EXPLORATION AND FUNCTIONALISATION OF PLASMA-EXFOLIATED GRAPHENE-BASED MATERIALS FOR ADVANCED APPLICATIONS

RACHEL LOUISE MCLAREN

A submission presented in partial fulfilment of the requirements of the University of South Wales / Prifysgol De Cymru for the degree of Doctor of Philosophy

This study was carried out in collaboration with Perpetuus Carbon Technologies

November 2021

Acknowledgements

The success and completion of this thesis would not have been possible without the guidance of my Director of Studies: Dr Gareth Owen. He has provided continual support over the past years and is an extremely hardworking individual who has dedicated vast amounts of time to myself and the rest of the research team. In addition, I am also grateful to Dr Christian Laycock, my supervisor, who has trained me to use the physisorption equipment and assisted in much of the surface area and porosity data interpretation, as well as pragmatics regarding instrument operation.

I would like to extend my sincere thanks to Dr David Morgan at Cardiff University who has carried out many XPS analyses and assisted in data interpretation. Furthermore, I am thankful to Dr Emmanuel Brousseau and Dr Greg Shaw from Cardiff University, who have conducted many AFM, Raman, TGA and XRD analyses over the course of the research. Moreover, Dr Uchechukwu Onwukwe, Dr Lorna Anguilano and Dr Ashley Howkins from Brunel University, have kindly conducted several SEM and TEM analyses, as well as hosting the SEM training course and providing continual support in relation to microscopy analysis.

I am additionally grateful the other members of my research team including Dr Rosenildo Costa, Dr Angelo Iannetelli and Dr Simon Thomas for their help and guidance, especially during early stages of the project. Furthermore, I would also like to express my gratitude to the rest of the research team and the USW Chemistry Department technicians who have always been willing to assist in providing necessary equipment and chemicals for research purposes.

I'd also like to recognise the KESS 2 programme and my company partner: Perpetuus Carbon Technologies who have financially supported this work and offered guidance throughout the course of the research. In particular, I would like to express my appreciation to the KESS 2 team at USW who have been especially welcoming and supportive throughout. In particular, Claire Naylor, an exceptionally hardworking individual who has worked closely with myself and Dr Gareth Owen regarding the pragmatics and progress of the PhD.

I would also like to express my deepest appreciation to my family and friends, particularly my mother and partner, who have continually provided support, especially during stressful times within the research.

Abstract

Graphitic materials describe those containing carbon within a honeycomb lattice structure and have attracted vast interest due to their novel and advantageous properties. Whilst large amounts of work have been conducted to investigate the nature of such materials, in the context of graphite, graphene and other carbon allotropes, there are still many voids in our understanding of these materials, extending to their structure, modification, characterisation, and application. Plasma-exfoliation offers a facile approach towards the large-scale synthesis of partially oxidised, multilayered stacks of graphitic layers. Within the scope of this thesis, plasma-exfoliated multilayer graphitic materials (NPs) are investigated in detail using a vast array of characterisation techniques to reveal information regarding their morphology, structure and elemental composition; including X-ray Photoelectron Spectroscopy (XPS), Raman spectroscopy, X-ray Diffraction (XRD), Scanning Electron Microscopy (SEM), Transmission Electron Microscopy (TEM), Atomic Force Microscopy (AFM), gas physisorption analysis, Nuclear Magnetic Resonance Spectroscopy (NMR), Fourier-Transform Infrared Spectroscopy (FT-IR), Thermogravimetric Analysis (TGA) and Energy-Dispersive X-ray (EDX) analysis. Various novel functionalisation strategies are also explored to covalently and non-covalently functionalise NPs.

Initially, an aryl boronic acid precursor is utilised as a radical source to provide a facile route towards the covalent functionalisation of NP. Such a methodology serves to identify safer aryl radical precursors as an alternative to commonly employed diazonium salt reagents, which are typically hazardous and undesirable for large-scale application. This functionalisation strategy enables the covalent attachment of 4-(trifluoromethyl)phenyl moieties to the edges of NP1 stacks. A percentage atomic composition (at.%) of 3.5 fluorine incorporation is revealed *via* XPS and Raman spectroscopy, TGA, FT-IR and EDX provide evidence of successful functionalisation. Brunauer-Emmett-Teller (BET), Barrett-Joyner-Halenda (BJH), SEM and TEM analyses are utilised to provide information relating to the surface area, porosity and morphological changes upon covalent addition. Furthermore, XRD is employed to assess the interlayer spacings and stacking types within the functionalised material and its precursor, revealing the presence of hexagonal and rhombohedral stacking, typical of those found within commercially derived graphene-based materials.

The thesis then moves towards investigating the porous structure of NPs in more detail. It is found that NP materials incorporate extensive slit pores between stacks of partially oxidised graphitic layers. These vary in size across the mesoporous and macroporous regions, where the average slit pore widths range between 6.3 – 10.4 nm. BJH data is utilised to provide an estimation of these slit pore widths within a model NP2 material, which are subsequently correlated with the distance between stacks. Slit pores between 2 to 131.2 nm in size are identified and thus, BJH analysis is shown to be a straightforward technique to offer an insight to the stack separations. This analysis coincides with data obtained using SEM, AFM and XRD techniques. Furthermore, the investigation also explores the surface area and porosity changes of NP material upon oxidation. Upon treatment of NP3 *via* the modified Hummers' method, the material suffers a substantial reduction in the BET surface area and porosity, due to the blockage and destruction of slit pores. As such, a novel pillaring strategy utilising the synthetic clay, laponite, as a pillaring device, enables the introduction of slit pores into the oxidised material. This enhances its surface area almost four-fold. The subsequent pillared material is explored utilising a range of characterisation methods, including solid-state NMR and XPS.

Finally, NP4 is non-covalently functionalised with polyelectrolyte and fluorosurfactant moieties to reveal its application within membrane technology. The subsequent composite material exhibits oleophobic properties and is used to synthesise free-standing films and to coat upon various substrates, including Kevlar, carbon fibre, glass fibre, nylon, and stainless-steel mesh. These materials found success in their ability to enable oil/water separation, thus granting them simultaneous oleophobic/hydrophilic properties. The composite structure, free-standing films and coated substrates are comprehensively investigated using various analytical and spectroscopic techniques, whilst contact angle measurements and sliding angle measurements provide evidence of oleophobic behaviour. High oil contact angles of up to 126.4° are obtained. SEM images reveal an interesting porous structure, which provides passage for water through the materials. The applications of the coated substrates are also investigated. It is found that coated carbon fibre can be used as a net to isolate oil from the surface of water, thus, granting it potential in the context of oil-spill clean-up. Meanwhile, coated nylon has properties which lend to its application as a membrane material which enables the passive removal of water from aircraft propellant tanks.

Whilst investigating the structures of NP, as well as exploring modification strategies and applications, many obstacles were encountered during the research. These typically related to the characterisation and processing of the materials. These issues are therefore also reviewed

and discussed in the context of the literature, providing an insight into some of the difficulties researchers may encounter whilst working with NPs and analogues materials. As such, the scope of this thesis provides various novel insights to enhance the understanding of NP materials and their modification.

Statement of Research Objectives

1. Understand the morphology, structure, surface area and porosity of plasma-exfoliated graphitic material
2. Investigate novel methodologies to functionalise plasma-exfoliated graphitic material
3. Investigate advanced applications of plasma-exfoliated graphitic material

Published and Presented Work

Publication Title/ Citation	Status	Chapter
Challenges Related to the Characterisation of Graphene-Based Materials Within Industry and Academia	Preparation of Manuscript	2
Boronic acids for functionalisation of commercial multi-layer graphitic material as an alternative to diazonium salts - R. L. McLaren, C. J. Laycock, D. J. Morgan and G. R. Owen, *New J. Chem.*, 2020, **44**, 19144–19154.	Accepted	4
Examining Slit Pore Widths within Plasma-Exfoliated Graphitic Material Utilising Barret-Joyner-Halenda Analysis - Rachel L. McLaren, Christian J. Laycock, Emmanuel Brousseau and Gareth R. Owen, *New J. Chem.*, 2021, **45**, 12071-12080.	Accepted	5
Laponite as a Pillaring Device to Enhance the Surface Area of Oxidised Plasma-Exfoliated Graphitic Material	Preparation of Manuscript	5
Oleophobic Composite Films Based on Multi-Layer Graphitic Scaffolding - Rachel L. McLaren, Rosenildo C. da Costa, Christian J. Laycock, David J. Morgan, Michael E. A. Warwick and Gareth R. Owen, *New J. Chem.*, 2021, **45**, 19210.	Accepted	6
Oleophobic Coated Composite Materials Based on Multi-Layer Graphitic Scaffolding for Application Within Aircraft Propellant Tanks and Oil-Spill Clean-Up	Submitted	6
Analysis Induced Reduction of a Polyelectrolyte Rachel L. McLaren, Gareth R. Owen and David J. Morgan, *Surfaces and Interfaces*.	Accepted	6

Conferences	Work presented	Year
RSC Coordination Chemistry Conference, University College Dublin, Dublin	Oral Presentation/ Poster Presentation- "*The Attachment of Poly-yne Compounds to Graphene*"	2018
Postgraduate Symposium, University of South Wales	Oral Presentation- "*The Functionalisation of Graphene Using Boronic Acid Radical Precursors*"	2018
MultiComp Spring Meeting, University of Aveiro, Portugal	Oral/ Poster Presentation- "*Plasma Synthesised Industrial Graphene*"	2019
MultiComp Autumn Meeting, University of Chemistry and Technology, Prague	Oral Presentation- "*The Functionalisation of Graphene Using Boronic Acid Radical Precursors*"	2019
Postgraduate Symposium, University of South Wales	3MT Presentation- "*Oleophobic/Hydrophilic Graphene-Based Membranes for Oil-Spill Clean-Up*"	2021

Outreach

A comic book sketch outlining the use of plasma-exfoliated graphitic material within membrane technology for oil-spill clean-up: https://multicomp-ca15107.eu/en/publications/ This comic book sketch was produced by Lottie Keene and Tony Keene as part of an initiative to inspire 10 year olds to explore the world of nanomaterials. This work involves a collaboration with MultiComp and CostAction.

Declaration

I declare that all the work in this thesis was carried out in accordance with the regulations of the University of South Wales. Unless indicated otherwise, all work is original and no part has been submitted for any other academic award. Any views expressed in this thesis are those of the author.

Table of Contents

Acknowledgements **i**

Abstract **ii**

Statement of Research Objectives **v**

Published and Presented Work **vi**

Outreach **vi**

Declaration **vii**

Table of Contents **viii**

Acronyms **xiii**

Figures **xvi**

Tables **xxxi**

Equations **xxxiii**

Schemes **xxxiv**

1 Introduction and Literature Review **1**

1.1 Introduction and Importance of Current Research 2

1.2 Introducing Graphene-Based Materials and Their Terminology 3

1.3 Single Layer Graphene 5

1.4 Stacked Forms of Graphene 7

1.5 Graphene Oxide and Reduced Graphene Oxide 8

1.6 Synthesis of Graphene-Based Materials 10

1.7 Introduction to Plasma and its Use in GBM Synthesis 15

1.8 Functionalisation and Modification of GBMs using Plasma 28

1.9 Functionalisation of GBMs without Plasma 37

1.10 Surface Area and Porosity in Plasma-Exfoliated Graphitic Material and Analogues 42

1.11 Applications of Plasma-Exfoliated Graphitic Materials and Other GBMs 45

2 Characterising Graphene-Based Materials **49**

2.1 Analysing Morphology using Microscopy 52

2.1.1 Scanning Electron Microscopy and Transmission Electron Microscopy 52

2.1.2 Atomic Force Microscopy 55

2.2 Analysing Graphitic Structure 58
2.2.1 Raman Spectroscopy 58
2.2.2 X-ray Diffraction 62
2.3 Elemental Composition Calculation 65
2.3.1 X-ray Photoelectron Spectroscopy 65
2.4 Thermal Decomposition Characteristics 69
2.4.1 Thermogravimetric Analysis 69
2.5 Bonding Analysis 71
2.5.1 Infrared Spectroscopy 71
2.5.2 Solution and Solid-State NMR 74
2.6 Surface Area and Porosity Analysis 77
2.6.1 Gas Physisorption 77
2.7 Additional Characterisation 81
2.7.1 Mass spectrometry 81
2.8 The Importance of Characterisation and the Challenges Associated with it 83
2.9 Analysed Area is Not Always Representative of the Sample as a Whole 84
2.10 Accurate Thickness Determination and Morphological Considerations 87
2.11 Elemental Composition Calculation 89
2.12 Inherent Challenges with Characterising Functionalised GBMs 90
2.13 Destructive and Non-Destructive Analysis 91

3 Materials and Methodology 96
3.1 Experimental 97
3.2 General Remarks 97
3.3 Characterisation of Materials Within this Thesis 98
3.3.1 Synthesis of Plasma-Exfoliated Graphitic Material 100
3.3.2 Synthesis of f-NP1 101
3.3.3 Control Reaction A- Reactivity of Radicals Generated from 4-(Trifluoromethyl)phenyl Boronic Acid in the Absence of NP1 101
3.3.4 Control Reaction 1- Synthesis of C1-NP1 102
3.3.5 Control Reaction 2- Synthesis of C2-NP1 102
3.3.6 Control Reaction 3- Synthesis of C3-NP1 102
3.3.7 Washing Procedure for f-NP1 and CX-NP (X = 1 – 3) 103

3.3.8 Characterisation of f-NP1 and CX-NP1 (X = 1 – 3) 103
3.3.9 Synthesis of O-NP3 103
3.3.10 Synthesis of Non-Covalent O-NP3/Laponite Composites 104
3.3.11 Synthesis of f-laponite 104
3.3.12 Synthesis of f-NP3 105
3.3.13 Synthesis of NP4-PP Composite 105
3.3.14 Preparation of NP4-PP Films 105
3.3.15 Preparation of NP4-PP Coated Substrates 106
3.3.16 Characterisation of NP4-PP Composite, NP4-PP Films and NP4-PP Coated Substrates 107

4 Boronic Acids for the Functionalisation of Plasma-Exfoliated Graphitic Material as an Alternative to Diazonium Salts 108
4.1 Synopsis 109
4.2 Results and Discussion 110
4.2.1 Mechanism of Radical Formation from Boronic Acid 110
4.2.2 Investigation into Control Reaction A 112
4.2.3 Characterisation of NP1 and f-NP1 and Various CX-NP1s 117
4.2.4 Elemental Analysis 118
4.2.4.1 XPS Analysis 118
4.2.4.2 SEM-EDX Analysis 126
4.2.5 Morphological Analysis using SEM/TEM 129
4.2.6 Graphitic Structure, Interlaying Spacings and Presence of Defects 133
4.2.6.1 Raman Spectroscopy 133
4.2.6.2 XRD 135
4.2.7 Bond Change Analysis by FT-IR 142
4.2.8 Surface Area and Porosity Studies using BET and BJH Measurements 143
4.2.9 Dispersibility in Common Solvents 146
4.2.10 Decomposition Characteristics using TGA 150
4.3 Conclusions 151

5 Exploring the Porous Structure and Pillaring of Plasma-Exfoliated Graphitic Material Using Laponite 153

5.1 Synopsis 154

5.2 Results and Discussion 154

5.2.1 Investigating the Surface Area and Porous Structure of Plasma-Exfoliated Graphitic Material 154

5.2.1.1 Surface Area and Morphological Analysis using BET and SEM 154

5.2.1.2 Graphitic Structure Analysis using Raman Spectroscopy 161

5.2.1.3 Investigating Pore Size Distribution using BJH Analysis 162

5.2.2 Application of BJH Data to Estimate the Distance Between Stacks in NPs 164

5.2.3 The Effect of Oxidation and Radical Functionalisation of Surface Area and Porosity 175

5.2.3.1 Investigating the Influence of Functionality on Surface Area and Porosity using XRD, BET, BJH, t-plot and XRD data 176

5.2.3.2 Graphitic Structure Analysis using Raman Spectroscopy 185

5.2.3.3 Thermal Decomposition Studies Using TGA 186

5.2.3.4 Investigating the Morphology using SEM 187

5.2.4 Laponite as a Pillaring Device to Enhance the Surface Area and Porosity of O-NP3 189

5.2.4.1 Introducing Laponite and its Surface Area and Porous Structure 189

5.2.4.2 Laponite as a Non-Covalent Pillaring Device 192

5.2.4.2.1 SEM Imaging of O-NP3/Laponite Non-Covalent Composites 195

5.2.4.2.2 Predicting the Structure of O-NP3/Laponite Composites 197

5.2.4.3 Laponite as a Covalent Pillaring Device 200

5.2.4.3.1 Attachment of Laponite to O-NP3 200

5.2.4.3.2 Characterisation 201

5.2.4.3.2.1 NMR Analysis 201

5.2.4.3.2.2 XPS Analysis 207

5.2.4.3.2.3 BET/BJH/t-Plot Analyses 213

5.2.4.3.2.4 FT-IR Analysis 217

5.2.4.3.2.5 SEM Analysis 219

5.2.4.3.3 Analysis of the Graphitic Structure of f-NP3 using Raman Spectroscopy 221

5.2.4.3.4 XRD Analysis 222

5.2.4.3.5 TGA 224

5.3 Conclusion 225

6 Development of Plasma-Exfoliated Graphitic Material-Based Oleophobic Hydrophilic Membranes for Advanced Applications 227

6.1 Synopsis 228

6.2 Introduction 228

6.3 Results and Discussion 233

6.3.1 NP4-PP Films and Coated Substrates 233

6.3.2 Chemical Composition of NP4-PP and Interactions Between Reagents using XPS 238

6.3.3 Investigating Oleophobic/Hydrophilic Behaviour 248

6.3.3.1 Testing of Water/Oil Passage Through NP4-PP Films and NP4-PP Coated Substrates 248

6.3.3.1.1 Silicone Oil/Water Passage Tests of NP4-PP Films 248

6.3.3.1.2 Silicone Oil/Water Passage Tests of NP4-PP Coated Substrates 252

6.3.3.2 Contact Angle Measurements 264

6.3.3.3 Sliding Angle Measurements 267

6.3.3.4 Comparison of NP4-PP Membranes with Existing Membrane Technology 268

6.3.4 Morphological Analysis 271

6.3.4.1 SEM analysis 271

6.3.4.2 AFM Analysis 281

6.3.5 Surface Area and Porosity Analysis 283

6.3.6 Bond Analysis using ATR-FT-IR 286

6.3.7 Graphitic Structure and Defects Analysis using Raman Spectroscopy 288

6.3.8 Stacking Orientation and Interlayer Spacing Analysis using XRD 289

6.3.9 Mechanism for Oleophobic/Hydrophilic Behaviour of NP4-PP Composite 290

6.3.10 Application of NP4-PP Coated Substrates 292

6.3.10.1 Application within Oil-Spill Clean-Up 292

6.3.10.2 Application within Aircraft Propellant Tanks 294

6.4 Conclusion 296

7 Conclusions and Future Work 298

References 303

Acronyms

Acronym	Terminology
Terminology Relating to Graphene Materials	
GBM	Graphene-based material
SLG	Single-layer graphene
2LG	Bilayer graphene
3LG	Trilayer graphene
FLG	Few-layer graphene
GO	Graphene oxide
rGO	Reduced graphene oxide
GBM	Graphene-based material
HOPG	Highly ordered pyrolytic graphite
CVD	Chemical vapour deposition
CNT	Carbon nanotube
Terminology Relating to Plasma-Exfoliated Graphitic Materials	
DBD	Dielectric barrier discharge
Perpetuus	Perpetuus Carbon Technologies LTD
NP	Plasma-exfoliated multilayer graphitic material/ nanoplate/ nanoplates
NP1	SDP 500 batch 1
NP2	SDP 150
NP3	SDP 500 batch 2
NP4	SDP 700
f-NP1	NP1 treated with 4-(trifluoromethyl)phenyl) boronic acid, $K_2S_2O_8$ and $AgNO_3$
C1-NP1	Control reaction 1. NP1 treated with 4-(trifluoromethyl)phenyl) boronic acid
C2-NP1	Control reaction 2. NP1 treated with $AgNO_3$
C3-NP1	Control reaction 3. NP1 treated with $K_2S_2O_8$
O-NP3	NP3 oxidised *via* the modified Hummers' method
f-laponite	Laponite treated with aminopropyltriethoxy silane (APTES)
f-NP3	O-NP3 treated with f-laponite in the presence of dicyclohexylcarbodiimide (DCC)
NP4-PP Composite	Composite containing NP4, PFO and PDDA
NP4-PP Thin Film	Thin film containing NP4-PP composite
NP4-PP Thin Film 2	Thinner film containing NP4-PP composite
NP4-PP Thick Film	Thick film containing NP4-PP composite
NP4-PP Coated Substrates	NP4-PP composite coated upon substrates
SW	Stone-Wales

Terminology Relating to Characterisation Methods	
XPS	X-ray photoelectron spectroscopy
UHV	Ultra-high vacuum
SEM	Scanning electron microscopy
SE	Secondary electron
BSE	Back scattered electron
FEG	Field emission gun
TEM	Transmission electron microscopy
HRTEM	High-resolution TEM
STM	Scanning tunnelling microscopy
AFM	Atomic force microscopy
PSPD	Position-sensitive photodetector
NMR	Nuclear magnetic resonance spectroscopy
CP-MAS	Cross-polarization magic angle spinning
HPDEC	High-power decoupled
ppm	Parts per million
XRF	X-ray fluorescence
BET	Brunauer-Emmett-Teller
BJH	Barrett-Joyner-Halenda
P/P_0	Relative pressure
HK	Horvath and Kawazoe
SF	Saito and Foley
MC	Monte Carlo
MD	Molecular dynamics
PSD	Pore size distribution
DFT	Density functional theory
IR	Infrared spectroscopy
FT-IR	Fourier-transform IR
ATR	Attenuated total reflection
EDX	Energy dispersive X-ray
XRD	X-ray diffraction
FWHM	Full width at half maximum
AB/2H stacking	Hexagonal stacking
ABC/3R stacking	Rhombohedral stacking
TGA	Thermogravimetric analysis
m/z	Mass-to-charge ratio
Terminology Relating to Reagents and Chemical Compounds	
AIBN	2,2’-azobisisobutyronitrile
APTES	Aminopropyltriethoxy silane
PPA	Polyphosphoric acid
P_2O_5	Phosphorus pentoxide
DCC	Dicyclohexylcarbodiimide
DCU	Dicyclohexylurea
DCM	Dichloromethane

MeOH	Methanol
$CDCl_3$	Deuterated chloroform
CD_3CN	Deuterated acetonitrile
IPA	Isopropyl alcohol
DMSO	Dimethyl sulfoxide
DMF	Dimethylformamide
NMP	N-methyl-pyrrolidone
GBL	gamma-butyrolactone
o-DCB	1,2-Dichlorobenzene
PDDA	Polydiallyldimethylammonium chloride
PFO	Perfluorooctanoate fluorosurfactant
Miscellaneous Terminology	
IUPAC	International Union of Pure and Applied Chemistry
ISO	The International Organisation for Standardisation
NPL	The National Physical Laboratory
RF	Radio frequency
DC	Direct current
at.%	Percentage atomic composition
wt.%	Weight percentage composition
sccm	Standard cubic centimetres per minute
Z	Atomic number
WCA	Water contact angle
OCA	Oil contact angle

Figures

Figure 1.1 Schematic representation of three sp^2 hybridised orbitals and an unhybridised $2p_z$ orbital present within each carbon atom in graphene. 5
Figure 1.2 The various stacking sequences between graphene layers within graphite and stacked forms of graphene including (a) AA stacking (b) hexagonal (AB/2H) stacking (c) rhombohedral (ABC/3R) stacking and (d) turbostratic stacking. 8
Figure 1.3 Common synthesis routes towards SLG and its stacked analogues. Green labels represent bottom-up methods and orange labels represent top-down methods. 11
Figure 1.4 A simplified representation of the stages within liquid-phase exfoliation of graphite. Cavitation bubbles and high-speed jets form due to ultrasonication and overcome the van der Waals forces between layers. This results in the formation of exfoliated stacks and individual layers, often comprising SLG, 2LG, 3LG and FLG. Ultracentrifugation eliminates un-exfoliated stacks and allows for an enhanced dispersion to form. Reprinted from reference [60]. 12
Figure 1.5 Schematic providing a simplified representation of the CVD growth steps to synthesise SLG film. (a) depicts the feeding of a hydrocarbon gas precursor into a heated chamber. Upon adsorption onto a metal substrate, pyrolysis of the gas occurs to form individual carbon atoms. These assemble onto the substrate to form graphene film shown in (b). Waste gases are subsequently removed by the exhaust system. 13
Figure 1.6 Schematic providing a simplified representation of the epitaxial growth of SLG. (a) depicts the structure of the SiC substrate and the desorbing of silicon from the surface of the substrate. (b) shows the formation of a graphene layer upon SiC. 14
Figure 1.7 Routes towards the oxidation of graphite, which are applicable to SLG and its staked forms. Reprinted from reference [88]. 15
Figure 1.8 Schematic representation of (a) a plasma consisting of charged particles moving in random directions and (b) the formation of plasma discharge between two electrodes. Reprinted from reference [89]. 16
Figure 1.9 Synthesis of exfoliated graphitic stacks including (a) instrument schematic comprising two graphite electrodes immersed in aqueous solution connected to a RF power supply and (b) the formation of plasma at the electrode. Reprinted from reference [112]. 19
Figure 1.10 (a) Photograph of DBD reactor utilised for the synthesis of NP and two NP products with trade names (b) SDP 150 and (c) SDP 500. 20
Figure 1.11 Schematic of (a) main components within the DBD reactor consisting of a central drum shown in more detail within (b) and with a rotated orientation in (c). 20
Figure 1.12 Formation of a Stone-Wales (SW) defect through the rotation of the π bond by 90° with respect to the midpoint. (a) shows the honeycomb lattice of graphene becoming rotated to form a Stone-Wales defect, as shown in (b). (c) and (e) show a sine-like Stone-Wales defect possessing a sine-like structure with a vertical displacement between the highest and lowest carbon atom of 1.4 Å. (d) and (f) show a cosine-like Stone-Wales defect

possessing a cosine-like structure with a vertical displacement between the highest and lowest carbon atom of 1.7 Å. Reprinted from reference [121]. 22
Figure 1.13 (a) and (b) SEM images at high and low magnifications respectively and (c) TEM image of partially oxidised graphitic stacks synthesised using plasma treatment. Reprinted from reference [93]. 22
Figure 1.14 Glow discharge formed within Haydales Ltd's plasma reactor (left) and a tunnelling electron microscopy image of an exfoliated NP. Reprinted from reference [131]. 24
Figure 1.15 (a) Apparatus to synthesis plasma exfoliated rGO consisting of a low voltage terminal (LVT) and a high voltage terminal (HVT). (b) depicts the expansion of the GO powders after treatment with the DBD plasma for 0 – 180 seconds and (c) discharge process. Reprinted from reference [135]. 25
Figure 1.16 Schematic representation of the exfoliation and reduction process experiences by GO during DBD plasma treatment. Reprinted from reference [135]. 25
Figure 1.17 Synthesis of FLG from graphite utilised H_2O_2 plasma etching. Reprinted from reference [136]. 26
Figure 1.18 Proposed three-stage mechanism for the synthesis of SLG, 2LG and 3LG during the exfoliation of graphite, consisting of (a) a schematic representation of the exfoliation mechanism (b) magnification of the laminar region of the plasma shown in (a) and (c) magnification of the turbulent region shown in (a). Reprinted from reference [138]. 28
Figure 1.19 (a) Proposed structure of SLG and 2LG treated with NH_3 plasma treatment consisting of various nitrogen functionalities (b) Raman spectra of NH_3 plasma treated 2LG on a Ni substrate after 0, 3, 6 and 9 minutes of exposure and (c) and (d) depict the evolution of the Raman G peak after 0, 3, 6 and 9 minutes of exposure, where the initial Fermi level lies in the conduction band and valence band respectively. Reprinted from reference [167]. 32
Figure 1.20 Proposed schematic of fluorinated CVD grown SLG. Reprinted from reference [179]. 35
Figure 1.21 Effect of DC bias voltage and treatment time on the C:Cl ratio (a) compares the DC bias to the Cl coverage using a constant treatment time of 300 seconds; (b) compares the treatment time to the Cl coverage using a constant DC bias (8 V) and (c) shows a map of the Cl coverage with changing DC bias and treatment time. Reprinted from reference [185]. 36
Figure 1.22 A side-view and top view of the proposed structures of a graphene layer before and after bromine plasma treatment. Reprinted from reference [188]. 37
Figure 1.23 (a) Nanoporous GBMs classified according to whether they possess in-plane pores, interlayered pores or 3D porous networks with broad applications of the materials and (b) applications associated with GBMs of varying pore sizes. Reprinted from reference [241]. 43
Figure 1.24 Various applications of GBMs. Reprinted from reference [275]. 46
Figure 1.25 SEM image of unreinforced cement mortar showing pores and voids (left) and reinforced cement mortar containing 0.5 wt.% of functionalised plasma exfoliated graphitic material possessing much smaller pores and voids. Reprinted from reference [137]. 47
Figure 2.1 Diagram outlining some of the key techniques used for GBM characterisation, categorised broadly as imaging, spectroscopic or analytical techniques. 50

Figure 2.2 (a) Schematic illustrating the various interactions resulting from electron beam irradiation onto a sample. (b), (c) and (d) outline the interaction of the incoming electron with the nuclei of an atom, resulting in the formation of a backscattered electron, a secondary electron and a secondary electron, an Auger electron and X-ray production respectively. Reprinted from reference [292]. 54
Figure 2.3 HRTEM images of various GBM samples corresponding to SLG, 2LG, 3LG and FLG containing 4 – 8 layers (left to right). Reprinted from reference [295]. 54
Figure 2.4 Schematic of TEM and SEM instruments outlining some of the main conponents. Reprinted from reference [290]. 55
Figure 2.5 (a) Diagram of AFM instrument schematic and (b) various modes of AFM operation including non-contact, tapping and contact mode with the respective distance between the cantilever and sample surface. (c) depicts a force-distance curve outlining how the attractive and repulsive regime combine to form a force response curve. 56
Figure 2.6 AFM image of a single layer of GO on a freshly cleaved mica substrate (scan area: 1 μm × 1 μm) (left) and corresponding height cross-sectional profile, acquired using tapping mode (right). The average thickness of the GO layer corresponds to 1.2 nm. Reprinted from reference [302]. 58
Figure 2.7 Energy-level diagram depicting several vibrational energy states and virtual energy states and transitions corresponding to infrared spectroscopy (IR), Rayleigh scattering, Raman Stokes scattering and Raman Anti-Stokes scattering. 59
Figure 2.8 Schematic of Raman spectrometer consisting of a laser (green beam) which is irradiated onto the sample through a cylindrical lens. When a spot is illuminated at the sample, the Raman-shifted light (red beam) is filtered out from the laser light by a dichroic mirror and dispersed along a vertical line on the two-dimensional CCD detector. Reprinted from reference [304]. 60
Figure 2.9 (a) The four components of the 2D band in 2LG at 514 and 633 nm and (b) Evolution of the 2D Raman band with increasing number of layers at (i) 514 nm and (ii) 633 nm. Reprinted from reference [312]. 62
Figure 2.10 The Bragg law for parallel planes depicting two incident X-ray beams becoming diffracted due to constructive interference. 64
Figure 2.11 XRD patterns of graphite, GO and FLG. 64
Figure 2.12 Diagram of the photoelectric effect. 65
Figure 2.13 Schematic of XPS emission processes including (a) photoelectron emission involving the emission of a photoelectron upon irradiation with photons and (b) Auger electron emission involving the emission of a photoelectron upon irradiation with photons, causing a vacancy to be produced and subsequent Auger electron emission as an electron fills this vacancy. 66
Figure 2.14 XPS instrument containing basic components including an UHV chamber, an X-ray source, a hemispherical energy analyser and a data acquisition system. Reprinted from reference [326]. 67
Figure 2.15 High-resolution XPS C 1s spectra of (a) graphite (b) GO prepared using a mixture of H_2SO_4, H_3PO_4, and HNO_3 (70:20:10) (c) GO prepared using a mixture of H_2SO_4, and H_3PO_4 (90:10) and (d) GO prepared using ultrasonic bath. Reprinted from reference [329]. 68
Figure 2.16 Schematic of TGA instrumentation and its basic components. 70
Figure 2.17 TGA plots in an air atmosphere for various (a) GO (b) FLG (Gr) and (c) graphite (Gft) samples. Reprinted from reference [333]. 70

Figure 2.18 Various modes of molecular vibration Reprinted from reference [334]. 72
Figure 2.19 Examples of IR methods including transmission and ATR modes. Reprinted from reference [338]. 73
Figure 2.20 IR spectra of (a) GO and (b) rGO. Reprinted from reference [339]. 73
Figure 2.21 Splitting of energy between alpha and beta states of nuclei containing spin upon application of an external magnetic field. 75
Figure 2.22 NMR instrument schematic. Reprinted from reference [341]. 76
Figure 2.23 Typical ^{13}C shifts within NMR spectroscopy. Reprinted from reference [342]. 76
Figure 2.24 The adsorption of gas adsorbate molecules on a solid's surface according to BET theory. Reprinted from reference [343]. 77
Figure 2.25 Gas physisorption analyser used to obtain adsorption-desorption data. Vacuum, calibration adsorbate, pressure gauge and valves are represented by VAC, CAL, ADS, P and V1 - V7, respectively. Reprinted from reference [353]. 79
Figure 2.26 N_2 adsorption-desorption isotherms at 77 K of two plasma-exfoliated FLG powders; the inset shows the differential pore size distributions derived by the quenched solid DFT method. Reprinted from reference [93]. 80
Figure 2.27 Basic components within a mass spectrometer. Reprinted from reference [359]. 82
Figure 2.28 m/z ratios vs relative abundance displayed as a mass spectrum (left) and within a table (right). Reprinted from reference [359]. 82
Figure 2.29 TEM analysis conducted on graphene flakes showing that flakes vary in morphology and lateral dimensions. Reprinted from reference [360]. 85
Figure 2.30 Depth of analysis profiles for various characterisation methods. Reprinted from reference [361] and modified from reference [362]. 85
Figure 2.31 (a) First and (b) second scanned topography images of graphene after 24 h. (c) Third and (d) fourth scanned topography images of graphene. Here, the arrows in (c) and (d) indicate the damage to the graphene surface over several repeat AFM scans, conducted using non-contact mode. Reprinted from reference [367]. 88
Figure 2.32 Suggested mechanism for adsorption of cationic and anionic contaminants onto date syrup-based graphene sand hybrid. Reprinted from reference [378]. 90
Figure 2.33 Mapping of the Raman G peak position after irradiation of 9.72 mC/cm^2 at 500 eV. The mapping in red (1573.6 cm^{-1}) and blue (1581.1 cm^{-1}) corresponds, respectively, to the red-shifted G peak (i.e., tensile strain) and the blue-shifted G peak (i.e., compressive strain) from the initial G peak position before irradiation (1577.3 cm^{-1}). Reprinted from reference [384] 94
Figure 4.1 Mass spectrum of the product of control reaction A consisting of a mixture of compound A and compound B 113
Figure 4.2 ^1H NMR spectrum of the product of control reaction A consisting of a mixture of compound A and compound B 114
Figure 4.3 ^{19}F NMR spectrum of the product of control reaction A consisting of a mixture of compound A and compound B 114
Figure 4.4 ^1H NMR spectrum of compound A. 115
Figure 4.5 ^{19}F NMR spectrum of compound A. 116
Figure 4.6 XPS survey spectra of; (a) NP1 and (b) f-NP1 118
Figure 4.7 Deconvoluted spectra of C 1s orbital; (a) NP1 and (b) f-NP1. 120
Figure 4.8 Deconvoluted spectra of O 1s orbital; (a) NP1 and (b) f-NP1. 121
Figure 4.9 XPS spectra of (a) F 1s and (b) Ag 3d $^5/_2$ orbital for f-NP1 at high resolution (deconvolution of the 3d peak indicates presence of Ag, Ag_2SO_4 and AgCl). 122

Figure 4.10 (a) Peak area integration of Ag 3d $^{5}/_{2}$ signal using OriginPro software and (b) Calculation of the % atomic composition of Ag_2SO_4 and AgCl/Ag through the integrated area of peaks. 123
Figure 4.11 SEM-EDX data for; (a) NP1 and (b) f-NP1. The origin of the K and M shells is explained within Chapter 2. 127
Figure 4.12 SEM images of NP1 at various magnifications including (a) 1.27 kx (b) 2.98 kx (c) 47.98 kx and (d) 115.30 kx. 130
Figure 4.13 TEM images of NP1. 130
Figure 4.14 SEM images of f-NP1 at various magnifications including (a) 1.93 kx (b) 29.50 kx (c) 45.30 kx (d) 50.90 kx (e) 50.0 kx (f) 81.7 kx (g) 94.86 kx and (h) 112.00 kx. 132
Figure 4.15 TEM images of f-NP1 flakes drop-casted onto a copper grid. 133
Figure 4.16 Raman spectra and respective I_D/I_G and I_{2D}/I_G ratios of (a) NP1 (b) f-NP1 (c) C1-NP1 (d) C2-NP1 and (e) C3-NP1. Peak deconvolution was performed using OriginPro software to discriminate the D and G bands from overlapping D^*, D'' and D' bands. 135
Figure 4.17 XRD patterns for NP1 and f-NP1 with increased magnification of the 2H (002) and 3R (003) planes and four-lined pattern associated with the 2H (100), 3R (101), 2H (101) and 3R (012) phases in the boxes on the right. An inset focused on the region 26.0° to 27.5° is shown on the main spectra. 137
Figure 4.18 The crystalline structure of graphite displaying the out of plane crystallite size, Lc and the in-plane crystallite size, La, as well as the interlayer spacing, d. 138
Figure 4.19 Gaussian and Lorentz fitting using OriginPro software for the overlapping (002) and (003) planes of the peak at $2\theta = 26.679$ for NP1 and f-NP1 shown in (a) and (b) respectively. Note: Within OriginPro the FWHM is denoted as "w" in degrees. 139
Figure 4.20 Gaussian fitting of the four-lined pattern associated with the 2H (100), 3R (101), 2H (101) and 3R (012) phases and the corresponding data, as provided by OriginPro software. 141
Figure 4.21 FT-IR-ATR spectra of NP1, f-NP1 and 4-(trifluoromethyl)phenyl boronic acid. 143
Figure 4.22 N2 adsorption-desorption isotherms for NP1, f-NP1and C3-NP1. 144
Figure 4.23 BJH adsorption data consisting of the average pore width vs dV/dlog(W) pore volume for NP1, f-NP1 and C3-NP1. 145
Figure 4.24 NP1 dispersed in solvents left to right: water, DMSO, acetonitrile, methanol, acetone, IPA, DCM, diethyl ether and hexane. A photograph of the dispersion is provided (a) instantly after sonication; (b) 1 hour after sonication; (c) 24 hours after sonication and (e) 2 weeks after sonication. 148
Figure 4.25 f-NP1 dispersed in solvents left to right: water, DMSO, acetonitrile, methanol, acetone, IPA, DCM, diethyl ether and hexane. A photograph of the dispersion is provided (a) instantly after sonication; (b) 1 hour after sonication; (c) 24 hours after sonication and (e) 2 weeks after sonication. 149
Figure 4.26 TGA curves for (a) NP1 and (b) f-NP1. 151
Figure 5.1 Stacks of NP material containing multiple graphene layers, defects, in-plane pores and oxygen functionality. Slit pores arise due to the presence of spacing between neighbouring stacks. 155
Figure 5.2 SEM images depicting pores within (a) NP2 at a magnification of 34.60 kx; (b) NP1 at a magnification of 20.67 kx; (c) f-NP1 at magnifications of (i) 81.7 kx (ii) 50.9 kx and (iii) 75.46 kx; (d) NP3 at a magnification of 51.96

kx and (e) NP4 at magnification of 10.39 kx. Green arrows and red arrows indicate the presence of slit pores and in-plane pores respectively. SEM images (a)(b)(d) and (e) were acquired on SEM 2, whilst SEM image (c) was acquired on SEM 1. 157
Figure 5.3 (a) N_2 adsorption-desorption isotherms typical of NPs incorporating their various features and the adsorption steps 1 - 3 and desorption corresponding to A1, A2, A3 and D respectively and (b) N_2 adsorption-desorption isotherms for various NP with the inset showing a magnified image of the contact closure point. 158
Figure 5.4 A graphical representation of the filling and emptying of open-ended cylindrical slit pores by nitrogen molecules inspired by the works of Ancilotto et al.[436] The diagram depicts how filling and emptying of slit pores proceeds as nitrogen pressure is increased (A1) - (A3) and decreased (D) respectively, and the incomplete filling occurs within relatively large slit pores found within NP materials. 160
Figure 5.5 Raman spectra of NP materials depicting their corresponding I_D/I_G and I_{2D}/I_G ratios. Peak deconvolution was performed using OriginPro software to discriminate the D and G bands from overlapping D^*, D'' and D' bands. 162
Figure 5.6 BJH adsorption data associated with the incremental pore volume for various NPs. 164
Figure 5.7 Morphology of NP2 shown by SEM images at a magnification of 34.60 kx, shown without (a) and with (b) a Sorbel filter. (c) depicts the presence of multiple aggregated stacks and (d) shows a magnified region of (c), indicating the presence of multiple graphitic layers within each stack and showing that the spacing between the stacks equates to the width, w, of the slit pore. SEM images were acquired on SEM 2. 166
Figure 5.8 SEM images of NP2 at magnifications of (a) 254,870 x and (b) 398,550 x with scale bars corresponding to 4.96 and 5.29 nm respectively acquired on SEM 3, and (c) TEM image of NP2 at a magnification of 50,000 x with a scale bar corresponding to 10 nm acquired on TEM 2. These images reveal an absence of any in-plane pores of 2 nm or larger in size, thus, suggesting that pores within the mesoporous and macroporous region primarily relate to slit pores. 167
Figure 5.9 SEM images outlining the width of slit pores found within NP2, which relate to the distance between the neighbouring stacks. Magnifications correspond to (a) 34.60 kx (b) 24.26 kx (c) 35.09 kx (d) 34.60 kx (e) 26.63 kx (f) 34.42 kx and (g) 20.60 kx and images were acquired on SEM 2. 168
Figure 5.10 SEM images of NP2 at magnifications of (a) 1.04 kx (b) 1.73 kx and (c) 4.15 kx acquired on SEM 2 170
Figure 5.11 TEM images of NP2 acquired on TEM 2. 170
Figure 5.12 AFM data acquired for NP2 using a mica substrate and non-contact mode, consisting of AFM images (a), (b) and (c). (d) depicts a representation of how the AFM tip scans over one stack, to the stack directly beneath during operation and (e) depicts line profiles acquired across the six marked regions of the AFM image (c), defined as line profiles 1 – 6. 171
Figure 5.13 XRD pattern for NP2 in the range between $2\Theta = 10°$ and 80° and expanded section in the range between $2\Theta = 40°$ and 50°. The pattern is labelled with the 2H and 3R planes. 172
Figure 5.14 Gaussian and Lorentz fitting using OriginPro software for the (002) plane of the peak at $2\theta = 26.611°$ for NP2. 173

Figure 5.15 SEM-EDX spectrum and quantitative data for NP2. 175
Figure 5.16 XPS spectra of NP3 including (a) survey spectrum (b) deconvoluted C 1s orbital and (c) deconvoluted O 1s orbital. 177
Figure 5.17 XPS spectra of O-NP3 including (a) survey spectrum (b) deconvoluted C 1s orbital (c) deconvoluted O 1s orbital (d) Si 2p orbital and (e) S 2p orbital. 178
Figure 5.18 A proposed diagram depicting the accessibility of (a) slit pores and (b) in-plane pores to nitrogen adsorbate molecules (represented by blue spheres) dependent on whether 4-(trifluoromethyl)phenyl) moieties and additional oxygen functionality are present. (a) depicts an accessible slit pore to adsorbate within NP1 (left) and an inaccessible slit pore to adsorbate within f-NP1 (right), whilst (b) depicts an accessible in-plane pore to adsorbate within NP1 (left) and an inaccessible in-plane pore to adsorbate within f-NP1 (right). Note: The diagram is not drawn to scale. 180
Figure 5.19 (a) N_2 adsorption-desorption isotherms and (b) BJH adsorption data associated with the incremental pore volume for NP1, f-NP1, C3-NP1, NP3 and O-NP3. 182
Figure 5.20 XRD patterns for NP3 and O-NP3 with peak assignment relating to the widened interlayer spacings due to oxidised regions within O-NP3, as well as the 2H and 3R phases. 184
Figure 5.21 A proposed diagram depicting the accessibility of (a) slit pores and (b) in-plane pores to nitrogen adsorbate molecules (represented by blue spheres) dependent on whether additional oxygen functionality is present. (a) depicts an accessible slit pore to adsorbate within NP3 (left) and many inaccessible slit pores to adsorbate within O-NP3 (right). O-NP3 also contains some newly formed slit pores due to the enlargement of interlayer spacings. (b) depicts an accessible in-plane pore to adsorbate within NP3 (left) and an inaccessible in-plane pore to adsorbate within O-NP3 (right). Note: The diagram is not drawn to scale. 184
Figure 5.22 Raman spectra of NP3 and O-NP3 depicting their corresponding I_D/I_G and I_{2D}/I_G ratios. Peak deconvolution was performed using OriginPro software to discriminate the D and G bands from overlapping D^*, D'' and D' bands. 186
Figure 5.23 TGA curves for NP3 and O-NP3. 187
Figure 5.24 SEM images of NP3 at magnifications of (a) 106 x (b) 415 x (c) 2.07 kx and (d) 20.71 kx acquired on SEM 2. 188
Figure 5.25 SEM images of O-NP3 at magnifications of (a) 106 x (b) 415 x (c) 2.08 kx and (d) 20.76 kx acquired on SEM 2. 188
Figure 5.26 Schematic depicting the structure of a laponite unit cell, adapted from previous works[469]. The stacking of individual laponite disks results in the formation of tactoids, which cluster to form aggregates. 190
Figure 5.27 (a) N_2 adsorption-desorption isotherm and (b) BJH adsorption data associated with the incremental pore volume for laponite, where the inset provides a magnified region of pore widths between 1.7 and 20 nm. 191
Figure 5.28 (a) N_2 adsorption-desorption isotherms and (b) BJH adsorption data associated with the incremental pore volume for O-NP3, laponite, controls, and O-NP3/laponite composites containing 6 wt.%, 11 wt.% and 20 wt.% laponite addition. 194
Figure 5.29 SEM images of (a) O-NP3 (b) O-NP3 control (c) laponite (d) laponite control and O-NP3/laponite composites consisting of (e) 6 wt.% laponite (f) 11 wt.% laponite and (g) 20 wt.% laponite with magnifications of (i) 208 x

(106 x for O-NP3) (ii) 415 x (iii) 2.08 kx and (iv) 20.76 kx acquired on SEM 2. 196
Figure 5.30 A proposed mechanism for the synthesis of the idealised pillaring structure; (d) and proposed structure based on experimental evidence; (e) associated with O-NP3/laponite composites. (a) depicts the structure of laponite within slit pores of O-NP3 and (c) depicts the entry of laponite into slit pores within aqueous media, resulting in widening of slit pores through the formation of a "house-of-cards" structure (shown within the inset (b)). Blue spheres represent nitrogen adsorbate molecules. 199
Figure 5.31 NMR studies including solution state spectra; (a) ^{1}H (b) ^{13}C and (c) ^{29}Si for APTES, and solid-state spectra; (d) ^{29}Si for laponite (e) ^{29}Si for f-laponite (f) ^{13}C for f-laponite (g) ^{13}C for O-NP3 (h) ^{13}C for f-NP3 and (i) ^{29}Si for f-NP3. ^{1}H and ^{13}C environments on APTES are annotated on (a), (b), (f) and (h), whilst the T and Q ^{29}Si environments are depicted on (d), (e) and (i). Peaks relating to sodium acetate impurity on (f) are assigned with an *. 204
Figure 5.32 The assignment of silanes with various denotations, where Q represents a silicon atom bonded to four oxygen atoms and T represents a silicon atom bonded to three oxygen atoms. The superscript integer represents the number of oxygen atoms bonded to a further silicon atom and R represents a variable group[485,486]. 204
Figure 5.33 Structure and magnified regions of (a) laponite depicting the Q^2 and Q^3 environments (highlighted by red and green circles respectively) and (b) f-laponite depicting Q^2, Q^3, T^2 and T^3 environments (highlighted by red, green, blue and purple circles respectively). Black spheres within the structure of f-laponite represent sodium acetate impurity and decomposed silica. 205
Figure 5.34 XPS spectra for laponite including (a) survey spectra (b) deconvoluted C 1s orbital (c) O 1s orbital (d) Si 2p orbital (e) Mg 2p orbital and (f) Na 1s orbital. 211
Figure 5.35 XPS spectra of f-laponite including (a) survey spectra (b) C 1s orbital (c) O 1s orbital (Note: the peak at 536.0 eV within the O 1s spectra of f-laponite relates to the Na Auger peak) (d) N 1s orbital (e) Na 1s orbital (f) Mg 2p orbital and (g) Si 2p orbital. 212
Figure 5.36 XPS analysis of f-NP3 including (a) survey spectra (b) deconvoluted C 1s orbital (c) deconvoluted O 1s orbital (d) N 1s orbital (e) Na 1s orbital (f) Mg 2p orbital and (g) Si 2p orbital. 213
Figure 5.37 (a) N_2 adsorption-desorption isotherms and (b) BJH adsorption data associated with the incremental pore volume for O-NP3, laponite, f-laponite and f-NP3. 215
Figure 5.38 Diagram outlining the blockage of pores within a f-laponite cluster due to functionalisation around the edges of the laponite disks, as well as the presence of sodium acetate within the pores. Nitrogen adsorbate molecules are shown by the diatomic blue spheres, and these are unable to access pores within the laponite cluster. 216
Figure 5.39 Proposed diagram depicting the pillaring effect within f-NP3. f-laponite is bonded to O-NP3 through an amide linkage and the pillared structure allows nitrogen adsorbate molecules (each nitrogen atom is denoted as a blue sphere) to access slit pores. A side on view of the pillared structure is provided within the inset. Note: the diagram is not drawn to scale. 217

Figure 5.40 FT-IR spectra of (a) NP3 (b) O-NP3 (c) laponite (d) APTES (e) f-laponite and (f) f-NP3 using KBr transmission method analyses for all NP3 containing samples, and the ATR method for APTES, laponite and f-laponite analyses. 219
Figure 5.41 SEM images of f-laponite at magnifications of (a) 208 x (b) 415 x (c) 2.08 kx and (d) 20.76 kx acquired on SEM 2. 220
Figure 5.42 SEM images of f-NP3 at magnifications of (a) 208 x (b) 415 x (c) 2.08 kx and (d) 20.76 kx acquired on SEM 2. 221
Figure 5.43 Raman spectra of NP3, O-NP3 and f-NP3 depicting their corresponding I_D/I_G and I_{2D}/I_G ratios. Peak deconvolution was performed using OriginPro software to discriminate the D and G bands from overlapping D^*, D'' and D' bands. 222
Figure 5.44 XRD patterns of NP3, O-NP3 and f-NP3. 223
Figure 5.45 TGA curves for NP3, O-NP3, laponite, f-laponite and f-NP3. 225
Figure 6.1 (a) A glass slide coated with PDDA/PFO/SiO_2 and treated with oxygen plasma to introduce hydrophilic polar groups to the surface to enhance favourable interaction with water and unfavourable interaction with hexadecane; (b) deposition of hexadecane on the surface causing the droplet to roll off easily; (c) deposition of water on the surface causing droplets to wet the surface rapidly; (d) the deposition of hexadecane upon the water-wetted surface causing droplets to roll off easily. Reprinted from reference [525]. 230
Figure 6.2 Schematic depicting the synthesis of NP4-PP thick film and NP4-PP thin film. The processes involved the redispersion of different concentrations of NP4-PP composite in methanol (1.75 g per 35 mL methanol and 0.80 g per 35 mL methanol for NP4-PP thick film and NP4-PP thin film respectively). The dispersions were subsequently poured into each section of an eight-sectioned metal tray. Through solvent evaporation overnight in air, free-standing films were fabricated. 235
Figure 6.3 SEM images showing the thickness of three edge regions of (a) NP4-PP thick film and (b) NP4-PP thin film at magnifications of 152 x and 198 x respectively. 236
Figure 6.4 Photographs of NP4-PP thick film (above) and NP4-PP thin film (below), illustrating the ability of the films to be bent with tweezers. NP4-PP thick film snapped easily as it was bent, whereas NP4-PP thin film could be bent repeatedly with no visible damage to the film. 236
Figure 6.5 Schematic depicting the synthesis of NP4-PP coated substrates. The process involved redispersion of 2.5 g NP4-PP composite in 150 mL methanol, followed by pouring of the dispersion over substrates: Kevlar, carbon fibre, glass fibre, nylon and stainless-steel mesh deposited within a single-sectioned metal tray. Solvent evaporation in air overnight resulted in a coating of NP4-PP over the substrates. In addition, nylon was also coated using the same methodology using less concentrated dispersions including 0.26 g NP4-PP composite in 150 mL MeOH and 0.16 g NP4-PP composite in 150 mL MeOH (referred to as coated nylon 2 and coated nylon 3 respectively). 237
Figure 6.6 XPS analysis of NP4 including (a) survey spectrum and high-resolution spectra of the (b) deconvoluted C 1s orbital (c) deconvoluted O 1s orbital and (d) N 1s orbital. 239

Figure 6.7 ^{13}C NMR spectrum of PDDA showing the presence of alkene peaks at 128.64 and 123.93 ppm. 240
Figure 6.8 XPS analysis of PDDA including (a) survey spectrum and high-resolution spectra of the (b) deconvoluted C 1s orbital (c) deconvoluted N 1s orbital (initial scan) (d) deconvoluted N 1s orbital (acquired 420 seconds after initial scan) (e) Na 1s orbital (f) deconvoluted Cl 2p orbital (g) deconvoluted O 1s orbital and (h) deconvoluted S 2p orbital. 242
Figure 6.9 XPS spectra of PDDA/NP4 including (a) survey spectrum and high-resolution spectra of the (b) deconvoluted C 1s orbital (c) deconvoluted O 1s orbital (d) deconvoluted N 1s orbital (e) Na 1s orbital (f) deconvoluted Cl 2p orbital and (g) deconvoluted F 1s orbital. 244
Figure 6.10 XPS analysis of PFO including (a) survey spectrum and high-resolution spectra of the (b) deconvoluted C 1s orbital (c) deconvoluted F 1s orbital (d) deconvoluted O 1s orbital and (e) Na 1s orbital. 245
Figure 6.11 XPS analysis of NP4-PP including (a) survey spectrum and high-resolution spectra of the (b) deconvoluted C 1s orbital (c) deconvoluted Cl 2p orbital (d) Na 1s orbital (e) deconvoluted N 1s orbital (f) O 1s orbital (g) deconvoluted F 1s orbital. 247
Figure 6.12 Silicone oil/water passage tests on NP4-PP thick film. (a) depicts the set-up of NP4-PP thick film on a beaker, beneath a burette filled with water and silicone oil. (b) shows the deposition of water on the film, resulting in formation of a droplet on the film instantaneously after deposition, and wetting of the film after approximately 20 seconds after deposition; (c). (d) depicts the addition of silicone oil showing that a droplet formed on the film with no occurrence of wetting. This droplet could easily be removed at any stage after its deposition by tilting the material, as shown in (e), and remained on top for at least 3 weeks. 249
Figure 6.13 Silicone oil/water passage tests on NP4-PP thin film. (a) depicts the set-up of NP4-PP thin film on a beaker, beneath a burette filled with water and silicone oil. (b) shows the deposition of water on the film, resulting in formation of a droplet on the film instantaneously after deposition, and wetting the film after approximately 20 seconds after deposition; (c). (d)(i)-(vii) depict the passage of water through the film after 2.5 hours after its deposition, showing that a droplet forms on the bottom of the film and is subsequently released into the beaker. (d) shows the deposition of silicone oil showing that a droplet formed on the film with no occurrence of wetting. This droplet could easily be removed at any stage after its deposition by tilting the material, as shown in (f), and remained on top for at least 3 weeks. 250
Figure 6.14 SEM image of NP4-PP thin film 2 showing the thickness of three edge regions of the film at a magnification of 787 x. 251
Figure 6.15 Water and silicone oil passage through each of the uncoated substrates including (a) Kevlar (b) carbon fibre (c) glass fibre (d) nylon and (e) stainless-steel mesh. 1 mL of each liquid was deposited on the surface of the substrate. It was observed that both liquids penetrated all materials instantaneously. 252
Figure 6.16 Silicone oil/water passage tests on NP4-PP coated Kevlar. (a) depicts the set-up of the coated substrate on a beaker, beneath a burette filled with water and silicone oil. (b) shows the deposition of water onto the coated substrate, resulting in wetting and subsequent penetration of 5 mL water

through the coated substrate and into the beaker after 10 seconds of its deposition. (c) shows the presence of a silicone oil droplet on the surface of the coated substrate, which undergoes no visible wetting or penetration of the coated substrate after at least 3 weeks, and (d) shows that the silicone oil can easily be poured off the coated substrate by tilting. 254
Figure 6.17 Silicone oil/water passage tests on NP4-PP coated Kevlar after washing with acetone and water to remove residual silicone oil. The tests displayed identical findings to that of the analogous unwashed coated substrate. (a) depicts the set-up of the coated substrate on a beaker, beneath a burette filled with water and silicone oil. (b) shows the deposition of water onto the coated substrate, resulting in wetting and subsequent penetration of 5 mL water through the coated substrate and into the beaker after 10 seconds of its deposition. (c) shows the presence of a silicone oil droplet on the surface of the coated substrate, which undergoes no visible wetting or penetration of the coated substrate after at least 3 weeks, and (d) shows that the silicone oil can easily be poured off the coated substrate by tilting. 254
Figure 6.18 Silicone oil/water passage tests on NP4-PP coated carbon fibre. (a) depicts the set-up of the coated substrate on a beaker, beneath a burette filled with water and silicone oil. (b) shows the deposition of water onto the coated substrate, resulting in wetting and subsequent penetration of 5 mL water through the coated substrate and into the beaker after 5 seconds of its deposition. (c) shows the presence of a silicone oil droplet on the surface of the coated substrate, which undergoes no visible wetting or penetration of the coated substrate after at least 3 weeks, and (d) shows that the silicone oil can easily be poured off the coated substrate by tilting. 255
Figure 6.19 Silicone oil/water passage tests on NP4-PP coated carbon fibre after washing with acetone and water to remove residual silicone oil. The tests displayed identical findings to that of the analogous unwashed coated substrate. (a) depicts the set-up of the coated substrate on a beaker, beneath a burette filled with water and silicone oil. (b) shows the deposition of water onto the coated substrate, resulting in wetting and subsequent penetration of 5 mL water through the coated substrate and into the beaker after 5 seconds of its deposition. (c) shows the presence of a silicone oil droplet on the surface of the coated substrate, which undergoes no visible wetting or penetration of the coated substrate after at least 3 weeks, and (d) shows that the silicone oil can easily be poured off the coated substrate by tilting. 255
Figure 6.20 Silicone oil/water passage tests on NP4-PP coated glass fibre. (a) depicts the set-up of the coated substrate on a beaker, beneath a burette filled with water and silicone oil. (b) shows the deposition of water onto the coated substrate, resulting in wetting and subsequent penetration of 5 mL water through the coated substrate and into the beaker after 5 seconds of its deposition. (c) shows the presence of a silicone oil droplet on the surface of the coated substrate, which undergoes no visible wetting or penetration of the coated substrate for up to 2 hours, and (d) shows that the silicone oil can easily be poured off the coated substrate by tilting, up to 2 hours after its deposition. (e) shows the penetration of silicone oil through the coated substrate after 2 hours. 256
Figure 6.21 Silicone oil/water passage tests on NP4-PP coated glass fibre after washing with acetone and water to remove residual silicone oil. The tests displayed

different findings to that of the analogous unwashed coated substrate. (a) depicts the set-up of the coated substrate on a beaker, beneath a burette filled with water and silicone oil. (b) shows the deposition of water onto the coated substrate, resulting in wetting and subsequent penetration of 5 mL water through the coated substrate and into the beaker after 5 seconds of its deposition. (c) shows the presence of a silicone oil droplet on the surface of the coated substrate, which undergoes no visible wetting or penetration of the coated substrate after at least 3 weeks, and (d) shows that the silicone oil can easily be poured off the coated substrate by tilting. 256

Figure 6.22 Silicone oil/water passage tests on NP4-PP coated nylon. (a) depicts the set-up of the coated substrate on a beaker, beneath a burette filled with water and silicone oil. (b) shows the deposition of water onto the coated substrate, resulting in wetting of the substrate but no penetration for up to 3 weeks (c) shows the presence of a silicone oil droplet on the surface of the coated substrate, which undergoes no visible wetting or penetration of the coated substrate after at least 3 weeks. 257

Figure 6.23 Silicone oil/water passage tests on NP4-PP coated nylon 3 (0.26 g per 150 mL MeOH) (a) depicts the set-up of the coated substrate on a beaker, beneath a burette filled with water and silicone oil. (b) shows the deposition of 5 mL water onto the coated substrate, resulting in instantaneous penetration through the coated substrate after its deposition. (c) shows the presence of a silicone oil droplet on the surface of the coated substrate, which undergoes no visible wetting or penetration of the coated substrate after at least 3 weeks, and (d) shows that subsequent water droplets penetrate through the silicone oil droplet and coated substrate. 258

Figure 6.24 Silicone oil/water passage tests on NP4-PP coated nylon 3 (0.26 g per 150 mL MeOH) after washing with acetone and water to remove residual silicone oil. The tests displayed identical findings to that of the analogous unwashed coated substrate. (a) depicts the partially washed away coating upon the substrate after acetone washes. (b) depicts the set-up of the coated substrate on a beaker, beneath a burette filled with water and silicone oil. (c) shows the deposition of 5 mL water onto the coated substrate, resulting in instantaneous penetration through the coated substrate after its deposition. (d) shows the presence of a silicone oil droplet on the surface of the coated substrate, which undergoes no visible wetting or penetration of the coated substrate after at least 3 weeks, and (e) shows that the silicone oil can easily be poured off the coated substrate by tilting. 258

Figure 6.25 Silicone oil/water passage tests on NP4-PP coated nylon 2 (0.16 g per 150 mL MeOH) (a) depicts the set-up of the coated substrate on a beaker, beneath a burette filled with water and silicone oil. (b) shows the deposition of 5 mL water onto the coated substrate, resulting in instantaneous penetration through the coated substrate after its deposition and (c) shows the presence of a silicone oil droplet on the surface of the coated substrate, which undergoes no visible wetting or penetration of the coated substrate after at least 3 weeks. 259

Figure 6.26 Silicone oil/water passage tests on NP4-PP coated nylon 2 (0.16 g per 150 mL MeOH) after washing with acetone and water to remove residual silicone oil. The tests displayed identical findings to that of the analogous unwashed coated substrate. (a) depicts the partially washed away coating upon the substrate after acetone washes. (b) depicts the set-up of the coated

substrate on a beaker, beneath a burette filled with water and silicone oil. (c) shows the deposition of 5 mL water onto the coated substrate, resulting in instantaneous penetration through the coated substrate after its deposition. (d) shows the presence of a silicone oil droplet on the surface of the coated substrate, which undergoes no visible wetting or penetration of the coated substrate after at least 3 weeks, and (e) shows that the silicone oil can easily be poured off the coated substrate by tilting. 259
Figure 6.27 oil/water passage tests on NP4-PP coated stainless-steel mesh. (a) depicts the set-up of the coated substrate on a beaker, beneath a burette filled with water and silicone oil. (b) shows the deposition of water onto the coated substrate, resulting in wetting and subsequent penetration of 5 mL water through the coated substrate and into the beaker after 5 minutes of its deposition. (c) shows the presence of a silicone oil droplet on the surface of the coated substrate, which undergoes no visible wetting or penetration of the coated substrate after at least 3 weeks, and (d) shows that the silicone oil can easily be poured off the coated substrate by tilting. 260
Figure 6.28 Silicone oil/water passage tests on NP4-PP coated stainless-steel mesh after washing with acetone and water to remove residual silicone oil. The tests displayed identical findings to that of the analogous unwashed coated substrate. (a) depicts the partially washed away coating upon the substrate after acetone washes. (b) depicts the set-up of the coated substrate on a beaker, beneath a burette filled with water and silicone oil. (c) shows the deposition of water onto the coated substrate, resulting in wetting and subsequent penetration of 5 mL water through the coated substrate and into the beaker after 5 minutes of its deposition. (d) shows the presence of a silicone oil droplet on the surface of the coated substrate, which undergoes no visible wetting or penetration of the coated substrate after at least 3 weeks, and (e) shows that the silicone oil can easily be poured off the coated substrate by tilting. 260
Figure 6.29 Diagram showing a simplified structure of NP4-PP composite and how it can be used to fabricate NP4-PP films and NP4-PP coated substrates. Blue and red arrows represent the passage of water and silicone oil onto the material and/or through the material. The time for water penetration is depicted below each material. This diagram refers to the results accompanying NP4-PP coated nylon 2 and 3. All materials, unless specified, prevented silicone oil passage for at least 3 weeks. 263
Figure 6.30 Sliding angle measurements conducted on an electronic goniometer. Materials were fixed to the goniometer with a small piece of tape (see photograph on the right). A droplet of silicone oil (approximately 0.05 mL) was deposited upon each material and the goniometer was lifted. When the droplet began to slide, the angle was recorded. The process was repeated five times for each material and an average sliding angle was recorded. 267
Figure 6.31 SEM image of NP4 at magnifications of (a) 415 x (b) 4.15 kx and (c) 20.74 kx. 271
Figure 6.32 SEM image of NP4-PP composite at magnifications of (a) 105 x (b) 415 x (c) 4.15 kx and (d) 20.76 kx. 272
Figure 6.33 SEM images of PDDA/PFO at magnifications of (a) 106 x (b) 415 x (c) 1.04 kx (d) 4.15 kx (e) 20.76 kx and (f) 34.60 kx. 273
Figure 6.34 SEM images of NP4-PP thick film at various magnifications including (a) 415 x and (b) 2.06 kx (c) 4.14 kx (d) 10.37 kx (e) 17.36 kx and (f) 34.71 kx. 274

Figure 6.35 SEM image of NP4-PP thin film at magnifications of (a) 414 x (b) 2.07 kx (c) 4.17 kx (d) 10.45 kx (e) 17.36 kx and (f) 34.56 kx. 274
Figure 6.36 SEM image of NP4-PP thin film at a magnification of 34.56 kx, depicting approximate dimensions in the form of diameters and areas (A). 275
Figure 6.37 SEM images obtained in wide field mode of NP4-PP coated (a) Kevlar (b) carbon fibre (c) glass fibre (d) nylon 3 and (e) stainless-steel mesh at magnifications of 20 x. 276
Figure 6.38 SEM images of (a) uncoated Kevlar at a magnification of 1.73 kx and coated Kevlar at magnifications of (b) 56 x (c) 589 x (d) 519 x (e) 10.38 kx and (f) 10.38 kx. 278
Figure 6.39 SEM images of (a) uncoated carbon fibre at a magnification of 1.38 kx and coated carbon fibre at magnifications of (b) 461 x (c) 2.08 kx (d) 830 kx (e) 4.15 kx and (f) 1.04 kx. 278
Figure 6.40 SEM images of (a) uncoated glass fibre at a magnification of 1.38 kx and coated glass fibre at magnifications of (b) 208 x (c) 1.38 kx (d) 1.38 kx (e) 4.15 kx and (f) 10.38 kx. 279
Figure 6.41 SEM images of (a) uncoated nylon at a magnification of 125 x and coated nylon 3 at magnifications of (b) 415 x (c) 10.38 kx (d) 10.39 kx (e) 20.75 kx and (f) 4.15 kx. 280
Figure 6.42 SEM images of (a) uncoated stainless-steel mesh at a magnification of 106 x and coated stainless-steel mesh at magnifications of (b) 208 x (c) 10.38 kx (d) 10.38 kx (e) 9.96 kx and (f) 692 x. 280
Figure 6.43 AFM images of NP4-PP thin film depicting: (a) a 10 by 10 μm AFM image of the surface of NP4-PP thin film, consisting of many aggregates; (b) a magnified image of (a) consisting of a 10 by 10 μm AFM image; (c) a magnified image of (b) consisting of a 2 by 2 μm AFM image of the surface of an aggregate; (d) a two-dimensional (2D) representation of image (b) containing line profiles 1 – 4, and corresponding plots (shown in (d)(i)), measured across four holes and (e) a two-dimensional representation of image (c) containing a line profile and its corresponding plot (shown in (e)(i)), measured across the surface of an aggregate. 282
Figure 6.44 BET curve for NP4, NP4-PP composite and NP4-PP thin film. 284
Figure 6.45 BJH incremental pore volume as a function of average pore width for NP4, NP4-PP composite and NP4-PP thin film 286
Figure 6.46 ATR-FT-IR spectra of PDDA, PFO and NP4-PP composite 287
Figure 6.47 Raman spectra of NP4 and NP4-PP composite with depicting their corresponding I_D/I_G and I_{2D}/I_G ratios. Peak deconvolution was performed using OriginPro software to discriminate the D and G bands from overlapping D^*, D'' and D' bands. 288
Figure 6.48 XRD patterns of NP4 and NP4-PP composite. 290
Figure 6.49 A proposed step-by-step process to remove oil from the surface of water in oceans, using an oleophobic/hydrophilic coated net to "mop up" the accumulated oil. 293
Figure 6.50 A step-by-step process implementing NP4-PP coated carbon fibre supported on a stainless-steel mesh to remove silicone oil from the surface of water. 293
Figure 6.51 Diagram outlining how a passive membrane allows the removal of water accumulation from the bottom of an aircraft propellant tank. 295

Figure 6.52 Apparatus used to replicate an aircraft propellant tank consisting of (a) a Whatman three-piece filter funnel and (b) NP4-PP coated nylon 3 which is sandwiched between two plates containing holes to replicate the membrane. 295
Figure 6.53 Apparatus to replicate an aircraft propellant tank, consisting of a Whatman three-piece filter funnel and NP4-PP coated nylon 3 sandwiched between two plates containing holes. (a) depicts the funnel filled with Jet A-1 fuel to resemble a propellant tank. 20 mL water was then added into the funnel and this water passed through the propellant and membrane within 30 seconds. The NP4-PP coated nylon 3 membrane therefore allows for the removal of water, whilst simultaneously retaining the Jet A-1 fuel. The Jet A-1 fuel was retained for at least 24 hours. (b) corresponds to a control experiment showing that Jet A-1 fuel penetrates uncoated nylon, and therefore passes freely through the apparatus and into the beaker, in the absence of NP4-PP coated nylon 3. 296

Tables

Table 1.1 Terminology associated with graphene-based materials according to definitions reported by ISO.[6] 4
Table 1.2 Comparison of the elemental compositions of FLG (MLGR) and HOPG samples treated at a different sample biases. Reprinted from reference [151]. 33
Table 1.3 Surface area and porosity data associated with plasma-exfoliated graphitic stacks. Reprinted from reference [93]. 44
Table 2.1 Destructive and non-destructive characterisation techniques. Some techniques may be non-destructive in nature, however, their preparation routes may introduce permanent change. 92
Table 4.1 XPS Quantitative data for NP1, f-NP1 and CX-NP1 (X = 1 – 3)*. 119
Table 4.2 Summary of parameters used within the Scherrer equation and Bragg equation. 138
Table 4.3 Calculations of Lc, La, Nc and $d_{(002)/(003)}$ for NP1 and f-NP1. 140
Table 4.4 BET and BJH adsorption data for NP1, f-NP1 and C3-NP1. 144
Table 5.1 BET surface area values for NPs. 158
Table 5.2 BET, BJH adsorption and t-plot data for NPs. 164
Table 5.3 Calculations of Lc, La, Nc and $d_{(002)/(003)}$ for NP2. 173
Table 5.4 XPS quantitative data for NP2. 174
Table 5.5 XPS Quantitative data for NP1, f-NP1, C3-NP1, NP3 and O-NP3. 177
Table 5.6 Data associated with BET, BJH adsorption and t-plot methods for NP-1, f-NP1, C3-NP1, NP3 and O-NP3. 179
Table 5.7 Data associated with BET, BJH adsorption and t-plot methods for O-NP3, laponite, controls and O-NP3/laponite composites containing 6 wt.%, 11 wt.% and 20 wt.% laponite addition. 194
Table 5.8 XPS quantitative element composition data for NP3, O-NP3, laponite, f-laponite and f-NP3. 208
Table 5.9 XPS quantitative element composition data for the C 1s orbital for NP3, O-NP3 and f-NP3. 208
Table 5.10 BET, BJH adsorption and t-plot data for O-NP3, laponite, f-laponite and f-NP3. 215
Table 6.1 XPS surface elemental composition data for NP4, PDDA, NP4/PDDA, PFO and NP4-PP composite. 238
Table 6.2 A summary of the silicone oil/water passage tests of various NP4-PP films and NP4-PP coated substrates. Washing procedures were conducted with water and acetone. 262
Table 6.3 Contact angle measurements for silicone oil, hexadecane and Jet A-1 fuel on NP4-PP film and NP4-PP coated substrates with subsequent photographs of the droplet. 266
Table 6.4 Surface tension of various liquids[566,567]. 267
Table 6.5 Sliding angle data for NP4-PP films and NP4-PP coated substrates using silicone oil. 268
Table 6.6 A comparison of the present membranes rate of water and oil passage with various gravity-based separation membrane technologies published within the literature. Note: In published examples, various membranes may have been tested, however, the most significant results are displayed here. 270
Table 6.7 BET and BJH data for NP4, NP4-PP composite and NP4-PP thin film. 285

Table 6.8 BJH and t-plot data for NP4, NP4-PP composite and NP4-PP thin film. 285

Equations

Equation 2.1 Hooke's Law. 57
Equation 2.2 Bragg Equation. 64
Equation 2.3 Calculation of binding energy of a photoelectron. 66
Equation 2.4 Electron ionisation of a molecule to form its corresponding radical cation. 81
Equation 4.1 Scherrer equation for out-plane crystallite size (K = 0.91). 138
Equation 4.2 Scherrer equation for in-plane crystallite size (K = 0.91). 138
Equation 4.3 Calculation for the number of graphene layers. 139

Schemes

Scheme 1.1 Oxygen plasma processing on a graphitic network to introduce oxygen in the form of (a) C–O and C–OH (b) C=O and (c) O–C=O. Modified from reference [120]. 30
Scheme 1.2 Formation of an aryl radical from a diazonium salt precursor and its subsequent covalent attachment to a graphene layer. R represents the presence of a variable group and X^- represents an appropriate counterion. 38
Scheme 1.3 Synthesis of 4-tert-butylphenyl functionalised graphene, synthesised via the intercalation and exfoliation of graphite with potassium ions to form a graphite intercalation compound. This compound then reacts with 4-tert-butylphenyldiazonium tetrafluoroborate to form the functionalised material. Reprinted from reference [194]. 39
Scheme 1.4 Functionalisation of graphitic material via the Friedel-Crafts acylation reaction with benzoic acid derivatives in the presence of polyphosphoric acid (PPA) and phosphorus pentoxide (P_2O_5). Reprinted from reference [220]. 41
Scheme 4.1 (a) Mechanism of aryl radical formation from 4-(trifluoromethyl)phenyl boronic acid in the presence of $K_2S_2O_8$ and $AgNO_3$ as proposed by Baran et al (Ref [387,388]) and (b) The proposed mechanism of reaction between generated 4-(trifuoromethyl)phenyl radicals with a graphitic layer of NP1 to afford covalent bond formation 111
Scheme 4.2 Control reaction A consisting of the reaction between 4-(trifluoromethyl)phenyl boronic acid with $K_2S_2O_8$ oxidant and $AgNO_3$ catalyst to form compounds A and B. 112
Scheme 4.3 Various reagent additions to NP1 corresponding to (a) f-NP1 synthesis (b) control reaction 1 (c) control reaction 2 and (d) control reaction 3 117
Scheme 4.4 Proposed mechanism of 4-(trifluoromethyl)phenyl boronic acid to diol-type structure on NP1. 122
Scheme 4.5 The hypothesised structures of (a) f-NP1 (b) C1-NP1 (c) C2-NP1 and (d) C3-NP1 synthesised from NP1. 125
Scheme 5.1 Modified Hummers' treatment of NP3 to form O-NP3. 176
Scheme 5.2 Schematic representation of the synthesis of f-laponite (i) and its attachment to O-NP3 (ii) to synthesise f-NP3. 201
Scheme 6.1 (a) Schematic of NP4-PP synthesis utilising a two-step approach consisting of (i) the addition of PDDA and NP4 resulting in adsorption of PDDA on NP4 and (ii) the addition of PFO to NP4/PDDA resulting in complexation of PDDA and PFO moieties within the NP4 material. PDDA reagent consists of three isomers, including the cis and trans isomers and an unsaturated species containing a pendent double bond, consistent with previous work.[541] A photograph of NP4-PP as an aqueous sludge is depicted within (b). 234
Scheme 6.2 The proposed reduction of PDDA resulting in the loss of a methyl radical and generation of an uncharged tertiary amine species. Methyl radicals may then undergo dimerisation, reaction with water or gain electrons, to form ethane, methane or hydroxide ions. 242

1 Introduction and Literature Review

1.1 Introduction and Importance of Current Research

This PhD project involves a collaboration between The University of South Wales and Perpetuus Carbon Technologies LTD (Perpetuus). The latter is a carbon nanomaterial manufacturing company based in South Wales, UK. The research within this thesis primarily focuses on the modification, manipulation, and application of plasma-exfoliated multilayer graphene-based material, also known as nano plates (NP). These NPs are manufactured by a patented technique involving a custom-made multielectrode dielectric barrier discharge (DBD) plasma reactor, which enables a top-down synthesis of raw graphite into exfoliated NP material. Further insight into this synthesis method is provided further on in the text.

Research into graphene and related materials is extensive over the globe, signifying the potential of such materials for a whole variety of applications. Unfortunately, there are still many voids in the understanding of these materials, within both an academic and industrial setting, leading to some significant hurdles relating to their utilisation in commercial products. Such voids relate to their synthesis, characterisation, functionalisation and application. Many of which are outlined within the beginning of this thesis. It is therefore essential that research continues to make progress within these areas, to help to speed up the process of graphene-based material (GBM) commercialisation. Within the current work, various NP materials are investigated with the aim to strengthen the understanding of their nature, as well as to develop novel functionalisation routes and to extend their application. As such, a plurality of characterisation methods are heavily employed throughout this work, to fully understand the characteristics and properties of such materials. An overview of some of the commonly utilised characterisation methods is provided within Chapter 2.

The experimental research enclosed is largely divided into three sections, corresponding to Chapters 4 – 6. Initially, a novel functionalisation strategy was investigated to covalently functionalise NP. The success of this strategy is explained in detail, and the subsequent functionalised material is fully characterised using a number of characterisation techniques. Within both an academic and industrial setting, it is increasingly important to develop new strategies to covalently and non-covalently functionalise the surface of GBMs, to tailor their properties and meet specific requirement for application. This research is outlined within Chapter 4 and published research can be accessed elsewhere.[1] Chapter 5 focuses on the surface area and porous structure associated with NPs. GBMs are renowned for their high surface areas

and interesting porous structures; however, plasma-derived NPs are yet to be analysed in such detail. Within this context, Barrett-Joyner-Halenda (BJH) and Scanning Electron Microscopy (SEM) techniques are applied for the first time to assess the size of slit pores within these materials, which in turn, allows for estimation of the distance between neighbouring graphitic stacks.[2] In addition, NPs were also investigated within the context of pillaring. Laponite was employed as a pillaring device to further manipulate the size of slit pores within a low surface area, oxidised, NP. This investigation is depicted within Chapter 5 and is paramount towards deepening the understanding of how NP surface area and porous structures can be manipulated. Chapter 6 comprises the synthesis of a novel NP/polyelectrolyte/fluorosurfactant-based composite, for the purpose of oil/water separation.[3] This composite was fabricated into free-standing films and coated upon various substrates to fabricate oleophobic/hydrophilic membranes. Two unique applications of such materials were investigated within the context of oil-spill clean-up and aircraft propellant tanks. The membranes showed outstanding potential to meet the requirements of these applications.

To begin, a brief overview of the structures, synthesis, functionalisation strategies and applications of single-layer graphene (SLG), stacked analogues and plasma derived NPs is provided. Some of the key literature within this field is examined to introduce and deliver a straightforward understanding of the present materials.

1.2 Introducing Graphene-Based Materials and Their Terminology

Carbon can exist in various allotropic forms. The most well-known include diamond, graphite and amorphous carbon, however, in more recent years, the list extends to graphene, carbon nanotubes (CNTs) and fullerenes. These have been well summarised within an article by Zboril.[4] Many allotropes of carbon comprise of a hexagonal array of carbon atoms, where each atom is bonded to three neighbouring atoms through σ bonding, leaving an unhybridised π orbital perpendicular to the plane. A single layer of this arrangement describes graphene, whilst an array of stacked layers, containing van der Waals forces between the layers, describes stacked forms of graphene. Moreover, this arrangement can also form spherical cage-like arrangements known as fullerenes, as well as scrolled formations, such as in the case of CNTs.[4]

In regard to terminology, compounds labelled as graphene typically consist of a broad spectrum of materials within the context of academia and industry. The rate at which the field of nanomaterials has grown and challenges associated with the characterisation of graphene have arisen (*vide infra*), have meant that the boundaries of what can be classified as "graphene" have become somewhat blurred. At present, the graphene market is dominated by a variety of forms including powder and dispersed forms of SLG, as well as stacked and functionalised forms including bilayer graphene (2LG), trilayer graphene (3LG), few layer graphene (FLG), NPs, graphite, graphite oxide, graphene oxide (GO), reduced graphene oxide (rGO), graphene nanoplatelets (GNPs) and their functionalised counterparts.[5] These have been defined by The International Organization for Standardization (ISO) in effort to provide widespread consistency across the emerging world-wide graphene industry and are broadly considered as GBMs within this work.[6] A handful of definitions are provided in Table 1.1. GBMs each display different properties and provide distinctive advantages for modification and application purposes, however, many academics and industrial researchers still employ terminology which is inconsistent with that of ISO.[7–9] With this in mind, the GBMs used within the current work; consisting of multiple-layered graphitic stacks with partially oxidised regions, are considered as nanoplates (NPs).[6]

Table 1.1 Terminology associated with graphene-based materials according to definitions reported by ISO.[6]

Terminology	Definition According to ISO[6]
Nanoplate (NP)	A nano-object with one external dimension in the nanoscale and the other two external dimensions significantly larger.
Graphene/Graphene Layer/ Single-Layer Graphene (SLG)	Single layer of carbon atoms with each atom bound to three neighbours in a honeycomb structure
Graphite	Allotropic form of the element carbon, consisting of graphene layers stacked parallel to each other in a three dimensional, crystalline, long-range order
Bilayer Graphene (2LG)	Two-dimensions material consisting of two well-defined stacked graphene layers
Trilayer Graphene (3LG)	Two-dimensions material consisting of three well-defined stacked graphene layers
Few-Layer Graphene (FLG)	Two-dimensions material consisting of three to ten well-defined stacked graphene layers
Graphene nanoplatelet (GNP)	A nanoplatelet consisting of graphene layers. Note 1 to entry: GNPs typically have a thickness of between 1 nm to 3 nm and lateral dimensions ranging from approximately 100 nm to 100 µm.
Graphite oxide	Chemically modified graphite prepared by extensive oxidative modification of the basal planes

Graphene oxide (GO)	Chemically modified graphene prepared by oxidation and exfoliation of graphite, causing extensive oxidative modification of the basal plane
Reduced Graphene Oxide (rGO)	Reduced oxygen content form of GO
Nanoribbon	Nanoplate with the two larger dimensions significantly different from each other

1.3 Single Layer Graphene

The structure of SLG comprises carbon only, where the C−C bond distances correspond to 0.142 nm; a value which is intermediate of Csp^3−Csp^3 and Csp^2=Csp^2 bond lengths (0.153 and 0.132 nm respectively).[10] The bonding can be described in the context of hybridisation. In ground state, the electronic configuration of carbon is $1s^2$, $2s^2$, $2p^2$. Upon excitation, an electron from the 2s orbital is promoted to the 2p orbital and hybridisation occurs, where there is a mixing of the 2s and two of the 2p orbitals to form 3 sp^2 bonds, and an unhybridised $2p_z$ orbital. The sp^2 hybridised orbitals are occupied in bonding with neighbouring carbon atoms, whilst the partially filled $2p_z$ orbital enables electron delocalisation across the structure, as shown in Figure 1.1.

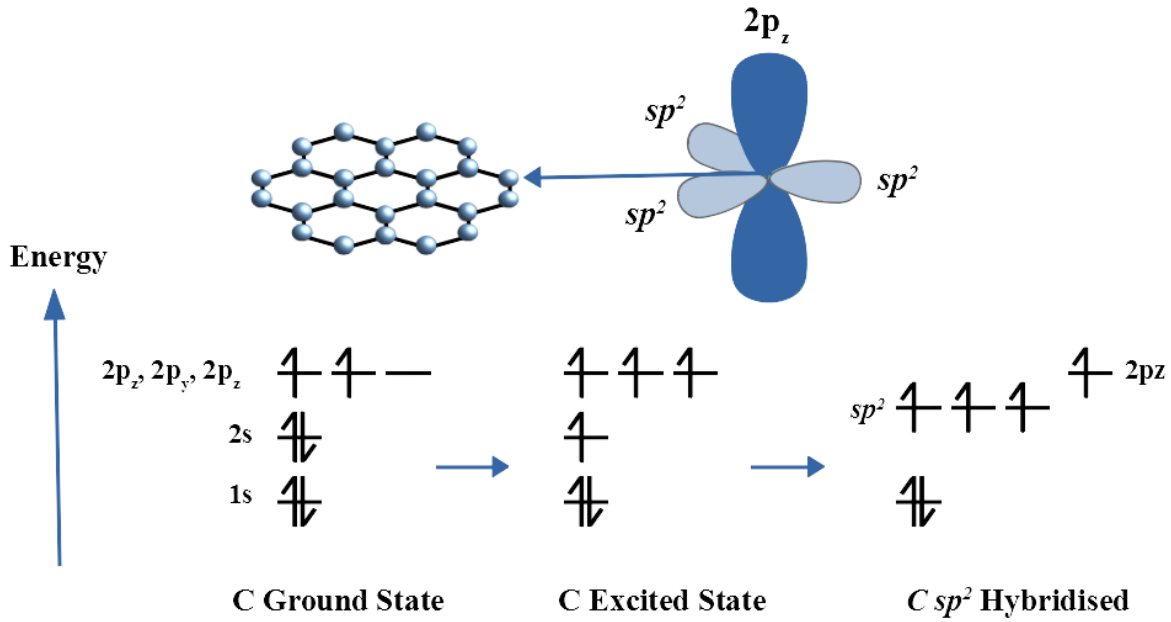

Figure 1.1 Schematic representation of three sp^2 hybridised orbitals and an unhybridised $2p_z$ orbital present within each carbon atom in graphene.

The existence of SLG was predicted several decades ago, however, it did not become isolated until 2004 at The University of Manchester, utilising micromechanical exfoliation of a single layer from highly ordered pyrolytic graphite (HOPG). This discovery was consequently awarded the Nobel Prize.[11–14] Since then, the material has gained overwhelming world-wide attention, due to the exciting properties it exhibits. SLG is a zero-band gap semi-conductor which exhibits semi-metallic behaviour and is recognised for its excellent electrical conductivity of 200,000 $cm^2\ V^{-1}\ S^{-1}$, high optical transparency (97.7% light transmitted), high thermal conductivity of up to $(5.30 \pm 0.48) \times 10^3\ W\ m^{-1}\ K^{-1}$, high theoretical surface area of around 2630 m^2/g, mechanical flexibility, biocompatibility and a Young's modulus value of around 1.0 TPa, resulting in its attraction within both academia and industry.[15–20] Whilst SLG has many exciting properties, it does come with some drawbacks. Firstly, even to date, it is still very difficult to synthesis reasonable quantities of pristine SLG. Secondly, it is a zero-band gap semi-conductor, limiting its ability to be used in active electronic devices such as field effect transistors.[21] Thirdly, it disperses poorly in common organic solvents, hindering many applications.[22] As such, strategies are often undertaken to improve these issues, including functionalisation and defect introduction to tailor the dispersion and electronic properties.[23–26] Furthermore, stacked forms of graphene are often used as an alternative for many applications, often due to their ease to synthesise.

In addition to the number of layers, the presence of defects also has an effect on the properties of SLG and its stacked counterparts, resulting in alteration of their properties. For instance, it has been found that there is an enhanced reactivity of the neighbouring carbons located within the vicinity of the defect.[27] In addition, it has been shown that the addition of defects within the lattice can result in band gap manipulation.[23,24] During covalent functionalisation upon the carbon network, defects are introduced in the form of sp^3 hybridised carbon atoms. As such, covalent functionalisation can transform the electronic properties of the material, such that the zero-band gap structure of SLG is opened. This expands its utilisation within electronic applications. An insight to the functionalisation methods are provided later on in this chapter.

1.4 Stacked Forms of Graphene

Stacked forms of graphene consider structures where multiple layers of graphene are held in alignment *via* van der Waals forces, such as in graphite, graphite oxide, 2LG, 3LG, FLG, NPs and GNPs. Within these structures, the C−C bond distances also correspond to 0.142 nm. Meanwhile, the distance between parallel layers describes the interlayer spacing, and typically corresponds to a value of around 0.335 nm, although slight deviations may occur depending on the synthesis method used.[28,29] Graphite describes the stacked form of graphene and is often used as its top-down precursor. Large quantities of graphite can be found naturally all over the world and are extracted from the ground. This type of graphite typically contains impurities such as trace metals.[30] Alternatively, graphite can also be made synthetically using stress annealing of pyrocarbon at high temperatures. HOPG is a typical example of graphite fabricated in this way and contains negligible impurities.[31] The manner in which the graphene layers orientate themselves within graphite and other stacked forms of graphene, depends on the stacking arrangement. These stacking arrangements can be defined according to four general categories: AA stacking, hexagonal (AB/2H) stacking, rhombohedral (ABC/3R) stacking and turbostratic stacking, as shown in Figure 1.2. AA stacking describes a stacking where each neighbouring layer is situated in the same position within space, directly above and below its neighbouring layer (Figure 1.2 (a)). Hexagonal stacking refers to stacking where a vacant centre of the hexagon in one layer is situated directly beneath and above a corner carbon of the neighbouring layer, in an alternating fashion (Figure 1.2 (b)). Rhombohedral stacking refers to stacking similar to hexagonal stacking; however, each third layer is also situated so the vacant centre of its hexagons sits directly below the corner atom of the layer above (Figure 1.2 (c)). Turbostratic stacking refers to a disordered form of graphite where layers are randomly rotated and translated with respect to one another and no stacking pattern takes place (Figure 1.2 (d)).[32] Hexagonal stacking is the preferred stacking arrangement in nature and is the thermodynamically stable form of graphite.[33] In contrast, rhombohedral stacking is the thermodynamically unstable form of graphite, formed due to shear deformation of hexagonal graphite. Rhombohedral graphite transforms progressively into hexagonal stacking upon heating above 1600 K.[33]

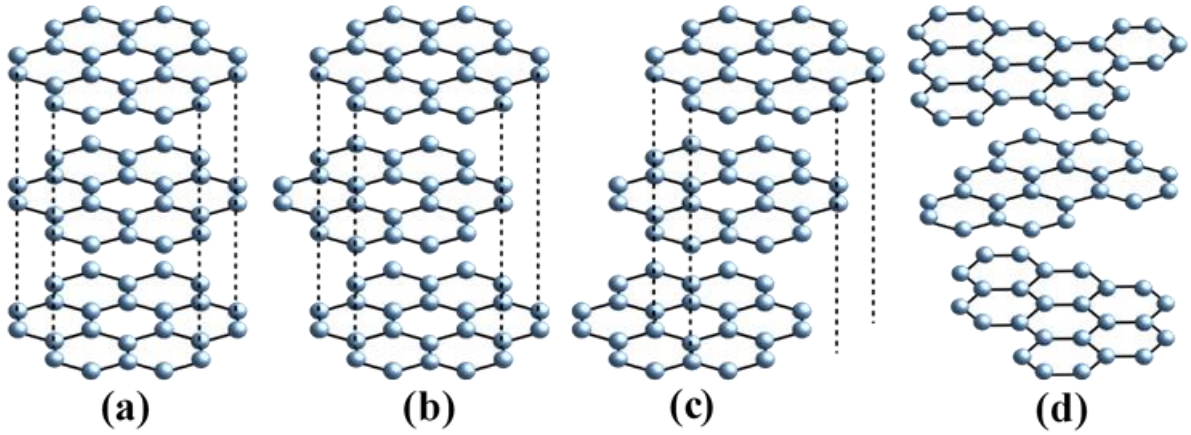

Figure 1.2 The various stacking sequences between graphene layers within graphite and stacked forms of graphene including (a) AA stacking (b) hexagonal (AB/2H) stacking (c) rhombohedral (ABC/3R) stacking and (d) turbostratic stacking.

Whilst stacked forms of graphene are often easier to synthesise and process, they differ to SLG in their properties and behaviour due to the presence of multiple layers. For example, it has been shown that SLG is 10 x more reactive than 2LG or graphene containing more than two layers.[34] Furthermore, in contrast with SLG, graphene containing multiple layers is also unable to undergo functionalisation on both sides of each sheet by functional moieties. The thermal stability of graphite and 2LG in air has also been found to exceed that of SLG. This was attributed to the presence of additional layer interactions which have the effect of increasing the energy barrier of the top graphene layer, causing it to be less easily oxidised.[35] Gas diffusion[36], optical transmittance[37] electronic properties[38] and mechanical properties[39] are also affected by the number of layers.

1.5 Graphene Oxide and Reduced Graphene Oxide

GO is commonly utilised as an alternative to graphene and its stacked forms in many applications, due to its differing properties. GO is an insulator and possesses oxygen functionality, most commonly in the form of epoxide, hydroxyl, carbonyl and carboxyl groups.[40] GO is not defined by a specific contribution of oxygen, since all samples vary depending on the material and synthesis route,[41] however, generally, the at.% of oxygen content is typically in the region of 30 − 50.[42–44] It is well known that the oxygen functionality across

the material is not uniformly distributed.[45] The Lerf-Klinowski model of GO predicted the structure and found that the material consists of epoxide and hydroxyl moieties on the basal plane, with carboxylic acid, ketone, lactone and quinoidal groups around the sheet edges and vacancy edges.[46] This general description of GO is, however, still in some debate.[47] Due to the extensive addition of oxygen and the presence of many defects, the properties of GO are very different from that of SLG or its various stacked forms. GO is hydrophilic and typically exhibits improved dispersibility in organic solvents.[48]

rGO is another commonly utilised precursor which is usually prepared *via* the reduction of GO.[49] rGO contains a much smaller oxygen content than GO, typically in the region of < 10 − 30 at.%.[50–52] rGO is also amorphous and possesses poor electrical and thermal conductivities. These conductivities are, however, improved compared with GO, due to partial restoration of the sp^2 network. The extent of this improvement relates to the degree of reduction.[53] In many applications GO and rGO are be favoured over non-oxidised GBMs due to their unique properties and practical aspects of handling. Oxygen functionality may serve as anchor points to assist functionalisation or provide enhanced interactions with various moieties.[47] This grants them the ability to be functionalised in such a way to tailor them for desired applications. Furthermore, they typically exhibit enhanced dispersibility, due to the existence of electrostatic repulsion between carboxylate groups, thereby preventing reaggregation.[48] It should emphasised, however, that covalent functionalisation introduces defects in the form of sp^3 hybridised carbons. This in turn, has an effect on many of the exceptional properties which graphene possesses, for example; high electronic conductivity, granting GO and rGO success in applications such as composite additives, where the quality is not essential.[54,55] As a result, the choice to functionalise graphene may serve as a compromise for enhancing one property but reducing another. Researchers should therefore be mindful of the "end-goal" of the targeted graphene material.[56]

1.6 Synthesis of Graphene-Based Materials

GBMs can be synthesised by a plethora of methods depending on their requirements for application. Typically, the target is to synthesise a high-quality product containing a narrow layer distribution. In addition, the technique should be reproducible and allow for synthesis on a large-scale.[57] A handful of the common synthesis methods are outlined within Figure 1.3 which enable the synthesis of SLG and other GBMs. In 2004, SLG was first synthesised by micromechanical exfoliation of HOPG using Scotch tape. The individual graphene layers could be cleaved from the bulk precursor and isolated by dissolving the tape in acetone. These flakes could then be sedimented to a silicon wafer for analysis. This method was effective in obtaining high quality, defect-free graphene film between 5 – 10 μm in width. Furthermore, the methodology could also be applied to isolate individual layers or multiple layers from graphite oxide.[13] Unfortunately, however, the large-scale capability of this method is poor due to the low production yield. As such, extensive research has endeavoured to develop new processing routes for efficient graphene and GBM production. These synthesis methods can be classified according to whether they are bottom-up or top-down. Top-down synthesis involves the separation of bulk graphite into exfoliated layers, through the negation of van der Waals attractions. Bottom-up synthesis involves the development of GBMs from various carbon precursors. The scotch tape method provides an example of a top-down mechanism. Many top-down syntheses are implemented within industry and show promise on a large-scale basis, thus, prove to be advantageous compared to the initial scotch tape method. However, these methods often struggle to synthesise the high quality, single-layer, defect-free structure of SLG, which is obtained *via* the Scotch tape method.

Figure 1.3 Common synthesis routes towards SLG and its stacked analogues. Green labels represent bottom-up methods and orange labels represent top-down methods.

Stacked forms of graphene are commonly synthesised *via* liquid-phase exfoliation of raw graphite. The process offers a route towards overcoming the energy to aggregation by negating van der Waals interactions between individual layers. Generally, a liquid media, such as a high surface tension solvent or water, often accompanied by stabilisers including surfactants, supercritical fluids or ionic liquids, promotes the formation of the dispersion.[48] Currently, liquid-phase exfoliation relies heavily on the use of sonication to create the dispersion itself. This process introduces shear stresses and cavitation in the solvent, which causes graphite to break apart and exfoliate into single layers and stacks of varying thicknesses.[58] Sonication can be conducted through the use of a bath or a probe and in general, uses ultrasonic frequencies (>20 kHz). The principle relies on a series of events through which cavitation bubbles are formed within the solvent, resulting in high-speed liquid jets. This process overcomes many of the van der Waals forces between the stacked layers, as shown in Figure 1.4.[59,60] Dispersions have been achieved using many solvents including N-methyl-pyrrolidone (NMP), acetone, chloroform, isopropyl alcohol (IPA) and cyclohexanone. Whilst this method offers a cost-effective and scalable synthesis, it results in materials which exhibit a wide thickness distribution and low exfoliation efficiencies.[7] Furthermore, long sonication is often required

(48 hours).[61] Sonication has also been shown to induce tearing of flakes, introduce defects and oxygen functionality and reduce flake size.[48,61–63] Moreover, many of the best solvents have high boiling points, such as NMP, which brings about practical struggles when removing solvent from solution.[48] The unzipping of carbon nanotubes offers an alternative top-down method. In this regard, single layer and stacked analogues can be synthesised from their respective singe walled or multi-walled CNTs using strong oxidising agents in solvents, laser irradiation and plasma etching. The resultant materials are described as nanoribbons according to the ISO definitions.[6] Similar to liquid-phase exfoliation, the exfoliation process also typically introduces defects into the graphitic structure.

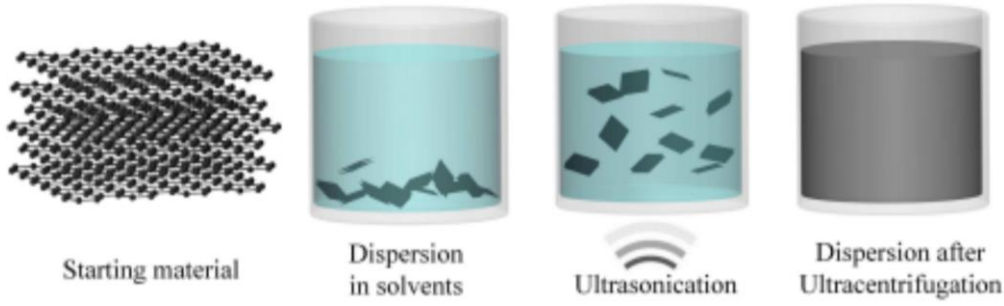

Figure 1.4 A simplified representation of the stages within liquid-phase exfoliation of graphite. Cavitation bubbles and high-speed jets form due to ultrasonication and overcome the van der Waals forces between layers. This results in the formation of exfoliated stacks and individual layers, often comprising SLG, 2LG, 3LG and FLG. Ultracentrifugation eliminates un-exfoliated stacks and allows for an enhanced dispersion to form. Reprinted from reference [60].

As previously mentioned, many commercially produced GBMs utilise top-down methods which are effective in producing high yields. These, however, often possess multilayered products with extensive defects and undesired functionality. Within industry, high quality graphene synthesis tends to involve chemical vapour deposition (CVD) or epitaxial growth on a metal substrate; methods which are considered "bottom-up". CVD is the most popular method for the synthesis of large area continuous film, comprising SLG and its stacked forms and involves a two-step synthesis process. The initial step involves pyrolysis of a hydrocarbon gas precursor, typically methane, which is fed into a heated chamber along with hydrogen.[64] Upon adsorption onto the metal substrate, this precursor is pyrolysed to form individual carbon atoms (Figure 1.5 (b)).[65] Examples of metal substrates include Pt, Ni, Co and Cu.[66] The second step involves subsequent rearrangement of these dissociated carbons atoms, which assemble on the substrate for lateral growth of graphene film (Figure 1.5 (b)). The waste gases are then

pumped from the reaction chamber. The subsequent CVD grown graphene film typically possesses large dimensions, consisting of several square meters in size and may comprise a single layer of graphene or several layers in thickness depending on the conditions.[64] Despite the extensive use of this synthesis route, especially for high quality GBM material synthesis, it does not come without its drawbacks. The waste gases are typically toxic and therefore suitable ventilation is required for their removal. In addition, the method is expensive, requiring high temperatures (typically around 1000˚C) and low pressures and defects can often become introduced if the conditions are not optimised.[67] CVD grown film is commonly utilised within electronic applications, panels and displays.[68–72] Alternatively, SLG and stacked analogues may also be synthesised using epitaxial growth on silicon carbide (SiC).[73] This utilises the SiC substrate as a carbon precursor. SiC contains carbon and silicon in a 1:1 stoichiometry with tetrahedral geometry where each carbon atom is bonded to four other silicon atoms, and each silicon atom is bonded to four other carbon atoms, as shown in Figure 1.6. This substrate is subjected to high temperatures resulting in the desorption of silicon from the surface due to its relatively high vapour pressure relative to carbon (Figure 1.6 (a)).[74] As such, carbon atoms remain on the surface as a continuous film (Figure 1.6 (b)). This method produces very high quality graphene film and is heavily exploited for electronic applications.[75] More recently, a number of novel methods have begun to emerge which enable the formation of SLG and stacked analogues.[76] For example, a scalable bottom-up method was patented by the industrial company; Applied Graphene Materials (AGM) and is subsequently referred to as the AGM method. This involves the use of a metal alkoxide as the carbon precursor, which undergoes thermal decomposition at high temperatures to afford graphitic layers.[77] SLG and stacked analogues of up to FLG can be synthesised this way.

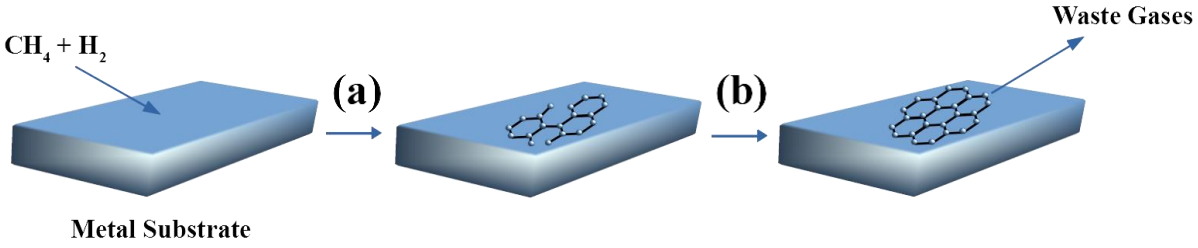

Figure 1.5 Schematic providing a simplified representation of the CVD growth steps to synthesise SLG film. (a) depicts the feeding of a hydrocarbon gas precursor into a heated chamber. Upon adsorption onto a metal substrate, pyrolysis of the gas occurs to form individual carbon atoms. These assemble onto the substrate to form graphene film shown in (b). Waste gases are subsequently removed by the exhaust system.

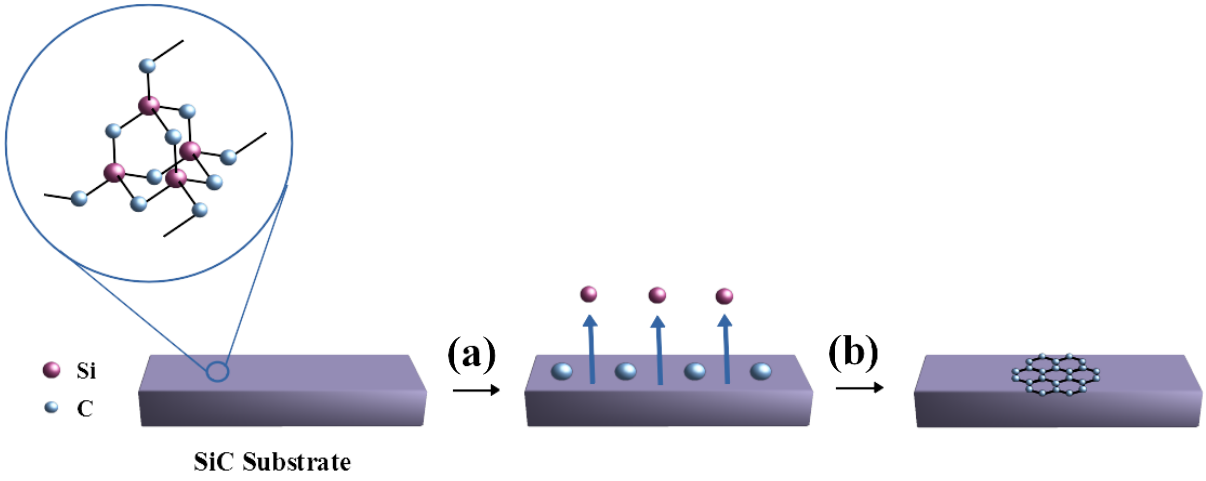

Figure 1.6 Schematic providing a simplified representation of the epitaxial growth of SLG. (a) depicts the structure of the SiC substrate and the desorbing of silicon from the surface of the substrate. (b) shows the formation of a graphene layer upon SiC.

GO and rGO are alternative precursors to pristine graphene and are often used in preference due to its abundance of oxygen functionalities which introduce different properties, such as a band gap and increased solubility. Well-established GO synthesis methods include the Brodie method,[78] Staudenmaier method[79], Hofmann method[80,81] and Hummers and modified Hummers methods, as outlined in Figure 1.7. Typically, these top-down oxidation reactions are carried out on bulk graphite, and exfoliation of the layers occurs simultaneously. In each case, an acid is required, such as HCl, H_2SO_4 or HNO_3, in conjunction with an intercalating alkali metal, such as potassium in $KClO_3$ or $KMnO_4$, which assists in the further exfoliation of the oxidised material. [79,82] Meanwhile, rGO is typically synthesised *via* the reduction of GO under thermal, chemical or electrochemical treatment.[83,84] These oxidation and reduction methods involve simple processes and utilise relatively cheap reagents, however, they are associated with challenges.[85] These include issues such as long reaction times, the need for strong oxidising and reducing agents, the release of toxic gases and a non-uniform distribution of oxygen functionality over the surfaces of the materials. Oxidising reagents, in particular, are extremely dangerous as they are capable of forming explosive mixtures when mixed with combustible material. Over the years, various adaptions and alternative synthesis routes have emerged to avoid these undesirable reagents and increase the efficiency of the oxidation process.[44] For example, plasma oxidation, microbial oxidation and electrochemical oxidation

have shown promise in providing routes which eliminate toxic gases, provide more homogenous oxidation and speed up the reaction times.[44,86,87]

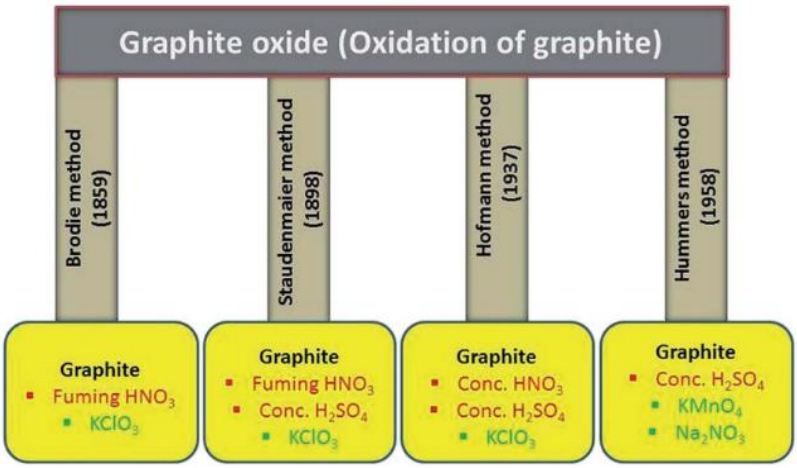

Figure 1.7 Routes towards the oxidation of graphite, which are applicable to SLG and its staked forms. Reprinted from reference [88].

Despite the overwhelming research into GBM synthesis processes, there are still many issues associated with them. Various reviews highlighting the advantages and disadvantages of existing methods can be accessed.[70,75,85] One of the key hurdles relates to the difficulty towards the synthesis of high-quality graphene. As mentioned above, defects can often become introduced during many existing syntheses which diminish the pristine nature of the graphitic lattice. Another hindrance relates to the scale-up and ability to synthesise GBMs in bulk. In light of this, academia and industry have sought to combat these. In regard to the latter, plasma synthesis routes have become increasingly desirable to synthesise bulk quantities of GBM, and the various plasma processes are discussed within the following sections.

1.7 Introduction to Plasma and its Use in GBM Synthesis

Plasma consists of an assemblage of free charged particles moving in random directions, as shown in Figure 1.8 (a).[89] These charged particles are typically generated within a gas *via* bond dissociation and ionisation upon application of thermal energy or electromagnetic fields.[89] Inelastic collisions take place between electrons and gas molecules, resulting in the formation of further reactive species including free radicals, ions and electrons.[90] The overall quantity of

electrons and ions within the gas is sufficient in providing an overall neutral charge.[87] A schematic outlining the formation of plasma through implementation of an electromagnetic field is shown in Figure 1.8 (b). This figure depicts a plasma discharge formed between two electrodes, where the plasma is ignited and sustained by applying a high frequency voltage to the gas.[89]

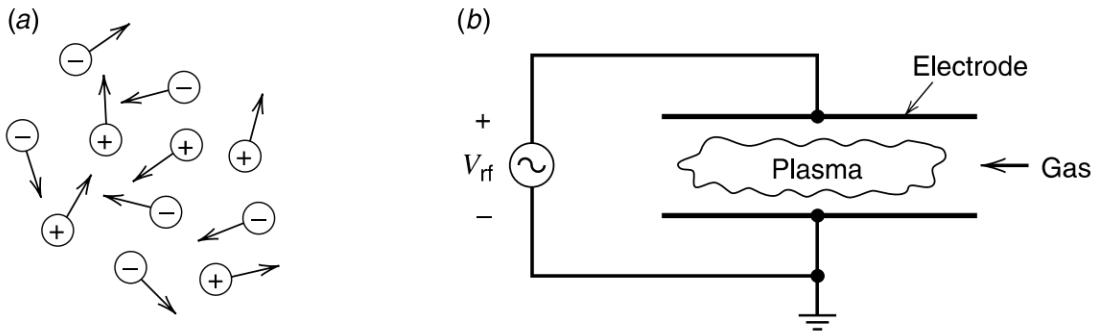

Figure 1.8 Schematic representation of (a) a plasma consisting of charged particles moving in random directions and (b) the formation of plasma discharge between two electrodes. Reprinted from reference [89].

When plasma is generated in the presence of a graphitic networks, it can physically modify the material's surface.[91] Such modifications involve etching, functionalisation, defect formation and cleaning.[87,92] As such, the properties of GBMs can be modified quite drastically, often providing desirable properties such as hydrophilicity, hydrophobicity, improved adhesion and enhanced conductivity.[87] The most common plasma treatments utilised in GBM modification involve oxygen, nitrogen, ammonia, methane, hydrogen and fluorine.[91] More information on these treatments are considered later on in the text, in relation to functionalisation procedures. In addition to these modifications, plasma is also capable of exfoliating bulk graphitic precursors into fewer-layered stacks and promoting nucleation and growth of carbon precursors into graphitic structures. As such, it is also considered as a synthesis route towards GBMs. Within the recent years, plasma has become an increasingly desirable route for the synthesis of SLG, 2LG, FLG and stacks containing multiple graphitic layers (often up to several hundred layers in thickness).[93–96] It possesses many advantageous over existing synthesis methods, such as lack of hazardous or toxic solvents or by-products and scalability.[94,97] As with the previously outlined synthesis methods, plasma syntheses can be classified according to whether they follow a bottom-up or top-down methodology. Top-down plasma methodologies typically rely

on the exfoliation of graphite into fewer-layered stacks, where the extensive van der Waals forces become weakened between the layers, often due to the introduction of defects and functionality.[70] These synthetic routes are particularly useful within industry as are able to produce bulk quantities of stacked graphitic layers. For example, it has been shown that 30 kg of FLG can be synthesised in around an hour using plasma exfoliation.[93] In contrast, bottom-up plasma syntheses commonly depend on the building of graphene from a gaseous precursor.[98–101] An example of a bottom-up plasma synthesis method includes plasma enhanced CVD (PECVD) which relies on the nucleation and growth of graphene under specialised conditions in the presence of a carbon source, such as methane.[66,102–104] PECVD commonly employees microwave or radio frequency (RF) to form the plasma, however, unlike conventional CVD, it typically does not utilise high temperatures.[105] This is because in CVD, the gas and surface reactions occur by thermal activation, whereas in PECVD, the electron temperature is sufficient for dissociation.[106] Carreon and co-workers provided an example of PECVD used to grow SLG from mango peel. It was found that the presence of the plasma was essential for the growth of the graphene and enabled the process to be conducted at relatively low temperatures (750˚C).[105] Furthermore, plasma also improves the graphene production rate and purity and may negate the need for catalyst addition.[90] For example, Kato and co-workers showed that PECVD could be utilised to grow high-quality SLG on a SiO_2 substrate in the absence of a metal catalyst.[107] This provided high quality SLG which was free of any metal impurities, and thus, extended the application of CVD grown graphene into biomedical applications where the absence of undesirable impurities is essential.

During top-down and bottom-up plasma syntheses, plasma can be generated through a variety of means. These include: RF (typically 13.56 MHz), direct current (DC), alternating current (AC), microwave (typically between 300 MHz to 300 GHz), DBD, corona discharge, capacitive, induction, electron beam, electric arc, plasma torch and hollow cathode discharge.[108–110] Furthermore, plasmas can also be categorised according to their temperature and pressure, which subsequently has a large influence on their properties.[109] Plasmas can be generated using both low and atmospheric pressures, low temperatures (< 1727˚C) and high temperatures (> 1727˚C). Low temperature (non-thermal) plasmas possess different thermodynamic properties than high temperature (thermal) plasmas. The former may be produced by RF or magnetron discharge and comprises electrons which are much higher in temperature than the ions and neutral species. Low temperature plasmas therefore do not exist in equilibrium and the gas is only weakly ionised. In contrast, high temperature plasmas possess

electrons, ions and neutral species all with the same temperature, thus exists in thermodynamic equilibrium. In high temperature plasmas, the gas is strongly ionised.[94] The common feature among all plasmas lays in their ability to ionise and dissociate gaseous precursors to form reactive plasma.[106] The generation route is chosen based on the conditions required to synthesise the desired GBM.[111] For example DC glow discharges offer a simple, cost-effective means towards plasma production, however, they are unsuitable for the deposition of non-conductive materials such as GO, due to charge build up. RF glow discharges, on the other hand, are widely used to modify insulating materials, due to their ability to neutralise charge build up by forcing the electrodes to act as cathodes and anodes alternatively.[106] A detailed insight to the applicability of the various plasma generation methods is outlined within an excellent review by Bogaerts.[106] Within this section, some of the key plasma-synthesis methods towards GBM synthesis are outlined.

Top-down plasma synthesis can take place both in dry state or in solution state. Saito and co-workers provided an example of exfoliated stacks of graphite made *via* graphite exfoliation in aqueous solution.[112] This incorporated a non-equilibrium, cold plasma produced by RF (between 10 to 60 kHz), which proved sufficient in exfoliating the graphite. A schematic of the instrumentation is depicted in Figure 1.9 (a). The setup incorporated two carbon electrodes containing graphite immersed in aqueous solution. The discharge was generated in the beaker between the two electrodes using a bipolar pulse power supply operating at a voltage of 1 – 2 kV and a pulse width from 1 to 4 μs. The mechanism for the exfoliation of graphite into fewer-layered stacks was attributed to the conversation of electrical energy into thermal energy on the electrode surface, resulting in the heating of water molecules and their subsequent vaporisation, as depicted within Figure 1.9 (b). The gas bubbles nucleate, and plasma is generated inside them due to the voltage applied between the electrodes, resulting in sufficient energy to overcome the extensive van der Waals interactions between layers.

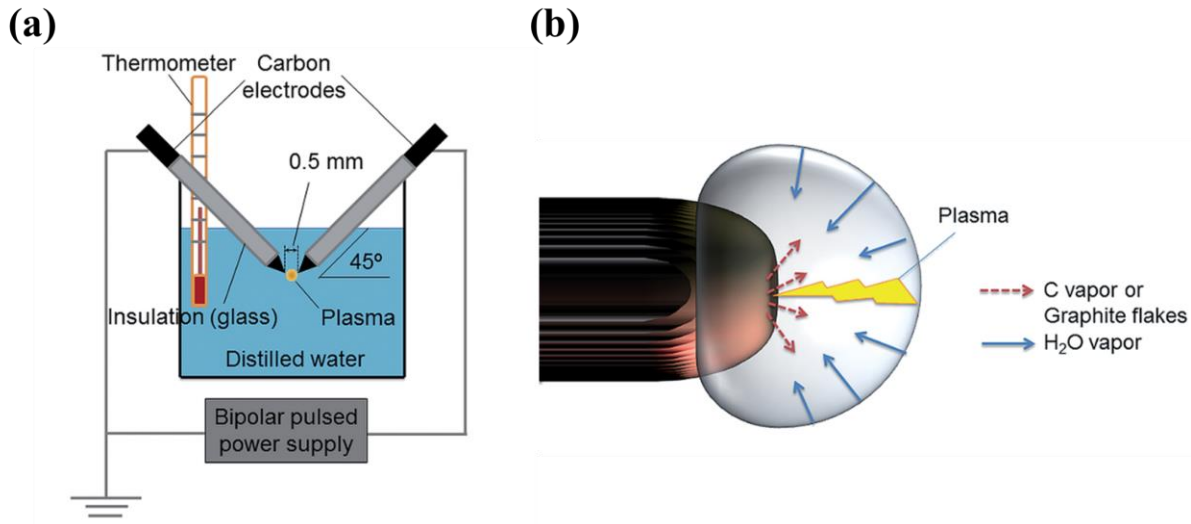

Figure 1.9 Synthesis of exfoliated graphitic stacks including (a) instrument schematic comprising two graphite electrodes immersed in aqueous solution connected to a RF power supply and (b) the formation of plasma at the electrode. Reprinted from reference [112].

Many examples of top-down wet plasma methods are described within the literature, and all show success in providing sufficient energy to overcome layer to layer interaction.[99,112–115] Unfortunately, however, wet plasma methods often involve the implementation of undesirable solvents, and subsequent drying of dispersions may result in re-stacking of layers. For this reason, dry plasma methods are often advantageous, as they do not form any toxic by-products or utilise hazardous solvents. Various dry plasma methods which utilise a top-down approach are outlined within the following sections. It is observed that most of these routes utilise a low-pressure reactor system, which helps to sustain the plasma. For example, exfoliated graphitic stacks (NPs), also referred to as "particles comprising stacked graphene layers" within their corresponding patent, are synthesised by the industrial manufacturer; Perpetuus. This manufacture utilise a trade-secret process relying on a low pressure custom-made DBD reactor, as shown in Figure 1.10 (a).[95] The subsequent NP products typically comprise of dark powders, as shown in Figure 1.10 (b) and (c). This reactor consists of multiple components; depicted within Figure 1.11. During synthesis, raw graphite is initially placed into the reactor and the motor rotates the chamber to agitate and displace the material during operation. The treatment chamber consists of a three-part system, incorporating the central drum and the first and second frusto-conical shaped sections. The central drum (see Figure 1.11 (b)) consists of a cylinder casing which encompasses two circular end plates (only one is shown) and a series of electrodes. The electrodes are arranged in a circular alignment, and project into the central

drum. This circular arrangement with the assistance of scoops, allows the graphitic particles to be further agitated and displaced during operation.

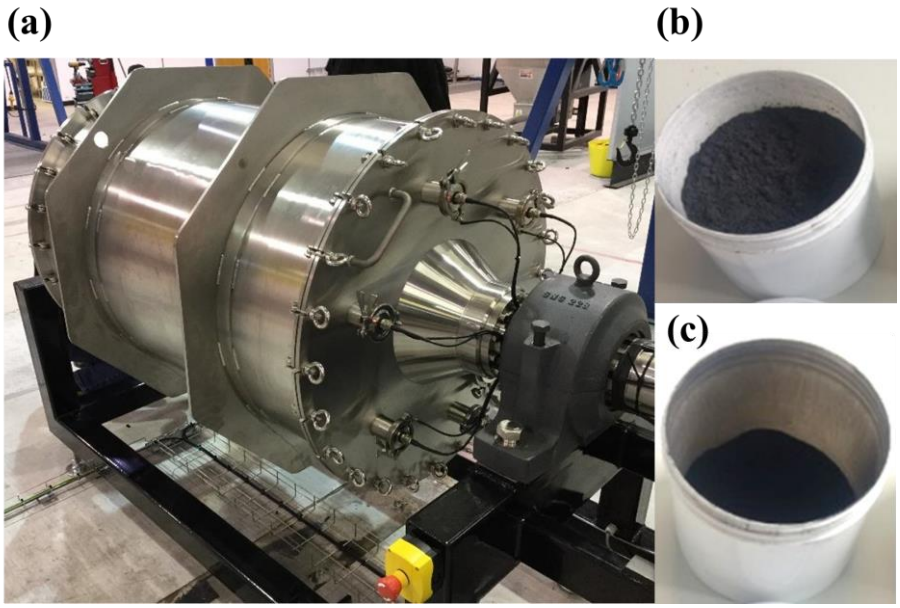

Figure 1.10 (a) Photograph of DBD reactor utilised for the synthesis of NP and two NP products with trade names (b) SDP 150 and (c) SDP 500.

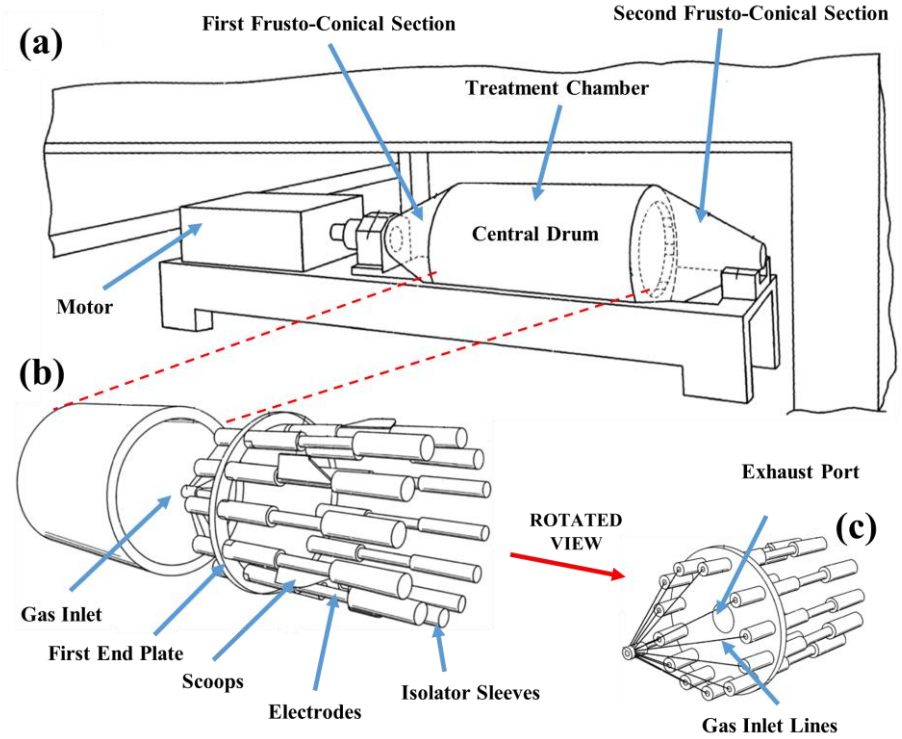

Figure 1.11 Schematic of (a) main components within the DBD reactor consisting of a central drum shown in more detail within (b) and with a rotated orientation in (c).

During operation, gas enters and exits the treatment chamber through the gas inlet, situated in the first frusto-conical section. From here, it is transferred up the gas inlet lines and flows through the hollow electrodes (Figure 1.11 (c)). The gas supply is controlled using a mass flow controller. The electrodes adopt the role of working electrodes within the glow discharge system, whilst the inside of the drum, coated with conductive boron silicate glass, acts as the counter electrode. This material also prevents unwanted sputtering. Prior to processing, the treatment chamber is evacuated and gases are introduced to the central drum through the hollow electrode manifold. During a typical synthesis operation, argon (Ar) gas is introduced through the gas inlet at a pressure of 0.01 mbar and a flow of 600 cm^3/min, and the treatment chamber is rotated. Meanwhile, RF power is applied to the electrodes (13.56 MHz) to establish a negative DC bias voltage on the electrodes, causing them to act as cathodes within the system. Typically each electrode delivers 240 V. As the electrodes continuously rotate, they form localised regions consisting of Ar plasma halo clouds around each working electrode. These regions consist of many high energy positive ions, free electrons, UV photons, radicals and other excited species. This plasma is irradiated onto the sample for a specified time and bombards the graphite particles. This introduces defects to the structure, likely to be in a variety of forms.[116] These include single vacancies, double vacancies or complex vacancies, which involve the removal of one atom, two atoms or more than two atoms respectively, from the structure. The presence of defects reduces the van der Waals forces between graphitic layers, causing many of the layers to dissociate to form stacks with improved friability.[95] Additionally, small pores become introduced, along with amorphous regions such as Stone-Wales defects which result from a 90°, in-plane rotation of two carbon atoms within the graphitic network, as shown in Figure 1.12.[117–120] Stone-Wales defects result in buckling of the planar graphitic layer, promoting the formation of non planar structures.[121–123] Kostoglou and co-workers investigated the various properties of these materials including their morphology. They found that the particles consisted of rigid aggregated particles with dimensions typically of several μm, as shown in Figure 1.13.[93] In addition the thickness of the individual particles was found to correspond to between 3 – 38 layers according to X-ray diffraction (XRD) studies. Within the current work, NPs are also synthesised using Perpetuus' patented plasma process.

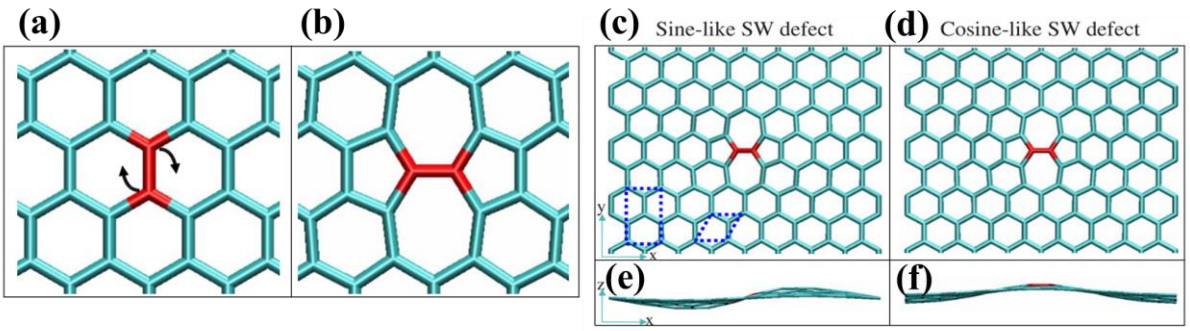

Figure 1.12 Formation of a Stone-Wales (SW) defect through the rotation of the π bond by 90° with respect to the midpoint. (a) shows the honeycomb lattice of graphene becoming rotated to form a Stone-Wales defect, as shown in (b). (c) and (e) show a sine-like Stone-Wales defect possessing a sine-like structure with a vertical displacement between the highest and lowest carbon atom of 1.4 Å. (d) and (f) show a cosine-like Stone-Wales defect possessing a cosine-like structure with a vertical displacement between the highest and lowest carbon atom of 1.7 Å. Reprinted from reference [121].

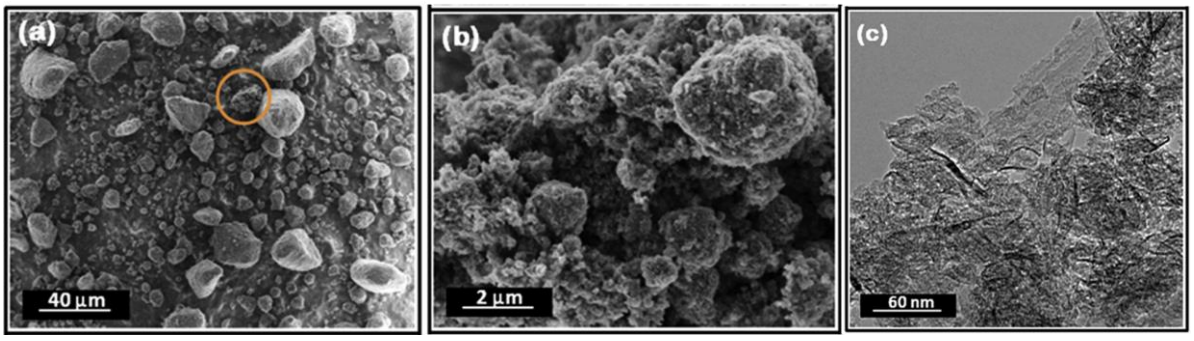

Figure 1.13 (a) and (b) SEM images at high and low magnifications respectively and (c) TEM image of partially oxidised graphitic stacks synthesised using plasma treatment. Reprinted from reference [93].

The combination of O_2 and Ar/H_2O mixtures has also been shown to effectively promote exfoliation and functionalisation of GBMs in various other literature examples.[116,124–129] The mechanism of this plasma exfoliation has attracted some interest over the years. Plasma radiation has been shown to promote the dissociation of π bonds, resulting in radical formation on the graphitic sheet. As outlined within several papers, the π bonds within the sp^2 network are described as being "active".[124–126] These bonds are higher in energy than σ bonds and hence more reactive. As such, they are more susceptible to plasma attack, resulting in radical generation on the dissociated π bond, creating these "active sites".[116,126] The quantity and presence of defects within GBMs depends on the energy of the incoming ions and the angle at

which they make contact with the graphitic sheet.[117] For example, molecular simulations by Keinonen revealed that ion beam energies between approximately 1 keV to 10,000 keV, produced single, double and complex vacancy defects within graphene, where the exact energy was dependent on the ion beam incident angle and the ion source. Lower energies (in the region of < 1 keV to 80 keV), on the other hand, generally yielded amorphisation as were incapable of displacing a target atom.[117,130] Such regions typically comprise Stone-Wales defects. These have been shown by density functional theory (DFT) and quantum Monte Carlo (MC) simulations to correspond to either sine-like buckling orientations or cosine-like buckling orientations, which cause a large verical displacement parallel to the defect core, revealing wavy structures, as shown in Figure 1.12 (e) and (f).[121] As such, both the energy and the angle of ion bombardment on the raw graphite material have a large influence on the types of defects produced during NP synthesis, as well as the planarity of the sheets.

A second industrial supplier of exfoliated graphitic material is the South Wales company; Haydale Ltd. Within their patented synthesis process, plasma is utilised to exfoliate graphite into "particulate carbon matter" *via* a glow discharge mechanism.[96] A photograph of this glow discharge is depicted within Figure 1.14 (a). The treatment vessel employed typically operates at a low pressure (< 500 Pa) and gas is fed into the chamber in a similar way to that described above. A range of functionalities including carboxy, carbonyl, hydroxy, amine, amide or halogens can be added to the exfoliated material, depending on the gaseous precursor introduced into the chamber. Examples include oxygen, water, hydrogen peroxide, alcohol, nitrogen, ammonia, amino-bearing organic compounds and halogens including fluorine, halohydrocarbons and noble gases. Graphite becomes exfoliated during the treatment to form NPs with thicknesses of < 100 nm and lateral dimensions of at least 10 times the thickness.[96] Increasing the gas concentration and treatment time, and subsequent plasma exposure, is found to enhance the degree of functionalisation.[96] The generated materials are typically utilised within composites and devices. In particular, Haydale Ltd manufacture a screen printable carbon ink which achieves a surface resistivity of < 15 ohm^2 and a surface covering of 550 cm^2 g^{-1}.[131] Furthermore, NPs can also be applied within composite coatings.[132] It has previously been found that the incorporation of nanomaterials enhances the capabilities of protective coatings, providing them with barrier fillers, and thus, providing tortuous diffusional pathways.[133,134] Chaudhry embarked upon an investigation to analyse the capability of Haydale's functionalised NPs within barrier coatings.[132] Composite coatings, consisting of polyvinyl butyral and NP treated with fluorine, oxygen and argon, were initially synthesised

and coated upon carbon steel samples. The barrier properties of these coatings were then investigated *via* electrochemical techniques, and it was found that the coatings were effective in blocking corrosive species. In addition, the composites were compared with that of their respective thermal rGO composites, and the barrier properties were found to be superior. This finding was attributed to the functionality on the NP surface, enhancing its dispersion within the polymer resin compared with rGO. This improved dispersion led to a reduction in the number of interfacial defects and an increase in the tortuous pathways. As a result, longer diffusional pathways for the corrosive solution were established through the coatings, granting them effective as barriers.

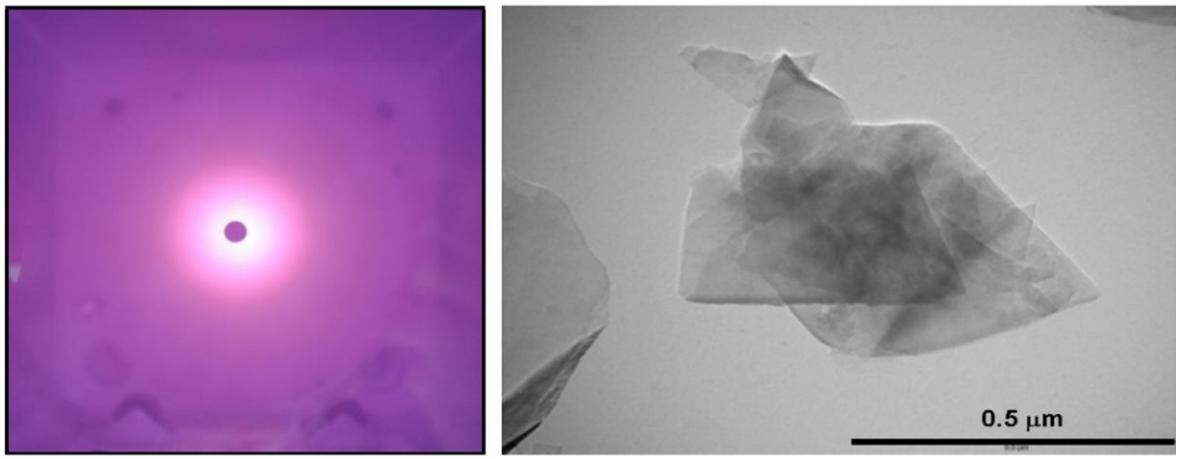

Figure 1.14 Glow discharge formed within Haydales Ltd's plasma reactor (left) and a tunnelling electron microscopy image of an exfoliated NP. Reprinted from reference [131].

Hong and co-workers reported another example of the use of a DBD reactor to synthesise plasma-exfoliated rGO, comprised of few-layered stacks.[135] Instead of utilising low pressures, this reactor operated at atmospheric pressure. Hydrogen plasma was responsible for reducing a GO precursor, whilst simultaneous enabling its exfoliation. The experimental set-up of the DBD process is depicted within Figure 1.15, outlining the presence of low voltage and high voltage terminals to form plasma. It was observed that increased plasma exposure time was accompanied by the production of a more expanded powder. This finding was attributed to an increase in exfoliation. During treatment, Hong outlined that the high energy electrons and ions within the plasma resulted in collisions with GO particles, whilst rapid discharge of H_2O and CO_2 gases, promoted exfoliation of GO into few-layered rGO stacks, as shown in Figure 1.16.

Again, it can be observed that as the treatment proceeded, the material underwent volumetric expansion, due to the exfoliation of the layers of GO.

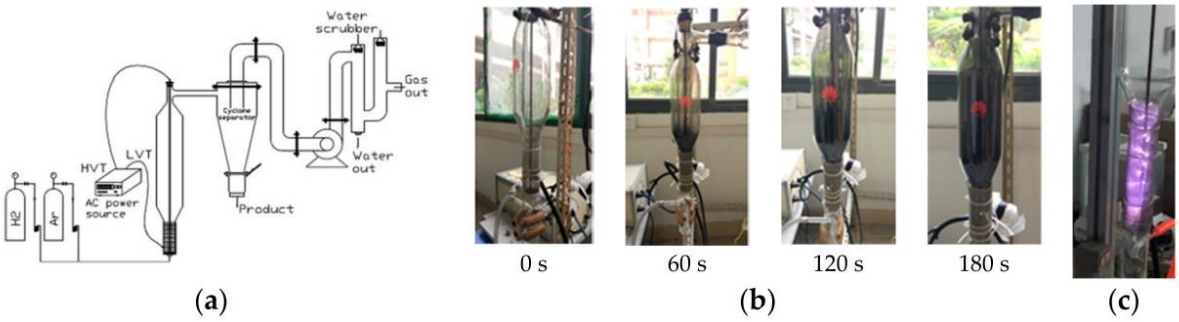

Figure 1.15 (a) Apparatus to synthesis plasma exfoliated rGO consisting of a low voltage terminal (LVT) and a high voltage terminal (HVT). (b) depicts the expansion of the GO powders after treatment with the DBD plasma for 0 – 180 seconds and (c) discharge process. Reprinted from reference [135].

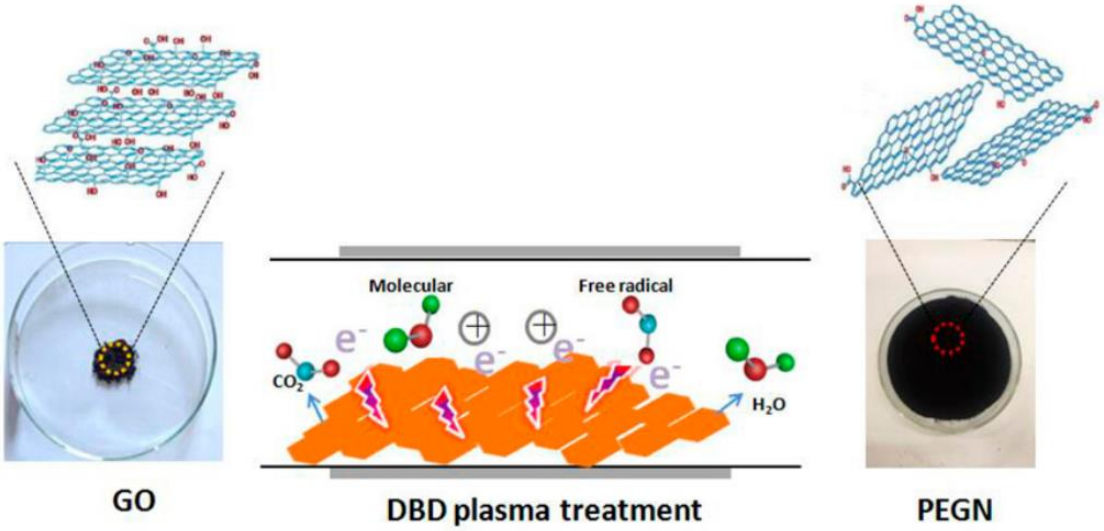

Figure 1.16 Schematic representation of the exfoliation and reduction process experiences by GO during DBD plasma treatment. Reprinted from reference [135].

Zhao and co-workers utilised an alternative precursor to synthesise exfoliated stacks from graphite. This consisted of H_2O_2, which enabled etching of the bulk structure upon plasma formation. The mechanism behind this top-down synthesis was attributed to the formation of strongly oxidising free radicals, in the form of OH, O, HO_2, upon excitation. These free radicals were found to be sufficient in enabling the unzipping of graphite, whilst oxidising many of the

carbon atoms to form partially oxidised FLG stacks, as shown in Figure 1.17. The plasma instrumentation incoorporated a custom-built reactor, operating at a pressure of 20 Pa and a power of 100 W. Respective voltages and currents of 850 V and 150 mA were utilised and treatment was allowed for 2 hours.[136]

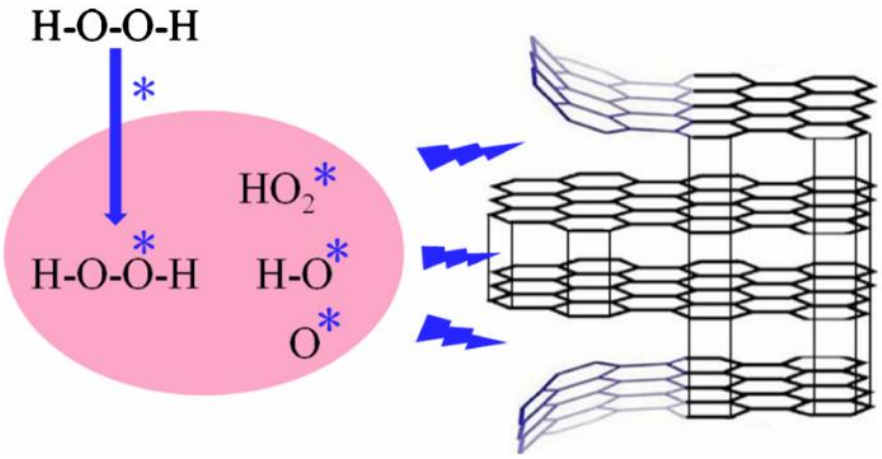

Figure 1.17 Synthesis of FLG from graphite utilised H_2O_2 plasma etching. Reprinted from reference [136].

More recently, Vasquez and co-workers utilised a combination of plasma treatment and liquid-phase exfoliation to synthesise stacks of partially oxidised graphitic layers.[137] Initially graphite was treated with RF capacitively-coupled plasma inside a glass bell jar chamber. This plasma was formed through the addition of an O_2 gas stream, and treatment continued for a duration of 15 minutes at 100 Pa. The treatment process was repeated three times and the particles were physically mixed between treatments, to ensure homogenous functionalisation. Afterwards, liquid-phase exfoliation and centrifugation were carried out to remove thick stacks, affording exfoliated functionalised particles containing 20 layers or less within the supernatant.

As previously highlighted, the aim for any synthesis route is to allow for the formation of high-quality graphene with a narrow layer distribution. In addition to this, the route should also be scalable, reproducible and cost-effective. Keshri and co-workers implemented a procedure for the synthesis of in-plane-defect free SLG, 2LG and 3LG on a large-scale, reaching a production rate of 48 g per hour. This synthesis utilised a DC bias to establish plasma within an Ar atmosphere and treatment was carried out for approximately 25 minutes at 20 Pa.[138] Centrifugation was employed post-plasma treatment to remove any un-exfoliated material from an aqueous dispersion. The combined processes led to the exfoliation of graphite into single

layers, two layers and three layers, where up to 85 % of flakes were believed to consist of single layers. The quality of the flakes was measured *via* Raman spectroscopy, revealing the absence of a D band within the planes, and a relatively low I_D/I_G ratio of 0.2 upon the edges. This suggested that the planes of the flakes were absent of any defects, whilst a small proportion of defects were present at edge sites. As such, this route shows promise towards the production of high-quality graphene with a narrow layer distribution, in high yield. The mechanism associated with the exfoliation was also proposed, consistent with Figure 1.18. This involved a three-stage process comprising thermal shock (stage 1) and shearing of the graphitic particles in the laminar (stage 2) and turbulent region (stage 3). Initially, thermal shock of graphite occurred by the hot plasma (3430˚C) (stage 1). During this stage, thermal damage to the graphitic structure was minimised due to the existence of inert Ar gas and short processing times. This thermal shock was believed to increase the graphitic interlayer spacings, leading to weakening of van der Waals forces. The particles then underwent shear forces within stage 2 and stage 3, which contributed to the exfoliation of graphite. This resulted from the combined effects of viscosity and velocity of the plasma within the laminar region and large-scale eddies of cold ambient gas within the turbulent region. In turn, the already exfoliated particles experienced extensive shear forces, resulting in additional exfoliation of stacked layers. Furthermore, the reproducibility of the exfoliated product was investigated. It was found that samples acquired across five batches of the same treatment process possessed similar Raman spectra, attributed to comparable graphitic structures. Moreover, 75 – 85 % of all samples consisted of single layers, indicating little variance in the thickness distributions across batches, and thus demonstrating the route's reproducibility.

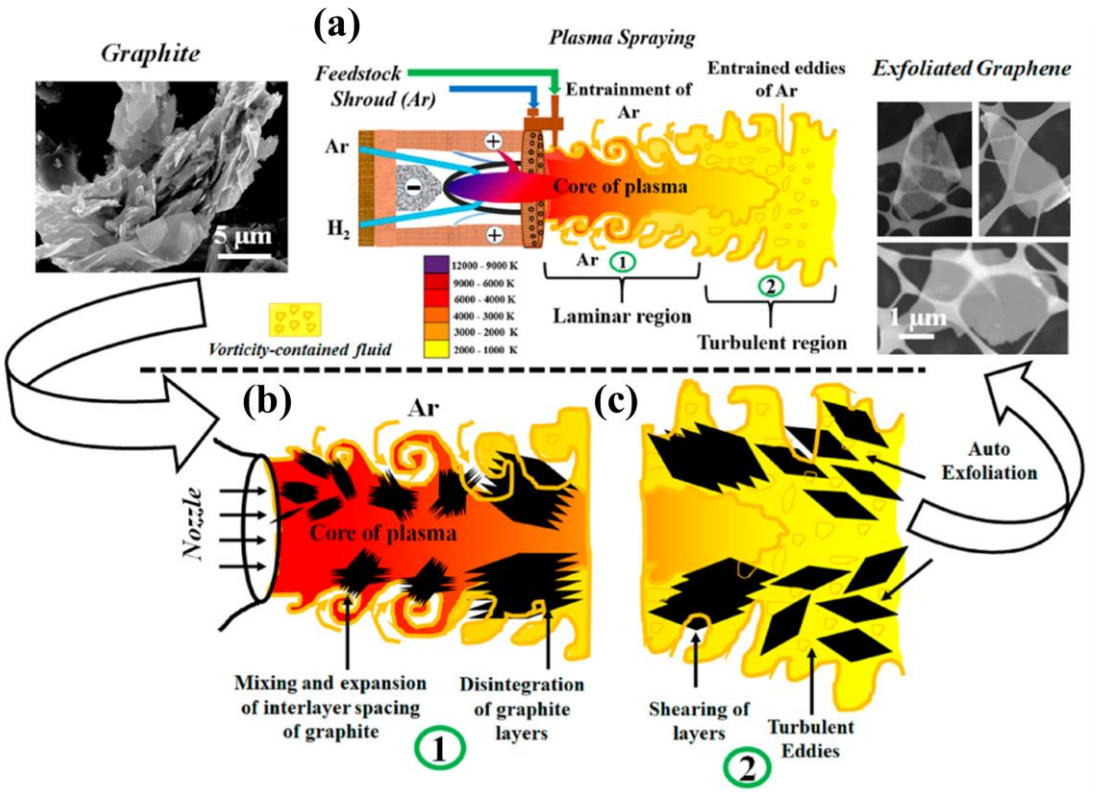

Figure 1.18 Proposed three-stage mechanism for the synthesis of SLG, 2LG and 3LG during the exfoliation of graphite, consisting of (a) a schematic representation of the exfoliation mechanism (b) magnification of the laminar region of the plasma shown in (a) and (c) magnification of the turbulent region shown in (a). Reprinted from reference [138].

1.8 Functionalisation and Modification of GBMs using Plasma

As previously mentioned, functionalisation serves as a useful tool to alter the properties of GBMs. For instance, the addition of external chemical moieties often improves issues associated with GBMs' poor dispersibility by introducing electrostatic or steric repulsion, in the form of functional moieties between the sheets. This is, of course, a common strategy to prevent reaggregation of the layers.[48,139,140] Furthermore, functionalisation may also serve as a strategy to enhance interaction of GBMs within composite materials, for the purpose of mechanical, energy and biomedical applications.[141–144] Functionalisation routes can be classified according to whether they are covalent or non-covalent. The former involves the formation of a covalent bond, typically either to the carbon network directly or to oxygen functionality present on the GBM's surface. The latter considers the functionalisation of GBMs through a non-covalent means, comprising various non-bonding interactions such as $\pi-\pi$

bonding, hydrogen bonding and van der Waals.[145] Strategies towards functionalised GBMs have been reviewed extensively within the literature.[25,47,146–150] Typically, covalent functionalisation methods rely on both wet and dry approaches. The former describes the use of a solvent to mediate the chemical reaction and is considered in more detail within the next section. The latter approach describes methods which do not implement liquid media and typically involve reactive species such as plasma, as described earlier on in the text.

Plasma conditions have been shown to provide success in introducing single atoms to the graphitic network of GBMs, as well providing active sites amongst the π network. These routes are particularly advantageous due to the fact that they: 1) are commonly solvent-free, and thus, eliminate the issues associated with reaggregation; 2) often utilise low energy sources and release negligible emissions[151]; 3) Typically, leave no contaminants in the resultant material, in contrast to wet chemical functionalisation methods such as oxidation[152] and 4) can be optimised to control the extent of functionalisation, by varying the plasma parameters including pressure, power and exposure time.[153] A commonly utilised plasma functionalisation method involves the oxidation of GBMs**.** This is often carried out in a combined exfoliation step where graphite forms fewer-layered stacks, such as that described previously within the work of Vasquez.[137] Generally, the plasma is generated through the addition of O_2 or O_2/Ar gas streams.[93,95,96,132,136,154,155] In the case of combined O_2/Ar plasma treatments, it has been shown that exposing graphite to Ar plasma prior to O_2 treatment, introduces defects and radicals onto the π network, providing active sites for oxidation.[124] Upon exposing the pre-treated material to oxygen plasma, it is believed that radicals present on the dissociated π bonds then react with highly reactive, "active", oxygen atoms.[120,156,157] These active oxygen atoms are formed during collisions between oxygen and electrons.[158,159] Choi and co-workers proposed a mechanism for plasma oxidation of multi-wall CNTs and activated carbon fibres, as shown in Scheme 1.1.[120,124] In this mechanism, radicals, formed during the dissociation of π bonds, reacted with active oxygen atoms to form C–O and C–OH bonds. This step entailed proton transfer, where a proton was abstracted from a source, such as atmospheric water or from the network itself, as depicted within Scheme 1.1 (a). Furthermore, C=O bond formation was also believed to take place during intramolecular reorganisation on the C–C bonds (Scheme 1.1 (b)), whilst O–C=O bonds formed due to combination of an existing C=O bond with plasma-generated radicals and active oxygen atoms, followed by proton transfer (Scheme 1.1 (c)). Moreover, plasma conditions may also have induced the formation of a lactone functional group from a carboxylic acid and a neighbouring C=O bond (not shown). Perpetuus employ a combination of Ar

plasma, followed by O_2 plasma, within their DBD plasma reactor, to functionalise graphitic stacks consisting of multiple layers.[93,95,160] This process introduces oxygen functionalities in the form of hydroxyl and epoxy groups, as well as ester and carboxyl groups, according to XPS data.[93,95] The total oxygen composition, determined from the O 1s spectrum, equates to ~ 5.5 at.%.

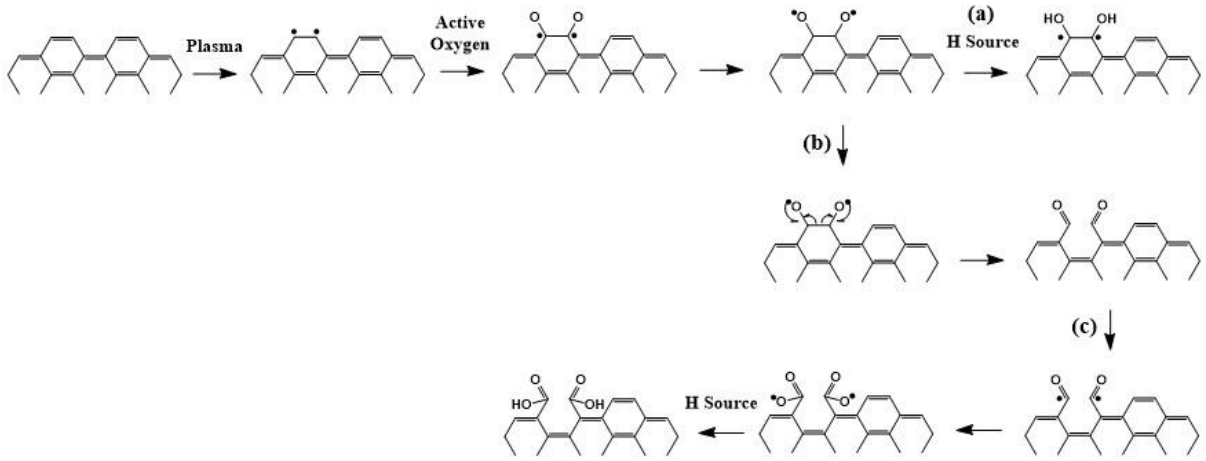

Scheme 1.1 Oxygen plasma processing on a graphitic network to introduce oxygen in the form of (a) C–O and C–OH (b) C=O and (c) O–C=O. Modified from reference [120].

The use of oxygen plasma is effective towards introducing a variety of oxygen functionality in the form of epoxy and carboxyl groups on the basal plane and edges of graphene, where epoxy groups are the most energetically favourable.[87] Covalent attachment of oxygen functionality coincides with the rehybridisation of the carbon of interest, from sp^2 to sp^3 and an increase in the amorphous nature of the graphitic structure.[91,161] As previously mentioned, functionalisation is a valuable method to alter the properties of GBMs. Childres and co-workers investigated the changes in electronic properties of CVD grown SLG on a Si/SiO_2 substrate, after treatment with short pulses of O_2 plasma.[161] They found that the oxidation process was accompanied by an increase in the disorder of the graphitic network, as evidenced by an increasing I_D/I_G ratio. This resulted in an up-shifting of the Dirac point, indicating hole doping. Nourbakhsch and co-workers also utilised O_2 plasma, in the absence of Ar, to functionalise the surface of SLG on Si/SiO_2, synthesised *via* micromechanical cleavage of HOPG. They found that the oxidation process had a large effect on the electronic properties, consistent with the previous findings. In this regard, it was observed that the time of the plasma treatment

influenced the semi-metallic/semiconducting behaviour, such that the bandgap became wider as the extent of functionalisation increased.[152] Duesberg and co-workers also carried out plasma functionalisation on CVD grown SLG and measured the corresponding wetting behaviour of the material, before and after the plasma treatment. In this case, plasma was generated using microwave AC with an O_2 gas stream (100 standard cubic centimetres per minute (sccm)), for a duration of between 10 – 300 seconds, at 133 Pa.[155] It was found that the material became increasingly hydrophilic upon oxidation, as shown by a decrease in the water contact angle (WCA). In addition, the plasma exposure was also found to degrade the electronic properties of the material. For example, cyclic voltammetry experiments revealed that the charging current depleted after plasma treatment.

Nitrogen functionality can also be introduced to the graphitic network through means of NH_3, and more commonly, N_2 generated plasmas.[162,163] Subsequent functionalised materials have shown promise within various applications, including supercapacitors, field effect transistors and lithium ion batteries.[164,165] Plasma initiated nitrogen doping typically introduces between 3 – 10 at.% nitrogen to the graphitic structure and a variety of functional groups can be formed.[151,155,166] Chiu and co-workers investigated the types of functionality present within SLG and 2LG upon treatment with plasma generated from NH_3 gas.[167,168] They observed that various atomic and molecular radicals were generated in the plasma, including H, N, NH and NH_2, which led to the formation of amine groups at edge and defect sites, pyrrole-type nitrogen rings, and quaternary nitrogen or graphite-like nitrogen, as shown in Figure 1.19 (a). These functional groups were found to be both stable in air and under high temperatures (up to 800˚C). Abel and co-workers also confirmed the presence of similar functional groups through treatment of SLG on caesium dihydrogen phosphate and Si wafer substrates with nitrogen plasma.[154] This was generated using a 20 W low-pressure microwave plasma system operating at 13.56 MHz with a N_2/Ar gas mixture in a 9:1 ratio. These conditions were effective in introducing various functionalities in the form of C−O, C=O and chemisorbed oxygen, as well as pyridinic-N, pyrrolic-N, and graphitic-N species.

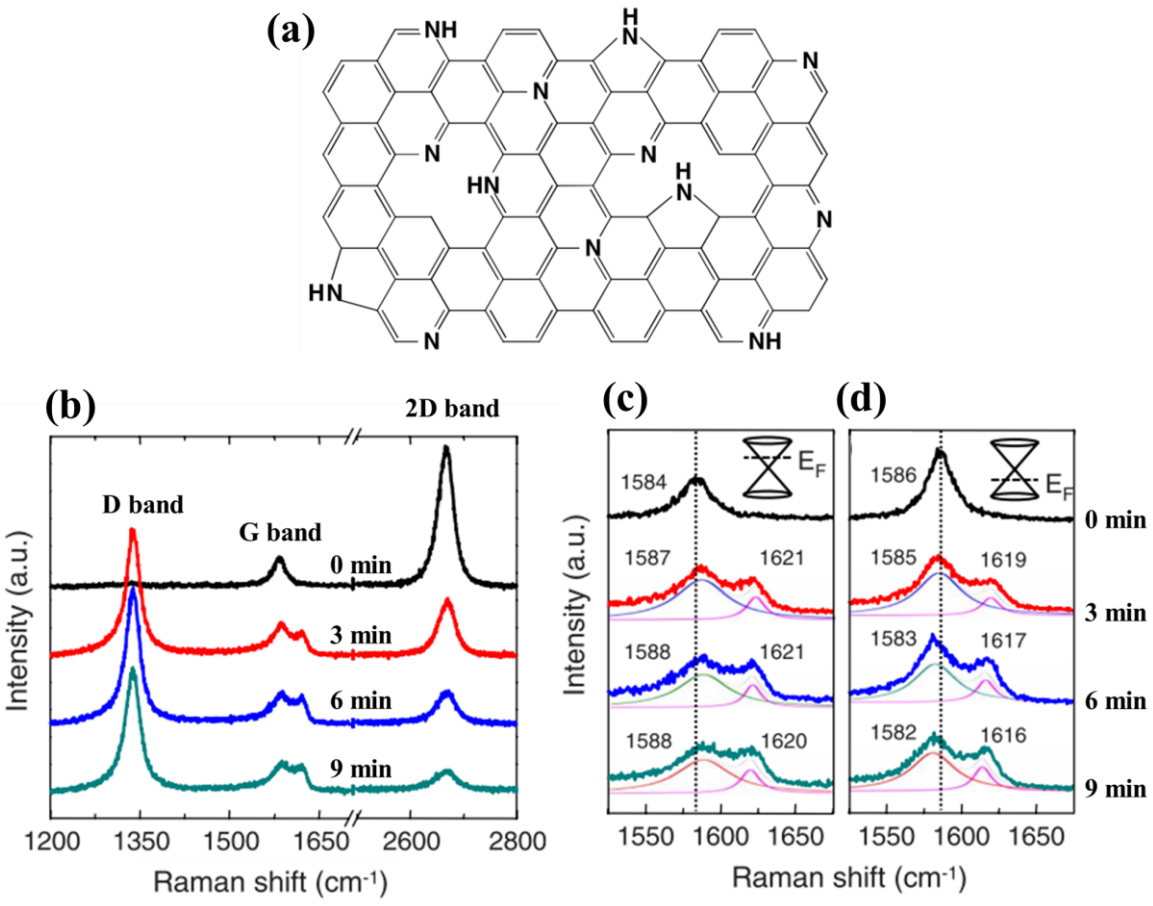

Figure 1.19 (a) Proposed structure of SLG and 2LG treated with NH_3 plasma treatment consisting of various nitrogen functionalities (b) Raman spectra of NH_3 plasma treated 2LG on a Ni substrate after 0, 3, 6 and 9 minutes of exposure and (c) and (d) depict the evolution of the Raman G peak after 0, 3, 6 and 9 minutes of exposure, where the initial Fermi level lies in the conduction band and valence band respectively. Reprinted from reference [167].

Nitrogen functionalised GBMs possess interesting electronic properties and modified band gap structures.[167,169] Nitrogen behaves as an n-type donor and thus, the density of states near the Fermi levels therefore decreases. As such, the Fermi level shifts above the Dirac point to create a gap between the valence and conduction bands. This promotes a decrease in conductivity and subsequently, an improved on/off ratio. Chiu and co-workers utilised Raman spectrometry to investigate the doping level of nitrogen within 2LG on Ni, under NH_3 plasma irradiation. Figure 1.19 (b) – (d) shows how the corresponding Raman peaks vary across a 3-minute period of plasma exposure.[167] A D band is introduced as plasma exposure proceeds, and increases in intensity with increasing exposure, before saturating at 3 minutes. Meanwhile, the 2D peak simultaneously decreases, and continues to decrease even after the D peak becomes saturated. This behaviour is attributed to the presence of excess charges from the dopant, and thus, the

corresponding I_{2D}/I_G ratio provides a measure of the doping level. The I_{2D}/I_G ratio subsequently shifts from 1.7 to 0.7, consistent with the Raman spectrum obtained in electrostatically gated graphene. Bertóti and co-workers investigated and compared the extent of nitrogen plasma functionalisation upon treatment of multi-wall CNTs, FLG and HOPG, at low and high pressures. In their initial report, they treated commercially available multi-wall CNTs with N_2 plasma, generated using RF power of 100 W at 13.56 MHz.[162] This introduced a composition of between 19 – 25 at.% nitrogen into the graphitic structure. More recently, they treated FLG and HOPG with low pressure N_2 plasma, using the same power.[151] This established a negative bias voltage of between 0 and 200 V, resulting in the positive plasma ions bombarding the material with controlled energy. Utilisation of a low bias voltage (≤ 50 V) resulted in the bonding of nitrogen only to pre-existing defects within the materials. As such, a much larger nitrogen incorporation took place within FLG compared to HOPG, due to the existence of more defects. In contrast, increasing the bias voltage (between 50 and 200 V for 10 minutes), promoted the generation of defect sites within both materials, promoting a similar nitrogen incorporation of between 4 – 10 at.% in both samples, as shown in Table 1.2. As such, it is realised that both the sample bias and extent of defects are important variables towards tailoring the extent of functionalisation.

Table 1.2 Comparison of the elemental compositions of FLG (MLGR) and HOPG samples treated at a different sample biases. Reprinted from reference [151].

Sample	Bias (V)	O	C	N
MLGR-0	Pristine	1.6	98.4	–
MLGR-1	0	4.2	89.6	6.1
MLGR-2	50	4.0	90.3	5.7
MLGR-3	100	4.2	89.0	6.7
MLGR-4	200	4.8	85.9	9.3
HOPG-0	Pristine	0.8	99.2	–
HOPG-1	0	5.0	91.2	3.8
HOPG-2	50	5.1	91.1	3.8
HOPG-3	100	5.6	88.9	5.5
HOPG-4	200	6.2	84.3	9.5

It is also possible to introduce hydrogen to GBMs through the means of plasma hydrogenation.[170] In this case, the π bond within the GBM participates in an addition reaction, resulting in the incorporation of hydrogen atoms across the double bonds. A complete 100%

hydrogen coverage of graphene forms a material known as "graphane". This material was theoretically studied by Sofo and co-workers.[171] Later, Elias reported the first example of graphane synthesis, through hydrogenation of exfoliated graphene on a Si/SiO_2 substrate.[172] During this synthesis, the graphene was treated for 2 hours with a low-pressure (0.1 mbar) H_2/Ar gas mixture (1:9 ratio), using a DC voltage between two aluminium electrodes. This route established covalent bond formation between carbon and hydrogen. Interestingly, the properties varied after treatment, where graphane possessed insulating behaviour, in contrast to the zero-band gap semi-metallic behaviour associated with graphene. It was observed that the original metallic behaviour could be restored by annealing the hydrogenated material at 450˚C for 24 hours in an argon atmosphere. Microwave plasma treatment has also been shown to assist the hydrogenation of GBMs. For example, Ray and co-workers treated CVD grown FLG, on a Si/SiO_2 substrate, with hydrogen plasma at 267 Pa, using a power of 150 W at various temperatures.[173] This successfully incorporated hydrogen to the graphitic network. Interestingly, varying the temperature of the plasma treatment resulted in different degrees of functionalisation. The C−H composition was estimated to correspond to 3:1.5:1 (~ 6:3:2) at 50, 100 and 200˚C respectively. This temperature-dependent behaviour was attributed to the penetration ability of hydrogen. It was believed that at lower temperatures (50˚C), hydrogenation only occurred on the surface layer of the FLG, however, at increased temperatures (between 100 and 200˚C), the hydrogen could passivate the surface, resulting in C−H bond formation in the stacked layers as well.

Halogen-based plasma offer an alternative strategy towards the functionalisation of GBMs. Fluorination, in particular, has become a common route towards the formation of derivatives with advantageous properties. Fluorination offers the opportunity for band gap modification.[174,175] For the fluorination of CVD grown graphene, plasma is commonly generated with SF_6, CF_4, XeF_2, fluoropolymers and Ar/F_2, due to their capability in forming fluorine radicals.[153,174–177] The fluorine content can be altered according to the fluorinating agent chosen and the treatment time used. The atomic ratio of fluorine to carbon typically ranges up to ~ 27%, although these values have been shown to rise up to 50% in SLG.[153,177,178] Zhu and co-workers provided an example of the fluorination of CVD grown SLG utilising CF_4 plasma.[179] The fluorine was found to bind to the surface of the graphitic network to form CF_x groups (where x = 1 – 3), as shown in Figure 1.20. It was observed that the functionalisation was more concentrated in some areas compared to others, forming an inhomogeneous coverage. Consequently, a conductive network was able to form in some regions, where charge

transport took place, resulting in electrical transport within the functionalised material. Fluorination reactions are generally fast and can be difficult to control due to their fast kinetics.[180] Furthermore, various bonding types are predicted within fluorinated SLG.[177] The dominant bonding types include semi-ionic bond formation between sp^2 carbon with an isolated fluorine, where fluorine acts as a p-dopant and covalent bond formation between C and F. This latter bond formation exists in the form of poly(carbon fluoride), where covalent C−F bonds alternate in ortho position to one another, on both sides of the graphitic sheet and/or in the form of poly(tetracarbon fluoride) where C−F bonds are in para positions to one another, on only one side of the graphitic sheet. The latter bonds exhibit a character intermediate between semi-ionic and covalent. Robinson and co-workers investigated the properties of fluorinated graphene films, functionalised with XeF_2 plasma.[174] This comprised graphene film grown on Cu foil which was functionalised on one or both sides. When both sides were exposed to plasma, a coverage of 100% fluorine was achieved (CF) and a band gap of 3.07 eV was observed. In contrast, when only one side was exposed to the plasma, a fluorine coverage of 25 % (C_4F) was observed and the material possessed a band gap of 2.93 eV and subsequent transparency. As such, they concluded that the single sided fluorination was effective in providing desirable electronic and optical changes for application in devices. In addition, graphene treated on both sides possessed a C 1s XPS spectrum which comprised of 86 % C−F, 12 % $C-F_2$ and 2% $C-F_3$, where the latter two bonds correspond to bonds at defective sites.

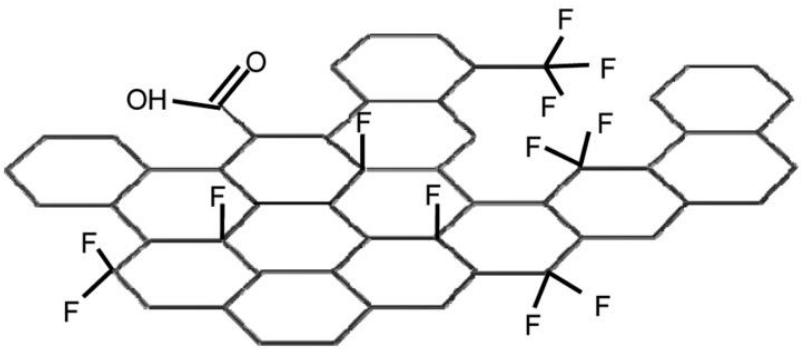

Figure 1.20 Proposed schematic of fluorinated CVD grown SLG. Reprinted from reference [179].

Chlorination is an alternative halogenation route for graphitic networks.[180–184] In contrast to fluorination, the kinetics are much slower and functionalisation tends to proceed to a lesser extent. Wu and co-workers showed that chlorine plasma was capable of doping graphene to

form a p-type material with increased conductivity and a chlorine coverage of 8.5%.[180] Zhang and co-workers improved this degree of functionalisation by utilising plasma generated in the presence of chlorine gas, to functionalise CVD grown SLG and SLG on a Si/SiO_2 substrate formed *via* micromechanical cleavage, for 30 seconds.[185] They achieved a high functionalisation, of up to 45.3 at.% (close to C_2Cl) and found that this coverage could be tuned according to treatment time and DC bias, as shown in Figure 1.21. Longer treatment times resulted in a lower Cl:C ratio, due to them exceeding the critical treatment time (Figure 1.21 (b)). At this critical point, further Cl plasma bombardment resulted in the activation and breaking of C−Cl bonds. At a treatment time of 300 seconds, it was found that a DC bias voltage of 8 V resulted in the maximum Cl functionalisation (Figure 1.21 (a)). This optimal bias voltage was dependent on the treatment time. For example, at 60 seconds, 16 V was optimal to maximise coverage. It was also observed that using a voltage of less than 8 V or over 16 V resulted in relatively low coverages. This was attributed to the interaction between C and Cl being too weak at low biases, whilst at high biases, the plasma was extremely energetic and thus, was able to break many C−Cl, resulting in the activation and desorption of Cl atoms.

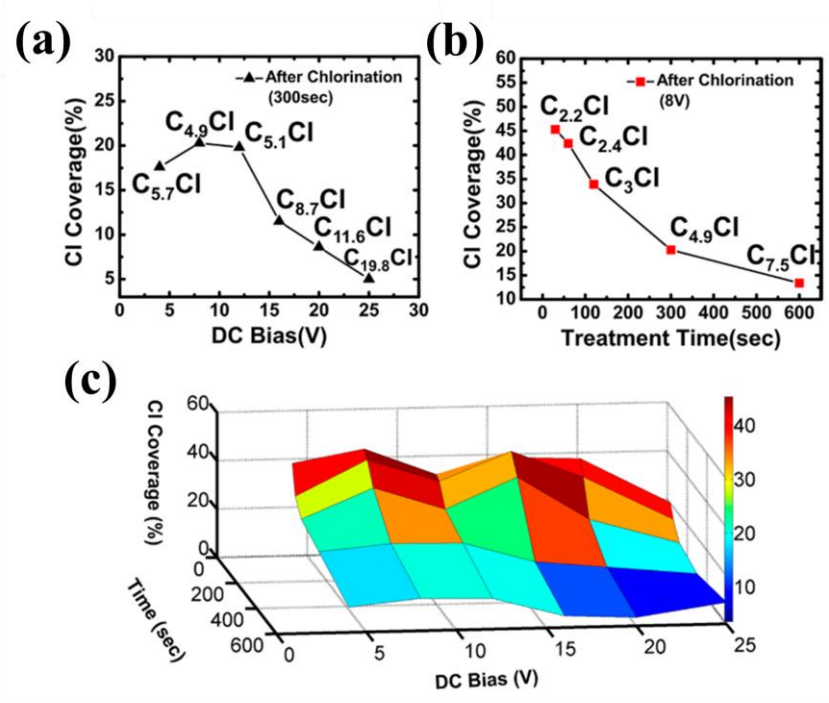

Figure 1.21 Effect of DC bias voltage and treatment time on the C:Cl ratio (a) compares the DC bias to the Cl coverage using a constant treatment time of 300 seconds; (b) compares the treatment time to the Cl coverage using a constant DC bias (8 V) and (c) shows a map of the Cl coverage with changing DC bias and treatment time. Reprinted from reference [185].

Bromination can also be carried out utilising plasma.[186–190] Friedrich and co-workers provided an example of bromination of HOPG.[188] This achieved more than 30 % Br:C ratios, using inductively or capacitively coupled low-pressure plasma. The morphology of the brominated graphene layers caused the plane topography to change, consistent with a rehybridisation of sp^2 to sp^3, from 180˚ to 109˚, as shown in Figure 1.22.

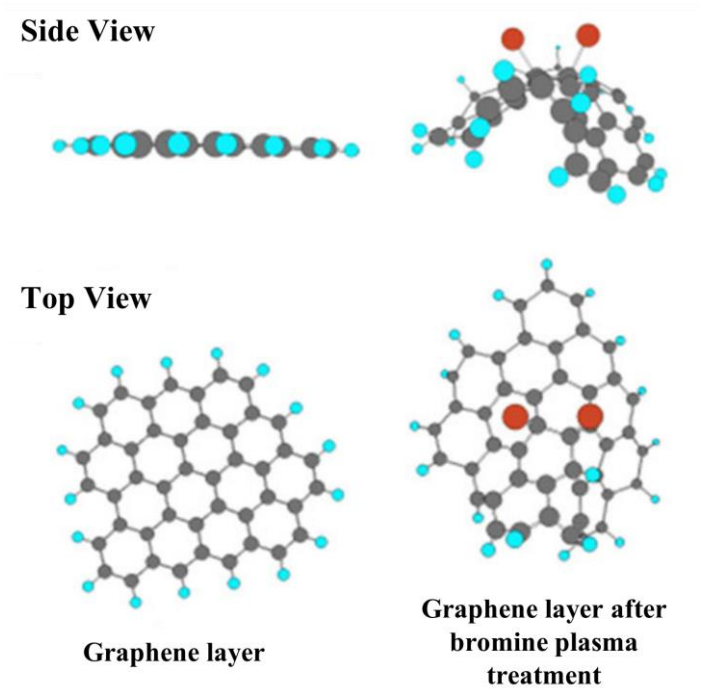

Figure 1.22 A side-view and top view of the proposed structures of a graphene layer before and after bromine plasma treatment. Reprinted from reference [188].

1.9 Functionalisation of GBMs without Plasma

As previously mentioned, covalent attachment can also take place without the requirement for plasma. There are a whole plethora of methodologies which enable functionalisation; allowing the covalent attachment of external moieties to GBMs, containing 1 to several hundred layers, defective or pristine structures and unfunctionalised or already functionalised lattices. Typically, these methodologies involve wet chemical approaches, thus, take place within a solvent medium.[47,191] Among these methodologies exists radical mediated bond formations; a functionalisation route which is commonly utilised for covalent bond establishment.[34,192–200]

For this purpose, diazonium salts are widely implemented radical precursors, due to their ease towards the formation of highly reactive intermediates, and have therefore been utilised to functionalise a range of GBMs. These compounds undergo C−N bond cleavage to eliminate nitrogen gas, resulting in the formation of radicals, which subsequently attack the sp^2 network of GBMs to form covalent bonds, as shown in Scheme 1.2.[192–194,197,201–203] Such steps are typically initiated under thermal or photolytic conditions.[204]

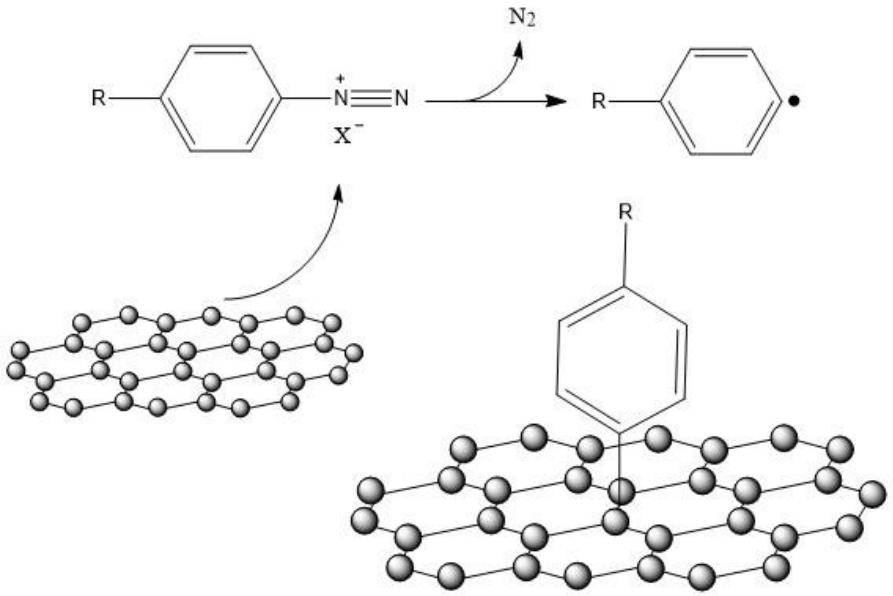

Scheme 1.2 Formation of an aryl radical from a diazonium salt precursor and its subsequent covalent attachment to a graphene layer. R represents the presence of a variable group and X^- represents an appropriate counterion.

Hirsch provided a good example of this functionalisation, as depicted within Scheme 1.3.[194] This work involved the functionalisation of graphite with 4-tert-butylphenyl moieties. Initially, the graphite was reduced with a potassium (or sodium) alloy, generating solvated electrons which activated the graphite and eased the exfoliation of sheets. This negative charge was balanced by the positive group 1 metal ion within the graphite intercalation compound. Subsequently, diazonium salt compounds within the vicinity of these solvated electrons became reduced, promoting nitrogen gas elimination and the formation of a reactive aryl radical. The *in situ* formed aryl radicals were believed to be consumed by covalent addition to the π network of the graphene. Of course, the use of diazonium salts can also be applied to plasma-exfoliated graphitic stacks. Aside of diazonium salts, another common precursor includes benzoyl peroxide, which readily undergoes free radical addition following the

formation of two phenyl radicals upon decomposition.[205] The reaction of benzoyl peroxide with graphite on a silicon substrate was carried out in toluene, using an argon-ion laser beam to photochemically initiate the decomposition of benzoyl peroxide into phenyl radicals. Subsequent covalent bond formation occurred between the graphitic sheets with the phenyl radicals.

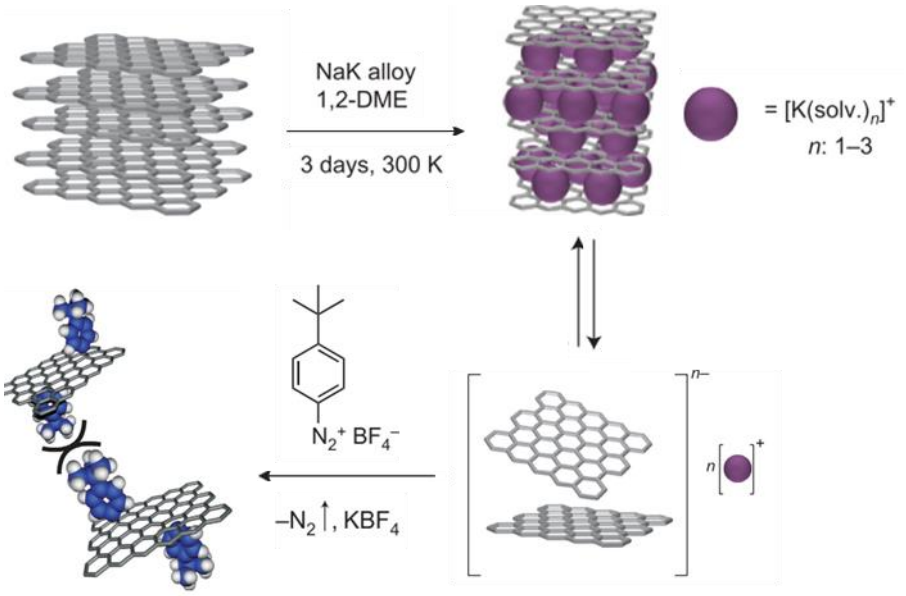

Scheme 1.3 Synthesis of 4-tert-butylphenyl functionalised graphene, synthesised via the intercalation and exfoliation of graphite with potassium ions to form a graphite intercalation compound. This compound then reacts with 4-tert-butylphenyldiazonium tetrafluoroborate to form the functionalised material. Reprinted from reference [194].

Other radical precursors have also been implemented during functionalisation methodologies, including 2,2'-azobisisobutyronitrile (AIBN) and styrene.[206,207] Suslick and Xu reported the synthesis of styrene radicals using high intensity ultrasound radiation to functionalise graphitic layers. They irradiated graphite powder for 2 hours at 0 °C under an argon flow, which afforded simultaneous exfoliation and functionalisation with polystyrene. The subsequent functionalised material contained an approximate weight composition of 18% polystyrene.[206] In a different report, Xu functionalised exfoliated graphitic material with isobutyronitrile radicals, generated through the decomposition of AIBN.[207] This afforded functionalisation, consistent with an isobutyronitrile group attached to 1 in every 50 carbon atoms. This degree of functionalisation related to a weight loss of 10%, as calculated by thermogravimetric analysis (TGA). AIBN has also been implemented as a radical initiator to functionalise

graphene.[208] In this regard, AIBN was used to promote radical formation on maleic anhydride, resulting in its covalent attachment to the graphitic material. A degree of functionalisation consistent with a weight composition of 13.2% maleic anhydride was reported.

Cycloaddition reactions are another common form of functionalisation which are formed upon addition to the π bonds within GBMs, to generate cyclic adducts. A variety of cycloadditions have shown promise for this purpose, including carbene, nitrene and azomethine ylide addition.[25] Furthermore, the graphitic network can also undergo Diels-Alder cycloaddition reactions, acting as both a diene and dienophile.[209,210] Carbenes provide a facile route towards functionalising the sp^2 carbon network of GBMs, behaving as electrophiles to form three membered rings.[47] Carbene units can be generated from various precursors, including chloroform[211] and bromoform.[212] Alternatively, azirine adducts can also react with the sp^2 carbon network to produce three membered rings. The reactive intermediate, in this case, involves nitrene, which is typically generated *via* thermal or photo-decomposition of an azide group.[25] Such a cycloaddition has been exploited within various investigations to functionalise graphene and FLG.[213–217]

It is well known that a small amount of hydrogen functionality typically exists at the edges of GBMs, which allows such materials to undergo electrophilic substitution reactions.[150,218–221] Friedel-Craft acylation is a typical example of such a reaction which has been shown promise in allowing the introduction of an aryl ketone group to the graphitic network, and proceeds *via* an acyl anion in the presence of polyphosphoric acid (PPA)/phosphorus pentoxide (P_2O_5), as shown in Scheme 1.4.[150,220] In this reaction, PPA acts as both an acidic catalyst and as the reaction medium.[220] An acylium ion becomes generated from the respective substituted benzoic acid, during the PPA catalysed protonation of the carbonyl group. Electrophilic aromatic substitution then occurs at C−H sp^2 hybridised edge sites of the graphene material. Alternatively, electrophilic aromatic substitution allows for the sulfonation of CVD grown graphene using chlorosulfonic acid to introduce sulfonate functionality to the edges of the sheets. This graphene sulfonate was further reduced to graphene thiol through the addition of PPh_3 and I_2.[221]

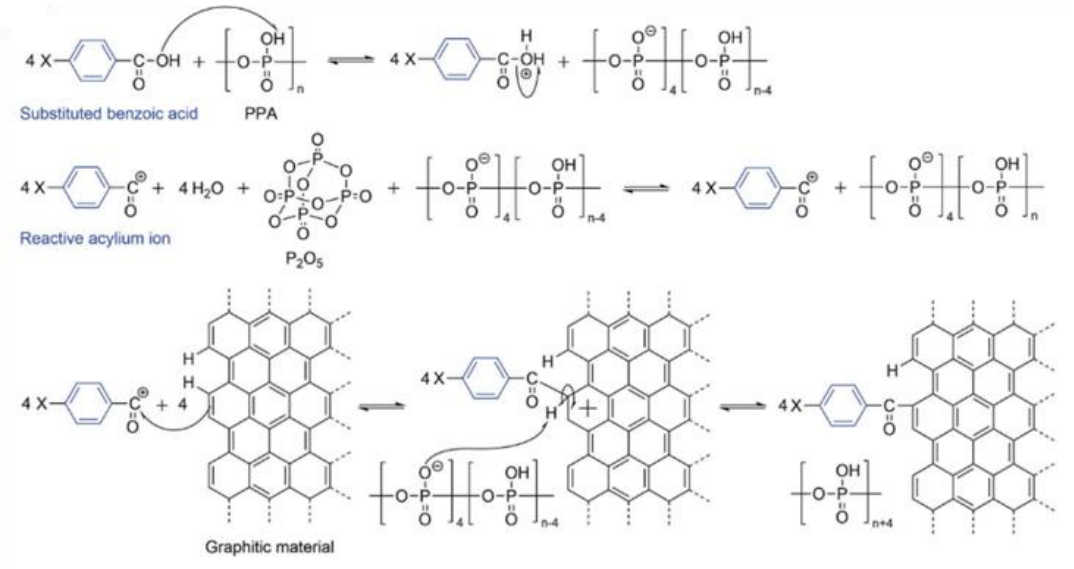

Scheme 1.4 Functionalisation of graphitic material via the Friedel-Crafts acylation reaction with benzoic acid derivatives in the presence of polyphosphoric acid (PPA) and phosphorus pentoxide (P_2O_5). Reprinted from reference [220].

Whilst the carbon network within GBMs is useful in allowing for functionalisation with a variety of species, the presence of oxygen functionality within GO and rGO, and partially oxidised stacks of graphene, provide additional functionalisation strategies, with the possibility for amidation, esterification and silanisation reactions.[200] In the former case, a variety of functional groups have been added to the carboxylic acid and lactone groups on GO, resulting in the establishment of an amide link.[222–224] For example, Kumar and co-workers attached various amine derivatives to GO, through condensation of the amine functionality with the lactone group of GO.[222] These functionalised materials possessed good dispersibility in common solvents, including water, DMSO and DMF. Moreover, esterification reactions take place through the reaction between a carboxylic acid group with a primary alcohol. By using this approach, a variety of functional groups have been added to oxygen containing GBMs, including ethylene glycol, 1,2-propylene glycol, butylene glycol, 1,6-hexylene glycol, neopentyl glycol, glycerol, pentaerythritol, 4-hydroxy-4′-n-pentylbiphenyl and meta-toluic acid.[225–227] In some cases, the carboxylic acid functionality upon GBMs combines with the hydroxyl group of the reacting moiety, whilst in others, the GBM's hydroxyl groups reacts with that of the carboxylic acid group of the reacting moiety. Silanisation reactions involve the attachment of silicon to hydroxyl groups. A number of different silane agents have been investigated for the purpose of functionalising GO, including, aminopropyltriethoxy silane (APTES), triethoxymethoxysilane, 3-glycidyloxypropyltrimethoxysilane,

vinyltrimethoxysilane and triethoxysilane.[228–231] Silanisation proceeds *via* a hydrolysis reaction, where typically, loss of aliphatic groups occurs from the silanising reagent.

1.10 Surface Area and Porosity in Plasma-Exfoliated Graphitic Material and Analogues

Surface area and porosity describe characteristics of materials. Surface area describes the total area of all of a material's surfaces, and thus, is important for determining its properties and behaviour with external species. Pristine SLG exhibits a large theoretical surface area of 2630 m^2/g and many other GBMs also possess large surface areas up to this value.[232] As such, these materials are desirable for providing additional surface for the interaction with chemical species and maximising permeance.[18,232] These properties allow such materials to prevent deformation and withstand vigorous environments. Consequently, GBMs have found extensive application within molecular separations,[233] energy storage[234] and sensor technology.[235,236]

The large surface area of SLG originates from the access to the whole two-dimensional structure. In many stacked analogues, this access is not enabled to many of the individual layers, and thus it is the outer dimensions of the stacks, holes within the graphitic layers and spaces between them, which govern the surface area. Pores describe the spacings between openings within the structure. Pores can also be distinguished according to their size, such that pores with dimensions of less than 2 nm, between 2 − 50 nm, or beyond 50 nm correspond to micropores, mesopores and macropores, respectively.[237–239]. Micropores can be further divided into super- (> 0.7 nm) and ultra-micropores (< 0.7 nm).[240] Pores can also be categorised according to their types. In the context of GBMs, these typically fall into the following categories, including: *in-plane pores*, *interlayer pores* and *three-dimensional (3D) porous networks*, where the latter of these may constitute both in-plane pores and interlayer pores. Figure 1.23 outlines the types of pores present within GBMs, their associated size distributions and corresponding relevant applications.[241] In-plane pores describe holes within the graphitic sheet and are commonly introduced *via* various approaches, including electron beam ablation,[242,243] focused ion beam irradiation,[244] ultraviolet-induced oxidative etching,[245] ion bombardment followed by chemical oxidative etching,[246] oxygen plasma etching,[119] laser irradiation[247] and MnO_2 etching,[248] as outlined in a review by Yang and co-workers.[241] The

manufacture of in-plane pores has found promise within the context of membranes. For instance, the generation of in-plane pores within SLG *via* oxygen plasma etching (20 W), has provided a material with application within desalination.[119] In one example, it was found that exposure time between < 1 to 6 seconds afforded porous SLG membranes containing nm-sized pores, which provided a nearly 100% salt rejection rate to ions, including K^+, Na^+, Li^+ and Cl^-. A rapid water transport of 10^6 g m^{-2} at 40 °C, using hydraulic pressure difference, was achieved through these membranes.

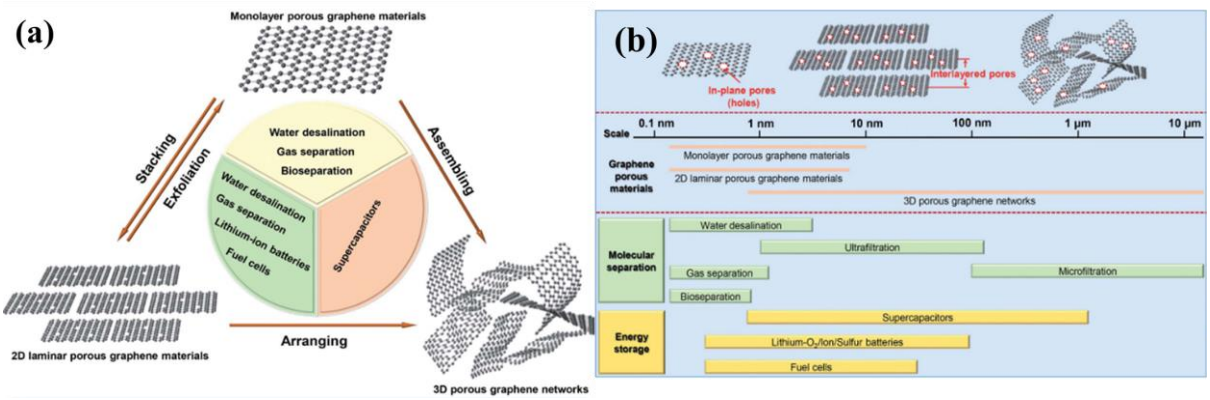

Figure 1.23 (a) Nanoporous GBMs classified according to whether they possess in-plane pores, interlayered pores or 3D porous networks with broad applications of the materials and (b) applications associated with GBMs of varying pore sizes. Reprinted from reference [241].

Kostoglou and co-workers also analysed plasma-exfoliated stacks, generated through DBD plasma irradiation of Ar and O_2 gas, and found that they possessed a high surface area and subsequent high H_2 storage capacity. In accordance with Chahine's rule[249,250], a large surface area is proportional to an increase in the hydrogen uptake. In addition, the pores act as "strong adsorption sites" due to overlapping potential fields from opposite pore walls. This resulted in an increased H_2 storage.[160] Their work also found that the addition of platinum promoted the strengthening of solid-H_2 interactions with a higher heat of adsorption. These stronger interactions improved the hydrogen storage capabilities of the material further.

Table 1.3 Surface area and porosity data associated with plasma-exfoliated graphitic stacks. Reprinted from reference [93].

Materials	S_{BET} [m^2/g]	S_{Micro} [m^2/g]	S_{Micro}/S_{BET} [%]	V_{Micro} [cm^3/g]	W_{QSDFT} [nm]
FLG-400	428.29	170.95	39.91	0.076	0.723
FLG-800	777.34	299.11	38.48	0.132	0.785

Interlayer pores describe the spacings between graphene layers, and commonly make up slit pores. Of course, the arrangement of GBMs containing an orderly alignment of graphitic materials, creates spacing between the layers, typically possessing distances of around 0.334 – 0.335 nm.[29] As such, during adsorption-desorption experiments, adsorbate molecules are unable to penetrate the layers, due to their kinetic diameters exceeding this size. For example, the kinetic diameter of nitrogen adsorbate exists between 0.364 – 0.380 nm.[251–253] As such, it is unsurprising that graphite exhibits a small surface area of 0.6 m^2/g.[254] Slit pores are therefore created through an expansion of orderly aligned stacked layers, such that adsorbate molecules can access the pore. Of course, the presence of numerous van der Waals forces between orderly aligned graphene layers gives rise to the tendency of GBMs to aggregate.[232,253] Generally speaking, the restacking of graphitic layers is undesirable for the creation of large surface area GBMs, and strategies to maintain separation are imperative. One way to prevent restacking is to introduce defective regions, which weaken the strong van der Waals.[95,255] Another common strategy used to tailor the slit pores within these materials is through the addition of external moieties to cause expansion of layers.[256,257] In this regard, templating has been employed to introduce bulky moieties between layers. Upon expansion of the layers, the templates are subsequently removed. For example, Fang and co-workers synthesised a highly wrinkled porous graphene film, using Fe_3O_4 nanoparticles as templating agents.[257] Through removal of these templates, the average pore size was found to be 27.7 nm, corresponding to slit pores between individual rGO layers and stacks of layers. A large BET surface area of 383 m^2/g was also achieved. Similarly, moieties may also be added permanently to the structure. Pillaring involves the addition of covalently/non-covalently bound external moieties to the interlayer regions of multilayer graphitic material, causing expansion of individual layers or multilayer stacks, and a subsequent increase in surface area.[253,256,258–267] A range of pillars have been implemented to GBMs including diboronic acid,[268] 1,4-diethynylbenzene,[258] chitosan,[269] iron oxide,[270] aminoalkanes[271–273] and tetrakis(4-aminophenyl)methane molecules.[259,260] In the

latter example, tetrakis(4-aminophenyl)methane molecules were inserted to GO, causing pillaring of the layers. Upon thermal annealing reduction, the rGO network was pillared, so that restacking was prevented and slit pores of 1.2 nm in size were created.[259,260]

Undoubtably, a large amount of work has been conducted on the tailoring of pores within GBMs. Investigating the porous structures is essential to understanding the nature of the material, and can have large implications on the subsequent applications.[241] Further to this, the development of strategies to tailor these porous structures is extremely beneficial to advance their scope of application. Unfortunately, limited research has been reported regarding the porous structure within the plasma-exfoliated materials incorporated into this thesis.[93] Without this fundamental understanding, efforts to tailor these porous networks becomes extremely challenging.

1.11 Applications of Plasma-Exfoliated Graphitic Materials and Other GBMs

The use of stacked graphene analogues have found application in a variety of fields.[144,274] Many of which are depicted within Figure 1.24.[275] For example, the application of GBMs within electronic devices has shown promise due to their high electron mobilities. The use of GBMs within conductive inks also shows great potential for creating the electrical pathway required across printed, flexible electrical devices.[276] For example, Kilduff and co-workers demonstrated that plasma functionalised GNPs, produced by Haydale, could be combined with polymer resin, to fabricate effective conductive inks for electrical devices.[96,277] The NH_3-plasma treated GNPs were mixed with thermoplastic polyurethane in diacetone alcohol and the subsequent composite showed desirable rheological properties for this application. The incorporation of graphitic material within conductive inks offers several advantageous. Many GBMs are relatively cheap and chemically inert, and can be functionalised to tailor their electronic and dispersive properties.[278]

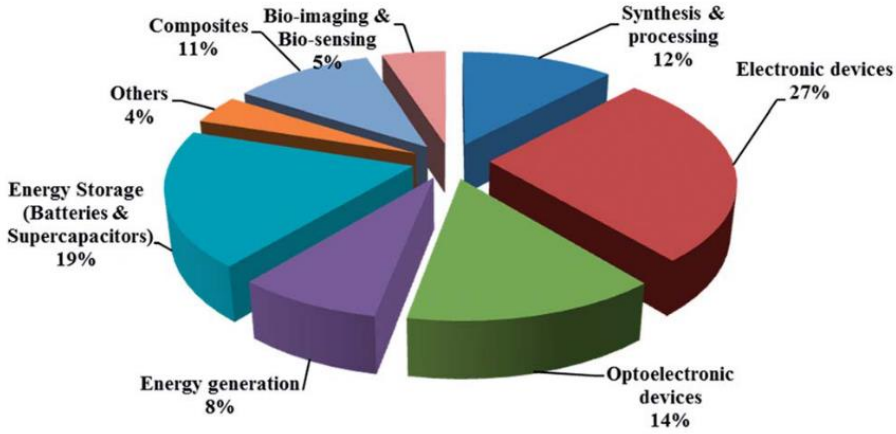

Figure 1.24 Various applications of GBMs. Reprinted from reference [275].

Furthermore, the atomic thickness and large surface area associated with GBMs, consisting of narrow thickness distributions, enables them to be highly sensitive to changes in the local environment, providing an indication of analytes present, and thus, granting them the ability to be used in sensor technology.[279] Their high surface areas are also advantageous within the context of electrodes. Doped GBMs have been investigated for their potential as both anodes and cathodes within fuel cells. Redox reactions take place at these electrodes, thereby, creating electric currents, which can be used to power desired devices. Such electrode materials could serve as cheaper alternatives to platinum.[280] In addition, GBMs have also been investigated for their application within the biomedical industry. The large surface area and biocompatible properties offer great potential in the area of drug delivery, allowing these materials to complex with drug molecules easily.[281] There are many applications which exploit the exciting properties associated with GBMs. Among these, composite applications are one of the most common. In this context, GBMs have been exhaustively investigated for their ability to enhance the strength of other materials, to form composites within industries. An example of such an industry which benefits from strong, corrosion-resistant composites for structural and engine components, is the aerospace industry. It has been shown that the incorporation of graphitic material improves the fracture toughness of silicon nitride ceramic matrices by 235%.[282] Jasquez and co-workers also provided an application of GBMs for strength enhancement. They showed that plasma functionalised graphene stacks, consisting of 20 layers and less and oxygen functionality, were effective in providing cement reinforcement.[137] It was found that the addition of 0.5 wt.% of the material resulted in a 56 % increase in the compressive strength of the cement mortar, compared to without the graphene material. The enhancement of these

mechanical properties was attributed to the high aspect ratio of the graphene material, therefore, allowing it to act as a nucleation site of the cement phase and aiding in cement hydration. In addition, the presence of small particles allowed them to act as nano fillers, which densified the structure, as shown within SEM images (Figure 1.25).

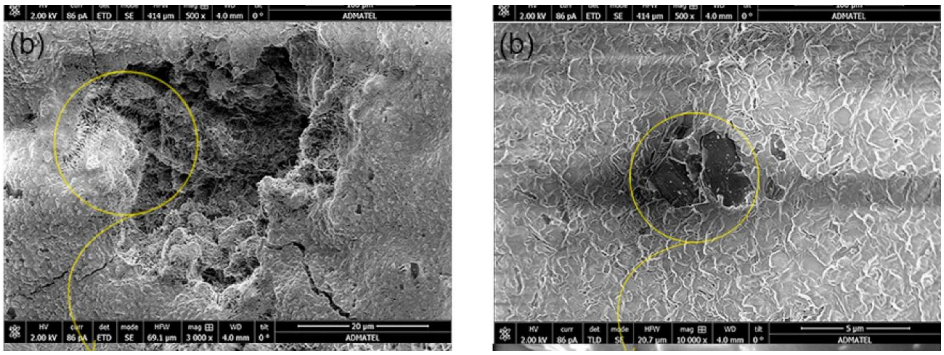

Figure 1.25 SEM image of unreinforced cement mortar showing pores and voids (left) and reinforced cement mortar containing 0.5 wt.% of functionalised plasma exfoliated graphitic material possessing much smaller pores and voids. Reprinted from reference [137].

Despite the overwhelming research which has been undertaken to apply GBMs for profitable application, it should be noted, that many applications investigated within the literature are still associated with laboratory-scale research, rather than commercial applications. Furthermore, many applications portrayed within the media consider that of SLG, rather than multi-layered stacks or their functionalised forms. Within a laboratory setting, the properties of GBMs have been extensively researched, and a whole plethora of applications have been proposed which exploit these. There is still, however, some significant progress needed to push GBMs through to their commercial breakthrough. Of course, delays in a material's market breakthrough are not uncommon and new materials often suffer substantial time delays between their initial discovery and commercial utilisation.[283] Furthermore, significant challenges still remain for GBMs; particularly those which relate to large-scale synthesis of high quality graphene, processing and characterisation. Despite this, however, recent years have seen several applications coming to market, particularly within the context of composites; taking advantages of the light weight, flexibility, and mechanical strength associated with graphene and many of its functionalised and stacked counterparts. Examples include a tennis racket developed by *Head*, which consists of a composite of carbon, graphene and the polymeric tubular material, Koroyd. The company claim that the addition of graphene provides the racket's shaft with

enhanced strength and lightweight properties, as well as delivering a better distribution in weight.[284] Other sport related products include graphene enhanced running trainers, manufactured by the company *inov-8*, in collaboration with The University of Manchester. The incorporation of graphene enhances the strength, elasticity, and wear of the rubbers within these products.[285] Furthermore, the UK-based company, *Versarien*, launched the graphene enhanced safety face mask, in response to the Covid-19 outbreak. These masks contain a graphene-based polymeric material, which prevents the passage of aerosol transmission of SARS-CoV-2.[286] It is also advertised that the masks can be sterilised through sunlight exposure. This ability is assigned to the light-absorbing capabilities of graphene, resulting in the establishment of high temperatures, which inactivate most viruses.

Within the next chapter, an insight to the characterisation of GBMs is provided. Details relating to the commonly exploited characterisation methods is outlined, and the conditions used during analysis of NP materials, within the current work, is described.

2 Characterising Graphene-Based Materials

The characterisation of GBMs is fundamental towards understanding their nature and properties. The contribution of various characterisation techniques provides an insight to the structure, morphology and elemental composition of any given material and such techniques have been examined in detail within the literature.[287–293] Many of the common characterisation techniques used within this work are described with this chapter, with relevance to their significance towards the analysis of GBMs. These characterisation techniques can be broadly divided into three categories, as depicted within Figure 2.1, encompassing imaging, spectroscopic and analytical techniques.

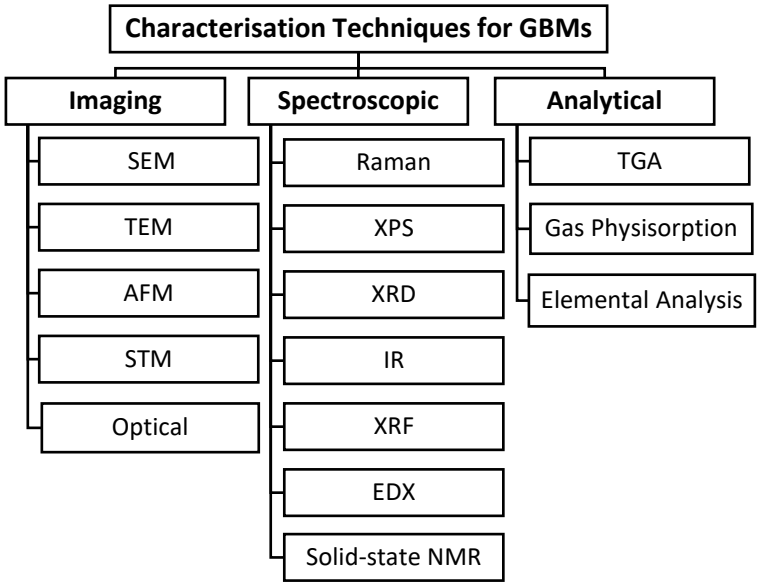

Figure 2.1 Diagram outlining some of the key techniques used for GBM characterisation, categorised broadly as imaging, spectroscopic or analytical techniques.

Imaging techniques incorporate a range of microscopic methods, which offer an understanding of the morphology and topography of a sample. As such, it is possible to determine the particle size, shape, and structural features. For instance, transmission electron microscopy (TEM) can be applied to view the number of graphene layers within a NP stack, whilst scanning tunnelling microscopy (STM) enables visualisation of dopants within the graphitic lattice. Scanning electron microscopy (SEM) and optical microscopy enable observation of the surface morphology and size distribution of particles, whilst atomic force microscopy (AFM) allows a three-dimensional image of the topographical features. Although imaging techniques may not

offer quantitative information regarding a sample, they allow for observation of the material's morphology and structural features, providing an insight to the nature of the GBM.

Spectroscopic techniques employ electromagnetic radiation to interact with matter and offer significant information regarding the structure and elemental composition of a GBM. For instance, X-ray photoelectron spectroscopy (XPS) provides rather detailed information of the chemical environment of specific elements at the surface of the sample to understand the proportion of elements and their bonding types. Raman spectroscopy, on the other hand, is used to examine the graphitic structure and the level of defects, which becomes especially useful when quantifying the number of layers and degree of functionalisation within GBMs. X-ray diffraction (XRD) is used to gain more detail on the interlayer spacing and orientation of planes. This is useful for determining stacking sequence, stack dimensions and uniformity of the material. Infrared spectroscopy (IR) is commonly implemented to analyse the bonding types present within materials, whilst energy dispersive X-ray (EDX) analysis and X-ray fluorescence (XRF) also enable calculation of the elemental composition of a material. EDX is commonly executed in conjunction with SEM or TEM. Lastly, solid-state nuclear magnetic resonance spectroscopy (NMR) provides information relating to various nuclei environments, allowing for probing of chemical structures. Within this context, ^{13}C is particularly useful for GBMs, whilst ^{1}H, ^{19}F, ^{15}N, ^{29}Si and other NMR active nuclei can also be useful for many functionalised analogues.

The final category relates to analytical techniques, which enable the characterisation of material but do not exploit electromagnetic radiation or imaging processes. These are related to the thermal stability, elemental composition and porosity of the material. Thermogravimetric analysis (TGA) is commonly implemented to GBMs to analyse their behaviour during thermal decomposition. This can provide evidence of the loss of specific functional groups which are either covalently or non-covalently bound within the sample. Elemental analysis also provides an indication of the elemental composition of a GBM, relying on the combustion of elements: carbon, hydrogen, nitrogen and sulfur into carbon dioxide, water, nitrogen gas/nitrogen oxides and sulfur dioxide, respectively. In addition, some instruments allow for oxygen composition analysis by measuring the quantity of carbon monoxide gas within an inert atmosphere. Gas physisorption experiments allow for the investigation of the surface area and porosity of the material. This is particularly useful during the synthesis of functionalised GBMs with enhanced surface areas.

Within the work presented in this thesis, a handful of these techniques are frequently implemented to characterise NP materials and their modified counterparts and assist with an understanding of their functionalisation mechanisms. These include, SEM, TEM, AFM, Raman spectroscopy, XPS, XRD, TGA, NMR, mass spectrometry and gas physisorption measurements. An overview of these techniques is therefore provided within this chapter, with particular focus towards the technique's theory and its application within the context of GBMs. Information relating to a vast array of characterisation techniques, as well as the remaining techniques within Figure 2.1, can be accessed within the literature.[287–293] Furthermore, the conditions and instrumentation associated with the characterisation methods used within this work are specified within the final section of this chapter.

2.1 Analysing Morphology using Microscopy

2.1.1 Scanning Electron Microscopy and Transmission Electron Microscopy

SEM and TEM are powerful techniques to discern the morphology of GBMs, revealing information relating to the structural features, lateral dimensions, and the assembly of particles. During operation, a high-energy beam of electrons is focused upon the sample, causing a number of interactions to take place.[292] As depicted within Figure 2.2 (a), Some electrons are transmitted through the sample, and are therefore unscattered, whilst other electrons become elastically or inelastically scattered. These phenomena are exploited during TEM imaging. In addition, electrons also become backscattered, forming backscattered electrons (BSEs) due to elastic collisions with the sample, resulting in a change in the electron's trajectory (Figure 2.2 (b)). Furthermore, the incident beam can knock out an electron from a core shell of the atom, resulting in the emission of a secondary electron (SE) (Figure 2.2 (c)). SEM typically generates images from the latter two scenarios where SEs are responsible for information relating to the morphology, topography and contrast within the surface regions, whilst BSEs are useful to differentiate between different phases, since they originate from much deeper within the sample. SEs are generally used more commonly than BSEs for imaging purposes. In addition to these phenomena, characteristic X-rays and Auger electrons are also emitted. If the inner

shell electrons of atoms become ejected, outer shell electrons fill the inner shell vacancies, resulting in an energy surplus (Figure 2.2 (d)).[291] The shell in which the electron is removed from can be defined such that the shell closest to the nucleus is the K shell, followed outwards by the L, M, N, O, P and Q shells. This energy surplus results in emission of X-rays or Auger electrons. The emission of X-rays differs for each element; hence the elemental composition of a sample can be obtained through their detection. This is the principle of EDX analysis, which can be used in conjunction with both SEM and TEM to provide elemental composition data. Moreover, visible light is created by catholuminescence phenomena, in addition to continuum X-ray emission (Bremsstrahlung X-rays) (not shown).[294] The transmitted electrons including unscattered, elastically scattered and inelastically scattered electrons contain the majority of the information during TEM. As such, both SEM and TEM focus on different phenomena, resulting from electron beam interaction with a sample. Furthermore, the wavelength and accelerating voltage of the radiation used differs for both types of microscopy, typically corresponding to respective values of 0.0080 nm and 20 kV for SEM and 0.0028 nm and 200 kV for TEM, depending on the working distance of the instrument.[290] For effective TEM analysis, samples must be thin enough to allow for penetration of electrons. In the context of GBMs, flakes are commonly analysed for their dimensions using this method, and each flake is analysed consecutively. This is because there is a relatively small viewing area associated with TEM, and thus, multiple flakes cannot typically be analysed at one time.[292] Some TEM instruments allow for high-resolution TEM (HRTEM) imaging which enables individual layers within GBM samples to be visualised. This is particularly useful to quantify the interlayer spacings and number of layers within a GBM. For example Lee and co-workers utilised HRTEM to discern the number of layers within several stacked graphene layers and SLG, as shown in Figure 2.3.[295] The grey and white regions provide evidence of individual layers, which were subsequently shown to correspond to SLG up to FLG samples containing 8 layers.

In contrast to TEM, SEM is only restricted on the size of the sample which can enter the chamber. As such, SEM imaging is particularly useful to analyse large areas of specimens at various magnifications, providing an insight to the GBM flake size, morphology and distribution and has been utilised in many published work.[293] The resolution capability of SEM is inferior to TEM, allowing for features of 1 nm to be distinguished. On the contrary, features of 0.1 nm are typically identified within TEM.[290]

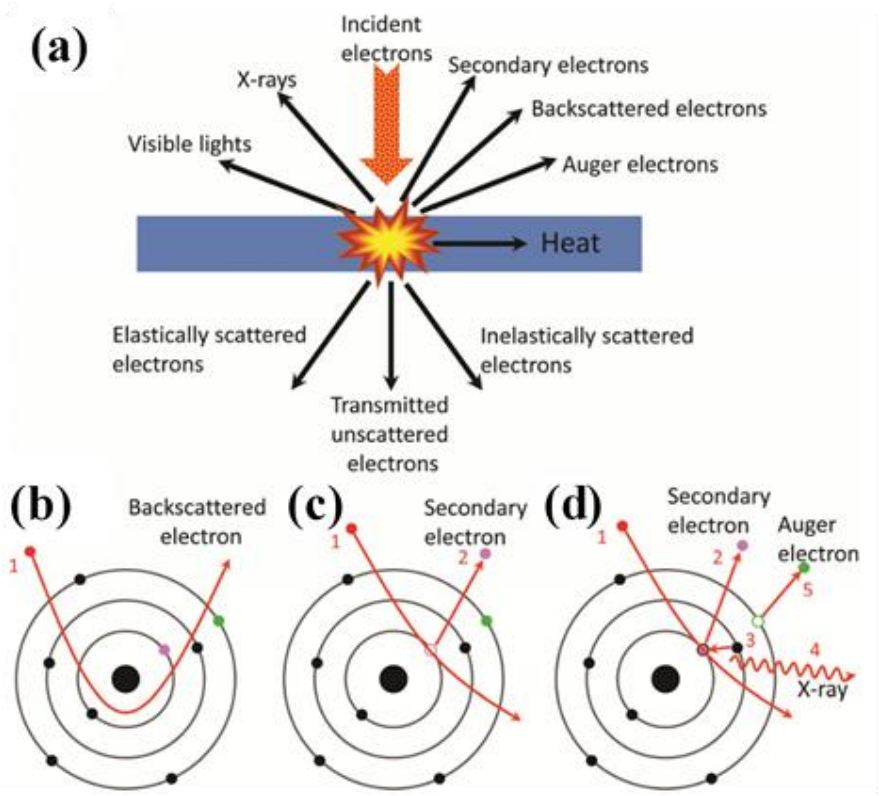

Figure 2.2 (a) Schematic illustrating the various interactions resulting from electron beam irradiation onto a sample. (b), (c) and (d) outline the interaction of the incoming electron with the nuclei of an atom, resulting in the formation of a backscattered electron, a secondary electron and a secondary electron, an Auger electron and X-ray production respectively. Reprinted from reference [292].

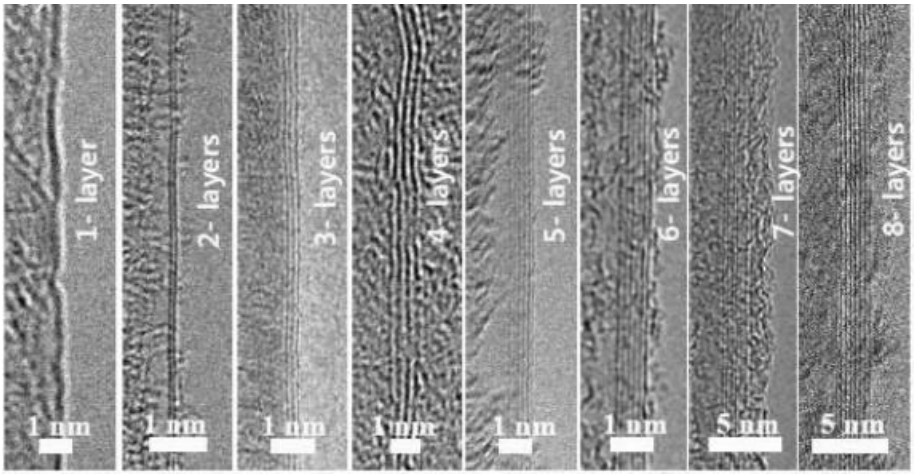

Figure 2.3 HRTEM images of various GBM samples corresponding to SLG, 2LG, 3LG and FLG containing 4 − 8 layers (left to right). Reprinted from reference [295].

The instrument set up of SEM and TEM is depicted in Figure 2.4.[290] Within both instruments, the electron source is positioned at the top of the microscope and electrons are accelerated through the microscope and towards the sample, through a series of lenses. Within TEM, electrons which are transmitted through the sample towards a fluorescent screen, where an image is generated, typically using bright field mode.[296] This mode depicts dark regions, where electrons have not passed through the sample due to the dense nature of these areas resulting in the scattering or absorbing of a large proportion of electrons. Bright regions can also be observed where electrons do not become scattered and penetrate the entirety of the sample. Grey regions may also be seen where electrons interact with the sample or become scattered to different extents. During SEM, electrons reach the sample, and undergo the aforementioned phenomena. As such, SE, BSE and EDX detectors are positioned suitably to detect the presence and quantity of their respective electrons and X-rays, and a reconstructed image is generated.

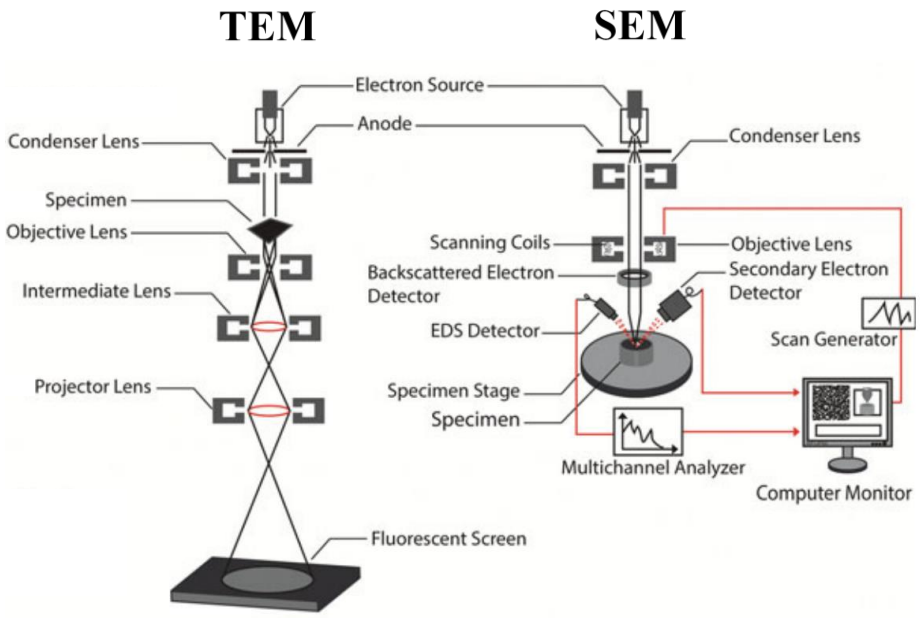

Figure 2.4 Schematic of TEM and SEM instruments outlining some of the main conponents. Reprinted from reference [290].

2.1.2 Atomic Force Microscopy

AFM is another example of an imaging technique and provides a three-dimensional profile of the surface of a material. As such, the surface topography of the material can be investigated. The principle of AFM relies on the force measurement between a sharp probe tip, supported

by a flexible cantilever, and the sample surface, as shown in Figure 2.5 (a). This force measurement depends on the distance between the probe tip and sample surface and relates to Hooke's Law (Equation 2.1) where F is the force between the probe tip and the sample, k is the spring constant and x is the distance of the cantilever deflection. As the probe tip scans over the surface, a feedback system is responsible for achieving high resolution during imaging and avoiding sample damage. This system involves the use of a laser beam and a position-sensitive photodetector (PSPD). As tip-surface interactions occur due to cantilever deflection, as well as changes to oscillation amplitude, frequency and phase, the position of the reflected laser spot on the PSPD changes in respect to the setpoint.[297] The PSPD detects these changes and a feedback loop is used to promote a corrected voltage signal to maintain the probe tip-sample interaction at the setpoint. These interactions can be used to generate a map of surface topography.

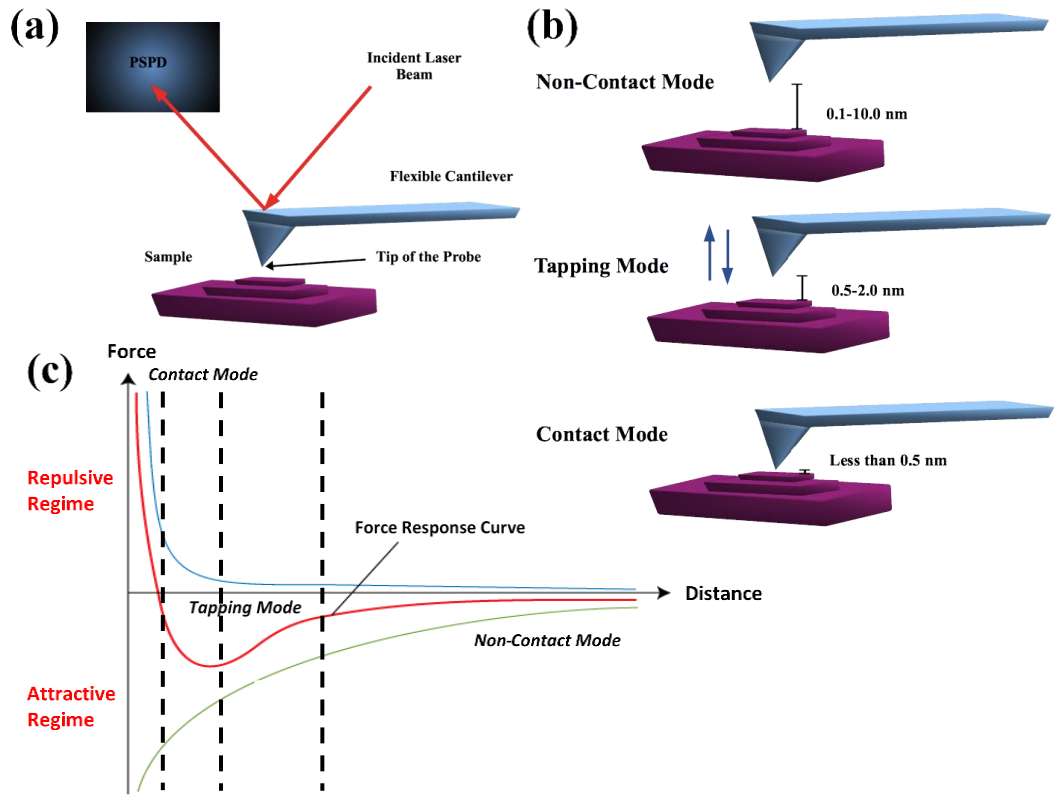

Figure 2.5 (a) Diagram of AFM instrument schematic and (b) various modes of AFM operation including non-contact, tapping and contact mode with the respective distance between the cantilever and sample surface. (c) depicts a force-distance curve outlining how the attractive and repulsive regime combine to form a force response curve.

$$F = – k x$$

Equation 2.1 Hooke's Law.

There are three primary modes of AFM operation which differ due to their distance between the cantilever and the sample surface (Figure 2.5 (b)).[297] A force curve can be used to summarise the types of modes and the interactions which take place within each, as shown in Figure 2.5 (c). Initially, when the probe tip resides far from the surface, the interaction forces are zero, and hence no repulsive or attractive regime takes place. As the tip is brought closer to the surface there are attractive van der Waals forces which cause the cantilever to deflect towards the sample which is measured by non-contact mode. Non-contact mode therefore refers to a static mode where the probe tip and sample are situated relatively far away from one another (approximately 0.1 – 10 nm). During operation, the tip never makes contact with the sample, but oscillates over it at its resonance frequency, and the oscillation amplitude is kept constant. As the tip and the sample interact, van der Waals forces result in attractive interactions and a feedback loop monitors changes in amplitude resulting from this. As the probe is brought closer towards the surface, there are both attractive and repulsive regimes taking place, and the tapping mode is used. This refers to a dynamic mode, where the probe tip and the sample are close to one another (approximately 0.5 – 2.0 nm). During operation, the cantilever oscillates at its resonant frequency, but the probe tip lightly taps on the surface, making contact each time. A constant oscillation amplitude is maintained for constant tip-sample interaction. This mode also eliminates frictional forces by intermittently contacting the surface and oscillating with sufficient amplitude to prevent the tip from being trapped by contaminants. As the distance between the probe tip and sample decreases further, repulsive van der Waals forces becomes dominant, and the cantilever deflects away from the sample. These repulsive forces are measured by contact mode. Here, the probe tip and the sample are less than 0.5 nm from each other. This mode therefore takes place within the repulsive van der Waals regime, as the electronic orbitals overlap. A constant cantilever deflection is maintained using feedback loops, so that the force between the probe and the sample remains constant. Many samples may become damaged by this method, and thus the image may be susceptible to distortion. All modes have shown success for GBMs.[298–300] AFM is extremely useful for analysing the lateral dimensions and thickness of GBMs, and was applied to the first isolated graphene material.[301]

In addition, it can also be used to quantify the presence of additional functionality on the surface of a GBM. For instance, Huang and co-workers utilised tapping mode to acquire an AFM image of a single layer of GO, as shown in Figure 2.6.[302] The corresponding height cross-sectional profile provided evidence of a layer thickness of 1.2 nm. This characterisation was consistent with successful oxidation of the material.

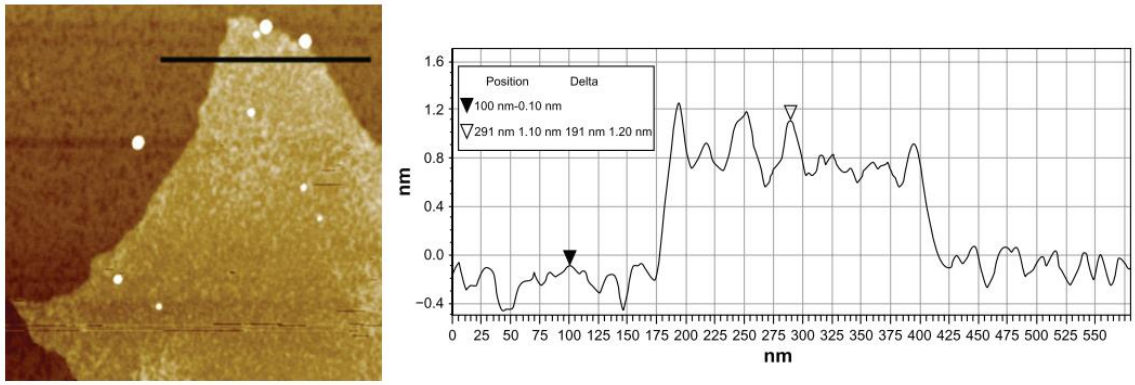

Figure 2.6 AFM image of a single layer of GO on a freshly cleaved mica substrate (scan area: 1 µm × 1 µm) (left) and corresponding height cross-sectional profile, acquired using tapping mode (right). The average thickness of the GO layer corresponds to 1.2 nm. Reprinted from reference [302].

2.2 Analysing Graphitic Structure

2.2.1 Raman Spectroscopy

Raman spectroscopy is a type of vibrational spectroscopy which relies on the scattering of light during vibrational excitations. Molecules can exist in various vibrational energy levels, however, tend to exist in the lowest energy level; denoted the ground state ($\nu = 0$) and only few molecules exist in higher energy states, denoted as ν = 1, 2, 3… (Figure 2.7). When monochromatic light is irradiated on a sample, molecules may absorb it or scatter it, as summarised in Figure 2.7.[303] The absorption process is exploited to identify functional groups during infrared spectroscopy, whilst the scattering phenomena is utilised during Raman spectroscopy. During scattering, the molecule becomes excited to a virtual state which is equal to the energy exhibited by the incoming monochromatic light. This virtual state is not a real energy level and is transient, thus, molecules undergo relaxation to a lower energy level

afterwards. During this relaxation step, a phonon is emitted by the molecule. If this phonon possesses identical energy to that of the incident photon, elastic scattering occurs, and the scattering is referred to as Rayleigh. No energy is lost or gained in this process, and this sort of scattering is exhibited by most molecules, thus Rayleigh scattering peaks are intense. If, however, the molecule emits a phonon of different energy than the incident photon, then inelastic scattering occurs, and the scattering is referred to as Raman. Furthermore, if the emitted phonon possesses less energy than that of the incident photon, then scattering is denoted as Raman Stokes, however, if the emitted phonon has more energy than the incident photon then scattering is denoted as Raman Anti-Stokes. Anti-Stokes is much less intense than Stokes since it relies on the molecule already being in an excited state, which is uncommon at room temperature. The change in energy of the emitted phonon corresponds to the difference between vibrational energy levels in a molecule. As a result, information regarding molecular vibrations of bonds is gained. For a molecule to be Raman active, it must obey the selection rule which requires its polarizability to change during the molecular vibration.[303] The Raman spectrometer consists of a laser source, which is typically irradiated onto a sample through a cylindrical lens, which focuses the beam, as shown in Figure 2.8. The scattered light is then filtered by a dichroic mirror, which is focused directly onto a charge-coupled device (CCD) detector.

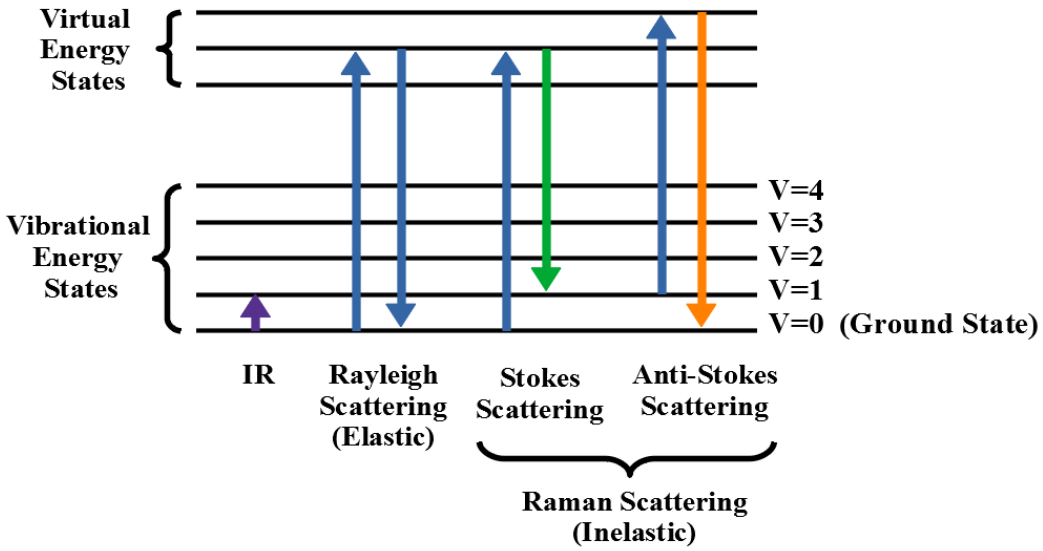

Figure 2.7 Energy-level diagram depicting several vibrational energy states and virtual energy states and transitions corresponding to infrared spectroscopy (IR), Rayleigh scattering, Raman Stokes scattering and Raman Anti-Stokes scattering.

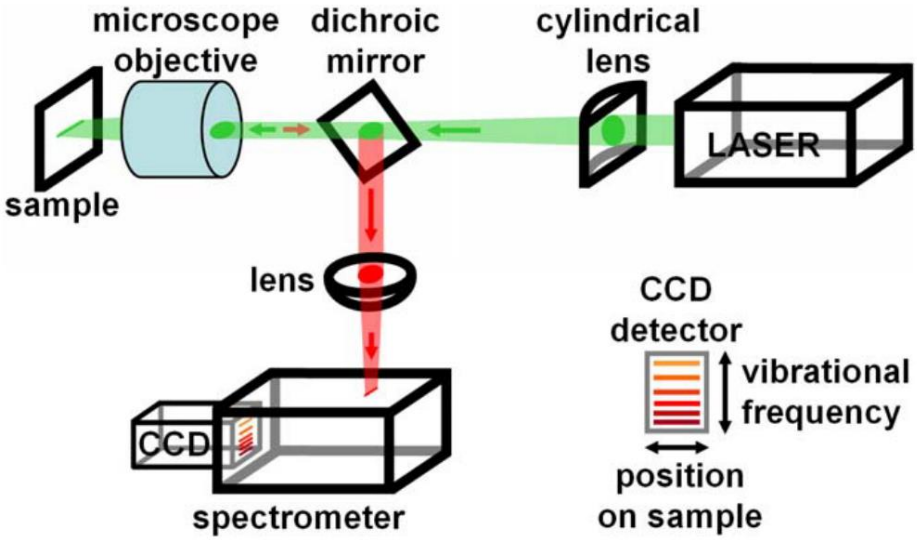

Figure 2.8 Schematic of Raman spectrometer consisting of a laser (green beam) which is irradiated onto the sample through a cylindrical lens. When a spot is illuminated at the sample, the Raman-shifted light (red beam) is filtered out from the laser light by a dichroic mirror and dispersed along a vertical line on the two-dimensional CCD detector. Reprinted from reference [304].

A Raman plot displays the shift in energy of the scattered light in relation to that of the incident light, enabling the generation of a spectrum containing phonon frequencies. Photons and phonons are both bosonic particles, however, a photon represents a quanta of light, whereas a phonon represents a quanta of atomic lattice vibration, which exists in systems where atoms can vibrate. Within sp^2 carbon structures such as graphitic materials, only a small number of possible phonon modes are Raman active. In the case of graphite, the E_{2g} modes correspond to the Raman active modes. SLG has the most fundamental spectrum of all sp^2 carbon materials. It contains two Raman-allowed features, including the G band and the 2D (often denoted G') band, which are common for all sp^2 carbon systems. The G band is due to the E_{2g} mode, whilst the 2D band corresponds to the second order symmetry allowed, overtone of the D band.[305–307] A third band may also be present, corresponding to the defect-activated Raman mode (first order D band), and is a breathing mode of A_{1g} symmetry.[308] It emerges in the presence of defects in the form of misarranged carbon lattice atoms, vacancies, substituted atoms or sp^2 carbon atoms.[309] It is highly dispersive as a function of the laser excitation energy. For a D peak to occur, a charge carrier must be excited and inelastically scattered by a phonon, prior to a second elastic scattering by a defect, to result in recombination. The D band represents a ring breathing mode of the sp^2 carbon ring and to be active, the ring must be adjacent to a graphene edge or defect. Additional peaks may emerge, corresponding to the D' and D + G peaks, when

disorder is present within the material. The D' peak resembles an intravalley double-resonance process caused by defects, whilst D + G corresponds to a combination mode.[172,310] Using this information, it is possible to estimate the quantity of defects within GBMs through implementation of the I_D/I_G ratio. It should be noted that this calculation may require the D band and G band to be deconvoluted to discriminate them from overlapping defect bands.[311] Within many literature studies, an increase in this ratio is attributed to an increase in covalent functionalisation, resulting from changes of hybridised carbon atoms from sp^2 to sp^3. These assumptions should be made tentatively, however, since it cannot be easy to discriminated between the types of defects mentioned.[289]

As well as being able to identify the presence of defects within the GBM, Raman spectroscopy also enables us to identify the number of layers within AB-stacked graphene materials, as shown in Figure 2.9. The 2D band experiences changes within its position and shape as the number of layers changes. For instance, SLG exhibits a sharp peak, however, increasing the number of stacked layers results in peak broadening and a shift towards higher energies. For 2LG and FLG possessing 2 – 5 layers, the 2D peak consists of four components: $2D_{1B}$, $2D_{1A}$, $2D_{2A}$ and $2D_{2B}$, where $2D_{1A}$ and $2D_{2A}$ have higher relative intensities. As the number of layers increases from 2 to 5, there is a significant decrease in the relative intensity of the lower frequency $2D_1$ peaks.[312] When the number of layers exceeds 5, the spectra looks almost indistinguishable from that of bulk graphite, which consists of two components: $2D_1$ and $2D_2$. It should be noted, however, that for turbostratic graphite, the 2D peak is a single, sharp peak, like graphene. Despite this, it does differ due to its full width at half maximum (FWHM) being 50 cm^{-1}, which is almost double that of graphene. In addition, it is associated with an upshift by 20 cm^{-1}. The 2D band is also generally broader for ABC stacked samples than ABA.[313] Increasing the number of layers of graphene also has influence on the G band. In this case, the band experiences a small shift towards lower energies as the number of layers increases.[314] In addition, there is also a linear increase in the G band intensity. As a result, the I_{2D}/I_G ratio can be applied to derive the number of layers. As such, Raman spectroscopy is an extremely useful tool to quantify the extent of defects and number of layers within GBMs.

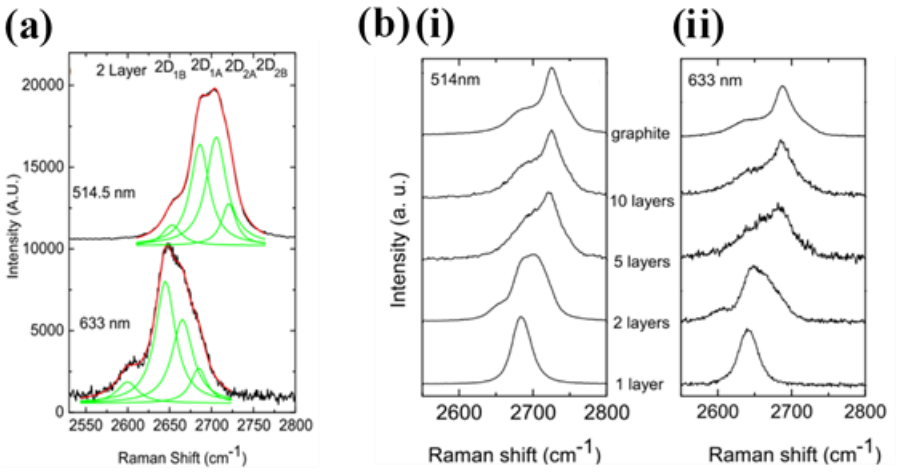

Figure 2.9 (a) The four components of the 2D band in 2LG at 514 and 633 nm and (b) Evolution of the 2D Raman band with increasing number of layers at (i) 514 nm and (ii) 633 nm. Reprinted from reference [312].

2.2.2 X-ray Diffraction

XRD is a useful tool to determine the arrangement of atoms or molecules within a crystalline material, such as a crystal or powder. It relies on the principle that when X-rays are focused onto a crystal or powder, they become diffracted in a characteristic pattern, depending on the structure of that crystal bulk material of that powder.[315] Different crystals and powders contain different planes, which have different spacings. In turn, information can be obtained regarding the crystallographic information to determine the crystallinity. A single crystal will produce only one set of peaks in the diffraction pattern, whilst a powder, containing various crystallites, will produce various diffraction peaks. This occurs because X-rays become partially scattered by the atoms, and that crystalline substances acts as three-dimensional diffraction gratings for X-rays of a similar wavelength to that of the spacing between planes in the lattice. In order for an X-ray to diffract, the sample must be crystalline and the spacing between the atom layers must be close to that of the incident X-ray wavelength. In incidences where beams diffract in phase from different layers, constructive interference occurs as shown in Figure 2.10, and the beam is scattered at a specific angle, resulting in a peak within the XRD pattern. If two beams are not in phase, destructive interference occurs and there is no peak. For diffraction to occur, the Bragg equation (See Equation 2.2) needs to be satisfied, where *d* is the spacing between

crystal planes (path difference), θ is the incident angle, n is an integer and λ is the wavelength of the X-ray.

During an XRD experiment, a detector records the position of the diffracted X-rays, observed at each angle 2θ. Using the Bragg equation, it is possible to calculate the interlayer spacing between planes. A characteristic lack of peaks within the XRD pattern for SLG arises due to the inability for constructive interference to occur in the two-dimensional structure.[316] As a result, peaks are only observed for stacked GBMs containing at least two layers. XRD is especially useful to give an indication of the interlayer spacings within GBMs. For instance, a strong peak in the region of 26° resembling that of the (002) basal reflection, provides evidence of graphitic stacking, corresponding to interlayer spacings of approximately 0.33 – 0.34 nm.[28,29] Within rGO and GO, the interlayer spacings are typically much larger than that of stacked graphene structures; the spacing is dependent on the extent of oxidation. For instance, rGO has been shown to possess an interlayer spacing of 0.385 nm whilst GO possesses larger interlayer spacings of above 0.6 nm.[317–320] Jung and co-workers utilised XRD to differentiate between graphite, GO and FLG consisting of between 2 − 4 layers in thickness, as shown in Figure 2.11.[321] It was observed that graphite possessed at peak at approximately 26˚, corresponding to an interlayer spacing of 0.336 nm. Upon oxidation of graphite to form GO, using an improved Hummers' method, the (001) reflection shifted to approximately 11˚, corresponding to an interlayer spacing of 0.833 nm. This provided evidence of the incorporation of oxygen-containing functional groups, which caused an increase in the distance between the layers. GO was then hydrothermally treated to remove the oxygen containing functional groups. The respective reduced material comprised of 2 − 4 layers. Its (001) reflection appeared at approximately 25˚, corresponding to an interlayer spacing of 0.370 nm. This was increased relative to graphite, indicating the presence of some remaining oxygen functional groups. In addition, it was also broad, suggesting that the stacking within the material was not well ordered.

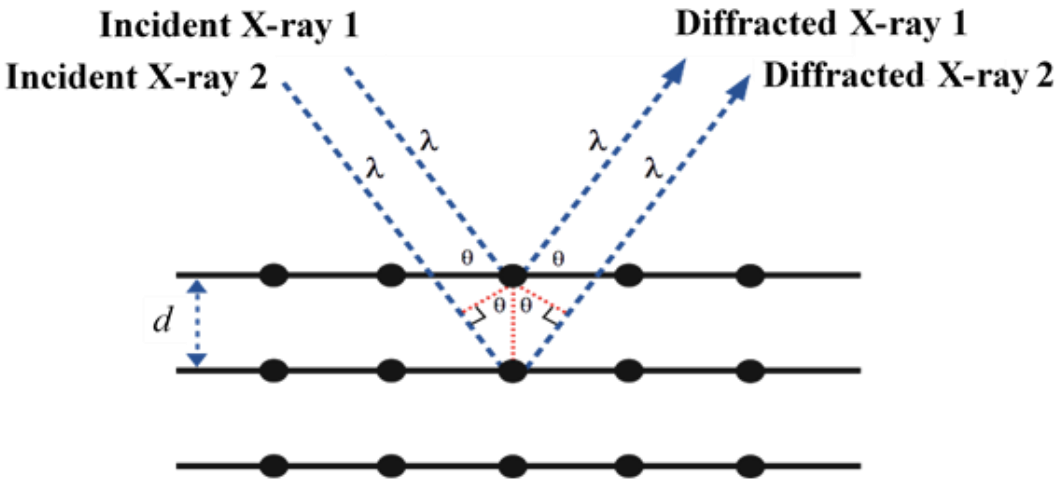

Figure 2.10 The Bragg law for parallel planes depicting two incident X-ray beams becoming diffracted due to constructive interference.

$$2d\sin\theta = n\lambda$$

Equation 2.2 Bragg Equation.

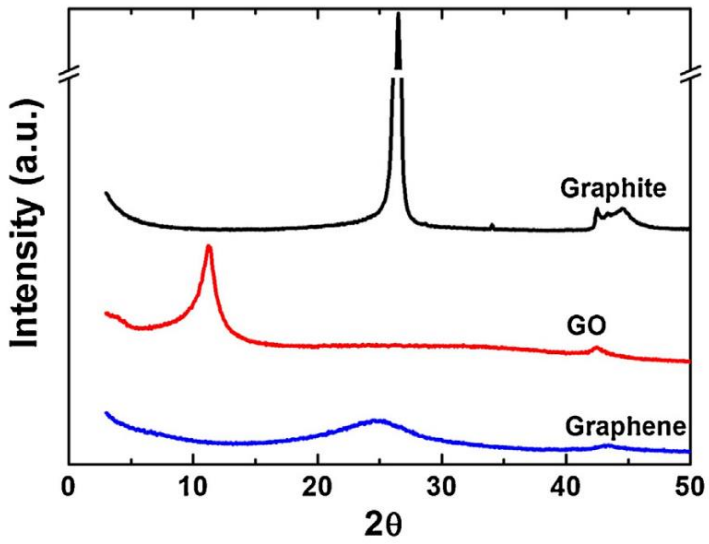

Figure 2.11 XRD patterns of graphite, GO and FLG.

2.3 Elemental Composition Calculation

2.3.1 X-ray Photoelectron Spectroscopy

XPS is an analytical technique which probes up to 10 nm of the sample, revealing information relating to the atomic composition within the surface regions.[322] It enables quantitative identification of surface elements, as well as providing information relating to their environments. The principle of this technique relies on the photoelectric effect. This phenomenon describes the interaction of X-rays photons with the core electrons within elements at the surface, resulting in the absorption of energy and emission of electrons as described within the works of Heinrich Hertz and Einstein.[323] During XPS, a sample is irradiated with X-rays of characteristic energy. If this energy is sufficient, core electrons can meet the threshold work function to pass the vacuum level and become ejected from the surface with kinetic energy, as shown in Figure 2.12. These emitted photoelectrons reach the detector within the instrument, and their kinetic energy is measured.[324,325]

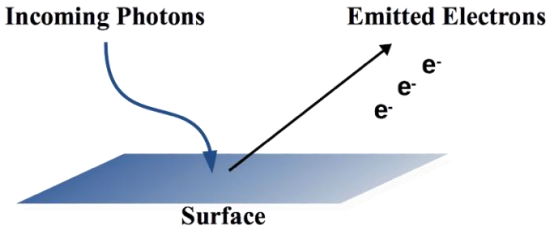

Figure 2.12 Diagram of the photoelectric effect.

The emitted photoelectrons possess kinetic energy (E_k), which equates to the difference between the X-ray photon energy, $h\upsilon$ (where h is Planck's constant and υ is the X-ray frequency) and the electron binding energy (E_b). During experimentation, the kinetic energy of the photoelectrons is determined, and through knowledge of the X-ray energy, the binding energy of the photoelectrons can be calculated, where Φ is the instrument's work function. The binding energy describes the energy required to remove the electron from the surface and can be calculated according to Equation 2.3.

$$E_b = h\upsilon - E_k - \Phi$$

Equation 2.3 Calculation of binding energy of a photoelectron.

The binding energy of an electron in a specific shell of a specific atom is unique and hence the atom can be identified. In fact, all elements (excluding hydrogen and helium) can be identified using this technique, and their relative compositions determined. An XPS spectrum is made up of spectral lines unique to a particular photoelectron emitted from different core shells (1s, 2s, 2p, 3s, 3p, 3d etc.) within an element. In general, various core levels are assigned by letters, such that the 1s shell = K, 2s shell = L_1 and 2p shell = L_2, L_3. Figure 2.13 (a) depicts the removal of an electron from the core K shell resulting in its emission. The intensity of the elemental peak is also proportional to the concentration of that element in the sample; hence the elemental composition of the surface can be calculated. The kinetic energy of these emitted photoelectrons is dependent on several factors including the incident photon energy, binding energy, element itself, orbital and chemical environment.

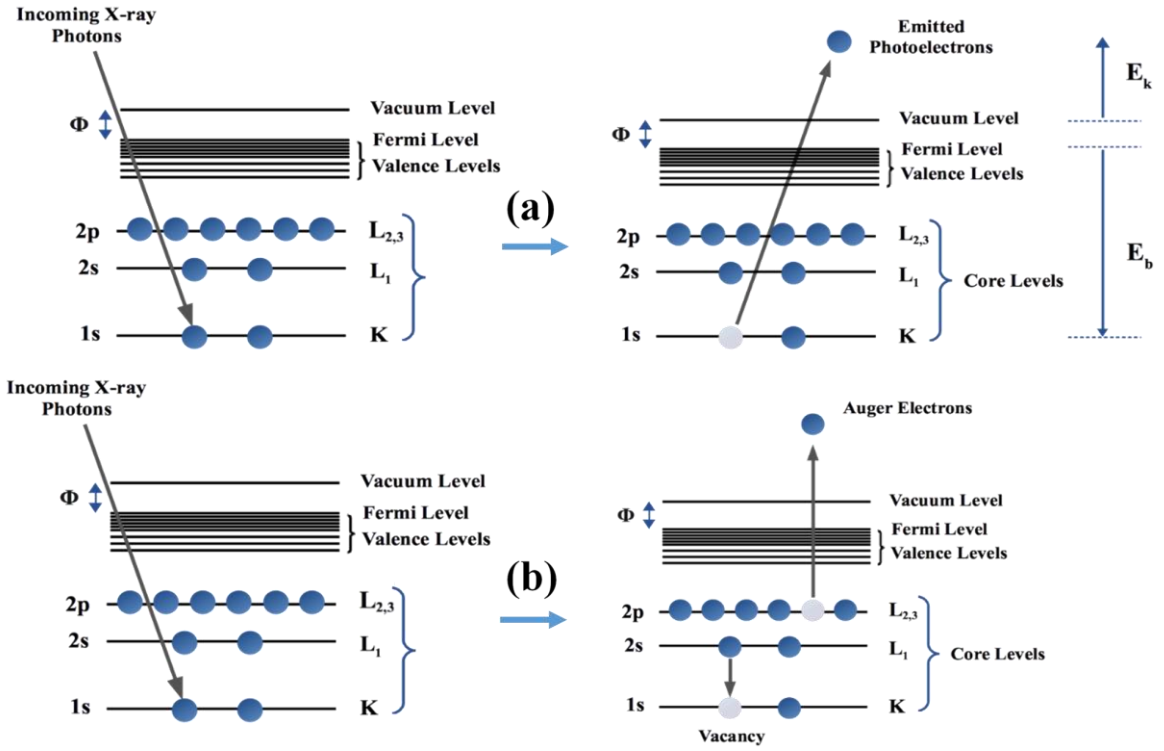

Figure 2.13 Schematic of XPS emission processes including (a) photoelectron emission involving the emission of a photoelectron upon irradiation with photons and (b) Auger electron emission involving the emission of a photoelectron upon irradiation with photons, causing a vacancy to be produced and subsequent Auger electron emission as an electron fills this vacancy.

In addition to the photoelectric process described, another phenomenon also occurs during XPS. Upon relaxation of the excited ion, Auger electrons or fluorescence X-ray photons may be emitted, as shown in Figure 2.13 (b). For lighter elements such as those with atomic number less than 30, Auger emission is dominant. The process occurs when a core electron is emitted due to interaction with an incoming X-ray photon. This creates a vacancy in the core level, which an electron from a higher energy level falls to occupy, resulting in emission of a third electron. This is the Auger electron, and its emission is due to conservation of the energy released. A typical XPS instrument is depicted in Figure 2.14.[326] This consists of an ultrahigh vacuum (UHV) chamber, an X-ray source, an electron energy analyser and a data acquisition system. Initially, X-rays are irradiated onto the sample, causing the emission of photoelectrons. The energy of the photoelectrons is counted by the energy dispersive analyser. This data is then processed by the data acquisition system.

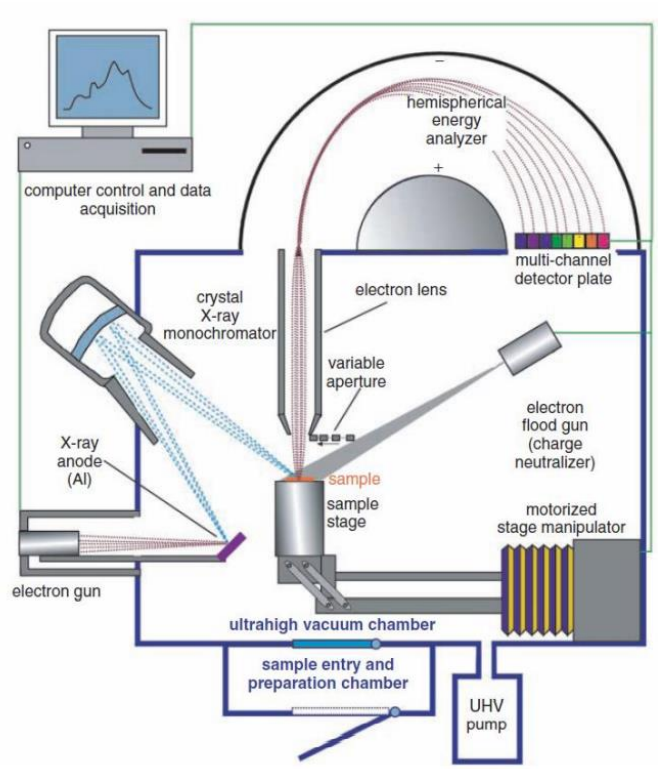

Figure 2.14 XPS instrument containing basic components including an UHV chamber, an X-ray source, a hemispherical energy analyser and a data acquisition system. Reprinted from reference [326].

In the context of GBMs, XPS becomes particularly useful to confirm the incorporation of a particular functional group containing other elements and their relative compositions, within the parts-per-thousand range.[1,327,328] In addition, it provides useful information on the various carbon and oxygen environments.[327] For instance, the C 1s spectrum may contain particular features including π–π* transitions, C=O, C–O, sp^2 hybridised carbon and sp^3 hybridised carbon.[329] This is clearly depicted within the work of Ateih and co-workers, who showed that graphite and GO samples, where the latter was synthesised *via* three different methods, contained variances in their concentration and types of carbon environments, as shown in Figure 2.15. It is observed that graphite primarily contained C=C bonding, originating from sp^2 carbon atoms, whilst the GO samples contained a significantly lower relative percentage of this carbon environment. Instead, these samples contained a large quantity of C–O, C=O and O–C=O bonding.

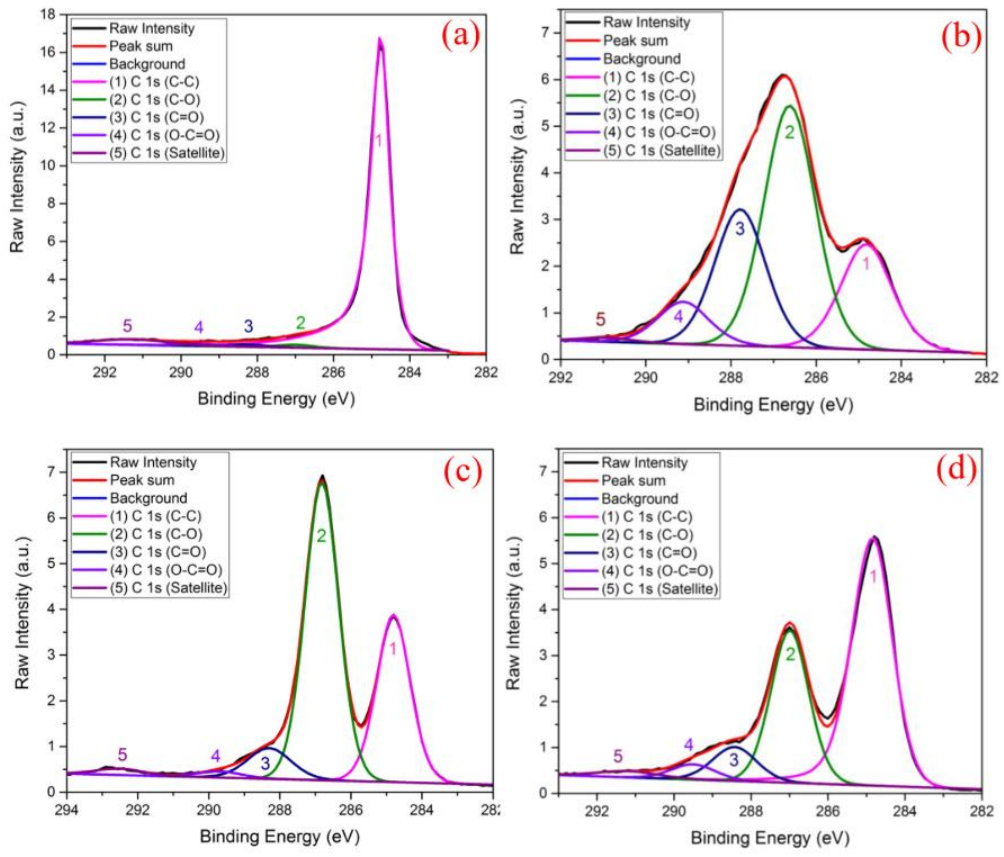

Figure 2.15 High-resolution XPS C 1s spectra of (a) graphite (b) GO prepared using a mixture of H_2SO_4, H_3PO_4, and HNO_3 (70:20:10) (c) GO prepared using a mixture of H_2SO_4, and H_3PO_4 (90:10) and (d) GO prepared using ultrasonic bath. Reprinted from reference [329].

2.4 Thermal Decomposition Characteristics

2.4.1 Thermogravimetric Analysis

TGA is a useful technique to provide an insight to the thermal stability of materials. During a typical TGA experiment, the mass of a sample is monitored as a function of temperature, and the temperature is altered at a controlled rate.[330] The various components of a sample may decompose at known temperatures and times, and thus the subsequent TGA curve provides an indication of the types of components within a material. During TGA operation, the sample is held within a sample pan, situated within a furnace, as shown in Figure 2.16. This pan is supported by a microbalance, which measures the mass of the sample throughout the analysis. The analysis takes place in the presence of various purge gases including oxygen, air, or under inert conditions, which are injected into the instrument through the gas inlet. These purge gases control the sample environment. In an example where the sample is heated, mass loss may result from a number of processes. The sample may undergo decomposition due to the breaking apart of chemical bonds, evaporation due to the release of volatiles, desorption of non-bonded components, or reduction where the sample interacts with a reducing atmosphere.[331] By measuring the mass of the sample during these losses, valuable information can be gained regarding the nature of the sample. For example, TGA is extremely useful for understanding the degree of covalently and non-covalently bonded functionality on the surface of GBMs. Graphite typically exhibits high thermal stability. The graphitic structure is usually maintained throughout the analysis, even at elevated temperatures.[332] Where additional functionality is present, however, decomposition occurs at lower temperatures. For instance, it has been shown that the thermally stability of GO is inferior compared to graphene and graphite, thus decomposition of oxygen functionalities occurs at much lower temperatures than the graphitic structure alone.[333] This was demonstrated by Losic and co-workers who analysed the TGA curves for various GO, graphene and graphite samples with different particle sizes, as shown in Figure 2.17.[333] The samples were heated up to 1000˚C in an air atmosphere. In all cases, the materials were completely burnt before 1000˚C with no residue left, indicating their high purity. There were variances in the decomposition rates between the materials, however. The mass loss in GO exhibited three distinct steps. Firstly, < 100˚C, water elimination resulted in a mass loss, followed by the removal of oxygen functional groups between 100 – 360˚C. Oxidative pyrolysis of the carbon framework then proceeded between 360 – 1000˚C. In

comparison, FLG and graphite did not contain oxygen functionality and their decompositions related to their carbon networks only. As such, FLG required more thermal energy for its decomposition. Moreover, a further increase in thermal energy was required to decompose graphite compared with FLG, due to its strong 3D carbon network comprising many stacked layers.

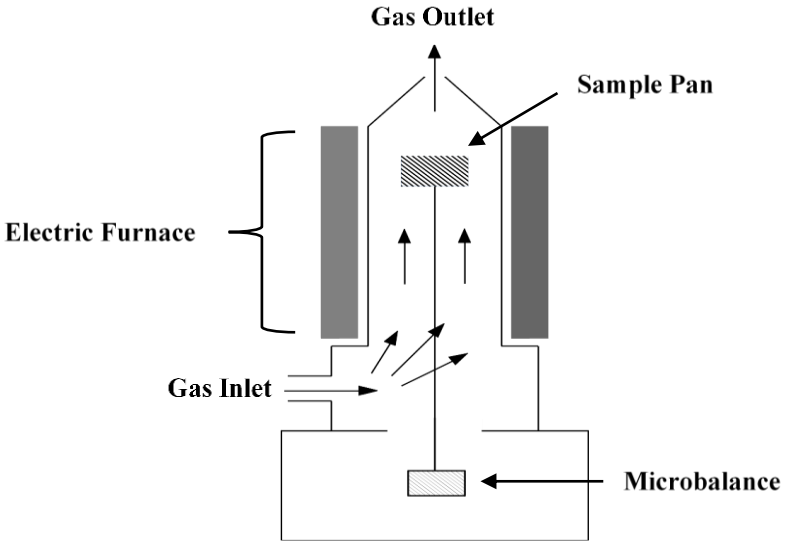

Figure 2.16 Schematic of TGA instrumentation and its basic components.

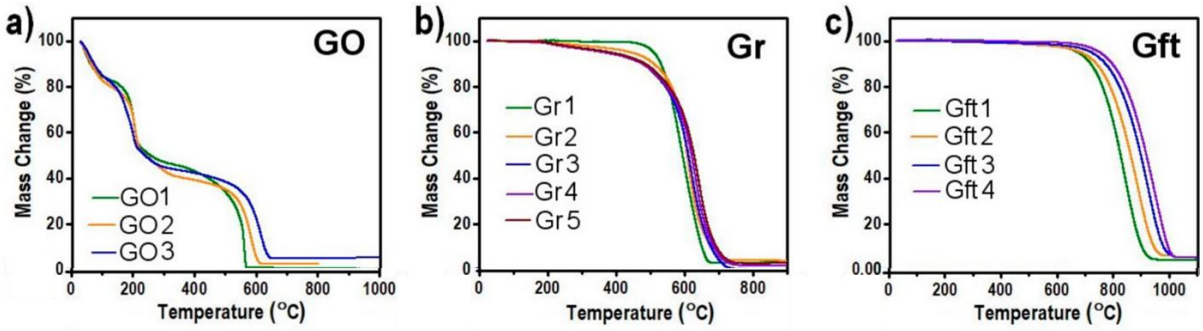

Figure 2.17 TGA plots in an air atmosphere for various (a) GO (b) FLG (Gr) and (c) graphite (Gft) samples. Reprinted from reference [333].

2.5 Bonding Analysis

2.5.1 Infrared Spectroscopy

FT-IR provides information about the chemical bonding present within samples and represents another type of vibrational spectroscopy. When infrared radiation is irradiated onto a sample, some of the energy may be absorbed for vibrations. Different bonds absorb different wavelengths of IR radiations. For example, single bonds are weaker than double bonds, which are weaker than triple bonds, hence, a single bond needs less energy to vibrate, therefore, peak absorptions occur at lower wavenumbers. The IR selection rule dictates whether a molecule is IR active; such that IR active vibrations occur if a molecule's dipole moment changes during a vibration. There is no dipole moment in diatomic molecules with the same atoms, and hence they cannot vibrate. For other molecules, such as water, a dipole moment exists. Figure 2.18 depicts the types of vibrations which occur in water. There are two main modes of vibration, including stretching and bending. In the former case, these can be symmetric (if the atoms move toward and away from the central atom simultaneously) or anti-symmetric (where one of the atoms moves towards the central atom, whilst the other moves away). Bending vibrations describe either rocking, scissoring, wagging and twisting.[334] The wavelength absorbed to undergo vibrations in molecules is plotted on an IR spectrum and the peaks can be compared with that of known absorptions of similar bonds.

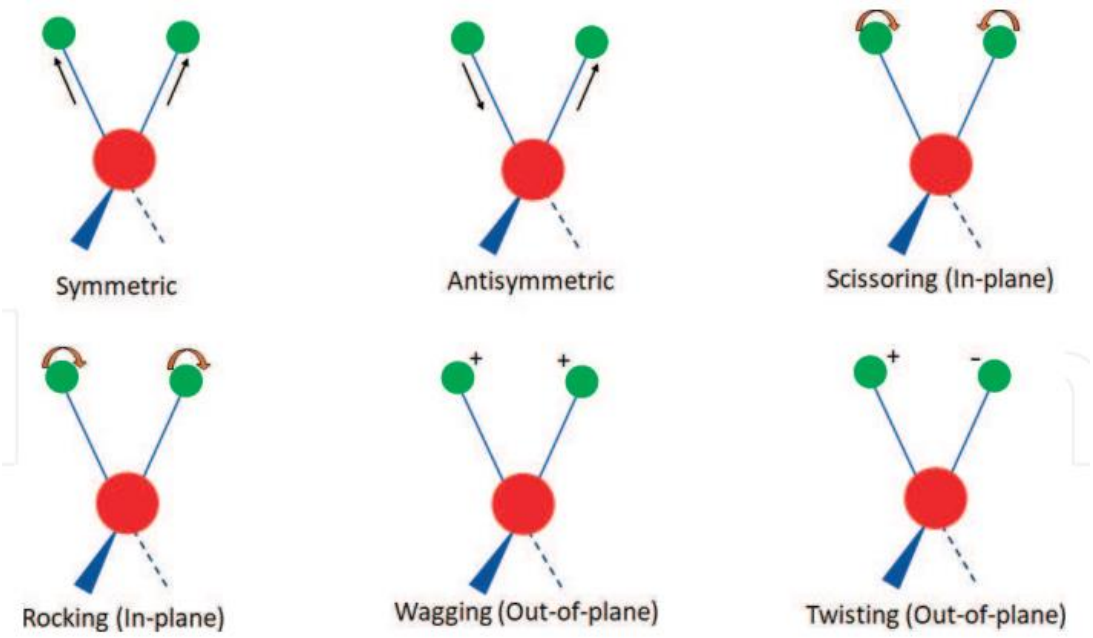

Figure 2.18 Various modes of molecular vibration Reprinted from reference [334].

There are various ways to carry out IR spectroscopy. Samples can be measured using various techniques, such as transmission or reflectance, as shown in Figure 2.19. In the former case, samples are typically prepared by grinding them with KBr powder and pressing this into a pellet. This pellet is then placed between the IR beam and the detector and the transmitted light is detected. In the case of reflectance techniques, attenuated total reflectance (ATR) IR is commonly implemented. This requires an ATR crystal with a high refractive index. Examples include diamond, germanium (Ge), zinc selenide (ZnSe) and silicon (Si). The crystal makes direct contact with the sample, and as the IR beam is irradiated onto the crystal, it experiences multiple internal reflections. This creates an evanescent wave which spreads to the sample. The detector measures the change in the internally reflected IR beam, after its contact with the sample. Both methods have found success in the analysis of GBMs, however, the transmission method often provides better spectra, due to its higher sensitivity, improved noise level and sharpening of peaks.[335,336] These advantages are extremely beneficial in the case of carbon samples, which are notoriously difficult to analyse using IR, due to their high absorptivity and tendency to scatter IR light.[337] Transmission IR does, however, require time-consuming sample preparation, unlike the ATR method.

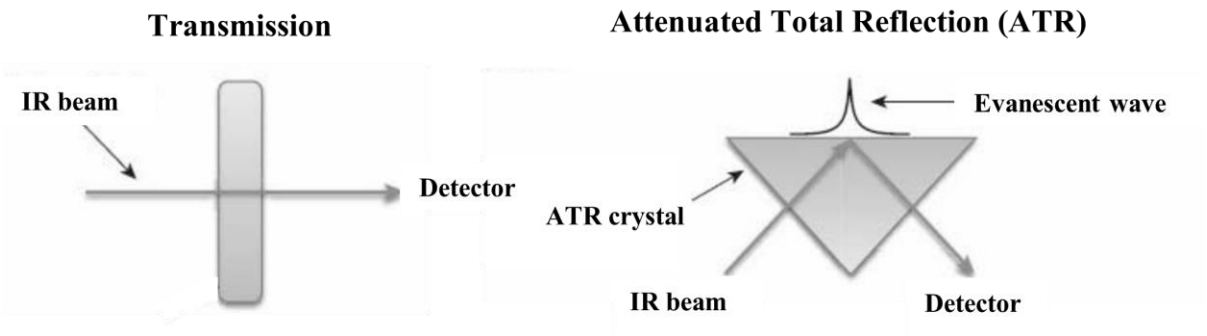

Figure 2.19 Examples of IR methods including transmission and ATR modes. Reprinted from reference [338].

Within the context of GBMs, IR is particularly useful to identify functional groups. Aziz and co-workers utilised the FT-IR spectra of GO and rGO to compare the types of bonding within the materials, as shown in Figure 2.20.[339] Both spectra contained a broad peak at high wavenumbers (3445.39 cm^{-1} for GO and 3400.18 cm^{-1} for rGO). In addition, peaks at 1583 cm^{-1} and 1563.80 cm^{-1} were present in GO and rGO respectively. These peaks correspond to the presence of O−H bonding, indicating the existence of adsorbed water within the materials. In contrast to rGO, however, GO possessed additional peaks at 1717.45, 1220.88 and 1050.79 cm^{-1}, which were attributed to C=O and C−O stretching. The spectrum therefore provided evidence of the existence of carbonyl functional groups within GO.

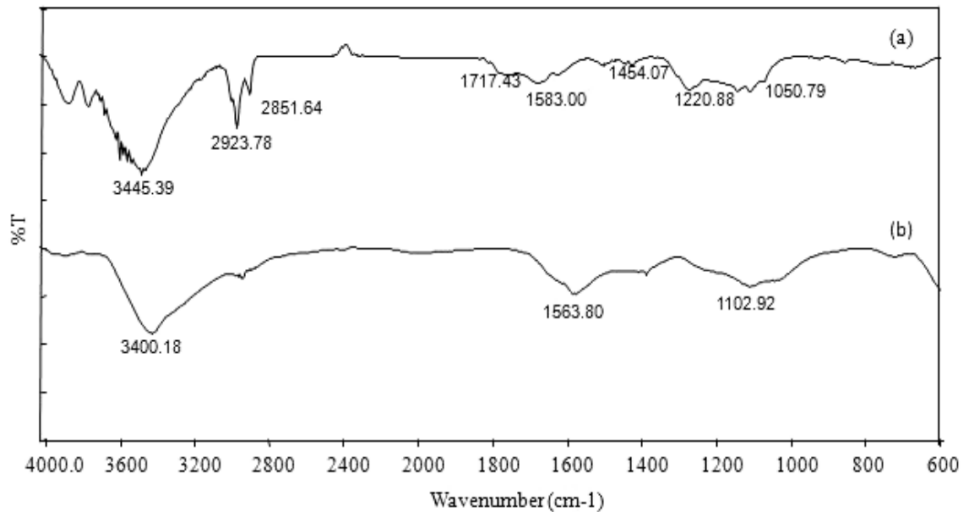

Figure 2.20 IR spectra of (a) GO and (b) rGO. Reprinted from reference [339].

2.5.2 Solution and Solid-State NMR

NMR spectroscopy can be applied to compounds to analyse their structures and chemical environments. It relies on the principle that some nuclei possess spin and therefore are NMR active. Typical nuclei include ^{1}H, ^{13}C, ^{19}F, ^{11}B, ^{31}P and ^{29}Si. There are two states for nuclei spin, corresponding the $+^{1}/_{2}$; alpha state and the $-^{1}/_{2}$; beta state. In the absence of a magnetic field, these states possess identical energy and hence an equal probability of the nuclei being in either state exists. If, however, an external magnetic field is applied, the nuclei behave like magnets and can either align with the field or align away from the field. This gives rise to an energy difference between the alpha and beta states, as shown in Figure 2.21, where the latter is slightly higher in energy, and therefore occupied to a lesser degree. During NMR, RF electromagnetic radiation is irradiated onto the sample, causing the nuclei to undergo transitions between the alpha to beta state. When energy is no longer provided, these nuclei relax back down to the lower energy, alpha state, and release energy in the process. It is this energy which is detected by the instrument and equates to a certain peak (or environment) within the NMR spectrum. Different molecules contain nuclei which exist in distinct environments, therefore the RF required to cause excitations depends on the precise nature of the molecule in question. As such, NMR offers an insight to the different chemical environments which surround the magnetically active nuclei. A thorough insight to the theory and applications of this analytical technique are provided elsewhere.[340]

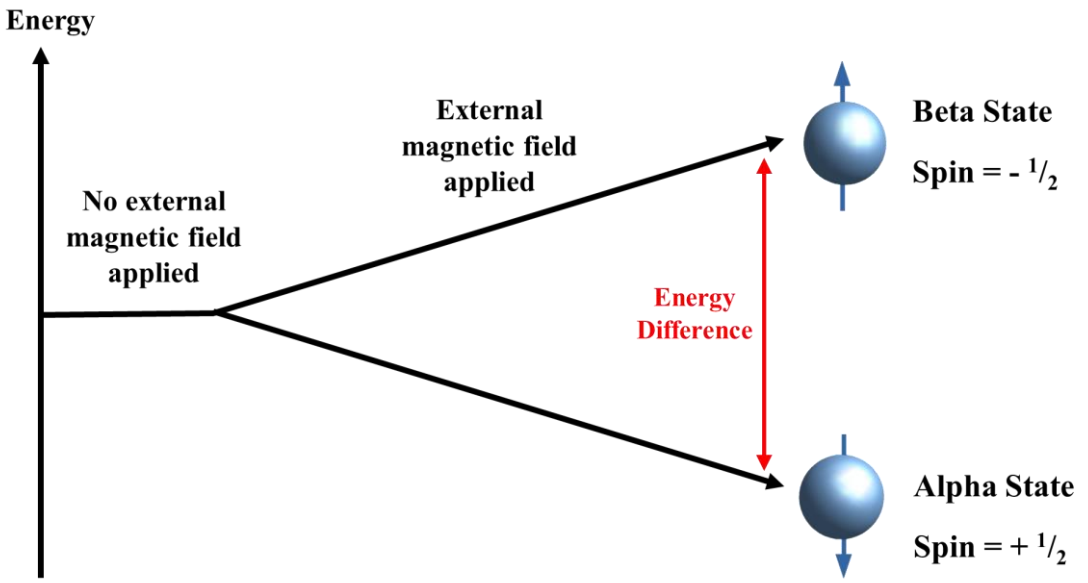

Figure 2.21 Splitting of energy between alpha and beta states of nuclei containing spin upon application of an external magnetic field.

A simplified diagram of the NMR spectrometer is depicted in Figure 2.22.[341] This contains a superconducting magnet which provides the magnetic field. This is immersed in liquid helium at 4K and a vacuum and a liquid nitrogen jacket surround this to prevent evaporation. A probe comprising a RF coil is situated at the bottom of the magnet and the sample is placed into the probe above a cushion of air. The superconducting magnet and RF then excite nuclei and collect information relating to the free-induction decay, as nuclei relax back to equilibrium. A signal is generated in the form of free-induction decay (FID) and the computer converts this signal into a spectrum.

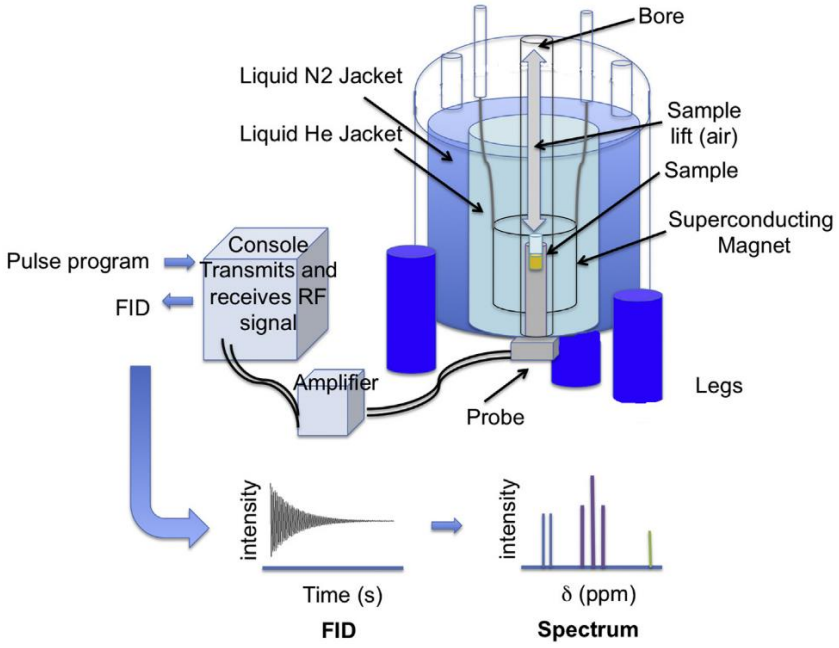

Figure 2.22 NMR instrument schematic. Reprinted from reference [341].

Whilst solution NMR is useful to detect molecules which can dissolve in deuteration solvent, GBMs do not possess solubility in this way, and therefore, solid-state NMR is of more use, as allows the analysis of solid samples. Solid-state NMR has been commonly utilised to analyse weakly ordered materials and nanomaterials. In the context of GBMs, ^{13}C NMR is particularly useful to provide an insight to the carbon lattice structure and various environments can exist, as shown in Figure 2.23.[342] The chemical shifts resemble different carbon environments. For example, sp^2 hybridised carbon atoms possess values in the range of 100 – 150 ppm. Furthermore, carbonyls possess signals in the region of 160 – 200 ppm.

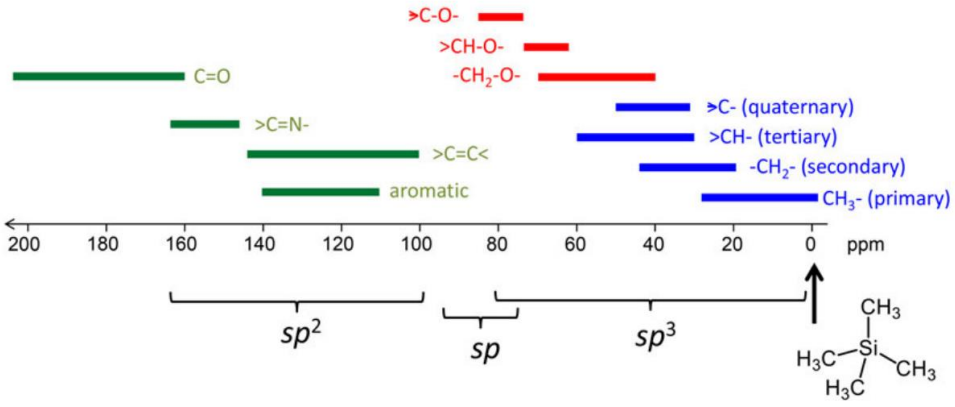

Figure 2.23 Typical ^{13}C shifts within NMR spectroscopy. Reprinted from reference [342].

2.6 Surface Area and Porosity Analysis

2.6.1 Gas Physisorption

The acquisition of physisorption equilibrium gas isotherms is a widely utilised method to characterise the surface area and porosity within solid materials. Typically, experimentally obtained isotherms are combined with a variety of different methodologies including Brunauer-Emmett-Teller (BET), Barrett-Joyner-Halenda (BJH) and DFT to reveal such information.[343–349] Adsorption describes the process where molecules, referred to as the adsorbate, approach a surface and interact with it *via* van der Waals forces. During a gas adsorption experiment, the pressure within the system is raised, resulting in increased adsorption of adsorbate. Initially, smaller pores fill at relatively low pressures due to the existence of enhanced adsorbent-adsorbate interactions within such pores, whilst larger pores then fill at higher relative pressures. As the relative pressure increases, more and more molecules adsorb onto the surface, covering the entire external surface and accessible internal pores, as shown in Figure 2.24. The volume of adsorbed gas is monitored during the process and an isotherm is constructed. Conforming to IUPAC definitions; pores may be characterised according to their dimensions, such that those of less than 2 nm, between 2 – 50 nm, or beyond 50 nm in size correspond to *micropores*, *mesopores* and *macropores*, respectively.[237] Micropores are further sub-divided into *ultra-micropores*, exhibiting dimensions of < 0.7 nm and *supermicropores* exhibiting dimensions of > 0.9 nm.[350] The results of the analysis are then obtained as an isotherm. The shape of the isotherm is dependent on the nature of the material. The IUPAC technical report of physisorption of gases by Sing outlines the types of isotherms and the respective structures of the materials.[239] Furthermore, the presence of hysteresis within isotherms results from capillary condensation in mesopores, providing further insight to the nature of the material.[351]

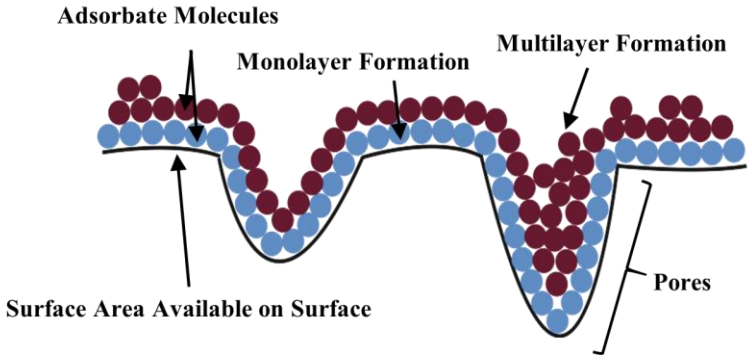

Figure 2.24 The adsorption of gas adsorbate molecules on a solid's surface according to BET theory. Reprinted from reference [343].

A variety of adsorbates can be utilised for these experiments, including N_2, Ar, CO_2 and Kr. N_2 is the most widely used adsorbate due to its availability in high purity, inert nature and low cost viability.[352,353] Investigations and measurements utilising this adsorbate are typically made at 77 K. This gas does, however, possess some disadvantages. Due to the low boiling point, there is restricted diffusion into very small micropores (< 0.45 nm). The use of CO_2 at 273 K or 298 K allows for access of these kinetically restricted pores (down to 0.35 nm).[354] Due to specific interactions between polar surfaces, however, this latter adsorbate is not suitable for polar materials. Ar is a monatomic adsorbate, therefore, does not possess a quadrupole moment. As such, it does not interact with surface functional groups. It is also utilised at an increased temperature of 87 K, meaning that the micropore filling step occurs at higher relative pressures, thus, smaller pores can be accessed. The choice of adsorbate is summarised within a review by Thommes, and each adsorbate possesses inherent advantages and disadvantages, thus, the choice should be made carefully according to the material of interest.[352]

Gas adsorption is an important technique to provide information relating to the surface area and porous structure of materials. SLG possesses a large theoretical surface area, which is desirable for a number of applications.[18] Furthermore, during synthesis and processing of SLG and other GBMs, the material's structure can become altered, and pores may be introduced due to etching or functionalisation.[241] On the contrary, particles may also be susceptible to agglomeration and/or experience pore blocking. Such effects have a major influence on the surface area of a given sample. The measurements of surface area are therefore extremely important. Once the isotherm has been measured, the surface area and porosity can be evaluated. Typically, the former of these is conventionally acquired using the BET method. The BET theory can be applied over a relative pressure range (P/P_0) = 0.05 to 0.3 in the adsorption branch of the isotherm, where monolayer adsorption takes place.[238–240,353] Furthermore, the micropore volume and the external surface area (pores of > 2 nm in size), are often calculated using the t-plot and more recently, the a_s-plot methods.[355,356] These methods represent classical models which utilise and compare an experimentally obtained isotherm with that of a reference or standard isotherm. This comparison yields a plot of the measured adsorbed amount as a function of the expected adsorbed amount. In the multilayer adsorption range, this plot displays a linear relationship, whereby the slope and extrapolated y intercept can be used to determine the external surface area and micropore volume respectively.[352]

To examine the pore size distribution (PSD), state-of-the-art methods involve DFT and molecular simulation methods including MC and molecular dynamics (MD). Classical,

macroscopic methods including BJH, Horvath and Kawazoe (HK) and Saito and Foley (SF) also exist.[352] BJH was first introduced by Barrett and co-workers who utilised the Kelvin equation to calculate PSDs.[344] This method is based on the physisorption equilibrium isotherm and considers the radius of the pore as a sum of the multilayer thickness and the meniscus radius, obtained from the Kelvin equation. In more recent years, however, it has been shown that this method does not realistically treat the behaviour of the molecules adsorbed in the structure, and may underestimate the pore size significantly, thus, methods such as DFT which rely on the theoretical description of the experimental isotherm, provide more reliable estimations of the PSD. Nevertheless, BJH offer a readily available and practical insight to the PSD of GBMs without the requirement for specialised software.[355]

To carry out a physisorption experiment, two steps are typically involved. Initially the sample is degassed to remove physically adsorbed water and other volatile species. This requires carefully chosen pressures and temperatures which depend on the nature of the sample. For materials which may decompose at high temperatures, milder temperatures are used, and for mechanically fragile materials, a stream of inert gas may be utilised in preference to a vacuum.[353] This is introduced through the adsorbate path shown in Figure 2.25. After degassing, the sample is then introduced to the adsorption configuration, and evacuated. Adsorbate is then presented to the sample cell and the pressure is measured.

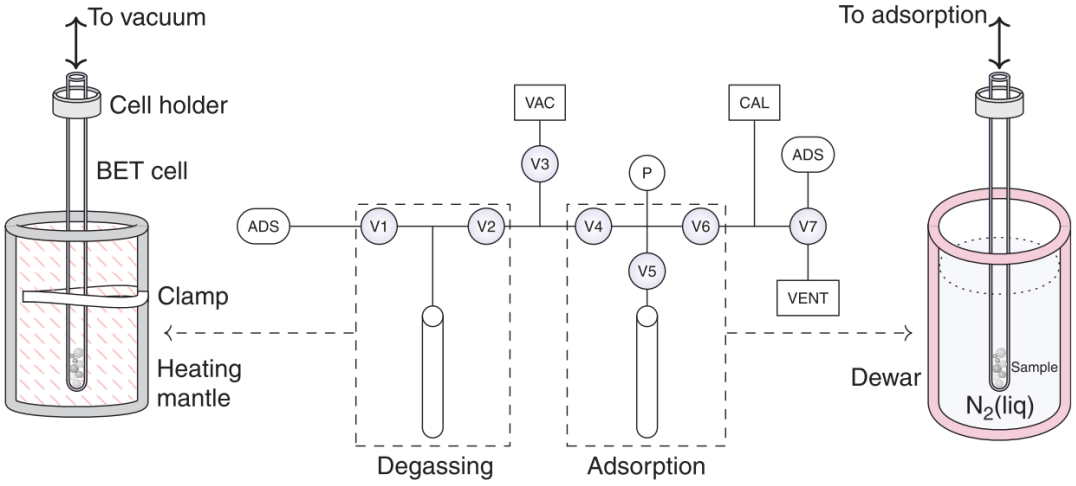

Figure 2.25 Gas physisorption analyser used to obtain adsorption-desorption data. Vacuum, calibration adsorbate, pressure gauge and valves are represented by VAC, CAL, ADS, P and V1 – V7, respectively. Reprinted from reference [353].

Physisorption analysis is a useful tool to provide information regarding the porous structure and surface area of GBMs. For example, Kostoglou and co-workers analysed the porosity and specific surface area of two plasma-exfoliated FLG materials. The corresponding nitrogen adsorption-desorption isotherms are depicted within Figure 2.26.[93] Kostoglou deduced that these materials possessed surface areas values corresponding to 428.3 and 777.4 m^2/g respectively, using the BET method. The type of hysteresis between the adsorption and desorption branch signified the presence of capillary condensation inside mesopores, proving their existence within the material. Furthermore, the t-plot method revealed that the FLG with the large surface area was associated with a larger a larger micropores volume (0.132 cm^3/g ca. 0.076 cm^3/g).

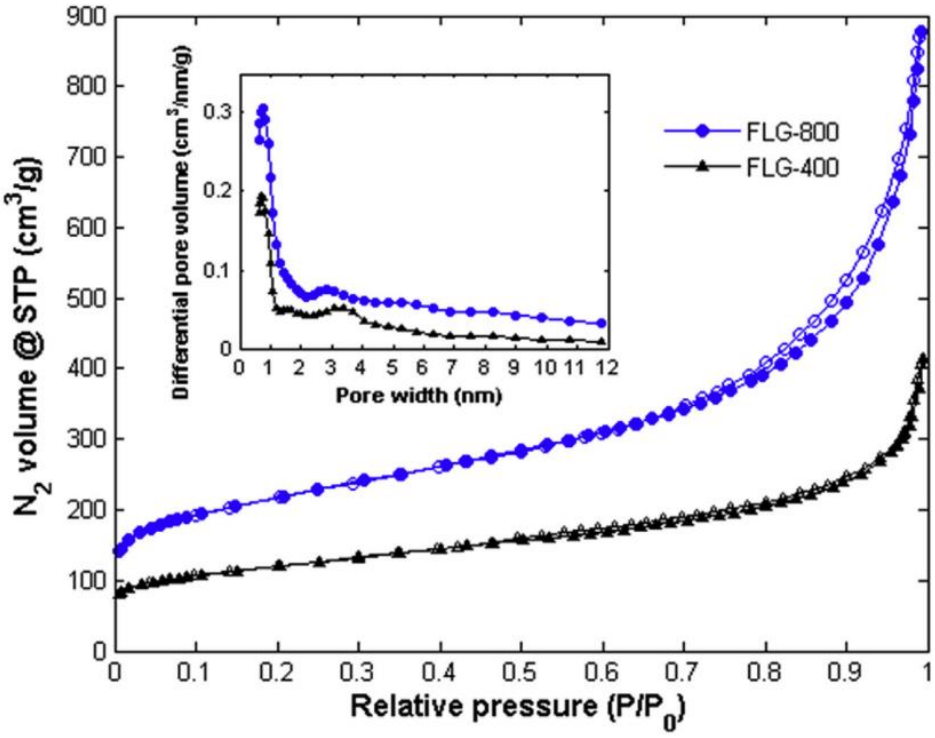

Figure 2.26 N_2 adsorption-desorption isotherms at 77 K of two plasma-exfoliated FLG powders; the inset shows the differential pore size distributions derived by the quenched solid DFT method. Reprinted from reference [93].

2.7 Additional Characterisation

2.7.1 Mass spectrometry

Mass spectrometry is a useful tool to identify a wide variety of compounds and quantify their structures.[357] It works by ionising a sample and detecting these ions based on their mass-to-charge ratios (m/z). Ionisation can proceed by providing thermal energy, an electric field, or by bombarding a gaseous sample with energetic particles in the form of electrons, ions or photons. An example of the ionisation process is provided in Equation 2.4, for electron ionisation.[358] The subsequent molecular ions may further fragment to form additional ions. All ions are separated in the mass spectrometer according to their m/z and their abundance is recorded to produce a mass spectrum.

$$M + e^- \rightarrow M^{\bullet+} + 2e^-$$

Equation 2.4 Electron ionisation of a molecule to form its corresponding radical cation.

The mass spectrometer consists of three primary components, corresponding to the ion source, mass analyser and detector (Figure 2.27). There are many different types of ion sources used in mass spectrometry and their application depends on the physical and chemical properties of the species present (molar mass, volatility, functionalities etc.) These techniques can be categorised according to the amount of energy they impart on the ions they form, which is considered as the relative hardness or softness of the technique. Hard ionisation techniques include thermal ionisation and electron ionisation, and result in a large degree of molecular fragmentation.[359] These techniques result in the acquisition of a detailed mass spectrum, allowing for precise structural determination. In contrast, soft ionisation techniques, including chemical ionisation, matrix-assisted laser desorption ionisation and electrospray ionisation impart less energy into the molecule and thus result in little fragmentation.[359] The subsequent mass spectrum therefore possesses much less molecular fragmentation, and may be more suitable for molecular ion detection. Several different mass analysers exist including quadrupole, linear ion, time of flight, Fourier transform ion cyclotron and orbitrap. Quadrupoles are the most commonly used and consist of four parallel circular metal rods which form an oscillating electric field when DC and RF frequency are applied to them. Only ions with a specific m/z will possess a stable trajectory to pass through the detector and the DC and

RF voltages can be varied to allow different ions through. One drawback of quadrupole mass analysers is their relatively low mass resolution. Whilst unit resolution is often suitable for the detection and quantification of known molecules, it is often useful to obtain high resolution spectra when identifying unknown molecules. As such, time of flight mass analysers are often implemented to provide high resolution and accurate mass measurements. Different types of detectors can also be applied including electron multipliers and array detectors.[359] These work on the principle that when an ion hits the detector, the charge becomes neutralised, causing an electric current to be generated. This electric current is proportional to the ion's abundance and a computer analyses this data to generate a mass spectrum, as shown in Figure 2.28.[359] A mass spectrum simply incorporates a plot of m/z *vs* the relative abundance of each ion. The most intense peak is referred to as the base peak and this is given a relatively abundance of 100%. In Figure 2.28, this refers to m/z=31. The acquired mass spectrum of a sample can be matched against a library to identify unknown compounds. As such, mass spectrometry is not only useful for elucidating the structure of compounds, but also identifying unknown species.

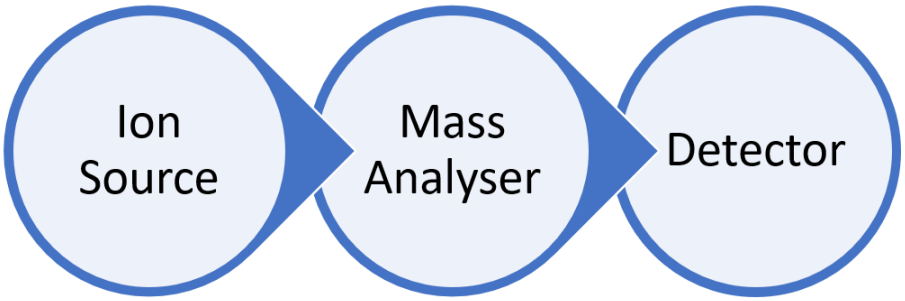

Figure 2.27 Basic components within a mass spectrometer. Reprinted from reference [359].

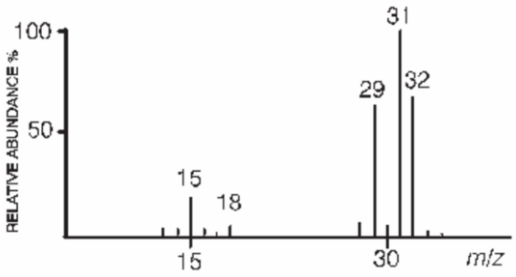

m/z	Relative abundance (%)	*m/z*	Relative abundance (%)
12	0.33	28	6.3
13	0.72	29	64
14	2.4	30	3.8
15	13	31	100
16	0.21	32	66
17	1.0	33	0.73
18	0.9	34	~0.1

Figure 2.28 m/z ratios vs relative abundance displayed as a mass spectrum (left) and within a table (right). Reprinted from reference [359].

2.8 The Importance of Characterisation and the Challenges Associated with it

Accurate characterisation is central towards building an understanding of the properties and behaviours that a given sample will exhibit. This is achieved *via* the implementation of multiple analytical techniques, such as those described above, which, when pieced together, provide a reasonably clear picture on the nature of the material studied. The various characterisation techniques can render precise distinctions on specific aspects of the material, such as the number of layers, the purity level and uniformity of the sample, as well as the quantity of defects. Characterisation is not only essential within an academic setting, where modifications are routinely carried out on GBMs, but is also fundamental within the graphene industry for quality control purposes. Within this context, accurate characterisation is crucial for obtaining reproducible GBMs and subsequent market products. This latter aspect is of course particularly crucial for applications within advanced level devices. There is no single technique which tells you everything you need to know to fully understand the nature of a GBM. Each technique provides relevant information to a specific property or characteristic. For example, XPS enables an understanding of the surface elements present within a GBM sample, however, offers little knowledge as to how they are bonded to the carbon network, though binding energies can provide clues. Whilst Raman spectroscopy enables one to recognise the presence of chemical bonding directly to the graphitic sheet, it gives no information about the morphological properties or the lateral dimensions, which requires a technique such as SEM. For this reason, samples tend to undergo analysis *via* a plurality of techniques within academia, to build up a clear understanding of the nature of the sample. As a result, the characterisation of GBMs can, in some respect, be considered as a "problem-solving" exercise, and hence comparisons between methods are typically made within the current results enclosed within Chapters 4 − 6, within this Thesis.

Unfortunately, the requirement for multiple specialised characterisation techniques is expensive. Each analytical technique requires a sample of the material in question, and some require a large quantity for adequate generation of results. Examples include solid-state NMR and BET, which typically require a minimum sample mass of approximately 1 g. One of the key hurdles encountered within the current research was the lack of suitable characterisation tools within the research institution, thus, meaning many samples required external analysis. Furthermore, purchasing of the explicit analytical equipment requires upfront costs and, in

many cases, maintenance costs which may not be feasible. As an example, an XPS instrument typically costs somewhere in the region of £250,000. If there is no access to analytical techniques within one's institution, there are often costs associated with the external analysis on an hourly or standard rate basis. For this reason, large volumes of analysis can quickly build up to large financial expenses. This was found to be a significant issue faced by the current research, and meant that in many cases, less analysis was conducted than desired. In all cases, a good understanding of what each technique has to offer was extremely valuable to prioritise characterisation and enable an understanding of the specific properties and features within the GBM in question. In the following sections, some more specific challenges that researchers face in making progress in the investigation of GBMs are outlined. Examples of many of the obstacles which were faced within the current work are also provided and compared with those within the literature.

2.9 Analysed Area is Not Always Representative of the Sample as a Whole

An inherent challenge among many characterisation techniques results from the restricted area of sample undertaking analysis. This is particularly difficult when the sample is non-uniform, and the analysis area is small. Analysis often provides information which is not representative of the rest of the material. There are various examples within this work which depict how stacks of NPs vary in thickness and lateral dimensions. This variance in morphology is also highlighted in literature. Castro Neto and co-workers, showed that liquid-phase exfoliation synthesis of graphene resulted in generation of exfoliated particles of graphene, adopting a large range in thicknesses, resulting from the statistical nature of the synthesis technique.[7] Inconsistencies in dimensions were also experienced by Banks who analysed a sample of graphene flakes containing lateral widths which varied between 1.5 mm − 0.5 µm (Figure 2.29) In this case, smaller flakes were also found to possess improved heterogeneous electron transfer kinetics within electrodes, due to an increase in the number of edge sites and defects available.[360] Such findings reveal the importance in understanding these morphological variations across the whole sample, particularly in applications which require homogenous properties.

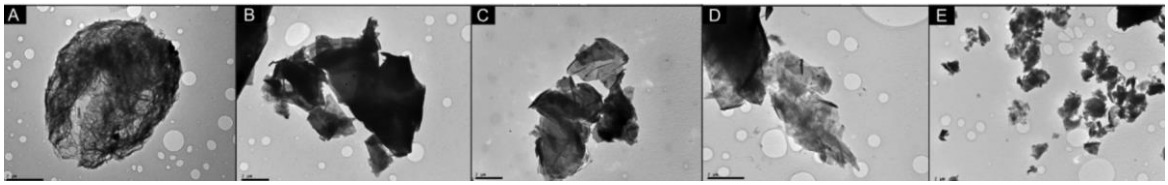

Figure 2.29 TEM analysis conducted on graphene flakes showing that flakes vary in morphology and lateral dimensions. Reprinted from reference [360].

As such, it was found to be extremely useful to conduct analysis across as many areas of the GBMs as possible, to gain a reliable insight to the variances of morphology and topography. Furthermore, it was also recognised that distinct techniques penetrate samples to different extents, resulting in acquisition of data associated with different depths of the sample. Accordingly, some techniques provide information on the surface of the material only, whilst others provide information on the bulk of the material. Figure 2.30 provides a representation of the penetrative nature of various characterisation techniques. Techniques such as XPS and Atomic Electron Spectroscopy (AES) are considered surface techniques since they examine only the top and near surface of a sample.

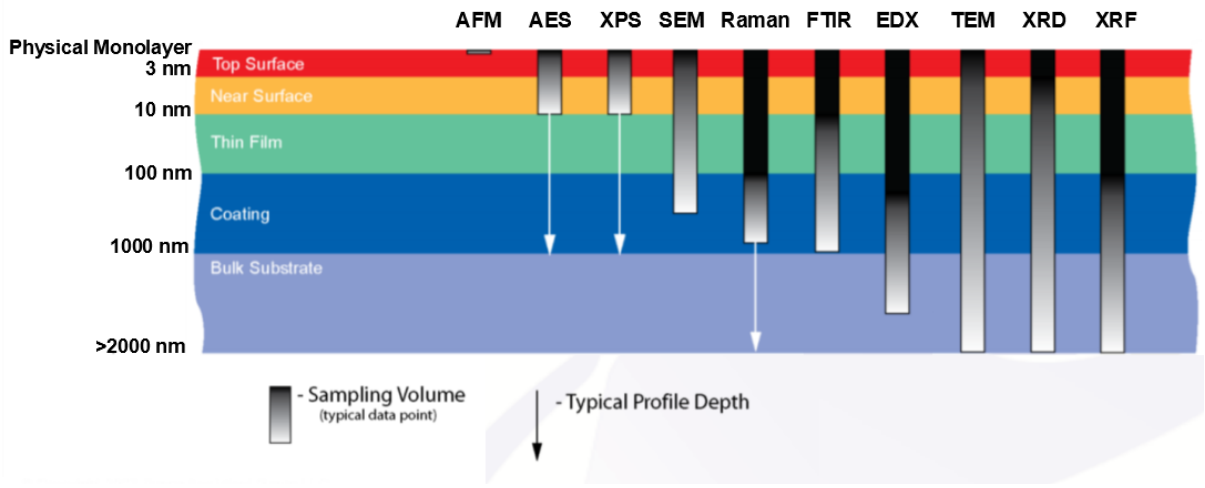

Figure 2.30 Depth of analysis profiles for various characterisation methods. Reprinted from reference [361] *and modified from reference* [362].

Other techniques such as FT-IR measure much deeper into the sample and therefore give information regarding the bulk properties. Moreover, techniques such as TEM penetrate the

whole sample. The importance of recognising the depth ability of a technique is critical when formulating conclusions about the properties of the material. For instance, XPS detects only elements present within the surface of a material; it provides no information about the elements present beneath the surface region. Clearly this has implications for heavily intercalated or stacked samples. If these trace elements are present much deeper than the depth of detection for XPS (approximately 10 nm), they would not be observed *via* this technique.[324] It is also important to note that elemental composition techniques may also render very different at.% values of the common elements; carbon and oxygen. Light elements ($Z < 10$) are extremely difficult to accurately quantify *via* EDX analysis due to the phenomena whereby Auger electron production is favoured over characteristic X-ray production, resulting in limited X-rays reaching the detector. For this reason, it is extremely important to be aware of the depth of analysis of a given technique to understand what information the data acquired is providing. The properties of a GBM have also been found to differ throughout a non-homogenous sample. It has been observed that the edges of GBMs typically contain more defects than the basal planes. Thus, when Raman spectroscopy is conducted at the edges of graphene samples, it reveals a relatively large D band.[34] Furthermore, rippled and crumbled regions associated with edges or defects, typically possess altered bond lengths.[363,364] These findings highlight the importance in carrying out a detailed survey of the material, since a routine Raman analysis may only focus on an unrepresentative region of the sample. To improve reliability and understand better the inconstancies in size and nature of graphene materials across a sample, it is recognised that more sites should be analysed, focusing across edges sites and various sites within the basal plane of GBMs. Unfortunately, these multiple analyses are often accompanied by a time and cost penalty, and therefore, a compromise may need to be met, such in the case of the current work. Aside of these issues with characterisation, the variances in size distribution across a sample can also trigger a number of practical implications, such as issues when washing and filtered. These are highlighted in more detail in the Experimental section within this Thesis.

2.10 Accurate Thickness Determination and Morphological Considerations

A common incentive behind characterising GBMs is to understand the numbers of layers present within the structure. This, of course, is especially important for applications whose properties are affected by particle thickness, since the number of layers has a large influence on the reactivity, thermal stability, electronic properties, optical transmittance and mechanical properties of GBMs.[34,35,37–39] Apart from SLG, GBMs commonly contain a broad distribution of layered stacks, including 2LG, 3LG, FLG, GNPs and NPs. Accordingly, accurate thickness determination can be difficult, and although there are several methods available to achieve this, a significant degree of uncertainty associated with their measurements remains. Raman spectroscopy is routinely used to quantify SLG, 2LG, 3LG and FLG materials. Ferrari noted that stacks of up to 5 layers can be determined by examining the 2D and G band shape and their intensity ratio.[312] SLG consists of a Raman spectrum where the 2D band is four times the intensity of the G band. On the other hand, graphite provides a spectrum where the G band exceeds that of the 2D band intensity. For this reason, the I_{2D}/I_G ratio is commonly implemented to provide an estimation to the number of graphene layers within a stack of < 5 layers. Unfortunately, when the layer thickness increases beyond 5, the 2D band spectra looks almost indistinguishable from that of bulk graphite, thus, it can no longer be used to estimate the number of layers. It should be noted that only a small number of commercially obtained materials, if any, would indeed only exclusively contain stacks of less than 5 layers.[7]

AFM analysis is also routinely used for layer thickness determination. AFM provides three-dimensional images, thereby enabling the calculation of the overall thickness of a stack by direct measurement. Since the interlayer spacing of stacked graphene layers within graphite typically corresponds to 0.335 nm, the number of layers within a stack can be calculated.[29,365] Unfortunately, literature values have been proven to provide inaccurate measurements of the values of SLG, ranging between 0.4 - 1.7 nm.[298] Practically, there are also some issues associated with gaining AFM measurements. To obtain an AFM image, one of three primary modes of operation is selected; including i) non-contact mode, ii) contact mode and iii) tapping mode, as described earlier in the text. All of these have been applied for the analysis of graphene samples reported in the literature, although tapping mode is the most commonly implemented. Unfortunately, imaging of the surface of GBMs can present challenges and some have noted that the contact mode should be avoided due to its ability to severely damage the sample or tip, and distort the image by displacing the sample.[298,366] Even, the non-contact mode

has also been found to damage the surface of GO over several repeat scans (Figure 2.31). It was shown that as more scans are undertaken, more damage was introduced to the graphene material due to a weakening of the van der Waals forces between the sample and the SiO_2 substrate.[367] Furthermore, challenges also exist due to tip-surface interactions, arising from substrate surface energies, interactions with the graphene surface itself and how the sample is prepared.[298,368] The nature of the ambient conditions, high humidity within the environment may also cause water adlayers to form between mica substrates and graphene, which would have implications on thickness measurements.[369,370]

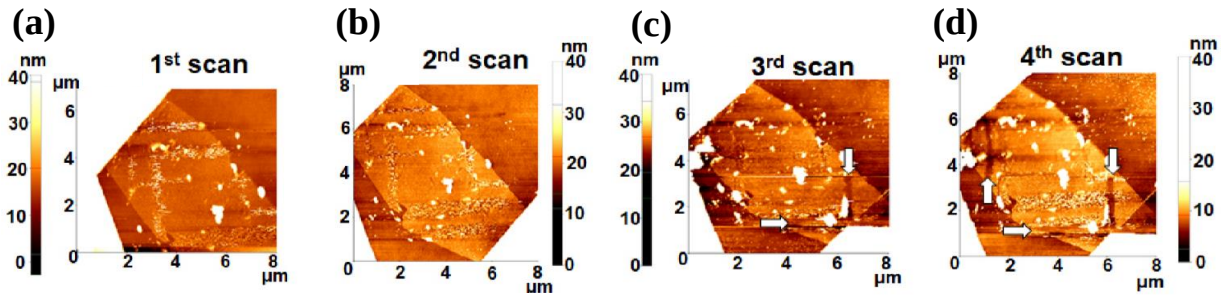

Figure 2.31 (a) First and (b) second scanned topography images of graphene after 24 h. (c) Third and (d) fourth scanned topography images of graphene. Here, the arrows in (c) and (d) indicate the damage to the graphene surface over several repeat AFM scans, conducted using non-contact mode. Reprinted from reference [367].

Finally, in terms of estimating the number of layers within GBMs, XRD offers an additional technique for this purpose. After obtaining an XRD spectrum, it is possible to calculate the thickness of a crystalline stack using; the Scherrer equation and the Laue function model.[371,372] It has been found that both determination methods are generally in good agreement with each other for samples with uniform thickness distributions. Unlike the Scherrer equation, however, the Laue function also provides reliable results for thickness determination within samples containing non-uniform thickness distributions.[373] In essence, a combination of Raman spectroscopy, AFM imaging and XRD data provide a good estimate of the number of layers.

2.11 Elemental Composition Calculation

Quantitative assessment of the elemental composition of GBMs is useful to understand the types of elements present, particularly when characterising functionalised materials. XPS is one of the key techniques used for this purpose due to its extreme surface sensitivity.[374] However, as noted above, the analysis is limited to the surface region, thus, provides no data regarding the bulk of the material. Nevertheless, it remains a vitally important technique since most functionalisation of graphene, indeed, occurs at the surface. The binding energies associated with the elements and the chemical environment in which they occupy provide an invaluable tool for quantifying specific functionality. The data obtained from the XPS analysis can be processed and compared with that of known compounds within databases. For this reason, XPS is a highly valuable technique in studies involving functionalised GBMs. As with all techniques, there are some challenges associated with the analysis and interpretation. Unfortunately, the databases do contain some uncertainties and errors in the experimental binding energy values, resulting from variances in instrument operators, calibration energies, C 1s charge referencing and analysis conditions.[375] As such, care must be taken during assignment. An understanding of the types of compounds present within a GBM sample is needed for the assignment and it should be supported by other evidence gained from the other analysis.

EDX is an alternative characterisation method to quantify the elemental composition of a sample, however, it is an inherently insensitive technique and struggles to detect elements in low concentrations; the detection limits are typically 0.2 – 0.5%.[374] Light elements with small atomic numbers (Be to F) also exhibit problems for EDX analysis. These elements lead to low fluorescence yield, absorption and peak overlaps with the L, M and N lines of heavier elements. Unfortunately, GBMs consist mostly of carbon and oxygen which both contain atomic numbers beneath the sensitivity threshold, hence accurate data is unlikely to be acquired. As such, it is unsurprising that discrepancies are often achieved between EDX and XPS quantitative elemental composition data, especially for light elements. In such cases, it is assumed that XPS provides a more accurate insight to the composition of carbon and oxygen.

Elemental analysis can also offer an insight to the composition and the elements present within a sample. Whilst this technique is useful in offering detection limited in order of ca. 0.01%, it typically only identifies a limited number of elements, namely carbon, hydrogen, nitrogen,

sulfur and oxygen. The facilities for the determination of the first three elements are standard in many research institutions. For sulfur and oxygen, there is less availability in most laboratories. Functionalised GBMs containing elements aside of these can be challenging to accurately quantify and many materials contain varying degrees of oxygen. Despite this, CHNS elemental analysis has shown to be successful in quantifying accurate sulfur incorporation within a functionalised GO within the surface and bulk, as explained within a previous report.[376]

2.12 Inherent Challenges with Characterising Functionalised GBMs

Characterising covalently functionalised samples is not always a straightforward task. It is especially challenging to identify and differentiate between covalently functionalised species bound to GBMs, with non-covalently bonded species. In the latter case, unreacted reagents and side products often remain strongly adsorbed to the surface *via* numerous interactions including π−π interactions, van der Waals forces, ionic interactions and hydrogen bonding.[377] For example, it has been shown within the work of Banat and co-workers, that cationic and anionic contaminants can interact strongly through these interactions with date syrup-based graphene sand hybrid, as shown in Figure 2.32.[378]

Figure 2.32 Suggested mechanism for adsorption of cationic and anionic contaminants onto date syrup-based graphene sand hybrid. Reprinted from reference [378].

Although non-covalently bonded species can be a desirable means of derivatising the material, showing extensive use for water decontamination for example, they are often undesirable in the form of unreacted reagents and side products. The nature of the graphitic surface mean that the undesirable entities remain strongly adsorbed by the above-mentioned bonding types or integrated within slit pores and stacks. Accordingly, copious amounts of washing may be required following any chemical modification, to prevent unwanted compounds remaining adsorbed to the surface. Unfortunately, the existence of remaining unwanted adsorbed species can have several undesirable implications, such as alteration of the properties of the GBM. Furthermore, they also confuse interpretation. In this regard, it may be believed that one has more of a particular element than is actually the case. As such, it makes it very difficult to quantify the amount of functionalisation which has occurred. Ambiguous assignments and tentative language are therefore used when drawing conclusions within published works relating to the covalent functionalisation of graphene, as it can be very difficult to differentiate adsorbed material from covalently attached material.

2.13 Destructive and Non-Destructive Analysis

All characterisation techniques can be differentiated according to their ability to cause permanent change to the sample or not during the analysis procedure. These are categorised as destructive and non-destructive characterisation methods, respectively. This is important since many early investigations are carried out on a small laboratory scale due to the availably and cost of GBMs. As such, only small quantities of sample may be synthesised, and thus, avoiding destructive testing or carrying it out at the end of several non-destructive techniques is desirable, to minimise the amount of "wasted" material. Table 2.1 classifies some of the key characterisation techniques, identifying whether the technique itself is destructive or non-destructive. Some techniques such as TGA and elemental analysis cause permanent change to the sample. In both cases, the sample is typically heated to high temperatures resulting in thermal decomposition, thus the sample cannot be recovered after testing. Other techniques are non-destructive in nature including Raman spectroscopy, BET, solid-state NMR and XRD, thus the material can be recovered and used for further testing or application. In some cases, techniques may generally be considered non-destructive in nature, however, when applied to

GBMs, the conditions used during analysis and the preparative routes, may result in permanent changes to the sample. As such, each technique is categorised according to whether it is typically non-destructive, non-destructive when applied to GBMs, or destructive due to the technique itself and/or the preparative routes. For these techniques, a comment is provided in the comments column to explain why the technique may result in it becoming destructive or non-destructive in relation to GBMs. In general, destructive characterisation is undesirable since it enforces significant change to the sample, thereby making it unsuitable for further analysis, as well as impeding the material's use in specific applications. As a result, when characterising a sample using multiple destructive characterisation methods, several batches of sample may need to be synthesised, solely for this purpose. Within this work, non-destructive characterisation was carried out prior to destructive testing on a sample, to minimise the quantity of sample needed to be synthesised.

Table 2.1 Destructive and non-destructive characterisation techniques. Some techniques may be non-destructive in nature, however, their preparation routes may introduce permanent change.

Characterisation Technique	Is the Technique Typically Considered Non-Destructive?	Is the Technique Non-Destructive with Graphene-Based Samples?	Is the Technique Destructive?		Comments
			By Technique	By Sample Preparation	
Raman Spectroscopy	✓	✓	-	-	No change implemented on sample during analysis or sample preparation
XPS‡	✓	-	✓	-	UHV (10^{-6} – 10^{-10} Pa) may remove desired volatile adsorbed species Electron beam may chemically modify some species
SEM/SEM-EDX‡	✓	-	✓	✓	Sample preparation can be destructive if conductive sputter coating is required High energy electron beam may damage sample
TEM/TEM-EDX‡	✓	-	✓	-	High energy electron beam may damage sample
TGA		-	✓	-	Sample is decomposed during high temperatures
AFM‡	✓	-	✓	-	Sample may become damaged/misplaced by cantilever
XRD	✓	✓	-	-	No change implemented on sample during analysis or sample preparation
BET‡	✓	-	-	✓	No change implemented on sample during analysis, however, thermally or mechanically sensitive samples may become chemically or physically changed if degas conditions are too extreme
FT-IR‡	✓	✓	-	✓	Generally, no change implemented on sample during analysis or sample preparation Sample preparation may be destructive if KBr disk is required
Elemental Analysis	-	-	✓	-	Sample is decomposed during high temperatures
Solid-state NMR	✓	✓	-	-	No change implemented on sample during analysis or sample preparation

‡ Technique is usually considered non-destructive, however, when applied to GBMs, permanent change may occur due to conditions required or sample preparation techniques.

Within the context of microscopy, samples can indeed undergo permanent change. During SEM and TEM analyses, a high energy beam of electrons propagates towards the sample through a series of lenses. The accelerating voltage of these electrons is typically in the range of 5 − 30 keV for SEM, and 100 − 200 keV for TEM, and the value chosen depends on the sample in question.[290] For example, the energy of this beam must overcome the critical ionisation energy of the inner shell electrons in the atoms of the sample. Whilst scattering enables data to be rendered, for elastic scattering, it has the side effect of causing specimen damage such that electrons transfer their energies to the atoms, thus, causing atoms to become displaced from the material. This is more severe for light elements (H, C, N and O), which unfortunately, are the most common elements incorporated into GBMs. To reduce beam damage, the accelerating voltage can be lowered and the working distance increased. It has been shown in several previous investigations that irradiation-induced damage can occur in GBMs, due to atomic displacement caused by electron beams.[130,379–384] Even relatively low beam voltages (5 − 30 keV) have been shown to induce defects in graphene, as evidenced by Raman spectroscopy, resulting in the degradation of the material's thermal and electronic properties.[382,383] Murakami and co-workers showed that as a low-energy electron beam (100 eV) was irradiated on graphene, internal strain was introduced.[384] Mapping of the Raman G peak shift of the graphene sample, subjected to low-energy electron irradiation, showed that biaxial tensile strain was introduced, as shown in Figure 2.33. With TEM, to reduce knock-on damage, the accelerating voltage of 80 keV is much less likely to damage the sample, however, it should be noted that although 80 keV is the threshold for knock-on damage in pristine graphene, defects and edges will have a lower threshold and thus may become damaged below this. It is also interesting to note that the quality of the vacuum in the microscope may also affect the damage susceptibility, such that ultra-high vacuum (UHV) instruments see lower damage rates.

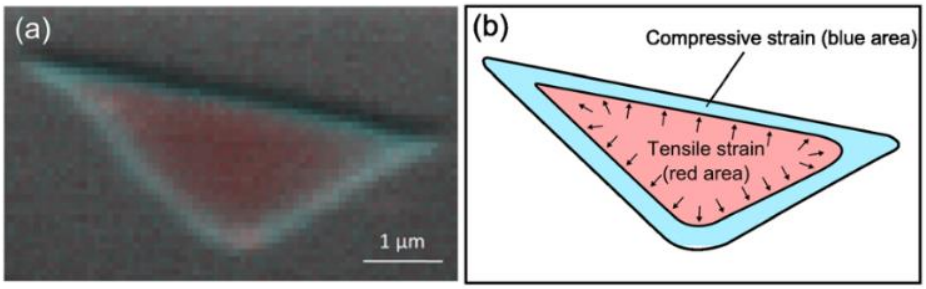

Figure 2.33 Mapping of the Raman G peak position after irradiation of 9.72 mC/cm^2 at 500 eV. The mapping in red (1573.6 cm^{-1}) and blue (1581.1 cm^{-1}) corresponds, respectively, to the red-shifted G peak (i.e., tensile strain) and the blue-shifted G peak (i.e., compressive strain) from the initial G peak position before irradiation (1577.3 cm^{-1}). Reprinted from reference [384]

Of course, using high resolution mode also implements more damage, and the longer the analysis period or scanning speed, the more obvious the effects. X-ray damage can also occur to GBMs upon XPS analysis. The X-ray photon energy is typically 1486.6 eV and thus, does not possess enough energy to displace atoms (typically 5 keV or more is needed), however, it has been shown to chemically modify samples. For example, reduction of a nitro functional group to an amine functional group has been observed in various previous investigations.[197,385,386] The XPS irradiation can also result in reduction of oxygenated graphitic material, especially after prolonger analysis, resulting in breaking of the C–O bonds. XPS measurements are also conducted under an UHV (10^{-6} – 10^{-10} Pa) to avoid collision between photoelectrons and gas molecules within the instrument, as well as to minimise potential surface contamination from residual gases. As such, volatile compounds will be driven off prior to analysis, and hence be undetected. This may pose issues when adsorbed volatile species are desired on the GBM.

Some techniques may be non-destructive in nature, but the preparation routes involve irreversible changes to the sample. For many samples, a conductive sputter coating is required to treat samples, prior to imaging. A common issue encountered with SEM/EDX when viewing insulating graphene samples such as GO or aggregated samples, is they undergo surface charging.[293] This phenomenon arises due to a lack of conductive paths for electrons to flow from the sample surface to the ground, which results in images which drift, blur and exhibit low contrast. Some samples may be conductive in nature, however, still experience charging. This may occur if the sample is not well dispersed on the SEM substrate, and instead, clumps together. Carbon leit tabs are commonly used to attach samples to the metal stub prior to

analysis, however, GBMs and the carbon tabs can be difficult to discern, therefore using a coating increases the number of secondary electrons which are detected from the sample, thus improving the signal to noise ratio. In effort to overcome these issues, samples are often coated with a thin layer of nanoparticles, such as gold. Unfortunately, this coating is not easy to remove after analysis, and hence the sample becomes permanently altered. Furthermore, the gold nanoparticles may also mask features on the sample. FT-IR is formally a non-destructive technique and upon ATR FT-IR analysis, no change is exhibited to the sample. However, in many cases, it can be advantageous to analyse the sample in the form of a KBr disk. This technique is often superior to ATR for the aforementioned reasons. To produce a KBr disk, a small quantity of the GBM is ground in a pestle and mortar with KBr powder, then pressed into pellet form. As such, it becomes exceptionally difficult to remove the GBM again from the newly made disk. In addition, KBr is extremely hygroscopic and therefore any water addition will result in a broad peak associated with water. It should also be noted that BET is not destructive in nature, however, some samples may be affected by extreme degas conditions, such as high vacuums or high temperatures. Meanwhile, eliminating these conditions may not result in effective removal of physisorbed water or volatiles. Any changes to the sample may affect the pore structure and subsequent surface area.[353] Finally, AFM is also not formally considered a destructive technique, however, as described in the previous section, many GBMs can become damaged or displaced by the cantilever during analysis. It is therefore important that the reproducibility of the sample under analysis is considered, and the appropriate amount of sample is synthesised prior to characterisation.

3 Materials and Methodology

3.1 Experimental

3.2 General Remarks

NPs were synthesised by Perpetuus *via* plasma treatment, as outlined below. All reagents and solvents were purchased from commercial sources and used as received. A Gallenkamp SGP-205-020X vortex mixer and a FB15055 FisherBrand ultrasonic bath (ultrasonic frequency 37 kHz and ultrasonic peak max corresponds to 600 W) were employed to create dispersions. A Sorvall Legend T Centrifuge from Kendro Laboratory Products was utilised to extract solids from dispersion at 4000 min^{-1} for 25 minutes.

NP4 was used to synthesise free-standing films and coatings, for the purpose of oil/water separation. The oleophobic/hydrophilic nature of these films and coated substates were investigated using simple oil/water passage tests, contact angle measurements and sliding angle measurements. Furthermore, the materials were fully characterised using various characterisation techniques.

Oil red O and brilliant blue R were used to dye oils and water, respectively. Jet II fuel was provided by Perpetuus. The eight-sectioned metal tray possessed external dimensions of 33 by 24 cm and each rectangular section possessed internal dimensions of 9.5 by 6 cm. The single-sectioned metal tray possessed external dimensions of 24.5 by 17.5 cm and internal dimensions of 23.5 by 16 cm. A5 size meshes were purchased from The Mesh Company and consist of industry standard woven wire mesh stainless-steel grade (#50). Nylon was purchased from Sefar LTD. Kevlar, carbon fibre and glass fibre were provided by The University of South Wales Engineering Department. NPs were synthesised by Perpetuus *via* plasma treatment. All reagents and solvents were purchased from commercial sources and used as received. A Gallenkamp SGP-205-020X vortex mixer and a FB15055 FisherBrand ultrasonic bath (ultrasonic frequency 37 kHz and ultrasonic peak max corresponds to 600 W) were employed to create the dispersions. A Sorvall Legend T Centrifuge from Kendro Laboratory Products was utilised to extract solids from dispersion at 4000 min^{-1} for 25 minutes. A standard burette was used to deposit silicone oil and water droplets onto substrates during oil/water passage tests.

Washing procedures- When filtering NPs using a simple Büchner filtration procedure, it was difficult to identify a suitable filter paper to enable the retainment of the solid NP, whilst allowing free passage of solvent. This became particularly difficult with NPs containing smaller aggregates, such as NP1, NP3 and NP4. In these cases, the smaller aggregates were able to penetrate the pores within the filter paper, whilst larger aggregates did not. This resulted in loss of material, both through the filter paper and within the filter paper, and insufficient filtering of solvent due to the blockage of pores. As such, even filter paper with pores of 0.22 μm in size become clogged. Due to this, filtration was often avoided and instead, solvent removal and product purification was conducted through multiple dispersion/centrifugation/decantation cycles.

3.3 Characterisation of Materials Within this Thesis

Within the work presented within this thesis, several characterisation methods are implemented to gain an understanding of the sample and its characteristics. A brief description of the instrument and preparative details are listed below.

AFM was conducted on an XE-100 atomic force microscope from Park Systems. Samples were dispersed in a volatile organic solvent, drop casted onto freshly cleaved mica and left to air-dry. Measurements were taken using non-contact mode.

XPS was performed using a Kratos Axis Ultra-DLD photoelectron spectrometer with a monochromatic Al K_α electron source (1486.6 eV). Samples were dispersed in a volatile organic solvent, drop casted onto a clean silicon wafer and left to air-dry. Data was analysed using CasaXPS software and binding energies were referenced to carbon core level for adventitious carbon at 284.8 eV possessing an uncertainty of approximately 0.2 eV. Curve fitting was carried out using Gaussian and Lorentzian line profiles.

TGA was carried out using a Perkin Elmer TGA 4000 instrument. Samples (*ca*. 35 mg) were deposited into ceramic crucibles and the temperature was increased from room temperature to 900 °C at a rate of 5 °C min^{-1} under a nitrogen flow (50 mL min^{-1}).

Raman spectroscopy measurements were performed using a Renishaw InVia confocal Raman microscope, equipped with an Ar^+ visible green laser with emission wavelength of 514 nm. A

magnification of 20 x was used over an extended wavenumber range of 100 – 3200 cm^{-1} (static, 625 – 1900 cm^{-1}). Measurements utilised a 5% laser power, with 5 accumulations (static, 20 accumulations) at 10 seconds exposure time (static, 2 seconds) for each material. Samples were deposited directly onto a slide and data was extracted from one spot of the sample. Spectra were collected in a reflective mode using a high sensitivity charge couple device (CCD) detector.

Powder XRD patterns were collected using a Panalytical X'Pert diffractometer with a Cu anode irradiation (λ = 1.5406 Å) operating at 40 kV and 40 mA. Samples were dispersed in volatile organic solvent, drop casted onto a planar substrate and left to air-dry. Phase identification was performed by matching experimental patterns against entries in the ICDD standard database.

Three **SEM** instruments were utilised within this research (SEMs 1 – 3). In all cases the samples were coated with a gold sputter coating to enhance resolution of imaging and accelerating voltages between 5 – 20 kV was utilised with a beam current of 12 kV. **SEM 1**: A Zeiss Supra 35VP (FEG) SEM instrument. The samples were dispersed in volatile organic solvent, drop casted onto metal stubs prepared with carbon leit tabs and left to air-dry. **SEM 2**: MIRA3 Tescan x 64 instrument. The samples were dispersed in volatile organic solvent, drop casted onto metal stubs prepared with double sided copper tape and left to air-dry. **SEM 3**: 1540XB from Carl Zeiss (FEG) SEM using the same preparation as SEM 2. SEM and EDX data within Chapter 4 utilised SEM 1, SEM images within Chapter 5 utilised SEM 1, 2 and 3. SEM images within Chapter 6 utilised SEM 2.

Two **TEM** instruments were utilised within this work (TEM 1 and TEM 2). In both cases, samples were dispersed in volatile organic solvent, drop casted onto a plasma-cleaned copper grid and left to air-dry and a 200 kV power source was utilised. **TEM 1**: JEOL 2100 FEG TEM. **TEM 2**: JEOL JEM 2100 TEM

The surface area and porosity characteristics of the materials were analysed using a Micromeritics ASAP 2020 physisorption analyser at 77 K with nitrogen adsorbate. Surface areas were calculated according to the **BET** method over a P/P_0 range where a linear relationship was maintained, whilst porous studies implemented the **BJH** and **t-plot** methods. All samples were degassed under 0.667 Pa for a defined period of time at a defined temperature. t-plot analysis utilised the Harkins Jura thickness equation and BJH cumulative pore volume methods utilised the *Halsey* equation *with Faas correction.*

Solution ^{1}H, ^{19}F, ^{29}Si, ^{11}B and ^{13}C **NMR** spectrometry were performed on a Bruker 400 MHz AscendTM 400, which operated at 400.13 MHz for ^{1}H nuclei, 376.50 MHz for ^{19}F nuclei, 79.49 MHz for ^{29}Si, 128.38 MHZ for ^{11}B and 100.61 MHz for ^{13}C nuclei. Chemical shifts are reported in parts per million (ppm). NMR spectra were obtained in CD_3CN or $CDCl_3$ solvent as specified.

Solid-state ^{13}C and ^{29}Si MAS **NMR** spectra were recorded on a Bruker AVANCE 400WB magnet and an ASCEND III HD Spectrometer, with a magnetic field strength of 9.4 T. The resonance frequency used for ^{13}C and ^{29}Si nuclei was 100.58 MHz and 79.47 MHz, respectively. Samples were packed into a zirconia rotor with a 4.0 mm outer diameter. Glycine was used to reference the ^{13}C chemical shift, and both kaolin and TMS were used to reference the ^{29}Si chemical shift. All the samples that were run that did not contain graphitic material were analysed using a ^{13}C CP-MAS program and a one pulse ^{29}Si program. If graphitic material was present, a HPDEC program was used to perform the ^{13}C and ^{29}Si analyses. The spectra were obtained at a spin speed of 10 kHz, with a recycle delay of 5 seconds for ^{13}C (CP-MAS) and 20 seconds for ^{29}Si. The ^{13}C CP-MAS program used 90° pulses of 2.5 microseconds and 1500 microseconds contact times. The HPDEC spectra was recorded with 2.5 microseconds 90° pulses and a recycle delay of 5 seconds for both ^{13}C and ^{29}Si.

Mass spectrometry was conducted on a Thermoscientific ISQ Single quad with direct insertion probe in positive electron impact mode. The identity of the compounds was confirmed for the preinstalled library of compounds.

FT-IR ATR analysis was conducted on a PerkinElmer Spectrum Two IR spectrometer. A resolution of 4 cm^{-1} was used with an accumulation of 8 scans. Samples were deposited onto a diamond crystal and a scan was conducted between 4000 and 500 cm^{-1}. Alternatively, some samples were prepared into a KBr disk and analysed *via* transmission mode.

3.3.1 Synthesis of Plasma-Exfoliated Graphitic Material

Natural flake plasma processing of natural graphite was carried out using a custom-made DBD plasma reactor as described elsewhere.[95]

3.3.2 Synthesis of f-NP1

4-(trifluoromethyl)phenylboronic acid (0.930 g, 4.91 x 10^{-3} mol) was added to NP1 (0.720 g) and dispersed in a solvent mixture consisting of water and DCM (1:1) (40 mL in total), followed by the addition of $K_2S_2O_8$ (2.600 g, 9.62 x 10^{-3} mol) and $AgNO_3$ (1.180 g, 7.00 x 10^{-3} mol). The mixture was allowed to stir for 44 hours at room temperature. The reaction mixture was then centrifuged and the resultant material, was extracted and washed repeatedly with water, acetonitrile, and DCM through several dispersion/centrifugation cycles. The resultant f-NP1 was then extracted and left on vacuum (10^{-6} bar) for 1 week to remove any potentially remaining solvents and volatile compounds.

3.3.3 Control Reaction A- Reactivity of Radicals Generated from 4-(Trifluoromethyl)phenyl Boronic Acid in the Absence of NP1

This reaction was carried out using similar conditions to that of previous works.[387,388] The reagent 4-(trifluoromethyl)phenyl boronic acid (0.092 g, 4.83 x 10^{-4} mol) was dissolved in a solvent mixture (40 mL) consisting of water and DCM (1:1), followed by the addition of $K_2S_2O_8$ (0.266 g, 9.85 x 10^{-4} mol) and $AgNO_3$ (0.027 g, 1.60 x 10^{-4} mol). The mixture was allowed to stir for 44 hours at room temperature. The biphasic mixture was filtered, and the DCM layer was separated from the filtrate using a separating funnel. The DCM layer was then evaporated to dryness to give a yellow oil consisting of two compounds: 4,4'-bis(trifluoromethyl)biphenyl (compound A) and bis((trifluoromethyl)-diphenyl)ether (compound B). Characterisation of compound A: ^{1}H NMR δ (CD_3CN): 7.87 (d, $^3J_{HH}$ = 8.2 Hz, 4H), 7.81 (d, $^3J_{HH}$ = 8.2 Hz, 4H). ^{19}F NMR d (CD_3CN): −63.06. EI-MS *m/z* $[M]^+$ calc. for $C_{14}H_8F_6$ 290 Da: found: 290 Da. Characterisation of compound B: 1H NMR d (CD_3CN): 7.72 (d, $^3J_{HH}$ = 8.2 Hz, 4H), 7.20 (d, $^3J_{HH}$ = 8.2 Hz, 4H). ^{19}F NMR d (CD_3CN): −62.42. EI-MS *m/z* $[M]^+$ calc. for $C_{14}H_8F_6$ 306 Da: found 306 Da.

3.3.4 Control Reaction 1- Synthesis of C1-NP1

NP1 (0.1531 g) and 4-(trifluoromethyl)phenyl boronic acid (0.1657 g, 8.724 x 10^{-4} mol) were dispersed in a solvent mixture (20 mL) consisting of water and DCM (1:1). The mixture was allowed to stir for 44 hours at room temperature. The reaction mixture was then centrifuged and the resultant C1-NP1, was extracted and washed repeatedly with water, acetonitrile, and DCM through several dispersion/centrifugation cycles. The resultant material was then extracted and left on vacuum (10^{-6} bar) for 1 week.

3.3.5 Control Reaction 2- Synthesis of C2-NP1

NP1 (0.1473 g) and $AgNO_3$ (0.187 g, 1.10 x 10^{-3} mol) were dispersed in a solvent mixture (20 mL) consisting of water and DCM (1:1). The mixture was allowed to stir for 44 hours at room temperature. The reaction mixture was then centrifuged and the resultant C2-NP1 was extracted and washed repeatedly with water, acetonitrile, and DCM through several dispersion/centrifugation cycles. The resultant material was then extracted and left on vacuum (10^{-6} bar) for 1 week.

3.3.6 Control Reaction 3- Synthesis of C3-NP1

NP1 (0.159 g) and $K_2S_2O_8$ (0.574 g, 2.12 x 10^{-3} mol) were dispersed in a in a solvent mixture (20 mL) consisting of water and DCM (1:1). The mixture was allowed to stir for 44 hours at room temperature. The reaction mixture was then centrifuged and the resultant C3-NP1, was extracted and washed repeatedly with water, acetonitrile, and DCM through several dispersion/centrifugation cycles. The resultant material was then extracted and left on vacuum (10^{-6} bar) for 1 week.

3.3.7 Washing Procedure for f-NP1 and CX-NP (X = 1 – 3)

After reaction, the treated samples (f-NP1 and CX-NP (X = 1 – 3)) were washed extensively to remove impurities and unreacted reagents. Ideally, Büchner filtration would have been implemented to wash the NP materials, however, the irregularity in particle size and contribution of tiny particles (less than 200 nm) meant that even some of the smallest pore size filter papers (0.2 μm pore size) became blocked, thereby impeding filtration. As a result, the washing procedure involved dispersing the treated NP in a solvent using a vortex mixer, then centrifuging the mixture to promote sedimentation of treated NP materials at the bottom of the centrifuge tube. The solution above was then decanted and disposed of. The process involved repeated washing until the solvent above was free of compounds or impurities. To test the presence of these, the pH was measured using standard pH indicator paper and ^{1}H, ^{19}F and ^{11}B NMR analysis was used to detect the presence of any unreacted reagents, impurities, or solvent. The treated NP samples were washed with various solvents, including water, acetonitrile, DCM and acetone. The samples were then dried under vacuum (10^{-6} bar) for 1 week, to remove any potentially remaining solvents and volatile compounds.

3.3.8 Characterisation of f-NP1 and CX-NP1 (X = 1 – 3)

SEM and EDX analyses were conducted on SEM 1, whilst TEM was conducted on TEM 1 (see Chapter 2 for details). XPS, FT-IR, Raman spectroscopy, XRD, BET/BJH/t-plot, TGA, solution-state NMR and mass spectrometry analyses were conducted in accordance with Chapter 2. During physisorption analysis, degas was conducted at 150 °C for 720 minutes.

3.3.9 Synthesis of O-NP3

O-NP3 was synthesised from NP3 using the modified Hummers method according to previous works.[389] In summary, H_2SO_4 (150 mL) was added to NP3 (5.02 g) and allowed to magnetically stir for 5 minutes. The flask was placed cooled to 0 °C (ice bath) then $KMnO_4$ (17.5 g) was

added slowly over a 30-minute period. After complete addition, the temperature was warmed to 35 °C and stirred for a further 2 hours. The mixture was then cooled to 0 °C (ice bath) and excess water was added followed by H_2O_2 (30 wt.% in water) until bubbling stopped. The subsequent oxidised material, O-NP3, was then extracted *via* centrifugation and washed several times with DI water. The sedimented material was then dried at 80 °C under vacuum for 12 hours and ground to a fine powder using a pestle and mortar.

3.3.10 Synthesis of Non-Covalent O-NP3/Laponite Composites

O-NP3 was placed into DI water and sonicated for 1 hour. Laponite was added to the O-NP3 dispersion, and the mixture was bath sonicated for a further 1 hour. The subsequent O-NP3/laponite composites were dried at 85 °C under vacuum for 2 hours to remove the water. (The composition of laponite within O-NP3/laponite was dependent on the ratio defined within the text, where a specific weight percentage of laponite (wt.%) is defined relative to the total weight of laponite and O-NP3).

3.3.11 Synthesis of f-laponite

F-laponite was synthesised in accordance with previous work.[390] Laponite (5.00 g) was stirred in 150 mL of deionized water at 50 °C for 30 minutes. A solution of aminopropyltriethoxy silane (APTES) (5 mL, 21.4 mmol) in 150 mL of DI water was prepared, and the pH adjusted to 5 with acetic acid. This solution was heated to 50 °C and allowed to stir for 10 minutes. The solution was poured into the laponite dispersion, immediately causing the solution to turn cloudy and viscous. Stirring continued at 50 °C for 16 hours. The pH was then adjusted to 9 with NaOH to neutralize the acetic acid and deprotonate the amines. The product was collected *via* vacuum filtration on a Büchner funnel as a white gel, washed with 500 mL water, then dried in a vacuum oven at 80 °C for 18 hours. To remove residual contaminants, the product was ground to a fine power with a mortar and pestle, stirred in 150 mL of water, filtered and washed

with 500 mL acetonitrile and 500 mL water. The subsequent material was then dried at 80 °C under vacuum for 12 hours.

3.3.12 Synthesis of f-NP3

O-NP3 (0.6067 g) was added to f-laponite (0.6175 g) in dry DMF (40 mL). dicyclohexylcarbodiimide (DCC) (0.343 g) was added and stirring was allowed for 6 hours at 60 °C. The subsequent solid was washed *via* multiple dispersion/centrifugation/decantation cycles using water, acetone and acetonitrile. The subsequent material was dried under vacuum for 12 hours, affording f-NP3.

3.3.13 Synthesis of NP4-PP Composite

PDDA aqueous solution (7.2 mL, 4.46 x 10^{-3} mol) was added to NP4 (0.5604 g) and placed in a beaker within an ultrasound bath for 10 minutes, to form a dispersion. The dispersion was then allowed to stir for a further 10 minutes. In a separate beaker, PFO (1.75 g, 4.01 x 10^{-3} mol) was dissolved in 10 mL DI water using an ultrasound bath (10 minutes) then the dispersion was slowly added to the NP4/PDDA dispersion over a 5-minute period. Upon addition of PFO to NP4/PDDA, a thick slurry was formed immediately. The slurry was dispersed in DI water and mixed, then centrifuged and decanted to remove any soluble material. This process was repeated twice. The sediment was then dried under vacuum for 12 hours and the subsequent solid (4.614 g) was denoted as NP4-PP composite.

3.3.14 Preparation of NP4-PP Films

To prepare “NP4-PP thick film”, 1.75 g of NP4-PP composite was dispersed in 35 mL MeOH *via* bath sonication for 15 minutes then poured into a single section of the eight-sectioned metal tray. This was left overnight for the solvent to evaporate, providing a thick film.

To prepare “NP4-PP thin film” 0.80 g of NP4-PP composite was dispersed in 35 mL MeOH *via* bath sonication for 15 minutes then poured into a single section of the eight-sectioned metal tray. This was left overnight for the solvent to evaporate, providing a thin film.

To prepared “NP4-PP thin film 2” 2.5 g of NP4-PP composite was dispersed in 150 mL MeOH *via* bath sonication for 15 minutes then poured into the single-sectioned metal tray. This was left overnight for the solvent to evaporate, providing a thin film.

3.3.15 Preparation of NP4-PP Coated Substrates

NP4-PP composite (2.56 g) was dispersed in 150 mL of MeOH *via* bath sonication for 15 minutes then poured into the single-sectioned metal tray over the Kevlar, carbon fibre, glass fibre, nylon and stainless-steel mesh and left to evaporate overnight, affording coated substrates. These were denoted as: NP4-PP coated Kevlar, NP4-PP coated carbon fibre, NP4-PP coated glass fibre, NP4-PP coated nylon and NP4-PP coated stainless-steel.

In addition, nylon was also coated using the same synthesis method, utilising MeOH dispersions of NP4-PP composite containing 0.16 g per 150 mL and 0.26 g per 150 mL. These are referred to as “NP4-PP coated nylon 2” and “NP4-PP coated nylon 3” respectively.

3.3.16 Characterisation of NP4-PP Composite, NP4-PP Films and NP4-PP Coated Substrates

SEM was conducted on SEM 2. XPS, AFM, FT-IR, Raman spectroscopy, XRD and BET/BJH/t-plot analyses were conducted in accordance with Chapter 2. During physisorption analysis, degas was conducted at 25 °C for 720 minutes for PDDA containing samples and 100 °C for 720 minutes for non-PDDA containing samples. Sliding angle measurements were conducted using an electronic goniometer purchased from Nestle. Silicone oil (ca. 0.05 mL) was deposited on each material, which was fixed to the apparatus, as shown in Figure 6.30 in Chapter 6. Contact angle measurements were conducted at Swansea University using a Krüss DSA25 Drop Shape Analyser using the sessile drop method to measure the static contact angles.

4 Boronic Acids for the Functionalisation of Plasma-Exfoliated Graphitic Material as an Alternative to Diazonium Salts

4.1 Synopsis

Within this chapter, a novel strategy for the synthesis of functionalised NP1 was investigated. The development of new functionalisation strategies on commercially derived GBMs is of great importance across materials science. At present, some of the most popular methods utilise undesirable reagents, such as diazonium salts, which are renowned for their explosive nature.[391] Aside of the hazards associated with diazonium salt reactions, the synthesis route also presents a number of challenges. Commonly, diazonium salt synthesis relies on the treatment of a primary amine with an aqueous solution of nitrous acid and a mineral acid.[392] Nitrous acid can, however, exert an unfavourable effect on diazonium salt stability, interfering with further processing. It also has the potential to decompose and release toxic NO_x gases.[393] As a result, access to aryl radicals through alternate precursors, is desirable for the purpose of large-scale functionalisation of industrial synthesised NPs. Within this chapter, a new methodology was investigated for the purpose of covalently functionalising NP1. The methodology involves the use of aryl boronic acids as aryl radical precursors. Such compounds have previously been shown to provide access to aryl radicals using various reagents including, $Mn(OAc)_3$,[394] $Ag(I)NO_3/K_2S_2O_8$,[387,388] $Fe(OTf)_3$/ *t*-BuOO*t*-Bu[395] and $[Ni(acac)_2]/K_3PO_4$/*t*-BuOO*t*-Bu[396], to enable coupling of aryl radicals with olefins through oxidative radical addition. A good review of the aryl radical pathways of aryl boronic acids has been reported by Yan and co-workers.[397] For this investigation, the Baran protocol was chosen to provide radical species from their corresponding aryl boronic acids. The protocol utilised inexpensive reagents including catalytic $Ag(I)NO_3$ in conjunction with $K_2S_2O_8$, as an oxidising reagent. As such, it was shown that radicals were generated with ease, upon removal of the boronic acid functional group within many boronic acids. Aryl boronic acids are safer precursors than diazonium salts since they do not release toxic gases, and therefore show promise as potential aryl radical precursors for large-scale, industrial synthesis of functionalised NPs. In addition, the radical functionalisation reaction consists of one step only; simply the removal of the boronic acid functional group to reveal the substituted aryl radical. Less desirably, diazonium salt reactions often consist of two steps, due to the treatment of a primary amine precursor prior to formation of the diazonium salt and subsequent aryl radical generation. Furthermore, diazonium salts

also require careful handling and storage. As such, this preliminary investigation shows promise as a scalable route towards the industrial synthesis of functionalised NPs.

The reaction of NP1 with the aryl boronic acid precursor 4-(trifluoromethyl)phenyl boronic acid was therefore investigated, and showed that covalent binding took place between the 4-(trifluoromethyl)phenyl moieties and the sheets of NP1 to form functionalised NP1 (denoted f-NP1). The success of this reaction is discussed in detail and the functionalised material is fully characterised *via* a plethora of techniques.

4.2 Results and Discussion

4.2.1 Mechanism of Radical Formation from Boronic Acid

As indicated above, Baran demonstrated that it was possible to form the 4-(trifluoromethyl)phenyl radical from its corresponding boronic acid, as shown in the proposed mechanism in Scheme 4.1 (a). This was achieved utilising a combination of $K_2S_2O_8$ oxidising reagent/$AgNO_3$ catalyst.[387,388] According to such work, it was suggested that the method proceeded *via* disproportionation of the persulfate anions to form the sulfate dianion and the sulfate radical anion in the presence of Ag(I). In Baran's case, this aryl radical was reacted with a protonated heterocycle to form a radical cation, which was re-oxidised by the Ag(I) catalyst, *via* a nucleophilic radical addition mechanism. In this present work, it was anticipated that the radical addition reaction would take place on the NP material *via* the transformation shown in Scheme 4.1 (b). It was postulated that the graphitic sheets, which contain extensive unsaturation, donate electrons which combine with 4-(trifluoromethyl)phenyl radicals to form covalent bonds. Bond formation in this way is believed to be accompanied by a re-hybridisation of the carbon atom at each site of reactivity from sp^2 to sp^3. It was also speculated that some 4-(trifluoromethyl)phenyl radicals would react

in the same manner with one another. As such, control reaction A was conducted to observe potential side-products formed in cases where radicals did not combine with NP1. The findings of this reaction are explained in more detail within the next section.

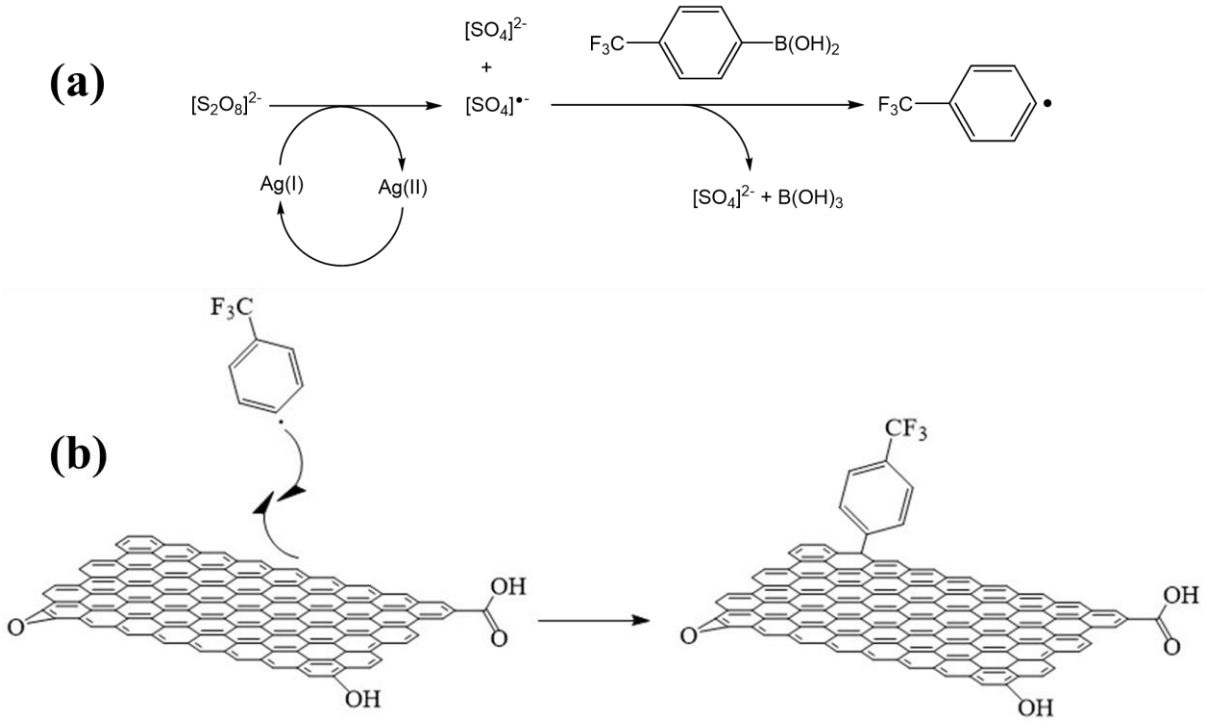

Scheme 4.1 (a) Mechanism of aryl radical formation from 4-(trifluoromethyl)phenyl boronic acid in the presence of $K_2S_2O_8$ and $AgNO_3$ as proposed by Baran et al (Ref [387,388]) and (b) The proposed mechanism of reaction between generated 4-(trifuoromethyl)phenyl radicals with a graphitic layer of NP1 to afford covalent bond formation

4.2.2 Investigation into Control Reaction A

Control reaction A was conducted to analyse the behaviour of the 4-(trifluoromethyl)phenyl radicals in the absence of NP1, to observe the potential side-product formation during f-NP1 synthesis. It is extremely important within this type of synthetic chemistry to recognise potential side-products to not only understand how the desired reaction could be influenced by them, but also enable their effective removal from the desired products (*vide infra*). Control reaction A formed a yellow oil within the DCM layer, following work up. This consisted of two components: the homo-coupled product 4,4′-bis(trifluoromethyl)biphenyl (compound A) and 4,4'-bis(trifluoromethyl)diphenyl) ether (compound B), as shown in Scheme 4.2. These compounds were formed in approximately a 1:1 stoichiometry and characterised *via* ^{1}H and ^{19}F NMR spectroscopy and mass spectrometry (as shown in Figures 4.1 − 4.3). It was found that 44 hours stirring at room temperature was sufficient for complete conversation of starting material. The synthesis of compound A was as expected, originating from the dimerisation of 4-(trifluoromethyl)phenyl radicals under catalytic/oxidative conditions, as explained within the previous section. The synthesis of compound B, however, was not. It is likely that this product derived from reaction between the radical species with water, to form 4-(trifluoromethyl)phenol, which then underwent a C–O coupling reaction to form the oxygen bridged ether product.

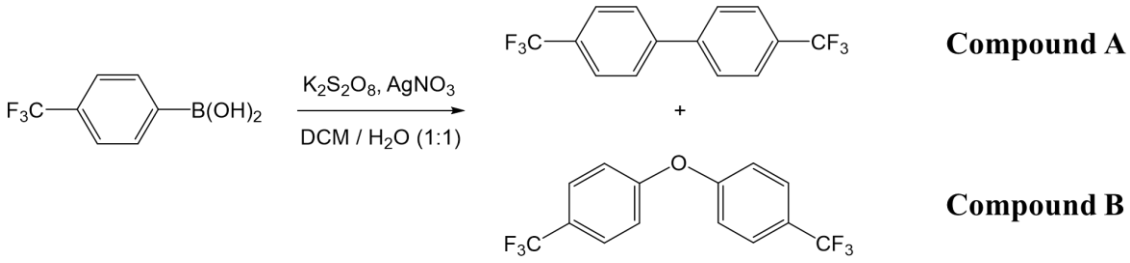

Scheme 4.2 Control reaction A consisting of the reaction between 4-(trifluoromethyl)phenyl boronic acid with $K_2S_2O_8$ oxidant and $AgNO_3$ catalyst to form compounds A and B.

Within the mass spectrum two large peaks were observed corresponding to 290.14 and 306.15 m/z (Figure 4.1). These relate to the molecular masses of compounds A and B, respectively. Within the ^{1}H NMR spectra, two sets of doublet pairs were visible, as shown in Figure 4.2. Their integration confirmed an approximate 1:1 stoichiometry. Those most downfield (at 7.87 ppm and 7.81 ppm were found to correspond to compound A, whilst those at 7.73 and 7.20 ppm were believed to correspond to compound B.[398] Within the ^{19}F NMR spectra (Figure 4.3), two peaks were observed corresponding to the CF_3 environments in both compounds. These signals were located at −63.08 ppm and −62.42 ppm and were assigned as compounds A and B, respectively.

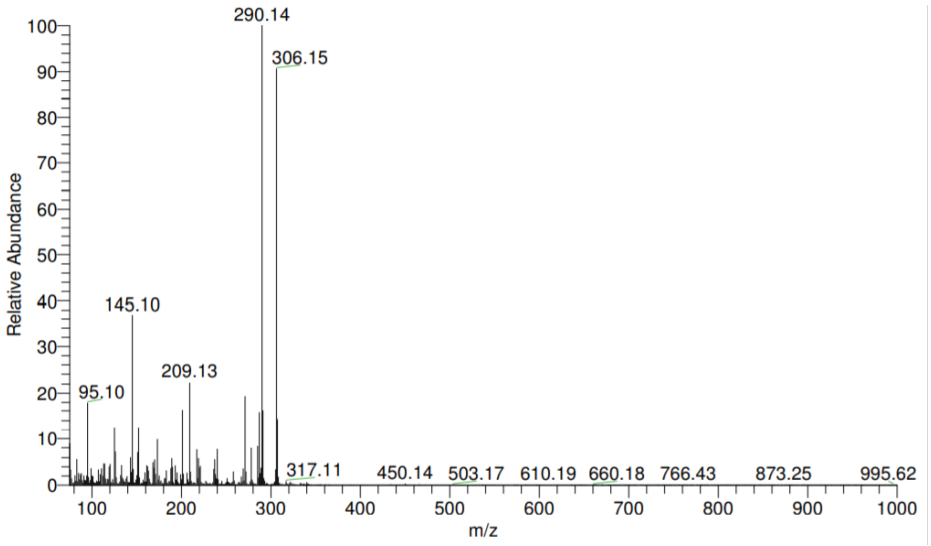

Figure 4.1 Mass spectrum of the product of control reaction A consisting of a mixture of compound A and compound B

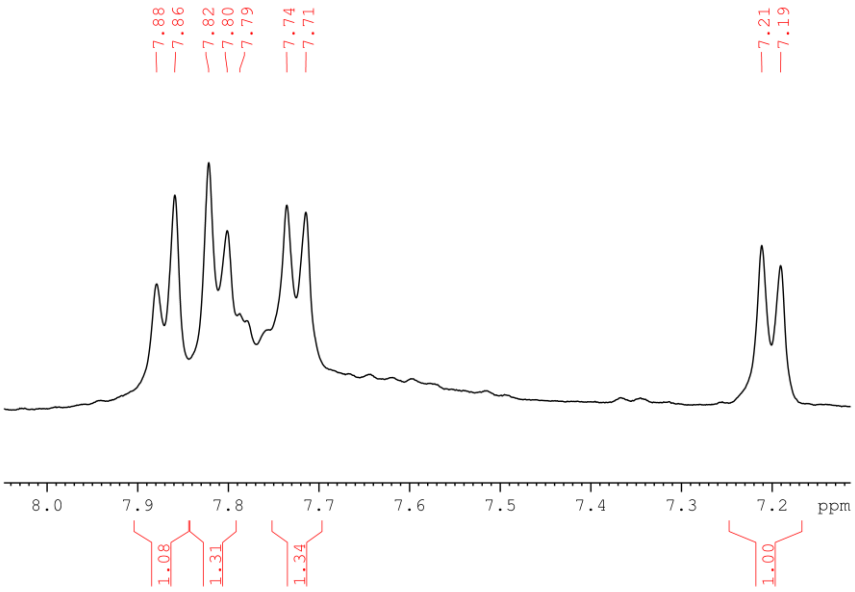

Figure 4.2 [1]H NMR spectrum of the product of control reaction A consisting of a mixture of compound A and compound B

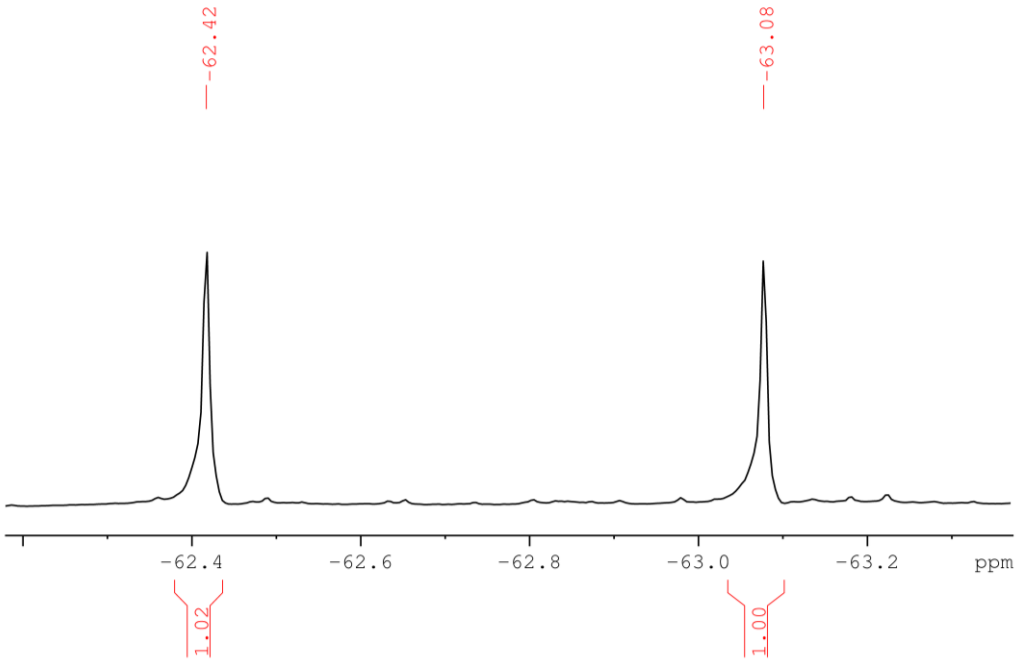

Figure 4.3 [19]F NMR spectrum of the product of control reaction A consisting of a mixture of compound A and compound B

Attempts were made to separate these components, with the vision to fully characterise them and understand their individual solubilities. For this, column chromatography, recrystallisation

and sublimation procedures were carried out. Unfortunately, it was not possible to separate these. It was therefore concluded that the compounds possessed extremely similar solubilities, thereby, hindering their separation. Attempts were then focused on the synthesis of compounds A and B individually. Compound A was successfully synthesised according to known procedure, and characterised by ^{1}H and ^{19}F NMR, as shown in Figure 4.4 and Figure 4.5 respectively.[398] A known procedure was also implemented in an attempt to synthesise compound B. This utilised 4-(trifluoromethyl)phenyl boronic acid with $Cu(OAc)_2$ and 10 equiv of water.[399] The reaction, however, led to an undesirable mixture containing both compounds A and B. No further efforts were made towards compound B synthesis.

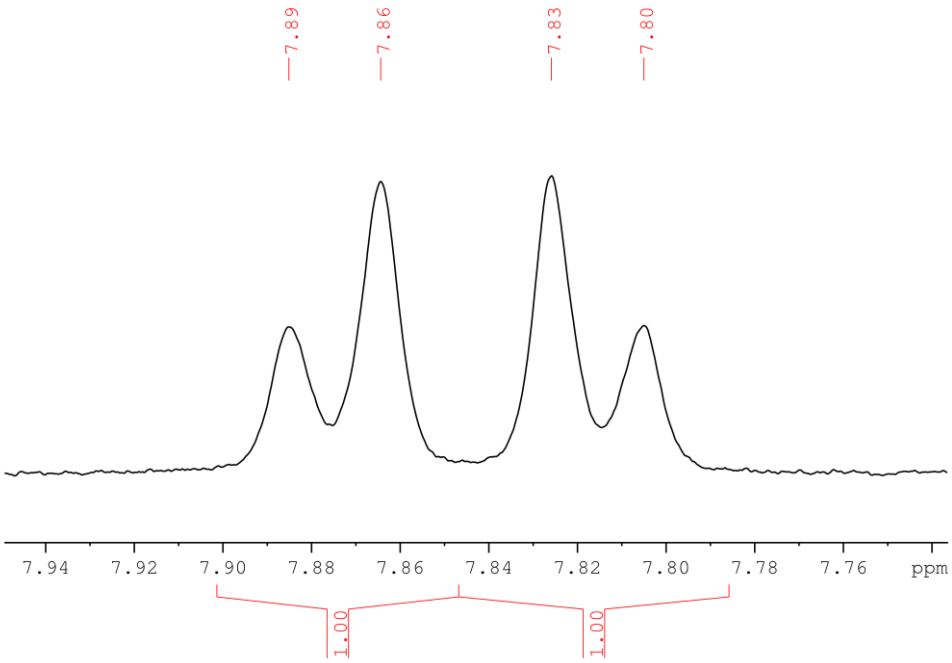

Figure 4.4 ^{1}H NMR spectrum of compound A.

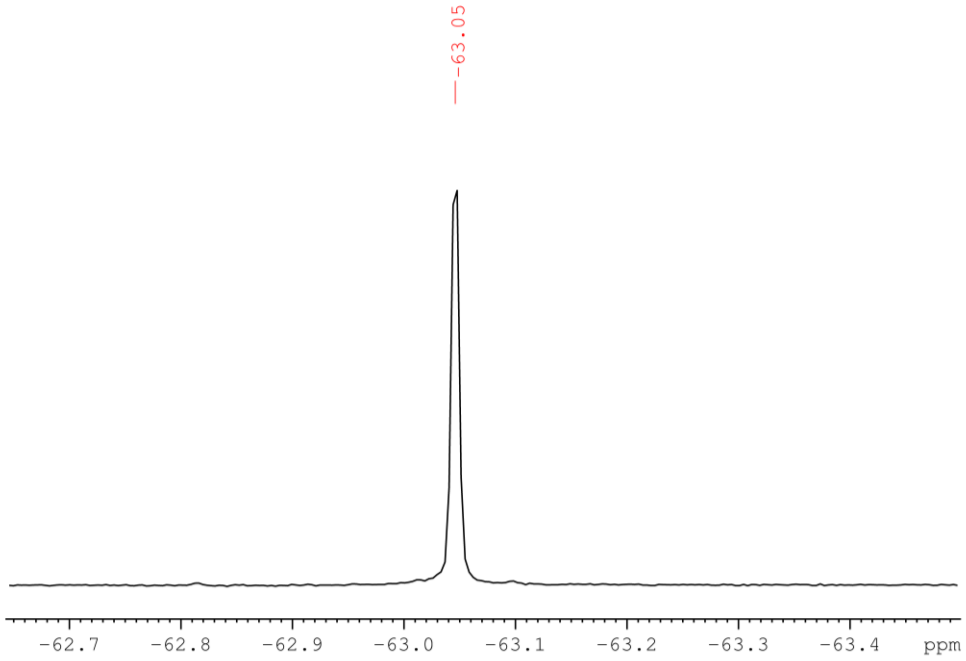

Figure 4.5 ^{19}F NMR spectrum of compound A.

Through the identification and characterisation of compounds A and B within the mixture, it became possible to identify their presence and absence within washing filtrates during f-NP1 synthesis, as described in Section 3.3.7. As a result, extensive washing could be continued until the filtrates were free of either compound. ^{19}F NMR analysis was particularly useful for detection of these compounds due to the high sensitivity of the ^{19}F isotope in NMR spectroscopy and natural abundance of 100%. Fluorine is also highly responsive to changes in its electronic environment, therefore different compounds have distinct chemical shifts. It was also possible to record the ^{19}F NMR spectra of the filtrates directly without the need for deuterated solvents. Due to this, it was assumed that an absence of peaks with the ^{19}F spectra, correlated to an absence of fluorine containing compounds A and B, non-covalently bonded to NP1. XPS quantitative data detects surface elements but is not able to recognise whether these elements are bonded to the graphitic sheets or loosely adsorbed within. Therefore, the efficient removal of these contaminants is extremely important. As previously mentioned, these compounds are also volatile and are thus, incompatible within the XPS chamber. The utilisation of the ultra-high vacuum (UHV) for extended time within the XPS chamber would have completely removed any residual traces. Therefore, the quantitative data for the F 1s state is assumed to provide an accurate representation of only 4-(trifluoromethyl)phenyl groups which are covalently bonded to NP1 materials, rather than any adsorbed compounds A or B.

4.2.3 Characterisation of NP1 and f-NP1 and Various CX-NP1s

To assist with the characterisation of f-NP1, the untreated precursor, NP1 was also fully characterised. Furthermore, various control reactions were also conducted, and their products were analysed to support interpretation. These involved the addition of each reagent individually to NP1 to form CX-NP1 (X = 1 – 3), consistent with the addition of 4-(trifluoromethyl)phenyl boronic acid (control reaction 1), $AgNO_3$ (control reaction 2) and $K_2S_2O_8$ (control reaction 3), respectively. All controls were conducted at room temperature for 44 hours, and the subsequent product was washed repeatedly, as outlined in Section 3.3.7. Scheme 4.3 outlines the reagent addition to NP1 to form f-NP1and CX-NP1 (X = 1 – 3).

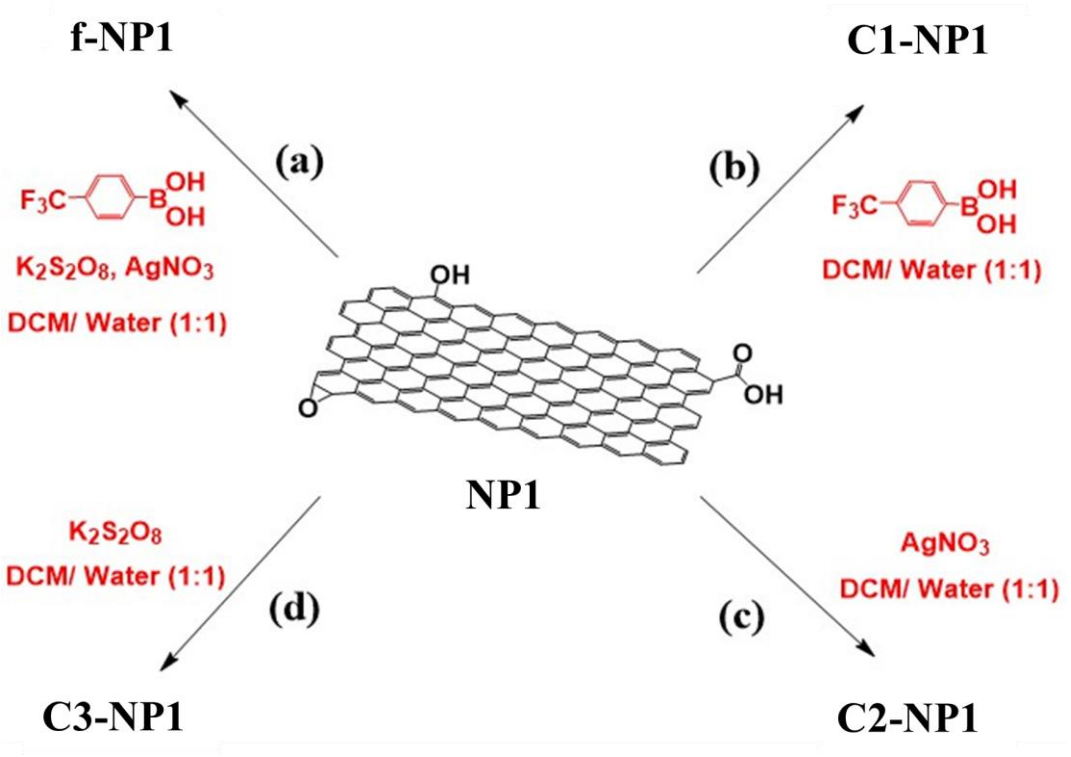

Scheme 4.3 Various reagent additions to NP1 corresponding to (a) f-NP1 synthesis (b) control reaction 1 (c) control reaction 2 and (d) control reaction 3

4.2.4 Elemental Analysis

Elemental surface analysis is a valuable tool to identify the elements present within solid-state materials. As such, both XPS and SEM-EDX analyses were implemented to determine the surface and bulk elements within f-NP1, thereby, providing an insight to the functionalisation process.

4.2.4.1 XPS Analysis

XPS analysis was utilised to identify and compare elemental presence within the surface regions of NP1, f-NP1 and CX-NP1 (X = 1 – 3). The corresponding quantitative elemental composition data is presented within Table 4.1. The survey spectra associated with NP1 and f-NP1 are also presented Figure 4.6. These show that all materials differ in their surface compositions by % atomic composition (at.%). As expected, all NP1 materials consist mostly of carbon, as well oxygen, which is introduced during plasma processing within the DBD reactor, as outlined in Chapter 3. Nitrogen surface impurities are also present within the untreated NP1 material, in small amounts (< 0.3 at.%), which, consequently, remain within f-NP1 and CX-NP1 (X = 1 – 3). The data confirms a large increase in the surface elements present within f-NP1, again consistent with the increased functionalisation of the material.

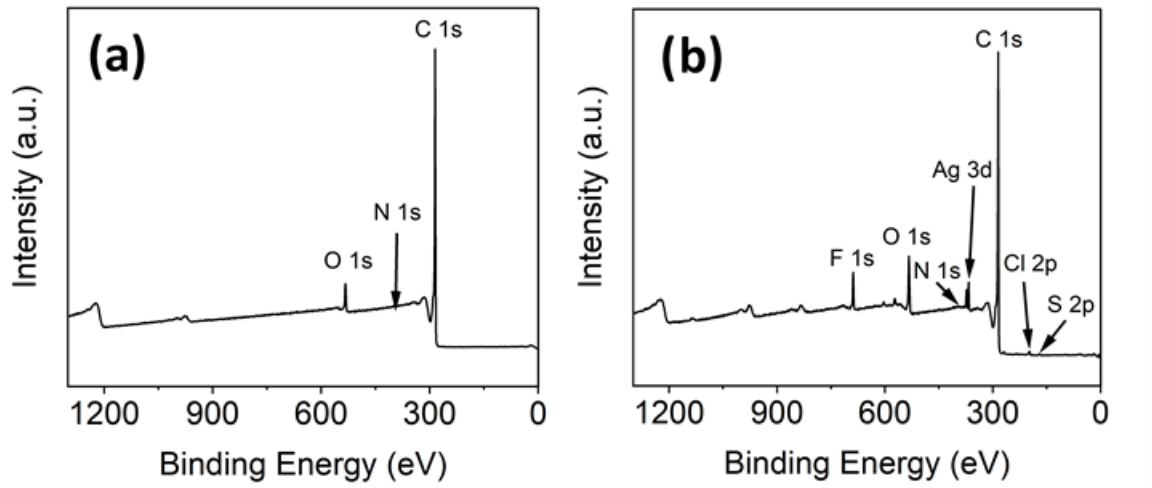

Figure 4.6 XPS survey spectra of; (a) NP1 and (b) f-NP1

Table 4.1 XPS Quantitative data for NP1, f-NP1 and CX-NP1 (X = 1 – 3).*

Orbital	% Atomic Composition				
	NP1	**f-NP1**	**C1-NP1**	**C2-NP1**	**C3-NP1**
C *sp²*	64.3	47.5	73.8	75.0	51.2
π–π*	10.3	7.5	8.5	8.2	8.7
C=O	3.8	3.4	2.8	2.9	4.3
C-O	6.5	6.2	2.6	2.4	6.2
C *sp³*	8.8	15.8	5.1	5.1	14.9
O-C=O	1.3	3.2	1.7	1.7	3.6
C–F_3	-	2.1	-	-	-
C–F_x	-	0.7	-	-	-
C 1s (total C)	94.9	86.5	94.4	95.3	88.8
O 1s	4.9	8.5	4.7	4.5	10.7
N 1s	0.3	0.3	0.1	0.2	0.2
F 1s	-	3.5	0.6	-	-
S 2p	-	0.3	-	-	0.3
Ag 3d $^5/_2$	-	0.7	-	0.1	-
Cl 2p	-	0.4	-	-	-
B 1s	-	-	0.2	-	-

*Incorporates the C 1s state, broken down into its various environments based on binding energy and the integrated area reveals the at.% of each environment. The total C 1s atomic percentage is calculated as a combination of the at.% of each environment.

Deconvolution of the high-resolution C 1s spectrum of NP1 Figure 4.7 (a) shows that the material consists of seven carbon environments. These include: C *sp²* (284.5 eV), π–π* (290.9 and 294.0 eV), C=O (288.3 eV), C−O (286.6 eV), C *sp³* (284.8 eV) and O−C=O (289.6 eV). The corresponding C 1s spectrum for f-NP1, as shown in Figure 4.7 (b), consists of nine components corresponding to C *sp²* (284.5 eV), π−π* (290.9 and 294.0 eV), C=O (287.7 eV), C−O (286.4 eV), C *sp³* (284.8 eV), O−C=O (289.0 eV), C−F_x (284.9 eV) and CF_3 (292.7 eV). These π−π* satellite structures give evidence of π bonding and arise due to π−π* transitions generating a continuum of excitations.[400,401] Whilst both show graphitic character, f-NP1 shows additional C–F functionality, originating from the incorporation of 4-(trifluoromethyl)phenyl moieties to the material. Overall, there is a reduction in the percentage carbon within the functionalised samples. There is also a large increase in the concentration of *sp³* hybridised carbon centres, with respect to *sp²* hybridised carbons, from 8.8 up to 15.8 at.% suggesting that covalent attachment to the conjugated *π* network has taken place within f-NP1. Some of this increase has been attributed to oxidation of the NP1 sample as a result of the oxidising conditions used, however, the

level of increase in oxygen content does not account for such a large increase in sp^3 hybridised centres (*vide infra).* These observations are consistent with some degree of covalent attachment of the 4-(trifluoromethyl)phenyl moieties to the sp^2 network within the functionalised material.

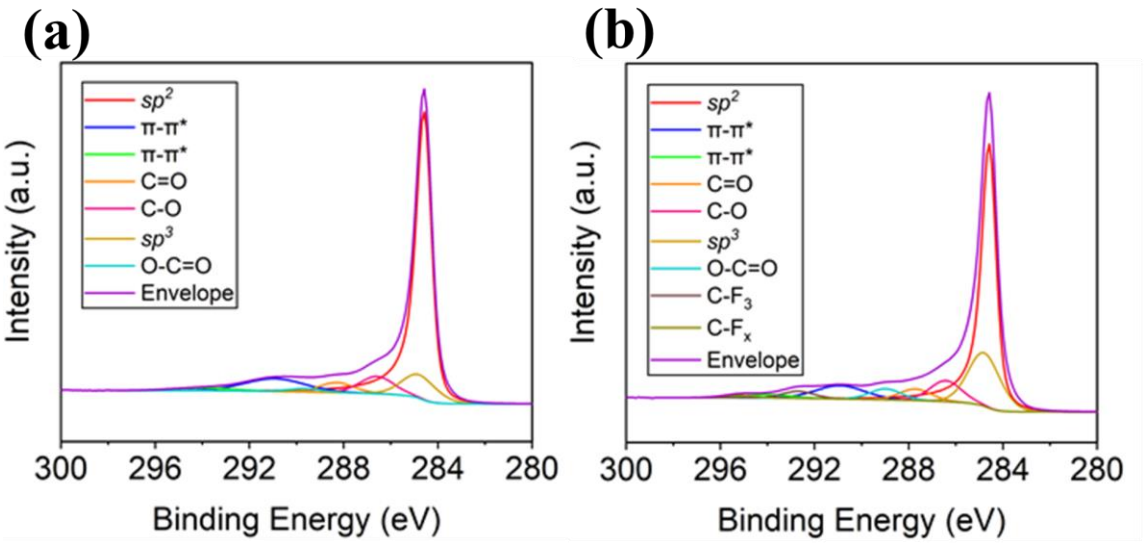

Figure 4.7 Deconvoluted spectra of C 1s orbital; (a) NP1 and (b) f-NP1.

The O 1s spectrum for NP1 (Figure 4.8 (a)) consists of five components C=O (531.7 eV), O 1s C–O–C (533.1 eV), C–OH (535.1 eV), and O 1s satellite structures (536.9 eV and 538.9 eV). The presence of these oxygen functionalities make up 4.8 at.% and originate from the plasma processing of the NP1 material. These satellite structures also arise due to π–π* transitions within carbonyl containing functionalities as a result of transitions between the bonding and antibonding orbitals. The O 1s spectrum for f-NP1 exhibits a similar spectrum to NP1 (Figure 4.8 (b)), displaying identical components corresponding to C=O (531.7 eV), C–O–C (533.1 eV), C–OH (535.1 eV) and O 1s satellite structures (536.9 and 538.9 eV), with similar respective ratios. Upon functionalisation however, its oxygen content almost doubled, increasing from 4.8 to 8.5 at.%. This increase in oxygen content is attributed to the oxidising reagent which is required for radical generation. In addition to generating the 4-(trifluoromethyl)phenyl radical, the reagent also increased the level of oxidation of the graphitic surface to some degree. To confirm this, control reaction 3 was carried out to synthesis C3-NP1 under the same conditions with only $K_2S_2O_8$ and a sample of NP1. Its surface elemental composition as determined by XPS is also presented in Table 4.1,

for comparison. In this case, a large increase in the oxygen concentration was indeed observed in the sample, up to 10.7 at.%. Even though the percentage of sp^3 carbon centres in f-NP1 is higher than C3-NP1, the increase in oxygen content is much lower (cf. 8.5 *vs* 10.7 at.%). This is consistent with the fact that the additional sp^3 centres originate from aryl group functionalisation. Furthermore, an increase in oxygen content may also be explained by the fact that a portion of 4-(trifluoromethyl)phenoxide [$OC_6H_4(CF_3)$] groups could also be covalently bonded to NP1 in addition to $C_6H_4(CF_3)$. The ether species (compound B) was, of course, found in the control reaction in the absence of NP1 (where both compound A and B were formed).

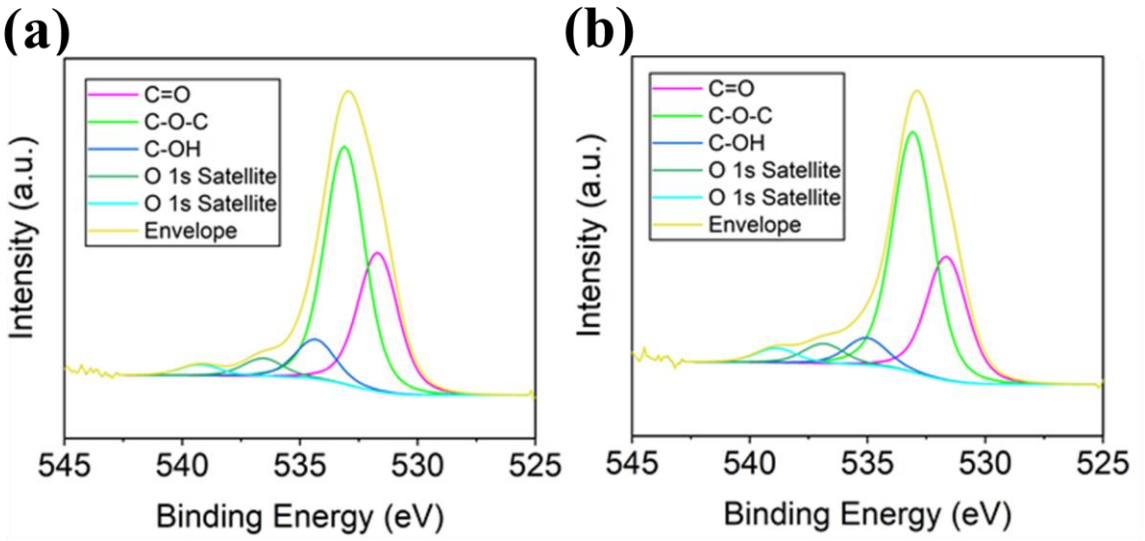

Figure 4.8 Deconvoluted spectra of O 1s orbital; (a) NP1 and (b) f-NP1.

Upon functionalisation, a peak at 687.9 eV confirms the presence of the F 1s state within f-NP1, as shown in Figure 4.9 (a). This binding energy relates to the presence of 4-(trifluoromethyl)phenyl functional group, as demonstrated in previous investigations.[402] The presence of an F 1s state can also be observed within C1-NP1 at 687.7 eV (see Scheme 4.3 for more details on control reaction synthesis). This peak corresponds to adsorbed 4-(trifluoromethyl)phenyl boronic acid. In addition to this peak, a binding energy of 191.38 eV is also present, resembling that of the B 1s state. Within C1-NP1, the ratio between the at.% for F and B 1s states corresponds to 0.2:0.6 (Table 4.1), which corresponds to the expected 1:3 ratio between B:F within the boronic acid starting

material. The presence of starting material was not detected within f-NP1 due to the absence of the B 1s state.

Despite the extensive washing which was undertaken on C1-NP1, F 1s and B 1s environments remained, resembling that of 4-(trifluoromethyl)phenyl boronic acid. As a result of this, it was suggested that this starting material remained strongly attached to the graphitic structure, through a covalent or non-covalent means. It was suggested that diol type functional groups on the graphitic system may complex with the boronic acid functional group to form a boronic ester, as shown in Scheme 4.4.[403,404] In the presence of radical generating conditions, however, it is believed that this complexation was not favoured since there is an absence of boron within f-NP1.

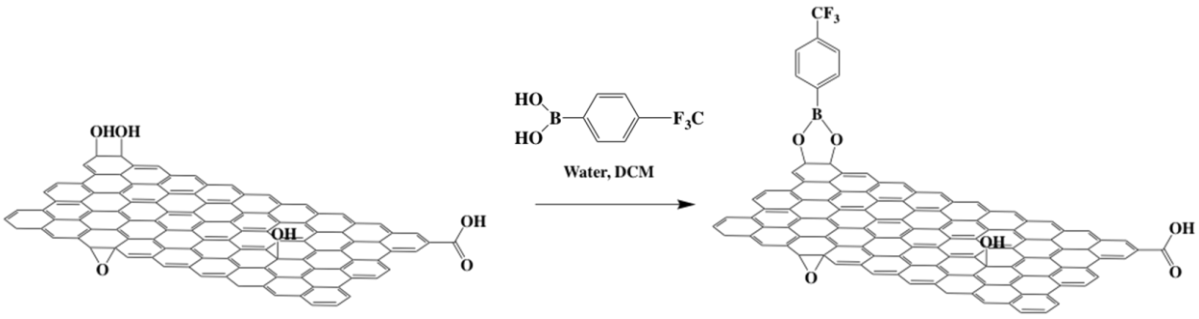

Scheme 4.4 Proposed mechanism of 4-(trifluoromethyl)phenyl boronic acid to diol-type structure on NP1.

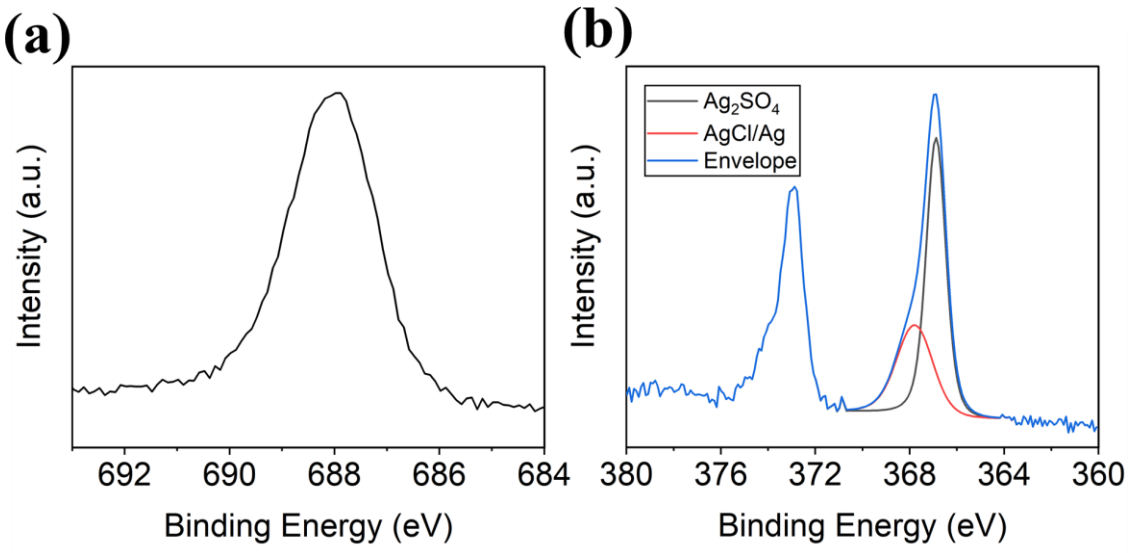

Figure 4.9 XPS spectra of (a) F 1s and (b) Ag 3d $^{5}/_{2}$ orbital for f-NP1 at high resolution (deconvolution of the 3d peak indicates presence of Ag, Ag_2SO_4 and AgCl).

The presence of silver (3d orbitals) was observed within f-NP1 and C3-NP1, resulting from the addition of $AgNO_3$ into the solvent mixtures. Within f-NP1, the Ag 3d $^3/_2$ and Ag 3d $^5/_2$ spin states are shown in Figure 4.9 (b) at 372.9 and 367.0 eV, respectively. Further deconvolution of the Ag 3d $^5/_2$ signal reveals peaks at 367.9 eV and 366.9 eV which resemble that of silver salts likely to be in the form of AgCl/Ag and Ag_2SO_4, respectively.[405,406] Unfortunately, binding energies are not always consistent for compounds within the NIST database and literature, thereby making unambiguous identification of specific silver salts difficult.[407] It was found that XRD data also confirmed the presence of silver salts, as outlined later on in this chapter.

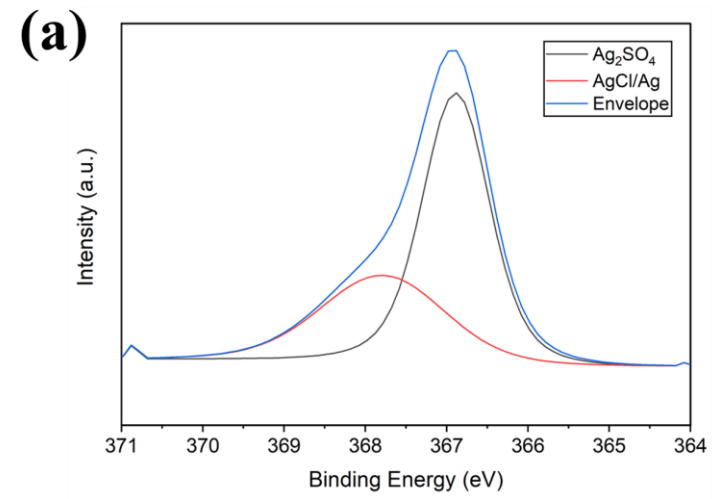

(b)

Peak	Integrated Area Under Peak	Percentage (%)	% Atomic Composition
Ag_2SO_4	10963.45	73.35	0.49
AgCl/Ag	3982.77	26.65	0.18

Figure 4.10 (a) Peak area integration of Ag 3d $^5/_2$ signal using OriginPro software and (b) Calculation of the % atomic composition of Ag_2SO_4 and AgCl/Ag through the integrated area of peaks.

The total composition of silver corresponds to 0.67 at.% within f-NP1. Through peak area integration of 3d $^5/_2$, it was found that 0.49 at.% originates from Ag_2SO_4 and 0.18 at.% originates from a combination of AgCl and Ag (as shown in Figure 4.10). Within C2-NP1, a trace amount of silver was present (0.09 at.%), which corresponded to unreacted $AgNO_3$ precursor, possessing a binding energy of 368.3 eV. It is believed that silver species within these samples were adsorbed to the surfaces of the NP1 stacks and integrated in

pores, proving rather challenging to remove even after extensive washing.[408,409] The porosity of NP1 materials is outlined in more detail later on within this thesis. Furthermore, both f-NP1 and C3-NP1 materials revealed a small percentage of sulfur incorporation as a result of the oxidising agent. Again, these proved challenging to remove completely. The presence of chlorine possessing a binding energy of 197.2 eV is also observed. This binding energy is characteristic of inorganic chlorine, originating from a chloride salt such as AgCl.[410] It is suggested that its presence originates from DCM solvent under radical conditions. Interestingly, Baran and co-workers did not report any reactivity occurring between the solvent and their reactions.

Under the assumption that all of the fluorine content determined by XPS corresponds to the 4-(trifluoromethyl)phenyl moieties only, it is estimated that the degree of functionalisation is consistent with 1 in every 65 graphitic carbon atoms functionalised by a 4-(trifluoromethyl)phenyl group. This is estimated as follows: The empirical formula of the 4-(trifluoromethyl)phenyl group is $C_7H_4F_3$. The prefunctionalied material within f-NP1 is assumed to consist of carbon atoms only and thus the empirical formula would be C_1. Assuming only carbon and fluorine elements within the material then, on the basis of the elemental composition determined by XPS, the ratio of C to F is 24.5:1. Incorporation of one 4-(trifluoromethyl)phenyl group per graphitic carbon would give a C:F ratio of 8:3 (assuming all F atoms are within the 4-(trifluoromethyl)phenyl group). This gives an approximate estimation of 1 4-(trifluoromethyl)phenyl group per 65 (24.5 x $^8/_3$) graphitic carbons at the surface of f-NP1.

A schematic summarising the components present within various NP1 materials, including f-NP1 and CX-NP1 (X = 1 – 3), is shown in Scheme 4.5. This has been determined based on the data obtained by XPS. NP1 materials consist of predominately carbon but also contain oxygen functionality. These are likely to be located around the edges of the sheets in the form of hydroxy, carboxyl and epoxy groups. C1-NP1 and C2-NP1 exhibit similar compositions of these elements to NP1, whereas f-NP1 and C3-NP1, contain a significantly larger percentage of oxygen, associated with the oxidising conditions. [F-NP1] also consists of 4-(trifluoromethyl)phenyl moieties, covalently bonded to the sheets; likely to also be situated around the edges. C1-NP1 consists of unreacted 4-(trifluoromethyl)phenyl boronic acid, intercalated between slit pores, and adsorbed to the surface through interactions such as hydrogen bonds. Trace amounts of silver species are found in f-NP1 and C2-NP1, and are attributed to the presence of Ag, AgCl and

Ag_2SO_4 and unreacted $AgNO_3$, respectively. It is likely that the silver species are well intercalated between the porous structure of the NP1 stacks. The retention of these impurities results from the inherent nature of the plasma-exfoliated graphitic material, which "traps" impurities within pores and defects.

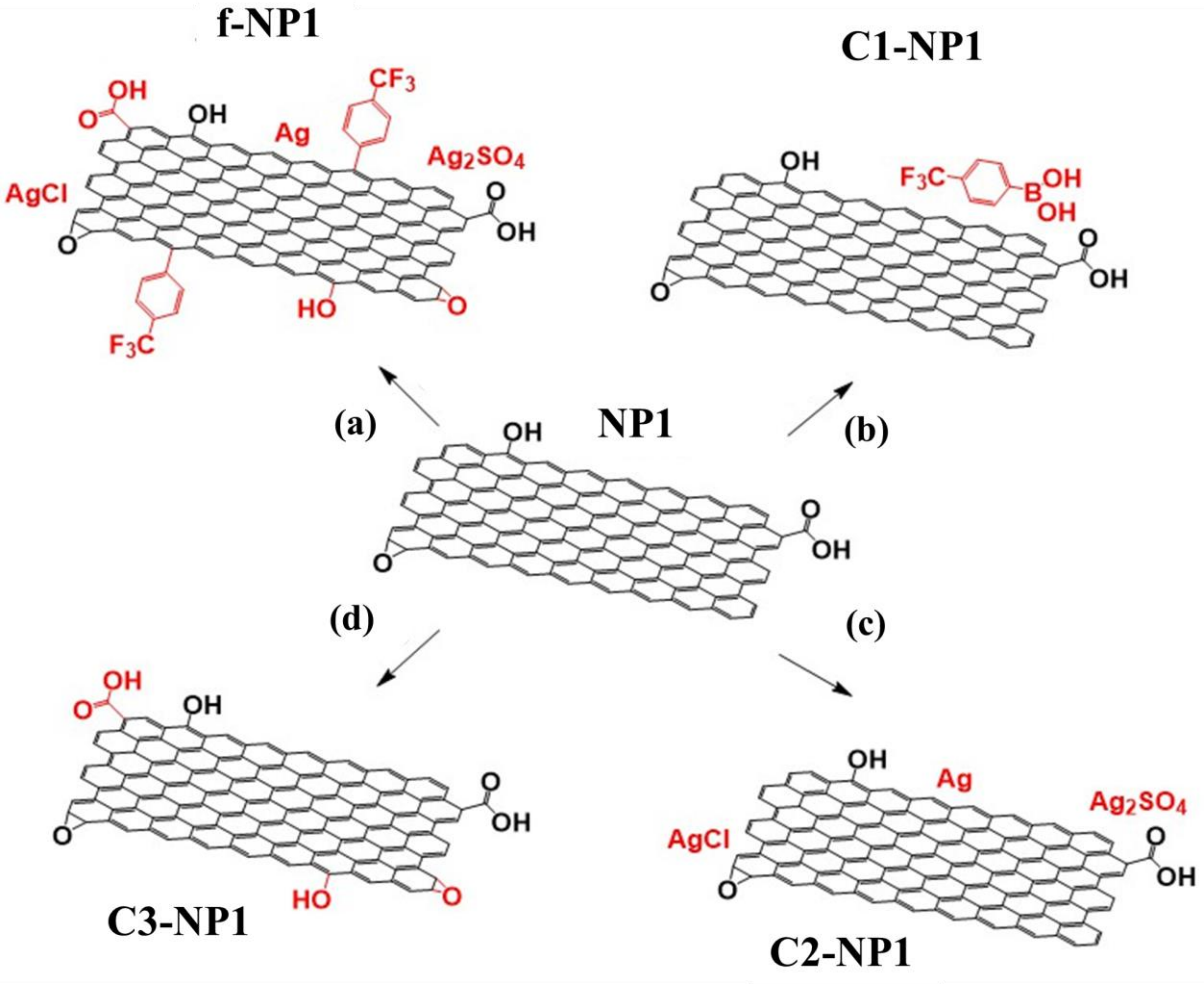

Scheme 4.5 The hypothesised structures of (a) f-NP1 (b) C1-NP1 (c) C2-NP1 and (d) C3-NP1 synthesised from NP1.

4.2.4.2 SEM-EDX Analysis

SEM-EDX data was acquired during SEM imaging for NP1 and f-NP1. The EDX data is depicted in Figure 4.11. Unfortunately, it can be extremely difficult to accurately quantify light elements (i.e., those which possess $Z < 10$) *via* EDX. This is due to the phenomena whereby Auger electron production is favoured over characteristic X-ray production, resulting in limited X-rays reaching the detector. Since NP1 and f-NP1 contain carbon, oxygen and fluorine in a high proportion, it is not believed that atomic quantification *via* EDX provides accurate results. As such the data presented may be considered less conclusive than that of XPS. As such, the XPS quantitative data is relied on instead, for the purpose of atomic concentration calculation. With this caveat in mind, it is believed, however, that it was useful to gain EDX data regardless of this, since XPS instruments rely on the detection of only surface elements. In contrast, however, EDX analysis determines elemental compositions much deeper within the sample, and thus, provides an insight to elements which XPS would not be able to detect. The raw data related to the elemental composition of NP1 and f-NP1 are depicted as weight percentages and atomic percentages. A gold sputter coating was introduced to these materials prior to SEM imaging and therefore a substantial degree of elemental gold is recognised upon EDX analysis. Due to this, the normalised atomic percentages were also calculated through exclusion of this element, and this data was used for comparative purposes.

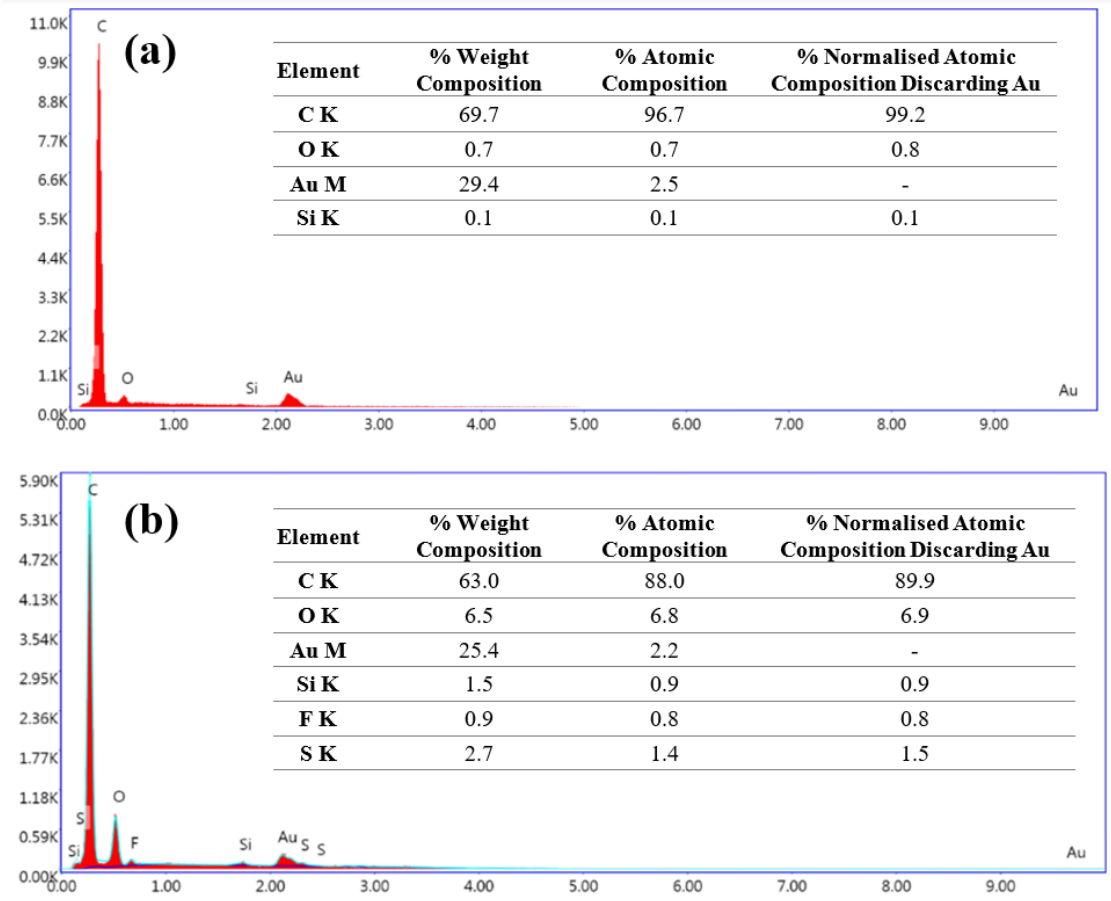

Element	% Weight Composition	% Atomic Composition	% Normalised Atomic Composition Discarding Au
C K	69.7	96.7	99.2
O K	0.7	0.7	0.8
Au M	29.4	2.5	-
Si K	0.1	0.1	0.1

Element	% Weight Composition	% Atomic Composition	% Normalised Atomic Composition Discarding Au
C K	63.0	88.0	89.9
O K	6.5	6.8	6.9
Au M	25.4	2.2	-
Si K	1.5	0.9	0.9
F K	0.9	0.8	0.8
S K	2.7	1.4	1.5

Figure 4.11 SEM-EDX data for; (a) NP1 and (b) f-NP1. The origin of the K and M shells is explained within Chapter 2.

As expected, the major elemental contribution results from carbon, contributing 99.2 and 89.9 at.% of NP1 and f-NP1, respectively. The next largest contribution originated from oxygen, corresponding to 0.8 and 6.9 at.% for NP1 and f-NP1, respectively. The value of oxygen associated with NP1 is much lower than that achieved through XPS characterisation, however, as previously mentioned, these values are much less accurate, due to the light weight associated with elements with $Z < 10$. An increase in oxygen content within f-NP1 is also observed, consistent with that acquired using XPS analysis (Table 4.1), due to the addition of the oxidising reagent. It was also observed that trace amounts of silicon were present within NP1 and f-NP1 which were not detected within XPS, suggesting that these were present much deeper into the sample, beyond the surface limit of XPS detection.

The analysis also revealed that f-NP1 possessed additional elements including fluorine and sulfur. Such findings coincide with that of XPS data. According to EDX, 0.80 at.% originates from fluorine. This is much lower than the 3.5 at.% detected within the

material *via* XPS analysis. This difference may relate to the inaccurate data acquired by the light element. Alternatively, 4-(trifluoromethyl)phenyl functionality may exist in much higher concentrations on the surface of the sample, rather than within deeper regions. Similarly, the sulfur content equals 1.5 at.% for f-NP1 within the EDX data, which exceeds than that of the 0.3 at.% acquired through XPS data. This is attributed to the presence of a larger proportion of this element, deeper into the sample. Based on EDX information, the number of 4-(trifluoromethyl)phenyl groups added to NP1 was calculated using the same methodology as that used to calculate the degree of functionalisation from XPS quantitative data (see Section 4.2.4.1).[1] An approximate estimation of 1 in every 300 carbon atoms functionalised by a 4-(trifluoromethyl)phenyl group was calculated.

[1] The degree of functionalisation based on EDX data was calculated as follows: The elemental composition determined by EDX, provides a ratio of C to F of 112.4:1. This gives an approximate estimation of one 4-(trifluoromethyl)phenyl group per 300 (112.4 x $^{8}/_{3}$) graphitic carbons within f-NP1

4.2.5 Morphological Analysis using SEM/TEM

SEM and TEM were used to investigate the surface morphology and lateral dimensions of the graphitic sheets. SEM images of NP1 at magnifications of 1.27 kx and 2.98 kx (Figure 4.12 (a) and (b)) reveal that the samples consist of loosely bound agglomerates with a powder like appearance. These agglomerates range quite substantially in diameter between < 10 to 30 µm. At higher magnifications (47.98 kx and 115.30 kx, Figure 4.12 (c) and (d)), it is observed that these agglomerates are irregularly arranged, consisting of flakes comprised of mostly multilayer stacks. These layers are physically aggregated by $\pi-\pi$ interactions. Some flakes adopt wavy morphology, displaying curled edges, whilst others are relatively flat. Moreover, these flakes possess a non-uniform range of sizes between 50 nm and 1 µm. The TEM images are consistent with these findings, showing that flakes deposited on the copper grid exhibit sizes of several hundred microns in size (Figure 4.13). The TEM images also suggest that the flakes consist of varying numbers of sheets. This is evidenced by darker and lighter regions present on the flakes, presenting more and less dense areas due to differences in thicknesses of the stack. It can be concluded from these images that stacks overlap in a non-uniform manner.

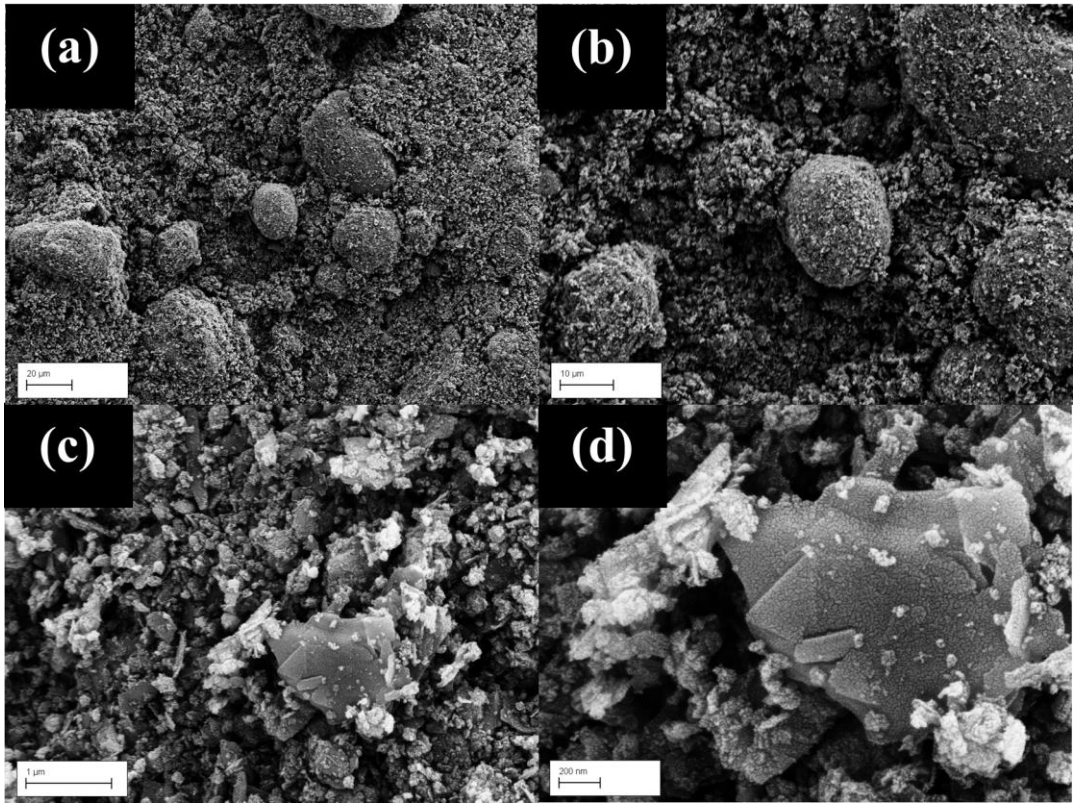

Figure 4.12 SEM images of NP1 at various magnifications including (a) 1.27 kx (b) 2.98 kx (c) 47.98 kx and (d) 115.30 kx.

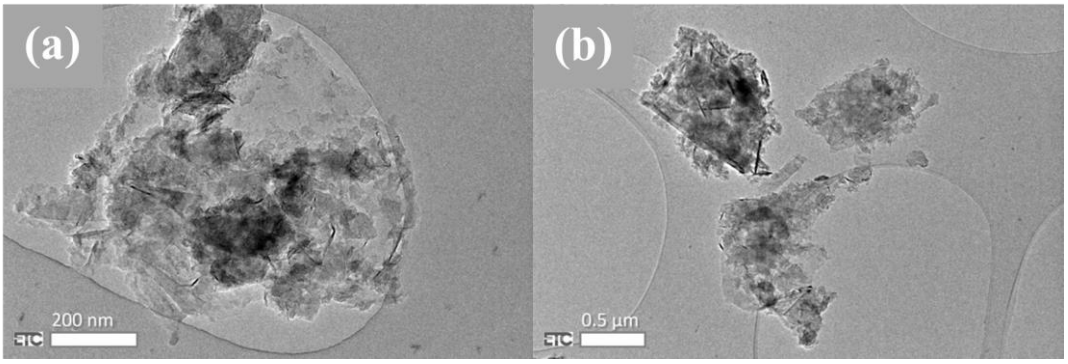

Figure 4.13 TEM images of NP1.

Upon functionalisation of NP1 to f-NP1, moieties in the form of oxygen functionality and 4-(trifluoromethyl)phenyl groups become bonded to the sheets. The SEM images (Figure 4.14) show that the functionalisation process results in changes to the morphology of the sample. In contrast to NP1, f-NP1 exhibits a smoother morphology, with less observable agglomerates at low magnification, as shown in Figure 4.14 (a). There are some agglomerates present, although these are typically < 10 µm in diameter. At increased

magnifications, the sample appears to consist of flakes of a variety of sizes (Figure 4.14 (b) – (h)). These flakes range in size between approximately 50 nm to several μms. TEM images (Figure 4.15) also show that flakes within f-NP1 possess dimensions of around several hundred nanometres in size. The nature of the less aggregated material also enables pore visualisation in f-NP1. A large macropore is apparent in Figure 4.14 (d) as highlighted within the red circle. This large macropore could originate from the etching of an existing smaller pore, due to the presence of radicals and oxidising conditions. It has been reported that vacancy defects can become etched to form micropores using acidic oxidants, such as potassium permanganate; a compound which is known to attack unsaturated double bonds.[246] Moreover, it appears that there are some smaller flakes which have become trapped within the in-plane pore. The presence of such pores and the ability of them to become blocked and therefore trap material, provides evidence of why it can often be very difficult to remove impurities during washing, such as silver species. Further to this, the presence of silver nanoparticles formed by nucleation of silver salts is also shown to the right-hand side of Figure 4.14 (e). Slit pores are also present between neighbouring stacks, as highlighted within Figure 4.14 (f), where orderly aligned stacks possess spaces between one another. The porous structure of these materials is analysed in more detail within Chapter 5. It is also observed that a scaley texture accompanies some of the high magnification images such as Figure 4.14 (g). This observation originates due to the deposition of a thin layer of gold during sputter coating addition. As an additional point of interest, samples were initially imaged in the absence of a sputter coating, however it was noticeable that the images underwent charging. As such, the addition of the gold nanoparticles enabled acquisition of images with increased contrast and higher resolution. The presence of the conductive coating also made it easier to discern between the carbon-based samples and the carbon leit tab, used during preparation for SEM analyses.

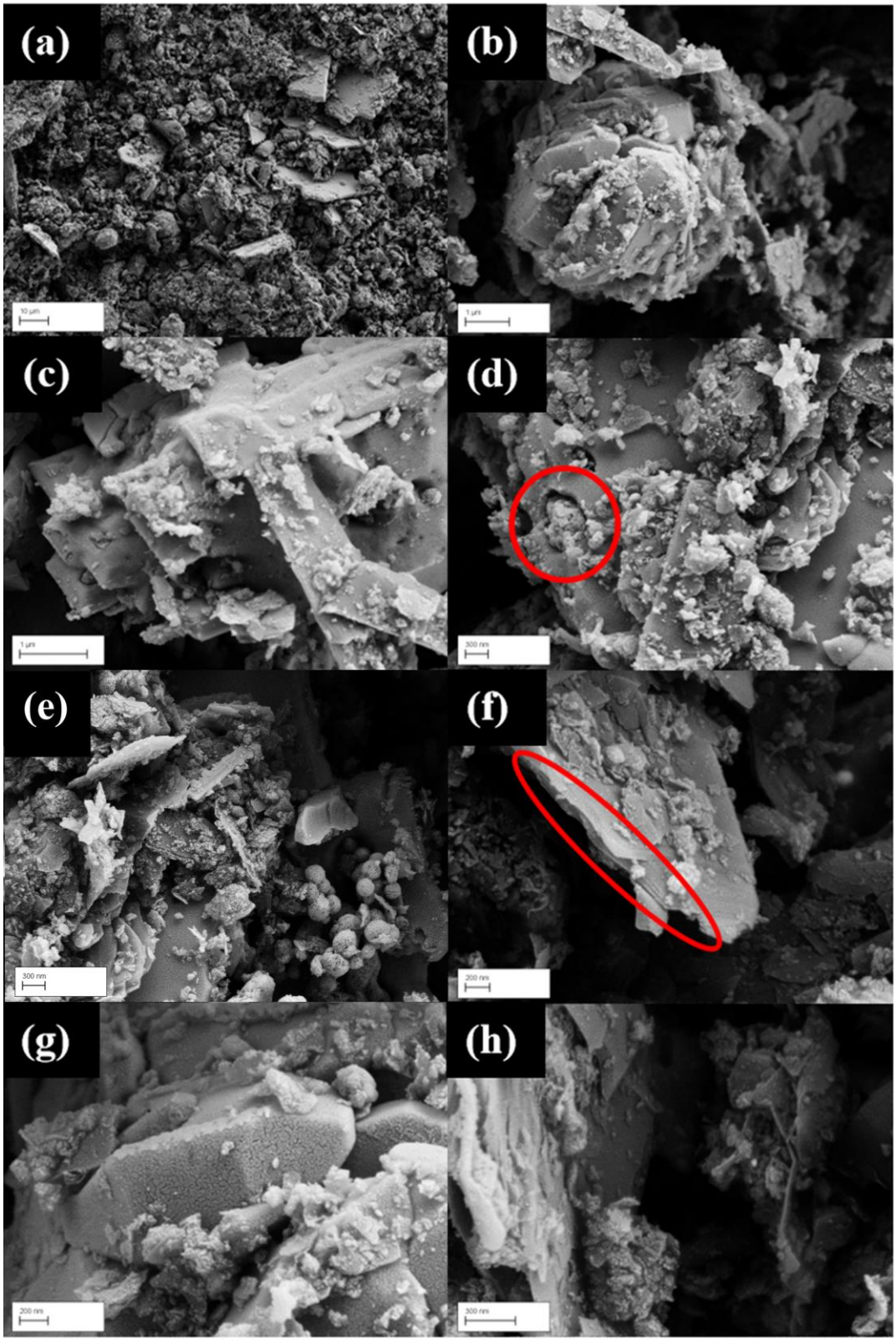

Figure 4.14 SEM images of f-NP1 at various magnifications including (a) 1.93 kx (b) 29.50 kx (c) 45.30 kx (d) 50.90 kx (e) 50.0 kx (f) 81.7 kx (g) 94.86 kx and (h) 112.00 kx.

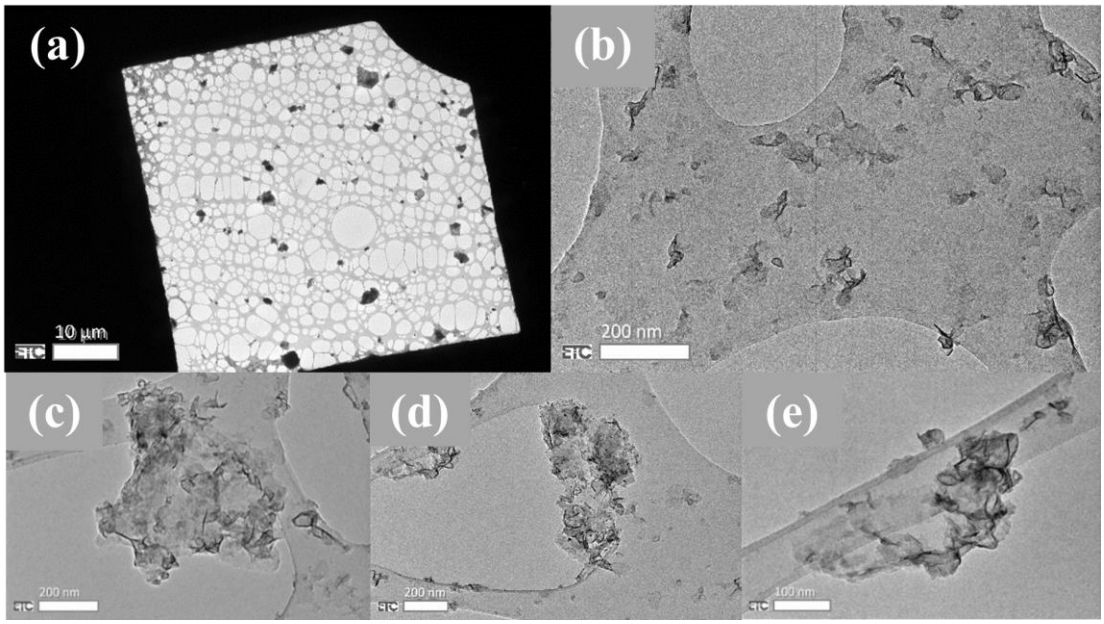

Figure 4.15 TEM images of f-NP1 flakes drop-casted onto a copper grid.

4.2.6 Graphitic Structure, Interlaying Spacings and Presence of Defects

Raman spectroscopy and XRD were conducted to gain information regarding the graphitic structure within NP1 and f-NP1. Such characterisation methods provide a valuable insight to information regarding the stacked nature of the graphitic material and orientation of planes within these stacks, as well as the extent of defects.

4.2.6.1 Raman Spectroscopy

Raman spectroscopy was used to investigate the graphitic structure of the materials and determine the extent of defects present within NP1, f-NP1 and CX-NP1 (X = 1 – 3), using a wavelength of 514 nm. Corresponding Raman spectra are shown in Figure 4.16. All spectra exhibit three characteristic peaks, corresponding to the G band, 2D band and D band, as outlined within Chapter 2. Within NP1, f-NP1 and CX-NP1 (X = 1 – 3), the

former of these three bands appears between 1570 and 1580 cm^{-1}. The 2D band spans between 2696 and 2707 cm^{-1} and is broad and heavily upshifted in respect to that of SLG, suggesting the presence of multiple layered stacks.[312] A relatively intense G band compared to the 2D band, with I_{2D}/I_G ratios, is also depicted in Figure 4.16.[312] Since these ratios lay beneath $I_{2D}/I_G = 2$, they are indicative of a multilayered structure.[411] The presence of defects is revealed by the appearance of the D band, which occurs between 1345 and 1350 cm^{-1} for all materials.[308] The presence of additional defect-induced bands corresponding to the D' (in the region of 1618 cm^{-1}) and D + G (in the region of 2930 cm^{-1}) peaks are also observed.[172,310] These bands are labelled on the spectrum for NP1 (Figure 4.16 (a)). Based on the knowledge gained on plasma-derived NP1s, it is likely that the origin of defects within NP1, originates from the plasma processing step during synthesis, where oxygen is covalent attached on the edges of the graphitic sheets (accompanied by a change in hybridisation from sp^2 to sp^3). The intensity ratio of the D band in relation to the G band (I_D/I_G) is indicative of the degree of functionalisation as a result of sp^3 hybridised carbon atoms. The calculated I_D/I_G ratios are shown on the Raman spectra within Figure 4.16 for all materials. The largest ratio is associated with f-NP1, which indicates the presence of the highest density of defects, thereby suggesting that successful covalent functionalisation has occurred, from the desired 4-(trifluoromethyl)phenyl incorporation, along with some additional oxygen functionality. As highlighted above, the XPS analysis indeed confirmed the addition of desired functionality, as well as an increase in oxygen functionality, which was attributed to the oxidising agent $K_2S_2O_8$. It was also found that the I_D/I_G ratio for C3-NP1 was also high with respect to NP1, although the material remained less defective than f-NP1. This is also expected due to the degree of covalent functionalisation associated with additional oxygen functionality. Both the Raman spectroscopic and XPS data are consistent with functionalisation of NP1 with 4-(trifluoromethyl)phenyl groups.

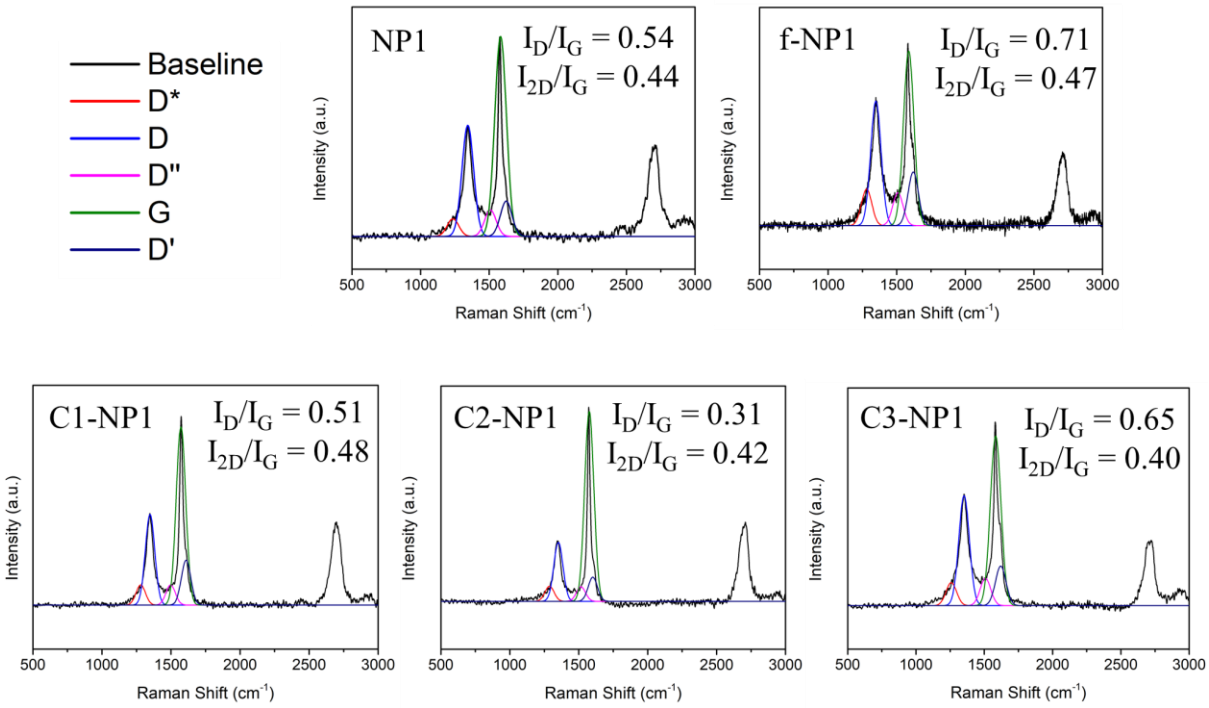

Figure 4.16 Raman spectra and respective I_D/I_G and I_{2D}/I_G ratios of (a) NP1 (b) f-NP1 (c) C1-NP1 (d) C2-NP1 and (e) C3-NP1. Peak deconvolution was performed using OriginPro software to discriminate the D and G bands from overlapping D, D'' and D' bands.*

4.2.6.2 XRD

NP1 and f-NP1 were then analysed *via* XRD to gain an insight into the interlayer spacings and orientation of planes between the two materials. Copper K_α radiation of wavelength 0.15406 nm, was implemented to acquire the spectra, as shown in Figure 4.17. The spectra suggest that both NP1 and f-NP1 consist of Bernal ABA stacking (2H) and Rhombohedral ABCA (3R) type-stacking, typical of that present within commercially available multilayer GBMs.[371] Strong diffraction peaks are present within both spectra at 26.7°, corresponding to graphitic 2H (002) and 3R (003) planes with an interlayer spacing (d) of 0.334 nm, calculated using the Bragg equation in Equation 2.2. For NP1, these planes overlap and therefore appear as one peak. For f-NP1, there is a high degree of overlap, however, the two planes can be distinguished. The (002) 2H peak appears at a slightly lower 2θ value of 26.67° compared with the 3R peak which appears at 26.73°. Smaller peaks are also observed at 42.6° and 44.6°, which correspond to 2H stacking of the (100) and (101) planes, as well as 3R type stacking at 43.4°

and 46.2°, which corresponds to the (101) and (012) planes. The presence of this four-lined pattern (shown in more detail within the expanded section) provides evidence of the 2H and 3R phases within the structures. This has been observed in various GBMs.[371,412] Peaks at 54.7° and 77.6° also correspond to graphite 2H (004) and 3R (006), and 2H/3R (110) planes, respectively, within both materials.

Many additional diffraction peaks were present within f-NP1 which were not present within NP1, as highlighted with asterisks (*) in Figure 4.17. These correspond to the diffraction of the crystalline AgCl, Ag and Ag_2SO_4 impurities incorporated into the material (PDF card numbers: 00-006-0480,[413] 01-073-6977[414] and 01-074-1739[415]). The presence of Ag_2SO_4 is recognised by the characteristic peaks at 2θ = 28.3°, 31.3°, 34.0°, 37.3° and 47.3° which correspond to (004), (131), (202), (133) and (135) reflections, respectively. AgCl is assigned to reflections at 2θ = 28.0°, 32.5°, 46.4°, 55.0°, 57.6°, 67.6°, 74.6° and 76.9° which correspond to (111), (200), (220), (311), (222), (400), (331) and (420) and Ag is assigned to reflections at 2θ = 38.3°, 44.6°, 64.7° and 77.6° which correspond to (111), (200), (220) and (311). Other reflections are also associated with these Ag salts, however, exist with too low intensity to be observed. As indicated above, the presence of these silver species was already established from the XPS data.

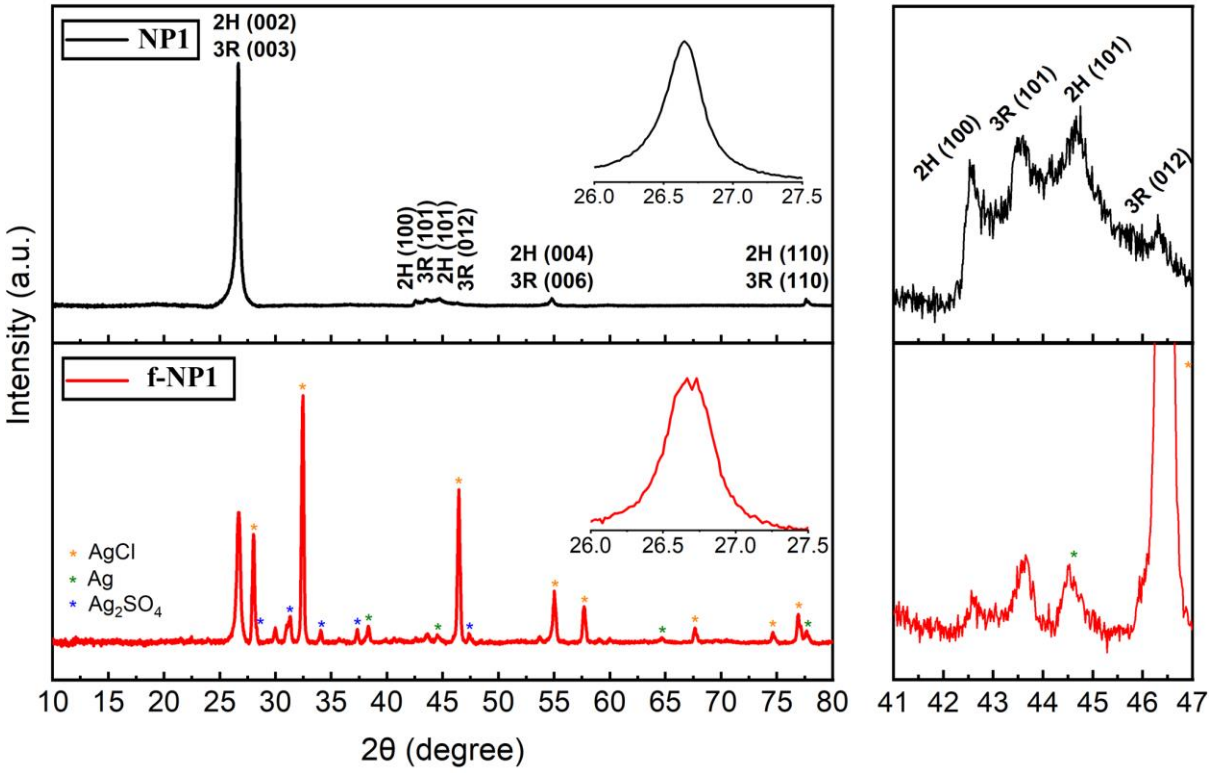

Figure 4.17 XRD patterns for NP1 and f-NP1 with increased magnification of the 2H (002) and 3R (003) planes and four-lined pattern associated with the 2H (100), 3R (101), 2H (101) and 3R (012) phases in the boxes on the right. An inset focused on the region 26.0° to 27.5° is shown on the main spectra.

In order to gain further insight into the nature of the materials, the data was used to calculate the dimensions of the graphitic stacks from the diffraction patterns. The Scherrer equation[2] is typically used to calculate the out of plane crystallite size, L_c (Equation 4.1) and the in-plane crystallite size, L_a (Equation 4.2).[416] The former of these provides an estimation of the thickness of a stack, whilst the latter provides an estimation of the width of a stack, as shown in Figure 4.18.[417] With this knowledge, the number of graphene layers within a crystallite, N_c (Equation 4.4) can be calculated through utilisation of the interlayer spacing, $d_{(002)/(003)}$ calculated *via* the Bragg equation (Equation 2.2).[418] Within these equations, K corresponds to the shape factor which takes values of 0.91 and 1.84 for equations corresponding to L_c and L_a respectively, λ corresponds to Cu K_α radiation (0.154185 nm), θ corresponds to the Bragg

[2] The Scherrer equation provides an estimation of the crystallite sizes, and various contributions of instrumental broadening, morphological effects and disorder to reflections widths all have an influence on the data acquired directly from the XRD spectra.[580]

angle, β corresponds to the full width at half maximum (FWHM) and n corresponds to the order of diffraction. These parameters are summarised in Table 4.2.

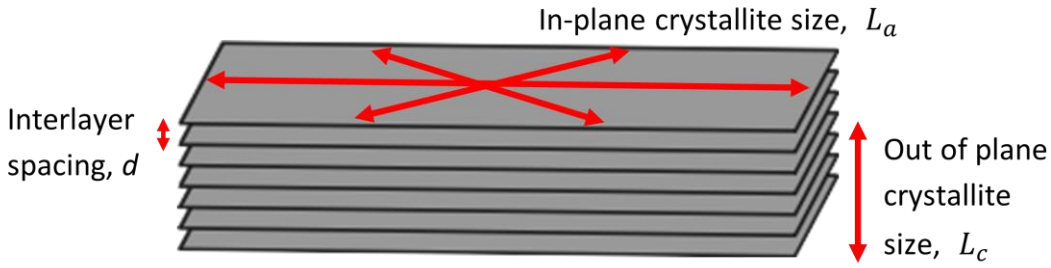

Figure 4.18 The crystalline structure of graphite displaying the out of plane crystallite size, L_c and the in-plane crystallite size, L_a, as well as the interlayer spacing, d.

Table 4.2 Summary of parameters used within the Scherrer equation and Bragg equation.

Parameter	Symbol
Out of Plane Crystallite Size	L_c
In-Plane Crystallite Size	L_a
Number of Graphitic Layers within a Crystallite	N_c
Shape Factor	K
Wavelength	λ
Bragg Angle	θ
Full Width at Half Maximum (FWHM)	β
Order of Diffraction	n
Interlayer Spacing	d

$$L_c = \frac{K\lambda}{\beta \cos\theta}$$

Equation 4.1 Scherrer equation for out-plane crystallite size (K = 0.91).

$$L_a = \frac{K\lambda}{\beta \cos\theta}$$

Equation 4.2 Scherrer equation for in-plane crystallite size (K = 0.91).

$$N_c = \frac{L_c}{d_{(002)/(003)}}$$

Equation 4.3 Calculation for the number of graphene layers.

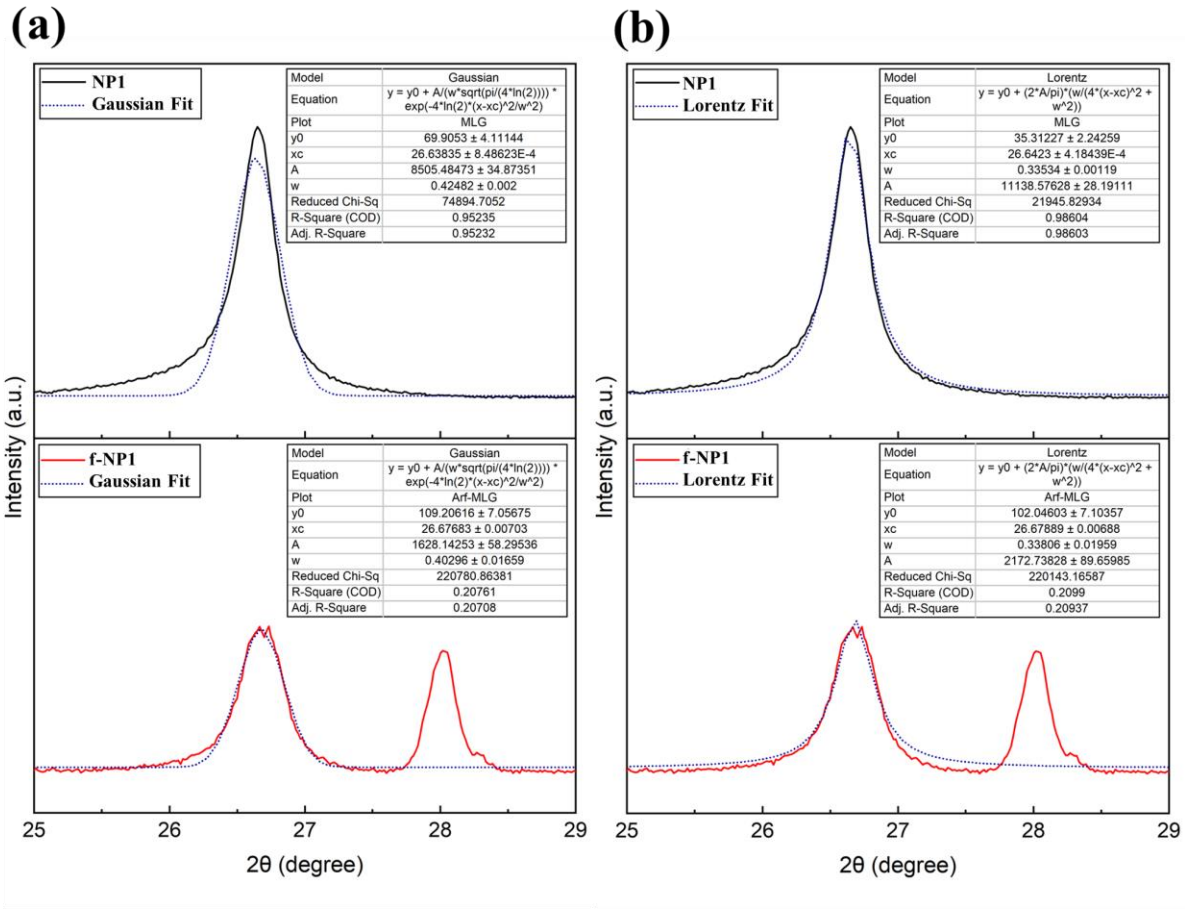

Figure 4.19 Gaussian and Lorentz fitting using OriginPro software for the overlapping (002) and (003) planes of the peak at 2θ = 26.679 for NP1 and f-NP1 shown in (a) and (b) respectively. Note: Within OriginPro the FWHM is denoted as "w" in degrees.

Table 4.3 Calculations of L_c, L_a, N_c and $d_{(002)/(003)}$ for NP1 and f-NP1.

	Material	Peak Position (2θ)	Interlayer Spacing ($d_{(002/003)}$) (nm)	FWHM (radians)	Crystallite Size, L_c(nm)	In-Plane Crystallite Size, L_a(nm)	Number of Graphene Layers, N_c
Gaussian Model	NP1	26.7	0.334	0.42	19.43	39.29	58.11
	f-NP1	26.7	0.334	0.40	20.49	41.42	61.36
Lorentz Model	NP1	26.7	0.334	0.34	24.61	49.77	73.63
	f-NP1	26.7	0.334	0.34	24.41	49.37	73.14

To carry out these calculations, the (002)/(003) graphitic peak corresponding to 2θ = 26.7° was employed for both NP1 and f-NP1 (see Figure 4.17). The interlayer spacing was calculated to be 0.334 nm for both materials. For the purposes of Equations 4.2 and 4.3, the FWHM was calculated using both Gaussian and Lorentz fittings, within OriginPro software, and β and θ were utilised in units of radians (Figure 4.19). The Gaussian plot fitted poorly for NP1 but more effectively for f-NP1, whereas the Lorentz plot fitted better for f-NP1and similar to the Gaussian plot for NP1. The crystallite size and in-plane crystallite size were calculated and displayed in Table 4.3 for NP1 and f-NP1. The crystallite size and in-plane crystallite size for NP1 and f-NP1 displayed very little deviation from one another, suggesting that both materials consist of crystallites with very similar structures. The Lorentz model, however, gave larger approximations of the crystallite size and in-plane crystallite size for both materials, compared with the Gaussian model, due to their differences in FWHM calculation. The number of graphene layers in a crystallite were then calculated for each material. It was found that the crystallites adopted stacks consisting of numerous graphitic layers, within the region of 58 to 74 layers for both models (see Table 4.3). As such, the materials could therefore also be described as graphite nanostructures.[5] There is little change in the number of graphene layers within a stack for NP1 and f-NP1, suggesting that the functionalisation procedure does not cause exfoliation or further stacking of graphene layers within a crystallite. Furthermore, in contrast to previous functionalisation methods, which have often caused enlargement of the interlayer spacings, there is no significant change to the distance between the graphene layers within a stack upon functionalisation.[419] It is therefore likely that functionalisation takes place predominately at the edges of the stacks, rather than on the plane, thereby, does not widen the layers through steric hindrance. In summary, it appears that functionalisation initiates negligible change to both the graphitic spacings and the number of layers within a stack.

To further understand the contribution of stacking types within the NP1 material, the ratio of 2H:3R phases within the material was calculated. For this, the four-lined pattern shown in the

XRD pattern for NP1 (Figure 4.17) was examined in more detail, and the ratio between the 3R (101) and 2H (101) peaks was discerned. Figure 4.20 depicts a deconvoluted spectra of the overlapping four-lined pattern consisting of the 2H (100), 3R (101), 2H (101) and 3R (012) phases. Gaussian fitting of the peaks revealed the corresponding areas associated with each peak. The integrated ratio of 3R (101) to 2H (101) corresponded to 658.0:688.2 (48.9%/51.1%). This is not dissimilar from values reported by Seehra for other commercially synthesised multilayer graphitic materials.[371] Unfortunately, the 3R (101) to 2H (101) peaks within f-NP1 could not be resolved and therefore were not deconvoluted. This was due to the presence of the Ag_2SO_4 reflection at 46.45°, and the weak intensity of the four-lined pattern.

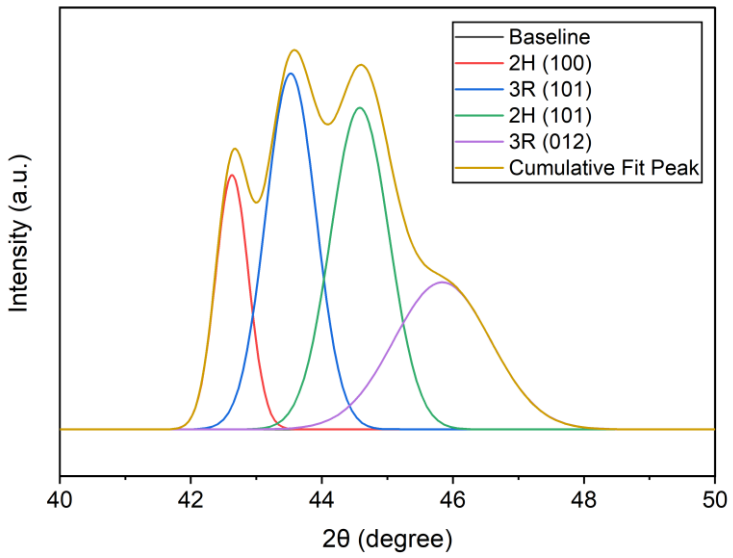

Peak Index	Peak Type	Area Intg	FWHM	Max Height	Center Grvty	Area IntgP
2H (100)	Gaussian	308.88756	0.59406	488.46971	42.62814	14.1802
3R (101)	Gaussian	658.04454	0.90418	683.70256	43.52429	30.20906
2H (101)	Gaussian	688.16695	1.04648	617.77677	44.57866	31.5919
3R (012)	Gaussian	523.20313	1.7396	282.5457	45.83542	24.01885

Figure 4.20 Gaussian fitting of the four-lined pattern associated with the 2H (100), 3R (101), 2H (101) and 3R (012) phases and the corresponding data, as provided by OriginPro software.

4.2.7 Bond Change Analysis by FT-IR

The FT-IR ATR spectra of NP1, f-NP1 and 4-(trifluoromethyl)phenyl boronic acid are shown in Figure 4.21. The ATR spectra of NP1 showed no obvious peaks. It might be expected that the sample should reveal the presence of C=C, C–O and C=O bonding, however, the high absorptivities associated with such a sample, grant it, and many other carbon-based samples notoriously difficult to analyse *via* the ATR technique.[337] FT-IR-ATR suffers from baseline sloping which descents at smaller wavenumbers. This is because the graphene displays absorption over the entire region (usually 4000 to 400 cm^{-1}), and the effect becomes amplified using ATR with deeper light penetration at lower wavenumbers (longer wavelengths). Despite this, this technique still provides an indication of the functionality introduced into the f-NP1 material. The corresponding spectrum for f-NP1 was also poorly resolved, however, it did provide some indication of the incorporation of additional functional groups to the material. Several peaks were observed within the spectra for f-NP1, corresponding to both oxygen and 4-(trifluoromethyl)phenyl functionality. Within f-NP1, a broad band exists around 1010 cm^{-1} with a shoulder at higher wavenumbers. It is likely that this band resulted from various overlapping absorptions including the CF_3 stretching vibrations and C−C antisymmetric vibrations. Further to this, based on assignments made on previously reported compounds, peaks at 1178 and 786 cm^{-1} correspond to the CF_3 stretch and the CF_3 deformation, respectively.[420] XPS has previously indicated the presence of oxygen functionality in the form of C=O, C–O and O–C=O. As expected, absorptions are observed at 3238, 1728, 1256 and 1050 cm^{-1}, corresponding to O–H, C=O, C–O–C and C–O stretching vibrations, respectively.[289] Such functionality coincides with that of GO, however, the lower degree of oxygen abundance correlates with a decreased peak intensity.[421] Peaks are also observed at 2914 and 2848 cm^{-1} which correspond to C–H stretching vibrations, likely to originate from aryl C–H groups present within the 4-(trifluoromethyl)phenyl functional groups.[422] Whilst the 4-(trifluoromethyl)phenyl boronic acid displays peaks corresponding to boronic acid functionality such as an intense B–O stretch at 1323 cm^{-1}, its presence is not observed within f-NP1, thereby, further confirming the efficient removal of any adsorbed starting material within the product.[423]

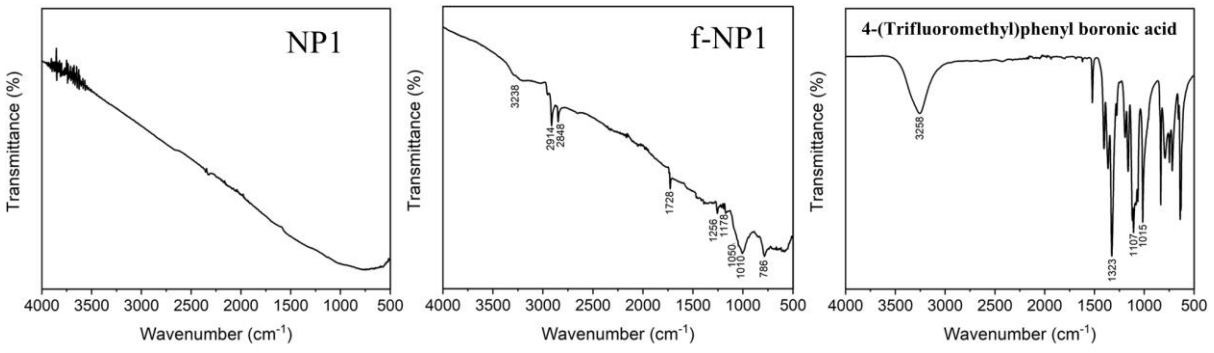

Figure 4.21 FT-IR-ATR spectra of NP1, f-NP1 and 4-(trifluoromethyl)phenyl boronic acid.

4.2.8 Surface Area and Porosity Studies using BET and BJH Measurements

Nitrogen adsorption-desorption measurements were implemented to determine the surface area and PSD of NP1 and f-NP1 materials, including BET and BJH analysis, whilst implementing the adsorption branch for the latter, as shown in Figure 4.22, Figure 4.23 and Table 4.4. The data was also compared with that of C3-NP1. The isotherms exhibit type IIb character, typical of materials composed of non-porous, plate-like particles, as observed in Figure 4.22.[238] A type H3 hysteresis loop is present in each isotherm, indicating the occurrence of capillary condensation within pores.[239] Hysteresis of this type is usually associated with plate-like aggregates or adsorbents containing slit-like pores. This agrees with the SEM images, where stacks of sheets are observed in a high magnification image of f-NP1 (Figure 4.14 (f)).[351] NP1 and f-NP1 possess surface areas corresponding to 380.2 and 192.1 m^2/g respectively, whilst the control material; C3-NP1 possesses a surface areas equivalent to 87.4 m^2/g.

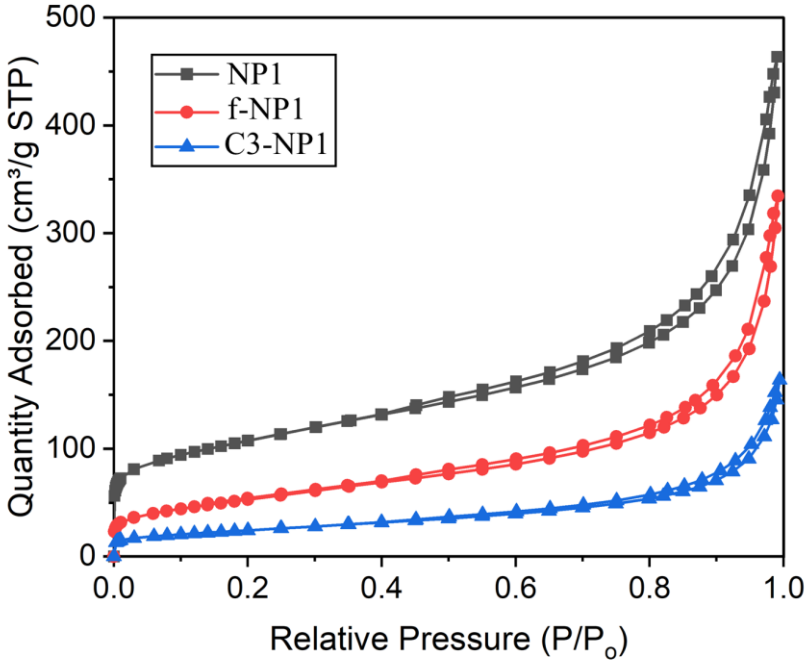

Figure 4.22 N2 adsorption-desorption isotherms for NP1, f-NP1and C3-NP1.

Table 4.4 BET and BJH adsorption data for NP1, f-NP1 and C3-NP1.

Material	BET Surface Area (m^2/g)	BJH adsorption cumulative volume of pores between 1.7 – 300 nm (cm^2/g)	BJH Average Pore Width (4V/A) (Adsorption) (nm)
NP1	380.2	0.746	7.0
f-NP1	192.1	0.490	10.0
C3-NP1	87.4	0.254	9.6

BJH data shows the materials exhibit pores spanning over the mesoporous and macroporous regions. The PSD profile was examined by plotting the average pore width as a function of dV/dlog(W) pore volume, using the adsorption branch of the isotherm (Figure 4.23). Overall, the curves reveal similar patterns for all materials, suggesting a minor impact to the overall structure upon functionalisation. Pores range in size extensively from 1.7 nm for all materials to 92.7, 103.7 and 128.1 nm for NP1, f-NP1 C3-NP1, respectively, according to the BJH data. Meanwhile, the average pore sizes for NP1, f-NP1 and C3-NP1 corresponded to 7.0, 10.0 and 9.6 nm, respectively. The main difference between the materials, however, is a decrease in the surface area and volume of pores. NP1 possesses a BJH adsorption cumulative volume of pores of 0.746 cm^3/g, which is significantly decreased to 0.490 and 0.254 cm^3/g for f-NP1 and C3-NP1, respectively. This is an indication that functionalisation resulted in a significant reduction

in the quantity of pores within the latter two materials. This finding coincides with the significant decrease in BET surface area. For f-NP1, the BET surface area reduced by almost half that of NP1. C3-NP1 suffered a further reduction in its BET surface area to 87.4 m^2/g although the PSD remained very similar to that of NP1 and f-NP1. As a result, it is assumed that the presence of oxygen functionality within C3-NP1 and f-NP1is the primary cause of pore blockage and reorientation of stacks, thereby causing significant reduction in BET surface area and the number of pores.[424] Since more oxygen functionality exists within C3-NP1 than f-NP1 and NP1, it is not surprising to observe a further decrease in surface area. The porous structure of these materials is considered in more detail within Chapter 5.

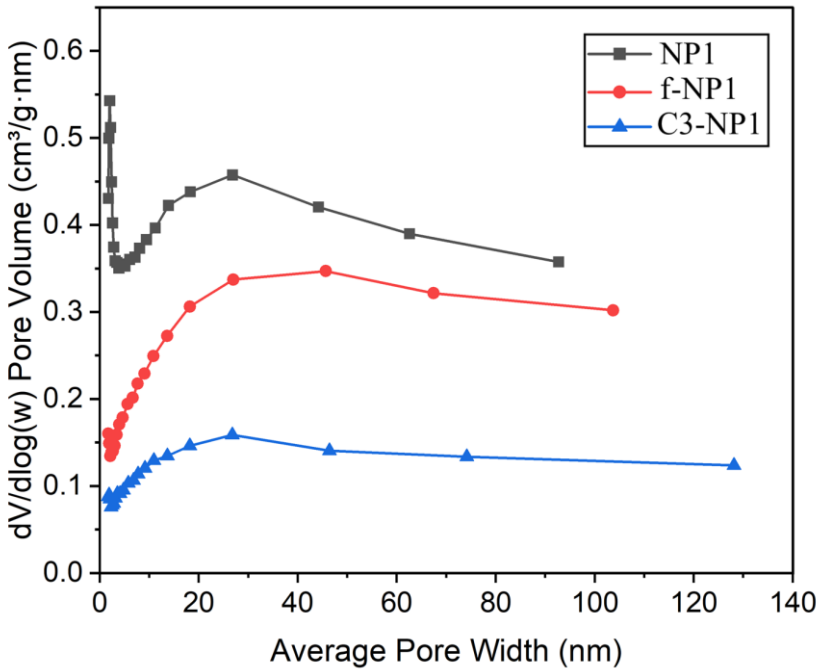

Figure 4.23 BJH adsorption data consisting of the average pore width vs dV/dlog(W) pore volume for NP1, f-NP1 and C3-NP1.

Since integration of the hexagonal (2H) and rhombohedral (3H) (002) and (002) peaks within the XRD spectra confirmed that the average number of layers within a stack remains unchanged upon functionalisation (see Figure 4.19 and Table 4.3), it is unlikely that changes to the stacking morphology of the material have occurred. It is more likely that the functionalised sheets re-orientate themselves to adopt curled, scroll-like edges due to enhanced interactions between the functionalised stacks. Further to this, it is also suggested that additional functionality, located around the edges of the sheets may result in further blockage of many

pores. With such a situation, many of the slit-like pores and channels between neighbouring stacks would become inaccessible to the nitrogen adsorbent molecules. This prospect is discussed in more detail within Chapter 5.

4.2.9 Dispersibility in Common Solvents

The solvent-solute interactions with NP1 and f-NP1 were investigated by obtaining dispersions of the materials across a range of organic solvents. Samples of NP1 and f-NP1 (0.007 g) were dispersed in 4 mL of each solvent then subjected to sonication for 5 minutes using the ultrasonic bath conditions described within the Experimental Section. Photographs were then taken of the dispersions at various intervals to observe how well the dispersions were maintained over time. This are depicted within Figure 4.24 and Figure 4.25 for NP1 and f-NP1 respectively. It should firstly be noted that the ultrasound conditions used to create the dispersions are likely to have had an impact on the particle size and thus dispersibility, consistent with the findings reported within the literature.[425] It is therefore likely that NP particles have undergone some degree of tearing to the planes of the sheets, as well as exfoliation of stacked layers, and thus, any subsequent application of the material would need to take this into account.

In the context of the current discussion, a poor dispersion refers to one which has undergone some sedimentation of solid and the dispersion subsequently appears visually less concentrated. The solvents used were water, dimethyl sulfoxide (DMSO), acetonitrile, methanol, acetone, isopropylalcohol (IPA), dichloromethane (DCM), diethyl ether and hexane. The dispersions were placed in order of solvent polarity; decreasing from left to right within the photographic images. As outlined above, the structure of f-NP1 differs to that of NP1, due to difference in functionality causing significant changes to the morphology and BET surface area. f-NP1 contains additional polar oxygen functionality, as well as non-polar 4-(trifluoromethyl)phenyl groups at the edges of the sheets. Since the composition of oxygen functionality exceeds that of the 4-(trifluoromethyl)phenyl moieties, it was envisioned that the material possesses an overall increase in polarity and interaction between functionality and solvent molecules. It was therefore predicted that the enhanced polar nature of f-NP1 would result in enhanced interaction with polar organic solvents. Interestingly, it was observed that

the dispersions of f-NP1 were in fact poorer than those of NP1, in all solvents. This indicates that it was much more difficult to overcome the barrier to aggregation in the functionalised material. Immediately after sonication, f-NP1 dispersed poorly in hexane and began to sediment to the bottom of the vial. Within an hour, its poor dispersive ability extended to acetonitrile, methanol, acetone, DCM, diethyl ether and hexane. NP1, on the other hand, remained dispersed in all solvents except from methanol and hexane after 1 hour. After 24 hours, f-NP1 had sedimented to the bottom of the vial for acetonitrile, methanol, acetone, IPA, DCM, diethyl ether and hexane. At this point, the water dispersion also began to deteriorate. After 2 weeks, the functionalised material remained only well dispersed in DMSO. On the contrary, NP1 remained well dispersed in all solvents except from methanol and hexane, even two weeks after sonication. In the cases of methanol and hexane, similar results were found within the work of Kymakis and co-workers, who found that methanol and diethyl ether also failed to maintain a good dispersion of GO or rGO, which was attributed to the relatively low surface tension of both solvents.[421] The current findings indicate that both materials remain well dispersed in DMSO. This finding coincides with previously findings that high surface tension solvents with high boiling points are generally best for dispersing graphitic materials.[48,426] The findings also indicate that NP1 was more effective in forming solvent interactions than f-NP1 in the remaining solvents. These findings were unexpected due to a number of reasons. Firstly, it would be expected that polar solvents would prevent aggregation to a better degree within f-NP1 than NP1. Secondly, the presence of additional oxygen functionality, in conjunction with 4-(trifluoromethyl)phenyl moieties should provide f-NP1 with much stronger interactions with strong hydrogen bonding solvents such as water, MeOH and IPA. In previous work, the presence of hydrophilic oxygen-containing groups on the surface of fluorinated GO do indeed facilitate dispersion in water.[153] Thirdly, there is little change in the number of layers in each stack within f-NP1 than NP1, according to XRD data, whereby both materials exhibit stacks corresponding to between 58 to 74 layers. The surface area of f-NP1 is also significantly reduced compared to NP1, indicating enhanced interaction between stacks. Since functionality exists around edges of the layers and the topmost and bottommost layer of each stack within the materials, it is probable that this functionality contributes towards governing how the stacks interact with one another. In the context of f-NP1, there is likely to be enhanced interaction between stacks resulting from hydrogen bonding between oxygen functionality, as well as multipolar interactions in the form of C−F---C=O holding stacks together.[427] As such, the energy to prevent aggregation would be increased, and thus sedimentation would occur much faster. Furthermore, fluorinated surfaces typically result

in decreased van der Waals interaction with solvent.[428,429] This phenomena occurs due to the low polarisability of fluorine and contributes to the overall low surface energy associated with such fluorocarbons. As such, solvent interaction with 4-(trifluoromethyl)phenyl groups may disfavoured, and this effect may outweigh the effect of enhanced interaction with oxygen functionalities. In addition, the 4-(trifluoromethyl)phenyl groups are relatively bulk in comparison with oxygen functionalities and thus, may encourage solvent molecules away from the polar oxygen functionality.

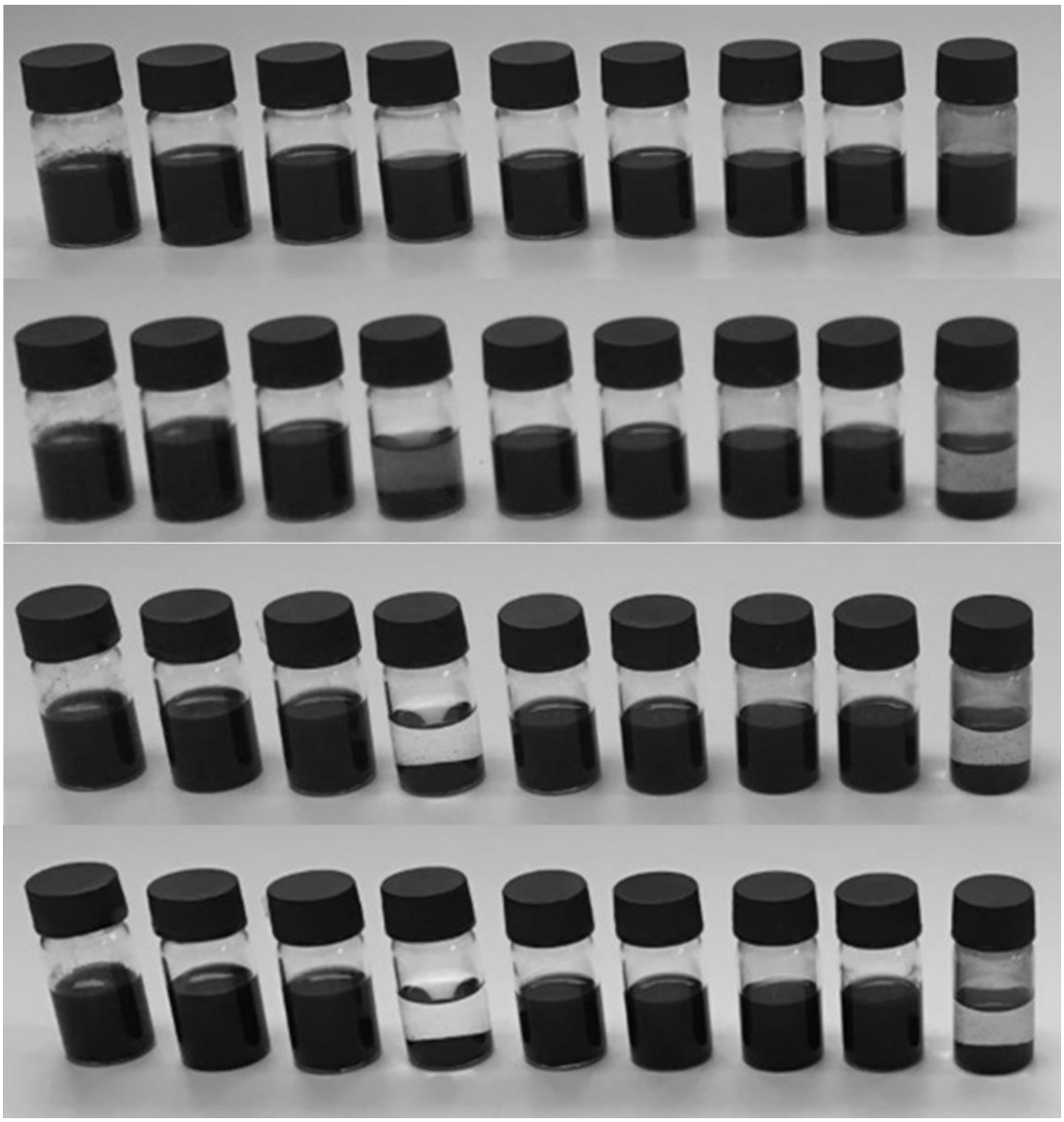

Figure 4.24 NP1 dispersed in solvents left to right: water, DMSO, acetonitrile, methanol, acetone, IPA, DCM, diethyl ether and hexane. A photograph of the dispersion is provided (a) instantly after sonication; (b) 1 hour after sonication; (c) 24 hours after sonication and (e) 2 weeks after sonication.

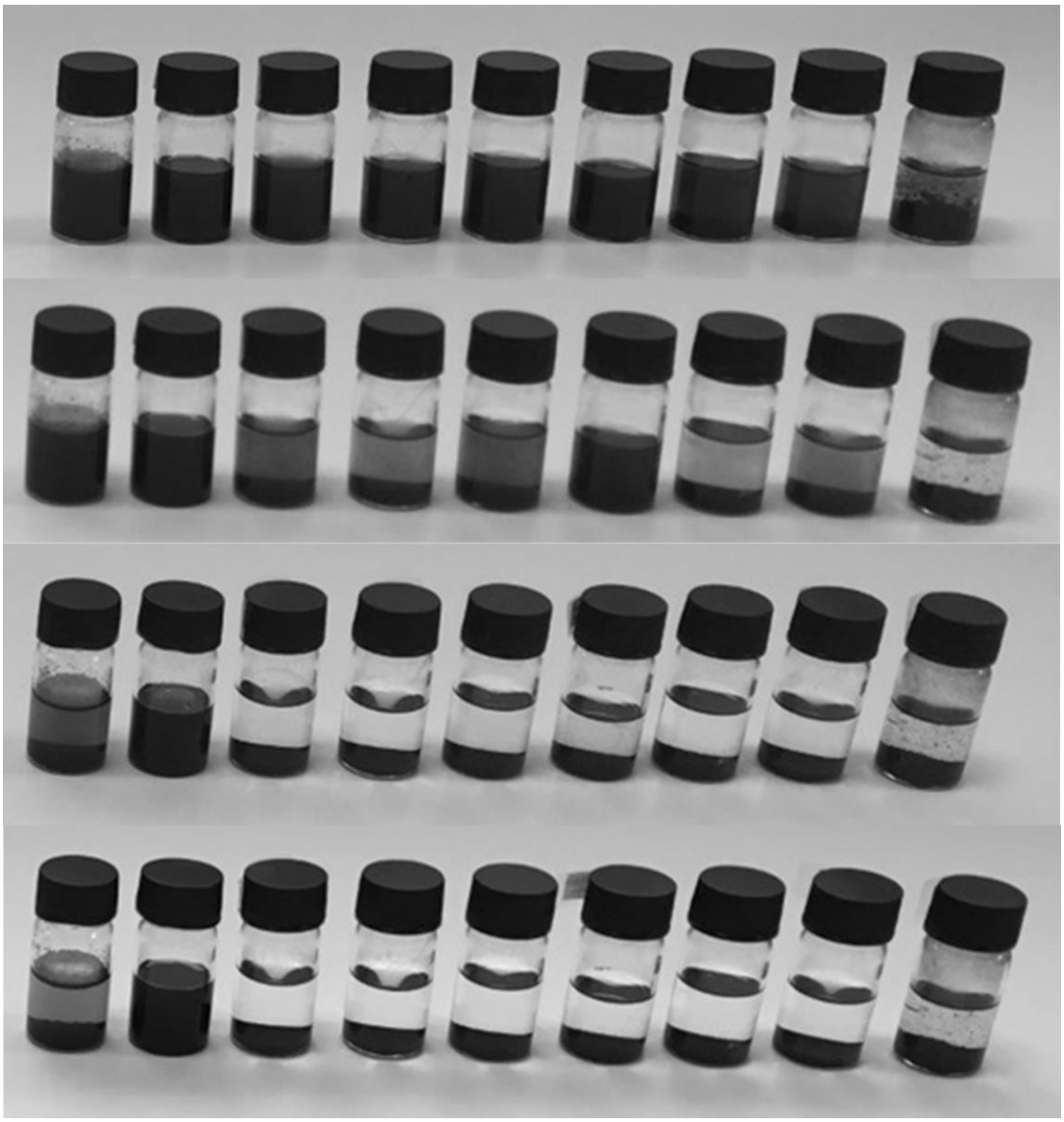

Figure 4.25 f-NP1 dispersed in solvents left to right: water, DMSO, acetonitrile, methanol, acetone, IPA, DCM, diethyl ether and hexane. A photograph of the dispersion is provided (a) instantly after sonication; (b) 1 hour after sonication; (c) 24 hours after sonication and (e) 2 weeks after sonication.

4.2.10 Decomposition Characteristics using TGA

Thermogravimetric analysis (TGA) enables the examination of how materials decompose, which can be very useful in confirming the nature and degree of functionalisation within the material. Accordingly, the thermal stability of both NP1 and f-NP1 were investigated using TGA measurements at temperatures up to 700 °C, within a nitrogen atmosphere. A comparison of the results is depicted in Figure 4.26. Graphitic materials containing oxygen functionality, such as GO, usually provide TGA curves with two distinct regions, corresponding to the decomposition of loosely bound oxygen functionality such as adsorbed water, gas molecules, and other volatile components and covalently bonded oxygen functionality.[430] Despite the presence of 4.82 and 8.46 at.% oxygen functionality in NP1 and f-NP1 respectively, there were no distinct regions of decomposition associated with either material. Instead, a gradual decomposition is observed with no distinct or well-defined mass loss regions. This is most likely due to the wide distribution of sizes, morphologies and degree of oxygen functionalisation of the commercial NP1 materials. Pristine graphite has been found to show little decomposition until 600 °C within an O_2 atmosphere and up to 1000 °C, within a nitrogen atmosphere. Accordingly, mass loss within both samples at these lower temperatures can be attributed to the decomposition of covalently and non-covalently bonded functionality over a gradual period.[431,432] Initial mass loss (up to 100 °C) is attributed to the removal of water from the surface. Decomposition from this point is then assigned to the removal of covalently bonded oxygen functionality. In the case of GO, it has been found that the decomposition of covalently bound oxygen functionality takes place above 150 °C.[433] f-NP1 shows a lower thermally stability than NP1, decomposing at a faster rate. This is attributed to the increased covalent functionality it possesses, including more oxygen functionality and 4-(trifluoromethyl)phenyl moieties. The presence of silver salts on the surface of f-NP1 may also lead to a more rapid and increased mass loss within the material.

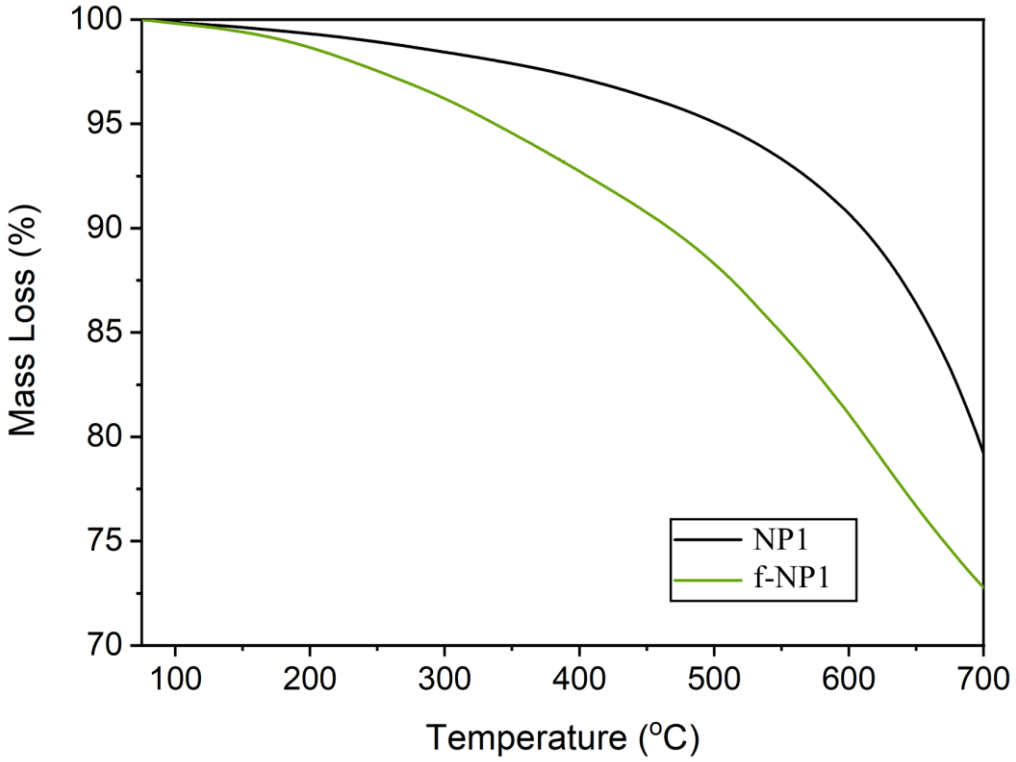

Figure 4.26 TGA curves for (a) NP1 and (b) f-NP1.

4.3 Conclusions

This chapter serves to provide an account outlining the successful covalent functionalisation of NP1 with 4-(trifluoromethyl)phenyl radicals. This was achieved through implementation of 4-(trifluoromethyl)phenyl boronic acid as an aryl radical precursor, utilising Baran's protocol. The success of this covalent functionalisation to form f-NP1 was confirmed using various imaging, spectroscopic and analytical techniques. A total 3.5 at.% fluorine was found to be incorporated into the material, as evidenced by XPS. In addition, an increase in the number of defects, evidenced by Raman spectroscopy, substantial weight loss during TGA and presence of CF_3 functionality within FT-IR, indicated successful covalent attachment of 4-(trifluoromethyl)phenyl moieties to the NP1 structure. In addition, it was observed that functionalisation had negligible effect on the interlayer spacings, quantity of layers or stacking sequence of individual layers within a stack. NP1 and f-NP1 possessed stacks containing multiple layers within the regions of 58 and 74, as determined from the Scherrer equation,

whilst the interlayer spacings corresponded to 0.334 nm. Furthermore, it was observed that the materials possessed both hexagonal and rhombohedral stacking, typical of commercially derived GBMs. Gas physisorption isotherms and utilisation of BET and BJH methodologies indicated a substantial decrease in BET surface area associated with functionalisation of NP1. This was consistent with a large reduction of porous area, resulting from loss of pores due to the reorientation of stacks with respect to one another, as well as blockage by functional groups. Whilst the purpose of this investigation was to identify an alternative aryl radical precursor to hazardous diazonium salts, f-NP1 also exhibits characteristics which could grant it useful in application. For example, its poorer water dispersibility is a reflection of its increased hydrophobicity relative to its un-functionalised counterpart. As such, this material may prove advantageous as a hydrophobic coating. Applications could therefore extend to waterproof clothing or treatment upon car windshields, where the wetting of water is undesirable. In addition, the entrapment of silver species within its structure, even after extensive washing, show its tendency to retain compounds to a large degree. This material could therefore be useful in the context of membrane technology, to remove toxic salts and heavy metals from solvents and water. As such, application could also extend to water treatment processes, where the presence of salts and metals within drinking water can cause threat to human health.

5 Exploring the Porous Structure and Pillaring of Plasma-Exfoliated Graphitic Material Using Laponite

5.1 Synopsis

As outlined in the previous chapters, it was found that NP1 consisted of a large surface area arising from the presence of pores spanning over the microporous, mesoporous and macroporous regions. Several investigations were therefore embarked upon within this chapter, to further understand the porous structure of NPs and how these can be altered to fabricate materials with increased surface areas. Initially, the porous structures and surface areas of NPs were investigated. The BJH data was utilised for the first time to provide effective estimation for the distance between stacks within such materials. Attention was then directed towards investigating how covalent functionalisation, including oxidation, impacted the porous structure and surface area of NP. In the final section, a novel strategy was utilised to enhance the surface area and porosity within oxidised NP, using laponite as a pillaring device to fabricate a scaffold-type structure.

5.2 Results and Discussion

5.2.1 Investigating the Surface Area and Porous Structure of Plasma-Exfoliated Graphitic Material

5.2.1.1 Surface Area and Morphological Analysis using BET and SEM

NPs possess interesting porous structures with a range of surface areas. During synthesis of these materials, the plasma processing initiates exfoliation of the bulk layered graphite into various multilayered substructures, referred to as stacks, as depicted in Figure 5.1. These stacks typically incorporate both in-plane pores or “holes” within the plane of the graphene layers, as

well as slit pores between subsequent neighbouring stacks. The stacks themselves incorporate assembled graphitic layers which are held together by extensive van der Waals forces such as π−π stacking between subsequent layers. Oxygen functionality is also introduced to the graphitic layers within the stacks.[95] NPs vary quite substantially in morphology due to differences in the dimensions and orientations of individual stacks. SEM images associated with NP2, NP1, f-NP1, NP3 and NP4 are shown below in Figure 5.2. NP2 displays a flake-like appearance consisting of many comparatively flat stacks, with large dimensions (Figure 5.2 (a)), whilst NP1, NP3 and NP4 consist of large aggregates comprised of many smaller stacks (Figure 5.2 (b)(d) and (e)). All stacks tend to adopt morphologies which consist of rippling and curvature, typical of such materials.[434] It has also been highlighted in previous works that the presence of Stone-Wales defects has been found to enhance the tendency of the graphitic layers to roll into nanotube and fullerene-type structures, as well as promoting intrinsic rumpling/buckling of graphitic layers as a way to relieve strain.[122,123,435] It is, therefore, unsurprising that the present materials adopt such morphologies.

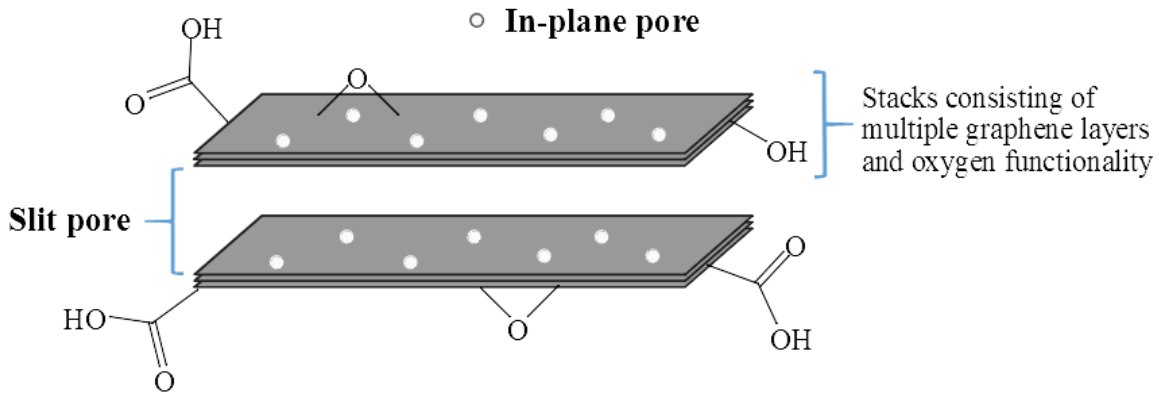

Figure 5.1 Stacks of NP material containing multiple graphene layers, defects, in-plane pores and oxygen functionality. Slit pores arise due to the presence of spacing between neighbouring stacks.

Initially SEM imaging was conducted to allow the observation of pore types within the materials. Slit pores are highlighted by green arrows within Figure 5.2, whilst in-plane pores are assigned by red arrows. Slit pores are present within all materials and result from the spacing between neighbouring stacks. These are easy to visualise in some materials such as Figure 5.2 (a) and (c)(i), however, are more difficult to observe within heavily aggregated materials such as NP4 (Figure 5.2 (e)). The 4-(trifluoromethyl)phenyl functionalised material

f-NP1, synthesised during Chapter 4, provides an example of a material which contains in-plane pores visible *via* SEM imaging, as shown within Figure 4.12 (d). Further SEM imaging reveals the presence of three additional in-plane pores possessing widths on the macro-scale corresponding to approximately 700, 300 and 150 nm. Such pores are likely to originate from the harsh radical conditions subjected upon the material causing etching of existing in-plane pores, as mentioned within Chapter 4. Smaller in-plane pores within the micro region also exist within the NP materials provided by Perpetuus, as highlighted by previous works.[93] It is believed that these are introduced into the materials during the plasma processing steps. Unfortunately, due to the limits with the SEM detection, these cannot be visualised by SEM imaging easily.

The plasma radiation modifies the graphitic surface both physically *via* ablation and through the generation of amorphous regions, as well as chemically through the introduction of oxygen functionality. Such physical modification results from single vacancies, double vacancies, complex vacancies and Stone-Wales defects. Complex vacancies, generated from the removal of multiple carbon atoms, consist of micro-scale holes within the graphitic lattice, which are considered as in-plane micropores, if indeed, they allow access to adsorbate molecules. It has been reported that etching proceeding at approximately 20 W, with several seconds of exposure time, introduces micropores of sizes between 0.5 – 1 nm into graphene. Furthermore micropores between 0.7 and 2 nm in size have been detected within activated carbon fibres, using low pressure (33.3 Pa) plasma treatment.[120] Furthermore, extension of the plasma exposure time has been found to not only increase the defect density, but also enlarge micropores.[119] In light of these findings, it is, therefore, suggested that the presence of micropores within NPs originate from the bombardment of ions/electrons, as well as due to etching of vacancy defects during oxygen plasma processing to enlarge existing vacancy defects.

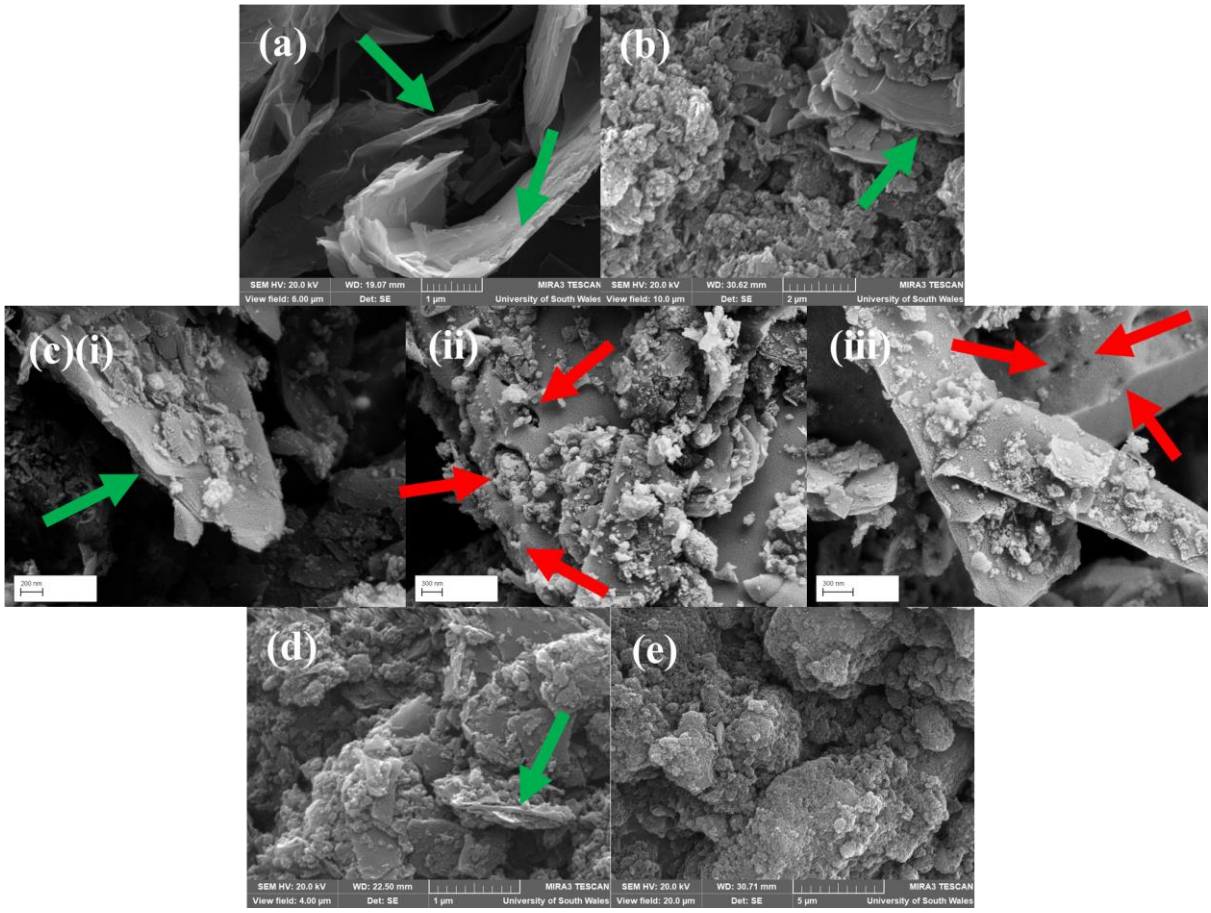

Figure 5.2 SEM images depicting pores within (a) NP2 at a magnification of 34.60 kx; (b) NP1 at a magnification of 20.67 kx; (c) f-NP1 at magnifications of (i) 81.7 kx (ii) 50.9 kx and (iii) 75.46 kx; (d) NP3 at a magnification of 51.96 kx and (e) NP4 at magnification of 10.39 kx. Green arrows and red arrows indicate the presence of slit pores and in-plane pores respectively. SEM images (a)(b)(d) and (e) were acquired on SEM 2, whilst SEM image (c) was acquired on SEM 1.

Information regarding the surface area and PSD was calculated using BET/BJH/t-plot data using nitrogen adsorption-desorption measurements. Since f-NP1 had previously been analysed in Chapter 4, it is discussed in no further detail within this section. BET isotherms for the four remaining materials were conducted using N_2 adsorption at 77 K, to gain an insight to the surface areas and adsorption-desorption pathways of the materials, as shown in Figure 5.3 (b). All isotherms possessed similar adsorption-desorption pathways to each other, displaying an initial sharp uptake at low P/P_0 (< 0.001), indicative of micropore filling. After monolayer formation at "the knee", an increase in P/P_0 results in a slower uptake of nitrogen, indicating the presence of mesopores within the samples. A further sharp rise at $P/P_0 > 0.9$, signifies the presence of macropores within the materials. In contrast to a type IV isotherm, no plateau is visible at high P/P_0, therefore, the isotherm is assigned as type IIb (pseudo-type II). The absence of a plateau suggests incomplete mesopore filling, suggesting that large mesopores and

macropores are not filled completely and thus, multilayer adsorption continues to proceed with no termination. The key features associated with this type of isotherm are depicted in Figure 5.3 (a) and discussed in further detail later on in the text. The overall BET surface represents a measure of the total surface area of the material, inclusive of micropores, mesopores and macropores. In this regard, the latter of these is considered to incorporate any pore exceeding 50 nm in pore width. The materials exhibit a range of BET surface areas, whereby NP4 displays the largest surface area corresponding to 670.9 m^2/g, NP1 and NP3 display surface areas of 380.2 and 450.5 m^2/g respectively, and NP2 possesses the smallest surface area of 88.8 m^2/g (Table 5.1)). It is believed that large surface areas are more prominent within materials with increased porosity (*vide infra*).

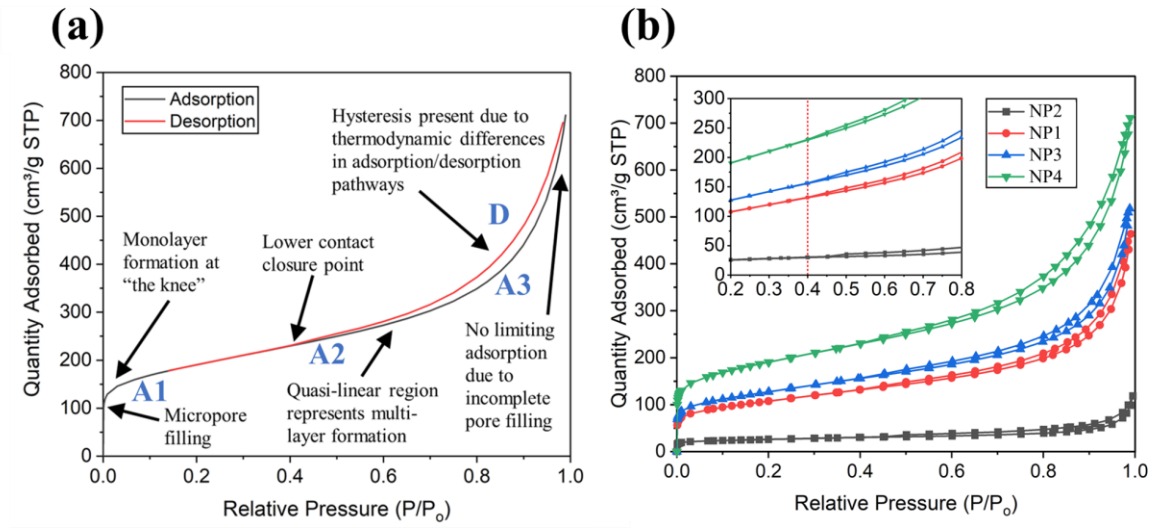

Figure 5.3 (a) N_2 adsorption-desorption isotherms typical of NPs incorporating their various features and the adsorption steps 1 – 3 and desorption corresponding to A1, A2, A3 and D respectively and (b) N_2 adsorption-desorption isotherms for various NP with the inset showing a magnified image of the contact closure point.

Table 5.1 BET surface area values for NPs.

	NP1	**NP2**	**NP3**	**NP4**
BET Surface Area (m^2/g)	380.2	88.8	450.5	670.9

Within the BET isotherms, H3 hysteresis is observed between the adsorption and desorption branches between 0.4 – 1.0 P/P_0, according to IUPAC classification.[351] The presence of hysteresis evolves from the behaviour differences of the adsorbate during adsorption and desorption. Such a hysteresis type indicates the presence of slit-like particles with non-rigid

nature, and non-uniform shape and size, consistent with SEM images in Figure 5.2. Since hysteresis is not present within materials containing solely micropores, where filling and emptying occurs *via* the same pathway, its presence provides additional evidence of mesopores and macropores within the materials.

Inspired by the work of Tiogo, who implemented argon density profiles on open-ended cylindrical pores, a simplified interpretation of the open-ended slit pore (Figure 5.4) was recreated.[436] This can be used to demonstrate how the filling and emptying occurs within pores within NP materials. Such steps can be directly compared with various regions within the BET curve, shown in Figure 5.3 (a), assigned as adsorption steps 1 − 3 and desorption, denoted as A1, A2, A3 and D, respectively for simplicity. Initially, the adsorption branch of the BET isotherm increases steeply, indicating monolayer formation of adsorbate over the surface of the material, relating to A1. Completion of this stage occurs at "the knee" of the isotherm, where the plot then exhibits a quasi-linear shape corresponding to that of multilayer formation, relating to A2. The isotherm then steepens (ca. 0.8 P/P_0), corresponding to macropore filling. Implementation of the grand canonical ensemble suggests that within the slit pores, adsorbate covers opposing walls, and at the lower contact point (ca. 0.4 P/P_0), their state changes from stable to metastable. The metastable adsorbed layer consists of three-regions: the dense adsorbed phase, the mass transfer zone, and the gas phase, as indicated within Figure 5.4. If the slit pore possesses a width, *w*, of a suitably small size, its mass transfer zones can interact *via* fluid-fluid interactions, forming a bi-convex liquid-embryo, causing condensation to occur, and more molecules to be drawn in. Two hemispherical menisci therefore form during A3. A further increase in pressure to the saturation vapour pressure further densifies the condensation.[437] In principle, this process provides a plateau within the isotherm during this adsorption step; however, no plateau is observed. This is because many of the slit pores are too wide for their mass transfer zones to interact, and hence condensation does not occur below the saturation vapour pressure. As a result, a steep line is observed within the isotherm, corresponding to incomplete filling. During desorption, D, the subsequent reduction in pressure then desorbs nitrogen molecules. In the case of pores where condensation occurs, the meniscus increases in curvature, while remaining pinned to the pore circular mouths.[436,438] However, in the situation observed within a large slit pore, *w* is relatively large, therefore not all pores become filled and condensation is not reached. As a result, no plateau is present, since there is no limiting adsorption at these high P/P_0 values. For these larger pores, the condensation exceeds the saturation vapour pressure, since the separation distance between opposing slit

pore walls is too large for liquid embryo formation.[437] According to the claims associated with NP materials, the distance between stacks is relatively large, thus, it is plausible that this incomplete filling occurs within these slit-pores.[95]

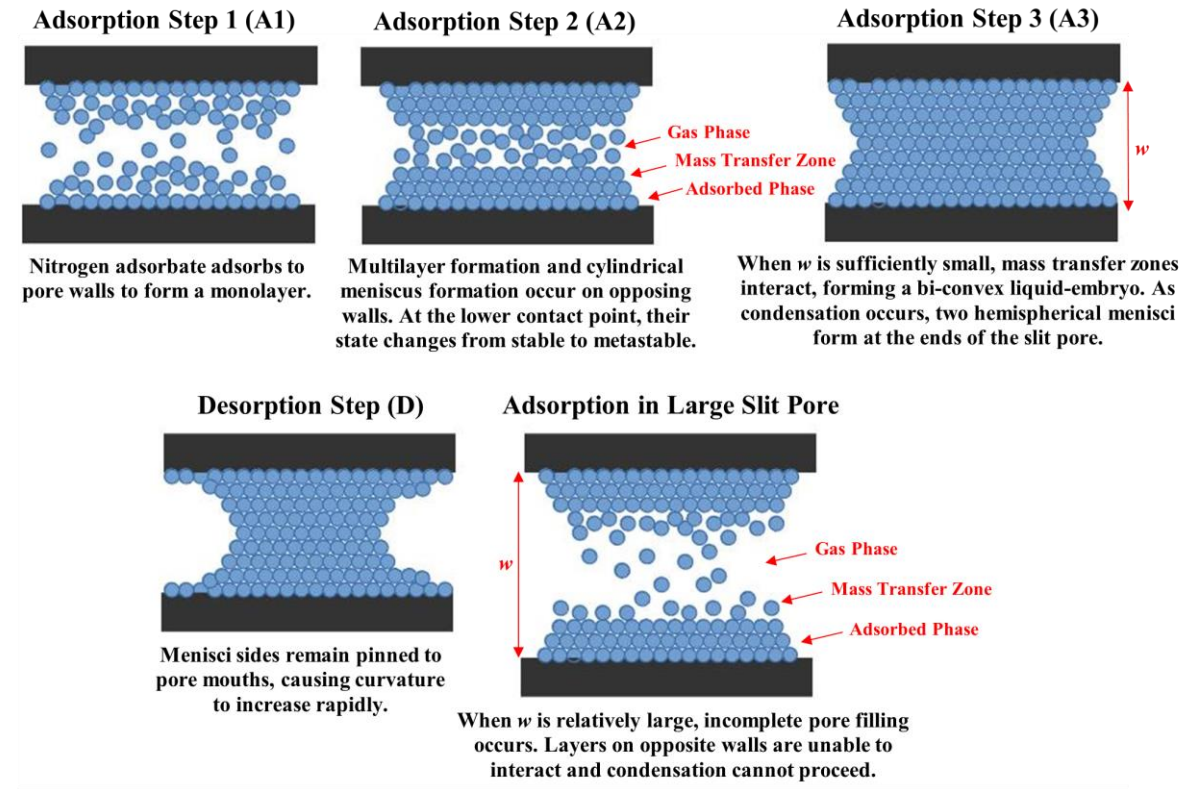

Figure 5.4 A graphical representation of the filling and emptying of open-ended cylindrical slit pores by nitrogen molecules inspired by the works of Ancilotto et al.[436] The diagram depicts how filling and emptying of slit pores proceeds as nitrogen pressure is increased (A1) – (A3) and decreased (D) respectively, and the incomplete filling occurs within relatively large slit pores found within NP materials.

Another feature of the BET isotherm (Figure 5.3) relates to the relatively low contact closure point. Such a property is attributed to the tensile strength effect of condensed liquid nitrogen which results from the instability of the meniscus condensation for pores around 4 nm in width. This unstable state is caused by the adsorption energy of the pore wall and an increased tensile strength in the adsorbed phase. As such, a forced closure of the hysteresis loop at relative pressure of approximately 0.4 P/P_0 occurs.[439–441]

5.2.1.2 Graphitic Structure Analysis using Raman Spectroscopy

Raman spectroscopy was conducted on these materials to understand how their graphitic structure and defect density compared with the BET surface area of the materials. The results are shown in Figure 5.5. Three characteristic peaks, corresponding to the G band, 2D band and D band are noticeable within all spectra, consistent with the spectra of f-NP1, within Chapter 4. Calculation of the I_{2D}/I_G ratio provides values ranging between 0.44 and 0.52, which all lay beneath that of SLG ($I_{2D}/I_G = 2 - 3$), and thus, a multilayer structure is consistent within all materials.[411] The 2D bands are also broad in appearance, and upshifted relative to SLG, therefore, this peak provides further evidence of the presence of multilayer stacks.[312] The presence of a D band indicates the existence of defects within the four materials. Using the I_D/I_G ratio as an indication of the number of defects, it is observed that NP4 is the most defective material, whilst NP2 is the least. These materials are associated with the largest and smallest BET surface area values respectively, thus suggesting that the defects serve to create a more porous structure. It is likely that increased plasma exposure results in an increase in the number of defects and hence more exfoliation.[3] In contrast, NP2 possesses a much smaller surface area, consistent with the far less defective structure, due to the reduced plasma exposure time. NP1 and NP3 represent two batches of the same material and were synthesised under the same plasma processing conditions. Their BET surface areas are therefore not too dissimilar from one another, as expected. Unexpectedly, the I_D/I_G ratio for NP1 is much larger than that of NP3 (0.54 *cf.* 0.24). This finding may be attributed to structural inconsistencies across different batches of the sample, originating from the plasma processing steps, or from their raw graphite precursor.

[3]Due to the patented technology, these assumptions are only speculative, and have not been confirmed by Perpetuus.

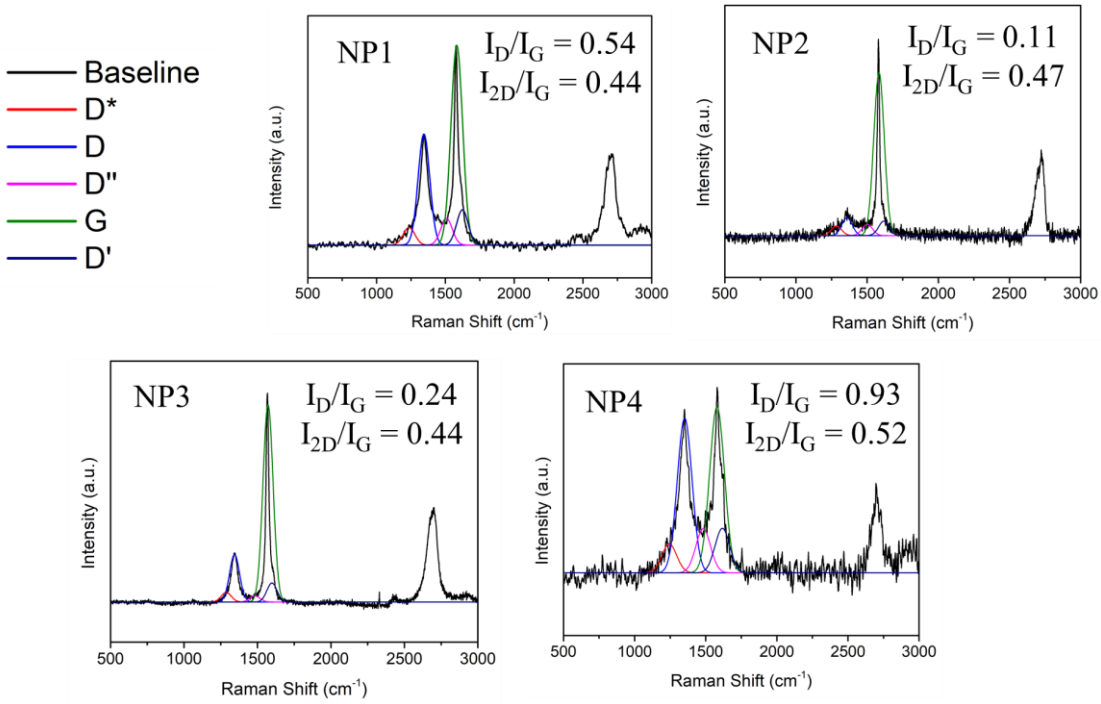

Figure 5.5 Raman spectra of NP materials depicting their corresponding I_D/I_G and I_{2D}/I_G ratios. Peak deconvolution was performed using OriginPro software to discriminate the D and G bands from overlapping D^*, D'' and D' bands.

5.2.1.3 Investigating Pore Size Distribution using BJH Analysis

BJH analysis, was also implemented to acquire information regarding the PSD of the four NP materials. Such analysis applies the Kelvin model for pore filling to experimental isotherms.[344] Whilst this method is useful in gaining an insight to the mesoporous region, it is constrained to a theoretical range between the limits of 1.7 − 300 nm. As a result, pore distribution data cannot be obtained outside of these limits. During BJH analysis, it is also extremely important to have an underlying understanding of the materials in question. To effectively carry out calculation using the BJH method on a sample, the fraction of pores open at both ends should be inputted prior to calculation. For NPs, this value was assumed to correspond to 0.8 (equating to 80% of

all pores). This estimation was made on the assumption that 80% of pores originate from open-ended slit pores (pores which can be accessed from both ends by adsorbate molecules)[4].

The BJH adsorption data associated with the incremental pore volume is presented in Figure 5.6 and Table 5.2. Adsorption data was favoured over desorption data for the purpose of interpretation and analysis, as the desorption process is heavily influenced by the pore volume/meniscus effects which become significant for macropores present within the material. Desorption data also presents an undesirable phantom peak at approximately 4 nm.[442] It is observed that the PSD varies quite substantially for all materials, ranging between the mesoporous and macroporous regions. NP2 possesses the largest PSD, ranging between 2 – 131.2 nm. Such pores are presumed to correlate primarily to slit pores between subsequent stacks (*vide infra*). Many of these pores present within NP are relatively large compared to those of similar materials.[443] Moreover, the BJH average pore size data signifies the large contribution of slit mesopores to the structures. These values range between the 6.3 – 10.4 nm for all materials (see Table 5.2).

Micropores are also present within all materials. The t-plot model was employed to estimate the volume and apparent surface area of micropores, using the Harkins and Jura thickness equation.[356,444,445] The addition of the t-plot micropore area and the t-plot mesopore/macropore area, which incorporates all pores within the mesoporous and macroporous regions, gave the total BET surface area associated with the material, as depicted within Table 5.1. As a result, it was possible to calculate the relative proportions of micropores, relative to mesopores and macropores, as a percentage. Such calculations show that NPs exhibited micropores associated with approximately 22 – 45% of the BET surface area. It is also observed that as the BET surface area increases, the t-plot micropore volume increases from 0.018 cm^3/g in NP2 to 0.081 cm^3/g in NP4. As a result, it is suggested that an increase in surface area correlates with an increase in slit and in-plane micropores. In the next section, BJH is employed to provide an estimation of the distance between the stacks within NP2 to provide a more detailed insight to its structure, and data is compared with that of SEM, AFM and XRD techniques.

[4] This value was postulated based on various assumptions using BET/BJH/t-plot data acquired for NP2: (1) Slit pores are primarily open-ended and that the vast majority of pores, although not all, are made up of slit pores within the current materials; (2) the t-plot external surface area likely corresponds to slit pores; (3) approximately half of the t-plot micropore area corresponds to slit pores and (4) the remaining half of the t-plot micropore area corresponds to in-plane pores. As such, a total of 80% of all pores are considered open-ended slit pores

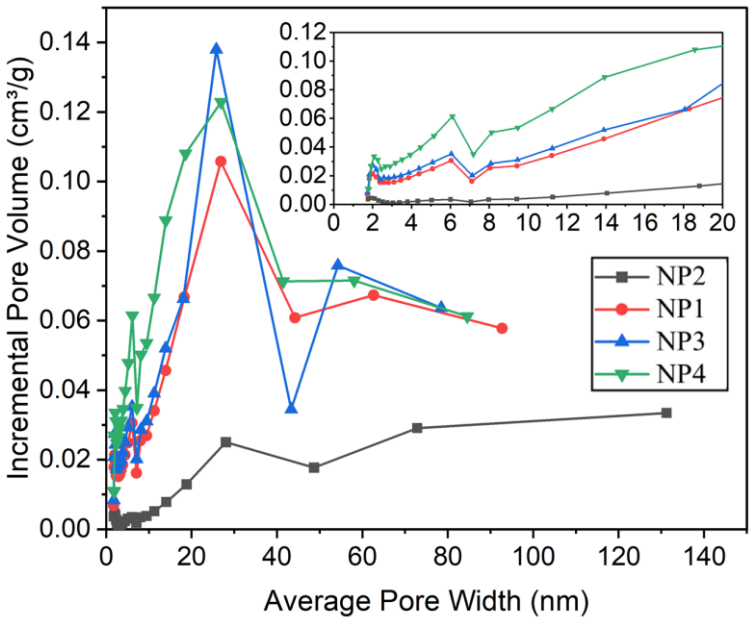

Figure 5.6 BJH adsorption data associated with the incremental pore volume for various NPs.

Table 5.2 BET, BJH adsorption and t-plot data for NPs.

	NP1	NP2	NP3	NP4
BJH Adsorption Average Pore Width (4V/A) (nm)	7.0	10.4	6.6	6.3
t-Plot Micropore Volume (cm^3/g)	0.037	0.018	0.043	0.081
t-Plot Micropore Area (m^2/g)	83.6	39.7	98.8	181.6
t-Plot Mesopore/Macropore Area (m^2/g)	296.6	49.2	351.7	489.3
t-Plot Micropore Area Compared to Total Area (%)	22.0	44.6	21.9	27.1

5.2.2 Application of BJH Data to Estimate the Distance Between Stacks in NPs

Within this section, it is shown that BJH data can be used as a valuable tool to estimate the distance between stacks within NPs. For this purpose, NP2 was employed as a model material due to its large flake size and less aggregated morphology, meaning that SEM imaging of slit pores were much easier to discern. The PSD within NP2 was previously found to range quite substantially; between 2 to 131.2 nm (Figure 5.6), and the material possessed a type IIb isotherm (Figure 5.3), which predicted a porous, slit-like structure. Slit pores simply describe

the porous space made up between two parallel stacks, as depicted in Figure 5.1, thus, the pore width coincides with the distance between these stacks. Whilst individual distances may be measured *via* imaging techniques, it is important to ascertain an average distance between stacks, and thus acquire information regarding the distribution of slit pores across the material. This is important since the spacings between stacks have a large influence on the properties of the material. The presence of large slit pores is particularly useful to improve friability and permits easy dispersion *via* shear type forces and sonication. Further to this, they provide accessibility for intercalation compounds such as sulfur and molecular hydrogen.[95] As such, a clear understanding of variations in stack separations is important for any manipulation of NP2 in this way. BJH data can therefore be applied to gain information on the size distribution of slit pores widths within the material, which subsequently, provides an estimate of the distance between the stacks.

Since no in-plane pores were visible *via* SEM or TEM imaging between the BJH PSD range of NP2, it is likely that the BJH data covers pores originating predominately from slits between neighbouring stacks within the material. High magnification SEM and TEM images do not provide any clear evidence of any in-plane pores of 2 nm or larger in size (Figure 5.8). The average pore size of NP2 corresponds to 10.4 nm (Table 5.2), which directly correlates with the average distance between the stacks between the ranges of 1.7 − 300 nm. A more detailed analysis of the SEM images associated with NP2 contextualises the presence of slit pores within the structure. Figure 5.7 (a) displays an SEM image of NP2, depicting the presence of two thick aggregated structures consisting of orderly aligned parallel stacks, which each contain many layers. The term aggregate applies to the assembly of individual stacks, typically containing slit pores and some degree of interparticle pores between them. Application of a sorbel filter (Figure 5.7 (b)) enhances the ability to observe these orderly aligned stacks. These aggregated structures possess thicknesses of 313 and 152 nm, as highlighted in the figure. The former of these structures has been used to provide a visual explanation of how multiple stacks aggregate with one another, forming slit pores within the regions between them (Figure 5.7 (c) and (d)). A thick structure with a thickness of 313 nm should have somewhere in the region of 18 stacks, assuming an average stack dimension of 7.2 nm (see AFM data below) and an average slit pore size of 10.4 nm (see BJH adsorption data). Only six stacks have been drawn within this diagram for the purpose of clarity. A closer look at these neighbouring stacks is outlined in Figure 5.7 (d). This shows that each stack consists of multiple graphitic layers, held

tightly to one another through π−π interactions, similar to the structure of graphite. The width of the slit pore, *w*, correlates with the distance between two neighbouring stacks.

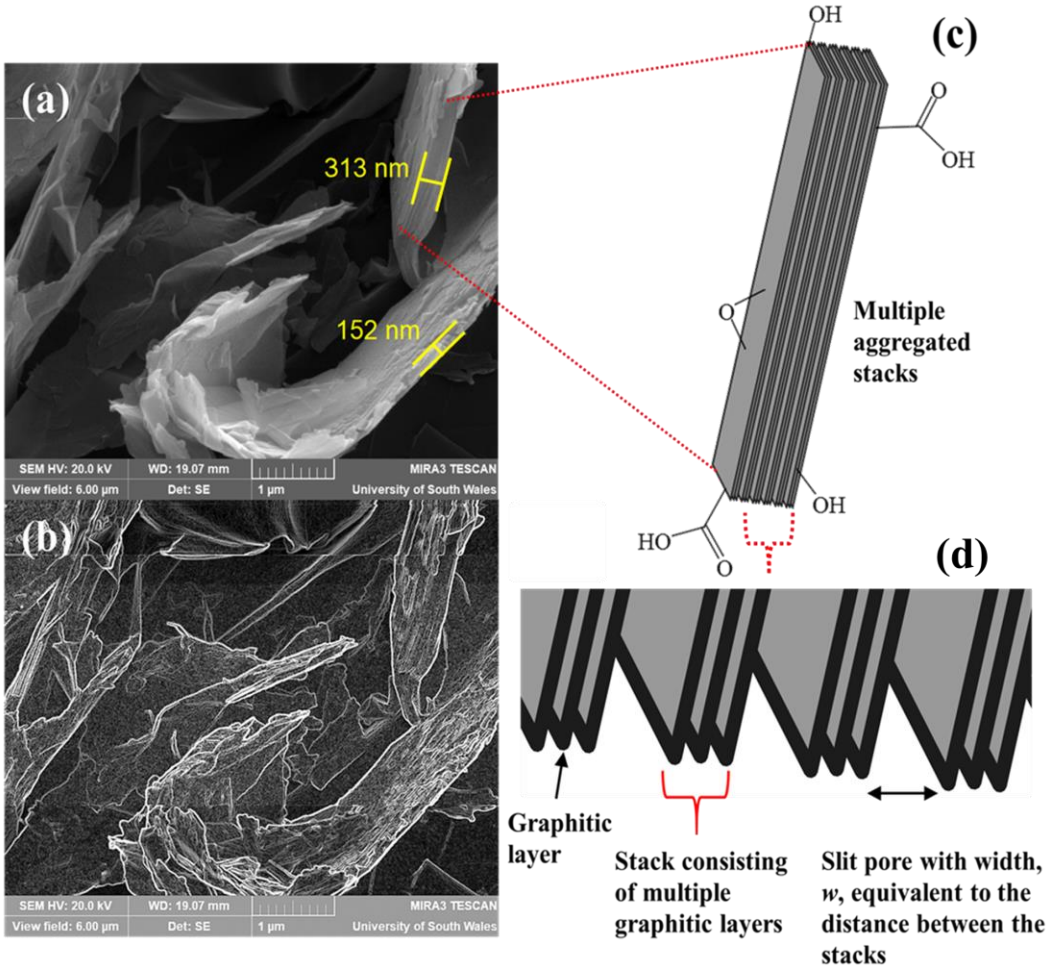

Figure 5.7 Morphology of NP2 shown by SEM images at a magnification of 34.60 kx, shown without (a) and with (b) a Sorbel filter. (c) depicts the presence of multiple aggregated stacks and (d) shows a magnified region of (c), indicating the presence of multiple graphitic layers within each stack and showing that the spacing between the stacks equates to the width, w, of the slit pore. SEM images were acquired on SEM 2.

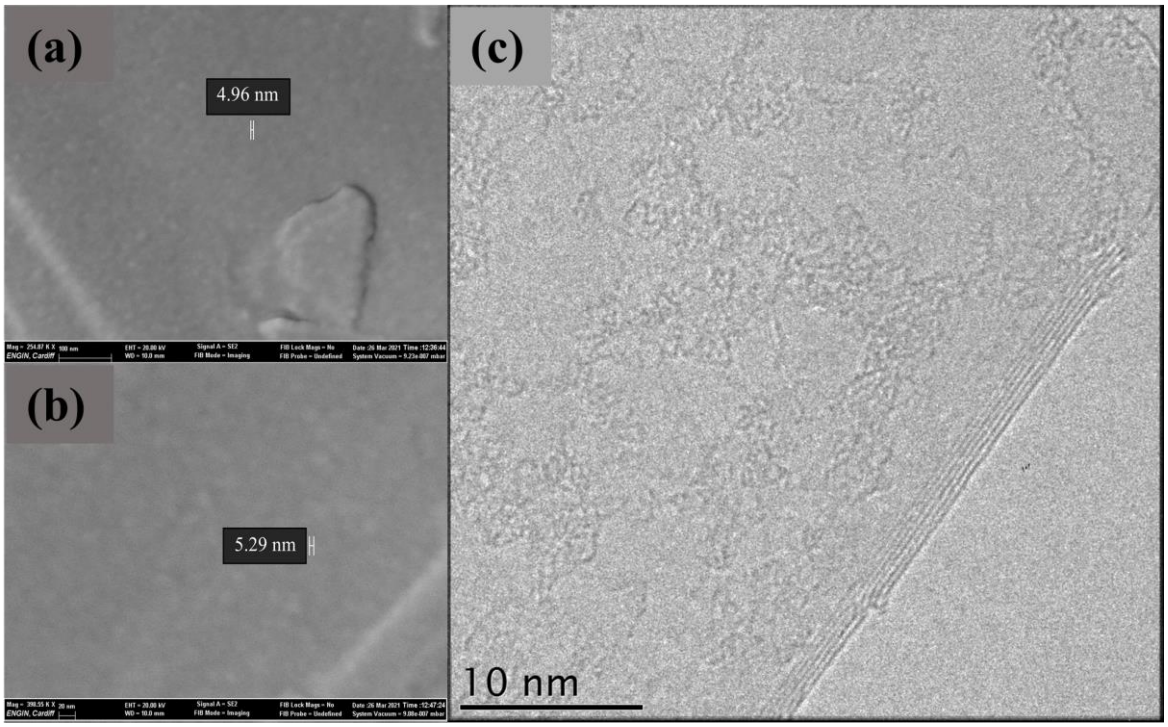

Figure 5.8 SEM images of NP2 at magnifications of (a) 254,870 x and (b) 398,550 x with scale bars corresponding to 4.96 and 5.29 nm respectively acquired on SEM 3, and (c) TEM image of NP2 at a magnification of 50,000 x with a scale bar corresponding to 10 nm acquired on TEM 2. These images reveal an absence of any in-plane pores of 2 nm or larger in size, thus, suggesting that pores within the mesoporous and macroporous region primarily relate to slit pores.

Further SEM imaging provides evidence of slit pores within NP2. Such data correlates with the slit pore widths acquired from BJH data. Figure 5.9 depicts seven representative SEM images of the NP2, showing that the distance between observed stacks vary from 9 nm up to 131 nm. The latter of these equates to the largest slit pore found during BJH analysis (Figure 5.9 (g)), whilst smaller widths (9, 10, 19, 23, 27, 32, 33, 70, and 92 nm, shown in Figure 5.9 (a) – (f)) correspond to slit pore widths observed within the BJH incremental pore volume plot (Figure 5.6). In addition, the distance between stacks, measured within Figure 5.9 (a) correlates with the average slit pore determined by BJH analysis. As such, SEM imaging also shows that many of these stacks possess large distances between each other, within the range found by the BJH data. Compared with similar graphitic materials reported within literature, these slit pores within NP2 are relatively large, which is beneficial due to the aforementioned reasons.[232]

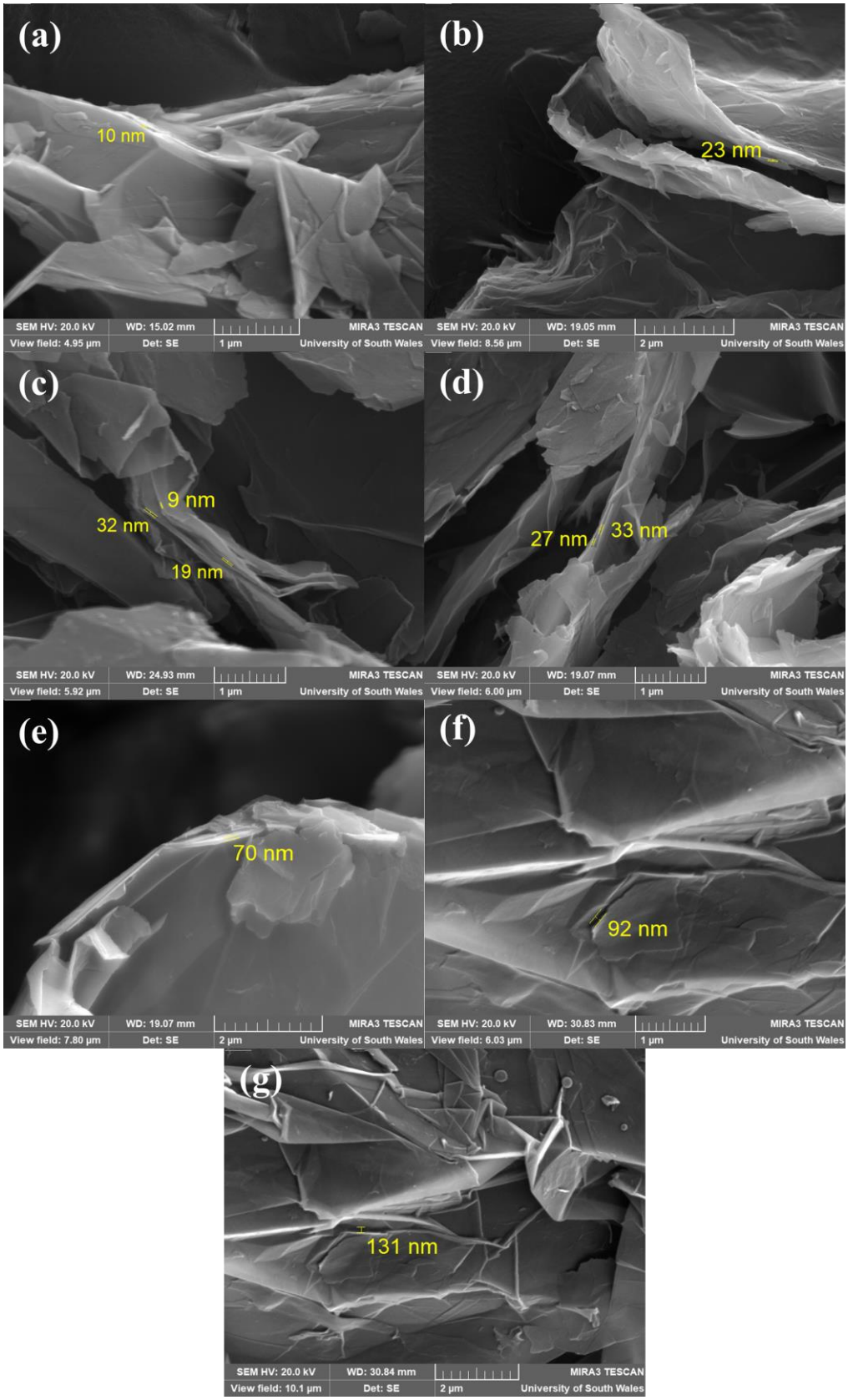

Figure 5.9 SEM images outlining the width of slit pores found within NP2, which relate to the distance between the neighbouring stacks. Magnifications correspond to (a) 34.60 kx (b) 24.26 kx (c) 35.09 kx (d) 34.60 kx (e) 26.63 kx (f) 34.42 kx and (g) 20.60 kx and images were acquired on SEM 2.

NP2 was also assessed further *via* TEM, SEM, AFM, XRD, XPS and SEM-EDX to provide a more thorough understanding of the morphology, elemental composition and structure of the material. Additionally, the contribution of AFM and XRD data supported the stack width and slit pore width estimations, acquired by SEM and BJH analysis (*vide infra*). Initially, TEM analysis and further SEM imaging were conducted to gain an insight to the dimensions of the material. It was observed that NP2 consists of stacks adopting a flake-like morphology and dimensions of < 1 to 50 µm, as shown by SEM and TEM images within Figure 5.10 and Figure 5.11, respectively. These flakes corresponded to individual stacks containing multiple graphitic layers. Within TEM imaging, it is observed that several flakes overlap with one another. Lighter regions correspond to relatively thin areas of the sample, where flakes do not overlap with other flakes, whilst dark regions indicate thicker areas, where flakes overlap with subsequent flakes (Figure 5.11).

AFM also provided evidence of the aggregated morphology (Figure 5.12). Images were used to gain an insight to the height distribution across overlaying stacks within the various aggregated structures. Magnification of the AFM image presented in Figure 5.12 (a) shows that these stacks display non-uniform dimensions of several micrometres. Additionally, it is observed that some stacks lay flat upon one another, whilst others protrude from the surface. A magnified and two-dimensional depiction of this figure is shown in Figure 5.12 (c) and contains a height scale bar which shows that the surface structure deviates in height by 415 nm. This indicates the presence of numerous stacked structures. Moreover, line profiles were recorded across six regions of Figure 5.12 (c), where the AFM tip was scanned directly over one stack and then over the stack directly beneath. As such, these line profiles provide representative thicknesses of each stack plus its associated slit pore, as demonstrated within Figure 5.12 (d). The relevant line profiles are depicted in Figure 5.12 (e) and correlate to regions 1 – 6 within Figure 5.12 (c). It is observed from these that there is a decrease in height of approximately 22, 83, 32, 26, 27 and 49 nm, respective to each region. The average decrease in thickness is therefore calculated to be 40 nm, consistent with the average thickness of the stack plus its associated slit pore.

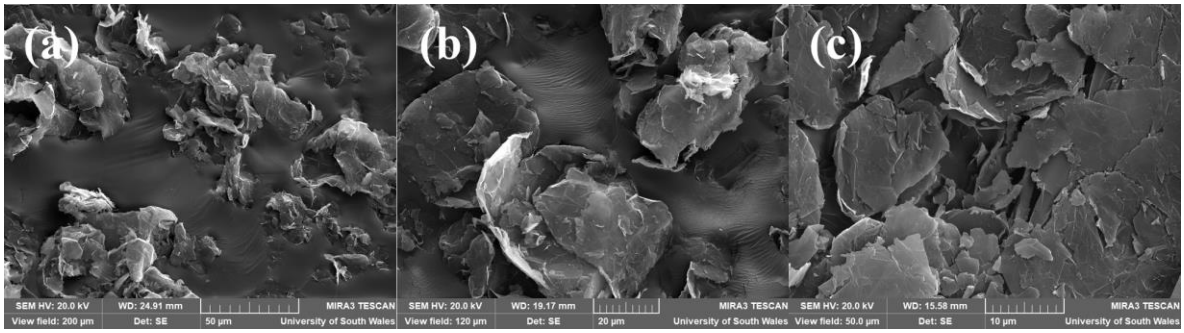

Figure 5.10 SEM images of NP2 at magnifications of (a) 1.04 kx (b) 1.73 kx and (c) 4.15 kx acquired on SEM 2

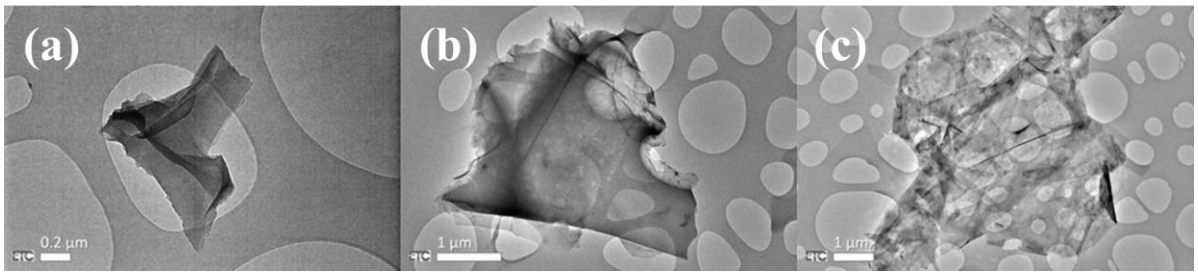

Figure 5.11 TEM images of NP2 acquired on TEM 2.

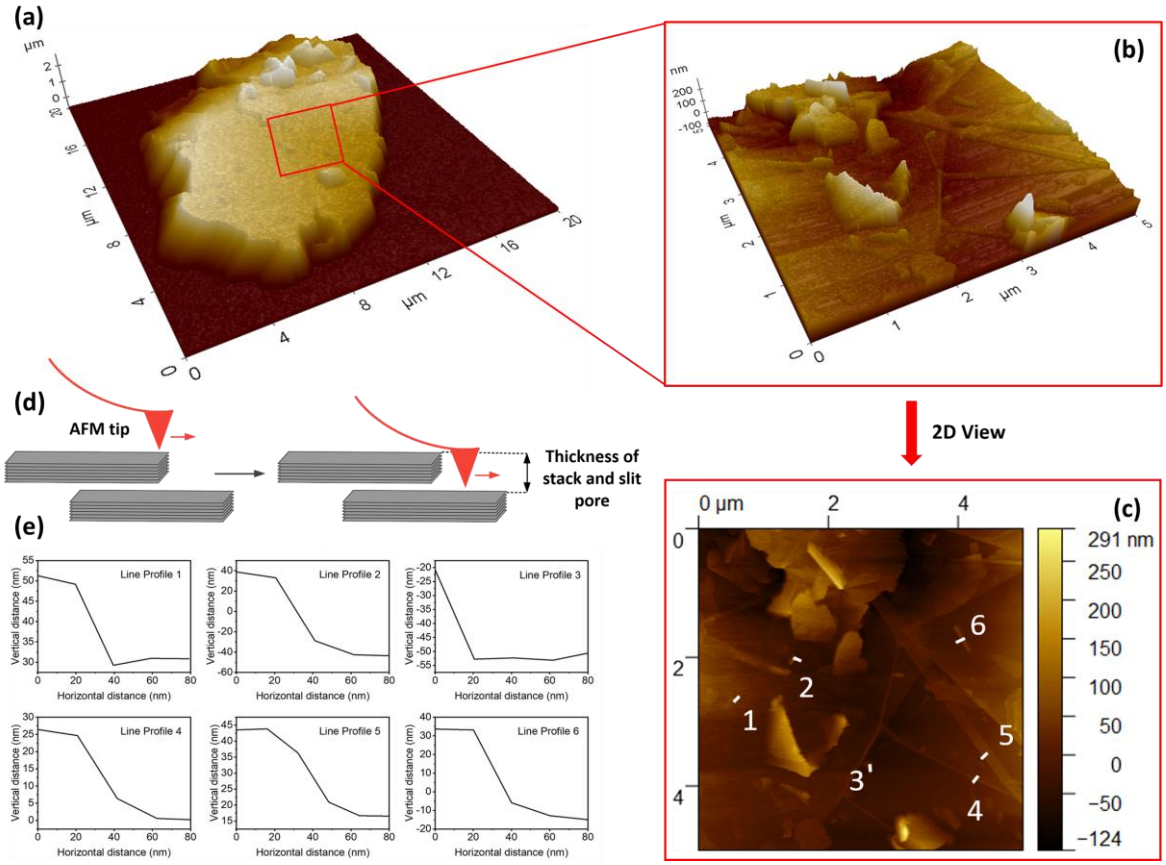

Figure 5.12 AFM data acquired for NP2 using a mica substrate and non-contact mode, consisting of AFM images (a), (b) and (c). (d) depicts a representation of how the AFM tip scans over one stack, to the stack directly beneath during operation and (e) depicts line profiles acquired across the six marked regions of the AFM image (c), defined as line profiles 1 – 6.

The XRD pattern of NP2 provides an insight to the interlayer spacings between the graphitic layers and the stacking within the material (Figure 5.13). It is observed that the material consists of hexagonal (2H) and rhombohedral (3R) stacking, resulting from an arrangement of layers with AB and ABC stacking sequences, respectively. This material therefore possesses a similar crystallographic structure to that of NP1 and f-NP1, as discussed within Chapter 4, whilst coinciding with that of commercially produced exfoliated graphite materials.[371] A strong diffraction peak, characteristic of graphite, is shown at 26.6°, resembling the overlapping (002) 2H and (003) 3R planes. This peak corresponds to an interlayer spacing of 0.335 nm. Additional, less prominent peaks are also observed as a four-lined pattern between 42° and 46°. Magnification of this four-lined pattern (shown in the inset of Figure 5.13), reveals peaks at 42.5° and 44.6° which correspond to the 2H stacking of the (100) and (101) planes, respectively. The remaining two peaks present at 43.5° and 46.3° resemble the 3R (101) and

(012) stacking planes. Additional small peaks are also present at 54.7° and 77.6°, corresponding to graphite 2H (004) and 3R (006) and 2H and 3R (110) planes, respectively. The intensity of the 2H peaks exceed that of the 3R peaks, suggesting that the majority of the stacking coincides with the AB orientation.

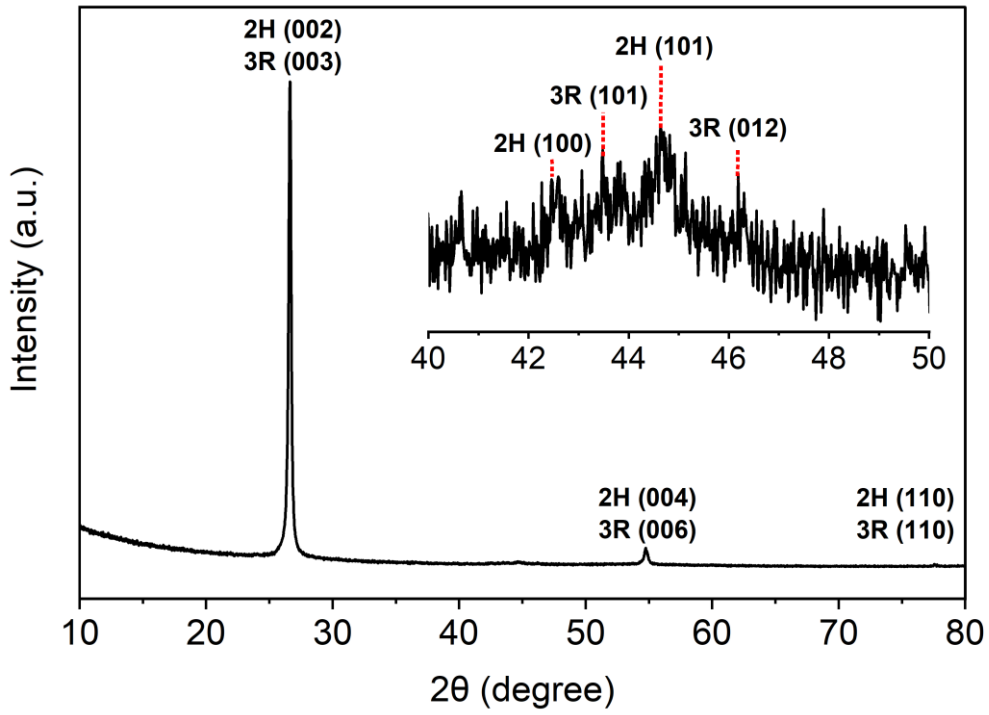

Figure 5.13 XRD pattern for NP2 in the range between 2Θ = 10° and 80° and expanded section in the range between 2Θ = 40° and 50°. The pattern is labelled with the 2H and 3R planes.

The overlapping hexagonal (2H) and rhombohedral (3R) planes present at around 2θ = 26° were utilised to calculate the out of plane crystallite size, L_c, the in-plane crystallite size, L_a, the number of graphene layers, N_c, and the interlayer spacing, $d_{(002)/(003)}$ for graphitic stacks using the Scherrer equation and Bragg equation.[416,418] These equations are described within Chapter 4. Utilising K, the shape factor, (possessing values of 0.91 and 1.84 for equations corresponding to L_c and L_a, respectively) and λ corresponding to Cu K_α radiation (0.154185 nm), allowed for calculation of L_c and L_a, as shown in Table 5.3 and Table 4.3. The value of β, corresponding to the full width at half maximum (FWHM) was calculated through application of both Gaussian and Lorentz fittings using OriginPro software, as shown in Figure 5.14. The subsequent fitting across both models was then compared. To three significant

figures, the values of β were calculated to be 0.236 and 0.220 for the Gaussian and Lorentz models, respectively. Through application of these equations and β values, the crystallites were found to possess crystallite sizes (L_c) of 32.57 and 35.53 nm and in-plane crystallite size (L_a) of 65.86 and 71.84 nm, where the former value in each case relates to the Gaussian model and the latter relates to the Lorentz model. As such, numerous graphitic layers, (97.23 for Gaussian model and 106.38 for Lorentz model) were predicted. As such, both models provide similar β values which correspond to similar values for L_c, L_a and N_c. It is, however, observed that the Lorentz fitting is slightly superior, in this case, to that of the Gaussian model, therefore the crystallite size (L_c) corresponding to 35.53 nm was assumed to be a more accurate value.

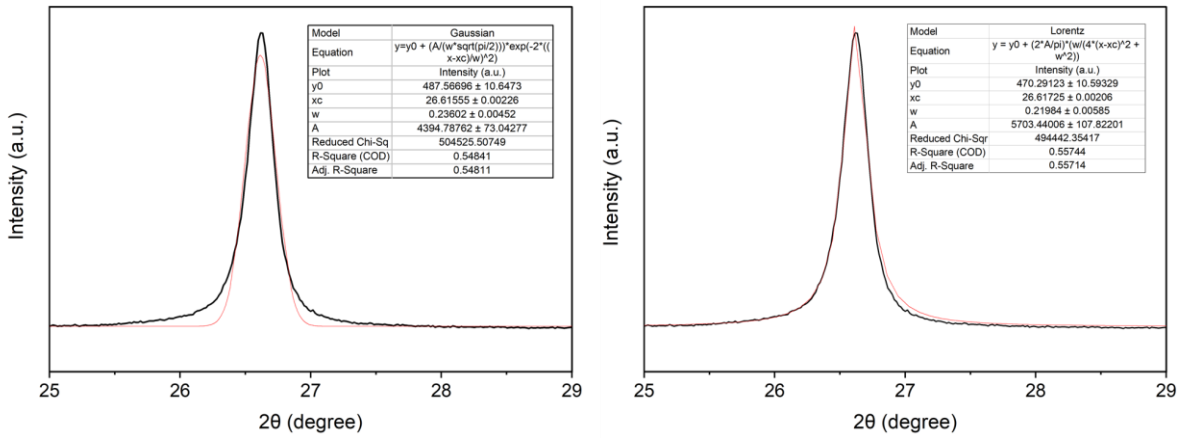

Figure 5.14 Gaussian and Lorentz fitting using OriginPro software for the (002) plane of the peak at 2θ = 26.611° for NP2[5].

Table 5.3 Calculations of L_c, L_a, N_c and $d_{(002)/(003)}$ for NP2.

	Peak Position (2θ)	**Interlayer Spacing ($d_{(002)}$) (nm)**	**FWHM (radians)**	**Crystallite size, L_c (nm)**	**In-Plane Crystallite Size, L_a(nm)**	**Number of graphene layers, N_c**
Gaussian Model	26.6	0.335	0.24	32.57	65.86	97.23
Lorentz Model	26.6	0.335	0.22	35.53	71.84	106.38

XPS analysis was utilised to identify the surface elements present within the NP2 material. The elemental composition data is shown in Table 5.4 and provides evidence of a large proportion of carbon within the material, equating to 93.4 at.%, with a binding energy of 284.5 eV. The presence of oxygen functionalities, in the form of C=O, C=O–C and C–OH, are also

[5] Note: Within OriginPro the FWHM is denoted as "w" in degrees.

recognised due to the existence of peaks with binding energies between 531.5 to 535.4 eV. The total oxygen at.% equates to 6.3 and its presence is attributed to the plasma processing step during synthesis. A satellite structure present at 538.0 eV is also associated with the O 1s state, indicating the presence of π–π* transitions due to bonding to antibonding transitions within carbonyl containing functionalities. Nitrogen impurities are also observed in trace amounts (0.3 at.%), similar to that of NP3 from Chapter 4.

Table 5.4 XPS quantitative data for NP2.

Orbital	Binding Energy (eV)	% Atomic Composition
C 1s	284.5	93.4
O 1s (C=O)	531.5	1.5
O 1s (C−O=C)	532.9	4.0
O 1s (C−OH)	535.4	0.5
O 1s (satellite structure)	538.0	0.2
Total O 1s	-	6.3
N 1s	400.4	0.3

SEM-EDX analysis was utilised to gain further information on the elemental composition within the bulk regions of NP2. The results are shown in Figure 5.15. A gold sputter coating was introduced to the material prior to SEM imaging, and a substantial degree of gold was detected upon quantitative elemental analysis. To eliminate this, the normalised atomic composition percentage was calculated, by discarding the percentage amount of gold. As with the data acquired by XPS, carbon was the largest elemental contributor to the sample, comprising of 99.7 at.%. The presence of oxygen was also detected with a composition of 1.8 at.%. Similar to NP1 within Chapter 4, trace amounts of silicon were also detected, likely to originate from the raw graphite itself. As previously explained within the context of this work, EDX does have limitations when quantifying the composition of light elements with $Z < 10$, and therefore, it is believed that XPS data provides a more accurate representation of the elements within approximately 10 nm depth of the sample.[324]

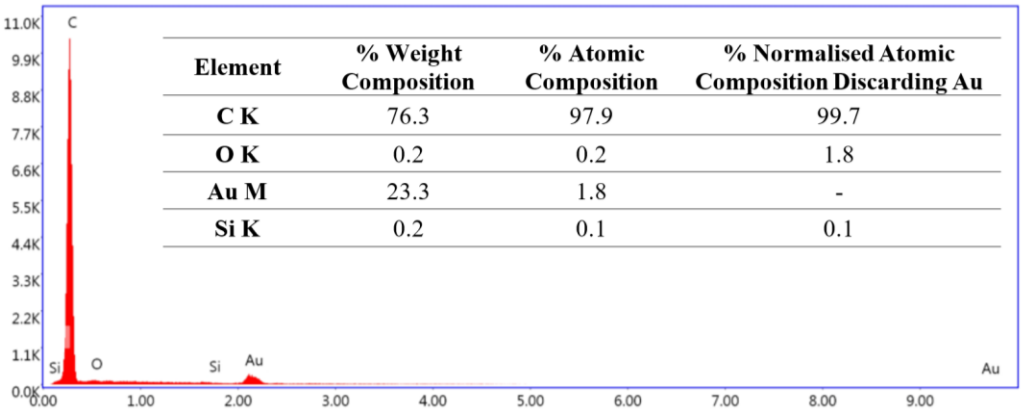

Element	% Weight Composition	% Atomic Composition	% Normalised Atomic Composition Discarding Au
C K	76.3	97.9	99.7
O K	0.2	0.2	1.8
Au M	23.3	1.8	-
Si K	0.2	0.1	0.1

Figure 5.15 SEM-EDX spectrum and quantitative data for NP2.

5.2.3 The Effect of Oxidation and Radical Functionalisation of Surface Area and Porosity

Within this section the effect of oxidation and radical functionalisation on NP is discussed in relation to the changes associated with the surface area and PSD. During Chapter 4, NP1 was treated with 4-(trifluoromethylphenyl)boronic acid, $K_2S_2O_8$ and $AgNO_3$ to synthesise f-NP1. In addition, NP1 was also treated with $K_2S_2O_8$, as a control, to synthesise C3-NP1. Within this current chapter, NP3 was treated *via* the modified Hummers' method to introduce additional oxygen functionality to the material to synthesise O-NP3, as shown in Scheme 5.1.[82,389] This oxidation comprised of the addition of H_2SO_4 followed by $KMnO_4$. It is believed that the oxidation mechanism proceeds *via* several steps. Initially sulfuric acid intercalates between slit pores and some layers within stacks of NP3. These H_2SO_4 intercalants then react with $KMnO_4$, to form MnO_3HSO_4 or $(MnO_3)SO_4$, which subsequently oxidise the material. Finally, further exfoliation of layers occurs upon addition of water, effecting mostly regions which are heavily oxidised, due to an increase in interlayer spacings within the stacks themselves.[446] The addition of H_2O_2 is required to terminate the reaction by reducing residual oxidants and intermediates to soluble sulfates.[447,448] Within the following section, the three materials, f-NP1, C3-NP1 and O-NP3 are compared with each other, to gain an understanding of how their functionalisation route altered their surface areas and PSDs.

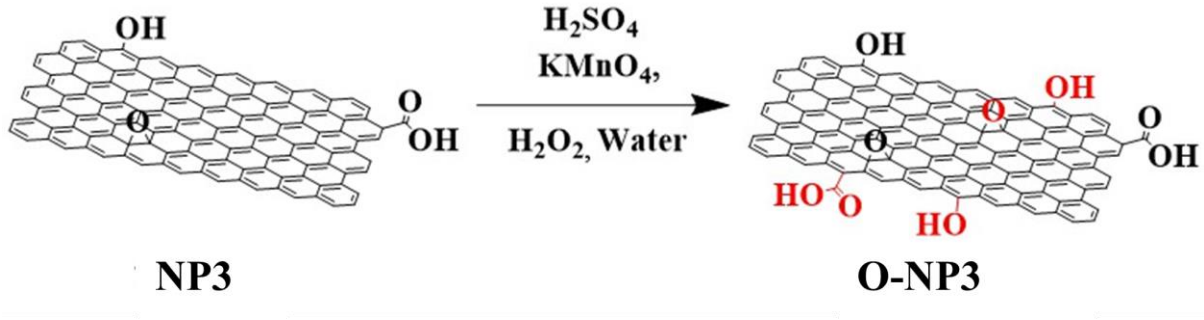

Scheme 5.1 Modified Hummers' treatment of NP3 to form O-NP3.

5.2.3.1 Investigating the Influence of Functionality on Surface Area and Porosity using XRD, BET, BJH, t-plot and XRD data

In terms of functionalities present, f-NP1 consists of both oxygen and 4-(trifluoromethyl)phenyl moieties, with trace amounts of silver and silver salts (denoted as * within Table 5.5). In comparison, C3-NP1 and O-NP3 consist of oxygen functionality only, with different atomic compositions, as shown in Table 5.5. XPS analyses of O-NP3 and its NP precursor are presented in Figure 5.16 and Figure 5.17, respectively. The O 1s spectra associated with O-NP3 provides evidence of a relatively large composition of oxygen; 23.5 at.%, relative to NP3 (5.7 at.%). Furthermore f-NP1 and C3-NP1 possess 8.5 and 10.7 at.% oxygen functionality respectively, relative to the 4.9 at.% in their NP precursor. It was therefore evident that the modified Hummers' oxidative treatment introduced a relatively large amount of oxygen functionality to the NP precursor. Additional details relating to XPS analyses of NP3 and O-NP3 are discussed in more detail later on in this chapter.

Table 5.5 XPS Quantitative data for NP1, f-NP1, C3-NP1, NP3 and O-NP3.

	% Atomic Composition				
	NP1	**f-NP1**	**C3-NP1**	**NP3**	**O-NP3**
Orbital	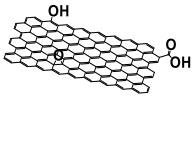	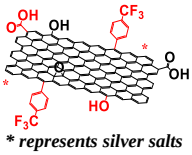 ** represents silver salts*	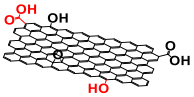	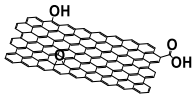	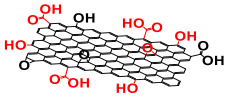
C 1s	94.9	86.5	88.8	94.3	73.5
O 1s	4.9	8.5	10.7	5.7	23.5
S 2p	-	0.3	0.3	-	0.8
Si 2p	-	-	-	-	2.2
N 1s	0.3	0.3	0.2	-	-
F 1s	-	3.5	-	-	-
Ag 3d $^{5}/_{2}$	0	0.7	-	-	-
Cl 2p	-	0.4	-	-	-

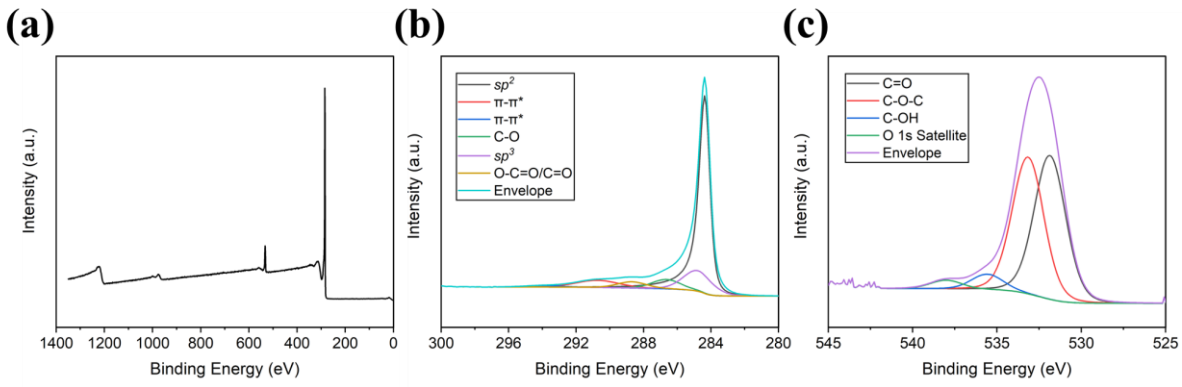

Figure 5.16 XPS spectra of NP3 including (a) survey spectrum (b) deconvoluted C 1s orbital and (c) deconvoluted O 1s orbital.

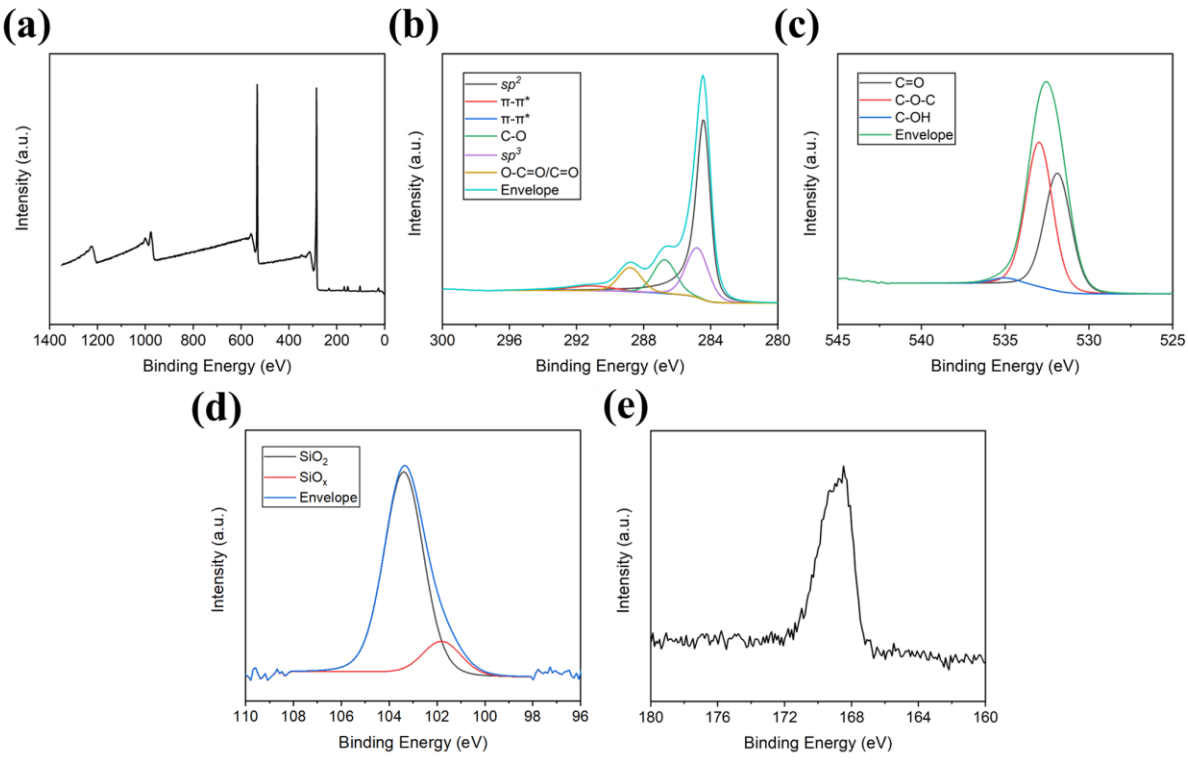

Figure 5.17 XPS spectra of O-NP3 including (a) survey spectrum (b) deconvoluted C 1s orbital (c) deconvoluted O 1s orbital (d) Si 2p orbital and (e) S 2p orbital.

f-NP1 and C3-NP1 possesses BET surface areas of 192.1 and 87.4 m^2/g which were significantly reduced compared with the NP1 precursor, which possessed a BET surface area of 380.2 m^2/g (see Table 5.6). This loss of surface area was associated with a reduction in the number of pores available to nitrogen adsorbate molecules, as explained within Chapter 4. BJH analysis showed that the pore volume reduced from 0.746 cm^3/g in NP1 to 0.490 and 0.254 cm^3/g for f-NP1 and C3-NP1, respectively. Furthermore, t-plot analysis also showed a substantial reduction in the area and volume associated with micropores within the materials. t-plot micropore analysis of f-NP1 indicated volume and area values of zero, whilst C3-NP1 possessed a t-plot micropore volume and area of 0.001 cm^3/g and 3.8 m^2/g, respectively. It was therefore evident that the functionalisation had a large effect on the pores and resultant surface area within the materials. During an investigation carried out by Toupin and Bélanger, it was found that a substantial loss in micropore volume and BET surface area was associated with the covalent functionalisation of carbon black and glassy carbon with 4-nitrophenyl moieties.[449] The authors postulated that micropores of 1 nm or smaller in size became blocked or filled by these organic moieties.

Table 5.6 Data associated with BET, BJH adsorption and t-plot methods for NP-1, f-NP1, C3-NP1, NP3 and O-NP3.

	Material				
	NP1	**f-NP1**	**C3-NP1**	**NP3**	**O-NP3**
BET Surface Area (m^2/g)	380.2	192.1	87.4	450.5	28.9
BJH Adsorption Average Pore Width (4V/A) (nm)	7.0	10.0	9.6	6.6	10.2
BJH Adsorption Cumulative Volume of Pores Between 1.7 – 300 nm (cm^3/g)	0.746	0.490	0.254	0.835	0.017
t-Plot Micropore Volume (cm^3/g)	0.037	0.000	0.001	0.043	0.010
t-Plot Micropore Area (m^2/g)	83.6	0.0	3.8	98.8	20.9
t-Plot Mesopore/Macropore Area (m^2/g)	296.6	192.1	83.6	351.7	8.0
t-Plot Micropore Area Compared to Total Area (%)	22.0	0.0	4.3	21.9	72.4

Within the current work, a similar scenario is likely in the case of f-NP1. It is predicted that the presence of 4-(trifluoromethyl)phenyl moieties in conjunction with oxygen moieties at the edges of sheets and the outer edges of pores, resulted in the blockage of slit pores and in-plane pores, as shown in Figure 5.18. This assumption is made on the belief that such sites possess an increased number of defects and thus, would be favourable towards functionalisation.[34,450,451] Furthermore, it is also likely that there is some degree of destruction to slit pores, resulting from enhanced alignment of stacks. As outlined in Figure 5.18, nitrogen adsorbate molecules are only granted access to slit pores and in-plane pores in the absence of additional functionality.

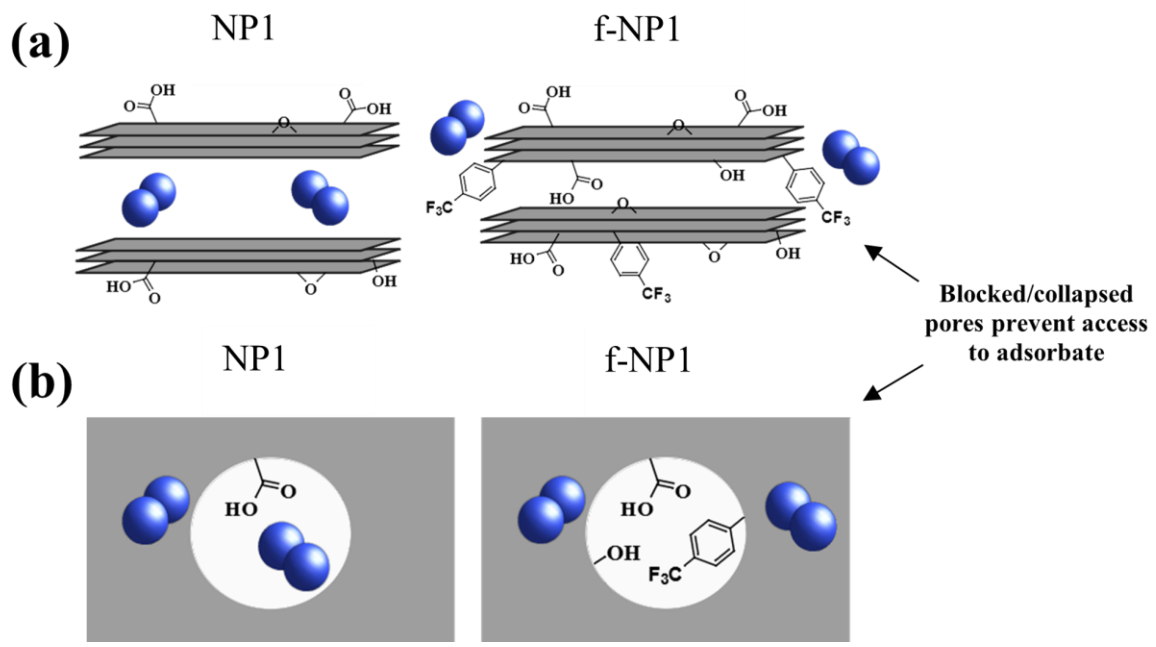

Figure 5.18 A proposed diagram depicting the accessibility of (a) slit pores and (b) in-plane pores to nitrogen adsorbate molecules (represented by blue spheres) dependent on whether 4-(trifluoromethyl)phenyl) moieties and additional oxygen functionality are present. (a) depicts an accessible slit pore to adsorbate within NP1 (left) and an inaccessible slit pore to adsorbate within f-NP1 (right), whilst (b) depicts an accessible in-plane pore to adsorbate within NP1 (left) and an inaccessible in-plane pore to adsorbate within f-NP1 (right). Note: The diagram is not drawn to scale.

Like f-NP1, C3-NP1 also exhibited a drastic decrease in micropores as evidenced by t-plot analysis. The micropore volume decreased by a factor of approximately 37, relative to its NP precursor, thus providing evidence of pore blockage to nitrogen adsorbate molecules. However, in contrast to f-NP1, a small proportion of micropores did remain. Whilst oxygen functionality introduced through $K_2S_2O_8$ addition caused inaccessibility to most micropores, it did not completely block all micropores and may have only partially blocked others. As a result, the contribution of both oxygen functionality and 4-(trifluoromethyl)phenyl moieties was required for complete blockage of micropores, as in the case of f-NP1.

The BET curve associated with O-NP3 is displayed in Figure 5.19 (a) and depicts an isotherm with Type IIb characteristics and H3 hysteresis, consistent with that of both NP precursors, f-NP1 and C3-NP1. Hysteresis of this type is usually associated with plate-like aggregates or adsorbents containing slit-like pores. The oxidation process also resulted in a drastic decrease in BET surface area (decreasing from 450.5 to 28.9 m^2/g), which was attributed to the blockage and collapsing of pores within O-NP3 (see Table 5.6 and Figure 5.19 (a)) This BET surface area value is very similar to that of graphite oxide, synthesised *via* an improved Hummers

method, indicating the presence of a heavily stacked material within O-NP3.[452] Previous reported investigations have also observed a severe reduction in surface area upon oxidation. For example, Külaots found that modified Hummers' oxidation of multilayer graphene material resulted in the formation of a low surface area GO film.[253] The surface area loss was attributed to restacking of sheets during the drying process, such that GO sheets tended to accumulate on the surfaces of water droplets and collapse due to capillary forces upon solvent evaporation.[453] Similarly, López-Garzón investigated the oxidation of glassy carbon *via* plasma treatment and found that the oxidised material possessed a substantially reduced surface area.[424] Similar to the proposed explanation within Figure 5.18, the authors proposed that the surface area reduction resulted from a loss of micropores due to attachment of oxygen functionality around the pore entrances.

Within O-NP3, there was a substantial decrease in the BJH adsorption cumulative volume of pores between 1.7 − 300 nm (cm^3/g), compared with the untreated precursor, decreasing from 0.835 to 0.017 cm^3/g for NP3 and O-NP3, respectively (Table 5.6). Much of the BET surface area of NP3 originates from external surface, incorporating both mesopores and macropores, contributing a t-plot external area of 351.7 m^2/g. In contrast, its oxidised counterpart accounts for only 8.0 m^2/g of this area. This is consistent with a significant reduction of mesopores and macropores within the material. Contrarily to the previous materials, it is suggested that the oxidation process results in pore blockage effects, as well as the destruction of many slit pores due to enhanced alignment of stacks, causing them to aggregate. This aggregation is also observed by SEM imaging, as outlined further on in the text. It is likely that oxygen functionality becomes introduced to the edges and basal planes of many graphitic layers. The oxidation preferentially occurs at defective areas, such as multivacancy sites on the basal planes, due to their higher reactivity.[450] As such, many pores become obstructed by oxygen functionality, leading to the loss of many mesopores and macropores. It is noticeable that the shape of the BJH plot remains similar for O-NP3 and NP3, suggesting that although the number of pores decreases upon oxidation, the PSD does not differ substantially (Figure 5.19 (b)). This suggests that the loss in BET surface area was associated with the destruction of slit pores consistently over the mesoporous and macroporous regions. In contrast, however, it was observed that the t-plot micropore volume decreased only by a factor of 4.5 (from 0.043 to 0.010 cm^3/g for NP3 and O-NP3, respectively). The extent of this reduction is significantly less than that of the previous materials, even though the extent of oxidation increased. In parallel, the t-plot micropore area (compared to the total area) increased from 21.9 to 72.4% for NP3

and O-NP3 respectively, suggesting that the destruction of micropores was less severe than that of the mesopores and macropores. This finding is explained by examining the XRD data below.

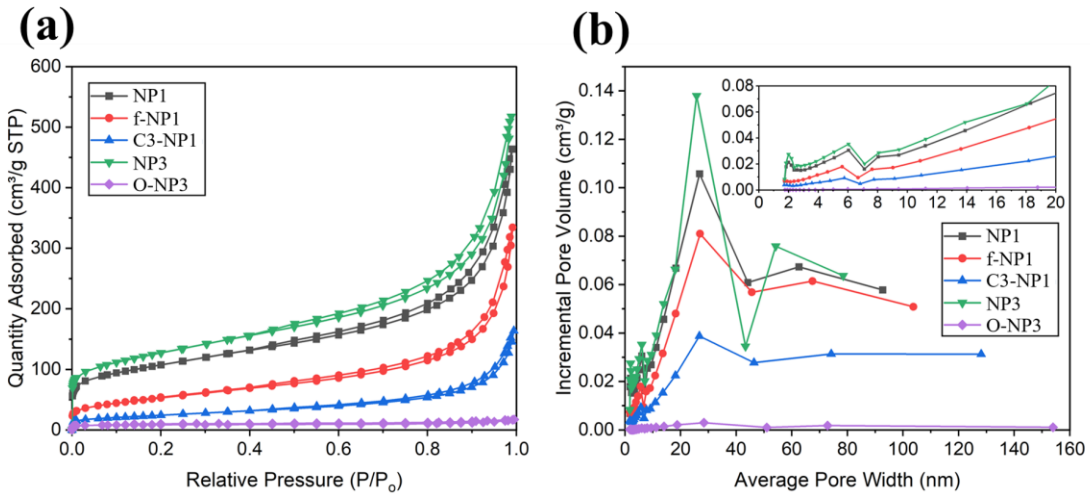

Figure 5.19 (a) N_2 adsorption-desorption isotherms and (b) BJH adsorption data associated with the incremental pore volume for NP1, f-NP1, C3-NP1, NP3 and O-NP3.

XRD patterns were obtained for NP3 and O-NP3, to compare the interlayer spacings, as shown in Figure 5.20. Within these, a four-lined pattern is observed between 43° and 45°, consistent with the 2H stacking of the (100) and (101) planes and the 3R stacking of the (101) and (012) planes. In addition, small peaks are also observed at 54.8° and 77.7°, corresponding to graphite 2H (004) and 3R (006) and 2H and 3R (110) planes, respectively. Furthermore, the XRD patterns both consist of a diffraction peak at 26.7°, which resembles the overlapping (002) 2H and (003) 3R graphitic planes, corresponding to an interlayer spacing of 0.344 nm. In the case of O-NP3, this peak overlaps with a diffraction peak at 23.6°, which indicates the presence of crystalline graphitic structure with partial oxidation, typical of that found within rGO samples.[454] This 2θ value corresponds to an increased interlayer spacing of 0.376 nm, resulting from the presence of additional oxygen functionality causing the sheets to widen in separations.[318] In addition, a peak at 10.9° was also observed within O-NP3, which corresponds to a much larger interlayer spacing of 0.814 nm, representing the (001) plane of GO. This is commonly observed within GO samples due to the introduction of epoxy, hydroxy and carboxyl functionality.[318] This increase in oxygen functionality causes the sheets to separate to much larger interlayer spacings, exceeding the kinetic diameter of nitrogen adsorbate

molecules.[251] This widening of these interlayer spacings therefore results in the introduction of slit micropores into the structure, similar to those found within rGO samples in previous works.[455] This explains why the overall reduction of micropores is much lower compared with those within the meso- and macro-regions. Figure 5.21 depicts the proposed accessibility of nitrogen adsorbate within NP3 and O-NP3. This outlines how adsorbate molecules are able to access slit pores and in-plane pores within NP3, however, are unable to access those within the oxidised material, due to blockage of pore entrances and the destruction of pores, resulting from an enhanced alignment of stacks. Furthermore, the presence of newly formed micropores is depicted. Such pores possess widths which correlate to the enlarged interlayer spacings, found within XRD data, resulting from the expansion of subsequent layers within a stack. In addition, it is also known that GO often contains holes with dimensions of < 5 nm^2, which originate from the evolution of CO and CO_2 gases during the oxidation and exfoliation conditions.[45] As such, the introduction of some newly formed in-plane pores within O-NP3 is also predicted, however, these too may also become blocked by functionality.

It is interesting to note that in contrast with NP3, there are three distinct interlayer spacings within O-NP3. This suggests that the oxidation process does not proceed homogenously throughout the sample. Some regions within the sample are unlikely to have become oxidised on their basal plane, resembling those possessing interlayer spacings of 0.344 nm. Other regions possess a much larger interlayer spacing (0.814 nm), suggesting the existence of densely packed regions of oxygen functionality. Meanwhile, other regions resemble a less densely oxidised basal plane (correlating with an interlayer spacing of 0.376 nm). It is well known that the structure of GO is inhomogeneous in nature, possessing graphic regions and areas of high oxidation.[45,51]

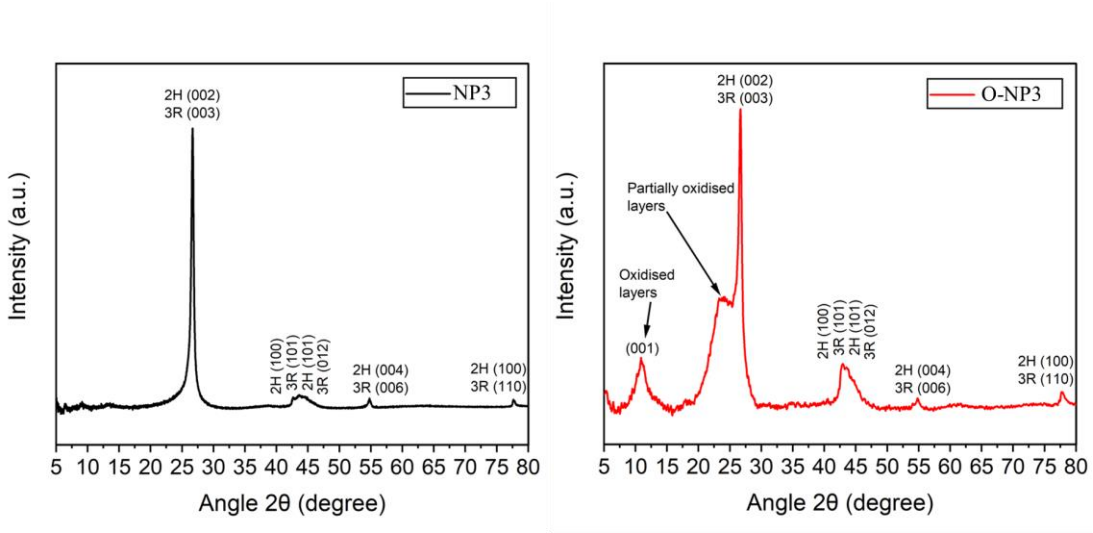

Figure 5.20 XRD patterns for NP3 and O-NP3 with peak assignment relating to the widened interlayer spacings due to oxidised regions within O-NP3, as well as the 2H and 3R phases.

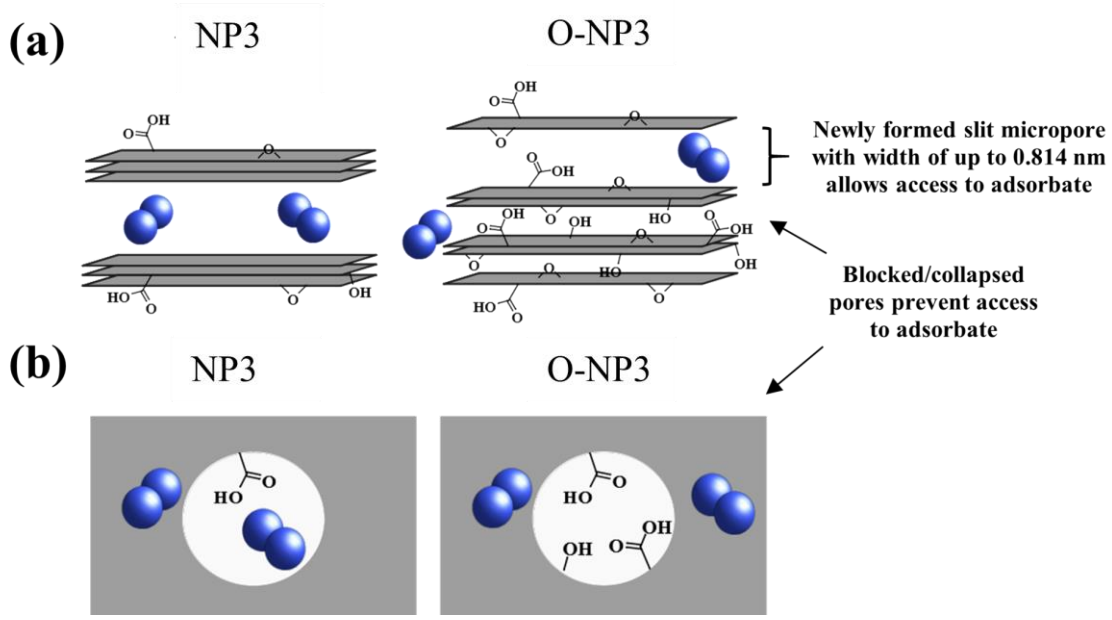

Figure 5.21 A proposed diagram depicting the accessibility of (a) slit pores and (b) in-plane pores to nitrogen adsorbate molecules (represented by blue spheres) dependent on whether additional oxygen functionality is present. (a) depicts an accessible slit pore to adsorbate within NP3 (left) and many inaccessible slit pores to adsorbate within O-NP3 (right). O-NP3 also contains some newly formed slit pores due to the enlargement of interlayer spacings. (b) depicts an accessible in-plane pore to adsorbate within NP3 (left) and an inaccessible in-plane pore to adsorbate within O-NP3 (right). Note: The diagram is not drawn to scale.

To explain the absence of newly formed micropores within f-NP1, the XRD patten within Figure 4.17 is reflected upon (see Chapter 4 for more details). This pattern exhibits a peak

corresponding to the overlapping graphitic 2H (002) and 3R (003) planes, with no peaks present at lower 2θ values. As a result, the distance between layers corresponds to 0.334 nm; a distance insufficient to allow nitrogen adsorbate access.[251–253] Due to this, it is suggested that during the functionalisation process, the reagents were unable to intercalate between individual layers within a stack and thus, are unlikely to functionalise the in-plane surface. If this had have occurred, it would be likely that the functionalisation process would have promoted an increased interlayer spacing. Instead, it is proposed that the outer regions of the stacks became functionalised at regions where in-plane micropores and other defective sites exist, as well upon the edges of individual stacked layers, resulting in overall pore reduction.

5.2.3.2 Graphitic Structure Analysis using Raman Spectroscopy

Raman spectroscopy was utilised to analyse the crystallinity of O-NP3 compared with NP3, and found that the same characteristic bands corresponding to the G band, D band and 2D band were also found within the oxidised material at 1600, 1353 and 2716 cm^{-1}, respectively (Figure 5.22).[305–308,312] Whilst some defects are attributed to vacancies, sp^3 sites and Stone-Wales defects within the structure, originating from the plasma-exfoliation synthesis process, it is evident that the number of defects is substantially larger in O-NP3 than its unoxidised counterpart.[95,116–120] It is likely that oxidation upon NP3 resulted in the generation of more sp^3 centres. As such, successful covalent functionalisation is assumed to have taken place between oxygen and the NP3 sheets. The intensity ratio between the D band and G band (I_D/I_G) increased from 0.24 to 0.99.[312] Moreover, the I_{2D}/I_G corresponded to 0.44 and 0.30 for NP3 and O-NP3 respectively, suggesting that the multilayer structure remains upon oxidation.[312] Additionally, the D' and (D + D') bands at 1600 and 2944 cm^{-1} respectively, possess an increased intensity, indicating the incorporation of more defects.[172,310] In the former band, the increased intensity results in broadening of the G peak.

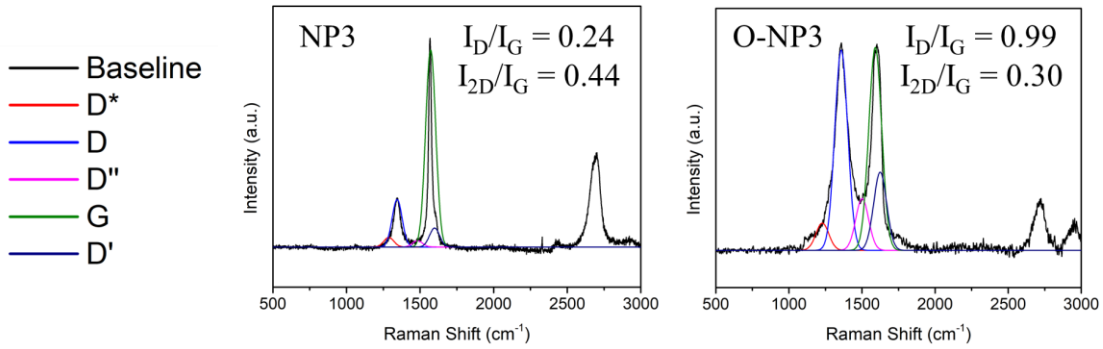

Figure 5.22 Raman spectra of NP3 and O-NP3 depicting their corresponding I_D/I_G and I_{2D}/I_G ratios. Peak deconvolution was performed using OriginPro software to discriminate the D and G bands from overlapping D, D'' and D' bands.*

5.2.3.3 Thermal Decomposition Studies Using TGA

TGA was conducted to understand the thermal decomposition pathways of NP3 and O-NP3, as shown in Figure 5.23. NP3 shows a gradual mass loss of 13.9%, indicating the decomposition of covalently and non-covalently bound oxygen moieties.[431,432] O-NP3 shows a much larger mass loss in comparison, corresponding to a percentage of 51.1% up to 770 °C. This mass loss was also assigned to the loss of oxygen functionality. Below 100 °C, a mass loss of 1% within NP3 and 14% within O-NP3 corresponds to the removal of adsorbed water.[456] As such, it is suggested that a substantially large amount of adsorbed water was present within O-NP3 compared to NP3, consistent with the nature of the oxidised material, where additional hydrogen bonding would be expected.[457]

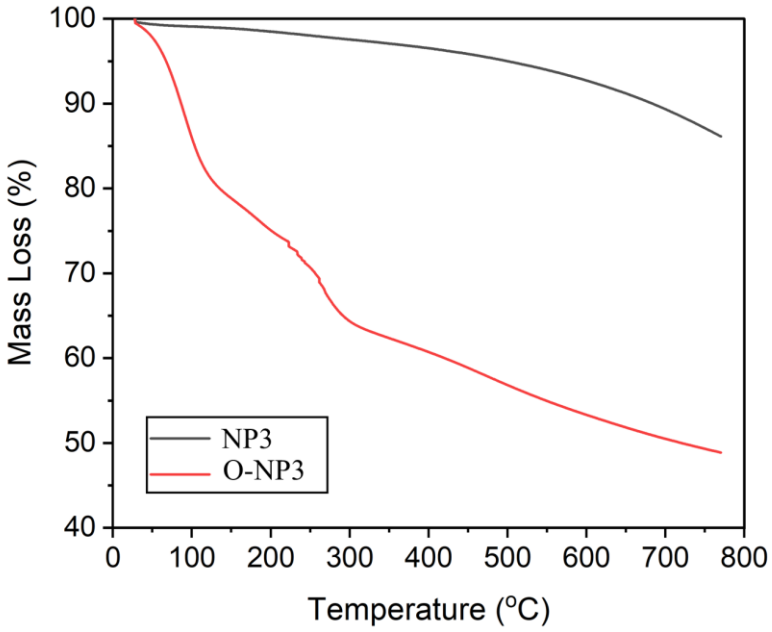

Figure 5.23 TGA curves for NP3 and O-NP3.

5.2.3.4 Investigating the Morphology using SEM

SEM images for NP3 and O-NP3 materials are depicted in Figure 5.24 and Figure 5.25, and show that oxidation causes a significant increase in aggregation. As such, O-NP3 consists of large particles with lengths ranging between 0.3 − 0.7 mm in size. These particles incorporate many closely packed aggregates. Since it was found that the BET surface area of this oxidised material was small: 28.9 m^2/g (Table 5.6), it is believed that the material is well-packed, due to enhanced interaction between neighbouring stacks and sheets. In fact, it is well known that the oxidation of GBMs promotes agglomeration when in dry state.[458] At high magnifications (Figure 5.25 (d)), it is observed that the aggregates within O-NP3 appear much smoother in texture, and visibly less porous on the meso and macro-scale, compared with that of those of its unoxidised counterpart (Figure 5.24 (d)), suggesting that alignment of stacks has taken place. This lack of visible porosity is consistent with the BJH data acquired (Figure 5.19 (b)). The morphologies of NP1 and f-NP1 are shown in Figure 4.12 and Figure 4.14 respectively, within Chapter 4. In this case, the functionalised material also displays a smoother appearance. This is likely to be attributed to an increased alignment of stacks. Furthermore, the blocking of

macropores is also observed within Figure 4.14 (d), which may contribute to the lower porosity and surface area associated with this material.

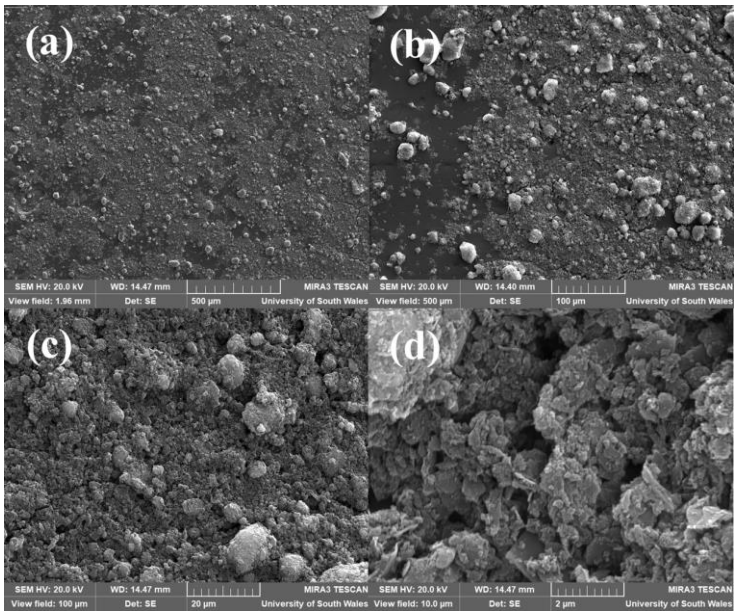

Figure 5.24 SEM images of NP3 at magnifications of (a) 106 x (b) 415 x (c) 2.07 kx and (d) 20.71 kx acquired on SEM 2.

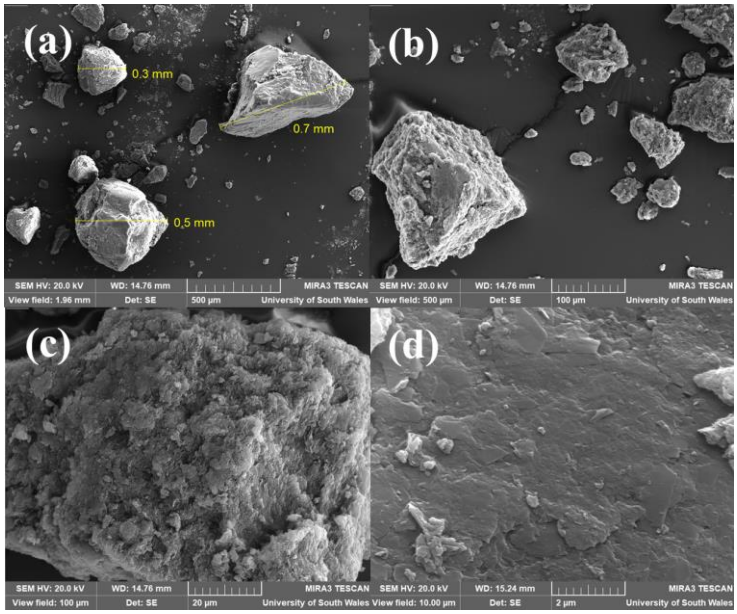

Figure 5.25 SEM images of O-NP3 at magnifications of (a) 106 x (b) 415 x (c) 2.08 kx and (d) 20.76 kx acquired on SEM 2.

5.2.4 Laponite as a Pillaring Device to Enhance the Surface Area and Porosity of O-NP3

In the previous section, it was found that O-NP3 exhibited a drastic decrease in both surface area and pore density, upon oxidation. As such, within this section an investigation was embarked upon to develop a strategy to increase the surface area of O-NP3. Such a strategy aimed to re-introduce slit pores into the heavily aggregated structure. Within this strategy, the synthetic silicate clay; laponite, was utilised as a pillaring device, to intercalate and expand slit pores within O-NP3. The combination of clays with GBMs has been investigated for various applications, by several research groups. Laponite and montmorillonite; another layered silicate clay material, have been shown to stabilise graphitic dispersions by preventing restacking.[459–461] In addition, the combination of clays with graphene/GO have been found to exhibit excellent barrier properties,[462] fire retardant properties,[460] improved mechanical properties,[463,464] enhanced capacity for dye adsorption[465] and enable the formation of homogeneous films for energy applications.[466] The realisation and application of laponite specifically as a pillaring device, however, has yet to be explored within the literature.

5.2.4.1 Introducing Laponite and its Surface Area and Porous Structure

Laponite consists of the unit cell depicted in Figure 5.26. The structure entails 6 octahedral magnesium ions (Mg^{2+}), which are sandwiched between two layers of 4 tetrahedral silicon atoms. 20 oxygen atoms and 4 hydroxyl groups balance these positive charges. The unit cell is repeated many times, in two directions, to form structures with a disc-shaped appearance. A laponite crystal typically consists of 2000 unit cells. The unit cell would, in theory, have a neutral charge, however, the unit cell does not provide a fully accurate description of the structure. In reality, some Mg^{2+} ions are substituted for monovalent, Li^{+} ions, whilst some octahedral sites remain empty, resulting in a composition which typically has the formula: $Na^{+}_{0.7}[(Si_8Mg_{5.5}Li_{0.3})O_{20}(OH)_4]^{-0.7}$. This has a negative charge of 0.7 per unit cell, which is neutralised by sodium ions, Na^{+}, which adsorb onto the surfaces. The unit cells become arranged into stacks, referred to as tactoids, which are held *via* electrostatic interactions through

the sharing of Na^+ ions within the interlayer regions between adjacent unit cells. Each laponite disk is around 25 nm in width and 0.92 nm in thickness.[467] Tactoids tend to cluster further into aggregates, which typically possess dimensions of < 1 – several hundred µm.[468]

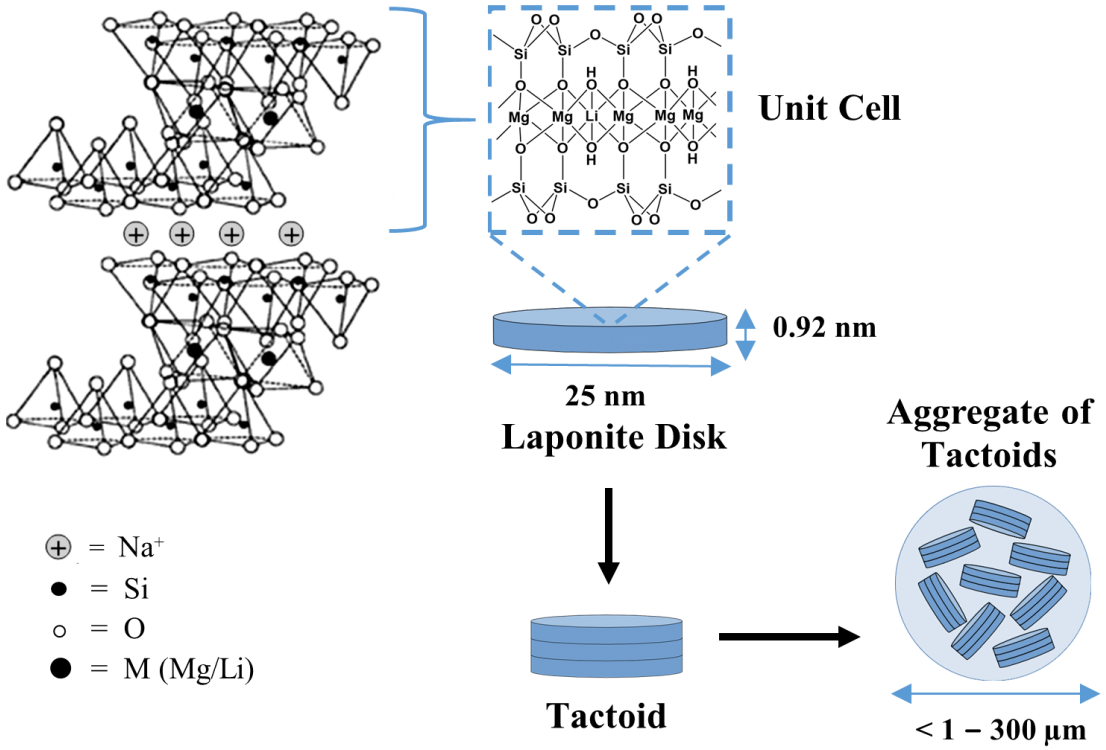

Figure 5.26 Schematic depicting the structure of a laponite unit cell, adapted from previous works[469]. The stacking of individual laponite disks results in the formation of tactoids, which cluster to form aggregates.

To gain an understanding of the surface area and porosity associated with laponite, Initially, BET analysis was conducted. The subsequent N_2 adsorption-desorption isotherm exhibited Type IVb character with H2(b) hysteresis, according to IUPAC recommendations and refinement by Rouquerol and co-workers, as shown in Figure 5.27 (a).[351,470,471] This isotherm type is characterised by its broad loop where the desorption branch is much steeper than the adsorption branch. A characteristic plateau of gas uptake also occurs at high P/P_0, unlike NPs. This indicates complete mesopore filling, consistent with the presence of pores within the microporous and mesoporous regions and an absence of macropores. Meanwhile, the hysteresis type signifies the presence of a complex porous structure made up of interconnected networks of pores of different sizes and shapes. In dry state, laponite powder comprises aggregates containing tactoids. These tactoids contain stacks of laponite disks with sodium ions occupying

the interlayer regions. The disks within the tactoid are held *via* long-range attractive forces. Between subsequent disks exists an interlayer spacing of approximately 0.26 nm.[472] Since this width is smaller than the kinetic diameter of nitrogen adsorbate molecules, these spacings do not contribute to surface area and porous data. Instead, the data originates from pores between particles themselves, resulting in interparticle pores and slit pores, very similar to that of NP materials. The BJH plot of the material is shown within Figure 5.27 (b). Here, it is observed that pores within laponite generally adsopt a PSD between 1.7 – 14 nm according to the data.

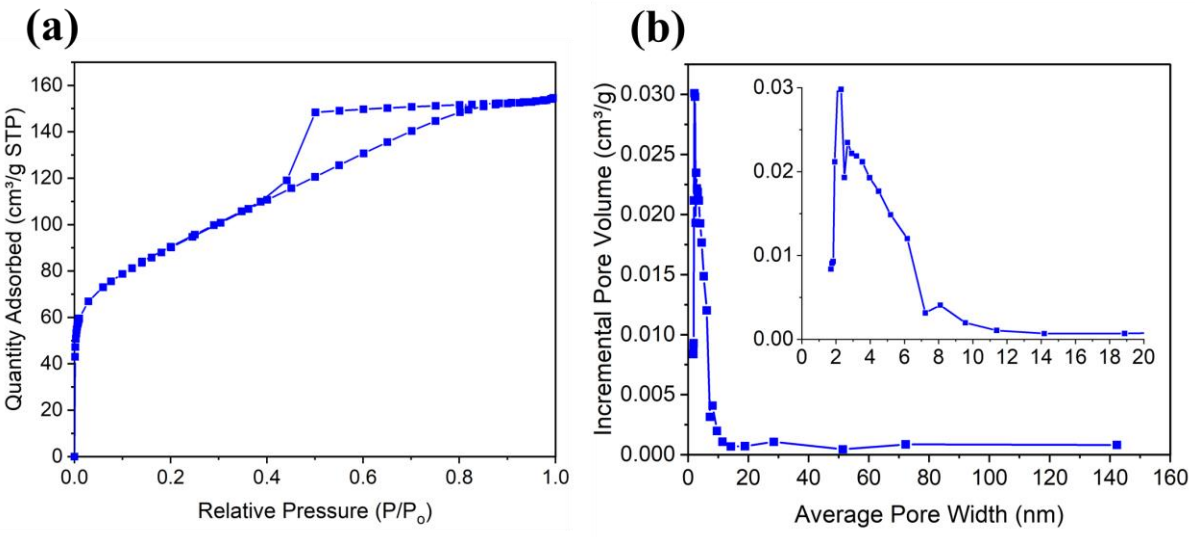

Figure 5.27 (a) N_2 adsorption-desorption isotherm and (b) BJH adsorption data associated with the incremental pore volume for laponite, where the inset provides a magnified region of pore widths between 1.7 and 20 nm.

The contribution of interlayer pores and interparticle pores results in an overall BET surface area of 319.4 m^2/g. Within the t-plot data, shown in Table 5.7, it is observed that the micropore area constitutes 21.2% of the total surface area, whilst the remaining surface area correlates to that of mesopores, since macropore presence is negligible. The micropores and mesopores within laponite result in a BJH adsorption cumulative volume of pores between 1.7 – 300 nm of 0.295 cm^3/g. The material possesses an average pore size of 2.8 nm, according to the BJH adsorption branch.

5.2.4.2 Laponite as a Non-Covalent Pillaring Device

To implement laponite as a pillaring device to O-NP3, its addition was initially conducted through a non-covalent means. This involved mixing laponite and O-NP3 *via* ultrasonic bath sonication in aqueous solution, to integrate the clay between the slit pores of the oxidised material as it swelled in water. The composition of laponite was varied as a percentage, and the subsequent O-NP3/laponite mixtures were dried to form composite structures. These O-NP3/laponite composites were then analysed using BET, BJH, t-plot and SEM techniques. Initially the surface area and porosity were studied for O-NP3/laponite composites, as depicted in Figure 5.28 and Table 5.7. Meanwhile, it was important that controls were carried out to enable effective comparison. In this regard, O-NP3 and laponite were also subjected to ultrasonic bath treatment in aqueous solution independently, consistent with the conditions used within the composite material synthesis. Upon drying, these treated counterparts were denoted "O-NP3 control" and "laponite control", respectively, and their results were also incorporated into Figure 5.28 and Table 5.7. O-NP3 control underwent a decrease in surface area from 28.9 to 12.1 m^2/g. This was accompanied by a large decrease in the t-plot micropore area from 20.9 to 1.9 m^2/g. Interestingly, the t-plot mesopore/macropore area underwent a slight increase from 8.0 to 10.2 m^2/g. As such, this demonstrates that the enhanced oxygen functionality results in the alignment of layers during the drying process of O-NP3 control, causing destruction of many slit pores.[253,473] The remaining porosity (mostly within the mesoporous region) is likely to originate from spatially irregular packing.[253] The largest pore width corresponds to 154.0 and 136.7 nm for O-NP3 and O-NP3 control, respectively. This coincides with the theory that the layers and stacks become aligned during the drying process.

Subjection of laponite to ultrasonic bath treatment was also associated with a reduction of the BET surface area (decreasing from 319.4 to 259.1 m^2/g), as shown by results for laponite control in Table 5.7. This reduction was associated with a large decrease in the t-plot mesopore/macropore from 251.5 m^2/g to 131.6 m^2/g. Interestingly, an increase in the t-plot micropore area was observed from 67.9 m^2/g to 127.5 m^2/g, which is attributed to the re-orientation of laponite tactoids during the drying process. Since the ultrasonic bath treatment takes place within aqueous media, the laponite disks undergo a gelification process, resulting from face-edge attractions, and thereby form a "house-of-cards" structure.[474,475] The laponite control was then dried, resulting in restacking of laponite disks to form tactoids. As such, it is likely that these disks aggregate to a greater extent, forming a more efficient packing

arrangement than that of its untreated counterpart. In turn, less surface area is available to nitrogen adsorbate molecules, however, more small pores within the microporous region are introduced within the regions between neighbouring tactoids. It is therefore evident that this dispersion/drying process has some effect on the arrangement and ordering of these tactoids within the laponite powder. The largest pore width associated with laponite and laponite control is 14 nm.6

For the O-NP3/laponite composites, it was observed that upon addition of laponite to O-NP3, the BET surface area increased. This was expected since the surface area of laponite exceeds that of O-NP3. Furthermore, O-NP3/laponite composites did not incorporate any larger slit macropores into O-NP3 upon laponite addition (see Figure 5.28 (b) and Table 5.7). As such it seems that laponite does not effectively act as a pillaring device to widen the slit pores within the material. This was concluded through observation of the BJH adsorption largest pore width, within Table 5.7. Whilst the largest pore within O-NP3 corresponds to 154.0 nm, laponite addition results in an overall reduction in the largest slit pores. The largest pore present within O-NP3/laponite composites corresponds to that containing 20 wt.% laponite addition, exhibiting a value of only 138.5 nm for the largest pore size. To explain this insufficient pillaring, it is believed that laponite integrates between stacks, and the enhanced interaction between positive edges of laponite disks and negative O-NP3 oxygen functionality results in narrowing of the slit pores.

O-NP3/laponite composites did not follow a straightforward pattern dependent on the percentage addition. It was predicted that as the percentage laponite addition increased, the BJH adsorption cumulative surface areas of pores between 1.7 − 300 nm and t-plot micropore area and volume would also increase. It was found that the t-plot micropore area increased upon addition of laponite from 4.8 to 15.2 to 23.4 m^2/g for 6, 11 and 20 wt.% laponite addition, respectively. Similarly, the t-plot micropore volume increased as the % laponite addition increased. In contrast, the BJH adsorption cumulative surface areas of pores between 1.7 − 300 nm decreased and increased from 3.0 to 1.6 to 39.8 m^2/g for 6, 11 and 20% respectively, which contrasts with the expected finding. Since only three O-NP3/laponite composites were synthesised, containing three different wt.% addition of laponite, it is recognised that better conclusions could be made between the relationship of BET surface area and pore composition if more composites with different weight atomic percentages were synthesised. Unfortunately,

[6] A very small quantity of pores (< 5.955 x 10^{-4} cm^3/g) are found to possess sizes on the macro-scale (up to 142.3 nm), however, within the context of this work, these are considered negligible.

the data from the three composites suggests that no larger slit pores were generated into the composites, suggesting that the presence of laponite within the slit pores of O-NP3 stacks was not causing pillared expansion.

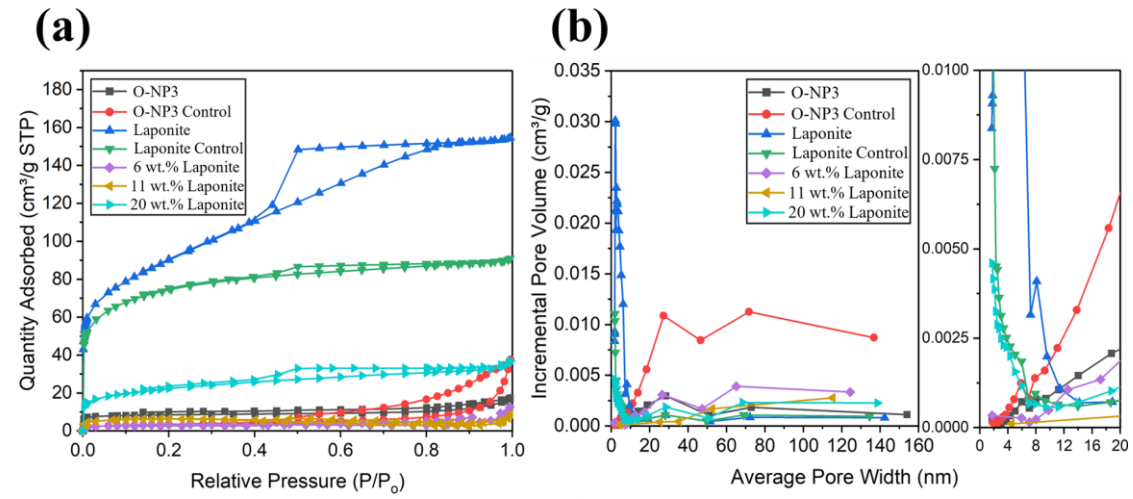

Figure 5.28 (a) N_2 adsorption-desorption isotherms and (b) BJH adsorption data associated with the incremental pore volume for O-NP3, laponite, controls, and O-NP3/laponite composites containing 6 wt.%, 11 wt.% and 20 wt.% laponite addition.

Table 5.7 Data associated with BET, BJH adsorption and t-plot methods for O-NP3, laponite, controls and O-NP3/laponite composites containing 6 wt.%, 11 wt.% and 20 wt.% laponite addition.

	Material						
	O-NP3	O-NP3 Control	Laponite	Laponite Control	O-NP3 /Laponite Composites (wt.% laponite addition)		
					6 wt.%	11 wt.%	20 wt.%
BET Surface Area (m^2/g)	28.9	12.1	319.4	259.1	11.4	21.9	79.1
BJH Adsorption Cumulative Volume of Pores Between 1.7 - 300 nm (cm^3/g)	0.017	0.058	0.295	0.064	0.016	0.005	0.045
BJH Adsorption Average Pore Width (4V/A) (nm)	10.2	18.7	2.8	2.6	21.5	50.4	3.2
BJH Adsorption Largest Pore Width (4V/A) (nm)	154.0	136.7	14.0	14.0	124.4	115.2	138.5
t-Plot Micropore Volume (cm^3/g)	0.010	0.001	0.029	0.057	0.002	0.007	0.010
t-Plot Micropore Area (m^2/g)	20.9	1.9	67.9	127.5	4.8	15.2	23.4
t-Plot Mesopore/Macropore Area (m^2/g)	8.0	10.2	251.5	131.6	6.7	6.8	55.7
t-Plot Micropore Area Compared to Total Area (%)	72.4	15.9	21.2	49.2	41.7	69.2	29.7

5.2.4.2.1 SEM Imaging of O-NP3/Laponite Non-Covalent Composites

As previously described earlier on in the text, O-NP3 consists of large particles of 0.3 – 0.7 mm in size. Subjection of O-NP3 to sonication (O-NP3 control) results in the breakage of these particles into slightly smaller particles of 0.25 mm – 1 μm in size. At high magnification (Figure 5.29 (b) (ii) and (iv)), it is observed that the morphology of the clustered aggregates within the particles remains similar to that of O-NP3.

SEM imaging of laponite shows that the clay consists of particles of non-uniform size and distribution as shown in Figure 5.29 (c). Although not visible within the current imaging, single laponite disks of diameter ca. 25 nm^2 have been recognised in previous works.[476] These disks align to form tactoids, which cluster and accumulate to form particles, which range in size between < 1 to 300 μm, in the current sample. These particles possess irregular shapes and smooth surfaces, where the latter of these properties relates to the ordered structure of the material, which exists due to edge-to-edge and face-to-face interactions.[477] Subjection of laponite to sonication (laponite control) shows that the particles become broken, similar to that of O-NP3 control. At higher magnifications, however, (Figure 5.29 (d) (iii) and (iv)), the morphology remains unchanged.

The O-NP3/laponite composites possess morphological features of both O-NP3 and laponite. Particles range in size between 800 to < 50 μm and exhibit plate-like morphology, with sharp edges. Moreover, the particles possess both smooth and rough regions. In general, the outer edges of the particles are smooth, indicating the presence of laponite around the edges, whilst inner regions and edges are typically rougher, resembling that of O-NP3. In the former case, it is believed that in dispersion, laponite disks, possessing positively charged edges and negatively charged faces would become electrostatically attracted to the negatively charged oxidised O-NP3 material. As such it is likely that upon drying, the laponite material encapsulates O-NP3 to form these smooth regions of laponite aggregates over the surface of O-NP3. This suggests a relatively strong non-bonding interaction exists between O-NP3 and laponite.

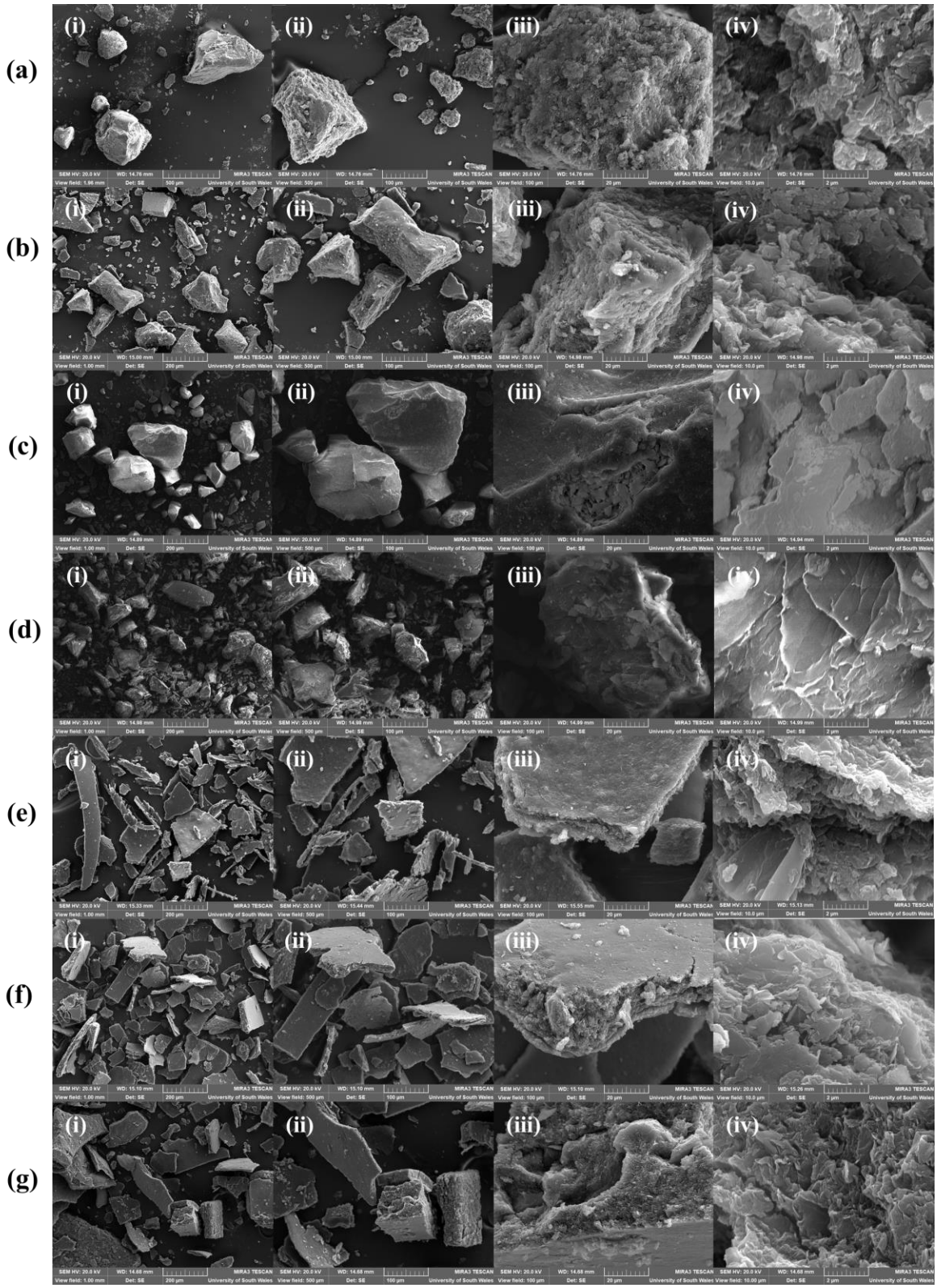

Figure 5.29 SEM images of (a) O-NP3 (b) O-NP3 control (c) laponite (d) laponite control and O-NP3/laponite composites consisting of (e) 6 wt.% laponite (f) 11 wt.% laponite and (g) 20 wt.% laponite with magnifications of (i) 208 x (106 x for O-NP3) (ii) 415 x (iii) 2.08 kx and (iv) 20.76 kx acquired on SEM 2.

5.2.4.2.2 Predicting the Structure of O-NP3/Laponite Composites

Figure 5.30 compares the hypothesised pillaring structure of O-NP3/laponite composites with the proposed structure, based on experimental evidence. It was initially envisioned that the presence of laponite within O-NP3, would open the collapsed slit pores within the structure, as shown in Figure 5.30 (d). In contrast, however, surface area and porosity data (Figure 5.28 and Table 5.7) suggested that the composites displayed a relatively small surface area which did not reflect any pillaring type mechanism. As such, the composites were likely to contain a mixture of densely packed O-NP3 and laponite moieties (Figure 5.30 (e)). These findings are believed to be attributed to the blockage of many O-NP3's slit pores due to laponite occupancy, whilst simultaneously promoting inaccessibility to laponite's porous structure. This densely packed composite is therefore unlikely to allow access to nitrogen adsorbate molecules within much of its structure.

The entry of laponite into the structure of O-NP3, and structure of the overall composite is explained in the context of work carried out by Joshi and co-workers.[468,478,479] In dry state, laponite aggregates range in size between < 1 to 300 μm and hence, are too large to enter the interlayer spacings of O-NP3 (Figure 5.30 (a)). In aqueous solution, however, water is able to enter the interlayer regions and solvate the sodium ions, rendering a permanent negative charge on the faces of the disks (Figure 5.30 (b)). This causes the distance between the disks to increase, due to inter-face repulsion, and the laponite undergoes swelling. Meanwhile, the edges of the laponite disks (specifically the middle octahedral layer) containing broken crystals of MgO and MgOH, exhibit positive charges.[479] As swelling continues, delamination of tactoids occurs, and these delaminated disks undergo thermal motion within the aqueous media.[478] The continuation of delamination, and the result of the opposing charges of the faces and edges of laponite disks, results in an edge-to-face interaction between disks and exfoliated tactoids, which overcome the initial repulsive energy barrier.[479] This results in the formation of clusters, which possess a "house-of-cards" structure. Some laponite tactoids become well-exfoliated, whilst other tactoids may not undergo complete delamination.[468] In both cases, there is an expansion of space in which the laponite disks occupy.

Moreover it is believed that O-NP3 undergoes swelling in aqueous solution, enabling expansion of the lattice to introduce permeation channels for the laponite dispersion.[480] As such, it is believed that the "house-of-cards" structure of laponite takes place both around, and

within the slit pores of O-NP3, as shown in Figure 5.30 (c). As such, this laponite forces the layers to expand further, acting as pillars within the aqueous dispersion. It is believed that the positive edges of the laponite disks interact with the negative functionality upon O-NP3.

Upon drying at 85 °C, under vacuum, the removal of water causes the delaminated laponite disks to re-stack, forming tactoids and aggregates. In such a case, many tactoids and aggregates now occupy slit pores of the oxidised material, probably filling the slit pore (Figure 5.30 (e)). During the initial hypothesis, it was believed that aggregates would pillar the layers (Figure 5.30 (d)), however, experimental evidence suggested that the laponite occupies the entirety of the pore instead, forming interactions with O-NP3. As such, access to nitrogen adsorbate molecules is denied into many of O-NP3's slit pores and within much of the laponite structure itself.

In parallel, some laponite disks may not enter the pores and remain around the edges of the pores, thus, nitrogen adsorbate molecules can freely access their porous network. An increase in BET surface area was found to be associated with the O-NP3/laponite containing the most laponite (20 wt.% addition), suggesting that the increased surface area was associated with non-integrated laponite around the edges of the composite. SEM imaging also revealed evidence of laponite around the edges of the material.

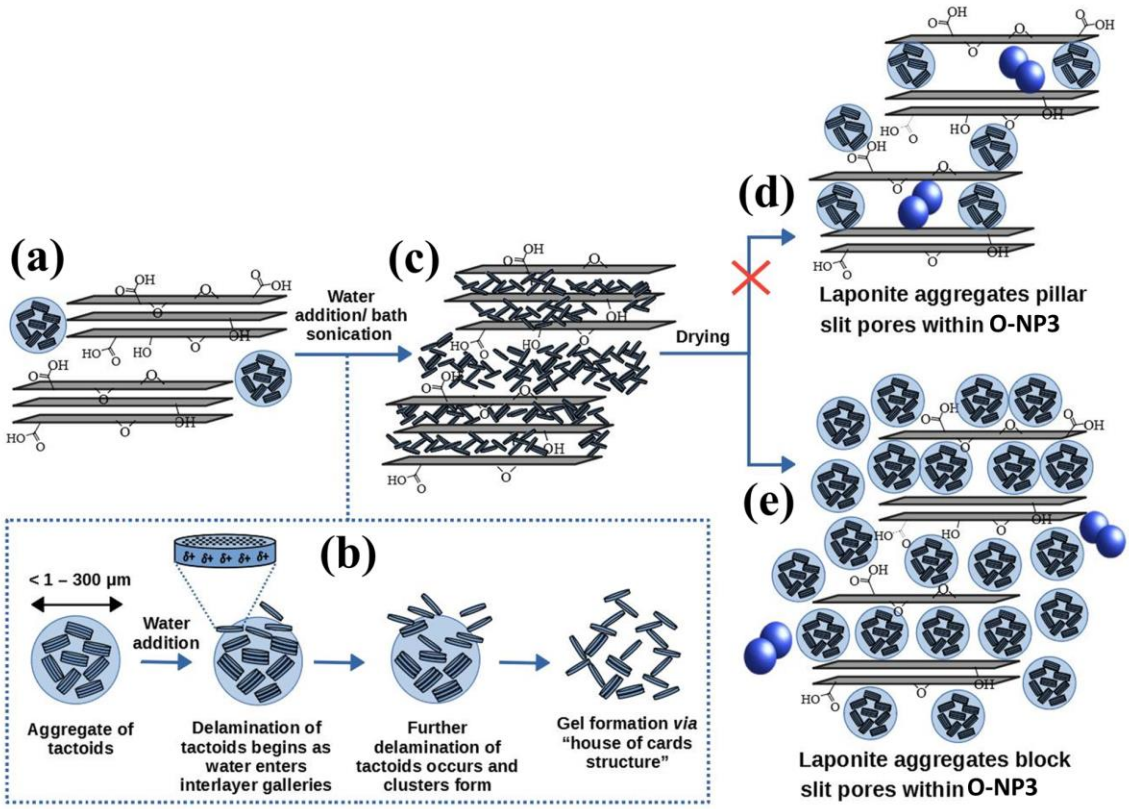

Figure 5.30 A proposed mechanism for the synthesis of the idealised pillaring structure; (d) and proposed structure based on experimental evidence; (e) associated with O-NP3/laponite composites. (a) depicts the structure of laponite within slit pores of O-NP3 and (c) depicts the entry of laponite into slit pores within aqueous media, resulting in widening of slit pores through the formation of a "house-of-cards" structure (shown within the inset (b)). Blue spheres represent nitrogen adsorbate molecules.

In summary, it was believed that the presence of oxygen functionality within O-NP3 was the primary cause of enhanced interaction with laponite edges, resulting in a densely packed composite with no enhanced surface area. As such, this non-covalent pillaring strategy was also investigated through the addition of laponite to the less oxidised material; NP4, to synthesise NP4/laponite composites. It was observed that this laponite addition resulted in expansion of some stacks, as well as the introduction of larger slit pores within the macroporous regions. There was, however, no significant increase in surface area values associated with these composites, thus, these were not investigated further. Since it was concluded that laponite did not effectively pillar the structure of O-NP3 to introduce slit pores and thus, did not enhance the surface area, it was suggested that laponite addition through a covalent means would prove

advantageous in providing a more well-defined, pillaring scaffold. This covalent strategy found more success and is described within the next section.

5.2.4.3 Laponite as a Covalent Pillaring Device

Since the previous section found that non-covalent laponite addition did not successfully introduce new slit pores to O-NP3 to create a high surface area material, attention was directed towards a modified functionalisation strategy. In this section, a covalent laponite functionalised O-NP3 composite was synthesised, and the subsequent surface area and porosity were studied.

5.2.4.3.1 Attachment of Laponite to O-NP3

O-NP3 was covalently bound to laponite through a two-step approach, as shown in Scheme 5.2. To facilitate covalent attachment between laponite and O-NP3, laponite was initially functionalised with primary amine moieties, to enable its coupling with carboxylic acid functionality on O-NP3's surface. In this regard, laponite was functionalised with aminopropyltriethoxy silane (APTES), a commercialy utilised silane coupling agent. This reaction is depicted within Scheme 5.2 (i), and involved a condensation reaction with surface silanol groups, present at broken edges, through the removal of ethanol. Previous investigations have found that APTES is able to functionalise silica and TiO_2 surfaces through a similar condensation reaction.[390,481–483] For the initial functionalisation, the protocol by Mathias was followed.[390] The product of (i) was the APTES functionalised laponite, containing terminal amine moieties, denoted f-laponite. Evidence of this species was found using solid-state NMR (^{13}C and ^{29}Si), FT-IR and XPS and supported by TGA, XRD and Raman spectroscopy. (ii) (Scheme 5.2) then involved the reaction of f-laponite with O-NP3, using the coupling reagent dicyclohexylcarbodiimide (DCC) to form f-NP3. DCC is renowned for its ability to couple amines with carboxylic acid functionality, to form the subsequent amide and the by-product dicyclohexylurea (DCU).[484] This by-product is usually insoluble in the reaction solvent,

therefore, is typically removed from soluble products *via* filtration. These steps enabled the reaction between the terminal primary amine of f-laponite and carboxylic acid functionality on O-NP3, to take place.

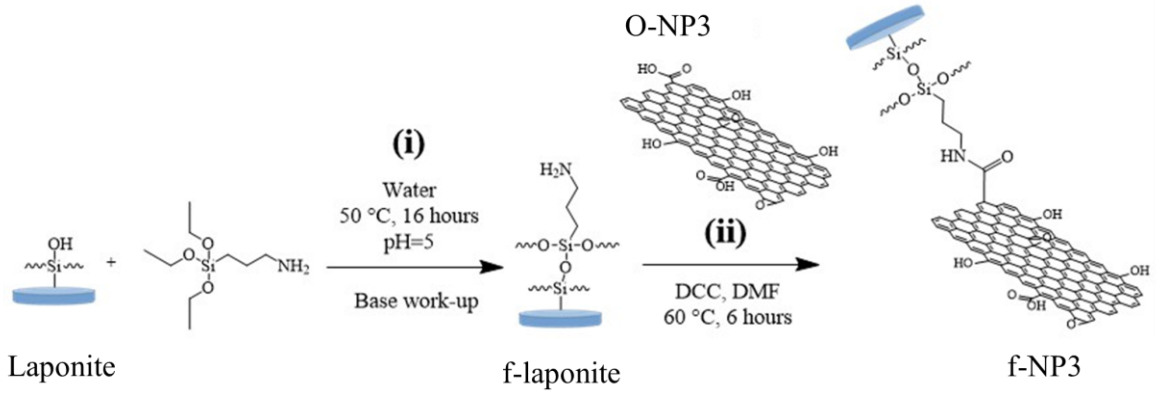

Scheme 5.2 Schematic representation of the synthesis of f-laponite (i) and its attachment to O-NP3 (ii) to synthesise f-NP3.

5.2.4.3.2 Characterisation

5.2.4.3.2.1 NMR Analysis

Solid-state NMR spectroscopy was employed to investigate the ^{13}C and ^{29}Si environments within O-NP3, f-laponite and f-NP3. In addition, APTES was also analysed *via* solution state NMR to aid comparison with APTES functionalised materials. The corresponding ^{1}H,^{13}C and ^{29}Si spectra are depicted within Figure 5.31 (a) – (i) respectively and the ^{1}H and ^{13}C environments are assigned by labels a – f and a – e within both spectra, to the APTES molecular structure. Five peaks were observed within the ^{1}H spectra, possessing an appoximate ratio of 6:2:2:10:2, consistent with the number of protons in each environment. The ^{13}C spectra also possessed five peaks, with an approximate ratio of 3:1:1:3:1, consistent with the number

of ^{13}C environments. Furthermore, the peak at −44.99 ppm within the ^{29}Si spectrum corresponds to silicon within the triethyoxy silane environment.

Within the ^{29}Si NMR spectra of laponite, two resonances were present at −95.03 and −85.38 ppm (Figure 5.31 (d)). These peaks can be assigned according to the various denotations, depending on how the silicon is bonded to oxygen. These denotations correspond to Q^n, T^n, D^n or M^n, where the letter correlates to the number of oxygen atoms the silicon is bonded to: Q = 4, T = 3, D = 2 and M = 1 and n correlates to the number of oxygen atoms which are further bonded to a silicon atom.[485,486] The Q^n and T^n denotations are outlined in more detail in Figure 5.32.

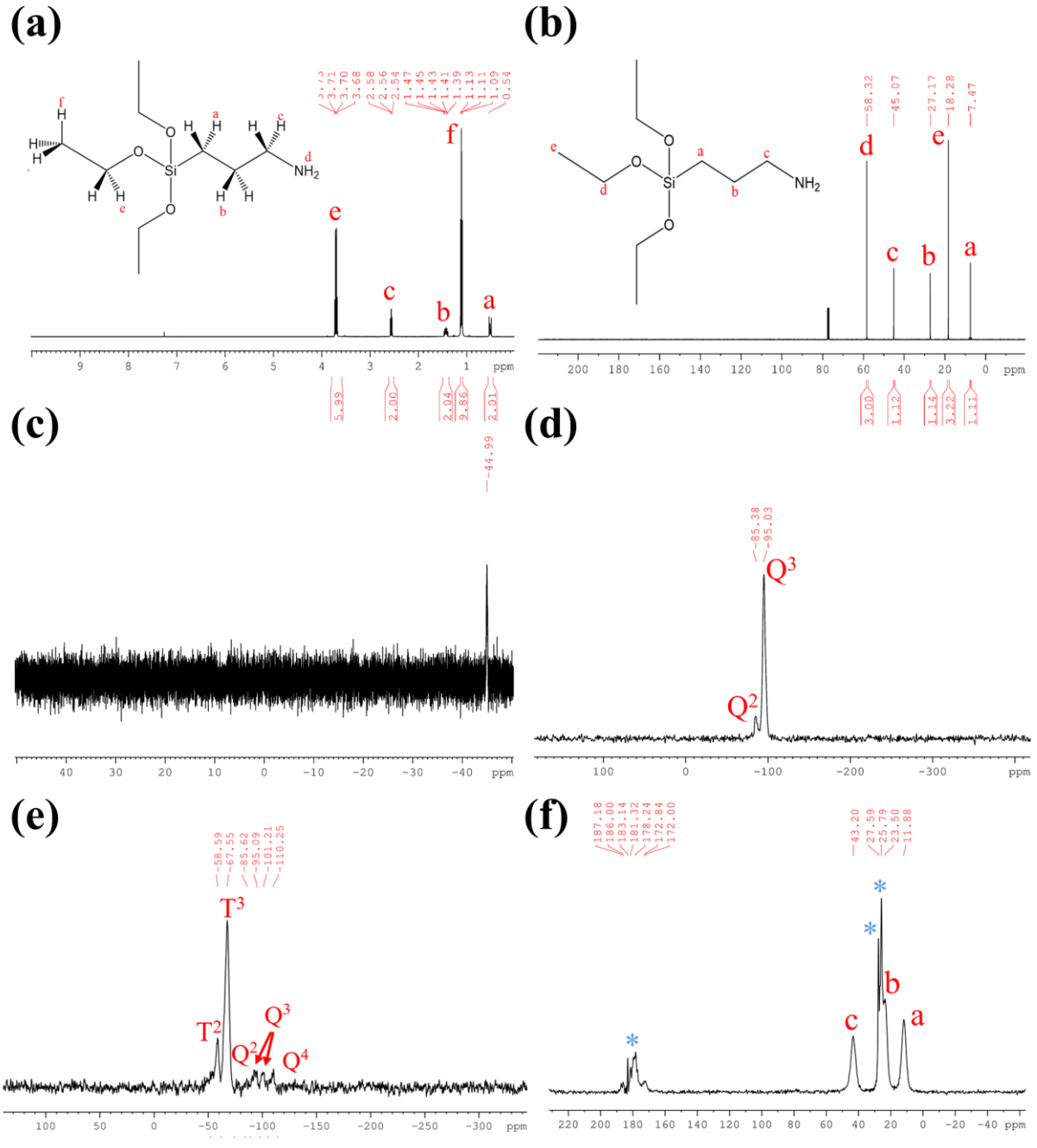
(a)
(b)
(c)
(d)
(e)
(f)
Q3
Q2
T3
T2
Q4
ppm

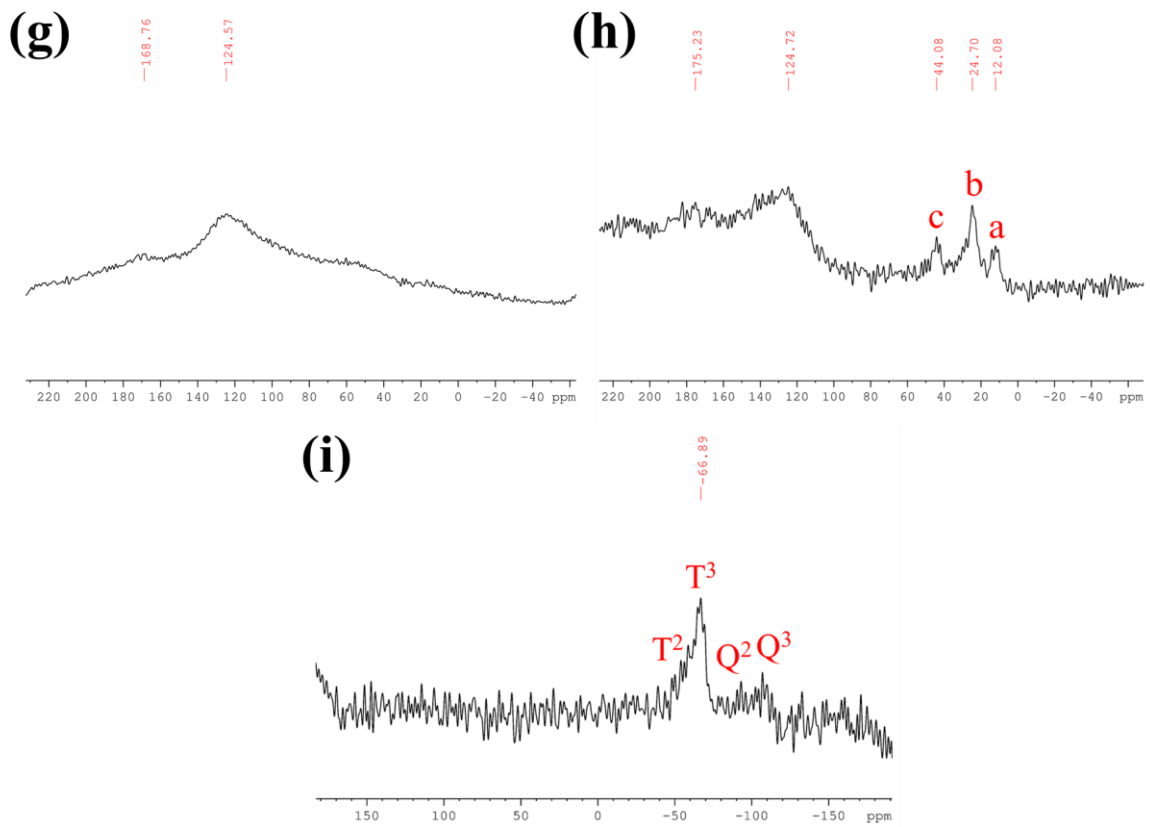

*Figure 5.31 NMR studies including solution state spectra; (a) ^{1}H (b) ^{13}C and (c) ^{29}Si for APTES, and solid-state spectra; (d) ^{29}Si for laponite (e) ^{29}Si for f-laponite (f) ^{13}C for f-laponite (g) ^{13}C for O-NP3 (h) ^{13}C for f-NP3 and (i) ^{29}Si for f-NP3. ^{1}H and ^{13}C environments on APTES are annotated on (a), (b), (f) and (h), whilst the T and Q ^{29}Si environments are depicted on (d), (e) and (i). Peaks relating to sodium acetate impurity on (f) are assigned with an *.*

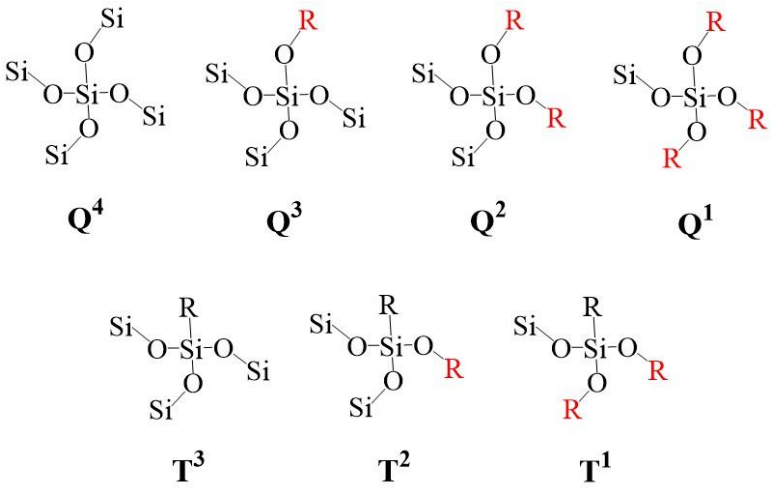

Figure 5.32 The assignment of silanes with various denotations, where Q represents a silicon atom bonded to four oxygen atoms and T represents a silicon atom bonded to three oxygen atoms. The superscript integer represents the number of oxygen atoms bonded to a further silicon atom and R represents a variable group[485,486].

By comparison with the literature, it can rationalised that the peak at −95.03 ppm relates to Q^3 trioxo silicon, where each silicon atom is bonded to four oxygen atoms, and three of these oxygen atoms are further bonded to silicon atoms. The peak at −85.38 ppm, corresponds to Q^2 sites at silicate sheet edges originating from isolated silanol groups. In these groups, each silicon atom is bonded to four oxygen atoms, and two of these oxygen atoms are further bonded to silicon atoms.[487] These environments are outlined within Figure 5.33 (a).

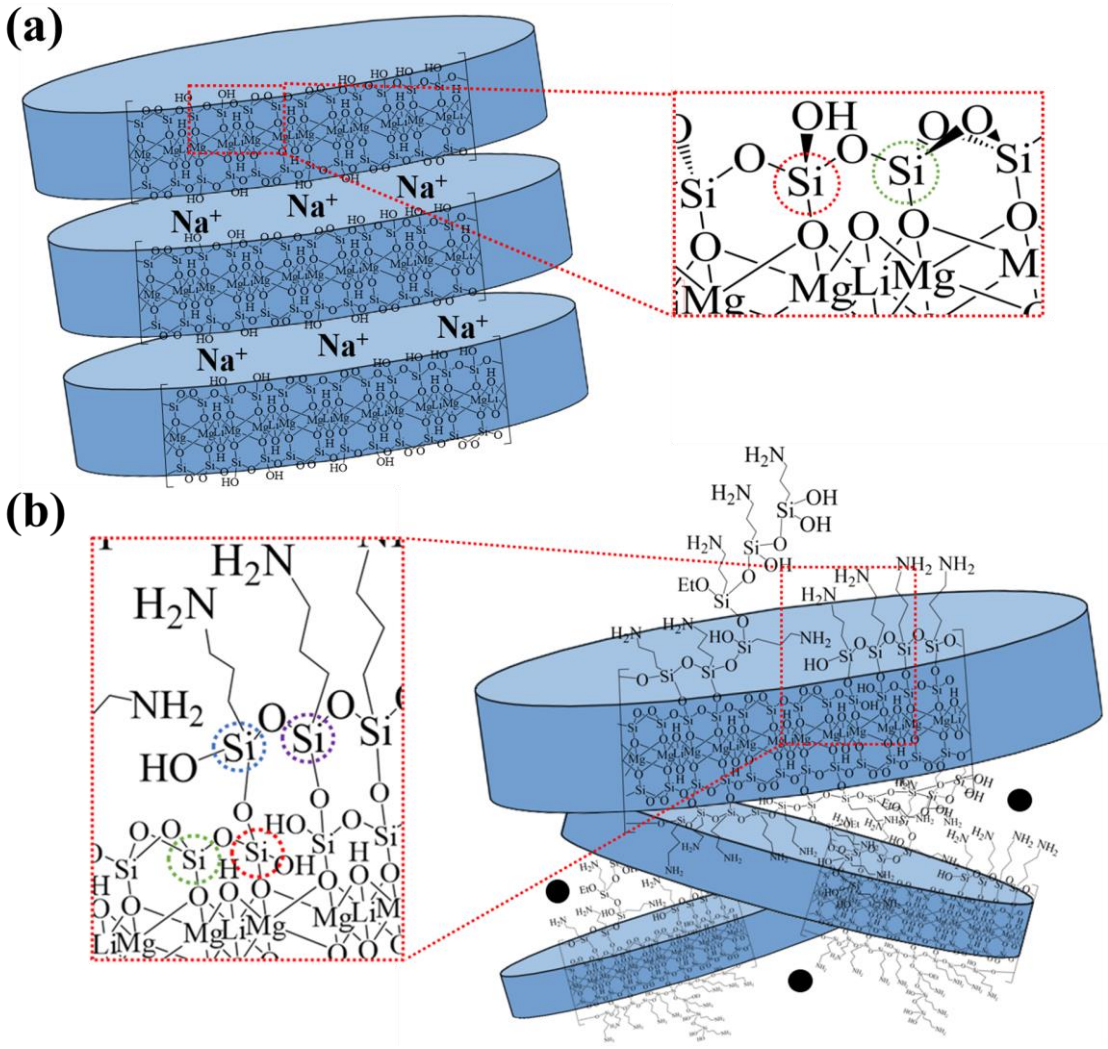

Figure 5.33 Structure and magnified regions of (a) laponite depicting the Q^2 and Q^3 environments (highlighted by red and green circles respectively) and (b) f-laponite depicting Q^2, Q^3, T^2 and T^3 environments (highlighted by red, green, blue and purple circles respectively). Black spheres within the structure of f-laponite represent sodium acetate impurity and decomposed silica.

NMR analysis of f-laponite, revealed changes within the ^{29}Si NMR spectra (Figure 5.31 (e)). Most noticeably, the appearance of two new peaks at −67.55 and −58.59 ppm were observed, which relate to the T^3 peaks and T^2 respectively.[488] As such, it can be concluded that the introduction of APTES has resulted in the presence of [RSi*(OMg)$(OSi)_2$] (T^3) and [RSi*(OMg)(OSi)−(Et)] (T^2) type environments, where R is the rest of the APTES chain. These peaks relate to APTES moieties where the three ethoxy groups become condensed (T^3) and only two ethoxy groups have condensed (T^2), as shown in Figure 5.33 (b). It is likely that these APTES moieties reacted at not only defective silanol sites on the outer edges of laponite, but also underwent self-polymerisation *via* condensation reactions with already attached APTES moieties. Furthermore, it may also be possible that the APTES moieties reacted with silanol groups within the laponite structure itself, resulting in the disruption to the "silica" like structure, and promoting a degree of decomposition within the structure. Additional peaks are also present within the ^{29}Si spectra at −101.21 and −110.25 ppm. The latter of these peaks has been observed within previous work, and was attributed to the [Si*$(OSi)_4$] (Q^4) functionality associated with silicon in quartz.[489] The former peak resembles silicon atoms within [Si*$(OSi)_3$(OH)] (Q^3) type environments.[490] Furthermore, the original Q^3 and Q^2 peaks, relating to the laponite structure, were observed at −85.62 and −95.09 ppm. The combination of the newly formed T^3 and T^2 peaks in conjunction with the Q^3 and Q^2 peaks has been recognised upon functionalisation of clays and silica using various silanising reagents.[390,488–493]

The subsequent ^{13}C spectra of the material (Figure 5.31 (f)) contained various peaks including 11.9, 23.5 and 43.2 ppm, which relate to carbons A, B and C respectively from APTES. An absence of ^{13}C peaks associated with carbons D and E from APTES, suggests that condensation occurs successfully between laponite and APTES. Additional peaks between 172.00 − 187.18, 25.79 and 27.59 ppm were also observed, corresponding to the carbonyl and methyl environments within acetate, likely to originate from primarily sodium acetate, in accordance with XPS and FT-IR data (*vide infra*).[494] It is likely that such species become well intercalated between laponite layers during synthesis, however, it is unlikely to be bound to any acidic NH_3^+ groups of APTES functionality, since a base work-up was carried out to neutralise any remaining acetic acid and to deprotonate any acidic protons. Acetate proved very difficult to remove even after repeated 60% methanol in water washes, as described within the work followed.[390] Furthermore, the washing produce was also difficult due to the ability of laponite to gelate during redispersion/sedimentation.

Analysis of the ^{13}C NMR spectrum associated with O-NP3 depicts the presence of three peaks corresponding to approximately 60, 124.6 and 168.8 ppm (Figure 5.31 (g)). The former, broad, low intensity peak indicates the presence of epoxide and hydroxyl groups.[55] The latter two peaks correspond to unoxidised sp^2 carbons of the graphitic network and carbonyl functionality, respectively.[495]

The corresponding f-NP3 ^{13}C NMR spectrum possesses five peaks at 175.2, 124.7, 44.1, 24.7 and 12.1 ppm (Figure 5.31 (h)). The latter three peaks related to carbons C, B and A respectively, within the APTES functionality, indicating the presence of f-laponite. The broad peak at 124.7 ppm corresponds to un-oxidised sp^2 carbons within the graphitic network, similar to that of O-NP3. Furthermore, the low intensity peak at 175.2 ppm corresponds to carbonyl functionality, consistent with oxygen functionality on the graphitic surface. The existence of acetate was no longer observed within the ^{13}C spectrum, and XPS data indicated the presence of much smaller quantities compared with that of f-laponite (*vide infra*), suggesting that the functionalisation process, shown within Scheme 5.2 (ii), was adequate in aiding its removal. In addition, the ^{29}Si spectrum for f-NP3 possesses a peak at −66.89 ppm, analogous of silicon within the Si−O−Si polymeric chain environment, consistent with the spectrum obtained for f-laponite (Figure 5.31 (i)).[496] This was much broader than that of f-laponite due very short relaxation times originating from the strong couplings between the nuclei and the unpaired electrons within graphitic material.[497]

5.2.4.3.2.2 XPS Analysis

XPS was utilised to investigate the surface elemental composition of NP3, O-NP3, laponite, f-laponite and f-NP3. The quantitative data and XPS spectra are provided in Tables 5.5, 5.8 and 5.9 and Figures 5.16, 5.17, 5.34, 5.35 and 5.36. NP3 was found to possess carbon and oxygen only, with corresponding compositions of 94.2 and 5.9 at.%, respectively. The deconvoluted high-resolution C 1s spectrum (Figure 5.16 (b)) contains several carbon environments corresponding to sp^2 (284.3 eV), sp^3 (284.8 eV), C−O (286.6 eV), O−C=O/C=O (288.7 eV), $\pi-\pi^*$ (290.7 and 294.0 eV). The incorporation of oxygen functionalities within NP3 originate from the oxygen plasma processing, described within Chapter 3. The O 1s spectra (Figure 5.16

(c)) depicts four peaks at 531.9 eV, 533.2 eV, 535.6 eV and 538.0 eV, which correspond to the C=O, C−O−C, C−OH and the O 1s satellite structure, respectively. XPS analysis of O-NP3 reveals a large increase in oxygen functionality, consistent with the oxidation method used (Scheme 5.1). O-NP3 contains a total of 23.8 at.% oxygen in the form of hydroxyl, epoxide, carbonyl and carboxyl moieties, as evidenced by the O 1s peak at 532.6 eV (Figure 5.17 (c)). As expected, the carbon atomic composition reduced to 73.2 at.%. Moreover, the concentration of sp^2 carbon also decreased from 62.7 to 40.3 at.% consistent with the change in hybridisation of the carbon atoms upon covalent bond formation. In parallel, the π−π* satellite structures at 291.1 and 293.8 eV also decreased, further supporting the fact that there was a decline in π bonding. Silicon and sulfur were also detected in trace amounts, as evidenced by the Si and S 2p peaks, at 103.4 eV/101.8 eV and 168.5 eV, respectively (Figure 5.17 (d) and (e)).

Table 5.8 XPS quantitative element composition data for NP3, O-NP3, laponite, f-laponite and f-NP3.

Orbital	**Atomic Concentration (%)**				
	NP3	O-NP3	Laponite	f-laponite	f-NP3
C 1s	94.2	73.2	6.3	45.5	64.2
Mg 2p	-	-	16.2	1.6	1.3
Na 1s	-	-	2.5	17.6	1.2
O 1s	5.9	23.8	52.8	30.9	23.4
Si 2p	-	2.2	20.8	2.8	5.8
N 1s	-	-	-	1.6	4.1
S 2p	-	0.8	-	-	-

Table 5.9 XPS quantitative element composition data for the C 1s orbital for NP3, O-NP3 and f-NP3.

C 1s Orbital	**Atomic Concentration (%)**		
	NP3	O-NP3	f-NP3
Sp²	62.7	40.3	21.5
π−π*	6.8	2.5	1.5
π−π*	1.2	0.5	-
C=O	(overlaps with O−C=O)	(overlaps with O−C=O)	5.0
C−O	6.0	9.4	10.2
Sp³	13.4	13.9	23.0
O−C=O	4.0	6.7	3.1

Analysis of laponite reveals the presence of carbon, oxygen, silicon, magnesium and sodium, consistent with that of previous work (Figure 5.34 and Table 5.8).[498] The origin of carbon is

suggested to relate to atmospheric contamination. The deconvoluted C 1s orbital depicts peaks at 285.0 , 287.1 and 289.2 eV, which correspond to adventitious carbon (C−C and C−H bonds), C−O bonds and carbonate, respectively (Figure 5.34 (b)).[499] Oxygen presence is evidenced by the binding energy at 532.3 eV, resembling that of single bonded oxygen atoms bonded to silicon, comprising a total 52.8 at.% of the material.[500] Further binding energies at 103.2, 50.1 and 1072.9 eV indicate the presence of silicon, magnesium and sodium, with atomic percentage compositions of 20.8, 50.1 and 2.5 respectively, as shown in Figure 5.34 (c) − (f). As described within the previous section, silicon, holding an oxidation state of +4, is bonded to four oxygen atoms, and is located within the tetrahedral sheets of the material. Mg^{2+} cations reside within the octahedral sheets, whilst Na^{+} ions are situated within the interlayers of the structure. The absence of lithium within the structure was attributed to the small cross section (the area at which a collision must take place in order for energy transfer to occur) of the XPS instrument. This means that it is notoriously difficult to observe lithium under XPS analysis, unless it is present in particularly high concentrations.[501]

XPS analysis of f-laponite reveals the presence of a peak at 398.9 eV within the N 1s spectrum (Figure 5.35 (d)), corresponding to 1.6 at.% nitrogen. This resembles nitrogen within primary amine moieties, consistent with those of APTES, indicating successful functionalisation. The binding energy associated with the nitrogen within primary amine moieties of 3-aminopropyltrimethoxysilane functionalised on a silicon (111) surface were also found to possess a similar binding energy, equivalent to 399 eV.[502] Moreover, the absence of a peak corresponding to nitrogen within NH_3^{+} type functionality provides further evidence that protonated amines associated with $Si{-}O^{-}$ are unlikely to exist, thus, suggesting that covalent bonding of APTES originated from condensation of ethoxy moieties, as opposed to ionic interactions.[503] Analysis of the C 1s spectrum (Figure 5.35 (c)) also reveals a large increase in carbon at 284.9 eV, indicating the incorporation of the APTES carbon chain, containing C−C, C−N and C−Si, as well as C−O bonds originating from sodium acetate. A further binding energy of 288.5 eV was also observed, consistent with the C=O bond within the acetate impurity. The deconvoluted O 1s spectrum (Figure 5.35 (d)) also signifies the presence of C=O associates with sodium acetate at 531.4 eV, in addition to single bonded oxygen to silicon atoms at 530.4 eV. Moreover, the Na 1s spectrum possesses a peak at 1071.4 eV, suggestive of Na^{+} ions bound to oxygen, typical of those within sodium acetate moieties (Figure 5.35 (e)).[325,504] It was also observable that f-laponite contained a considerable decline in the atomic concentration of magnesium and silicon (Table 5.8 and Figure 5.35 (f) and (g)). This was

explained through consideration of the orientation of APTES moieties. The presence of APTES moieties extending out from the surface of laponite results in partial coverage of the clay, meaning magnesium and silicon reside much deeper into the sample, and thus, would be detected to a lesser extent.[322] It was also observed that the Si 2p peak also shifted towards a slightly lower binding energy value from 103.2 eV in laponite to 102.1 eV in the f-laponite. This implies a change to the silicon environment, consistent with NMR analysis. It is believed that silicon atoms bonded to four oxygen atoms, such as that of laponite, would possess a higher binding energy than those bonded to only three oxygen atoms, such as that of f-laponite. An increase in electronegative atoms such as oxygen would indeed mean that the removal of an electron from that atom would be more difficult, since more electron density is pulled away from that atom.

XPS analysis of f-NP3 reveals the presence of nitrogen, carbon, oxygen, magnesium, sodium and silicon. Nitrogen was evidenced by a peak at binding energy of 400.2 eV, equating to a total nitrogen content of 4.1 at.% (Figure 5.36 (d)). A small increase in binding energy relative to f-laponite was indicative of the nitrogen within the amide functional group, possessing an electronegative oxygen atom within a close proximity to nitrogen. As such, electron density is withdrawn away from nitrogen, thus, inducing an increased binding energy.[505] f-NP3 consists of a substantial increase in carbon relative to f-laponite (Figure 5.36 (b)). This carbon originates from the carbon network within O-NP3, in conjunction with APTES functional groups. More specifically, a large increase in sp^3 carbon compared with sp^2 is consistent with the addition of the APTES aliphatic carbon chain. Furthermore, the presence of carbon within the amide functional group (N−C=O) is likely to overlap with that of C=O of the graphitic network, whilst the C−N peak probably overlaps with the C−O peak. The presence of O−C=O functionality was also evidenced by the peak at 288.9 eV, suggesting that some carboxylic acid functional groups on the surface of f-NP3 remain unreacted with primary amine groups of f-laponite. Oxygen was present with a total atomic percentage composition of 23.4 (Figure 5.36 (c)). The O 1s spectra revealed a peak at 102.9 eV, which was deconvoluted into peaks corresponding to C=O/Si−O/C−O, C−O−C, C−OH, and O 1s satellite environments. 1.2 at.% sodium was also observed within the Na 1s spectrum at a binding energy of 1071.6 eV, corresponding to residual sodium acetate (Figure 5.36 (e)). The concentration is drastically reduced compared with that of f-laponite, suggesting that the majority of the contaminant was removed upon composite synthesis. Its removal may have been assisted by the functionalisation procedure causing exfoliation of f-laponite, such that the trapped sodium acetate became freed prior to f-

NP3 washing. Magnesium and silicon were also observed at binding energies of 50.4 and 102.9 eV and at.% of 1.3 and 5.8, respectively (Figure 5.36 (f) and (g)). These indicate the presence of Mg^{2+} cations within the octahedral sheets and silicon within the tetrahedral sheets, holding a formal charge of +4.

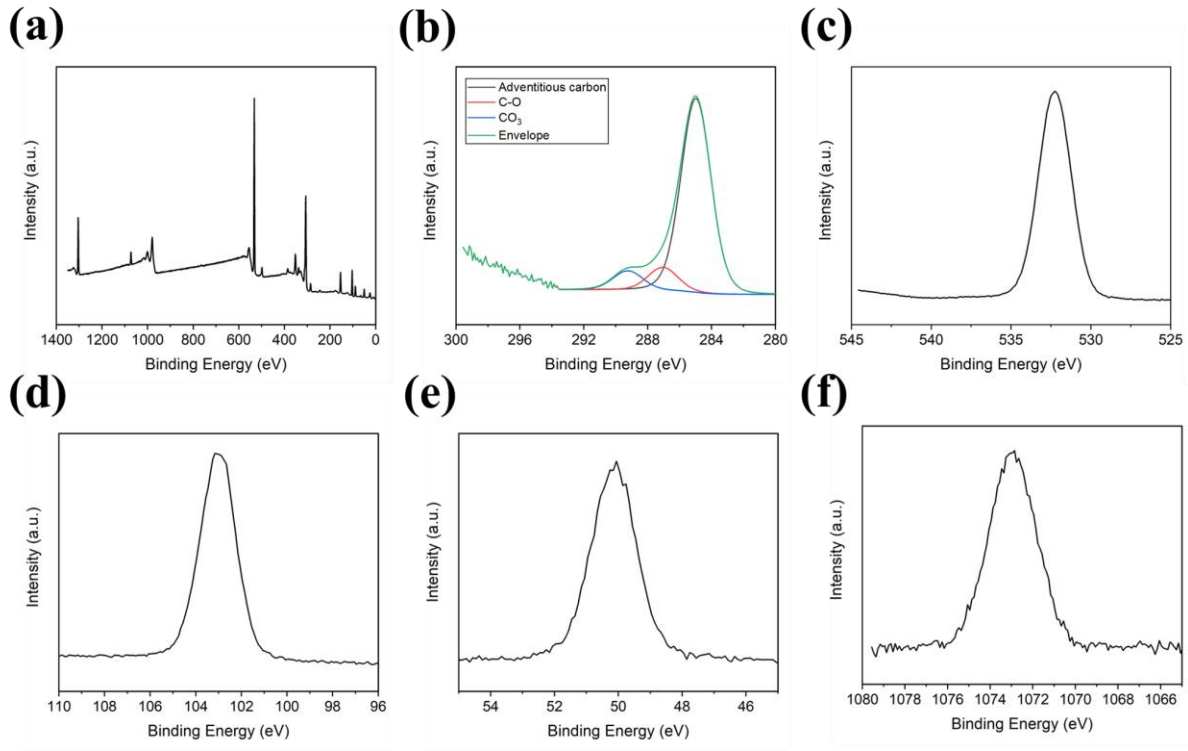

Figure 5.34 XPS spectra for laponite including (a) survey spectra (b) deconvoluted C 1s orbital (c) O 1s orbital (d) Si 2p orbital (e) Mg 2p orbital and (f) Na 1s orbital.

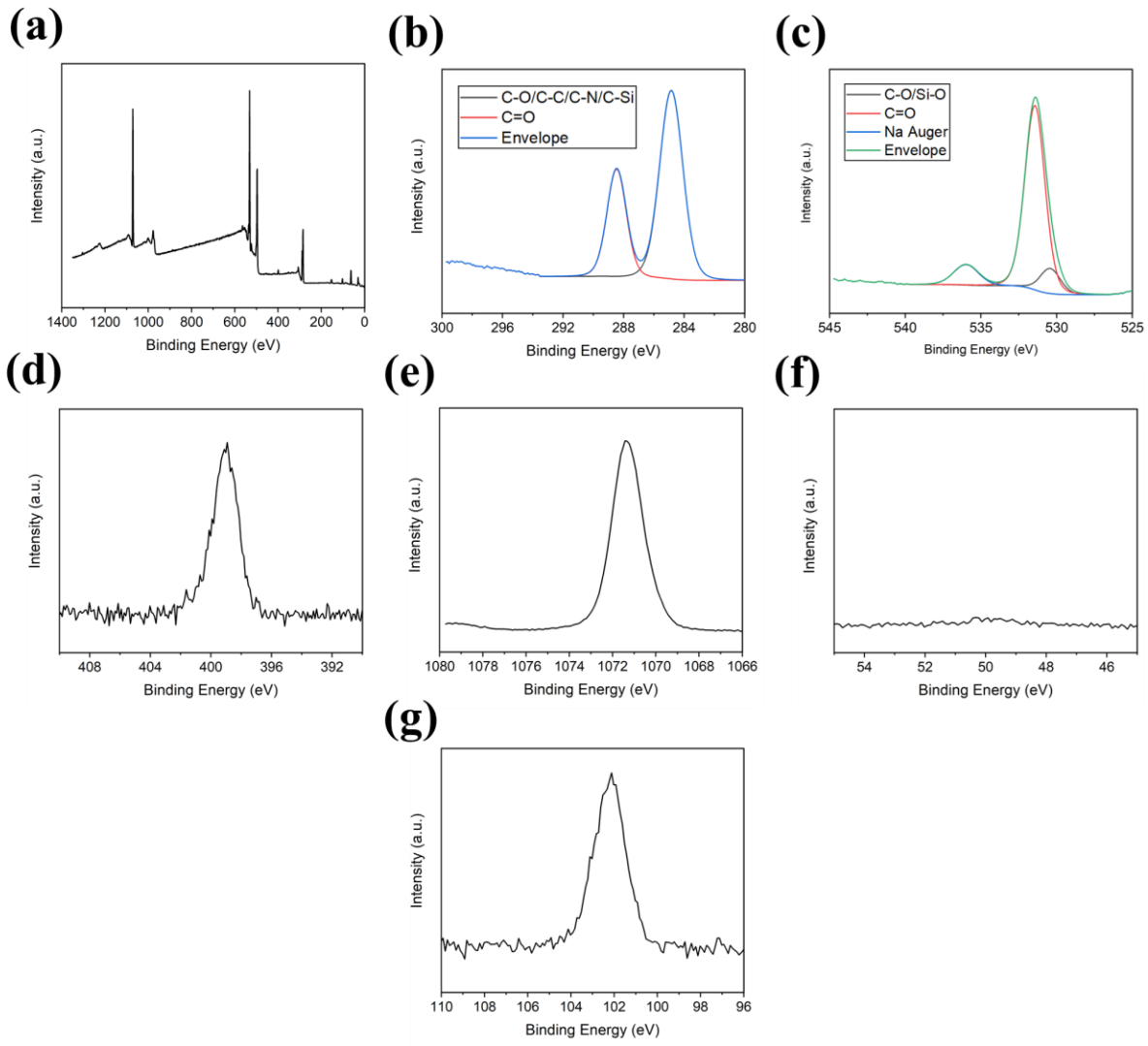

Figure 5.35 XPS spectra of f-laponite including (a) survey spectra (b) C 1s orbital (c) O 1s orbital (Note: the peak at 536.0 eV within the O 1s spectra of f-laponite relates to the Na Auger peak) (d) N 1s orbital (e) Na 1s orbital (f) Mg 2p orbital and (g) Si 2p orbital.

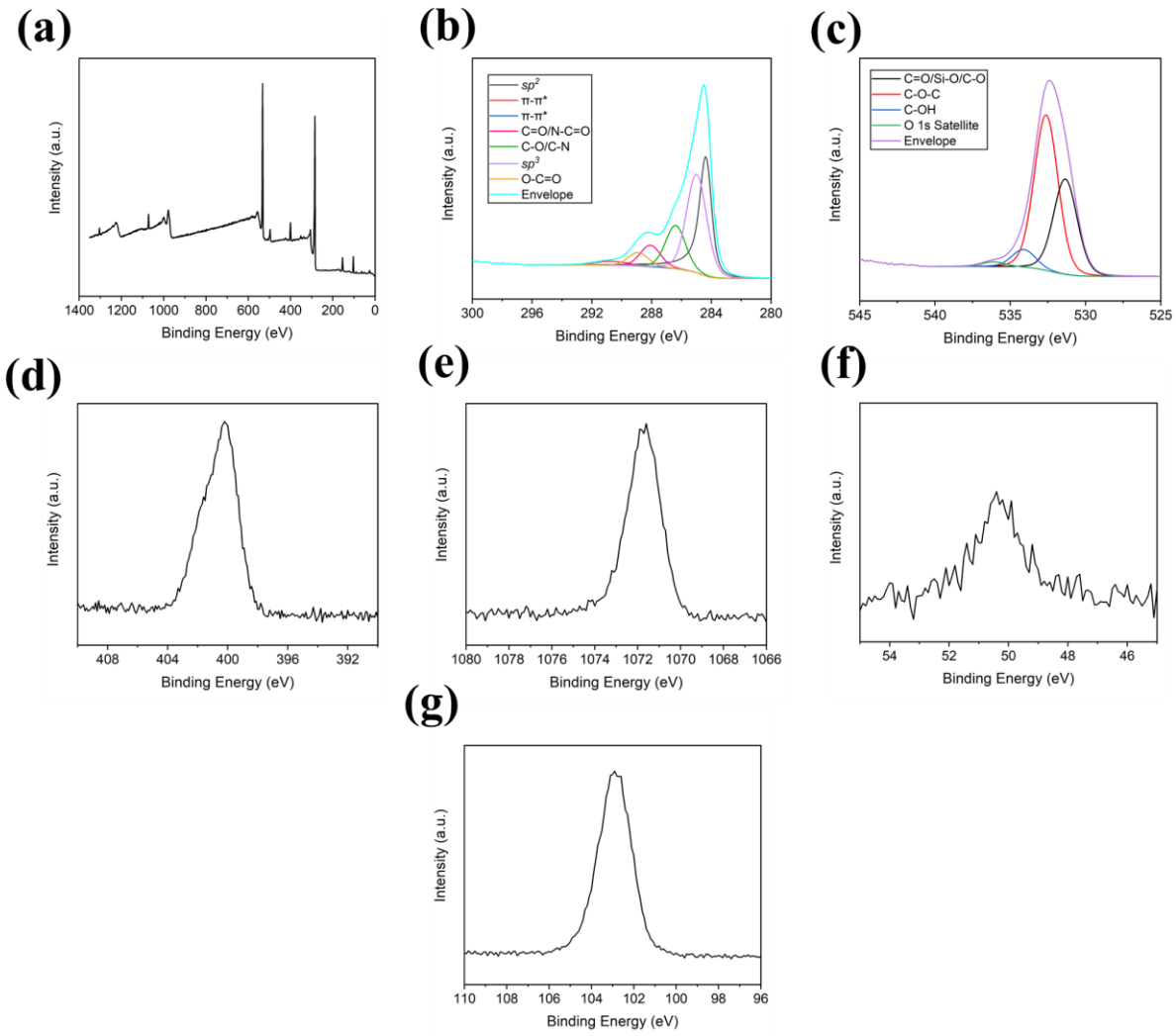

Figure 5.36 XPS analysis of f-NP3 *including (a) survey spectra (b) deconvoluted C 1s orbital (c) deconvoluted O 1s orbital (d) N 1s orbital (e) Na 1s orbital (f) Mg 2p orbital and (g) Si 2p orbital.*

5.2.4.3.2.3 BET/BJH/t-Plot Analyses

Surface area and porosity analysis was conducted on f-laponite and f-NP3, and the data compared with that of O-NP3 and laponite (Table 5.10 and Figure 5.37). The surface area and porous structures of the latter two materials are described within Sections 5.2.3 and 5.2.4. Initially, f-laponite was analysed, and it was found that in contrast to laponite's Type IVb character with H2 hysteresis, f-laponite possessed a pseudo-type II isotherm with a small H3 hysteresis, indicating the presence of slit-like particles with non-rigid nature, and non-uniform

shape and size (Figure 5.37 (a)).[351] The absence of a plateau was one of the most noticeable differences between the isotherm of f-laponite compared to laponite, suggesting the occurrence of incomplete mesopore filling, resulting in multilayer proceeding until high $P/P_{0,}$ with no termination. Quite clearly changes occurred to the porous structure of the newly functionalised material. A second difference between laponite and f-laponite relates to the surface area. A relatively low BET surface area was associated with f-laponite, reducing from 319.4 m^2/g within laponite to 0.4 m^2/g within the functionalised material (Table 5.10). This reduction was associated with a complete loss micropores as confirmed by t-plot data, as well as a substantial reduction in t-plot mesopore/macropore area and BJH absorption cumulative volume of pores between 1.7 – 300 nm. It is believed that the functionalisation process led to a significant blockage of pores. It has been postulated within previous works that the functionalisation occurs at the edges of the laponite sheets, therefore, it is assumed that these regions prevent access to nitrogen adsorbate molecules.[390] In fact, a reduction in surface area has been associated with the functionalisation of laponite with alkoxysilanes in previous work.[488,491] For example, Bourgeat-Lami observed a decrease in surface area upon functionalisation of laponite with trifunctional *γ*-methacryloxypropyl trimethoxy silane from 370 m^2/g down to 76 m^2/g. As such, it is believed that in the case of f-laponite, APTES functionality, in conjunction with trapped sodium acetate contaminants, blocked passage of nitrogen adsorbate molecules into pores, as depicted within Figure 5.38 for f-laponite. Upon functionalisation of O-NP3 with f-laponite, its surface area increased from 28.9 m^2/g and 0.4 m^2/g, within the independent materials, to 112.6 m^2/g within the f-NP3 composite. As such it was evident that new pores had been created within the covalently bound composite structure. The BET curve for f-NP3 displayed pseudo-type II character (Figure 5.38 (a)). Similar to the isotherm of f-laponite, the absence of a plateau suggests no indication of complete mesopore filling, suggesting the presence of relatively large pores. H3 hysteresis was observed between the adsorption and desorption branches between 0.4 – 1.0 P/P_0, according to IUPAC classification.[351] This hysteresis type also indicates the presence of slit-like particles with non-rigid nature and non-uniform shape and size. The BJH adsorption cumulative volume of pores between 1.7 – 300 nm is 0.431 cm^3/g, suggesting a substantial increase in volume compared with that of the individual components of the composite. Similarly, the t-plot mesopore/macropore area increased drastically. In contrast, however, the t-plot micropore area and volume equal zero, suggesting a lack of pores on the micro-scale. As such, it is concluded that the increase in BET surface area was associated with an introduction of pores within the mesoporous and macroporous regions. Such pores are believed to result from a pillaring effect between the f-

laponite tactoids within the O-NP3 stacks and layers, forming a pillared network which acts as a scaffold (Figure 5.39). In turn, more surface area is revealed to nitrogen adsorbate molecules.

Table 5.10 BET, BJH adsorption and t-plot data for O-NP3, laponite, f-laponite and f-NP3.

	Material			
	O-NP3	Laponite	f-laponite	f-NP3
BET Surface Area (m^2/g)	28.9	319.4	0.4	112.6
BJH Adsorption Cumulative Volume of Pores Between 1.7 – 300 nm (cm^3/g)	0.0167	0.295	0.002	0.431
BJH Adsorption Average Pore Width (4V/A) (nm)	10.2	2.8	40.0	11.6
BJH Adsorption Largest Pore Width (4V/A) (nm)	154.0	142.3	122.1	97.5
t-Plot Micropore Volume (cm^3/g)	0.0097	0.029	0.000	0.000
t-Plot Micropore Area (m^2/g)	20.9	67.9	0.0	0.0
t-Plot Mesopore/Macropore Area (m^2/g)	8.0	251.5	0.4	112.6
t-Plot Micropore Area Compared to External (%)	72.4	21.2	0.0	0.0

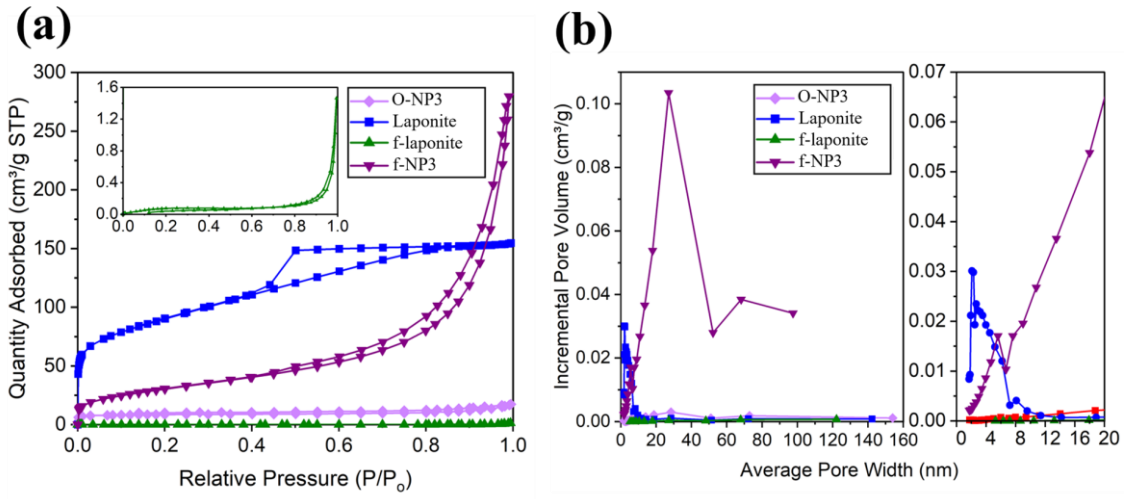

Figure 5.37 (a) N_2 adsorption-desorption isotherms and (b) BJH adsorption data associated with the incremental pore volume for O-NP3, laponite, f-laponite and f-NP3.

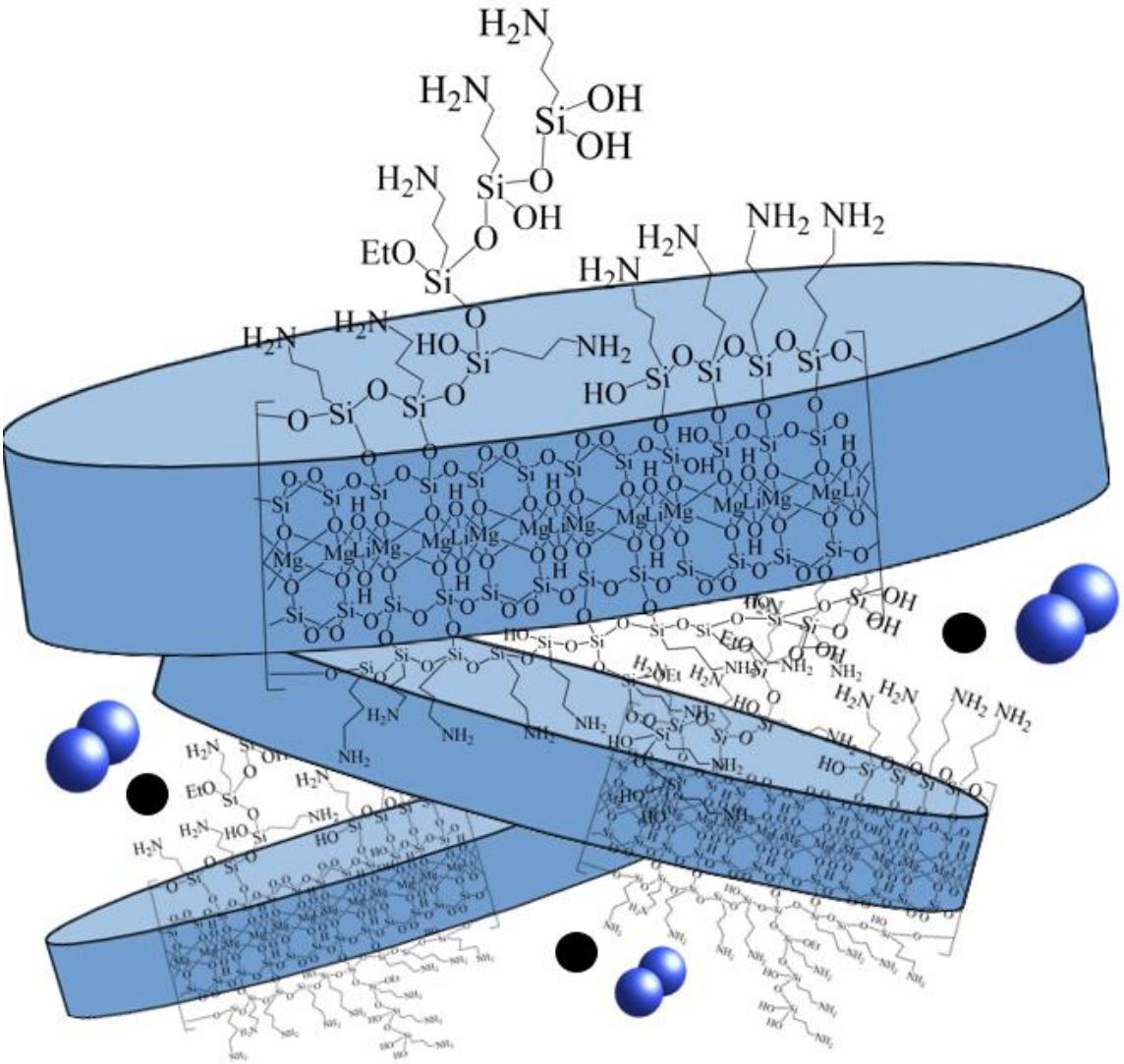

Figure 5.38 Diagram outlining the blockage of pores within a f-laponite cluster due to functionalisation around the edges of the laponite disks, as well as the presence of sodium acetate within the pores. Nitrogen adsorbate molecules are shown by the diatomic blue spheres, and these are unable to access pores within the laponite cluster.

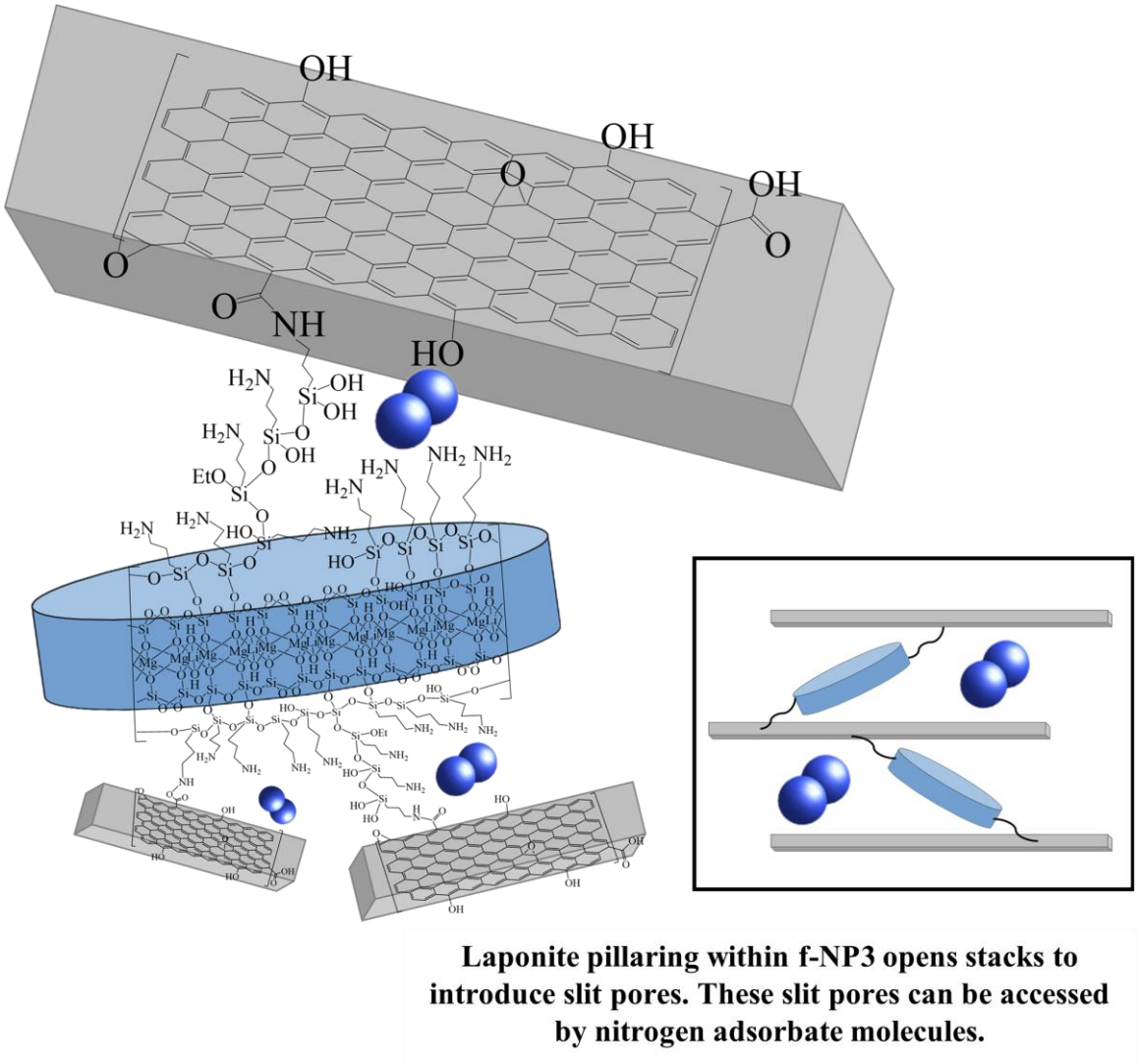

Figure 5.39 Proposed diagram depicting the pillaring effect within f-NP3. f-laponite is bonded to O-NP3 through an amide linkage and the pillared structure allows nitrogen adsorbate molecules (each nitrogen atom is denoted as a blue sphere) to access slit pores. A side on view of the pillared structure is provided within the inset. Note: the diagram is not drawn to scale.

5.2.4.3.2.4 FT-IR Analysis

The FT-IR spectra of O-NP3, laponite, f-laponite, APTES and f-NP3 are shown in Figure 5.40. The spectra were obtained using the KBr disk technique for NP3 containing samples, to reduce noise and achieve more pronounced peaks. The ATR technique was utilised for the remaining samples. The FT-IR spectra of NP3 possessed three broad, low intensity peaks at 3206, 1722 and 1441 cm^{-1}. The former of these was attributed to O–H bend, whilst the peak at 1722 cm^{-1}

was attributed to the C=O stretching vibration, relating to ketones or aldehydes overlapping with the bending mode of water molecules.[289] Furthermore, the peak at 1441 cm^{-1} was assigned to the O–H deformation vibrations of tertiary C–OH.[506] It was observed that O-NP3 also possesses few, low intensity peaks. Mostly noticeably, a peak corresponding to the O–H bend of adsorbed water; present at 3445 cm^{-1}. A peak corresponding to overlapping C=C and C=O stretches can also be observed at 1637 cm^{-1}. In addition, a small peak at 1386 cm^{-1} is attributed to the O−H deformation vibrations of tertiary C−OH moieties. The FT-IR spectra of laponite contained four major peaks corresponding to 3409, 1631, 975 and 648 cm^{-1}. The former of these is broad and relates to overlapping Si–OH and Mg–OH stretching vibrations, as well as the O–H stretching frequency due to physiosorbed water. Peaks at 1631 and 648 cm^{-1} correlate to the O–H deformation band and the O–H bending vibration of adsorbed water, providing further evidence of water. The remaining peak at 975 cm^{-1} represents the Si–O and Si–O–Si stretching vibrations.[477,507,508] Within the FT-IR spectra of APTES, a peak was observed at 3382 cm^{-1} corresponding to the NH_2 stretching of primary amines.[483] Meanwhile, bands at 2974, 2927 and 2884 cm^{-1}, correspond to the $–CH_3$, $–CH_2$ and –CH asymmetric stretching vibrations respectively.[509] $–CH_3$ and $–CH_2$ functional groups also display bending vibrations at 1390 and 1480 cm^{-1} respectively.[509] Bands at 1295 and 1608 cm^{-1} were also present within the spectrum, relating to the $Si–CH_3$ stretching vibration and the –NH bending vibration of amines.[509] In addition, intense bands are present between 1166 and 1075 cm^{-1}, which relate to $Si–O–CH_3$ and $Si–CH_2–R$ vibrational modes.[483,509] In comparison with laponite, the FT-IR spectra for f-laponite contains some key differences. Most notably was the incorporation of sodium acetate into the material, signified by two peaks were at 1573 and 1409 cm^{-1}, which correspond to the stretching frequency of the carbonyl group and the CH_3 deformation respectively.[510,511] In addition, strong bands can also be observed between 1119 – 1010 cm^{-1}, which correspond to $S–CH_2–R$ and Si–O–Si stretches.[483,509]. Furthermore, peaks at 2996 and 2939 cm^{-1} were assigned to the $–CH_2$ and –CH asymmetric stretching vibrations respectively, whilst the O–H deformation band and O–H bending vibration of water correlate with the peak at 648 cm^{-1}.[509] The FT-IR spectra of f-NP3 reveals the presence of a broad peak at 3429 cm^{-1}, consistent with the O–H stretch. Various other peaks were also introduced into the spectrum, located at 1385, 2925 and 2876 cm^{-1}. These correspond to the C–N stretch of amide functionality and $–CH_2$ and –CH asymmetric stretching vibrations respectively, originating from the APTES carbon chain.[509] Moreover, a peak at 1578 cm^{-1} was believed to relate to the N−H in-plane bend of the amide group.[512] This appears to overlap with the C=O/C=C stretches

between 1650 – 1578 cm^{-1}. Additional peaks at 1124 and 1050 cm^{-1} were also observed, correlating with Si–CH_2–R and Si–O–Si stretches.[483,509]

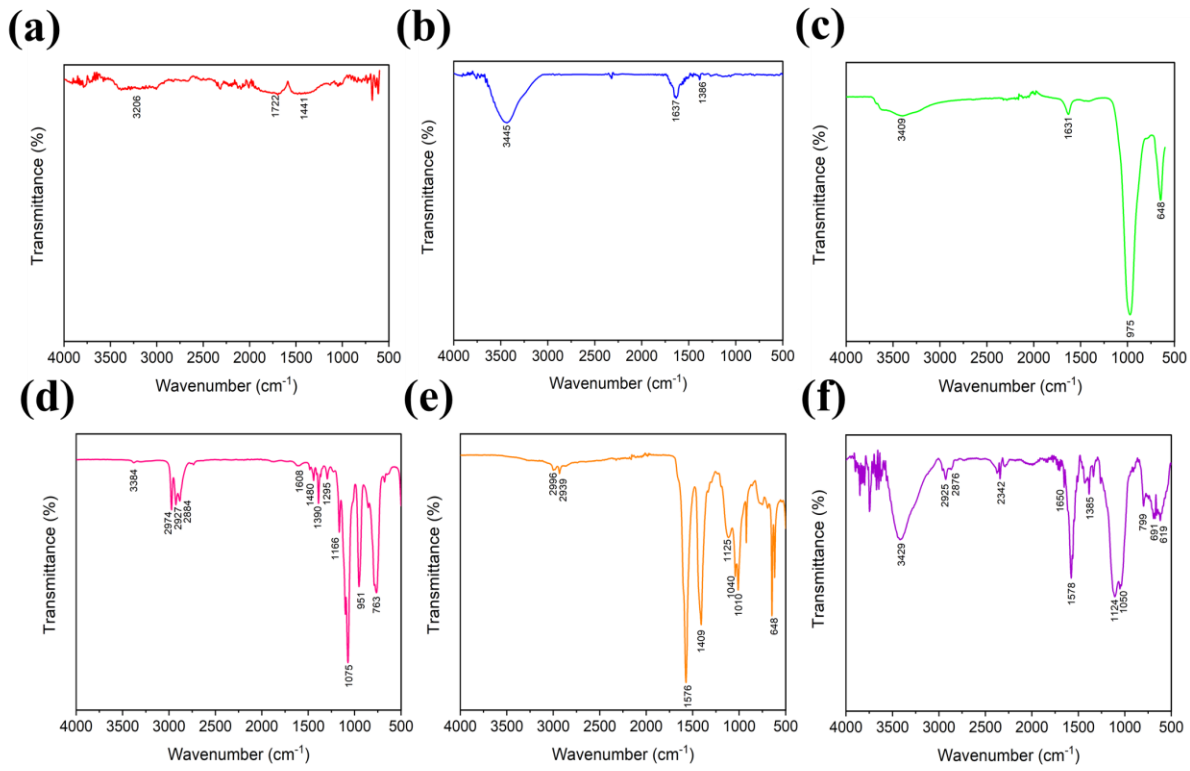

Figure 5.40 FT-IR spectra of (a) NP3 (b) O-NP3 (c) laponite (d) APTES (e) f-laponite and (f) f-NP3 using KBr transmission method analyses for all NP3 containing samples, and the ATR method for APTES, laponite and f-laponite analyses.

5.2.4.3.2.5 SEM Analysis

The structure of f-laponite differs quite significantly compared with that of laponite. During previous analysis of laponite *via* SEM imaging (Figure 5.29 (c)), it was observed that the particles possessed dimensions of between < 1 to 300 µm. In contrast, the particle sizes within f-laponite are typically much smaller, ranging in dimensions between < 1 µm to 100 µm, as shown in Figure 5.41. Such a particle size reduction was also found during laponite control, where laponite was subjected to sonication (Figure 5.29 (d)). As such, this decrease in particle size could be attributed to the mechanical mixing of laponite in dispersion, resulting in the fracturing of large particles. Furthermore, a decrease in particle size may also be attributed to

the presence of APTES moieties, extending out from the surface of the laponite disks and tactoids. These particles appear rougher in texture and drastically much less ordered than that of laponite. This indicates a reduction in edge-to-edge and face-to-face interactions between laponite disks, creating disordered and less cohesive aggregates, thus reducing their ability to form densely packed particles.[477] It may, therefore, be expected that a more porous structure would be achieved through this functionalisation, however, this does not coincide with physisorption data. As such, it is likely that the presence of APTES and sodium acetate contaminant result in the blocking of any newly formed porosity. f-NP3 consists of particles which are much less aggregated than O-NP3 or f-laponite, possessing dimensions of < 20 µm (Figure 5.42). It is believed that the reaction between O-NP3 and f-laponite results in destruction of the highly aggregated structure of O-NP3, due to the steric hindrance of f-laponite moieties within O-NP3 slit pores, revealing the presence of macro- and meso-porosity.

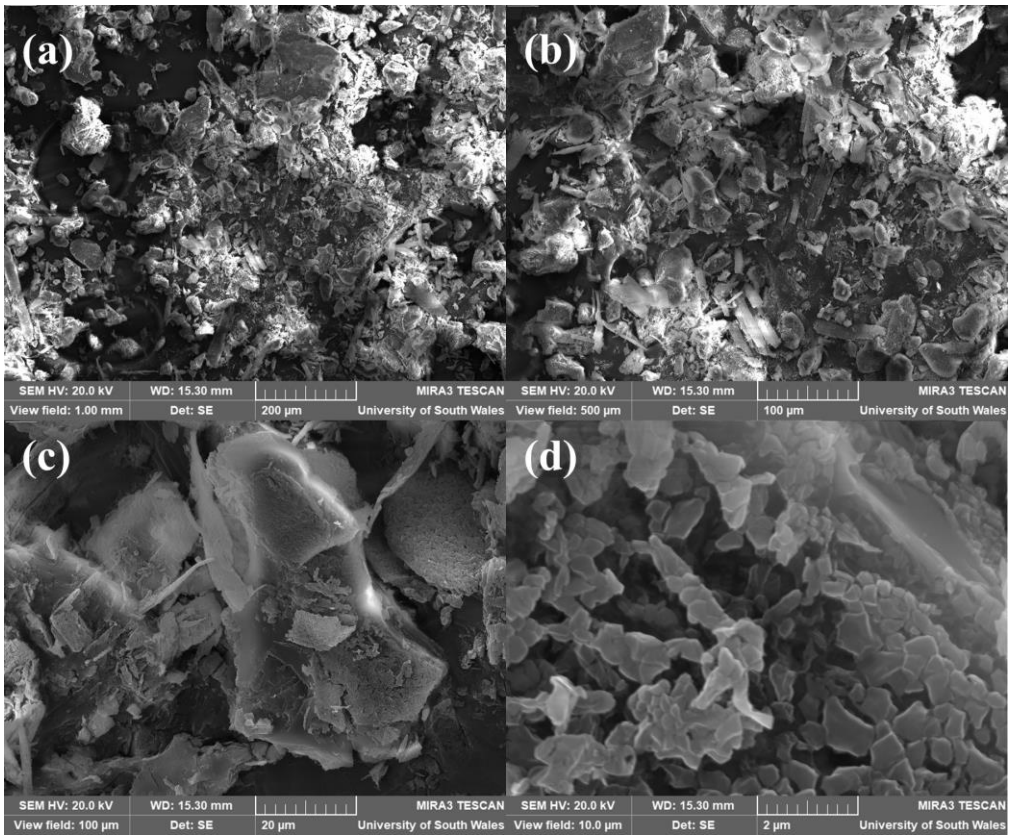

Figure 5.41 SEM images of f-laponite at magnifications of (a) 208 x (b) 415 x (c) 2.08 kx and (d) 20.76 kx acquired on SEM 2.

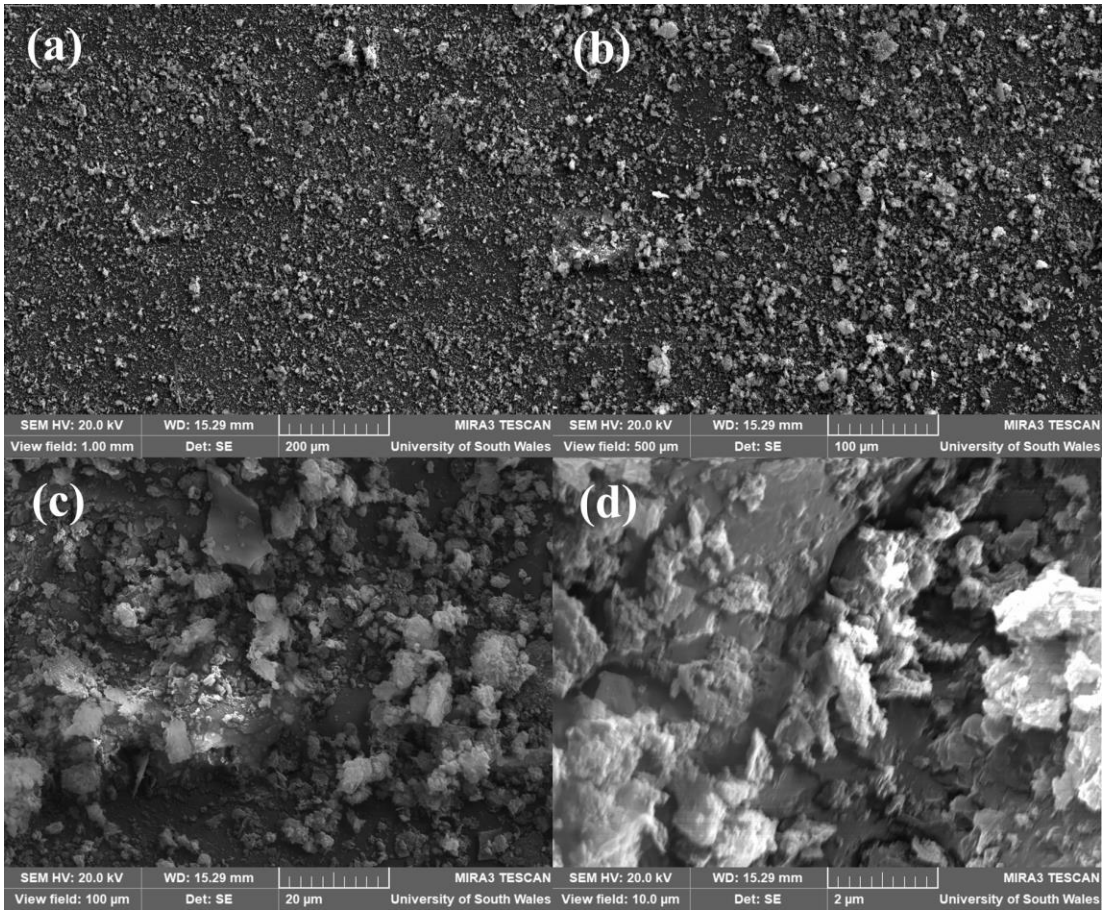

Figure 5.42 SEM images of f-NP3 at magnifications of (a) 208 x (b) 415 x (c) 2.08 kx and (d) 20.76 kx acquired on SEM 2.

5.2.4.3.3 Analysis of the Graphitic Structure of f-NP3 using Raman Spectroscopy

The Raman spectrum of f-NP3 is similar to that of NP3 and O-NP3, depicting a D band, G band and 2D band at 1353, 1580 and 2702 cm^{-1} respectively, as shown in Figure 5.43.[305–308,312] In addition, the D' peak and (D + D') peaks can also be observed at 1600 and 2933 cm^{-1} respectively, where the former band overlaps with that of the G band.[172,310] The I_D/I_G ratio of f-NP3 equates to 0.99, suggesting a similar number of defects as that of O-NP3.[312] Since the f-laponite moieties are covalently bonded to an existing carboxylic acid functional group, additional defects are not be expected to arise within the material, consistent with the findings. Furthermore, an I_{2D}/I_G ratio of 0.30 also predicts a multilayered structure, consistent with that of NP3 and O-NP3.[312] This suggests many graphitic layers remained as stacks, indicating that f-laponite moieties do not result in pillaring of individual

layers within the stacks themselves, and rather, pillar of the stacks. The Raman spectra of laponite and f-laponite (not shown) displayed no Raman peaks.

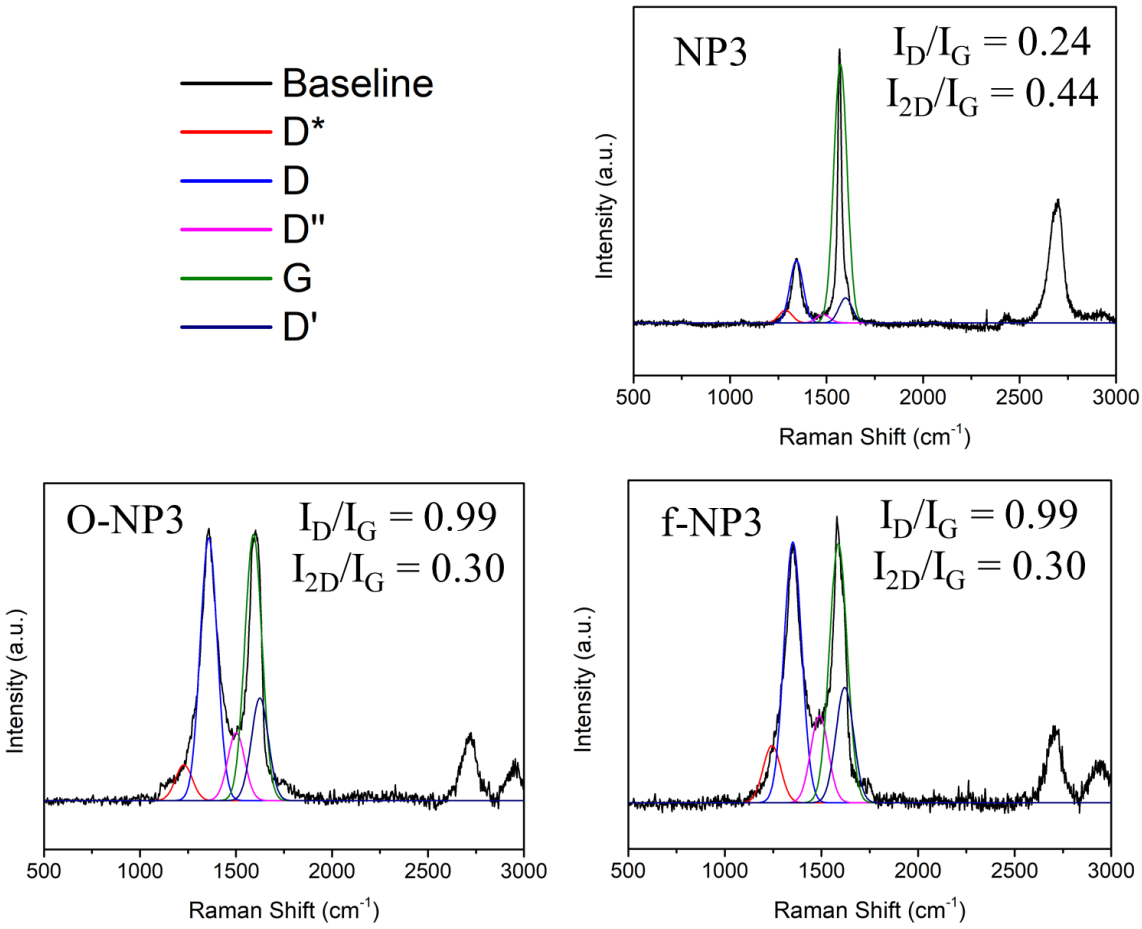

Figure 5.43 Raman spectra of NP3, O-NP3 and f-NP3 depicting their corresponding I_D/I_G and I_{2D}/I_G ratios. Peak deconvolution was performed using OriginPro software to discriminate the D and G bands from overlapping D, D'' and D' bands.*

5.2.4.3.4 XRD Analysis

The XRD pattern associated with f-NP3 displayed a strong resemblance to that of NP3 and O-NP3, as shown in Figure 5.44, possessing peaks at identical positions of 26.7, 54.8, 77.7° and peaks in the range 43° – 45° corresponding to the 2H (002)/3R (003), 2H (004)/3R (006), 2H (100)/3R (110) and 2H (100)/3R (101)/ 2H (101)/ 3R (012) phases,

respectively. More details on these peaks are provided earlier on in the text. There was, however, a small shift in the peaks corresponding to the largest interlayer spacings within f-NP3. The (001) peak can be observed at 7.3°, corresponding to an interlayer spacing of 1.211 nm. Furthermore, the peak at 23.6° within O-NP3 was shifted to 21.7° within f-NP3, corresponding to an increased interlayer spacing of 0.410 nm. As it was previously concluded that not all graphitic planes became oxidised during oxidation of NP3 to O-NP3, it was expected that many of the graphitic planes would remain within f-NP3, consistent with the findings. As such, it is likely that it was the oxidised regions within O-NP3 that underwent covalent functionalisation upon synthesis of f-NP3. During this functionalisation, an increased interlayer spacing is consistent with the expansion of oxidised layers due to large pillaring f-laponite moieties forcing widening of layers.

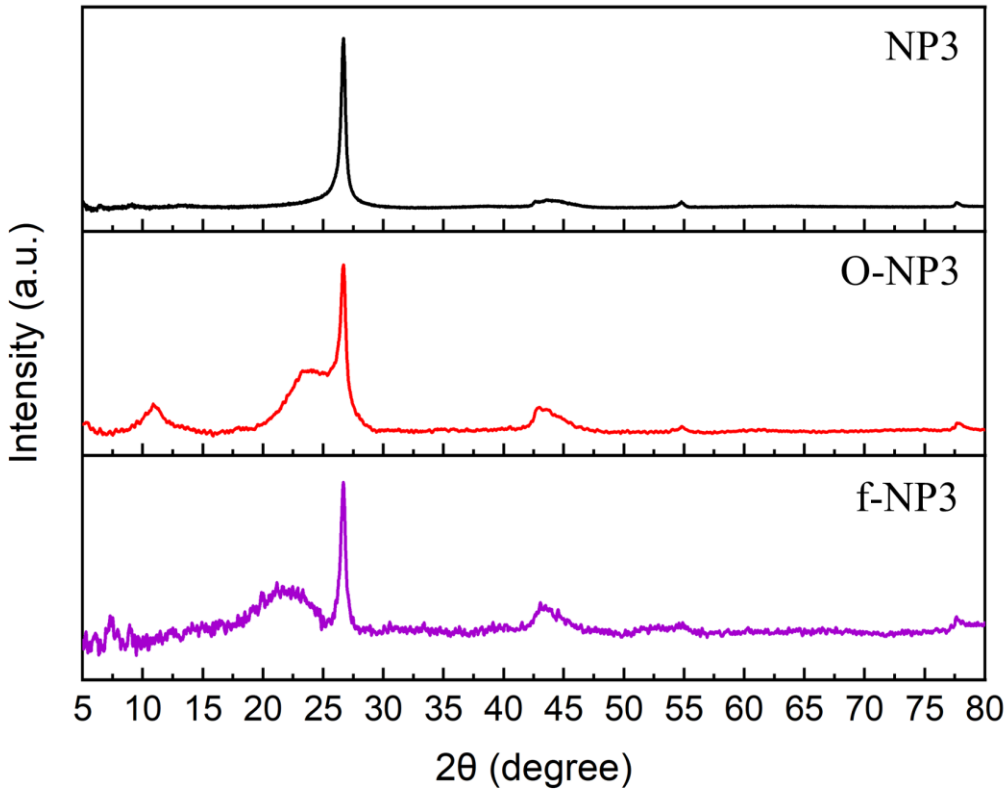

Figure 5.44 XRD patterns of NP3, O-NP3 and f-NP3.

5.2.4.3.5 TGA

TGA analysis was conducted to understand the thermal decomposition pathway of NP3, O-NP3, laponite, f-laponite and f-NP3, as shown in Figure 5.45. During this analysis, NP3 underwent a gradual mass loss corresponding to 13.9%, indicative of the decomposition of covalently and non-covalently bound oxygen moieties, after being heated to temperatures up to 770 °C.[431,432] O-NP3 underwent a larger mass loss than NP3, corresponding to 51.1% up to these temperature, indicating the presence of a large amount of oxygen functionality. Below 100 °C, mass losses of 1% within NP3 and 14% within O-NP3 were attributed to the removal of adsorbed water.[456] As such, it can be concluded that a substantially larger amount of adsorbed water resides within O-NP3 compared to O-NP3, consistent with the nature of the oxidised material and an increase in hydrogen bonding to with the water molecules.[457]

Within laponite, a total mass loss of 14.8% was observed. Initially, a rapid mass loss occurred, up to 150 °C, which corresponded to the removal of adsorbed water. Between 200 - 550 °C, additional water occupying the interlayer spacings of the material was removed. A final mass loss was also present between 550 to 800 °C corresponding to the dehydroxylation of laponite.[485]

A much larger mass loss was associated with f-laponite, corresponding to 60.6%. This mass loss occurred in two main stages (8% loss between 150 and 210 °C and 40% loss between 250 to 450 °C). This increased mass loss was attributed to the decomposition of further functionality, consistent with APTES moieties and sodium acetate respectively. In the latter species, a similar decomposition pathway was observed between 350 and 450 °C within previous work.[513] Furthermore, the removal of APTES moieties from $La_{0.8}Sr_{0.2}MnO_3$ was also shown to proceed between 150 and 400 °C, consistent with the current data.[514] It was also observed that a smaller mass loss up to 150 °C was associated with f-laponite compared with laponite, indicating the presence of less adsorbed water. This is consistent with the existence of less Si–O surface groups, which bond to water easily. Within f-NP3, a total weight loss of 42.4%, was observed, relating to the decomposition of oxygen functionality from O-NP3 and APTES moieties from f-laponite. The overall mass loss, however, was much less than that of f-laponite or O-NP3 alone, indicating an increased thermal stability for the composite structure. This increase in

stability is attributed to the composite structure being more tightly held due to covalent interaction between f-laponite and O-^{N}P3, which prevent facile loss of APTES moieties upon heating. In addition, some oxygen functionality within the O-NP3 structure is likely to be "protected" by the presence of f-laponite linkers. This increase in thermal stability was also observed within previous works upon composite addition.[466]

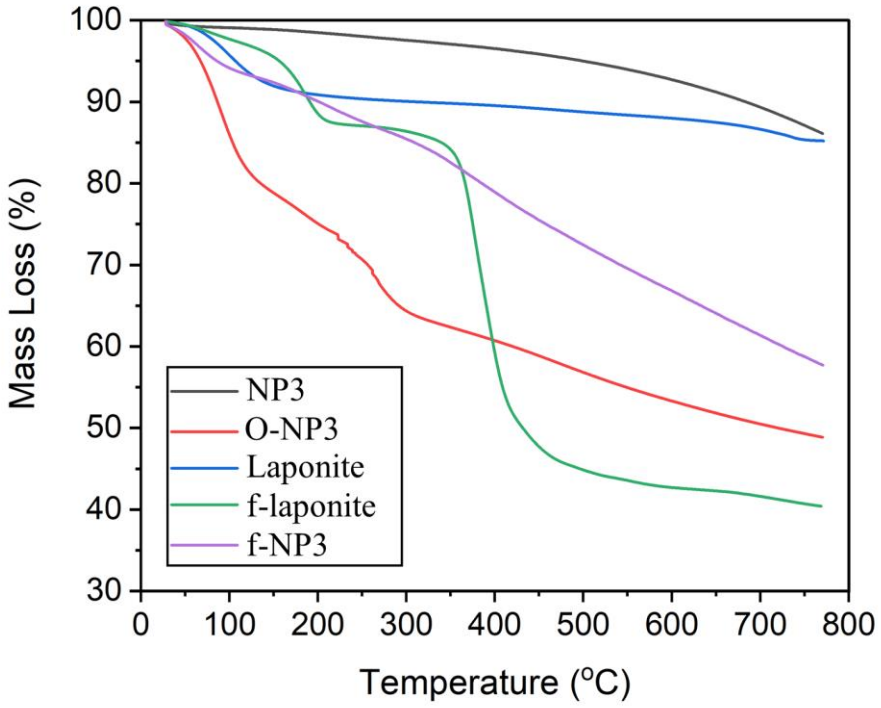

Figure 5.45 TGA curves for NP3, O-NP3, laponite, f-laponite and f-NP3.

5.3 Conclusion

This chapter explores the surface area and porosity of NP materials which were found to contain extensive slit pores between stacks of orderly aligned layers. These slit pores were estimated to range in size between the mesoporous and macroporous regions, possessing relatively large average BJH pore width between 6.3 – 10.4 nm. BJH data was applied to provide an estimation of these slit pore widths, thereby enabling subsequent estimation of the distance between stacks within NP4. Such a methodology coincided with measurements

obtained *via* SEM imaging and AFM and XRD analyses. Upon investigation into the effects of oxidation on surface area and porosity, it was determined that oxidation of NP3 *via* the modified Hummers' method resulted in a substantial reduction in the BET surface area. This was attributed to a decrease in porosity available to nitrogen adsorbate molecules, due to blockage of slit-like micropores and mesopores. XRD provided evidence of interlayer spacing expansion, suggesting that newly formed micropores were created during the oxidation process. SEM images showed that oxidation of the material caused considerable aggregation. Employing laponite as a covalently attached pillaring device served to introduce further slit pores into the structure, to increase the BET surface area. This was found to increase from 28.9 m^2/g in O-NP3 to 112.6 m^2/g in f-NP3. Moreover, the novel composite: f-NP3 could serve as an advantageous material within composite applications. For example, the addition of high surface area NP, with high aspect ratios, to laponite, could enhance the clay's barrier properties, acting as a filler within the interparticle regions.[232] Furthermore, the application of laponite within surface coatings could be improved through the addition of NP, providing it with additional strength and flexibility.[463,515] In summary, this chapter enhances the knowledge of the porous structure of NPs, identifies a novel application of BJH analysis and distinguishes a novel functionalisation strategy to pillar slit pores, to obtain oxidised NP materials with enhanced surface areas.

6 Development of Plasma-Exfoliated Graphitic Material-Based Oleophobic Hydrophilic Membranes for Advanced Applications

6.1 Synopsis

Within this chapter, a novel oleophobic/hydrophilic NP-based composite was developed, comprising of NP4, polydiallyldimethylammonium chloride (PDDA) polyelectrolyte and sodium perfluorooactanoate (PFO) fluorosurfactant. This unique composite was rendered into free-standing films, and also coated upon various substrates including Kevlar, carbon fibre, glass fibre, nylon and stainless-steel mesh. Tests were performed on the films and coated substrates to assess their ability to retain oil, whilst simultaneously allowing the passive release of water. Meanwhile the morphology, structure, and oleophobic/hydrophilic properties associated with the films and coated substrates, were investigated. Selected coated substrates were then applied as membranes for oil/water separation within the context of oil-spill clean-up and within aircraft propellant tanks.

6.2 Introduction

Oil/water separation is imperative for a number of applications, including oil-spill clean-up, anti-fogging films, detergent free-cleaning surfaces, liquid-liquid separation membranes and within bearing liners and pressure vessels, to prevent moisture build-up within aircraft equipment.[516–518] In regard to the former, there are huge economic and environmental impacts associated with the spilling of oil in oceans. The removal of this oil from water is not a straightforward process since the oil undergoes a number of processes concurrently. These include spreading, evaporation, emulsification, photo-oxidation, dispersion, sinking, resurfacing, tar ball formation and biodegradation.[519] At present there are various methods to remove and contain the oil, including *in-situ* burning of oil slick and the use of mechanical techniques such as booms, bioremediation, dispersants and sorbents.[519] Unfortunately, these methods are not free of drawbacks and it is therefore, beneficial to continue investigation into alternative strategies for oil removal.

Another key issue associated with undesirable water/oil mixing occurs within aircraft fuel tanks. Within fuel tanks exists small openings which allow the pressure to be maintained within

the interior of the tank. Whilst these openings are crucial within many fuel tank designs, they cause the tank to become susceptible to an ingress of atmospheric water. If water is drawn into the tank, water/fuel mixing can occur, resulting in the inevitable accumulation of water at the base of the tank, due to its increased density.[520] As water build-up continues in this manner, several issues arise. The presence of water reduces the fuel-storage capacity, increases the fuel tank mass, raises the risk of biocontamination and may become frozen within colder conditions, causing obstruction to the normal working function. In practice, this water is removed through a scavenger pump or drainage valves, or a combination of both. Unfortunately, scavenger pumps are susceptible to malfunction and drainage valves require manual operation, resulting in additional costs.

Oil/water separation may proceed through the removal of oil from water using a hydrophobic/oleophilic material or *via* the removal of water from oil, relating to a hydrophilic/oleophobic material. The former of this has been investigated in some detail, however, such materials suffer the major drawback of fouling, where unwanted oil deposits remain in the surface and reduce the material's ability to be recycled.[516] Hydrophilic/oleophobic materials are less common since it is widely accepted that liquids with higher surface tensions possess large contact angles. As such, the water contact angle (WCA) will typically exceed that of the oil contact angle (OCA), since most oils possess much lower surface tension values than water.[520] In essence, a given solid surface is typically more wettable to oil than water. Of course, there are some exceptions, and the morphology and properties of surfaces which are more wettable to water than oil are specifically designed to overcome these considerations. These types of surfaces are highly desirable for the applications described above, and have been reviewed by Wang and Gong.[518]

Common reagents which are implemented into oleophobic/hydrophilic membranes and surfaces involve fluorosurfactants, which typically possess ultralow surface energies (< 20 mN/m using hexadecane).[521] In principle these low surface energy surfaces should not be wettable to oil or water, however, it has been found that water can penetrate the reagents with much success. For example, Badyal reported the use of cationic fluorosurfactants complexed to well-defined plasma-deposited acrylic acid and maleic anhydride surfaces, which in turn allowed for simultaneous oleophobic/hydrophilic behaviour.[522,523] It was believed that the ultrathin array of aligned perfluorocarbon fluorosurfactant tails, present at the liquid-solid interface, were effective in repelling non-polar liquids, whilst allowing wetting of polar water

molecules. The latter were believed to be able to penetrate into the hydrophilic subsurface or cause the perfluoro tails to reorganise to expose non-hydrophilic regions.

Furthermore, a combination of polydiallyldimethylammonium chloride (PDDA) and sodium perfluorooctanoate fluorosurfactant (PFO) with SiO_2 nanoparticles have also been implemented commonly within several research groups.[524–526] Zhou applied this combination as a coating upon various substrates including a glass slide, *via* a spray coating technique.[525] The surface was then plasma-treated in air to introduce hydrophilic polar groups to enhance favourable interaction with water and unfavourable interaction with hexadecane. Zhou found that water droplets wet the coating rapidly, whilst oil droplets rolled off the coating at low tilt angles, as shown in Figure 6.1.

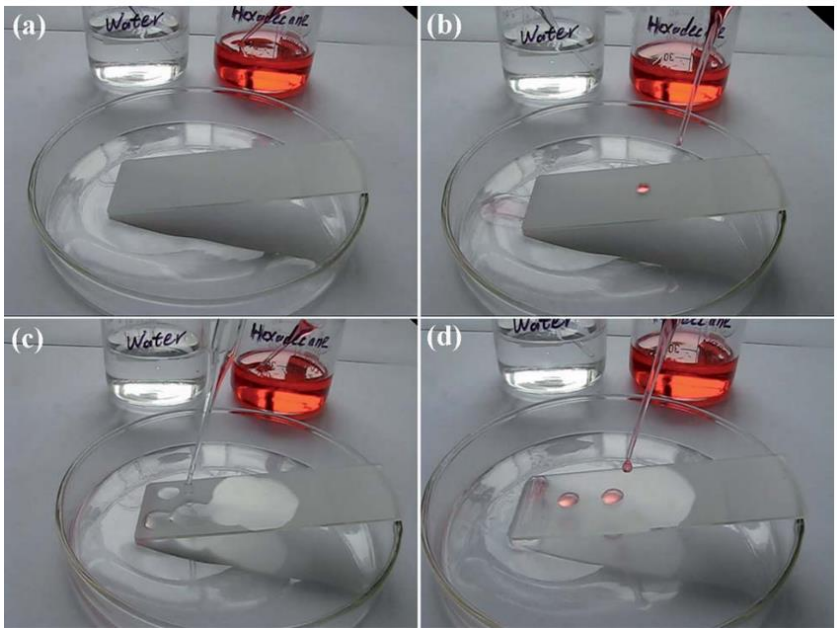

Figure 6.1 (a) A glass slide coated with PDDA/PFO/SiO_2 and treated with oxygen plasma to introduce hydrophilic polar groups to the surface to enhance favourable interaction with water and unfavourable interaction with hexadecane; (b) deposition of hexadecane on the surface causing the droplet to roll off easily; (c) deposition of water on the surface causing droplets to wet the surface rapidly; (d) the deposition of hexadecane upon the water-wetted surface causing droplets to roll off easily. Reprinted from reference [525].

Yoon and co-workers also exploited this reagent system during the coating of stainless-steel mesh.[526] They tested the ability of the coated mesh to enable oil/water separation by passing hexadecane, dyed with Oil Red O, and water, dyed with methylene blue, through their mesh.

It was found that the coated mesh was successful in preventing oil passage, whilst allowing passage of water through. Furthermore, they also introduced a graphene plug which was able to purify the water by extracting methylene blue dye from the separated water. In this regard, the plug prevented the passage of the dye molecules by promoting their adsorption upon the surface of the graphene sheets, *via* π–π stacking interactions, thus, allowing for colourless water to pass through. This provided the mesh with the potential application as a membrane for wastewater clean-up, within the dyeing industry. The group also achieved contact angles of hexadecane and water of 95 (± 2)° and 0°, respectively, on the coated mesh. Yang and co-workers utilised the same combination of reagents, and found that PDDA adsorbed to the surface of SiO_2 readily, meanwhile PFO anions coordinated to quaternary ammonium groups of PDDA to form a new composite.[524] They synthesised an aqueous dispersion of these reagents and coated them upon a stainless-steel mesh using a spray gun. Brown and Bhushan also employed PDDA polyelectrolyte, but with Capstone™ FS-50 fluorosurfactant and SiO_2 nanoparticles.[527,528] They coated this onto glass and found that the surface displayed oleophobic/superhydrophilic behaviour, achieving hexadecane contact angles exceeding 155°, and tilt angles of < 4°.

Within many examples of oleophobic/hydrophilic surfaces, SiO_2 nanoparticles are often applied.[516] The incentive behind this addition relates to their role as a "roughness component", which has the effect of amplifying the oleophobic/hydrophilic behaviour of the material. It is found that the introduction of roughness is effective in providing more pores to the material. As such, a larger surface area is provided, thus, enhancing the contact made between the material and the liquid droplets, leading to amplification of the solid-liquid interactions. This scenario is described by the Wenzel regime.[529,530]

The mechanisms behind the oleophobic/hydrophilic behaviour of fluorosurfactant/polyelectrolyte coupled surfaces have been discussed in some detail by Wang and Gong, although these remain under debate.[518] An early suggestion related to surface rearrangement or the "flip-flop" mechanism, as first proposed by Sawada in 1996.[531] When water molecules make contact with the surface, rearrangement takes place so that the surface exposes its hydrophilic regions, thereby attracting water. When oil molecules make contact however, no rearrangement takes place and the topmost fluorinated chains, with low surface energy, repel the oil. This ability for the different liquids to "see" different aspects of the surface was utilised to describe the behaviour of various oleophobic/hydrophilic surfaces.[522,523,531–535] An alternate theory relates to the Cassie-Baxter model.[536] Within nano-scale rough surfaces,

containing hierarchical structures underwater, water becomes trapped below the oil droplet, resulting in formation of an oil/water/solid interface within the water system.[537] Such structures were detected by the extremely low adhesive force between the oil droplet and the surface. Further developments on the mechanism were made in the last decade. When water molecules make contact with a silicon surface, coated with perfluoropolyether, they pass down towards the hydrophilic sub-surface, causing wetting to occur. It is thought that this occurs through defects in the fluorinated layer. Since water penetrates the polymer layer and is attracted to the high surface tension subsurface, it would make sense that oil would also be attracted to the high surface tension substrate also, to a much larger extent that the perfluorinated moieties.[538] However, in contrast to water molecules, the oil molecules are too large to penetrate these gaps instantly.[538] This is due to size exclusion and the size of the polymer layer is therefore crucial in optimising the passage of water, whilst preventing the passage of oil, for a substantial time. Within Li's work, it was observed that the OCA decreased over time, therefore, its initial contact angle was considered kinetic in nature, rather than the equilibrium value.[538,539] According to this size exclusion theory, oil molecules will ultimately penetrate these defects also. In this context, the initial rearrangement mechanism proposed by Sawada, was disregarded. The surface within Li's work comprised of polymers containing polar hydroxy groups which were believed to favour interaction with the silicon substrate, rather than the deposited water molecules. It was therefore deemed improbable that the polymers would flip, to reveal their polar hydroxy groups to water molecules in preference.[539,540]

In light of the success of these literature investigations, a combination of PDDA and PFO reagents were utilised in this work to synthesise free-standing NP4 films and coatings with oleophobic/hydrophilic properties. It was hypothesised that the large surface area associated with NP4 would act as a platform for the adsorption of PDDA/PFO, as well as providing the necessary roughness component to amplify oleophobic/hydrophilic behaviour. The application of these films and coated substrates was postulated and tested within the context of aircraft propellant tanks and oil-spill clean-up. This chapter therefore provides a novel application for NP material within the context of oil/water separation.

6.3 Results and Discussion

6.3.1 NP4-PP Films and Coated Substrates

NP4-PP composite was synthesised *via* a two-step procedure as shown in Scheme 6.1 (a) . Initially step (i) involved the addition of PDDA to NP4, to promote adsorption of the polyelectrolyte onto the graphitic surface, as well to encourage access of PDDA moieties into NP4's slit pores. The resultant material is denoted PDDA/NP4. During step (ii), PFO was then added dropwise to enable polyelectrolyte/fluorosurfactant complexation, in accordance with previous investigations, as outlined in the introductory section of this chapter.[524–526] The addition of PFO coincided with an approximate 1:1 stoichiometry relative to PDDA, and resulted in the formation of a thick black sludge, as shown in Scheme 6.1 (a) (b). Upon repeated washing cycles, to remove NaCl and loosely bound PDDA/PFO reagents, and subsequent drying under vacuum for 12 hours, a solid composite material, denoted as NP4-PP composite, was formed.

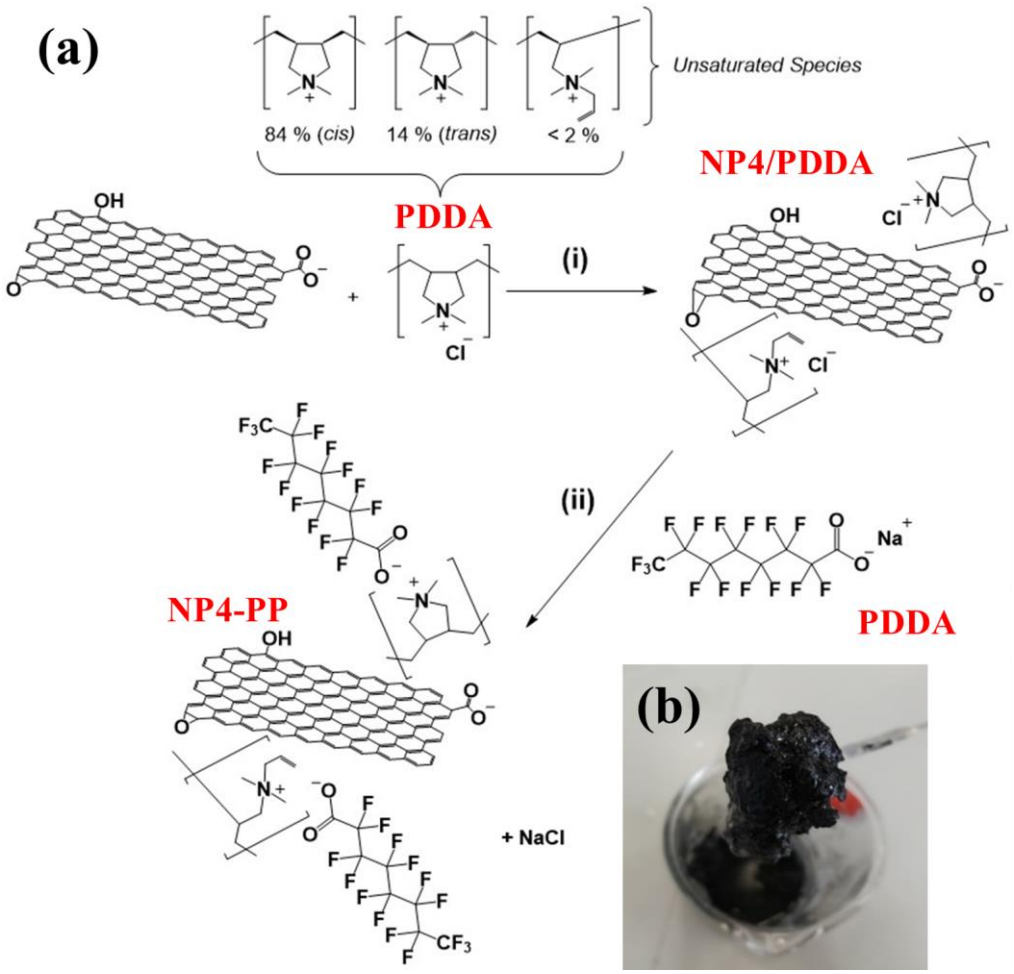

Scheme 6.1 (a) Schematic of NP4-PP synthesis utilising a two-step approach consisting of (i) the addition of PDDA and NP4 resulting in adsorption of PDDA on NP4 and (ii) the addition of PFO to NP4/PDDA resulting in complexation of PDDA and PFO moieties within the NP4 material. PDDA reagent consists of three isomers, including the cis and trans isomers and an unsaturated species containing a pendent double bond, consistent with previous work.[541] *A photograph of NP4-PP as an aqueous sludge is depicted within (b).*

Redispersion of NP4-PP composite in methanol allowed the formation of free-standing films and coated substrates. Bath sonication was used to assist the formation of the dispersion. In the case of film formation, two concentrations of this dispersion were initially synthesised. In the first instance, 1.75 g of NP4-PP was added to 35 mL of methanol and poured into a section of the eight-sectioned metal tray shown in Figure 6.2. This was repeated eight times to fill all sections of the tray. Solvent evaporation under ambient conditions was then allowed overnight, affording eight identical free-standing films comprised of NP4-PP (each denoted as NP4-PP thick film). The latter concentration consisted of only 0.80 g of NP4-PP in 35 mL of methanol. The same process was repeated in this case, affording a further eight free-standing films; each denoted as NP4-PP thin film.

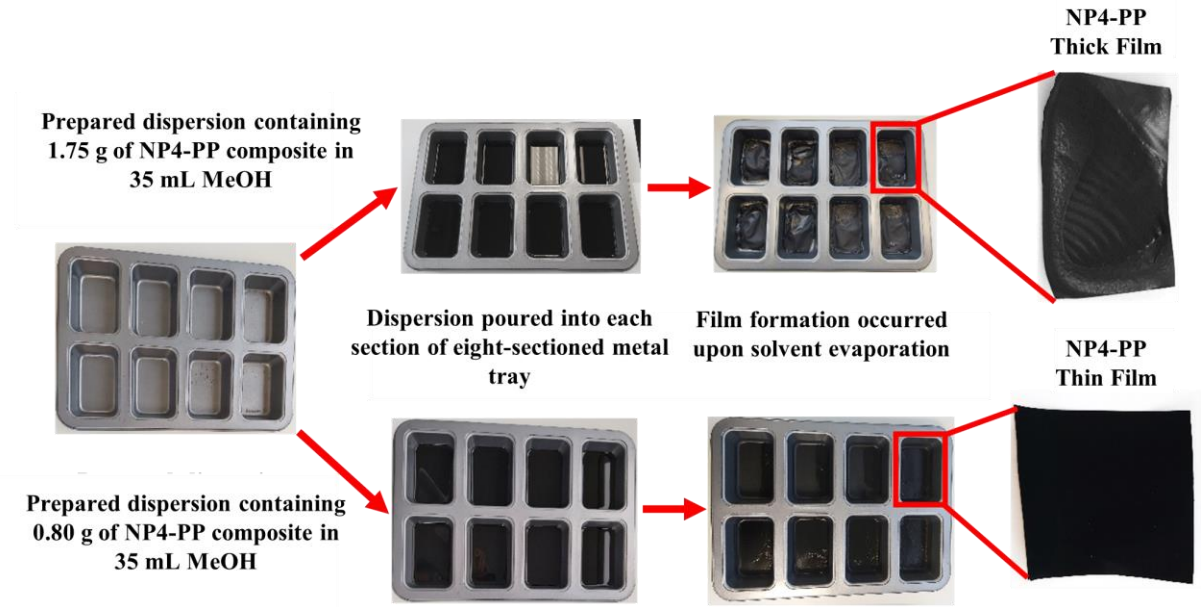

Figure 6.2 Schematic depicting the synthesis of NP4-PP thick film and NP4-PP thin film. The processes involved the redispersion of different concentrations of NP4-PP composite in methanol (1.75 g per 35 mL methanol and 0.80 g per 35 mL methanol for NP4-PP thick film and NP4-PP thin film respectively). The dispersions were subsequently poured into each section of an eight-sectioned metal tray. Through solvent evaporation overnight in air, free-standing films were fabricated.

NP4-PP thick film and NP4-PP thin film possessed similar appearances, both consisting of black films. NP4-PP thick film, however, possessed much thicker dimensions, as expected. SEM imaging was conducted on the side of each film to determine the dimensions across three regions of the edge, to gain an understanding of the film thickness (Figure 6.3). NP4-PP thick film possesses thicknesses which vary quite drastically across different regions of the film edge, corresponding to 471, 318 and 285 µm. In contrast, NP4-PP thin film possesses a more even thickness distribution, where thicknesses correspond to 121, 130 and 142 µm. As such, the thickness of NP4-PP thick film is approximately three times that of NP4-PP thin film. In addition, NP4-PP thick film was more brittle in nature. In fact, upon bending a section of each film with tweezers, it was observed that the NP4-PP thick film was susceptible to snapping, whilst the NP4-PP thin film could be bent repeatedly with no observable damage, thus showing improved flexibility Figure 6.4.

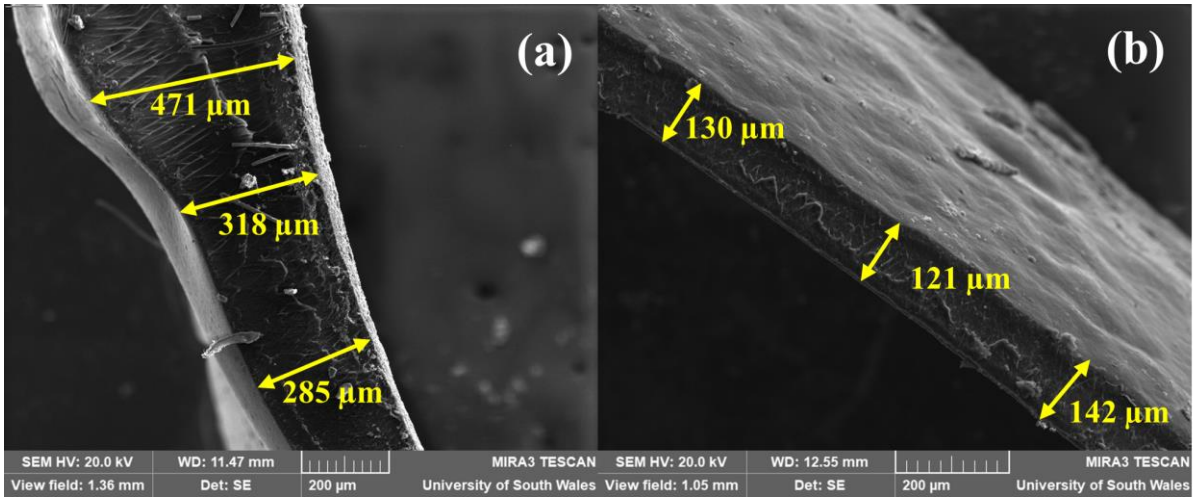

Figure 6.3 SEM images showing the thickness of three edge regions of (a) NP4-PP thick film and (b) NP4-PP thin film at magnifications of 152 x and 198 x respectively.

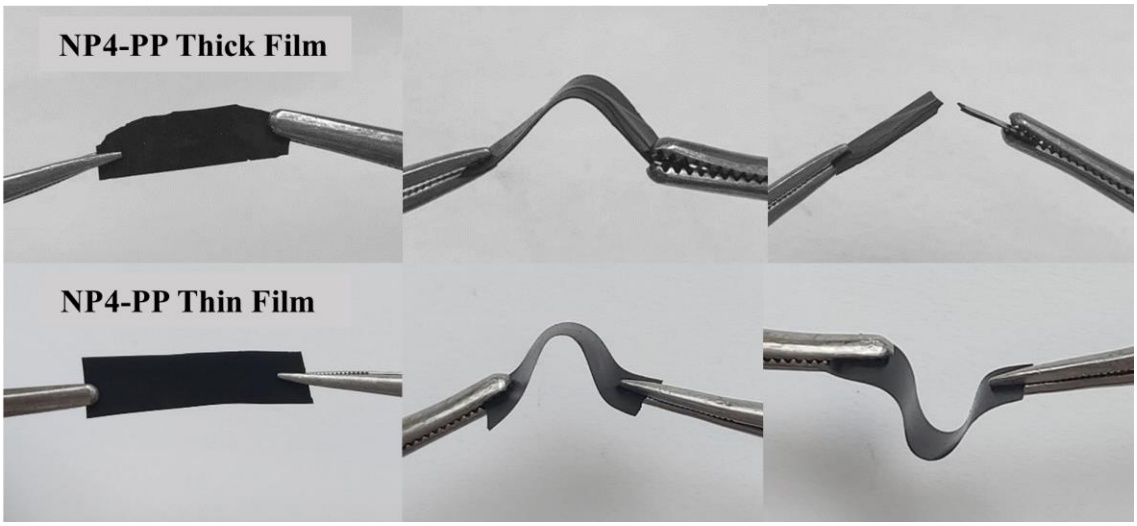

Figure 6.4 Photographs of NP4-PP thick film (above) and NP4-PP thin film (below), illustrating the ability of the films to be bent with tweezers. NP4-PP thick film snapped easily as it was bent, whereas NP4-PP thin film could be bent repeatedly with no visible damage to the film.

The coated substrates were synthesised using a similar methodology to that of the NP4-PP films and are depicted in Figure 6.5. The substrates (Kevlar, carbon fibre, glass fibre, nylon and stainless-steel mesh) were deposited within the bottom of a single-sectioned metal tray, and a dispersion consisting of 2.5 g of NP4-PP in 150 mL methanol was then poured over the substrates. The tray was left overnight, to enable solvent evaporation, thereby affording a black NP4-PP coating upon each substrate. In addition, nylon was also coated with two slightly less

concentrated dispersions of NP4-PP composite, including 0.26 g per 150 mL and 0.16 g per 150 mL, referred to as NP4-PP coated nylon 3 and NP4-PP coated nylon 2 respectively. It was found that the coating upon Kevlar, carbon fibre and glass fibre appeared homogeneous. These coatings were uniformly black in colour. Coated nylon and coated stainless-steel mesh, however, appeared to acquire a less homogenous coating, where some regions appeared darker, indicating well coated regions, whilst other regions appeared lighter, indicating less well-coated regions. This was particularly obvious for coated nylon synthesised with lower concentrations of NP4-PP dispersions.

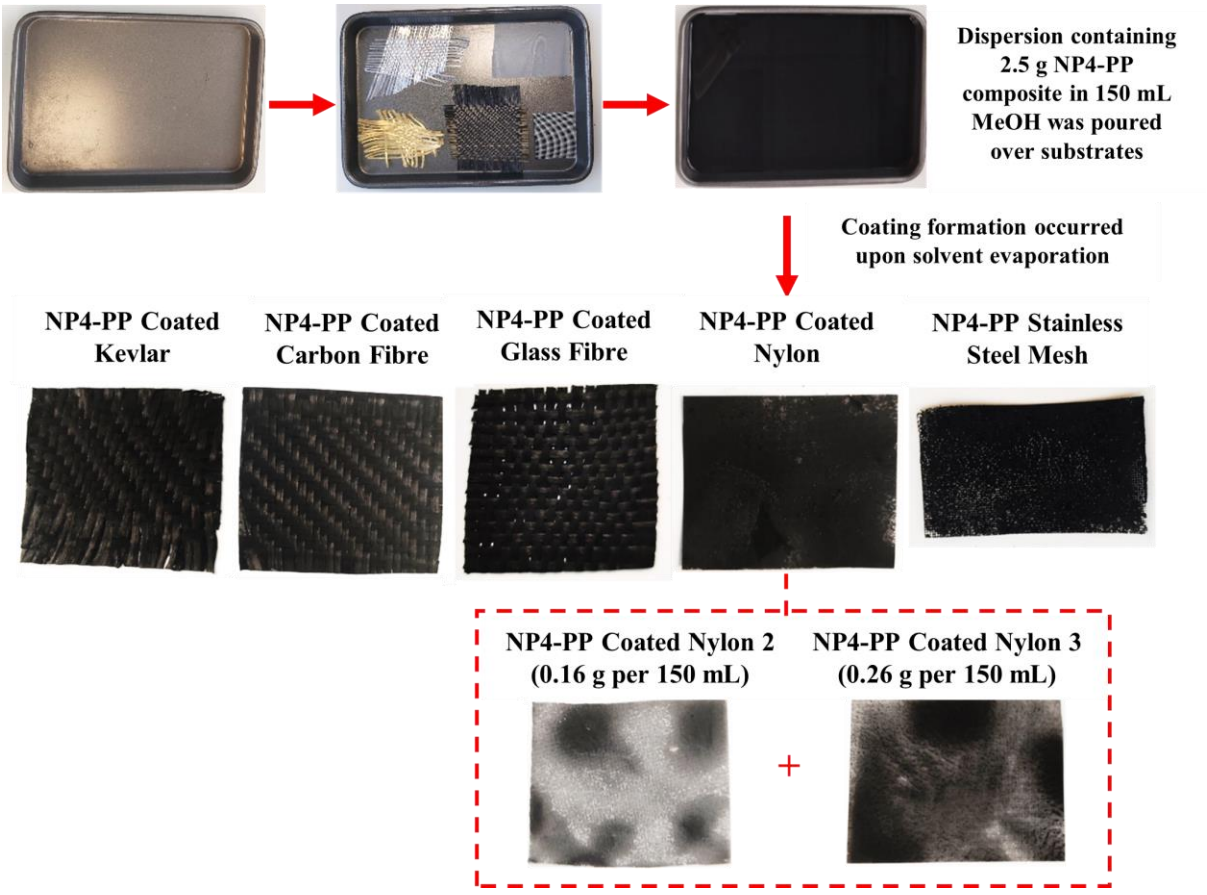

Figure 6.5 Schematic depicting the synthesis of NP4-PP coated substrates. The process involved redispersion of 2.5 g NP4-PP composite in 150 mL methanol, followed by pouring of the dispersion over substrates: Kevlar, carbon fibre, glass fibre, nylon and stainless-steel mesh deposited within a single-sectioned metal tray. Solvent evaporation in air overnight resulted in a coating of NP4-PP over the substrates. In addition, nylon was also coated using the same methodology using less concentrated dispersions including 0.26 g NP4-PP composite in 150 mL MeOH and 0.16 g NP4-PP composite in 150 mL MeOH (referred to as coated nylon 2 and coated nylon 3 respectively).

6.3.2 Chemical Composition of NP4-PP and Interactions Between Reagents using XPS

XPS was employed to analyse the surface elemental composition present within NP4, PDDA, NP4/PDDA, PFO and NP4-PP composite to build an understanding of the interactions between reagents. As such, the nature of the products obtained from steps (i) and (ii) within Scheme 6.1 (a) could be determined (*vide infra*). The quantitative data associated with this analysis is presented within Table 6.1, and the corresponding survey spectra and high-resolution spectra are depicted in Figures 6.6 and Figures 6.8 − 6.11. Initial analysis of NP4 suggested that the material incorporated carbon, oxygen and nitrogen with atomic percentage compositions (at.%) of 93.4, 0.3 and 6.3, respectively (Table 6.1 and Figure 6.6 (a)). Deconvolution of the high-resolution C 1s spectrum indicated the presence of seven carbon environments, as shown in Figure 6.6 (b). These environments corresponded to binding energies of 284.4, 284.8, 286.2, 287.7, 289.3, 290.8 and 293.9 eV, relating to sp^2, sp^3, C−O, C=O, O−C=O and π−π* satellite components, respectively. The presence of π−π* satellite structure, in combination with a large proportion of sp^2 character, signify the presence of extensive π bonding within the graphitic material.[542] The appearance of oxygen functionality is also observed in the form of C=O, C−O and O−C=O, suggesting the presence of hydroxy, epoxide, carboxyl, and carbonyl functional groups.[543] These functionalities are further evidenced within the O 1s state (Figure 6.6 (c)). The O 1s spectra contains four peaks at 531.5, 532.9, 535.4 and 538.0 eV, which correspond to C=O, C−O−C, C−OH and the O 1s satellite structure, respectively. A trace amount of nitrogen is also indicated by the N 1s state at 400.4 eV (see Figure 6.6 (d)). This binding energy is characteristic of a nitrogen contaminant in the form of NH_2/NH_x. This may have been introduced to NP4 during the gas feed within the plasma-synthesis procedure.

Table 6.1 XPS surface elemental composition data for NP4, PDDA, NP4/PDDA, PFO and NP4-PP composite.

Orbital	Atomic Concentration (%)				
	NP4	PDDA	NP4/PDDA	PFO	NP4-PP
C 1s	93.4	69.3	73.5	28.5	55.1
N 1s	0.3	7.4	8.2	−	3.4
O 1s	6.3	11.2	6.0	4.7	4.7
Cl 2p	-	7.6	9.1	−	1.1
Na 1s	-	2.5	2.3	4.7	0.3
S 2p	-	2.0	-	-	-
F 1s	-	-	0.97	62.1	35.4

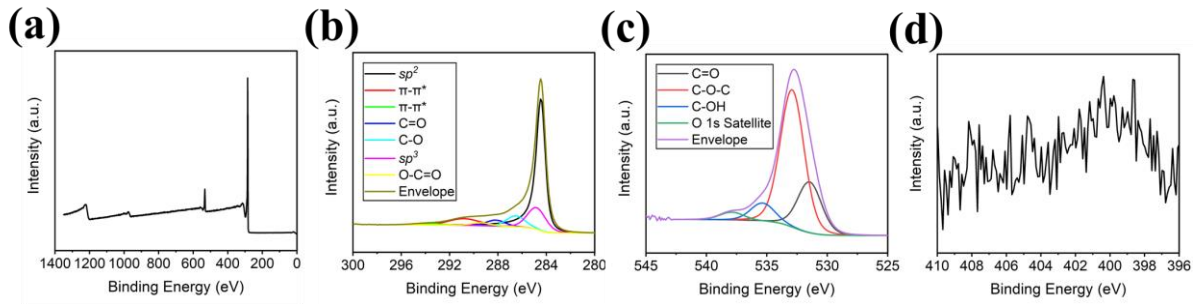

Figure 6.6 XPS analysis of NP4 including (a) survey spectrum and high-resolution spectra of the (b) deconvoluted C 1s orbital (c) deconvoluted O 1s orbital and (d) N 1s orbital.

XPS analysis was subsequently carried out on PDDA (Figure 6.8). This enables comparisons to be made between NP4-PP and NP4, to understand any surface elemental changes which occur as PDDA is adsorbed onto NP4. Previous investigations have discussed the adsorption of PDDA upon graphitic materials including CNTs, rGO and GO.[544–550] It was suggested by several of these authors that an electrostatic interaction exists between the negatively charged structures of GO or rGO and the positive charge of the PDDA.[548–551] It is well-established that the presence of −COOH and −OH functional groups on the surface of such materials are capable of ionising in aqueous solution, therefore, providing the surface with a negative charge.[552–554] As such, electrostatic interaction was considered as a potential adsorption bonding process between the NP4 and PDDA components. In contrast, other research has suggested that adsorption may take place *via* π−π bonding between the unsaturated species, containing pendant residual double bonds, present within PDDA reagent (shown in Scheme 6.1 (a)), with the conjugated π system of the graphitic network. This unsaturated species is believed to originate from the polymerisation synthesis of PDDA, whilst accounting for < 2 at.% of the structure. It was reported that its presence was recognised by a shake-up peak at 290.9 eV, associated with the π→π* transitions within the XPS spectrum.[541,547] Within this current work, XPS analysis of PDDA did not reveal the presence of any shake-up peak within the C 1s spectrum, as evidenced in Figure 6.8 (b). Instead, two peaks at 284.4 and 285.6 eV were observed; corresponding to the carbons bonded to carbon and hydrogen only (CH_x), and carbons bonded to the quaternary ammonium group ($N-CH_x$) within the polyelectrolyte, respectively.[547] The ^{13}C NMR spectra of PDDA did, however, indicate the presence of alkene-

type species, depicting two small peaks at 128.64 and 123.93 ppm (see Figure 6.7), which correspond to the unsaturated species of PDDA.

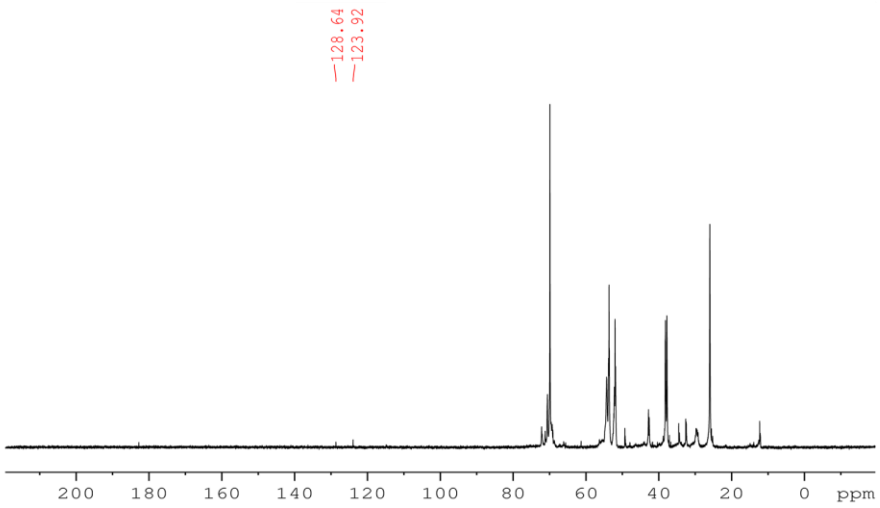

Figure 6.7 ^{13}C NMR spectrum of PDDA showing the presence of alkene peaks at 128.64 and 123.93 ppm.

Several explanations may be used to explain the absence of this shake-up peak from the XPS spectrum including: (1) PDDA may possess an orientation where the C=C bond within the unsaturated species do not reside at the surface region; (2) The unsaturated species is present in too small concentration at the surface region to be detected; and/or (3) the binding energy associated with the unsaturated species overlaps with that of the CH_X and $N-CH_X$ environments of the cis/trans isomers. Since previous works have detected the presence of this unsaturated impurity and evidence of unsaturation is obtained within the ^{13}C NMR spectrum, it is deemed plausible that interactions may take place through $\pi-\pi$ bonding in some regions of the sample.

The N 1s spectra of PDDA reveals the presence of four nitrogen environments at 401.7, 405.9, 398.1 and 399.2 eV (Figure 6.8 (c)). The former of these relates to the quaternary (4^o) ammonium group present within all isomeric forms of PDDA, including the cis/trans isomer and unsaturated species (see Scheme 6.1 (a)). These each possess negligible deviations from each other in their binding energy values due to the presence of the positively charged nitrogen centre.[547] The binding energy at 405.9 eV is characteristic of N−O environments, likely in the form of NO_2 or NO_3.[555] Such species may have contaminated PDDA, perhaps during the synthesis procedure. Moreover, the peak at 399.2 eV is likely to correspond to a trace amount

of contamination in the form of polymeric amines. The final peak at 398.1 eV, relates to a reduced form of nitrogen. When analysing PDDA *via* XPS, several authors have also observed a peak between 399 – 400 eV, which they have assigned to "the uncharged side product" of the quaternary ammonium group, correlating to approximately 7% of the total nitrogen composition.[547,556–558] Marinoiu and co-workers suggested that this product originated from the partial loss of Cl^+ from PDDA.[557] During our investigations, we sought to examine the N 1s spectrum in more detail to explain and identify the origin of the uncharged side product. It was hypothesised that the XPS analysis promoted reduction of the quaternary ammonium group to form the uncharged side product. In order to explore this further, the XPS analysis was repeated on the same sample 420 seconds after the initial nitrogen scan (Figure 6.8 (d)). It was found that the atomic composition of this peak did in fact increase from 0.1 to 0.5 at.%, suggesting that the XPS conditions were indeed, causing reduction. The reduction process is likely to proceed *via* elimination of methyl chloride from the quaternary R_4N^+, resulting in the formation of a neutrally charged species, as shown in Scheme 6.2. Alternatively, this peak may also correspond to nitrogen within an NH_2 type environment, formed during the reduction NO_2 to NH_2, if indeed, the nitro species was present. X-ray beam reduction has been observed in this way within previous reports and this serves to demonstrate that functional group changes can occur during XPS analysis.[197,385,386] This latter scenario, however, is less likely since a peak at approximately 406 eV, resembling the NO_2 environment, is not observed within the N 1s spectra of NP4/PDDA (Figure 6.9 (d)), despite the fact that two peaks associated with reduced nitrogen are present at 398.1 and 398.4 eV.

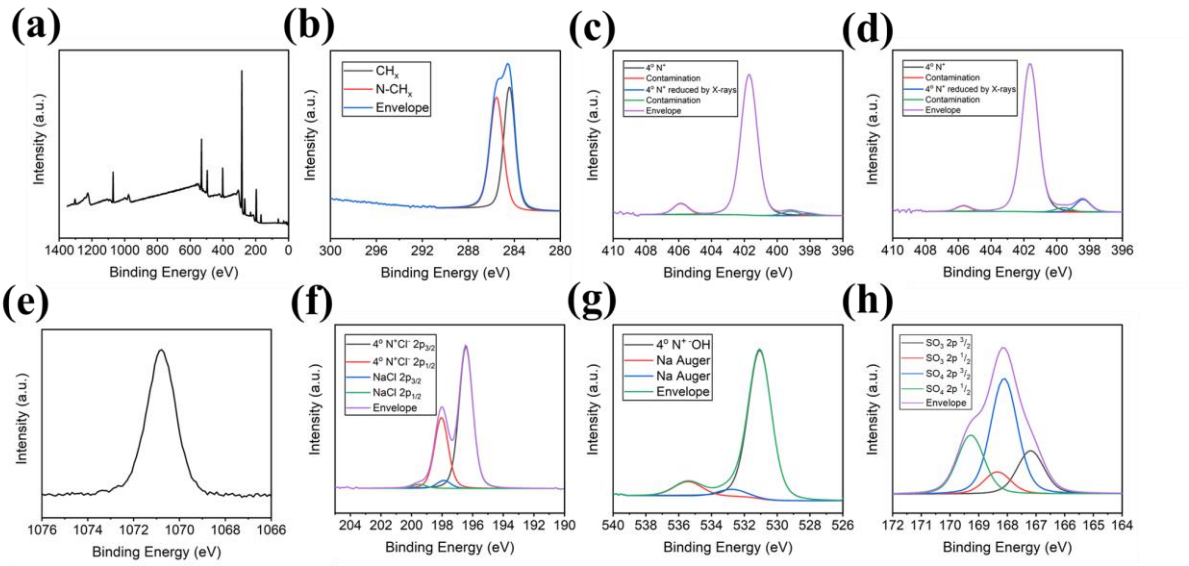

Figure 6.8 XPS analysis of PDDA including (a) survey spectrum and high-resolution spectra of the (b) deconvoluted C 1s orbital (c) deconvoluted N 1s orbital (initial scan) (d) deconvoluted N 1s orbital (acquired 420 seconds after initial scan) (e) Na 1s orbital (f) deconvoluted Cl 2p orbital (g) deconvoluted O 1s orbital and (h) deconvoluted S 2p orbital.

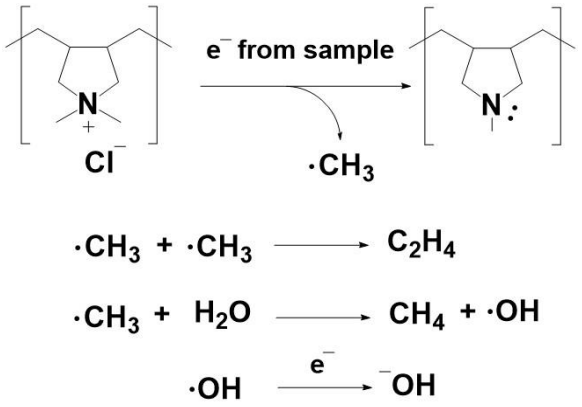

Scheme 6.2 The proposed reduction of PDDA resulting in the loss of a methyl radical and generation of an uncharged tertiary amine species. Methyl radicals may then undergo dimerisation, reaction with water or gain electrons, to form ethane, methane or hydroxide ions.

XPS analysis of PDDA also revealed the presence of the Na 1s state at 1070.8 eV, which is likely to correspond to NaCl impurities in the aqueous solution (Figure 6.8 (e)). In addition, the Cl 2p spectrum depicts two chlorine species, as observed in (Figure 6.8 (f)). The former relates to chloride (Cl^-), associated with the quaternary ammonium R_4N^+ of PDDA, corresponding to binding energies, and respective spin states of 196.5 (Cl 2p $^3/_2$) and 198.1 eV

(Cl 2p $^{1}/_{2}$). The second corresponds to NaCl, possessing binding energies, and respective orbitals of 197.9 (Cl 2p $^{3}/_{2}$) and 199.5 eV (Cl 2p $^{1}/_{2}$).[559] Through peak integration, it was found that 7.2 at.% of the total chlorine related to Cl^- associated with the quaternary ammonium R_4N^+ of PDDA. This value is not dissimilar to the at.% of nitrogen within the quaternary ammonium R_4N^+ of PDDA, which corresponds to 6.7. This finding is not surprising since an approximate 1:1 ratio is predicted between nitrogen and chlorine within $R_4N^+Cl^-$. Furthermore, a large proportion of oxygen (11.2 at.%) is also observed within PDDA, as evidenced by the O 1s spectrum (Figure 6.8 (g)). This is likely to correspond to the presence of the ^-OH anion associated with PDDA, formed during the removal of the Cl^- anion in aqueous solution, in the form of HCl gas.[547] In addition, some oxygen may also be associated with sulfur in the form of SO_3 or SO_4-based compounds (See Figure 6.8 (h)).

Full characterisation of PDDA by XPS, enables comparisons to be made between PDDA, NP4/PDDA and NP4-PP, to determine the nature of the composite materials. XPS analysis was then conducted on NP4/PDDA, as shown in Figure 6.9. The C 1s spectrum (Figure 6.9 (b)) closely resembles that of PDDA, displaying peaks at 284.4 and 285.6 eV, which relate to N−CH_X and CH_X carbon environments, respectively. Interestingly, there are an absence of peaks associated with the π−π* satellite structure, C−O, C=O and O−C=O functionality within NP4. Of course, any sp^2 and sp^3 associated with NP4 would overlap with that of the CH_x functionality of PDDA and thus, may not be visible within the NP4/PDDA mixture. This absence of peaks suggests that a large proportion of PDDA exists within the surface region of the NP4/PDDA mixture, therefore, the underlaying NP4 was not analysed. A reduction in oxygen content was also observed in comparison with PDDA, reducing from 11.2 at.% in PDDA to 6.0 at.% in NP4/PDDA (Figure 6.9 (c) and Table 6.1), despite both NP4 and PDDA containing oxygen. This may be due to loss of ^-OH anions from PDDA hydroxide or due to attenuation of the O 1s state, resulting from a reduction of oxygen concentration within the surface region. NP4/PDDA also contains an N 1s peak at 401.5 eV, indicating the presence of quaternary ammonium groups, relating to PDDA (see Figure 6.9 (d)). This binding energy is similar to that of free PDDA, as discussed above. The Na 1s and Cl 2p orbitals (Figure 6.9 (e) and (f)) possess identical spectra to that of PDDA, indicating the presence of NaCl intercalated within the material and Cl^- interacting with quaternary ammonium R_4N^+ groups. The unexpected presence of fluorine was also recognised by a F 1s peak at 688.7 eV (Figure 6.9 (g)) This peak correlates with a small amount of contamination, likely to originate from the synthesis

procedure. It is believed that this contamination has no effect on the reactivity of the data presented and thus, it is not considered further.

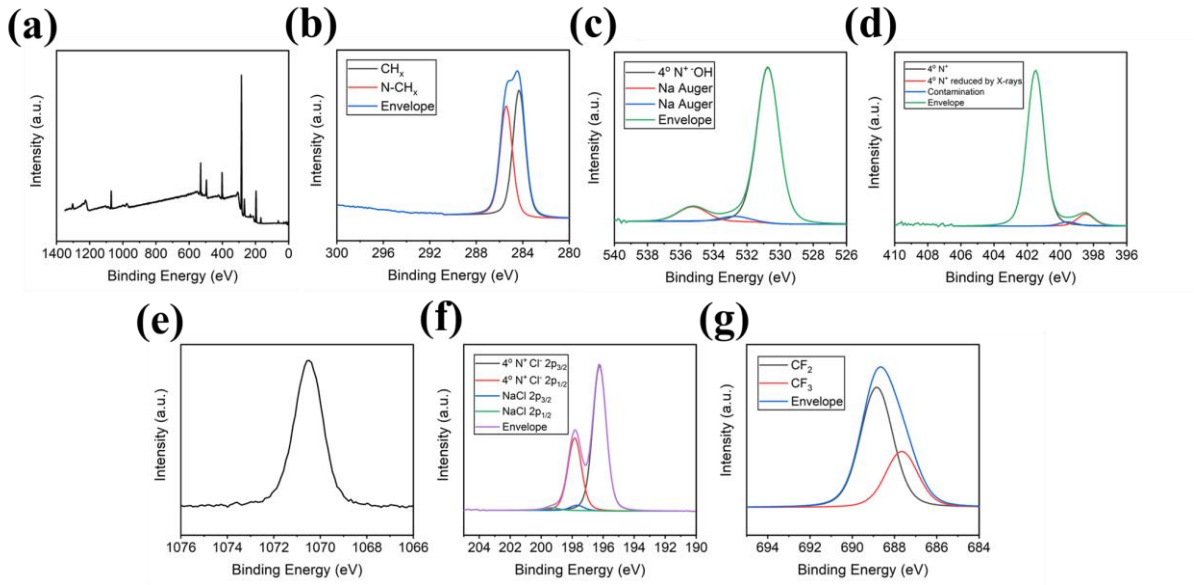

Figure 6.9 XPS spectra of PDDA/NP4 including (a) survey spectrum and high-resolution spectra of the (b) deconvoluted C 1s orbital (c) deconvoluted O 1s orbital (d) deconvoluted N 1s orbital (e) Na 1s orbital (f) deconvoluted Cl 2p orbital and (g) deconvoluted F 1s orbital.

XPS analysis of PFO revealed the presence of four elements, including carbon, oxygen, sodium, and fluorine (Figure 6.10 (a) and Table 6.1). The C 1s spectrum contained four peaks at 286.0, 290.0, 292.0 and 294.0 eV (Figure 6.10 (b)). These correspond to various environments including C−O, O−C=O, CF_2 and CF_3, consistent with the structure of PFO.[525] The presence of CF_3 and CF_2 environments were also evidenced by peaks at 689.2 and 690.2 eV, within the deconvoluted F 1s spectrum (Figure 6.10 (c)).[499] Furthermore, peaks at 532.8 and 1072.4 eV relate to the O 1s and Na 1s environments respectively, corresponding to oxygen and sodium within the sodium carboxylate functionality of the fluorosurfactant (see Figure 6.10 (d) and (e)).

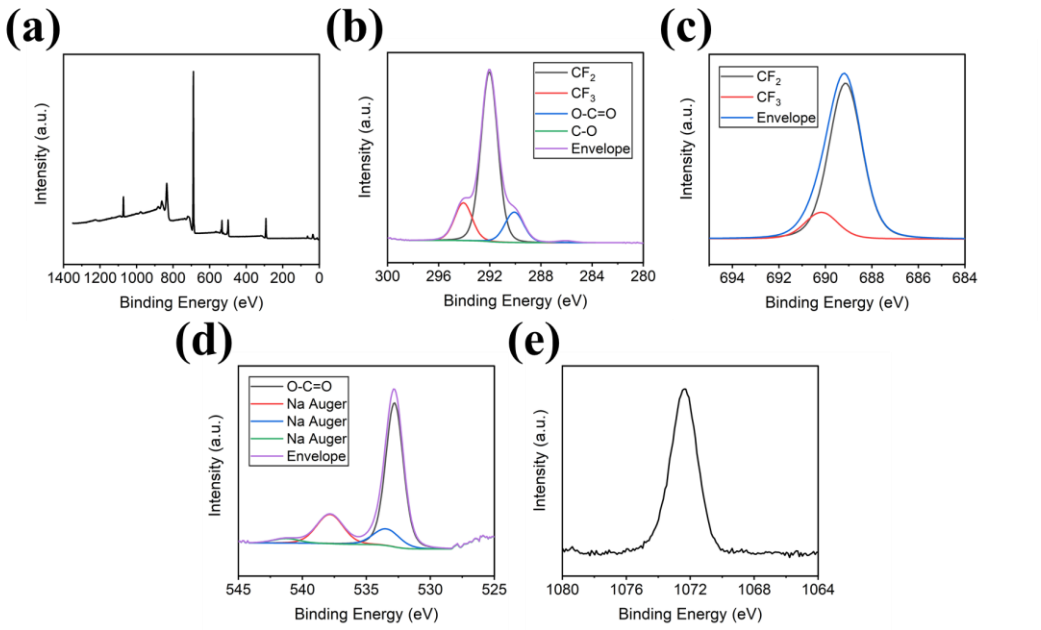

Figure 6.10 XPS analysis of PFO including (a) survey spectrum and high-resolution spectra of the (b) deconvoluted C 1s orbital (c) deconvoluted F 1s orbital (d) deconvoluted O 1s orbital and (e) Na 1s orbital.

XPS analysis of NP4-PP composite, provided evidence of carbon, nitrogen, oxygen, chlorine, sodium, and fluorine (Figure 6.11 and Table 6.1). These elements originate from a contribution of NP4, PDDA and PFO within the surface regions. The C 1s spectrum (Figure 6.11 (a)) depicts six peaks located at 284.6, 286.0, 288.1, 290.5, 291.5 and 293.8 eV. The latter three binding energies correspond to the O−C=O, CF_2 and CF_3 environments within PFO, whilst the former two correspond to CH_X and N−CH_X environments within PDDA. Furthermore, a peak at 288.1 eV, and a slight broadening of the peak at 286.0 eV, indicate the presence of C 1s environments originating from NP4. The former of these peaks most likely corresponds to C=O within NP4, whilst the broadening of PDDA's CH_X peak indicates additional C−O bonding. Moreover, it is plausible that the remaining environments within NP4 overlap with the C 1s environments of PDDA and PFO. A substantial reduction in the atomic concentration of chlorine between PDDA and NP4-PP composite is observed (Figure 6.11 (c)). This finding is attributed to the polyelectrolyte/fluorosurfactant complex formation, and the establishment of NaCl through counterion exchange. The presence of NaCl is evidenced by peaks at 199.8 and 1070.8 eV, corresponding to Cl 2p $^3/_2$ and Na 1s orbitals, respectively (see Figure 6.11 (c) and (d)). The washing procedure for NP4-PP involved a succession of dispersion-centrifugation-decantation cycles in effort to remove NaCl, which proved successful due to the presence of only trace quantities of the salt remaining within NP4-PP (0.3 at.% according to the sodium atomic

concentration shown in Table 6.1). Furthermore, a small quantity of Cl^- remained bound to quaternary ammonium groups as evidenced by the Cl 2p $^3/_2$ peak at 196.8 eV, suggesting that PFO did not complex to all quaternary ammonium group present on PDDA. As such, the polyelectrolyte/fluorosurfactant complex was unlikely to have formed in a 1:1 stoichiometry, contrarily to previous works.[560–562] It is believed that some quaternary ammonium functionality within PDDA may have been inaccessible to PFO moieties due to the morphology of NP4. Some regions of PDDA may have become blocked within the porous structure. Whilst the stoichiometry was not directly quantified, it was found that upon washing of NP4-PP, both PDDA and PFO were present in the filtrate, suggesting that they were in excess upon addition. This finding supports the inaccessibility theory since it would be reasonable to assume that an excess of PFO would bind in a 1:1 stoichiometry with PDDA.

The presence of four nitrogen species was also observed within the N 1s spectrum associated with NP4-PP, consistent with the N 1s spectrum for PDDA (Figure 6.11 (e)) A shift in the binding energy for the quaternary ammonium species was also observed from 401.7 eV in PDDA to 402.1 eV in NP4-PP. This increase in binding energy, by 0.5 eV, was attributed to complexation of quaternary ammonium groups within PDDA with carboxylate functionality within PFO. This shift can be explained by the ability of oxygen to form strong electrostatic interactions with the positively charged nitrogen species. Interestingly, this shift in binding energy was not observed for NP4/PDDA, suggesting that PDDA moieties did not form electrostatic interaction with carboxylate groups present on NP4, or indicating that any electrostatic interaction present was comparatively weaker. Analysis of the O 1s spectrum for NP4-PP also provided evidence of oxygen within the material, displaying a peak at 530.8 eV (Figure 6.11 (f)). This oxygen originates from NP4, PDDA and PFO. The F 1s spectrum also signifies the presence of fluorine in the form of CF_3 and CF_2, corresponding to 687.9 and 688.9 eV, respectively (Figure 6.11 (g)). Theoretically, a 1:1 stoichiometry between PDDA and PFO would be consistent with 15 fluorine atoms for every 1 nitrogen atom.[560–562] Within NP4-PP, the nitrogen to fluorine ratio was approximated to be 13:1, providing further evidence that some quaternary ammonium groups remained un-complexed to PFO moieties within NP4-PP.

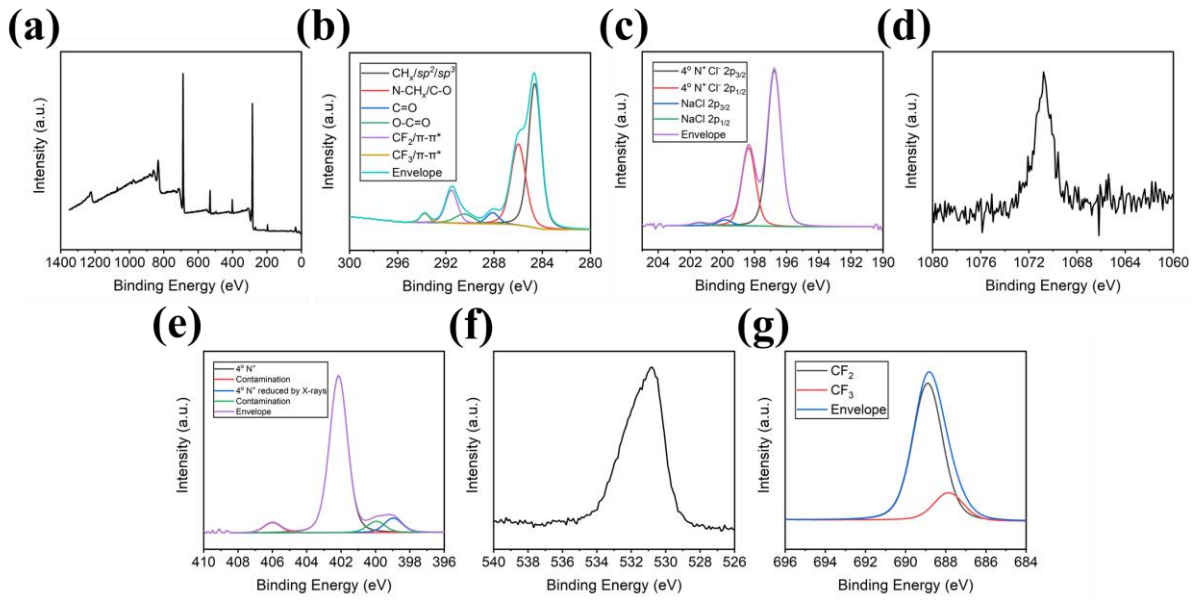

Figure 6.11 XPS analysis of NP4-PP including (a) survey spectrum and high-resolution spectra of the (b) deconvoluted C 1s orbital (c) deconvoluted Cl 2p orbital (d) Na 1s orbital (e) deconvoluted N 1s orbital (f) O 1s orbital (g) deconvoluted F 1s orbital.

Reflection upon the XPS elemental surface data enables several assumptions to be made regarding the nature of NP4/PDDA and NP4-PP. The data provides no evidence of the existence of an electrostatic interaction between positive quaternary ammonium groups and the carboxylate groups on NP4 upon addition of PDDA to NP4, shown in step (i) of Scheme 6.1 (a). Instead, it is believed that adsorption occurs *via* $\pi-\pi$ interactions between the unsaturated species of PDDA, and the graphitic network of NP4, since unsaturated presence was recognised within the ^{13}C NMR spectra. Furthermore, it is likely that PDDA moieties become well intercalated into pores present within NP4. In step (ii) (Scheme 6.1 (a)), PFO addition proceeds and polyelectrolyte/fluorosurfactant complexation occurs between many positive quaternary ammonium groups of PDDA with carboxylate functionality of PFO. In turn, some entrapped PDDA moieties remain un-complexed with NP4. As such, the resultant NP4-PP remains well bound through entrapment of PDDA/PFO complex within NP4's porous structure and through non-covalent bonding interactions. Within the following sections, the oleophobic/hydrophilic nature of the NP4-PP films and coated substrates are investigated and their application within the context of oil-water separation is explored.

6.3.3 Investigating Oleophobic/Hydrophilic Behaviour

6.3.3.1 Testing of Water/Oil Passage Through NP4-PP Films and NP4-PP Coated Substrates

The films and coated substrates were tested for their ability to allow passage of silicone oil and water through the material. In this regard, drops of each liquid were deposited upon the surface of each material, at a rate of approximately 1 drop per second, using a burette, using a gravity-based separation. For clarity of observation, DI water was dyed with brilliant blue R dye, whilst silicone oil was dyed with oil red O dye. The wetting and passage of liquid through each material was then observed. Photographs were taken over the period of testing. In total, 5 mL of silicone oil and 5 mL of DI water were added onto the films and coated substates. The water and silicone oil were mixed and poured into the burette. Due to differences in densities between the liquids, water tended to settle to the bottom of the burette and hence the deposition of water typically occurred before that of silicone oil. The ease in which silicone oil could be poured off the film/substrate was also shown by simply tilting the material to enable it to slide off.

6.3.3.1.1 Silicone Oil/Water Passage Tests of NP4-PP Films

Initially, NP4-PP thick film and NP4-PP thin film were tested for their ability to allow water/silicone oil passage through the materials. It was found that neither water nor silicone oil were able to penetrate the thick film (as shown in Figure 6.12). The addition of water resulted in partial wetting of the material after approximately 20 seconds (Figure 6.12 (b) and (c)), causing the film to become partially saturated. Subsequent water, however, formed droplets on the surface which failed to wet the material further. This excess water was removed with a paper towel prior to silicone oil deposition. Upon deposition of silicone oil, it was observed that minimal wetting occurred, and the silicone oil could be poured off with ease, at any stage after its deposition (see Figure 6.12 (d)) and (e)). It was also observed that silicone oil was capable of remaining on the surface of the film for at least 3 weeks with no visible wetting

occurring over this time.[7] Water and silicone oil were deposited on five different thick films in this way, and the same results were achieved each time.

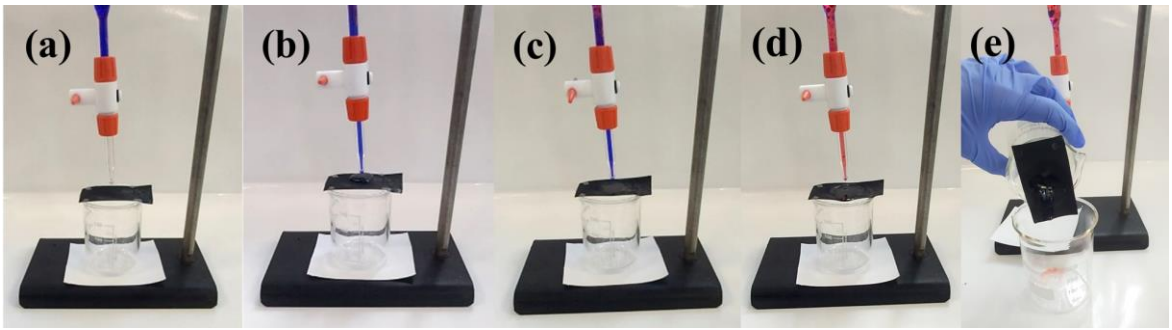

Figure 6.12 Silicone oil/water passage tests on NP4-PP thick film. (a) depicts the set-up of NP4-PP thick film on a beaker, beneath a burette filled with water and silicone oil. (b) shows the deposition of water on the film, resulting in formation of a droplet on the film instantaneously after deposition, and wetting of the film after approximately 20 seconds after deposition; (c). (d) depicts the addition of silicone oil showing that a droplet formed on the film with no occurrence of wetting. This droplet could easily be removed at any stage after its deposition by tilting the material, as shown in (e), and remained on top for at least 3 weeks.

NP4-PP thin film was then tested under the same conditions as those described above, as shown in Figure 6.13. It was found that complete wetting of the surface occurred after approximately 20 seconds (Figure 6.13 (c)). In contrast to NP4-PP thick film, it was found that water was able to pass through the material passively. Figure 6.13 (d) shows the process of a water droplet forming on the bottom of the film, before becoming released into the beaker. Five different thin films were tested in this way, and found that in contrast to the thick film, complete water penetration was enabled during 4 out of the 5 tests. This water penetration, however, was very slow, taking 2.5 hours on average to occur. During one of the tests however, it was observed that the thin film did not allow water penetration at all, and like the thick film, water wetted the surface, but remained on top for at least 3 weeks. In a similar way with the thick film, the thin film also prevented silicone oil passage for at least 3 weeks. Deposition of silicone oil resulted in a droplet, which did not wet the surface of the film, and could easily be poured off (Figure 6.13 (e) and (f)).

[7] 3 weeks was the limit of observation, however, there was no evidence to suggest that the silicone oil would have wet the film after this time

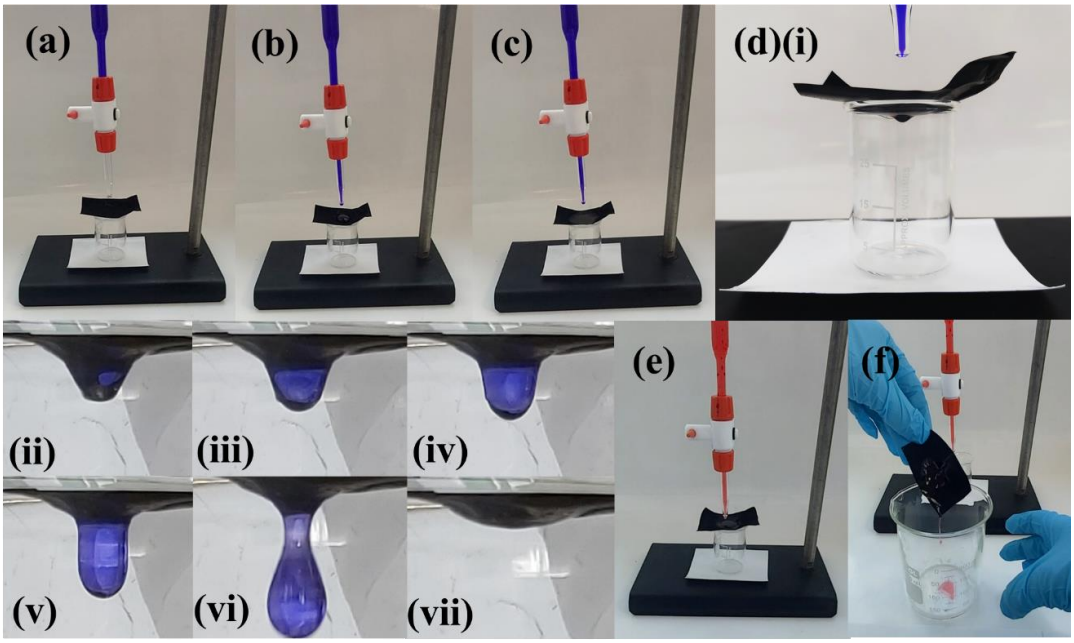

Figure 6.13 Silicone oil/water passage tests on NP4-PP thin film. (a) depicts the set-up of NP4-PP thin film on a beaker, beneath a burette filled with water and silicone oil. (b) shows the deposition of water on the film, resulting in formation of a droplet on the film instantaneously after deposition, and wetting the film after approximately 20 seconds after deposition; (c). (d)(i)-(vii) depict the passage of water through the film after 2.5 hours after its deposition, showing that a droplet forms on the bottom of the film and is subsequently released into the beaker. (d) shows the deposition of silicone oil showing that a droplet formed on the film with no occurrence of wetting. This droplet could easily be removed at any stage after its deposition by tilting the material, as shown in (f), and remained on top for at least 3 weeks.

These findings reveal that both NP4-PP thick film and NP4-PP thin film are successful in displaying oleophobic/hydrophilic behaviour due to their enhanced wetting capacity towards water than silicone oil. As previously discussed, this finding is unusual since theoretically, a surface should always be more wettable to oil than water due to the higher surface tension associated with water.[563,564] Unfortunately, however, many applications, such as those described further on in the text, require a material which not only enables wetting of water, but also allows its facile passage through the material. In the case of NP4-PP films, water did indeed wet the films. However, its passage through the materials was either very slow (in the case of the thin films) or redundant (in the case of the thick films). The differences in thickness between the film sizes meant that water passage could occur only through the thin material, due to much shorter pathways. In order to explore this further, a third film was also synthesised (NP4-PP thin film 2) using a dispersion of 2.5 g in 150 mL methanol using the single-sectioned metal tray shown in Figure 6.5. This film was visibly much thinner than NP4-PP thin film, possessing thicknesses across three regions of the film edge of 28.5, 26.2 and 25.9 µm (see

Figure 6.14). As such, it can be concluded that NP4-PP thin film 2 is approximately five times smaller than that of NP4-PP thin film. NP4-PP thin film 2 allows water penetration after only 1 hour, whilst still preventing silicone oil passage. It was, however, much weaker in strength and easily ripped when handling. Furthermore, after 4 hours, a small volume of silicone oil residing on its surface (10 mL) formed a large tear. The silicone oil droplet therefore passed through the tear and into the beaker. As with the former films, the test was repeated on five identical samples and the same results were obtained. As such, it was concluded that minimising the thickness of NP4-PP film enhanced the rate of water passage, however, jeopardised the mechanical strength of the film, resulting in its failure to withstand the physical weight of the deposited oil on its surface. For practical application, this latter observation grants such a thin film unsuitable.

As such, the NP4-PP composite was then coated upon substrates, to provide additional support to the thin film-like coating, thus reducing the potential for film breakage. Moreover, all substrates contained apertures which simultaneously provided passages to enhance the rate of water penetration through the materials.

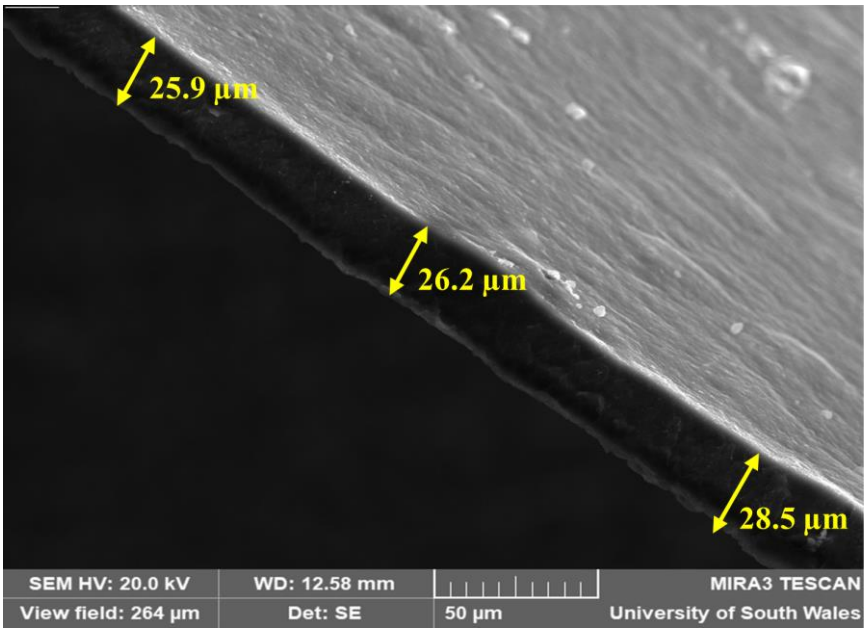

Figure 6.14 SEM image of NP4-PP thin film 2 showing the thickness of three edge regions of the film at a magnification of 787 x.

6.3.3.1.2 Silicone Oil/Water Passage Tests of NP4-PP Coated Substrates

The NP4-PP composite was coated upon various substrates including Kevlar, carbon fibre, glass fibre, nylon and stainless-steel mesh using a dispersion with a concentration of 2.5 g per 150 mL MeOH (identical to that of NP4-PP thin film 2 synthesis).[8] The coated substrates were then investigated for their silicone oil/water passage ability, again, using an identical process to that of the NP4-PP films. The reproducibility of the coatings were also assessed on the various coated substrates to observe how robust the coatings were and whether they were retained following washing and usage. In this regard, the coated substrates were repeatedly washed with DI water and acetone to remove residual silicone oil, before drying in air. The coated substrates were then re-tested under the same conditions. Furthermore, as controls, water and silicone oil were also deposited onto the substrates in the absence of coating, to show that free passage of both liquids was allowed instantaneously after their deposition (Figure 6.15 (a) – (e)). It was apparent that the addition of a coating was required to provide oleophobic behaviour to the substrates, whilst simultaneously allowing free passage of water.

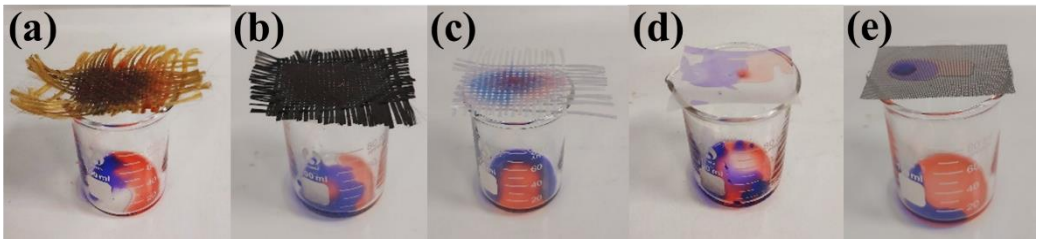

Figure 6.15 Water and silicone oil passage through each of the uncoated substrates including (a) Kevlar (b) carbon fibre (c) glass fibre (d) nylon and (e) stainless-steel mesh. 1 mL of each liquid was deposited on the surface of the substrate. It was observed that both liquids penetrated all materials instantaneously.

The findings revealed that coated Kevlar was effective in allowing the passage of water within 10 seconds (approximately 10 drops of water added) of deposition (Figure 6.16 (b)). Further water addition resulted in continuous water passage through the material, suggesting that the prior wetting of the substrate assisted in the penetration of further water molecules. 5 mL water

[8] During early stages of this investigation, a spray coating technique was employed using a spray gun; a method which found success in previous works to coat substrates with nanocomposite/polymer coatings.[524,525,581–583] In the current work, however, the spray gun became rapidly clogged with NP4-PP composite, leading to extremely poor coated substrates. As such, the solvent evaporation coating method was utilised.

passed through the coated substrate effectively. Furthermore, coated Kevlar simultaneously prevented the passage of silicone oil, even after at least three weeks, as shown in Figure 6.16 (c). Silicone oil could be removed from the surface with ease, by simply tilting the substrate and decanting off the liquid (Figure 6.16 (d)). Following washing of the coated substrate, there were no visible differences in the material's appearance (see Figure 6.17). Identical findings were obtained to its unwashed counterpart in enabling water passage and preventing silicone oil passage, as shown in Figure 6.17 (b) – (d). This indicated that the coating remained well adsorbed and integrated into the fibres.

Similar results were obtained during tests of the coated carbon fibre, as shown in Figure 6.18. Silicone oil was unable to penetrate the coated material even after 3 weeks of deposition and could easily be poured off with ease (Figure 6.18 (c) and (d)). The passage of water was also allowed through the material and occurred at a faster rate than that of the coated Kevlar substrate. Water rapidly passed through the material within 5 seconds of deposition and then continuously from then onwards, allowing a total of 5 mL water through (Figure 6.18 (b)). There were no visual differences in the appearance of the coated carbon fibre after washing, or in its ability to allow water passage and prevent silicone oil passage (Figure 6.19). As such, the material also reflected the good adsorption and integration of the coating within the fibres.

Next, the coated glass fibre was tested. In this case it was found that water passage was enabled through the coated substrate within 5 seconds of its deposition, as shown in Figure 6.20 (b). In contrast to coated Kevlar and coated carbon fibre, however, silicone oil passage was only prevented for periods of up to 2 hours after initial deposition onto the surface. After 2 hours, the oil was found to penetrate through the coated substrate, falling into the beaker, as shown in Figure 6.20 (e). Prior to this, silicone oil could easily be removed at any stage by pouring off the surface Figure 6.20 (d)). This demonstrates a temporary blockage of the oil through the coated substrate. This difference in behaviour was attributed to the larger apertures present within coated glass fibre (See SEM analysis within 6.3.4.1 for more detail). Photographs provide evidence of much larger uncoated holes within the substrate in comparison with coated Kevlar and coated carbon fibre (Figure 6.5). After washing of coated glass fibre, no visual differences were observed in the appearance of this coated substrate (see Figure 6.21), suggesting that, again, the coating remained well adsorbed and integrated into the fibres. Subsequent tests were repeated, and it was found that water passage was enabled through the coated substrate, consistent with its unwashed counterpart (Figure 6.21 (b)). In contrast however, silicone oil passage was prevented for at least 3 weeks after deposition (substantially

longer than the initial test) and could also be extracted by tilting the coated substrate, as shown in Figure 6.21 (c) and (d). This finding appears to be due to the flexible nature of this coated glass fibre, meaning that fibres were very susceptible to moving. Whilst carrying out the second test on the washed coated substrate, it appeared that the fibres may have moved slightly, altering the size of the holes within the grid. By revealing much smaller holes, it is believed that the silicone oil passage is prevented for a much longer time period.

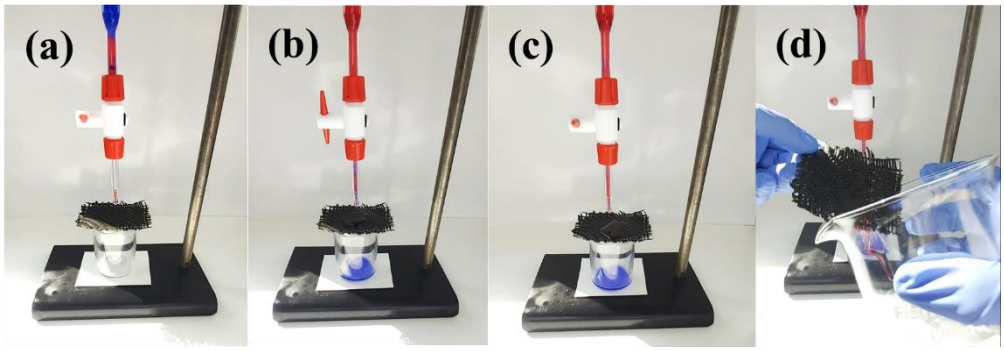

Figure 6.16 Silicone oil/water passage tests on NP4-PP coated Kevlar. (a) depicts the set-up of the coated substrate on a beaker, beneath a burette filled with water and silicone oil. (b) shows the deposition of water onto the coated substrate, resulting in wetting and subsequent penetration of 5 mL water through the coated substrate and into the beaker after 10 seconds of its deposition. (c) shows the presence of a silicone oil droplet on the surface of the coated substrate, which undergoes no visible wetting or penetration of the coated substrate after at least 3 weeks, and (d) shows that the silicone oil can easily be poured off the coated substrate by tilting.

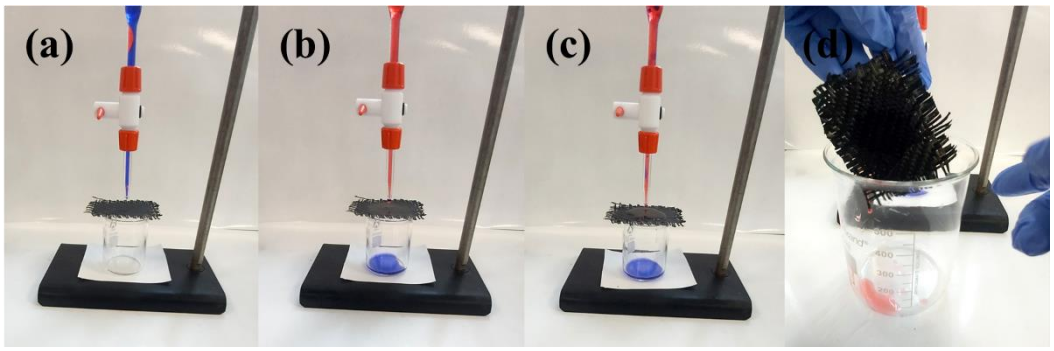

Figure 6.17 Silicone oil/water passage tests on NP4-PP coated Kevlar after washing with acetone and water to remove residual silicone oil. The tests displayed identical findings to that of the analogous unwashed coated substrate. (a) depicts the set-up of the coated substrate on a beaker, beneath a burette filled with water and silicone oil. (b) shows the deposition of water onto the coated substrate, resulting in wetting and subsequent penetration of 5 mL water through the coated substrate and into the beaker after 10 seconds of its deposition. (c) shows the presence of a silicone oil droplet on the surface of the coated substrate, which undergoes no visible wetting or penetration of the coated substrate after at least 3 weeks, and (d) shows that the silicone oil can easily be poured off the coated substrate by tilting.

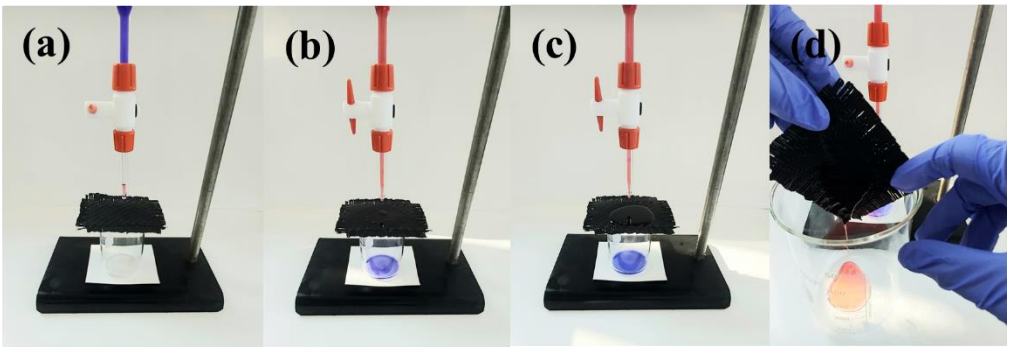

Figure 6.18 Silicone oil/water passage tests on NP4-PP coated carbon fibre. (a) depicts the set-up of the coated substrate on a beaker, beneath a burette filled with water and silicone oil. (b) shows the deposition of water onto the coated substrate, resulting in wetting and subsequent penetration of 5 mL water through the coated substrate and into the beaker after 5 seconds of its deposition. (c) shows the presence of a silicone oil droplet on the surface of the coated substrate, which undergoes no visible wetting or penetration of the coated substrate after at least 3 weeks, and (d) shows that the silicone oil can easily be poured off the coated substrate by tilting.

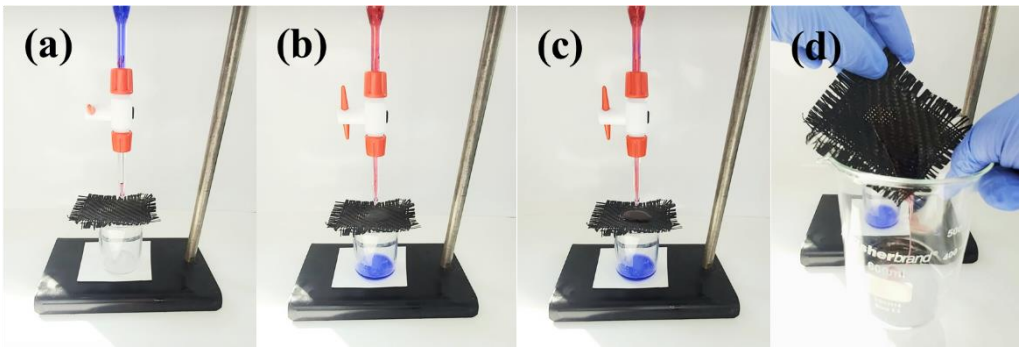

Figure 6.19 Silicone oil/water passage tests on NP4-PP coated carbon fibre after washing with acetone and water to remove residual silicone oil. The tests displayed identical findings to that of the analogous unwashed coated substrate. (a) depicts the set-up of the coated substrate on a beaker, beneath a burette filled with water and silicone oil. (b) shows the deposition of water onto the coated substrate, resulting in wetting and subsequent penetration of 5 mL water through the coated substrate and into the beaker after 5 seconds of its deposition. (c) shows the presence of a silicone oil droplet on the surface of the coated substrate, which undergoes no visible wetting or penetration of the coated substrate after at least 3 weeks, and (d) shows that the silicone oil can easily be poured off the coated substrate by tilting.

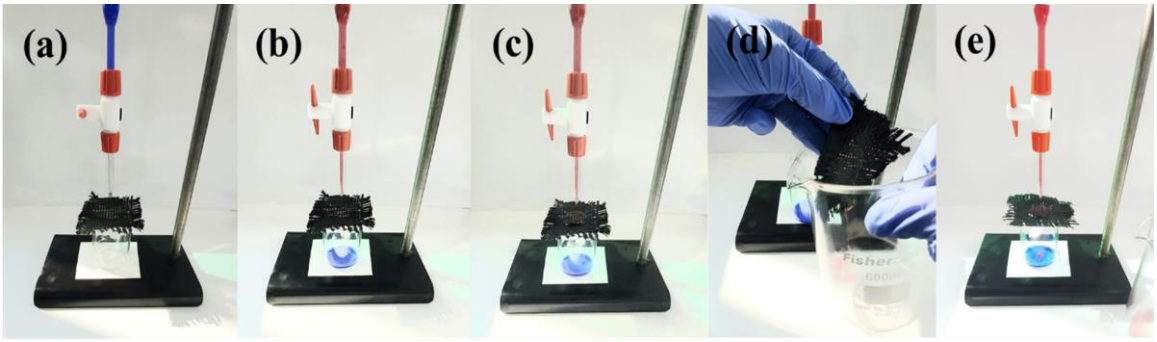

Figure 6.20 Silicone oil/water passage tests on NP4-PP coated glass fibre. (a) depicts the set-up of the coated substrate on a beaker, beneath a burette filled with water and silicone oil. (b) shows the deposition of water onto the coated substrate, resulting in wetting and subsequent penetration of 5 mL water through the coated substrate and into the beaker after 5 seconds of its deposition. (c) shows the presence of a silicone oil droplet on the surface of the coated substrate, which undergoes no visible wetting or penetration of the coated substrate for up to 2 hours, and (d) shows that the silicone oil can easily be poured off the coated substrate by tilting, up to 2 hours after its deposition. (e) shows the penetration of silicone oil through the coated substrate after 2 hours.

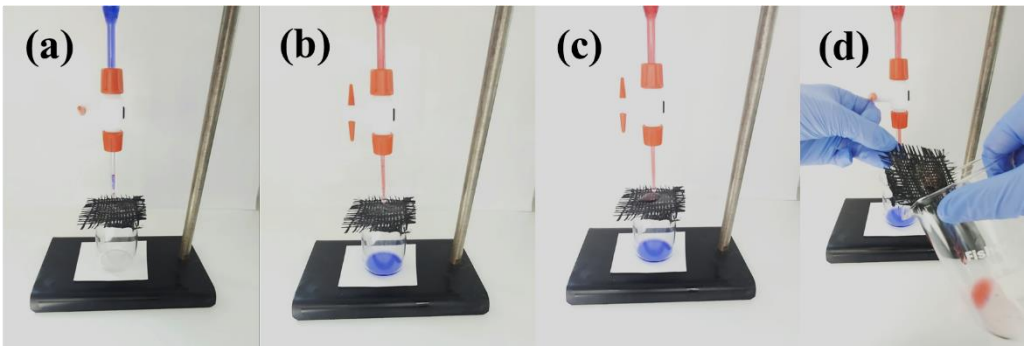

Figure 6.21 Silicone oil/water passage tests on NP4-PP coated glass fibre after washing with acetone and water to remove residual silicone oil. The tests displayed different findings to that of the analogous unwashed coated substrate. (a) depicts the set-up of the coated substrate on a beaker, beneath a burette filled with water and silicone oil. (b) shows the deposition of water onto the coated substrate, resulting in wetting and subsequent penetration of 5 mL water through the coated substrate and into the beaker after 5 seconds of its deposition. (c) shows the presence of a silicone oil droplet on the surface of the coated substrate, which undergoes no visible wetting or penetration of the coated substrate after at least 3 weeks, and (d) shows that the silicone oil can easily be poured off the coated substrate by tilting.

The next step in the investigation involved coating nylon substrate. Three coated nylon substrates were synthesised using various concentrations of NP4-PP composite dispersion, as described in the Experimental. Coated nylon prepared using a concentrated dispersion of NP4-PP (2.5 g in 150 mL MeOH) was found to prevent the passage of both water and silicone oil, for at least 3 weeks, as shown in Figure 6.22 (b) and (c). It was observed that like the thick film, water wetted the surface of the coated substrate to a much greater extent than silicone oil,

however, it was unable to pass through the material. This was likely due there being complete coverage of all holes within the nylon, and thus, it behaved similar to that of the thick film. In order to facilitate water passage, a thinner coating was targeted by using less concentrated dispersions of NP4-PP coated upon nylon. These included NP4-PP coated nylon 3 (synthesised using 0.26 g in 150 mL MeOH) and NP4-PP coated nylon 2 (synthesised using 0.16 g in 150 mL MeOH). Differences in coating concentrations were evidenced by direct observation, where the more concentrated the coating, the darker and more homogeneous the coating appeared (see Figure 6.5). It was observed that these lower concentrated dispersions were sufficient in providing coated nylon substrates which allowed free passage of water instantly after deposition (Figure 6.23 and Figure 6.25). Meanwhile, silicone oil passage was prevented for at least 3 weeks in both cases (see Figure 6.23 (c) and Figure 6.25 (c)). Silicone oil could easily be poured off the surface of these coated substrates. Upon washing of these latter two materials, partial removal of the coating from the nylon substrate was observed during the acetone washing steps. The subsequent partially washed away coatings are presented in Figure 6.24 (a) and Figure 6.26 (a). Despite this, the coated nylon materials performed just as efficiently as their unwashed counterparts, providing silicone oil passage prevention for at least 3 weeks, and allowing passive flow of water (Figure 6.24 and Figure 6.26). It was therefore suggested that the remaining coating, which was not washed away, must have been satisfactory to enable the oleophobic behaviour. In addition, it was desirable that the coating was not washed away during the water wash since this could hinder its practical application when separating water/oil mixtures.

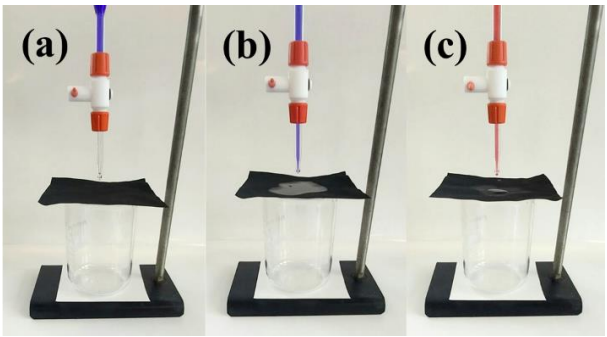

Figure 6.22 Silicone oil/water passage tests on NP4-PP coated nylon. (a) depicts the set-up of the coated substrate on a beaker, beneath a burette filled with water and silicone oil. (b) shows the deposition of water onto the coated substrate, resulting in wetting of the substrate but no penetration for up to 3 weeks (c) shows the presence of a silicone oil droplet on the surface of the coated substrate, which undergoes no visible wetting or penetration of the coated substrate after at least 3 weeks.

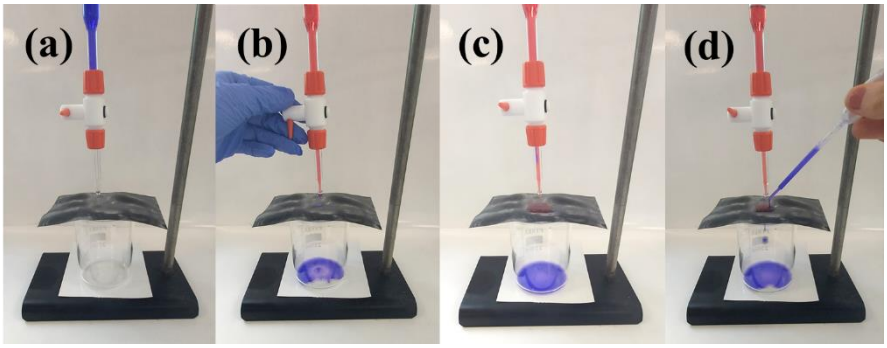

Figure 6.23 Silicone oil/water passage tests on NP4-PP coated nylon 3 (0.26 g per 150 mL MeOH) (a) depicts the set-up of the coated substrate on a beaker, beneath a burette filled with water and silicone oil. (b) shows the deposition of 5 mL water onto the coated substrate, resulting in instantaneous penetration through the coated substrate after its deposition. (c) shows the presence of a silicone oil droplet on the surface of the coated substrate, which undergoes no visible wetting or penetration of the coated substrate after at least 3 weeks, and (d) shows that subsequent water droplets penetrate through the silicone oil droplet and coated substrate.

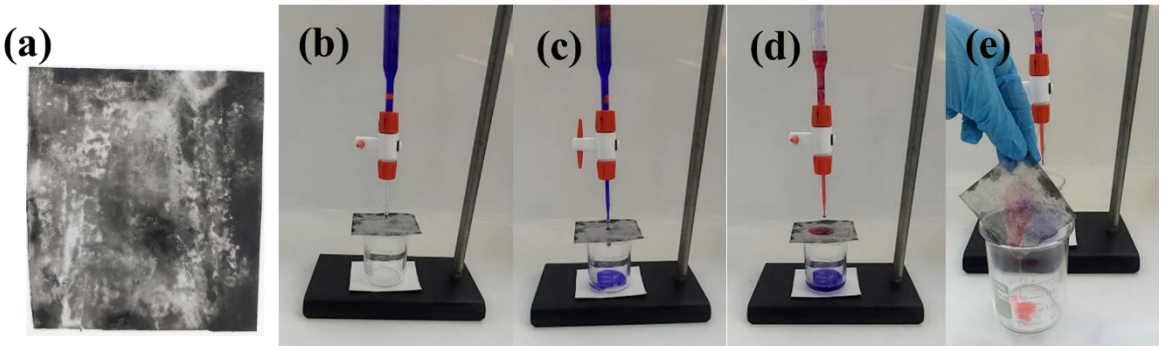

Figure 6.24 Silicone oil/water passage tests on NP4-PP coated nylon 3 (0.26 g per 150 mL MeOH) after washing with acetone and water to remove residual silicone oil. The tests displayed identical findings to that of the analogous unwashed coated substrate. (a) depicts the partially washed away coating upon the substrate after acetone washes. (b) depicts the set-up of the coated substrate on a beaker, beneath a burette filled with water and silicone oil. (c) shows the deposition of 5 mL water onto the coated substrate, resulting in instantaneous penetration through the coated substrate after its deposition. (d) shows the presence of a silicone oil droplet on the surface of the coated substrate, which undergoes no visible wetting or penetration of the coated substrate after at least 3 weeks, and (e) shows that the silicone oil can easily be poured off the coated substrate by tilting.

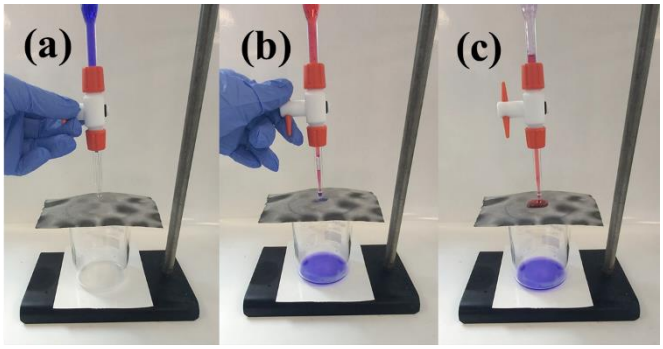

Figure 6.25 Silicone oil/water passage tests on NP4-PP coated nylon 2 (0.16 g per 150 mL MeOH) (a) depicts the set-up of the coated substrate on a beaker, beneath a burette filled with water and silicone oil. (b) shows the deposition of 5 mL water onto the coated substrate, resulting in instantaneous penetration through the coated substrate after its deposition and (c) shows the presence of a silicone oil droplet on the surface of the coated substrate, which undergoes no visible wetting or penetration of the coated substrate after at least 3 weeks.

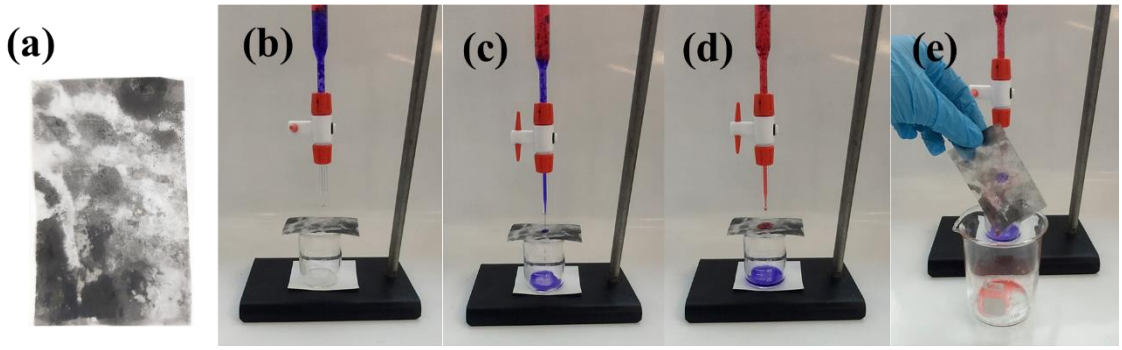

Figure 6.26 Silicone oil/water passage tests on NP4-PP coated nylon 2 (0.16 g per 150 mL MeOH) after washing with acetone and water to remove residual silicone oil. The tests displayed identical findings to that of the analogous unwashed coated substrate. (a) depicts the partially washed away coating upon the substrate after acetone washes. (b) depicts the set-up of the coated substrate on a beaker, beneath a burette filled with water and silicone oil. (c) shows the deposition of 5 mL water onto the coated substrate, resulting in instantaneous penetration through the coated substrate after its deposition. (d) shows the presence of a silicone oil droplet on the surface of the coated substrate, which undergoes no visible wetting or penetration of the coated substrate after at least 3 weeks, and (e) shows that the silicone oil can easily be poured off the coated substrate by tilting.

Upon analysis of coated stainless-steel mesh, it was observed that water penetrated the coated material after approximately 5 minutes after deposition (after 20 drops of silicone oil were also added) as shown in Figure 6.27 (b). Meanwhile, silicone oil passage was prevented, even after 3 weeks (Figure 6.27 (c)). The silicone oil could easily be poured off the surface of the coated mesh as shown in Figure 6.27 (d). After washing, it was observed that the coating had partially

washed away from the mesh, but to a much lesser extent than that of the coated nylon 2 and 3 (see Figure 6.28 (a)). Despite this, identical findings were acquired when assessing the water/silicone oil passage ability (Figure 6.28 (b) – (e)).

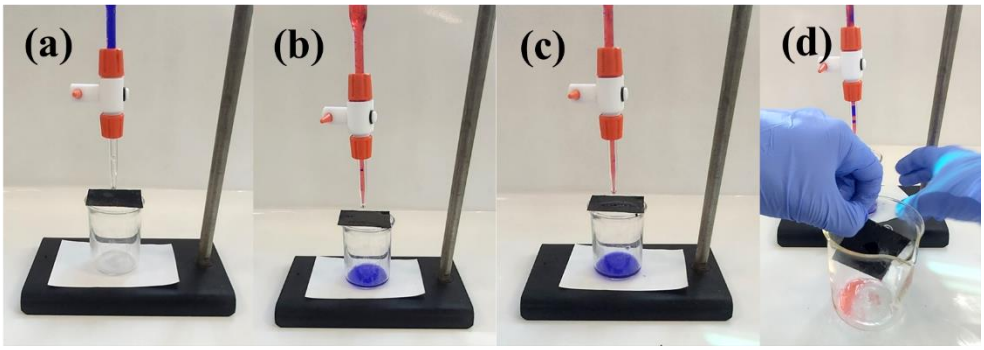

Figure 6.27 oil/water passage tests on NP4-PP coated stainless-steel mesh. (a) depicts the set-up of the coated substrate on a beaker, beneath a burette filled with water and silicone oil. (b) shows the deposition of water onto the coated substrate, resulting in wetting and subsequent penetration of 5 mL water through the coated substrate and into the beaker after 5 minutes of its deposition. (c) shows the presence of a silicone oil droplet on the surface of the coated substrate, which undergoes no visible wetting or penetration of the coated substrate after at least 3 weeks, and (d) shows that the silicone oil can easily be poured off the coated substrate by tilting.

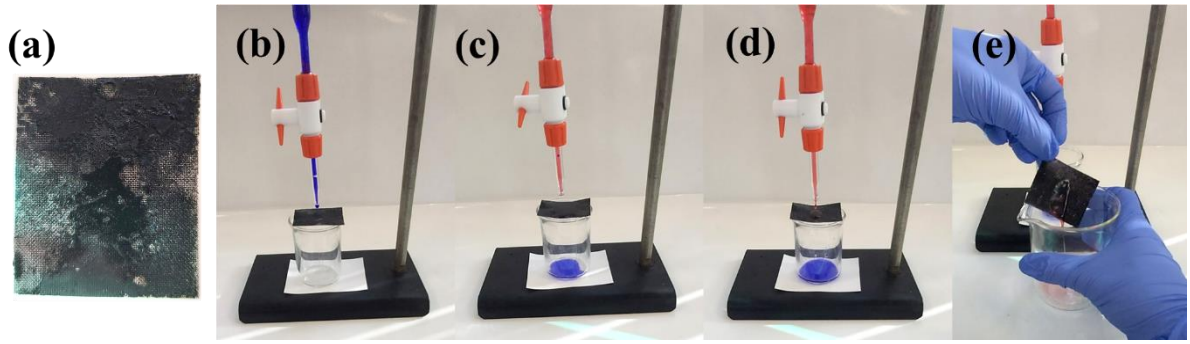

Figure 6.28 Silicone oil/water passage tests on NP4-PP coated stainless-steel mesh after washing with acetone and water to remove residual silicone oil. The tests displayed identical findings to that of the analogous unwashed coated substrate. (a) depicts the partially washed away coating upon the substrate after acetone washes. (b) depicts the set-up of the coated substrate on a beaker, beneath a burette filled with water and silicone oil. (c) shows the deposition of water onto the coated substrate, resulting in wetting and subsequent penetration of 5 mL water through the coated substrate and into the beaker after 5 minutes of its deposition. (d) shows the presence of a silicone oil droplet on the surface of the coated substrate, which undergoes no visible wetting or penetration of the coated substrate after at least 3 weeks, and (e) shows that the silicone oil can easily be poured off the coated substrate by tilting.

The results of the coated substrates tests suggested that the presence of a substrate was much more effective in providing passage for water penetration through the material, whilst also improving the mechanical integrity of the NP4-PP film-type coating. In no incidence was there a tear observed in the coating, such as that obtained for NP4-PP thin film 2. Furthermore, silicone oil did not wet any of the coated substrates, thus, it is believed that these coated substrates show potential as membranes for oil/water separation.

The results of these water/silicone oil passage tests for NP4-PP films and coated substrates are summarised in Table 6.2. They show that all films and coated substrates successfully exhibited oleophobic character. In all cases, films and substrates did not allow the passing of oil, even after a substantial length of time with silicone oil deposited on the top. The free passage of water, however, required optimisation. Whilst coated Kevlar, carbon fibre, glass fibre and stainless-steel mesh possess pores large enough to allow water to flow through passively, coated nylon synthesised with a relatively concentrated dispersion of the NP4-PP composite (2.5 g per 150 mL) prevented water passage. As a result, the thickness of the coating was decreased using less concentrated dispersions. These proved effective in allowing the free passage of water. Similarly, it was also found that the thick film did not enable water penetration through the material, whereas the thin film did, during 4 out of the 5 tests, although took an average of 2.5 hours for complete penetration. It is likely that the water passage proceeds as it finds suitable pathways through the films, thus, the thinner the film, the quicker the rate of passage.

Table 6.2 A summary of the silicone oil/water passage tests of various NP4-PP films and NP4-PP coated substrates. Washing procedures were conducted with water and acetone.

Substrate	Was water allowed through?	Was oil passage prevented (for at least 3 weeks)?	Did the film/coated break?	Could the silicone oil be poured off easily?	Were there any visual changes to the coated substrate after washing?	Did the silicone oil/water passage behaviour remain consistent after washing?
NP4-PP Thick Film	No	Yes	No	Yes	N/A	N/A
NP4-PP Thin Film	Yes (after ~ 2.5 hours)	Yes	No	Yes	N/A	N/A
NP4-PP Thin Film 2	Yes (after 1 hour)	No (film was too weak and tore)	Yes (film was too weak and tore)	Yes	N/A	N/A
NP4-PP Coated Kevlar	Yes (after 10 seconds)	Yes	No	Yes	No	Yes
NP4-PP Coated Carbon Fibre	Yes (after 5 seconds)	Yes	No	Yes	No	Yes
NP4-PP Coated Glass Fibre	Yes (after 5 seconds)	No (silicone oil passed through apertures after 2 hours)	No	Yes	No	No, oleophobic behaviour improved and oil passage was prevented for at least 3 weeks
NP4-PP Coated Nylon	No	Yes	No	Yes	N/A	N/A
NP4-PP Coated Nylon 3	Yes (instantly)	Yes	No	Yes	Yes, coating was partially washed away	Yes
NP4-PP Coated Nylon 2	Yes (instantly)	Yes	No	Yes	Yes, coating was partially washed away	Yes
NP4-PP Coated Stainless-Steel Mesh	Yes (after ~ 5 minutes)	Yes	No	Yes	Yes, coating was partially washed away	Yes

Figure 6.29 provides an illustrative outline of the NP4-PP composite synthesised into NP4-PP thin film, NP4-PP thick film and NP4-PP coated substrates. The passage of water through films and coated substrates is depicted by a blue arrow; such that an arrow above the material represents water deposition upon the material, and a second blue arrow beneath the material depicts the water penetration through the entire material. Red arrows represent the deposition of silicone oil on the surface of the material, however, the absence of a second red arrow beneath the material signifies the prevention of silicone oil penetration.

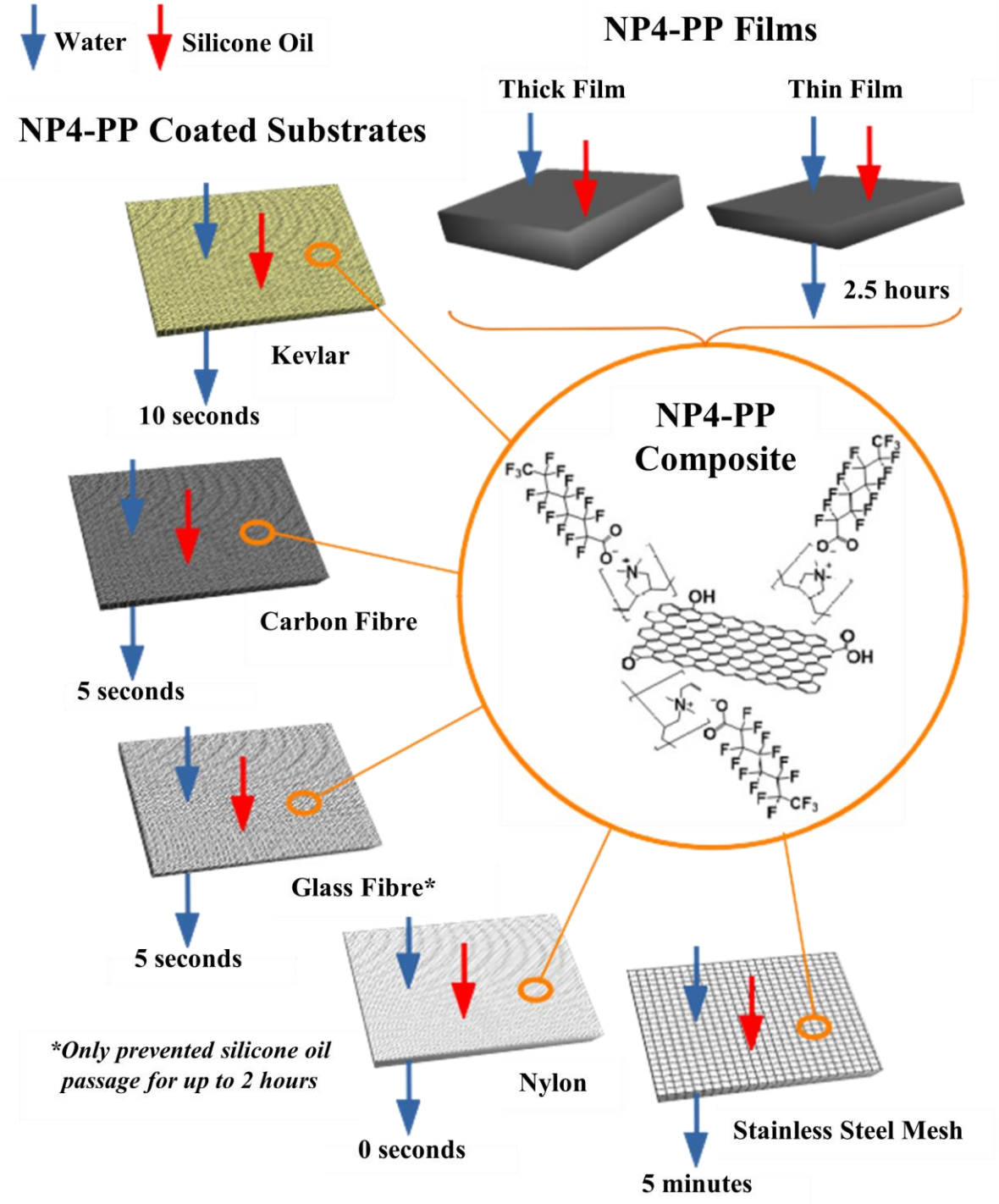

Figure 6.29 Diagram showing a simplified structure of NP4-PP composite and how it can be used to fabricate NP4-PP films and NP4-PP coated substrates. Blue and red arrows represent the passage of water and silicone oil onto the material and/or through the material. The time for water penetration is depicted below each material. This diagram refers to the results accompanying NP4-PP coated nylon 2 and 3. All materials, unless specified, prevented silicone oil passage for at least 3 weeks.

In light of these findings, it is suggested that all materials containing the NP4-PP composite display desirable oleophobic properties. In general, NP4-PP coated substrates afford much more facile water penetration, whilst simultaneously displaying oleophobic behaviour to silicone oil, granting them particularly desirable for application within the context of oil/water separation for oil-spill clean-up and within aircraft technology (*vide infra*). To further examine the oleophobic behaviour of such materials, contact angle and sliding angle measurements and were conducted.

6.3.3.2 Contact Angle Measurements

Contact angle measurements were measured on NP4-PP films and NP4-PP coated substrates using three different oils, including silicone oil, hexadecane, and Jet A-1 fuel. In each case, a small droplet (1 − 3 μL) of each liquid was deposited onto three different regions of the material's surface, thereby allowing the measurement of their contact angles. Average contact angles for each material are depicted in Table 6.3. WCAs in all cases were unmeasurable, due to the instantaneous wetting of each material. As such, WCAs were deemed to correspond to 0°. In regards to contact angles associated with the oils, it is generally accepted that a contact angle of less than 90° shows no oleophobic behaviour, between 90 and 150° shows oleophobic behaviour and angles exceeding 150° show superoleophobic behaviour.[565] During the present measurements, it was found that all materials possessed oleophobic behaviour to hexadecane, whilst the majority of the materials demonstrated oleophobic behaviour towards silicone oil and Jet A-1 fuel, with all contact angles being greater than 70.6°. Very high contact angles were observed for NP4-PP thin film corresponding to 126.4, 111.9 and 105.9° for hexadecane, Jet A-1 fuel and silicone oil, respectively, demonstrating that the NP4/PDDA/PFO composite provides the targeted properties. In some cases, the contact angles for Jet A-1 fuel and silicone oil were generally slightly lower for each material, with the former oil generally associated with slightly higher contact angles than the latter. These findings are attributed to the differences in surface tension. The surface tension values are in order of magnitude corresponding to hexadecane > Jet A-1 fuel > silicone oil, as shown in Table 6.4.[566,567] Many contact angles with Jet A-1 fuel and silicone oil also reflected oleophobic behaviour, possessing contact angles of over 90° in both cases. It was noticeable, however, that NP4-PP coated carbon

fibre and NP4-PP coated nylon possess lower contact angles with silicone oil and that NP4-PP thick film possesses a relatively low contact angle with Jet A-1 fuel. These findings were attributed to the non-uniformity of the materials, as well as due to the presence of large pores, particularly in the case of the coated substrates. The porous structures were observed directly *via* SEM imaging (*vide infra*). It is believed that during both contact angle analyses, it is possible that the oil droplet was deposited over a large pore, and therefore, the oil droplet may have partially resided in the pore space. As such, a lower contact angle could have been generated this way. Whilst it is often desirable to obtain extremely high contract angles exceeding 150°, such as many of those within literature, they are not necessary within the current investigation, since the NP4-PP films and coated substrates all succeeded in preventing oil passage.

Table 6.3 Contact angle measurements for silicone oil, hexadecane and Jet A-1 fuel on NP4-PP film and NP4-PP coated substrates with subsequent photographs of the droplet.

Material	Average Contact Angle (°)		
	Silicone Oil	Hexadecane	Jet A-1 Fuel
NP4-PP Thick Film	70.6 	95.1 	78.6 
NP4-PP Thin Film	105.9 	126.4 	111.9 
NP4-PP Coated Kevlar	78.3 	116.1 	103.6 
NP4-PP Coated Carbon Fibre	103.3 	117.6 	107.0 
NP4-PP Coated Glass Fibre	90.3 	120.3 	106.0 
NP4-PP Coated Nylon	74.5 	90.6 	97.2 
NP4-PP Coated Stainless-steel Mesh	92.3 	109.3 	96.9 

Table 6.4 Surface tension of various liquids[566,567].

Liquid	Surface Tension (mN/m) (20 °C)
Water	73
Hexadecane	27
Silicone Oil	21
Jet A-1 Fuel	24

6.3.3.3 Sliding Angle Measurements

In order to gain an understanding of the surface properties of the NP4-PP films and coated substrates, sliding angle measurements were conducted using an electronic goniometer (see Figure 6.30). These involved the deposition of silicone oil onto each material, before tilting the material using an electronic goniometer until the droplet began to roll. This process was repeated 5 times for each material and an average sliding angle was recorded, as shown in Table 6.5. Small sliding angles are typically associated with a low lateral adhesion between the silicone oil droplet and the surface.[568]

Figure 6.30 Sliding angle measurements conducted on an electronic goniometer. Materials were fixed to the goniometer with a small piece of tape (see photograph on the right). A droplet of silicone oil (approximately 0.05 mL) was deposited upon each material and the goniometer was lifted. When the droplet began to slide, the angle was recorded. The process was repeated five times for each material and an average sliding angle was recorded.

It was found that all sliding angles ranged between 16.0° − 33.8°. The ability of the oil droplets to roll off the surface with no visible contamination is a beneficial commodity and results from the oleophobic behaviour of the surface, causing repellence towards the oil droplet. The ease towards oil removal by tilting each material was also discussed during silicone/oil passage tests. An example of an application where it is necessary that the oil can be poured off with

ease is discussed in more detail further on in the chapter and considers the use of NP4-PP coated carbon fibre as a net to scoop up oil from the surface of water. It should be noted, however, that these angles are higher than several other oleophobic surfaces containing PDDA with fluorosurfactant, which typically range between 4° to 10°.[525,527] As such, it is believed that the higher sliding angle measurements within the current work reflect the presence of pores within the NP4-based materials, which provide grooves for the oil to partially situate in. As such, the oil is required to overcome a relatively large resistance (friction) to slide across the material.[529]

Table 6.5 Sliding angle data for NP4-PP films and NP4-PP coated substrates using silicone oil.

Material	Average Sliding Angle (°)
NP4-PP Thick Film	32.7
NP4-PP Thin Film	23.2
NP4-PP Coated Kevlar	16.0
NP4-PP Coated Carbon Fibre	23.7
NP4-PP Coated Glass Fibre	16.6
NP4-PP Coated Nylon	33.8
NP4-PP Coated Stainless Steel Mesh	26.7

6.3.3.4 Comparison of NP4-PP Membranes with Existing Membrane Technology

A comparison of NP4-PP membranes with various membranes within literature is summarised within Table 6.6. This compares the rate of water and oil passage through the various oleophobic/hydrophilic membranes, as well as the OCA associated with various oils. Since NP4-PP membranes (describing NP4-PP thin films and NP4-PP coated substrates) rely on a gravity-based separation, only literature examples of this type are provided. Gravity-based separations are, of course, particularly desirable to provide passive separations with no need for pumping technology.[569] Within these published works, it is observed that water passage through the membranes is typically within the region of several seconds to several minutes. These differences in passage rates primarily relate to the chemical composition, morphology and pore size of the membrane.[525,570] In some of these examples, the water was unable to penetrate the membrane, even though the OCA exceeded that of the WCA. This was observed within the work by Sultanov and co-workers, who coated methoxytrimethylsilane

functionalised SiO_2 nanoparticles onto stainless steel mesh containing various aperatures.[569,570] The penetration of oil through the membranes was found to be related to the pore size, where the stainless steel mesh substrate with larger pore sizes accommodated passage for oil flow, whilst the smaller pores sizes prevented it. Through comparison of these rates of water passage within these examples, it was suggested that the water passage through NP4-PP coated substrates occurred relatively fast, where times for complete passage through the membranes corresponded to between 0 – 5 minutes, depending on the substrate used. The present results also indicated that substrates with large pore sizes typically allowed much faster water passage. Further comparative analysis of the ability of the membrane to retain oil, revealed that several of the oleophobic/hydrophilic membranes allowed water to pass through, but also allowed oil passage, albeit at a slower rate than the water passage. Whilst these differences in separation times between oil and liquid may be sufficient for many separation applications, they require the separated water to be removed prior to the passage of oil to avoid further water/oil mixing. In the context of the applications presented within this thesis, this is undesirable. Any passage of oil through the NP4-PP coated nylon membrane would result in Jet A-1 fuel being lost from the propellant tank, in the context of aircraft tanks. Meanwhile, passage of oil through the NP4-PP coated carbon fibre membrane, which is shown to be act as a successful "net" to scoop up oil from the surface of ocean water, would result in further oil contamination of the water. Details relating to these applications are discussed further on in the chapter. Furthermore, the penetration of oil into the membrane can result in fouling of the membrane.[525] Within the current work, oil passage was typically prevented for at least 3 weeks. As such, the oil was successfully retained at the membrane surface and could be easily poured off. Furthermore, OCAs acquired within the current work were comparable with those achieved within published work, typically correlating with "oleophobic contact angles" (those with an OCA > 90°).[565]

Table 6.6 A comparison of the present membranes rate of water and oil passage with various gravity-based separation membrane technologies published within the literature. Note: In published examples, various membranes may have been tested, however, the most significant results are displayed here.

Membrane and its Composition	Rate of water passage (sec/min/hour)	Rate of oil passage (if any) (min/hour) *	Oil Contact Angle (°)	Reference
Various substrates coated with NP/PDDA/PFO	2.5 hour (NP4-PP thin film) Instantly – 5 min (coated substrates)	No oil passage (silicone oil)	105.9 (silicone oil) 126.4 (hexadecane) 111.9 (Jet A-1 fuel) (NP4-PP thin film) Up to 103.3 (silicone oil) up to 120.3 (hexadecane) Up to 107.0 (Jet A-1 fuel) (Coated substrates)	Current work
Stainless steel mesh spray coated with hydrolysed methoxytrimethylsilane/ SiO_2 nanoparticles	1.5 sec – 2 min	No oil passage (vacuum-pump oil) Oil passage occurs between 25 – 28 mins (kerosene)	128 (organic liquid[ǂ])	[569]
Stainless steel mesh spray coated with PDDA/ Pentadecafluorooctanoic acid/ SiO_2	4 – 5 sec	Oil passage occurs between 20 – 21 min (vacuum pump oil) No oil passage (kerosene)	116 (kerosene)	[570]
Cellulose filter paper dip coated in acetonitrile solution of toluene diisocyanate/ N-(2,4-diaminophenyl) maleimide	< 2 min	No oil passage (dibromoethane)	139.7 (dibromoethane)	[571]
Stainless steel mesh dip coated with PDDA/PFO/SiO_2 nanoparticles	12 min	No oil passage (hexadecane)	95 (hexadecane)	[526]
Stainless steel mesh spray coated with PDDA/PFO/SiO_2 nanoparticles	~ 7 sec	No oil passage (paraffin oil)	162 (paraffin oil)	[524]

*No oil passage refers to the oil being retained at the surface of the membrane. The length of time in which the oil is retained is not always specified within literature, however, in the present work, this refers to at least 3 weeks

ǂThe specific organic liquid is unspecified within the literature

6.3.4 Morphological Analysis

6.3.4.1 SEM analysis

SEM analysis was conducted to gain an insight to the structure and morphology of NP4-PP films and NP4-PP coated substrates. Initially SEM imaging was performed on NP4 for comparative purposes, and three different magnification images were recorded, as shown in Figure 6.31. These images reveal the presence of many aggregated stacks, forming particles which range drastically in size, spanning between several hundred microns to several hundred nanometers, as described in 5.2.1.1 of Chapter 5. Figure 6.31 (a) depicts the presence of particles with lengths of up to 300 µm. At high magnification, it is observed that these particles possess a powdery, clumped appearance (Figure 6.31 (c)).

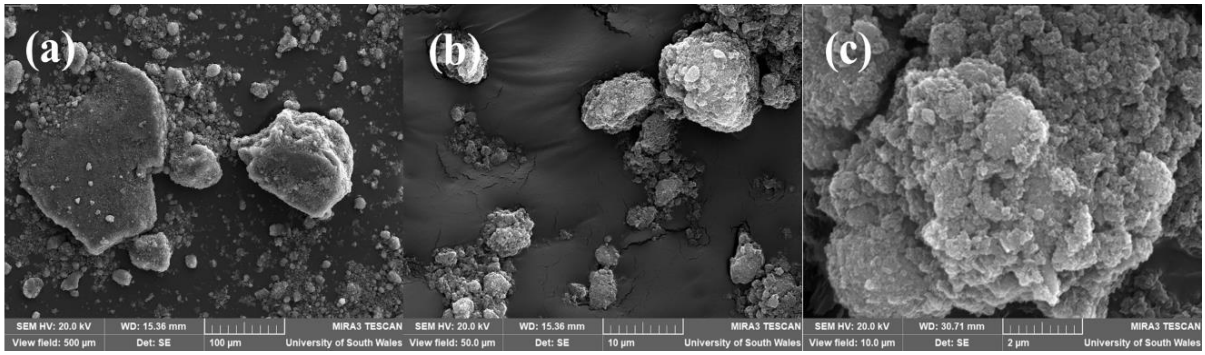

Figure 6.31 SEM image of NP4 at magnifications of (a) 415 x (b) 4.15 kx and (c) 20.74 kx.

Images of the NP4-PP composite contain a unique morphology, which differs from that of NP4. The SEM images (Figure 6.32) comprise of larger particles containing aggregates consisting of NP4 stacks in conjunction with PDDA and PFO. These particles possess lengths of several hundred microns to several millimetres. High magnification images (Figure 6.32 (c) and (d)) reveal that the outer regions of these aggregates also possess a smooth morphology, with a scaley appearance (Figure 6.32 (d)). In parallel, SEM imaging was also conducted on a mixture of PDDA and PFO in the absence of NP4, for comparative purposes. Corresponding images

are depicted within Figure 6.33 and show that this material consists of a single large particle, with a length of approximately 2 mm. The particle possesses a smooth morphology and at higher magnifications, the surface structure also appears scaly, with a rippling effect (Figure 6.33 (e) and (f)). As such, this scaly, rippling effect within NP4-PP, was attributed to the presence of the PDDA/PFO mixture. It is also noteworthy that the physical texture of the NP4-PP varied across the sample when physically handling the material. Some areas were brittle and could be snapped easily, whilst others were more flexible and could be stretched. The PDDA/PFO mixture possessed a more flexible texture, which is typical of many polymer-containing materials. As such, it is believed that within NP4-PP composite, the contribution of rigidity and flexibility, originates from the presence of both NP4 and PDDA/PFO components in the material.

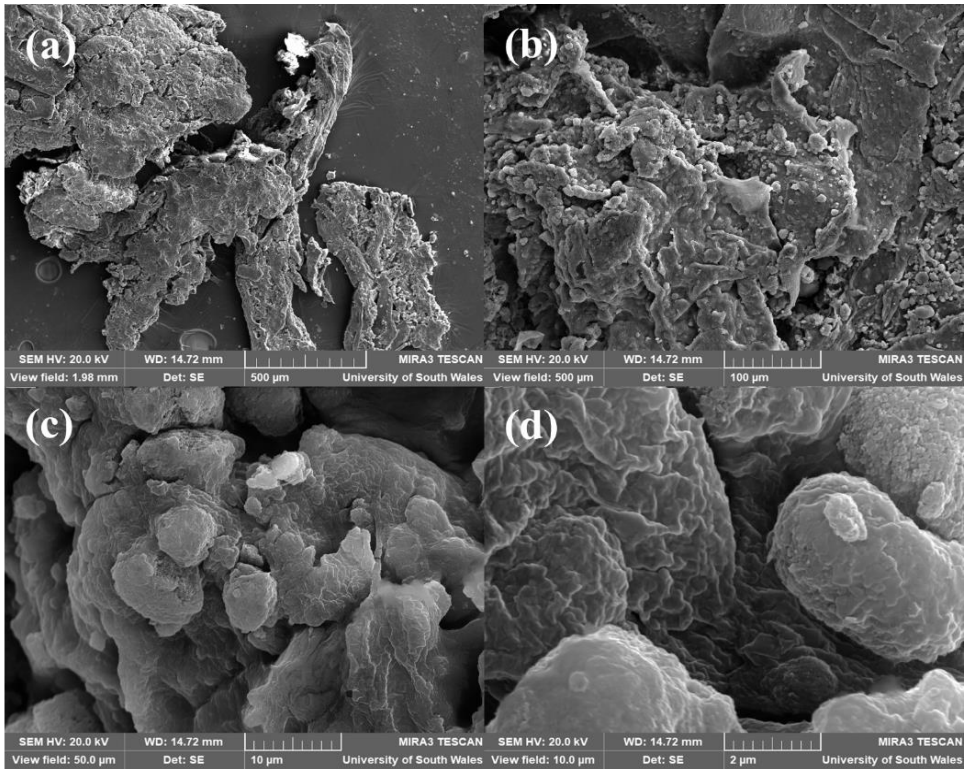

Figure 6.32 SEM image of NP4-PP composite at magnifications of (a) 105 x (b) 415 x (c) 4.15 kx and (d) 20.76 kx.

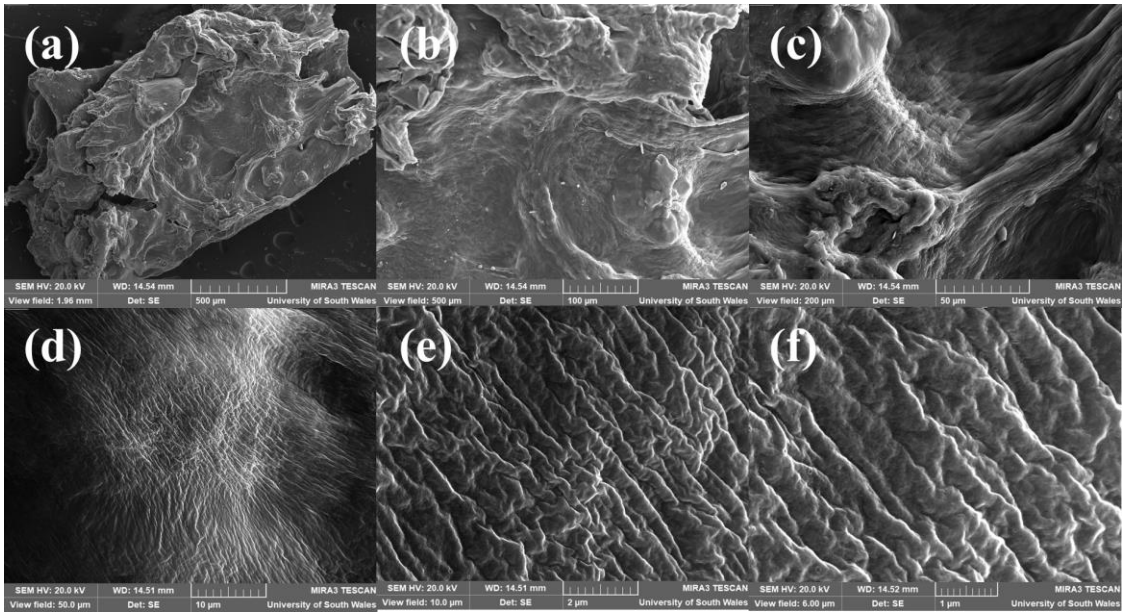

Figure 6.33 SEM images of PDDA/PFO at magnifications of (a) 106 x (b) 415 x (c) 1.04 kx (d) 4.15 kx (e) 20.76 kx and (f) 34.60 kx.

For the NP4-PP films, it was found that the morphologies consisted of an extended array of aggregates, comprising NP4 stacks and PDDA/PFO reagents (see Figure 6.34 and Figure 6.35). NP4-PP thick film possesses aggregates which exhibit lengths of 1 − 20 µm (Figure 6.34 (a) and (b)), whilst NP4-PP thin film possesses aggregates with lengths typically around 1 − 10 µm, with a few larger aggregates possessing lengths of up to 100 µm (Figure 6.35 (a) and (b)). In both films, some aggregates appeared cross-linked with one another, presumably by PDDA/PFO complex. This can be observed within (d) − (f) of Figure 6.34 and Figure 6.35. These images also enable the observation of a scaly, rippling texture, consistent with that of NP4-PP and PDDA/PFO. The arrangement of aggregates and the presence of cross-linking within both films resulted in the formation of pores, which were quite clearly observed throughout the films. Several large pores of 1 µm in size can be observed within NP4-PP thick film in Figure 6.34 (d) (e) and (f). NP4-PP thin film also contains pores between the aggregates, as shown within Figure 6.35 (f). Approximations were made to estimate the widths and areas associated within the pores of NP4-PP thin film, as outlined within Figure 6.36. Pores were observed to exhibit approximate widths of 0.5, 1.0 and 2.0 µm with corresponding areas of 0.1, 0.2, 0.3, 1.0 and 2.0 μm^2. These pores between NP4-PP aggregates form a network which extends throughout NP4-PP film and were observable within multiple SEM images taken across different positions on the film. As such, this porous network most likely provides a path for water passage through the material.

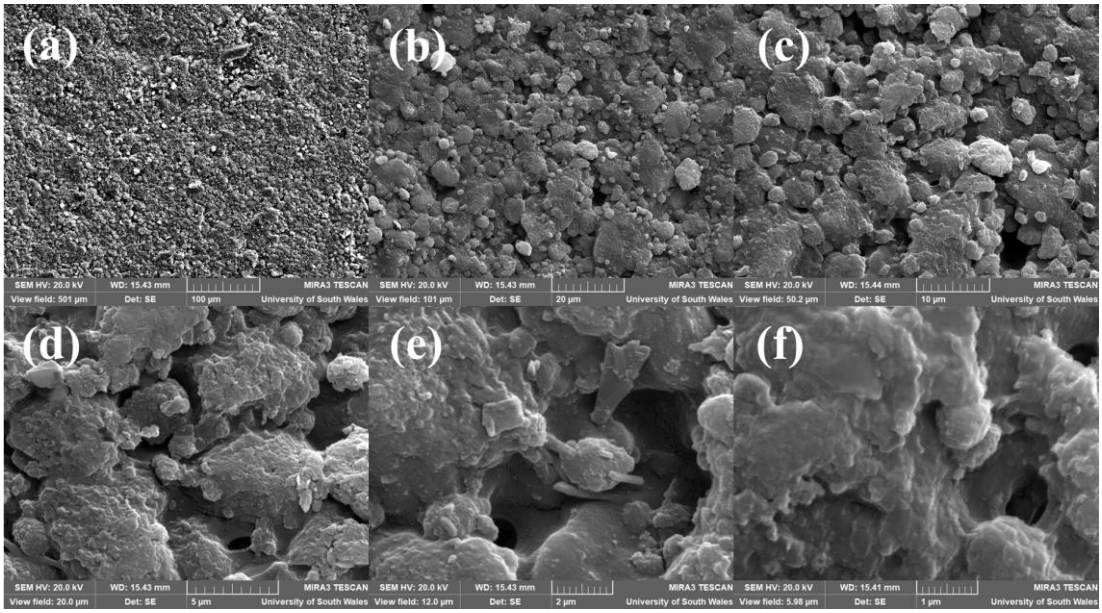

Figure 6.34 SEM images of NP4-PP thick film at various magnifications including (a) 415 x and (b) 2.06 kx (c) 4.14 kx (d) 10.37 kx (e) 17.36 kx and (f) 34.71 kx.

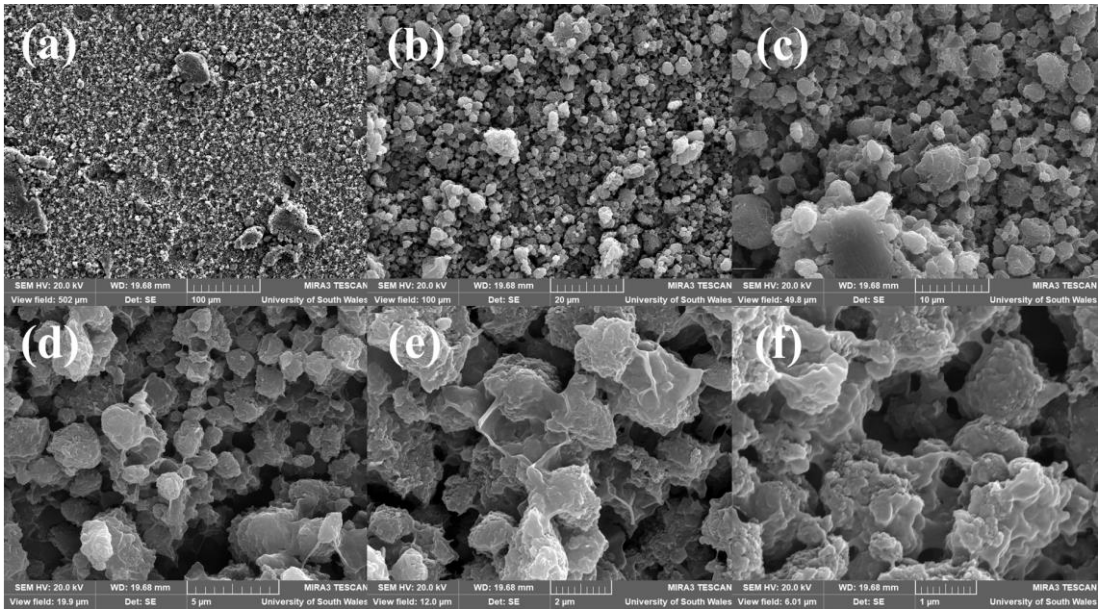

Figure 6.35 SEM image of NP4-PP thin film at magnifications of (a) 414 x (b) 2.07 kx (c) 4.17 kx (d) 10.45 kx (e) 17.36 kx and (f) 34.56 kx.

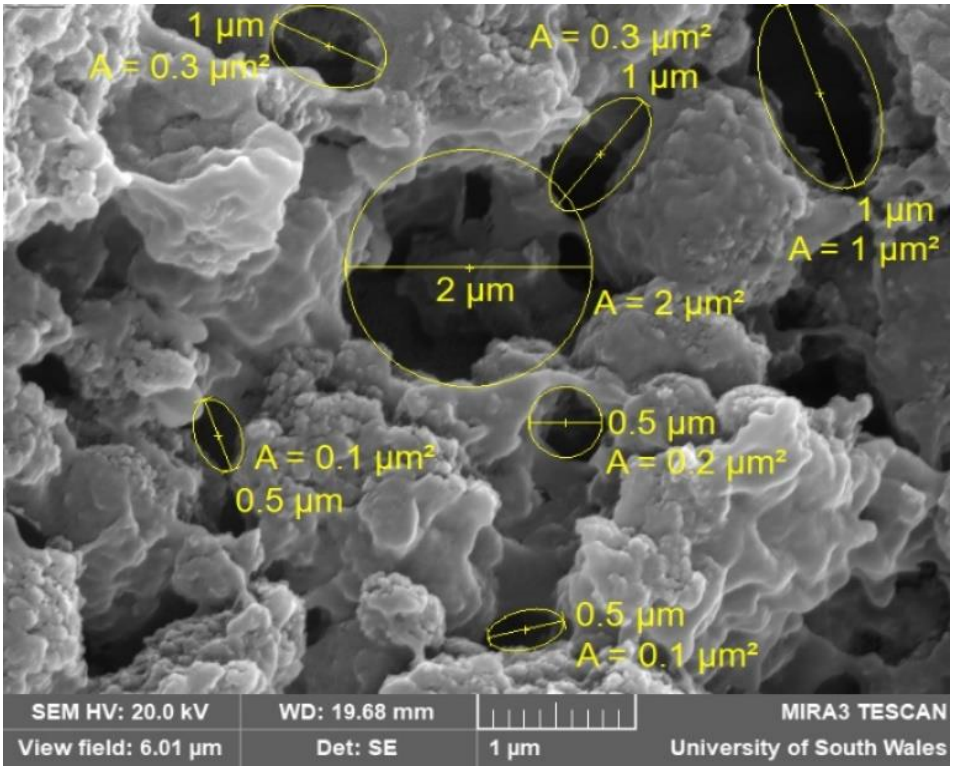

Figure 6.36 SEM image of NP4-PP thin film at a magnification of 34.56 kx, depicting approximate dimensions in the form of diameters and areas (A).

SEM imaging was also conducted on the coated substrates, as shown in Figure 6.37. Kevlar, carbon fibre and glass fibre contain fibrous strands with respective diameters of 15, 7.5 and 15.1 µm, as shown in (a) of Figures 6.38 – 6.40. Within these materials, many strands run parallel to one another, whilst other strands run perpendicular, resulting in a crosshatched arrangement of fibres. This orientation allows for the formation of gaps between both parallel and perpendicular strands. These gaps result in the presence of numerous pores within the overall material. Nylon and stainless-steel mesh also consist of a crosshatched arrangement, however, do not consist of the parallel fibrous structure present in the other substrates. Nylon contains an aperture and width of 0.1 mm, whilst stainless-steel mesh consists of apertures of 0.28 mm and widths of 0.16 mm, as observed in Figure 6.41 (a) and Figure 6.42 (a), respectively. Low magnification, wide field imaging of these showed that the coating on the substrates was homogeneous in some regions of the substrates and inhomogeneous in others (Figure 6.37). For example, in coated Kevlar, carbon fibre and glass fibre, it can be observed that some of the gaps between the fibres remained uncoated, as shown in Figure 6.37 (a) – (c). High magnification SEM analysis reveals the presence of pores within the three-coated substrates, corresponding to widths of 64 and 90 µm in coated Kevlar (Figure 6.38 (b) and (c)),

52, 15 and 14 µm in coated carbon fibre (Figure 6.39 (b)(c) and (d)) and 101 µm in coated glass fibre (Figure 6.40 (b)). Furthermore, additional pores are also observed between coated regions of the substrate and the fibres themselves, with areas corresponding to 114 and 232 μm^2 as shown by SEM imaging of coated glass fibre (Figure 6.40 (c)).

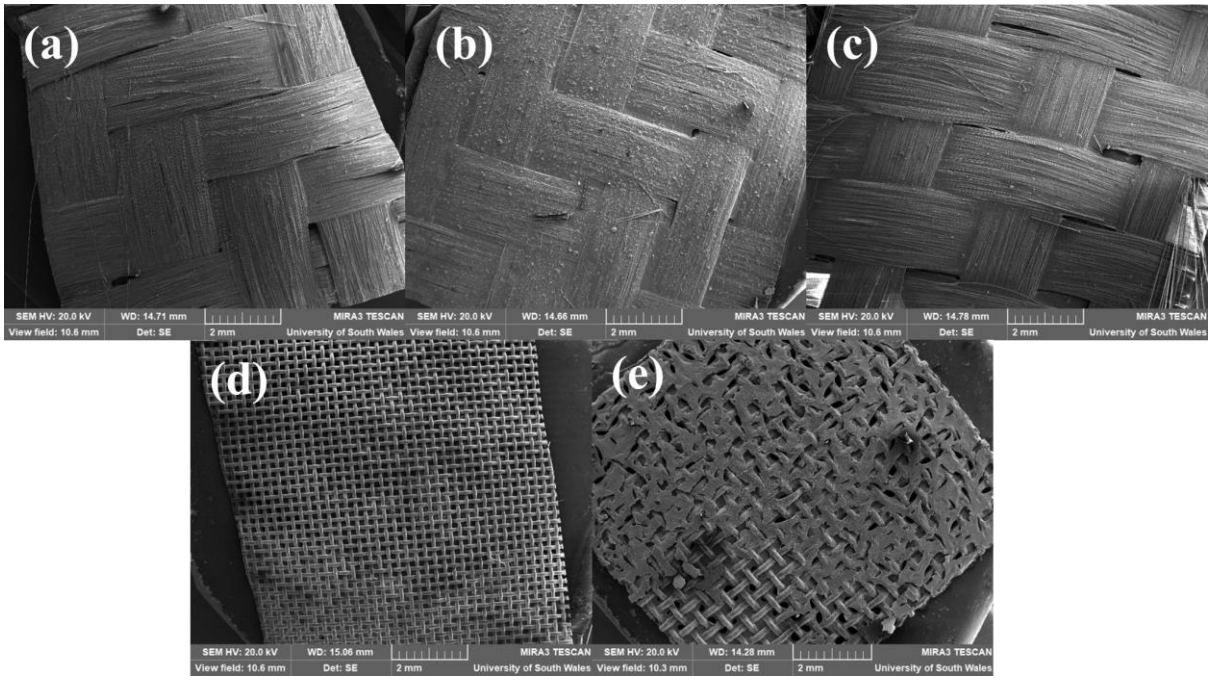

Figure 6.37 SEM images obtained in wide field mode of NP4-PP coated (a) Kevlar (b) carbon fibre (c) glass fibre (d) nylon 3 and (e) stainless-steel mesh at magnifications of 20 x.

In general, the coating process on Kevlar, carbon fibre and glass fibre resulted in NP4-PP film formation across the majority of the substrate. Some regions acquired film morphology directly over the strands, whilst other regions consist of film suspended between strands, however, the strands remain very much visible, as observed in Figure 6.38 (d), Figure 6.39 (e) and (f) and Figure 6.40 (d) and (f). Furthermore, some regions do not acquire NP4-PP film morphology at all, as evidenced by the large pores present within the coated substrates. In regions where coating consists of NP4-PP film formation suspended between strands, it is observed that the morphology differs significantly. Some regions comprise a smooth film formation, as shown in Figure 6.38 (e), Figure 6.39 (e) and Figure 6.40 (c) and (e), likely to be due to the presence of large concentrations of PDDA and PFO polymer. These regions possess no pores observable by SEM imaging. Other regions possess a similar aggregated morphology to that of NP4-PP

film, as shown in Figure 6.38 (f), Figure 6.39 (e) and (f) and Figure 6.40 (f), consisting of a more cluster-like appearance. In this case, pores are also present within the film forming areas themselves. For example, it is observed that coated Kevlar possesses pores with corresponding approximate areas of 5.0, 0.4, 5.0 and 1.0 μm^2 (Figure 6.38 (f)). In regions where film formation is acquired over the strands directly, a smooth morphology is observed. These are comparable with strands which do not acquire film formation, which display a different contrast, and appear much darker in colour. This is clearly observed within images associated with coated carbon fibre and coated glass fibre in Figure 6.39 (f) and Figure 6.40 (d), respectively. It is evident that pores are formed both within the film itself and within regions where film formation is not present. In the latter case, these regions may not have become coated during the process or may have become coated, but the flexible nature of the substrate may have led to tearing of the film. Within the SEM image for coated carbon fibre, as shown in Figure 6.39 (d), it is likely that this situation has occurred. This image depicts a very smooth crevasse within the film, where each side of this crevasse appears to perfectly match its opposing side, indicating that it was once conjoined. As such, it is evident that a large variety of pores exists within NP4-PP coated Kevlar, carbon fibre and glass fibre substrates, which provide facile passages for the passing of water. In the case with glass fibre, SEM imaging suggests that many of the pores are much larger than that of the other substrates. In particular, those pores present between non-coated areas and between parallel and neighbouring strands. This may explain why silicone oil passes through this coated substrate 2 hours after deposition in some cases, during silicone oil/water passage tests (see 6.3.3.1.2). With the remaining NP4-PP coated substrates and NP4-PP films, it is believed that oil may reside partially in the pores within the upmost regions (since high sliding angles were obtained), however, the oleophobic nature of the PFO moieties prevented any passage through the materials, and hence, silicone oil droplets remained on the surface with no visible wetting, for at least 3 weeks.

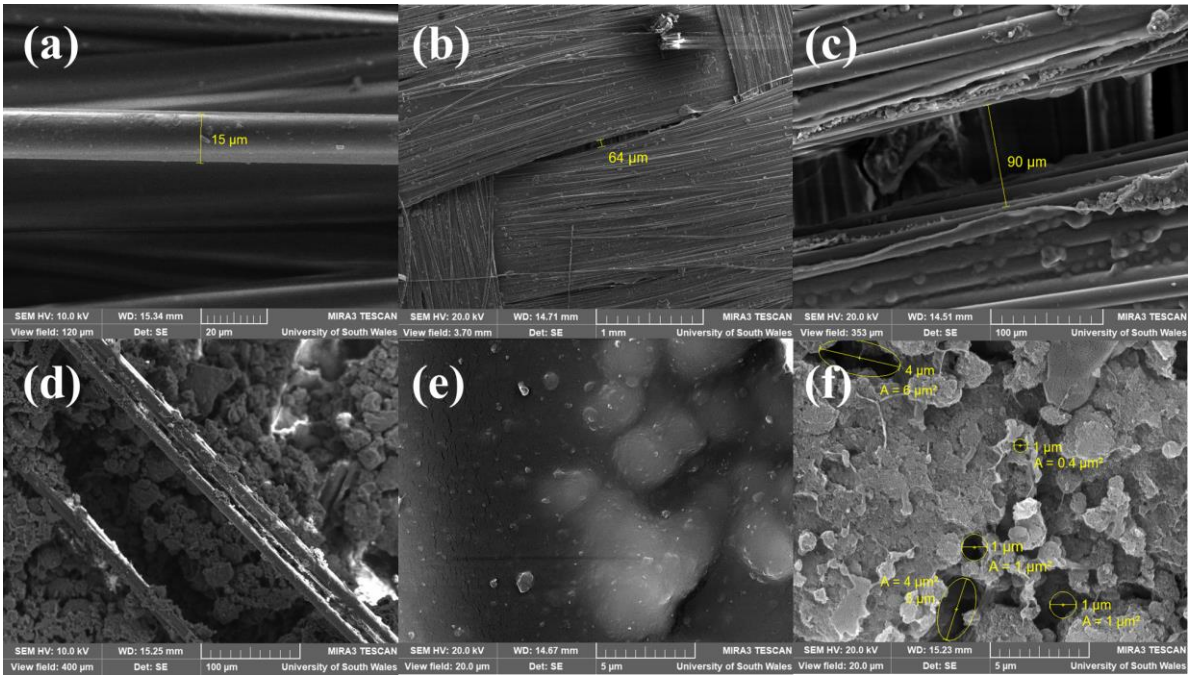

Figure 6.38 SEM images of (a) uncoated Kevlar at a magnification of 1.73 kx and coated Kevlar at magnifications of (b) 56 x (c) 589 x (d) 519 x (e) 10.38 kx and (f) 10.38 kx.

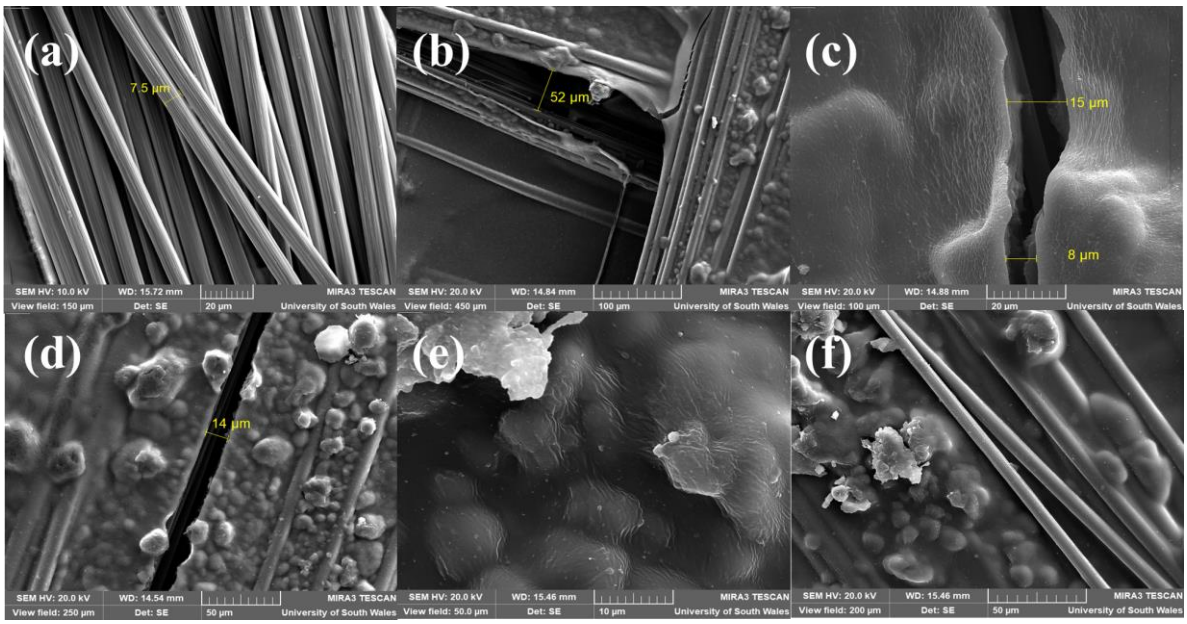

Figure 6.39 SEM images of (a) uncoated carbon fibre at a magnification of 1.38 kx and coated carbon fibre at magnifications of (b) 461 x (c) 2.08 kx (d) 830 kx (e) 4.15 kx and (f) 1.04 kx.

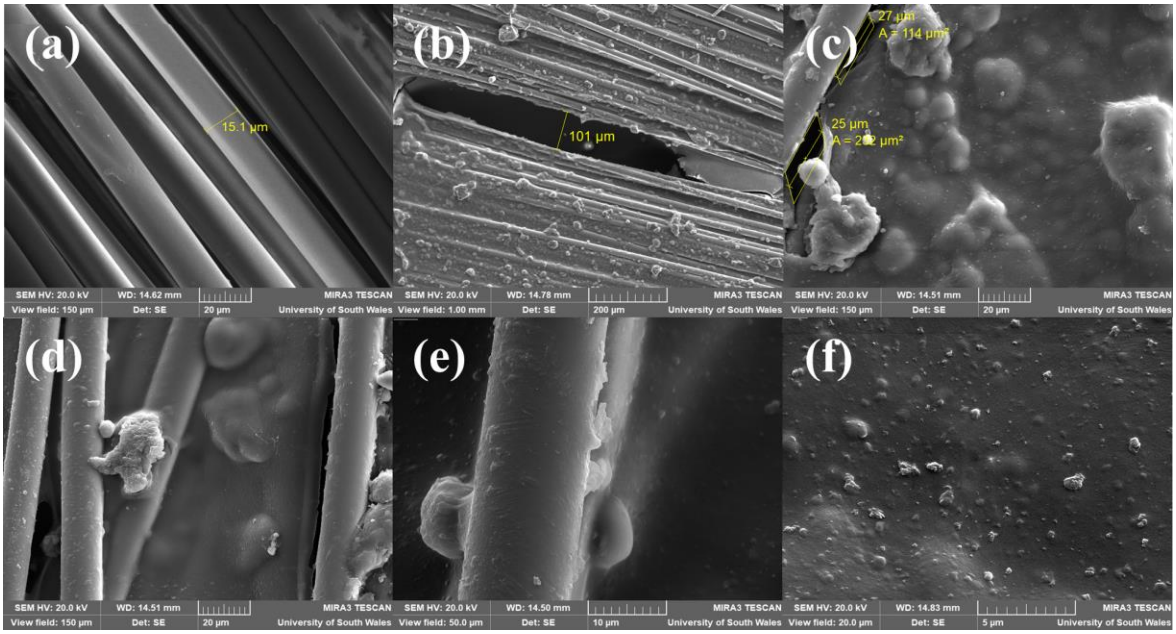

Figure 6.40 SEM images of (a) uncoated glass fibre at a magnification of 1.38 kx and coated glass fibre at magnifications of (b) 208 x (c) 1.38 kx (d) 1.38 kx (e) 4.15 kx and (f) 10.38 kx.

Within coated nylon 3 and stainless-steel mesh, it was observed that many apertures acquired a suspended film across them, however, some did not acquire coating or became partially coated (Figure 6.37). As such, large pores were created in the latter cases, as shown in Figure 6.41 (b) and Figure 6.42 (b). Coated stainless-steel mesh contained pores with corresponding areas of 0.02 and 0.04 mm^2 (Figure 6.42 (b)). It was also observed that regions which did acquire coating, displayed varying morphologies, similar to those of the previous coated substrates. Many regions displayed a smooth film-like morphology, indicating the presence of concentrated regions of PDDA/PFO reagents, as evidenced by Figure 6.41 (c) and Figure 6.42 (c). Other regions comprised of a coating, possessing strong similarity to that of NP4-PP films, as shown in Figure 6.41 (d) and Figure 6.42 (d). These possessed a cluster-like appearance. Pores were also created within the coated areas themselves. High magnification images also revealed the presence of pores with areas corresponding to 3 and 5 μm^2 in Figure 6.41 (e) for coated nylon 3 and 0.2 μm^2 in Figure 6.42 (e) for stainless-steel mesh. Pore formation also occurred within the spacing between suspended film and the substrate itself, likely to be due to the flexibility of the substrate. An example is depicted in the coated nylon 3 (Figure 6.41 (f)), which contains a pore of 13 µm in width. Moreover, a large crevasse-like pore can be observed within a coated region of the stainless-steel mesh, possessing a width of 31 µm, also likely to be formed due to movements of the substrate (Figure 6.42 (f)).

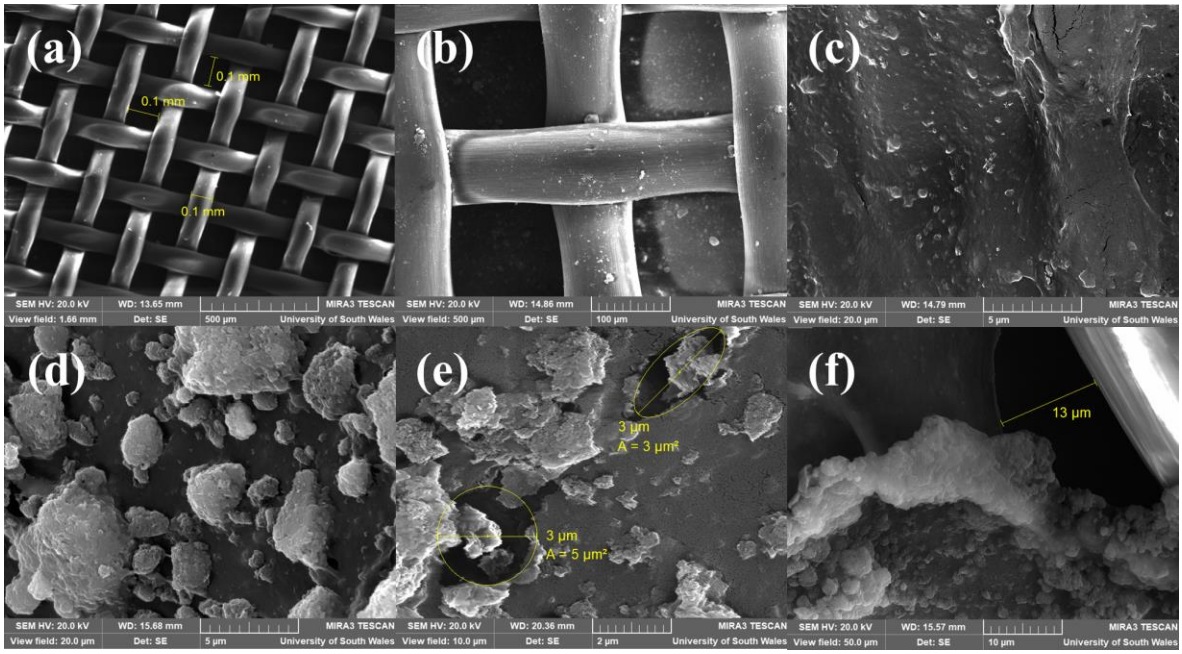

Figure 6.41 SEM images of (a) uncoated nylon at a magnification of 125 x and coated nylon 3 at magnifications of (b) 415 x (c) 10.38 kx (d) 10.39 kx (e) 20.75 kx and (f) 4.15 kx.

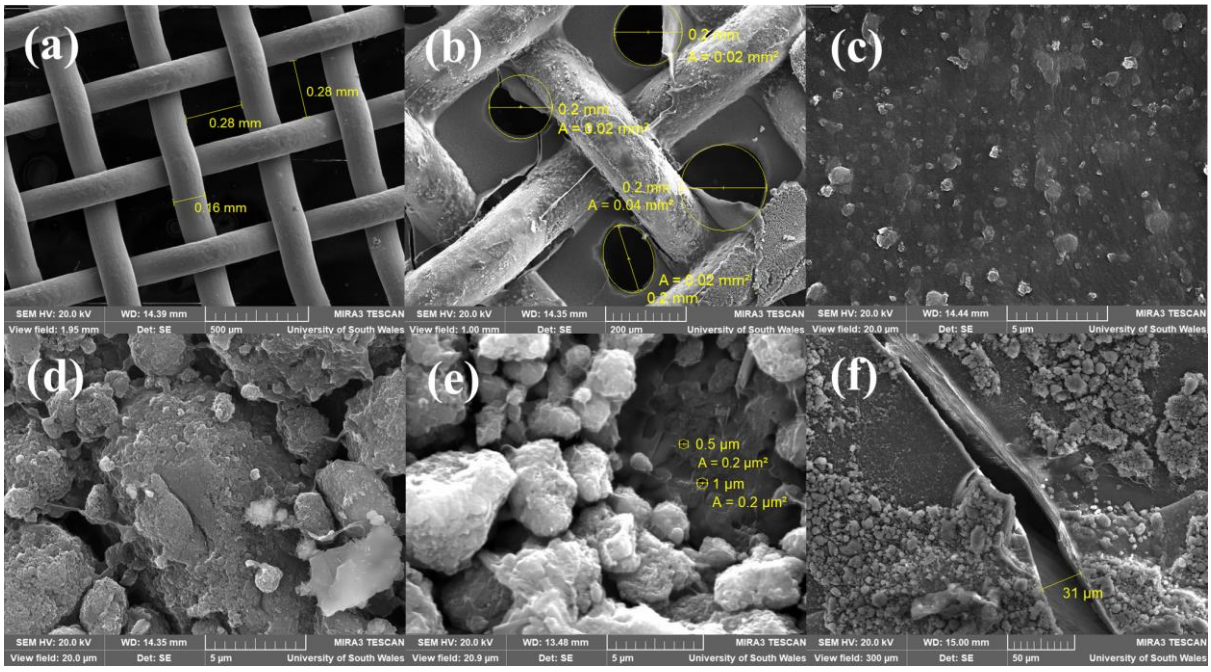

Figure 6.42 SEM images of (a) uncoated stainless-steel mesh at a magnification of 106 x and coated stainless-steel mesh at magnifications of (b) 208 x (c) 10.38 kx (d) 10.38 kx (e) 9.96 kx and (f) 692 x.

SEM imaging revealed the presence of a wide variety of pores within NP4-PP films and NP4-PP coated substrates. In the latter materials, the size of the largest pores in each material reflects the order as follows: glass fibre (232 µm) > stainless-steel mesh (200 µm) > nylon 3 (100 µm) > Kevlar (90 µm) > carbon fibre (52 µm). The presence of relatively large pores within glass fibre provide an explanation to why it allowed silicone oil passage, as previously mentioned in Section 6.3.3.1.2. It was also noticed that although SEM imaging of coated stainless-steel mesh revealed the presence of relatively large pores, this coated substrate showed very slow water penetration during the same silicone oil/water passage tests. It is believed that if a water droplet was deposited on an extremely well-coated region of this substrate, the passage would have been much slower than if deposition had have occurred on a less well-coated region. As such, this reasoning could explain why the passage for this coated substrate was much slower than expected.

6.3.4.2 AFM Analysis

The morphology of NP4-PP thin film was also analysed using AFM, as shown in Figure 6.43. It is observed that the film possesses a rough texture, consisting of aggregates of NP4, PDDA and PFO with dimensions of several microns (Figure 6.43 (a) and (b)). The coloured contrast within the images enables identification of the height variations of the film, such that lighter areas depict regions where the film protrudes from the surface, and darker regions correspond to holes within the film. It is evident that the NP4-PP thin film is not flat, and instead, contains many features which extend out from the surface. Further analysis of the holes is observed within the two-dimensional representation of Figure 6.43 (b), where measured line profiles provide an indication of the height variations across holes (see line profiles in Figure 6.43 (d)(i)). These line profiles indicate that a relatively large drop in height exists within these holes, including 37, 307, 240 and 276 nm for line profiles 1 − 4, respectively. A line profile was also produced across Figure 6.43 (c) and is depicted as a 2D representation in Figure 6.43 (e)). The respective line profile plot (Figure 6.43 (e) (i)) shows that the surface of the aggregate does not possess a flat topography. It is observed that the vertical distance varies between a minimum value of −109 nm to a maximum value of 77 nm, indicating that the height variations range quite substantially across a single aggregate.

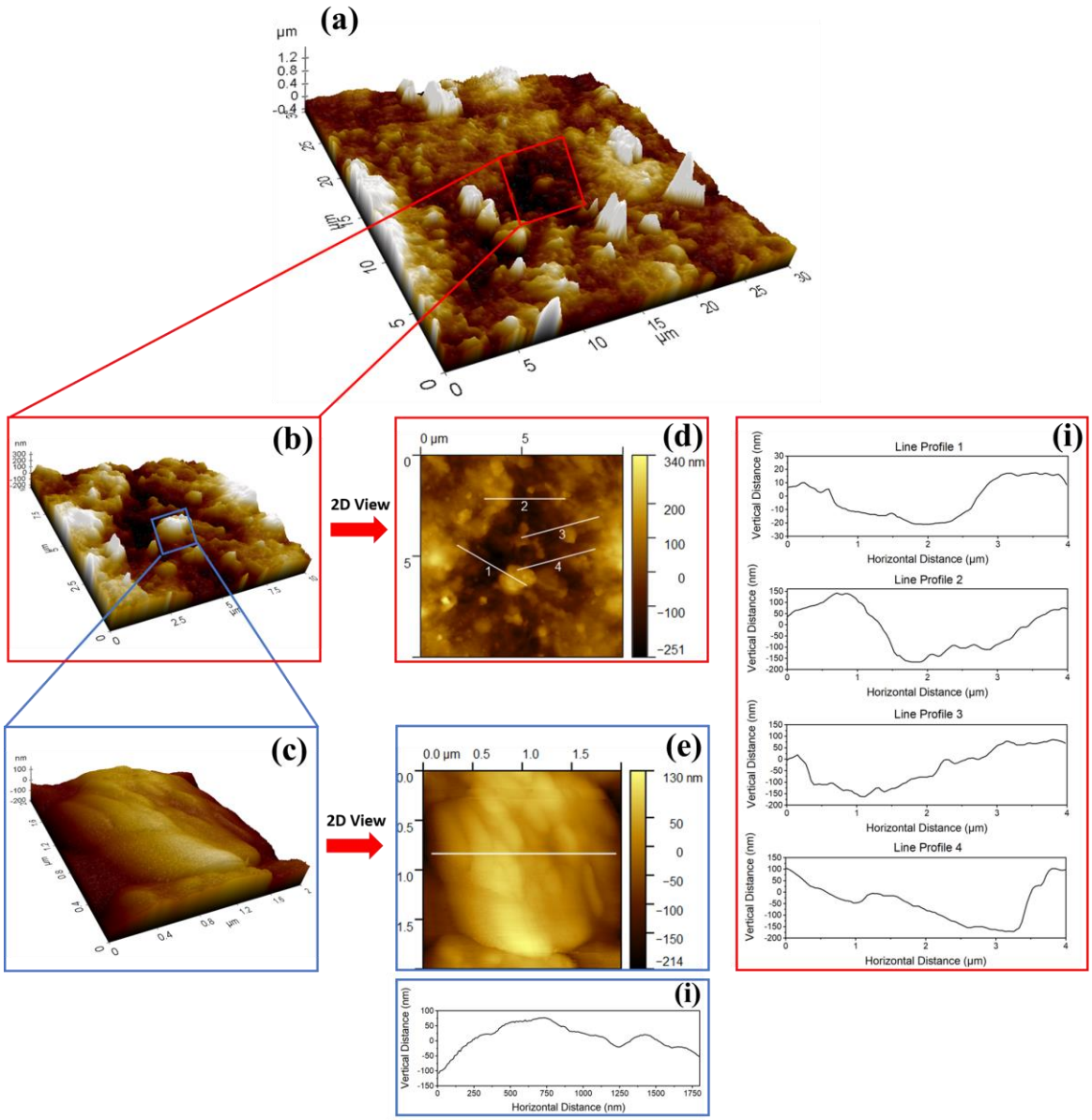

Figure 6.43 AFM images of NP4-PP thin film depicting: (a) a 10 by 10 µm AFM image of the surface of NP4-PP thin film, consisting of many aggregates; (b) a magnified image of (a) consisting of a 10 by 10 µm AFM image; (c) a magnified image of (b) consisting of a 2 by 2 µm AFM image of the surface of an aggregate; (d) a two-dimensional (2D) representation of image (b) containing line profiles 1 – 4, and corresponding plots (shown in (d)(i)), measured across four holes and (e) a two-dimensional representation of image (c) containing a line profile and its corresponding plot (shown in (e)(i)), measured across the surface of an aggregate.

6.3.5 Surface Area and Porosity Analysis

BET, BJH and t-plot analysis were conducted to gain an understanding of the surface area and porosity associated with NP4, NP4-PP composite and NP4-PP thin film.[9] The BET curves provided data on the adsorption-desorption characteristics of the materials, as shown within Figure 6.44. NP4 was previously characterised using BET, BJH and t-plot techniques within Chapter 5 (referred to as NP4), and contains a H3 hysteresis loop according to IUPAC classification,[239,351] indicating the presence of slit-like particles with non-rigid nature, and non-uniform shape and size. The other materials display similar isotherms, also possessing H3 hysteresis with a pseudo-type II isotherm. Like NP4, the absence of the plateau within NP4-PP composite and NP4-PP thin film suggests that the materials contain large pores which do not become completely filled during adsorption. As such, multilayer adsorption continues to proceed with no termination, until high P/P_0. In contrast to NP4, there is no steep uptake of nitrogen adsorbate at $P/P_0 < 0.001$, indicating an absence of micropores within the material. The BET surface area associated with NP4-PP composite and thin film correspond to 4.3 and 1.8 m^2/g, which is drastically lower than the surface area of NP4 (670.9 m^2/g) (see Table 6.7). The large surface of NP4 was desirable to maximise PDDA/PFO adsorption.

[9] The BET surface area data gave negligible surface area values for Kevlar, carbon fibre, glass fibre, nylon, stainless-steel mesh and their NP4-PP coated counterparts

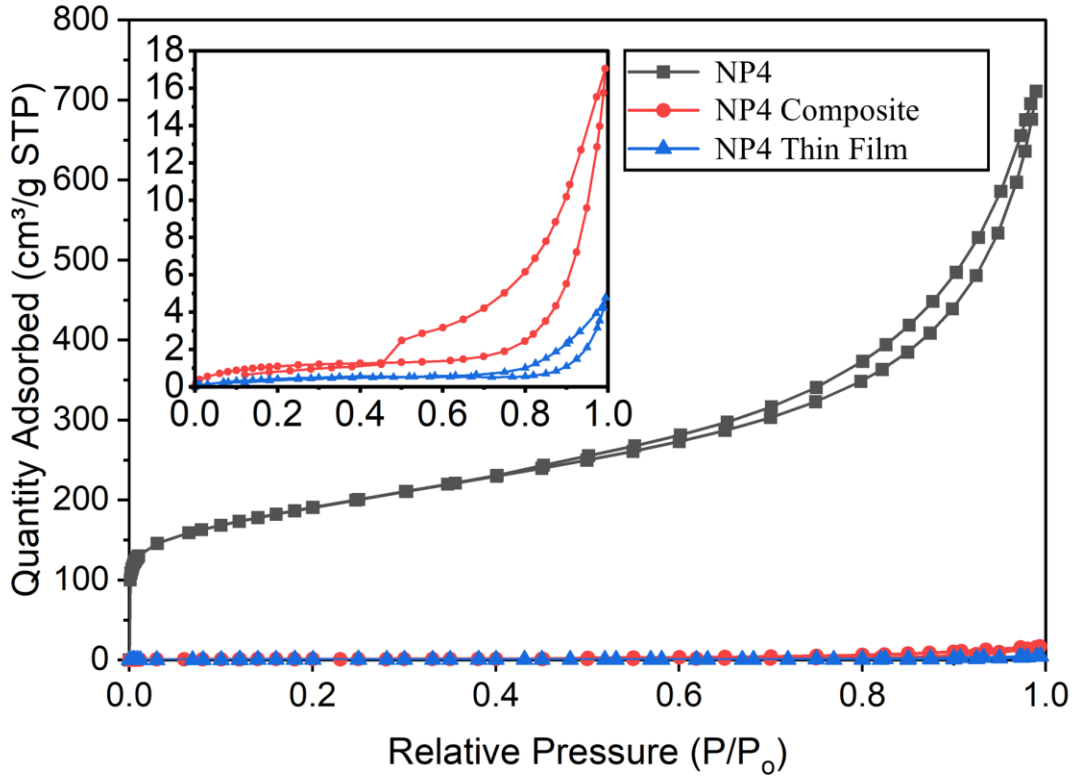

Figure 6.44 BET curve for NP4, NP4-PP composite and NP4-PP thin film.

The BJH PSD is depicted in Figure 6.45. The BJH pore volume associated with NP4-PP composite and thin film was found to correspond to 0.03 and 0.01 cm^3/g, which contrasts quite dramatically from 1.16 cm^3/g associated with NP4, as shown in Table 6.7. T-plot data also provided evidence of a decrease in the mesopore and macropore surface areas associated with NP4-PP composite and NP4-PP thin film, corresponding to 4.3 and 1.8 m^2/g, relative to 489.3 m^2/g for NP4 (Table 6.8). It is believed that the addition of PDDA/PFO results in a severe loss of pore volume and area, which remains consistent with the large decrease in surface area available to nitrogen adsorbate. This suggests that many mesopores and macropores within NP4 become diminished through the addition of PDDA and PFO, due to the physical blocking and occupancy of pores (both in-plane and slit pores). Interestingly film formation decreases the pore volume, pore area and subsequent BET surface area further, relative to NP4-PP composite, suggesting that a more orderly alignment of NP4 stacks and PDDA/PFO moieties exists. The BJH PSD of NP4-PP composite and thin film also varies from NP4. NP4 possesses a PSD between 1.7 – 84.5 nm, suggesting the presence of micropores, mesopores and macropores the material. In contrast, NP4-PP composite and NP4-PP thin film possess larger

PSDs corresponding to 4.1 – 123.8 and 5.9 – 130.3 nm, respectively, indicating mesopore and macropore presence only, with the loss of micropores. This finding is confirmed due to the absence of t-plot micropore area and volume associated with these materials. This absence of micropores is consistent with the lack of a sharp nitrogen uptake within the BET curves. Moreover, a loss of small mesopores with widths between 1.7 − 4.1 nm for NP4-PP and 1.7 − 5.9 nm for NP4-PP thin film also suggests that these small pores are heavily impacted by the presence of PDDA and PFO. Interestingly, it is also observed that the PSD increases over the macroporous region for NP4-PP composite and NP4-PP thin film, suggesting that larger pores were introduced into the materials, albeit in very low amounts. It is thus believed that the presence of PDDA and PFO moieties causes widening of some slit pores, whilst simultaneously establishing new pores through the linkage of aggregated NP4 stacks with PDDA/PFO networks.

Table 6.7 BET and BJH data for NP4, NP4-PP composite and NP4-PP thin film.

Material	BET Surface Area (m^2/g)	BJH Adsorption Volume of Pores Between 1.7 – 300 nm (cm^3/g)	BJH Average Pore Width (Adsorption)(4V/A) (nm)
NP4	670.9	1.16	6.3
NP4-PP Composite	4.3	0.03	16.7
NP4-PP Thin Film	1.8	0.01	23.1

Table 6.8 BJH and t-plot data for NP4, NP4-PP composite and NP4-PP thin film.

Material	t-plot Micropore Volume (cm^3/g)	t-plot Micropore Surface Area (m^2/g)	t-Plot Mesopore/Macropore Area (m^2/g)
NP4	0.0806	181.6	489.3
NP4-PP Composite	0	0	4.3
NP4-PP Thin Film	0	0	1.8

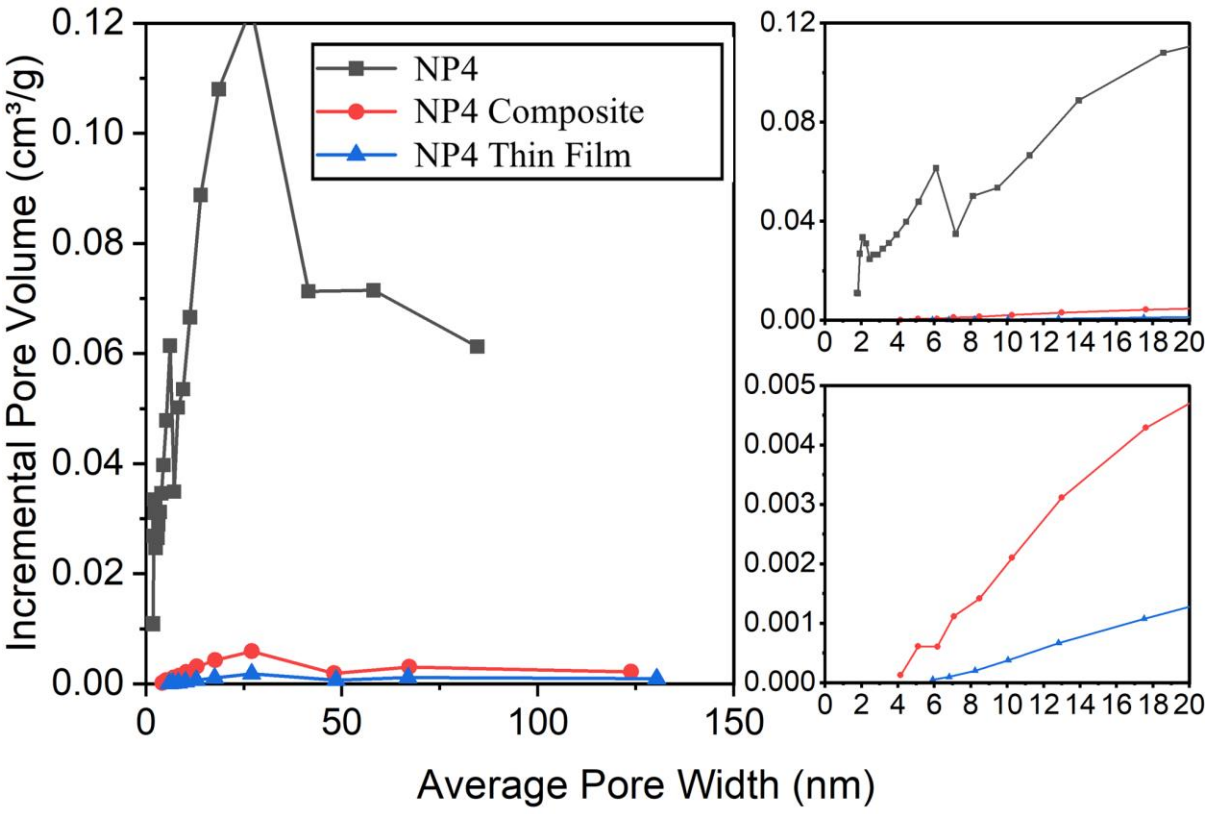

Figure 6.45 BJH incremental pore volume as a function of average pore width for NP4, NP4-PP composite and NP4-PP thin film

SEM imaging provided evidence of large macropores within the NP4-PP thin film, possessing widths of approximately 0.5 – 2 µm in size (Figure 6.36). It is worth noting that the surface area and volume associated with these pores contributes to the BET and t-plot mesopore/macropore area data, however does not contribute to BJH data, which analyses pores between the widths of 1.7 – 300 nm.[344,572]

6.3.6 Bond Analysis using ATR-FT-IR

The ATR-FT-IR spectra of PDDA, PFO and NP4-PP are depicted in Figure 6.46. The FT-IR spectrum of NP4 exhibited no significant peaks, which is assumed to be due to the nature of the material displaying absorption over the entire region of the spectrum. As such, the spectrum

is not presented. The most prominent absorptions within the spectrum of PDDA relates to the O−H stretch at approximately 3315 cm^{-1}. This peak exhibits a small shoulder around approximately 2900 cm^{-1} resembling that of the C−H asymmetrical stretch. An O−H symmetric deformation is also observed at 1633 cm^{-1}, whilst the O−H asymmetric deformation and O−H deformation are present at 1473 and 720 cm^{-1}, respectively.[573] The corresponding spectrum for PFO, exhibits prominent peaks at 1688 cm^{-1} corresponding to ν_{as} (COO^-), 1421 cm^{-1} corresponding to $\nu_{as}(COO^-)$ and 1363 cm^{-1} corresponding to $\nu_{ax}(CF_2)$. Furthermore, peaks at 1230, 1195 and 1146 cm^{-1} correspond to the CF_2 and CF_3 groups within PFO.[574] The spectrum of NP4-PP composite consists of a combination of both PDDA and PFO peaks, indicating the presence of both reagents within the composite material.

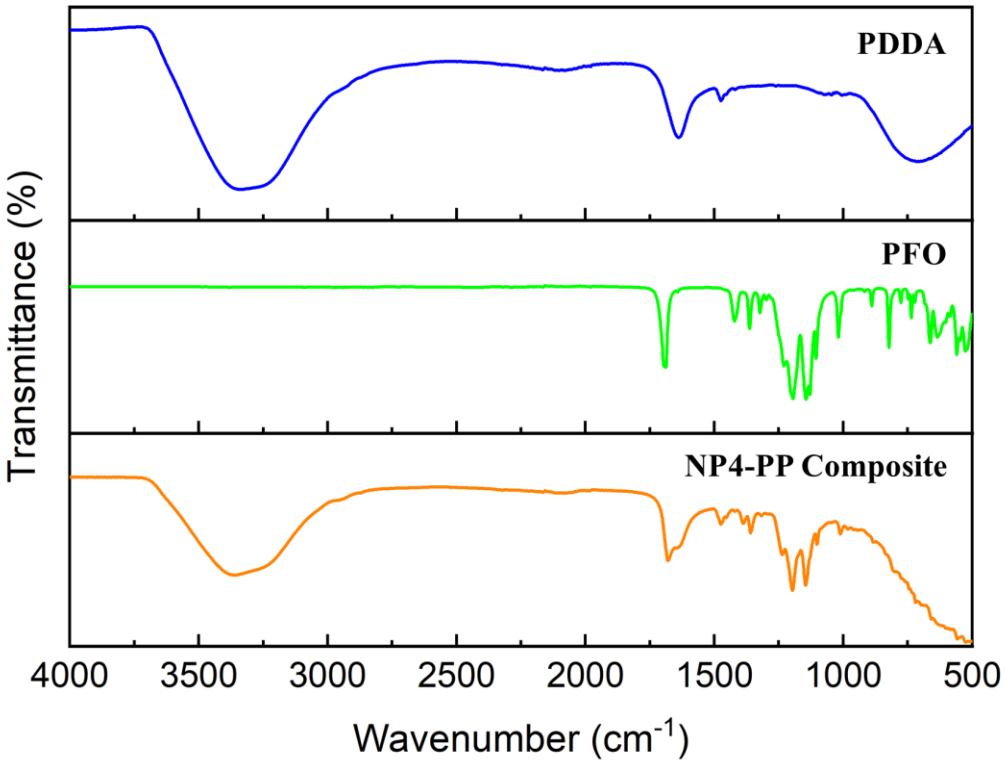

Figure 6.46 ATR-FT-IR spectra of PDDA, PFO and NP4-PP composite

6.3.7 Graphitic Structure and Defects Analysis using Raman Spectroscopy

The Raman spectra of NP4 and NP4-PP are presented within Figure 6.47. In accordance with the NP4's Raman spectra (originally presented in Section 5.4.1.2 within Chapter 5), the Raman spectrum associated with NP4-PP also contains three distinct peaks corresponding to the D band (1348 cm^{-1}), G band (1582 cm^{-1}) and 2D band (2700 cm^{-1}). The identify of these bands is discussed in more detail in the previous chapters. The D band signifies the presence of defects within NP4-PP, whilst the G band indicates the presence of sp^2centres.[305–308] Deconvolution of the D and G band with the overlapping D*, D'' and D' bands, allows for the I_D/I_G ratio of NP4-PP to be calculated.[311] This value corresponds to 0.96, which exceeds that for NP4 (0.93). This indicates an increase in the number of defects within the composite material. Furthermore, an additional defect band is present in NP4-PP at 2944 cm^{-1}, which corresponds to the combination mode (D + D').[172,310] Whilst defects within NP4 can be attributed to its plasma-exfoliation synthesis,[95] it is clear that the treatment of NP4 to form NP4-PP enhances its defective nature further. It is believed that the stirring within aqueous conditions may result in a small proportion of covalently bound oxygen becoming introduced into the graphitic network, thus, rehybridisation of some carbon atoms would occur from sp^2 to sp^3. The Raman spectra also provide an insight to the structure within both materials. The intensity ratio of the G band in respect to the 2D band (I_{2G}/I_G) is not dissimilar to that of NP4, possessing a value of 0.52, *cf.* 0.55 for NP4. Since this value is smaller than 1, the multilayer graphitic structure is confirmed, indicating that NP4 still consists of stacks comprising orderly aligned sheets.[312]

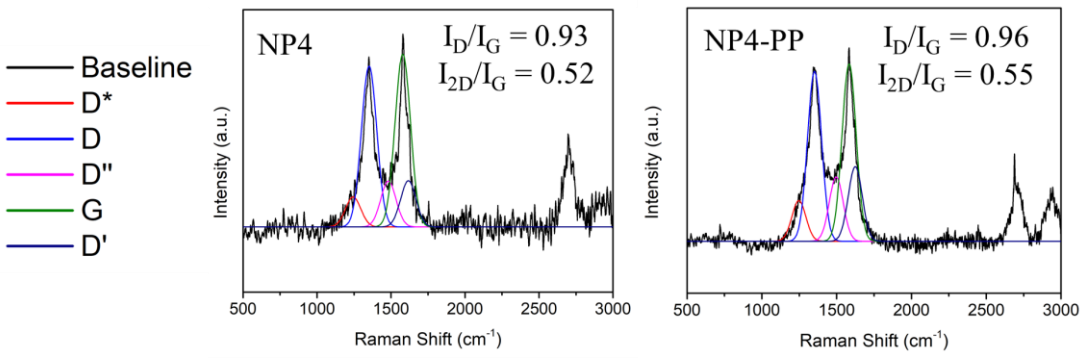

Figure 6.47 Raman spectra of NP4 and NP4-PP composite with depicting their corresponding I_D/I_G and I_{2D}/I_G ratios. Peak deconvolution was performed using OriginPro software to discriminate the D and G bands from overlapping D, D'' and D' bands.*

6.3.8 Stacking Orientation and Interlayer Spacing Analysis using XRD

The XRD patterns for NP4 and NP4-PP are presented in Figure 6.48. NP4 displays an intense peak at 2θ = 26.6°, which resembles the hexagonal (2H) (002) and rhombohedral (3R) (003) planes. These planes are associated with an interlayer spacing of 0.335 nm, thus, providing evidence of graphitic stacking. Slightly larger interlayer spacings are also present within the material, corresponding to 0.465 and 0.372 nm. These spacings relate to peaks at 2θ = 19.1° and 23.9° and suggest that the material consists of regions where graphitic layers have become expanded, probably due to the presence of covalently bound oxygen moieties.[318,454] A broad peak is also present between 43° and 46°, consistent with the presence of 2H (100) and (101) and 3R (101) and (012) stacking planes.[371] Additional peaks at 55.6° and 77.8° are also observed, resembling the graphite 2H (004) and (110) planes. The pattern associated with NP4-PP displays some key differences. Although a peak at 2θ = 26.6° is also present, it is much less intense. The most intense peak is observed at 2θ = 17.3°, which relates to an interlayer spacing of 0.513 nm. Further peaks are also observed at 19.9° and 24.2°, relating to interlayer spacing values of 0.446 and 0.363 nm, respectively. These widened interlayer spacings indicate the expansion of graphitic layers due to the presence of PDDA and PFO reagents. These widened interlayer spacings do not contribute to any significant porous area however, since the reagents cause complete occupancy, and therefore blockage of the pore as explained during BET/BJH analysis.

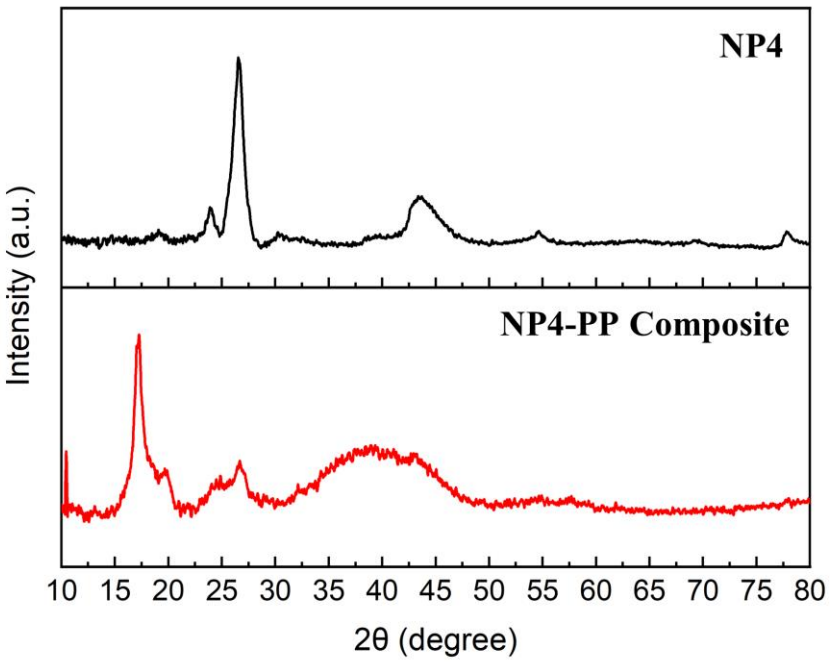

Figure 6.48 XRD patterns of NP4 and NP4-PP composite.

6.3.9 Mechanism for Oleophobic/Hydrophilic Behaviour of NP4-PP Composite

As previously outlined, it is believed that PDDA and PFO result in physical blockage of a large proportion of slit pores and in-plane pores within NP4. Furthermore, an electrostatic bond exists between PDDA and PFO moieties, forming the polyelectrolyte/fluorosurfactant complex, which has been utilised in complex formation in various other investigations.[518,522–528,575–577] Within these complexes exists the perfluorinated tail of PFO, which extends out towards the air/solid interface. This tail provides a sufficiently low dispersive component of its surface tension, whilst the polar carboxylate head group and PDDA moieties provide a sufficiently high polar component to the complex, thus providing effective oleophobic/hydrophilic behaviour, complimentary to previous works.[518,522–528,575–577] It has been found that a low dispersive component and a higher non-dispersive component are required for simultaneous oleophobic/hydrophilic behaviour.[578] When water is deposited on the surface it also encounters PFO's tails first, however, a stronger interaction exists between water and hydrophilic groups, thus water experiences a pull through the composite and pores

within the coated substrates.[577] During the dynamic process, more hydrophilic groups therefore reside at the top, resulting in an ease of passage for subsequent water molecules.

Cassie-Baxter and Wenzel regimes were also considered as alternative mechanisms for the existence of oleophobicity and hydrophilicity within the NP4-PP films and coated substrates.[530,536] In theory, a Cassie-Baxter wetting scenario could occur if a solid-water-oil or solid-air-oil interface was created. In regard to the former, it may have been possible that such an interface evolved when water was deposited onto the NP4-PP film and coated substrates, prior to oil deposition. In such a case, water could enter the surface pores of the material and create a "composite interface" for the oil to reside on, thus preventing its passage through the material. Whilst it is believed that this mechanism may be possible, it is unlikely that it is the key contributor towards the oleophobic behaviour. As explained previously, a test was conducted involving the deposition of oil onto coated nylon 3, prior to the deposition of water. During this test, no visible wetting occurred with the oil, however, water passed through the coated substrate with ease, consistent with the initial test on coated nylon 3. As such, it was concluded that the prior wetting of the NP4-PP films and coated substrates was not necessary to provide the oleophobic behaviour. Moreover, the roughness of the nanostructure may also result in the entrapment of air, resulting in a composite interface to both water and oil droplets. If indeed this had occurred, both water and oil wetting would have been equally reduced.

Finally, in relation to the Wenzel regime, it is believed that the nano-scale roughness of NP4-PP film and coated substrates resulted in increased oleophobic behaviour due to a larger oleophobic surface area being available. In parallel, it is believed that an increase in surface area would also increase the interaction between polar moieties with water droplets. As such, the oleophobic and hydrophilic behaviour becomes amplified.[579] AFM imaging provided evidence of the nano-scale rough texture of the NP4-PP aggregates; moreover, SEM analysis showed that many pores exist between the aggregates themselves. Whilst it is believed that these large pores should be large enough to provide passage for both water and oil droplets, the presence of the sufficiently low dispersive component associated with the PFO tails is sufficient in preventing the passage of oil.[578]

Reflection upon silicone oil/water passage tests, contact angle and sliding angle analyses and extensive characterisation of NP4-PP composite grants it success within the context of enabling oil/water separation. In addition, it was deemed a suitable candidate to be fabricated into free-standing films and coated upon substrates. These materials are deemed suitable as membranes

to separate oil/water mixtures. The porous morphology of these films and coated membranes, created due to the presence of NP4, is effective in providing a porous network which creates channels for water passage. In addition, the inhomogeneous coating coverage upon substrates also assisted in providing facile routes for water to pass through. In light of these findings, the applicability of NP4-PP composite within membrane applications is investigated within the context of oil-spill clean-up and within aircraft propellant tanks.

6.3.10 Application of NP4-PP Coated Substrates

6.3.10.1 Application within Oil-Spill Clean-Up

A well-known and desirable application for oleophobic/hydrophilic materials relates to oil/water separation. In the context of oil-spill clean-up, it can be extremely challenging to remove oil from water, especially when the oil disperses into many small droplets. As described within the introduction, there are a number of economic and environmental issues associated with the presence of oil in the oceans, and hence research into more effective strategies to enable its removal is vital.[519] When oil is spilt into water, it tends to accumulate at the water surface, due to the differences in densities associated with the liquids, as shown in Figure 6.49. As such, NP4-PP coated carbon fibre was employed as a coated net to "mop up" the surface-accumulated oil (Figure 6.49). The choice of this coated substrate over NP4-PP films and the remaining NP4-PP coated substrates lies in its suitability for application. Carbon fibre is mechanically strong, whilst flexible in nature. As such, it is suitable to withstand the weight of becoming saturated with water, without becoming damaged. Furthermore, its flexible nature means that it can be bent in the water to act as a scoop as it is lifts from the liquid's surface. In addition, this coated substrate also showed relatively fast water penetration during silicone/oil passage tests, as well as the highest OCA to silicone oil, relative to the other NP4-PP coated substrates. To test the application of NP4-PP coated carbon fibre, apparatus was set up, as shown in Figure 6.50. Water was placed into a round flask and silicone oil was poured over the top. These liquids contained the same dyes as outlined above. Naturally, the silicone oil

dispersed into several small droplets, which resided on the surface of the water. Coated carbon fibre was placed onto a stainless-steel mesh to ease its submersion into the water, and the coated substrate was scooped under the oil layer, before lifting from the water. The water then passed back through the coated carbon fibre, whilst the silicone oil remained on the coated substrate surface. The silicone oil was then deposited into a separate beaker by simply tilting the coated substrate. This process was repeated several times until no more silicone oil was observed on the water.

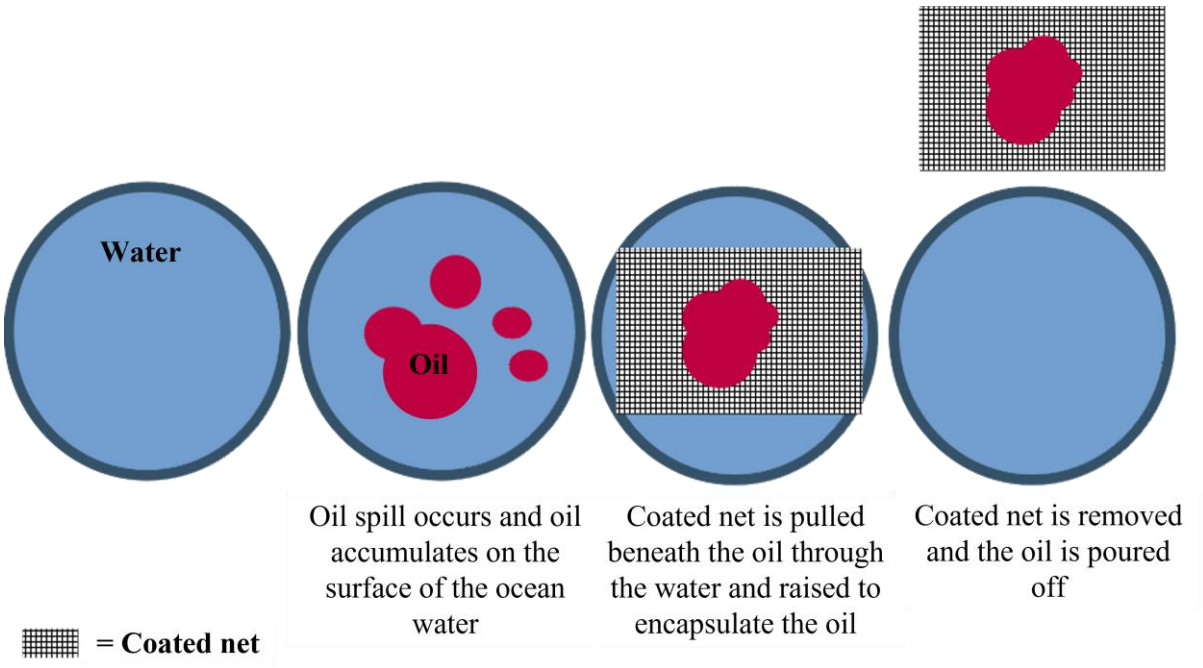

Figure 6.49 A proposed step-by-step process to remove oil from the surface of water in oceans, using an oleophobic/hydrophilic coated net to "mop up" the accumulated oil.

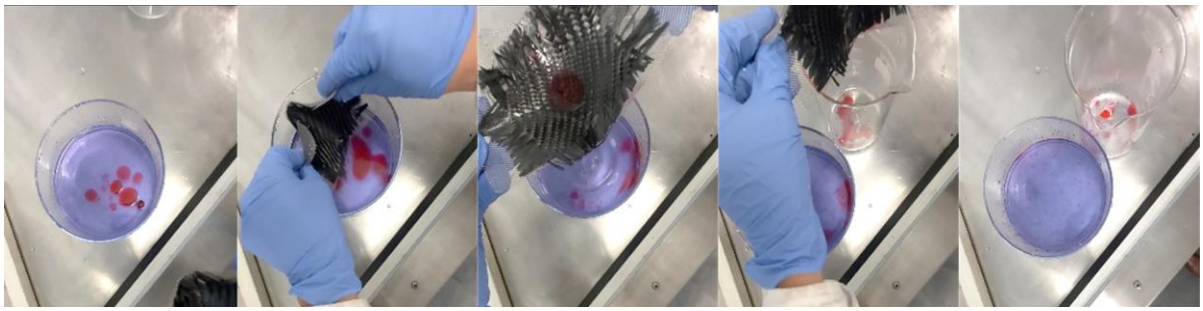

Figure 6.50 A step-by-step process implementing NP4-PP coated carbon fibre supported on a stainless-steel mesh to remove silicone oil from the surface of water.

6.3.10.2 Application within Aircraft Propellant Tanks

A second application which exploits the use of oleophobic/hydrophilic materials is proposed in the context of aircraft propellant tanks. As explained within the Introduction, a passive membrane which allows the removal of built-up water from a propellant tank, whilst simultaneously retaining propellant inside the tank, would be desirable. A simplified diagram of a propellant tank is shown in Figure 6.51, and depicts how engrossed water can accumulate at the bottom of tanks. The presence of a suitable oleophobic/hydrophilic membrane is therefore desirable to allow the removal of the water, whilst simultaneously retaining the propellant within the tank. For this purpose, NP4-PP coated nylon 3 was utilised as a passive filter membrane. This coated substrate was chosen due to its ease to cut into a suitable shape, and thin nature, enabling it to be manipulated into suitable apparatus. In addition, it also possessed a relatively high OCA using Jet A-1 fuel. To replicate an aircraft propellant tank, a Whatman three-piece filter funnel was used, and a homogenously coated section of NP4-PP coated nylon 3 was cut into a circular shape and sandwiched between two plates containing holes, as shown in Figure 6.52. The funnel was then filled with Jet A-1 fuel, to replicate a tank containing propellant. 20 mL of water was then pipetted into the Jet A-1 fuel, and it was observed that the coated nylon 3 was effective in allowing the passing of the water only, whilst retaining the Jet A-1 fuel within the tank. The water was released from the bottom of the funnel within 30 seconds. The Jet A-1 fuel was retained in the apparatus for at least 24 hours. A further 20 mL of water was then pipetted into the Jet A-1 fuel (not shown), and it was observed that the coated nylon 3 remained effective in allowing water passage through, within 30 seconds. As a control, it was shown that in the absence of NP4-PP coating, nylon was unable to prevent the passing of Jet A-1 fuel, thereby enabling it to pass freely through the apparatus, as shown in Figure 6.53.

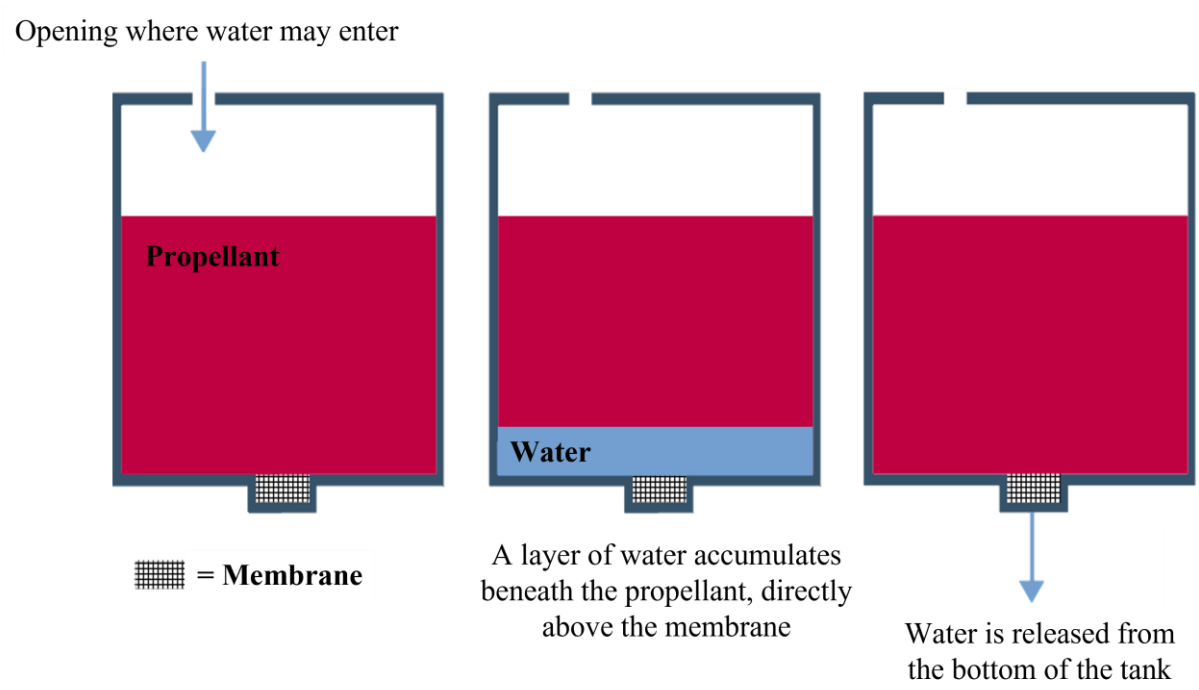

Figure 6.51 Diagram outlining how a passive membrane allows the removal of water accumulation from the bottom of an aircraft propellant tank.

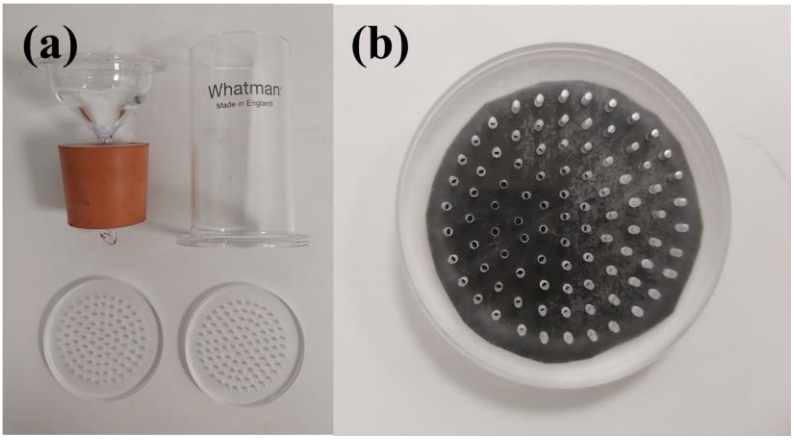

Figure 6.52 Apparatus used to replicate an aircraft propellant tank consisting of (a) a Whatman three-piece filter funnel and (b) NP4-PP coated nylon 3 which is sandwiched between two plates containing holes to replicate the membrane.

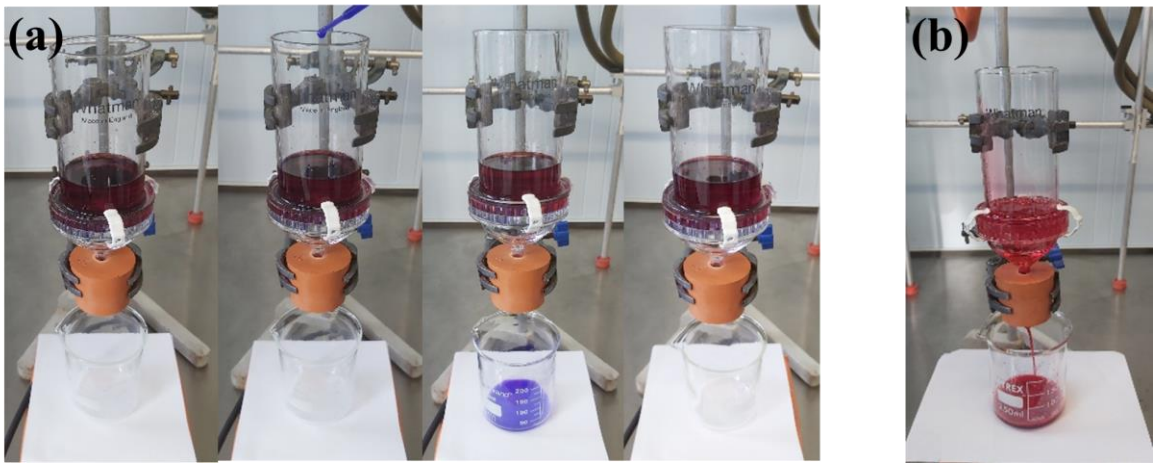

Figure 6.53 Apparatus to replicate an aircraft propellant tank, consisting of a Whatman three-piece filter funnel and NP4-PP coated nylon 3 sandwiched between two plates containing holes. (a) depicts the funnel filled with Jet A-1 fuel to resemble a propellant tank. 20 mL water was then added into the funnel and this water passed through the propellant and membrane within 30 seconds. The NP4-PP coated nylon 3 membrane therefore allows for the removal of water, whilst simultaneously retaining the Jet A-1 fuel. The Jet A-1 fuel was retained for at least 24 hours. (b) corresponds to a control experiment showing that Jet A-1 fuel penetrates uncoated nylon, and therefore passes freely through the apparatus and into the beaker, in the absence of NP4-PP coated nylon 3.

6.4 Conclusion

Within this chapter, a novel NP based composite comprising PDDA and PFO (NP4-PP) was synthesised and fabricated into free-standing films and coated upon various substrates, including Kevlar, carbon fibre, glass fibre, nylon and stainless-steel mesh. The NP4-PP films and NP4-PP coated substrates were found to display oleophobic character, preventing the wetting and passage of silicone oil, whilst simultaneously allowing water passage. High oil contact angles of up to 126.4° using silicone oil, hexadecane and Jet A-1 fuel, were associated with the materials. In addition, sliding angle measurements provided evidence of the ability for an oil droplet to be poured off from the surface of the materials by simply tilting them to angles in the range of 16.0° − 33.8°. The NP4-PP composite, NP4-PP films and NP4-PP coated substrates were investigated in some detail using XPS, XRD, BET/BJH/t-plot, FT-IR, Raman spectroscopy, AFM and SEM techniques. SEM analysis provided evidence of a unique porous network within the NP4-PP films. Furthermore, additional pores were observed upon the NP4-

PP coated substrates within regions of no coating. These additional pores served to decrease the time for water passage through these materials with respect to the NP4-PP films. Finally, the application of NP4-PP coated carbon fibre and NP4-PP coated nylon within the context of oil-spill clean-up and aircraft propellant tanks was investigated, revealing the capability of these coated substrates as membranes. In the former case, coated carbon fibre was effective in acting as a net to scoop up oil from the surface of water, whilst in the latter case, the coated nylon was used to allow removal of water from an aircraft propellant tank passively. The advantages of these membranes and free-standing films lays in their ability to allow water/oil separation in the absence of a vacuum. Passive gravity-driven separation is, of course, desirable to minimise the need for pump technology. In addition, the time for water passage through the coated substrates, is relatively fast compared to many literature examples of oil/water separation membranes and the oil passage is prevented for a considerably longer period of time. In summary, this chapter serves to identify a unique membrane and coating technology for oil/water separation which could benefit applications such as oil-spill clean-up and within aircraft propellant tanks.

7 Conclusions and Future Work

The entirety of this PhD work has involved the investigation into the understanding of the nature and modification of NP. In this regard, a number of novel strategies have been implemented to tailor the structure and nature of this material for advanced applications. Initially, a covalent functionalisation strategy, utilising aryl boronic acids, was investigated as an alternative to hazardous diazonium salts, with the objective to develop a safer and more industrially desirable route to large-scale synthesis of functionalised GBMs. This functionalisation strategy proved successful in decorating the edges of NP1 stacks with 4-(trifluoromethyl)phenyl moieties. The functionalised material was investigated in detail, revealing changes to the elemental composition, number of defects, morphology, and thermal stability as well as the surface area and porous characteristics. Unfortunately, at this stage of development, some challenges were associated with the methodology. Functionalisation was not solely obtained from the desired 4-(trifluoromethyl)phenyl units, and a portion of undesirable functionalities arose from oxidation caused by the presence of the oxidising reagent required for the catalytic conversion of Ag(I) to Ag(II). Furthermore, the integration of a small quantity of non-covalently bound, entrapped, silver impurities were also detected and assumed to be well in integrated to the porous structure of the material. As such, the development of strategies to avoid this unwanted functionality would be attractive. Despite these drawbacks, this functionalisation approach proved successful as a preliminary investigation towards the use of alternate aryl radical precursors for the safe synthesis of functionalised GBMs. In light of these findings, this work opens up the possibility for the decoration of NP and related materials with a variety of functional groups.

Following from this initial investigation, an alternate functionalisation strategy was then embarked upon with the aim to modify the surface area and porosity of oxidised NP. It was observed that the oxidation of NP3 led to a drastic decrease in its surface area upon drying, resulting from the disappearance of porous area within the material due to enhanced interaction between successive layers and stacks. Such a finding has only been reported in a handful of literature examples, despite the overwhelming research into oxidised GBMs. As such, the pillaring functionalisation strategy sought to re-introduce surface area to oxidised NP3, by establishing slit pores back into the structure. In this strategy, the synthetic clay material, laponite, was utilised as a unique pillaring device. Initially, laponite was functionalised with aminopropyltriethoxy silane *via* a silanisation reaction and was subsequently characterised, revealing the successful integration of terminal primary amine functionality from its surface. Afterwards, covalent functionalisation progressed *via* a coupling reaction between the

functionalised laponite, and carboxylic acid moieties present on the oxidised NP3. This two-step functionalisation found success in promoting expansion of the oxidised NP3 structure, resulting in the generation of slit pores and an almost four-fold increase in the BET surface area. As such, the employment of laponite as a pillaring device could open new avenues towards the expansion of multilayered and stacked materials. Consistent with the previous investigation, the entrapment of contaminant within the functionalised material once again proved challenging to remove. The undesirable presence of sodium acetate within f-laponite was believed to have a large influence on its surface area and porosity characteristics by causing physical blocking of the material. Upon addressing said challenges, a future perspective on this work would involve optimising the concentration of laponite attachment to enhance the surface area further. In addition, alternative clay materials with larger dimensions, such as montmorillonite, may also prove advantageous in the pillaring of such materials to different degrees.

Success was also found during the non-covalent functionalisation of NP4 with polyelectrolyte and fluorosurfactant moieties, providing opportunities for NP4 as a scaffold within oleophobic composite materials. Such a composite found success during the synthesis of free-standing films and as a coating for a variety of substrates. Interest was sparked in the potential application of this composite within the perspective of membrane technology for oil-spill clean-up and within aircraft propellant tanks, and its utility was demonstrated within a small laboratory-scale context. The morphology and nature of the composite, free-standing films and coated substrates also attracted vast interest, inspiring extensive microscopy analysis. SEM and AFM images revealed the obtainment of a unique porous structure, entailing a network of macropores, linked by NP4 aggregates and polymeric strands. In regard to future perspective on this investigation, the mechanism of oleophobic/hydrophilic behaviour should be investigated further. Whilst it is believed that the presence of fluorosurfactant grants the composite its oleophobic properties, it is still not well understood as to how exactly these proceed. For example, it would be extremely useful to assess the contact angle measurements over time, to see if there is any deterioration in the oleophobic properties of the materials. Furthermore, the contact angle measurements may also be measured using a wider range of oils to expand application. There are a range of jet fuels, containing slightly different compositions of hydrocarbon components, and thus the assessment of each would be necessary for implementation of the oleophobic composite membranes for specific aircraft propellant tank applications. In addition, varying the composition of polyelectrolyte/fluorosurfactant/NP4

within the composite may also result in changes to the oleophobic behaviour. Again, as an example, the length of the perfluorinated chain could be altered to tune oleophobic behaviour. Furthermore, practical considerations would also need to be considered upon utilising the composite material as a potential membrane within the stated applications. For instance, the longevity of the membranes would need to be examined in more detail, requiring tests on the reusability of the membranes after repeated use. Whilst it was shown within the current work that the coated substrates found success in their ability to prevent silicone oil passage whilst simultaneously allowing water passage, even after washing, this would need to be repeated to determine the reusability of the membranes and the quantity of reagents lost upon washing (if any at all). Such an investigation becomes particularly important to the application of the membranes within the context of oil-spill clean-up, where loss of any reagent to the sea could have detrimental impacts on aquatic life and the environment. Furthermore, it is also believed that the use of NPs within oleophobic/hydrophilic membranes could serve as an effective way of filtering contaminated water containing compounds such as polyaromatic hydrocarbons which often possess high toxicity, even at low concentrations. As such, these compounds are of great concern within the environment. It is well known that the extensive π system intrinsic to graphitic material is exceptionally good at forming $\pi-\pi$ interactions with aromatic compounds. As such, a further avenue of research could serve to investigate the ability of the free-standing films and coated substrates to retain unwanted contaminants as the water passes through the membrane material, to enable its purification.

The structure and morphology of these plasma derived materials was also investigated in detail, revealing interesting porous structures and the presence of a large range of slit pore widths. In this context, BJH analysis was uniquely applied to assess the distance between the stacks in the present materials. In recent years, BJH analysis has become much less commonly used to assess pore size distributions in carbon materials containing slit pores, due its shortcomings, and DFT has rapidly emerged as an alternative strategy. Despite this, however, the present work shows that BJH still remains a valuable and straightforward method to measure the distance between the stacks within materials such as NP2.

In all investigations, the requirement for characterisation was vital in effectively drawing conclusions about NPs and their functionalised counterparts. In this context, a number of practical struggles were encountered. For example, it was recognised that a great difficulty lies in the ability to identify whether covalent functionalisation or non-covalent functionalisation has occurred. In addition, the relatively inert nature of graphitic materials such as NPs brings

about a number of pragmatic issues when obtaining large degrees of functionalisation. Such hurdles have been reviewed in detail within this work, and in many cases, the strategies to overcome these issues have been identified.

As such, this PhD work offers a deeper understanding of the nature of plasma-exfoliated graphitic material, which is crucial for academic users working with analogous materials, as well as industrial manufacturers such as Perpetuus. In addition, the extensive investigations into novel covalent and non-covalent strategies allows for facile modification of NPs to alter their structure and properties and expand their application into a plurality of fields.

References

1 R. L. McLaren, C. J. Laycock, D. J. Morgan and G. R. Owen, *New J. Chem.*, 2020, **44**, 19144–19154.

2 R. L. McLaren, C. J. Laycock, E. Brousseau and G. R. Owen, *New J. Chem.*, 2021, **45**, 12071–12080.

3 R. L. McLaren, R. C. da Costa, C. J. Laycock, D. J. Morgan, M. E. A. Warwick and G. R. Owen, *New J. Chem.*, 2021, **45**, 19210–19214.

4 V. Georgakilas, J. A. Perman, J. Tucek and R. Zboril, *Chem. Rev.*, 2015, **115**, 4744–4822.

5 A. Bianco, H.-M. Cheng, T. Enoki, Y. Gogotsi, R. H. Hurt, N. Koratkar, T. Kyotani, M. Monthioux, C. R. Park, J. M. D. Tascon and J. Zhang, *Carbon N. Y.*, 2013, **65**, 1–6.

6 *International Organization for Standardization (ISO) Nanotechnologies Vocabulary Part 13: Graphene and Related Two-Dimensional (2D) Materials, BSI Standards Publication, London, UK, 2017. Retrieved from https://www.iso.org/standard/64741.html*, 2017.

7 A. P. Kauling, A. T. Seefeldt, D. P. Pisoni, R. C. Pradeep, R. Bentini, R. V. B. Oliveira, K. S. Novoselov and A. H. Castro Neto, *Adv. Mater.*, 2018, **30**, 1–6.

8 P. Bøggild, *Nature*, 2018, **562**, 502–503.

9 A. Kovtun, E. Treossi, N. Mirotta, A. Scidà, A. Liscio, M. Christian, F. Valorosi, A. Boschi, R. J. Young, C. Galiotis, I. A. Kinloch, V. Morandi and V. Palermo, *2D Mater.*, 2019, **6**, 025006.

10 D. M. Chen, P. M. Shenai and Y. Zhao, *Phys. Chem. Chem. Phys.*, 2011, **13**, 1515–1520.

11 P. R. Wallace, *Phys. Rev.*, 1947, **71**, 622–634.

12 H. P. Boehm., A. Clauss, G. O. Fischer and U. Hofmann, *Zeitschrift für Naturforsch. B*, 1962, **17**, 150–153.

13 K. S. Novoselov, A. K. Geim, S. V. Morozov, D. Jiang, Y. Zhang, S. V. Dubonos, I. V. Grigorieva and A. A. Firsov, *Science*, 2004, **306**, 666–669.

14 A. K. Geim, *Phys. Scr.*, 2012, **T146**, 014003.

15 K. I. Bolotin, K. J. Sikes, Z. Jiang, M. Klima, G. Fudenberg, J. Hone, P. Kim and H. L. Stormer, *Solid State Commun.*, 2008, **146**, 351–355.

16 R. R. Nair, P. Blake, A. N. Grigorenko, K. S. Novoselov, T. J. Booth, T. Stauber, N. M. R. Peres and A. K. Geim, *Science*, 2008, **320**, 1308–1308.

17 A. A. Balandin, S. Ghosh, W. Bao, I. Calizo, D. Teweldebrhan, F. Miao and C. N. Lau, *Nano Lett.*, 2008, **8**, 902–907.

18 A. Peigney, C. Laurent, E. Flahaut, R. R. Bacsa and A. Rousset, *Carbon N. Y.*, 2001, **39**, 507–514.

19 J. S. Bunch, A. M. Van Der Zande, S. S. Verbridge, I. W. Frank, D. M. Tanenbaum, J.

M. Parpia, H. G. Craighead and P. L. McEuen, *Science*, 2007, **315**, 490–493.

20 A. H. Castro Neto, F. Guinea, N. M. R. Peres, K. S. Novoselov and A. K. Geim, *Rev. Mod. Phys.*, 2009, **81**, 109–162.

21 F. Xia, D. B. Farmer, Y. Lin and P. Avouris, *Nano Lett.*, 2010, **10**, 715–718.

22 A. Liang, X. Jiang, X. Hong, Y. Jiang, Z. Shao and D. Zhu, *Coatings*, 2018, **8**, 33.

23 D. Jariwala, A. Srivastava and P. M. Ajayan, *J. Nanosci. Nanotechnol.*, 2011, **11**, 6621–6641.

24 L. Liu, M. Qing, Y. Wang and S. Chen, *J. Mater. Sci. Technol.*, 2015, **31**, 599–606.

25 C. K. Chua and M. Pumera, *Chem. Soc. Rev.*, 2013, **42**, 3222.

26 J. H. Wong, B. R. Wu and M. F. Lin, in *Computer Physics Communications*, 2011, vol. 182, pp. 77–80.

27 X. Gao, Y. Wang, X. Liu, T. L. Chan, S. Irle, Y. Zhao and S. B. Zhang, *Phys. Chem. Chem. Phys.*, 2011, **13**, 19449–19453.

28 G. E. Bacon, *Acta Crystallogr.*, 1951, **4**, 558–561.

29 G. Çakmak and T. Öztürk, *Diam. Relat. Mater.*, 2019, **96**, 134–139.

30 A. Ambrosi, C. K. Chua, B. Khezri, Z. Sofer, R. D. Webster and M. Pumera, *Proc. Natl. Acad. Sci. U. S. A.*, 2012, **109**, 12899–12904.

31 E. Fitzer, K.-H. Kochling, H. P. Boehm and H. Marsh, *Pure Appl. Chem.*, 1995, **67**, 473–506.

32 N. Kumar, R. Pandian, P. K. Das, T. R. Ravindran, S. Dash and A. K. Tyagi, *J. Phys. D. Appl. Phys.*, 2013, **46**, 395305.

33 H. Marsh and F. Rodríguez-Reinoso, in *Activated Carbon*, Elsevier, 2006, pp. 454–508.

34 R. Sharma, J. H. Baik, C. J. Perera and M. S. Strano, *Nano Lett.*, 2010, **10**, 398–405.

35 H. Y. Nan, Z. H. Ni, J. Wang, Z. Zafar, Z. X. Shi and Y. Y. Wang, *J. Raman Spectrosc.*, 2013, **44**, 1018–1021.

36 C. Sun and B. Bai, *Appl. Therm. Eng.*, 2017, **116**, 724–730.

37 S.-E. Zhu, S. Yuan and G. C. A. M. Janssen, *EPL (Europhysics Lett.*, 2014, **108**, 17007.

38 S. Zhao, Y. Lv and X. Yang, *Nanoscale Res. Lett.*, 2011, **6**, 498.

39 Y. Zhang and C. Pan, *Diam. Relat. Mater.*, 2012, **24**, 1–5.

40 C. Gómez-Navarro, R. T. Weitz, A. M. Bittner, M. Scolari, A. Mews, M. Burghard and K. Kern, *Nano Lett.*, 2009, **9**, 2206–2206.

41 D. Roy Chowdhury, C. Singh and A. Paul, *RSC Adv.*, 2014, **4**, 15138.

42 M. Mazurkiewicz-Pawlicka, M. Nowak, A. Malolepszy, A. Witowski, D. Wasik, Y. Hu and L. Stobinski, *Nanomaterials*, 2019, **10**, 32.

43 M. Nováček, O. Jankovský, J. Luxa, D. Sedmidubský, M. Pumera, V. Fila, M. Lhotka, K. Klímová, S. Matějková and Z. Sofer, *J. Mater. Chem. A*, 2017, **5**, 2739–2748.

44 P. P. Brisebois and M. Siaj, *J. Mater. Chem. C*, 2020, **8**, 1517–1547.

45 K. Erickson, R. Erni, Z. Lee, N. Alem, W. Gannett and A. Zettl, *Adv. Mater.*, 2010, **22**, 4467–4472.

46 H. He, T. Riedl, A. Lerf and J. Klinowski, *J. Phys. Chem.*, 1996, **100**, 19954–19958.

47 V. Georgakilas, M. Otyepka, A. B. Bourlinos, V. Chandra, N. Kim, K. C. Kemp, P. Hobza, R. Zboril and K. S. Kim, *Chem. Rev.*, 2012, **112**, 6156–6214.

48 D. W. Johnson, B. P. Dobson and K. S. Coleman, *Curr. Opin. Colloid Interface Sci.*, 2015, 20, 367–382.

49 D. R. Dreyer, S. Park, C. W. Bielawski and R. S. Ruoff, *Chem. Soc. Rev.*, 2010, **39**, 228–240.

50 W. Liu and G. Speranza, *ACS Omega*, 2021, **6**, 6195–6205.

51 N. Morimoto, T. Kubo and Y. Nishina, *Sci. Rep.*, 2016, **6**, 21715.

52 S. Azizighannad and S. Mitra, *Sci. Rep.*, 2018, **8**, 10083.

53 S. Pei and H.-M. Cheng, *Carbon N. Y.*, 2012, **50**, 3210–3228.

54 S. Stankovich, D. A. Dikin, G. H. B. Dommett, K. M. Kohlhaas, E. J. Zimney, E. A. Stach, R. D. Piner, S. B. T. Nguyen and R. S. Ruoff, *Nature*, 2006, **442**, 282–286.

55 S. Stankovich, D. A. Dikin, R. D. Piner, K. A. Kohlhaas, A. Kleinhammes, Y. Jia, Y. Wu, S. T. Nguyen and R. S. Ruoff, *Carbon N. Y.*, 2007, **45**, 1558–1565.

56 R. S. Edwards and K. S. Coleman, *Nanoscale*, 2013, **5**, 38–51.

57 S. S. Shams, R. Zhang and J. Zhu, *Mater. Sci. Pol.*, 2015, 33, 566–578.

58 Y. Arao and M. Kubouchi, *Carbon N. Y.*, 2015, **95**, 802–808.

59 K. Muthoosamy and S. Manickam, *Ultrason. Sonochem.*, 2017, **39**, 478–493.

60 B. T. Hogan, E. Kovalska, M. F. Craciun and A. Baldycheva, *J. Mater. Chem. C*, 2017, **5**, 11185–11195.

61 A. O'Neill, U. Khan, P. N. Nirmalraj, J. Boland and J. N. Coleman, *J. Phys. Chem. C*, 2011, **115**, 5422–5428.

62 Y. Hernandez, V. Nicolosi, M. Lotya, F. M. Blighe, Z. Sun, S. De, I. T. McGovern, B. Holland, M. Byrne, Y. K. Gun'ko, J. J. Boland, P. Niraj, G. Duesberg, S. Krishnamurthy, R. Goodhue, J. Hutchison, V. Scardaci, A. C. Ferrari and J. N. Coleman, *Nat. Nanotechnol.*, 2008, **3**, 563–568.

63 T. Skaltsas, X. Ke, C. Bittencourt and N. Tagmatarchis, *J. Phys. Chem. C*, 2013, **117**, 23272–23278.

64 M. Saeed, Y. Alshammari, S. A. Majeed and E. Al-Nasrallah, *Molecules*, 2020, **25**, 3856.

65 R. S. Edwards and K. S. Coleman, *Acc. Chem. Res.*, 2013, **46**, 23–30.

66 K. Ostrikov, E. C. Neyts and M. Meyyappan, *Adv. Phys.*, 2013, **62**, 113–224.

67 Z. Ereš and S. Hrabar, *Automatika*, 2018, **59**, 254–260.

68 X. Li, C. W. Magnuson, A. Venugopal, J. An, J. W. Suk, B. Han, M. Borysiak, W. Cai, A. Velamakanni, Y. Zhu, L. Fu, E. M. Vogel, E. Voelkl, L. Colombo and R. S. Ruoff, *Nano Lett.*, 2010, **10**, 4328–4334.

69 A. Reina, X. Jia, J. Ho, D. Nezich, H. Son, V. Bulovic, M. S. Dresselhaus and J. Kong, *Nano Lett.*, 2009, **9**, 30–35.

70 M. S. A. Bhuyan, M. N. Uddin, M. M. Islam, F. A. Bipasha and S. S. Hossain, *Int. Nano Lett.*, 2016, **6**, 65–83.

71 J. Du, S. Pei, L. Ma and H. Cheng, *Adv. Mater.*, 2014, **26**, 1958–1991.

72 D. Sun, C. Liu, W. Ren and H. Cheng, *Adv. Electron. Mater.*, 2016, **2**, 1600229.

73 G. Yazdi, T. Iakimov and R. Yakimova, *Crystals*, 2016, **6**, 53.

74 S. K. Lilov, *Mater. Sci. Eng. B*, 1993, **21**, 65–69.

75 H. Tan, D. Wang and Y. Guo, *Coatings*, 2018, **8**, 40.

76 L. Lin, H. Peng and Z. Liu, *Nat. Mater.*, 2019, **18**, 520–524.

77 K. Coleman, Applied Graphene Nanomaterials Limited, US Pat., US 2012/0114551A1, 2012, 1.

78 B. C. Brodie, *Philos. Trans. R. Soc. London*, 1859, **149**, 249–259.

79 L. Staudenmaier, *Berichte der Dtsch. Chem. Gesellschaft*, 1898, **31**, 1481–1487.

80 U. Hofmann and E. König, *Zeitschrift für Anorg. und Allg. Chemie*, 1937, **234**, 311–336.

81 U. Hofmann and R. Holst, *Berichte der Dtsch. Chem. Gesellschaft (A B Ser.*, 1939, **72**, 754–771.

82 W. S. Hummers and R. E. Offeman, *J. Am. Chem. Soc.*, 1958, **80**, 1339–1339.

83 A. T. Smith, A. M. LaChance, S. Zeng, B. Liu and L. Sun, *Nano Mater. Sci.*, 2019, **1**, 31–47.

84 W. Yu, L. Sisi, Y. Haiyan and L. Jie, *RSC Adv.*, 2020, **10**, 15328–15345.

85 K. E. Whitener and P. E. Sheehan, *Diam. Relat. Mater.*, 2014, **46**, 25–34.

86 M. C. F. Costa, V. S. Marangoni, P. R. Ng, H. T. L. Nguyen, A. Carvalho and A. H. Castro Neto, *Nanomaterials*, 2021, **11**, 551.

87 A. Dey, A. Chroneos, N. S. J. Braithwaite, R. P. Gandhiraman and S. Krishnamurthy, *Appl. Phys. Rev.*, 2016, **3**, 021301.

88 R. K. Singh, R. Kumar and D. P. Singh, *RSC Adv.*, 2016, 6, 64993–65011.

89 M. B. Structures, *Principles of Plasma Discharges and Materials Processing*, John Wiley & Sons, Inc., Hoboken, New Jersey, 2nd edn., 2005.

90 A. Kashyap, N. K. Singh, M. Soni and A. Soni, in *Chemical Solution Synthesis for Materials Design and Thin Film Device Applications*, Elsevier, 2021, pp. 79–117.

91 E. P. Neustroev, in *Graphene Oxide - Applications and Opportunities*, 2018.

92 P. V. Pham, *R. Soc. Open Sci.*, 2018, **5**, 172395.

93 N. Kostoglou, A. Tarat, I. Walters, V. Ryzhkov, C. Tampaxis, G. Charalambopoulou, T. Steriotis, C. Mitterer and C. Rebholz, *Microporous Mesoporous Mater.*, 2016, **225**, 482–487.

94 I. Levchenko, K. K. Ostrikov, J. Zheng, X. Li, M. Keidar and K. B. K. Teo, *Nanoscale*, 2016, **8**, 10511–10527.

95 I. Walters and D. Walters, Perpetuus Research & Development Limited, EU Pat., EP3129323B1, 2019.

96 US20130320274, 2011, 1–14.

97 Y. Sun and J. Zhang, *CCS Chem.*, 2021, **3**, 1058–1077.

98 A. Dato and M. Frenklach, *New J. Phys.*, 2010, **12**, 125013.

99 R. R. Kumal, A. Gharpure, V. Viswanathan, A. Mantri, G. Skoptsov and R. Vander Wal, *C*, 2020, **6**, 70.

100 E. Tatarova, A. Dias, J. Henriques, M. Abrashev, N. Bundaleska, E. Kovacevic, N. Bundaleski, U. Cvelbar, E. Valcheva, B. Arnaudov, A. M. B. do Rego, A. M. Ferraria, J. Berndt, E. Felizardo, O. M. N. D. Teodoro, T. Strunskus, L. L. Alves and B. Gonçalves, *Sci. Rep.*, 2017, **7**, 10175.

101 K. S. Subrahmanyam, L. S. Panchakarla, A. Govindaraj and C. N. R. Rao, *J. Phys. Chem. C*, 2009, **113**, 4257–4259.

102 J. Wang, M. Zhu, R. A. Outlaw, X. Zhao, D. M. Manos and B. C. Holloway, *Carbon N. Y.*, 2004, **42**, 2867–2872.

103 O. Baranov, K. Bazaka, H. Kersten, M. Keidar, U. Cvelbar, S. Xu and I. Levchenko, *Appl. Phys. Rev.*, 2017, **4**, 041302.

104 R. K. Amirov, I. N. Atamanuk, N. A. Vorobieva, E. H. Isakaev, M. B. Shavelkina and E. I. Shkolnikov, *J. Phys. Conf. Ser.*, 2015, **653**, 012161.

105 J. Shah, J. Lopez-Mercado, M. G. Carreon, A. Lopez-Miranda and M. L. Carreon, *ACS Omega*, 2018, **3**, 455–463.

106 A. Bogaerts, E. Neyts, R. Gijbels and J. van der Mullen, *Spectrochim. Acta Part B At. Spectrosc.*, 2002, **57**, 609–658.

107 T. Kato, *Nanosci. Technol. Open Access*, 2013, **1**, 0–3.

108 F. Mehmood, T. Kamal and U. Ashraf, , DOI:10.20944/preprints201810.0061.

109 D. Szabó and S. Schlabach, *Inorganics*, 2014, **2**, 468–507.

110 A. Kane, A. H. Barry, S. M. Chérif and S. Farhat, 2020, **02**, 30–36.

111 N. Santhosh, G. Filipič, E. Tatarova, O. Baranov, H. Kondo, M. Sekine, M. Hori, K. Ostrikov and U. Cvelbar, *Micromachines*, 2018, **9**, 565.

112 H. Lee, M. A. Bratescu, T. Ueno and N. Saito, *RSC Adv.*, 2014, **4**, 51758–51765.

113 V.-T. Nguyen, P. A. Le, Y.-C. Hsu and K.-H. Wei, *ACS Appl. Mater. Interfaces*, 2020, **12**, 11533–11542.

114 N. Van Hao, N. Van Dang, D. H. Tung, P. T. Tan, N. Van Tu and P. Van Trinh, *RSC Adv.*, 2020, **10**, 41237–41247.

115 T. Morishita, T. Ueno, G. Panomsuwan, J. Hieda, A. Yoshida, M. A. Bratescu and N. Saito, *Sci. Rep.*, 2016, **6**, 36880.

116 M. S. D. C. Dela Vega and M. R. Vasquez, *Compos. Part B Eng.*, 2019, **160**, 573–585.

117 O. Lehtinen, J. Kotakoski, A. V. Krasheninnikov and J. Keinonen, *Nanotechnology*, 2011, **22**, 175306.

118 T. Xu and L. Sun, in *Defects in Advanced Electronic Materials and Novel Low Dimensional Structures*, Elsevier, 2018, vol. 5, pp. 137–160.

119 S. P. Surwade, S. N. Smirnov, I. V. Vlassiouk, R. R. Unocic, G. M. Veith, S. Dai and S. M. Mahurin, *Nat. Nanotechnol.*, 2015, **10**, 459–464.

120 S. Tang, N. Lu, J. K. Wang, S.-K. Ryu and H.-S. Choi, *J. Phys. Chem. C*, 2007, **111**, 1820–1829.

121 J. Ma, D. Alfè, A. Michaelides and E. Wang, *Phys. Rev. B*, 2009, **80**, 033407.

122 L. A. Openov and A. I. Podlivaev, *Phys. Solid State*, 2015, **57**, 1477–1481.

123 A. I. Podlivaev and L. A. Openov, *Phys. Lett. A*, 2015, **379**, 1757–1761.

124 C. Chen, B. Liang, A. Ogino, X. Wang and M. Nagatsu, *J. Phys. Chem. C*, 2009, **113**, 7659–7665.

125 C. Chen, A. Ogino, X. Wang and M. Nagatsu, *Diam. Relat. Mater.*, 2011, **20**, 153–156.

126 B. Zhao, L. Zhang, X. Wang and J. Yang, *Carbon N. Y.*, 2012, **50**, 2710–2716.

127 M. Nakahara and Y. Sanada, *J. Mater. Sci.*, 1993, **28**, 1327–1333.

128 J. Duch, P. Kubisiak, K. H. Adolfsson, M. Hakkarainen, M. Golda-Cepa and A. Kotarba, *Appl. Surf. Sci.*, 2017, **419**, 439–446.

129 W.-H. Wang, B.-C. Huang, L.-S. Wang and D.-Q. Ye, *Surf. Coatings Technol.*, 2011, **205**, 4896–4901.

130 J. C. Meyer, C. Kisielowski, R. Erni, M. D. Rossell, M. F. Crommie and A. Zettl, *Nano Lett.*, 2008, **8**, 3582–3586.

131 M. Williams, K. Seunarine, R. Gibbs and C. Spacie, *Nano Newsl.*, 2013, 23–27.

132 A. U. Chaudhry, V. Mittal and B. Mishra, *Prog. Org. Coatings*, 2017, **110**, 97–103.

133 M. Calovi, S. Rossi, F. Deflorian, S. Dirè and R. Ceccato, *Materials (Basel).*, 2020, **13**, 1–27.

134 A. K. Hussain, I. Sudin, U. M. Basheer and M. Z. M. Yusop, *Corros. Rev.*, 2019, **37**, 343–363.

135 Z. Luo, Y. Li, F. Wang and R. Hong, *Materials (Basel).*, 2019, **12**, 707.

136 G. Zhao, D. Shao, C. Chen and X. Wang, *Appl. Phys. Lett.*, 2011, **98**, 183114.

137 M. S. D. C. Dela Vega and M. R. Vasquez, *Compos. Part B Eng.*, 2019, **160**, 573–585.

138 A. Islam, B. Mukherjee, K. K. Pandey and A. K. Keshri, *ACS Nano*, 2021, **15**, 1775–1784.

139 B. J. Hong, O. C. Compton, Z. An, I. Eryazici and S. T. Nguyen, *ACS Nano*, 2012, **6**, 63–73.

140 T. Kuila, S. Bose, A. K. Mishra, P. Khanra, N. H. Kim and J. H. Lee, *Prog. Mater. Sci.*, 2012, **57**, 1061–1105.

141 E. W. Hill, A. Vijayaragahvan and K. Novoselov, *IEEE Sens. J.*, 2011, **11**, 3161–3170.

142 R. J. Young, I. A. Kinloch, L. Gong and K. S. Novoselov, *Compos. Sci. Technol.*, 2012, **72**, 1459–1476.

143 T. P. Dasari Shareena, D. McShan, A. K. Dasmahapatra and P. B. Tchounwou, *Nano-Micro Lett.*, 2018, **10**, 53.

144 B. L. Dasari, J. M. Nouri, D. Brabazon and S. Naher, *Energy*, 2017, **140**, 766–778.

145 V. Georgakilas, J. N. Tiwari, K. C. Kemp, J. A. Perman, A. B. Bourlinos, K. S. Kim and R. Zboril, *Chem. Rev.*, 2016, **116**, 5464–5519.

146 I. A. Vacchi, C. Ménard-Moyon and A. Bianco, *Phys. Sci. Rev.*, 2017, **2**, 1–18.

147 T. Kuila, S. Bose, A. K. Mishra, P. Khanra, N. H. Kim and J. H. Lee, *Prog. Mater. Sci.*, 2012, 57, 1061–1105.

148 G. Bottari, M. Á. Herranz, L. Wibmer, M. Volland, L. Rodríguez-Pérez, D. M. Guldi, A. Hirsch, N. Martín, F. D'Souza and T. Torres, *Chem. Soc. Rev.*, 2017, **46**, 4464–4500.

149 J. Park and M. Yan, *Acc. Chem. Res.*, 2013, **46**, 181–189.

150 S. Aliyeva, R. Alosmanov, I. Buniyatzadeh, A. Azizov and A. Maharramov, *Soft Mater.*, 2019, **17**, 448–466.

151 I. Bertóti, M. Mohai and K. László, *Carbon N. Y.*, 2015, **84**, 185–196.

152 A. Nourbakhsh, M. Cantoro, T. Vosch, G. Pourtois, F. Clemente, M. H. van der Veen, J. Hofkens, M. M. Heyns, S. De Gendt and B. F. Sels, *Nanotechnology*, 2010, **21**, 435203.

153 Y. Ahmad, N. Batisse, X. Chen and M. Dubois, *C*, 2021, **7**, 20.

154 X. Lu, X. Yang, M. Tariq, F. Li, M. Steimecke, J. Li, A. Varga, M. Bron and B. Abel, *J. Mater. Chem. A*, 2020, **8**, 2445–2452.

155 N. McEvoy, H. Nolan, N. Ashok Kumar, T. Hallam and G. S. Duesberg, *Carbon N. Y.*, 2013, **54**, 283–290.

156 D. M. Coates and S. L. Kaplan, *MRS Bull.*, 1996, **21**, 43–45.

157 J. Chai, F. Lu, B. Li and D. Y. Kwok, *Langmuir*, 2004, **20**, 10919–10927.

158 V. Hrachová and A. Kaňka, *Vacuum*, 1997, **48**, 689–692.

159 J. Konno, A. Nezu, H. Matsuura and H. Akatsuka, *J. Adv. Oxid. Technol.*, 2017, **20**, 5–8.

160 N. Kostoglou, C.-W. Liao, C.-Y. Wang, J. N. Kondo, C. Tampaxis, T. Steriotis, K.

Giannakopoulos, A. G. Kontos, S. Hinder, M. Baker, E. Bousser, A. Matthews, C. Rebholz and C. Mitterer, *Carbon N. Y.*, 2021, **171**, 294–305.

161 I. Childres, L. A. Jauregui, J. Tian and Y. P. Chen, *New J. Phys.*, 2011, **13**, 025008.

162 I. Bertóti, I. Mohai, M. Mohai and J. Szépvölgyi, *Diam. Relat. Mater.*, 2011, **20**, 965–968.

163 Y. Wang, F. Yu, M. Zhu, C. Ma, D. Zhao, C. Wang, A. Zhou, B. Dai, J. Ji and X. Guo, *J. Mater. Chem. A*, 2018, **6**, 2011–2017.

164 C. P. Ewels and M. Glerup, *J. Nanosci. Nanotechnol.*, 2005, **5**, 1345–1363.

165 H. S. Kim, H. S. Kim, S. S. Kim and Y.-H. Kim, *Nanoscale*, 2014, **6**, 14911–14918.

166 R. Yadav and C. K. Dixit, *J. Sci. Adv. Mater. Devices*, 2017, **2**, 141–149.

167 Y.-C. Lin, C.-Y. Lin and P.-W. Chiu, *Appl. Phys. Lett.*, 2010, **96**, 133110.

168 D. Ding, Z. L. Song, Z. Q. Cheng, W. N. Liu, X. K. Nie, X. Bian, Z. Chen and W. Tan, *J. Mater. Chem. A*, 2014, **2**, 472–477.

169 D. Wei, Y. Liu, Y. Wang, H. Zhang, L. Huang and G. Yu, *Nano Lett.*, 2009, **9**, 1752–1758.

170 L. Xie, X. Wang, J. Lu, Z. Ni, Z. Luo, H. Mao, R. Wang, Y. Wang, D. Qi, R. Liu, T. Yu, Z. Shen, T. Wu, H. Peng, B. Özyilmaz, K. Loh, A. T. S. Wee, W. Chen, L. Xie, X. Wang, J. Lu, Z. Ni, Z. Luo and H. Mao, 2012, **193113**, 2012–2015.

171 J. O. Sofo, A. S. Chaudhari and G. D. Barber, *Phys. Rev. B*, 2007, **75**, 153401.

172 D. C. Elias, R. R. Nair, T. M. G. Mohiuddin, S. V. Morozov, P. Blake, M. P. Halsall, A. C. Ferrari, D. W. Boukhvalov, M. I. Katsnelson, A. K. Geim and K. S. Novoselov, *Science*, 2009, **323**, 610–613.

173 S. C. Ray, N. Soin, T. Makgato, C. H. Chuang, W. F. Pong, S. S. Roy, S. K. Ghosh, A. M. Strydom and J. A. McLaughlin, *Sci. Rep.*, 2015, **4**, 3862.

174 J. T. Robinson, J. S. Burgess, C. E. Junkermeier, S. C. Badescu, T. L. Reinecke, F. K. Perkins, M. K. Zalalutdniov, J. W. Baldwin, J. C. Culbertson, P. E. Sheehan and E. S. Snow, *Nano Lett.*, 2010, **10**, 3001–3005.

175 K.-J. Jeon, Z. Lee, E. Pollak, L. Moreschini, A. Bostwick, C.-M. Park, R. Mendelsberg, V. Radmilovic, R. Kostecki, T. J. Richardson and E. Rotenberg, *ACS Nano*, 2011, **5**, 1042–1046.

176 F. Karlický, K. Kumara Ramanatha Datta, M. Otyepka and R. Zbořil, *ACS Nano*, 2013, 7, 6434–6464.

177 S. Zhou, S. D. Sherpa, D. W. Hess and A. Bongiorno, *J. Phys. Chem. C*, 2014, **118**, 26402–26408.

178 X. Yu, K. Lin, K. Qiu, H. Cai, X. Li, J. Liu, N. Pan, S. Fu, Y. Luo and X. Wang, *Carbon N. Y.*, 2012, **50**, 4512–4517.

179 B. Wang, J. Wang and J. Zhu, *ACS Nano*, 2014, **8**, 1862–1870.

180 J. Wu, L. Xie, Y. Li, H. Wang, Y. Ouyang, J. Guo and H. Dai, *J. am. Chem. Soc.*, 2011,

133, 19668–19671.

181 M. Yang, L. Zhou, J. Wang, Z. Liu and Z. Liu, *J. Phys. Chem. C*, 2012, **116**, 844–850.

182 H. L. Poh, P. Šimek, Z. Sofer and M. Pumera, *Chem. - A Eur. J.*, 2013, **19**, 2655–2662.

183 H. Takehira, M. R. Karim, Y. Shudo, M. Fukuda, T. Mashimo and S. Hayami, *Sci. Rep.*, 2018, **8**, 1–8.

184 D. Bouša, J. Luxa, V. Mazánek, O. Jankovský, D. Sedmidubský, K. Klímová, M. Pumera and Z. Sofer, *RSC Adv.*, 2016, **6**, 66884–66892.

185 X. Zhang, A. Hsu, H. Wang, Y. Song, J. Kong, M. S. Dresselhaus and T. Palacios, *ACS Nano*, 2013, **7**, 7262–7270.

186 T. M. Bezugla, L. M. Grishchenko, A. V. Vakaliuk, V. E. Diyuk, O. V. Mischanchuk and V. V. Lisnyak, *Mol. Cryst. Liq. Cryst.*, 2018, **661**, 58–67.

187 A. E. Mansour, S. Dey, A. Amassian and M. H. Tanielian, *ACS Appl. Mater. Interfaces*, 2015, **7**, 17692–17699.

188 J. F. Friedrich, G. Hidde, A. Lippitz and W. E. S. Unger, in *Plasma Chemistry and Plasma Processing*, 2014, vol. 34, pp. 621–645.

189 F. Karlický, K. Kumara Ramanatha Datta, M. Otyepka and R. Zbořil, *ACS Nano*, 2013, **7**, 6434–6464.

190 J. F. Friedrich, S. Wettmarshausen, S. Hanelt, R. Mach, R. Mix, E. B. Zeynalov and A. Meyer-Plath, *Carbon N. Y.*, 2010, **48**, 3884–3894.

191 A. Hirsch, J. M. Englert and F. Hauke, *Acc. Chem. Res.*, 2013, **46**, 87–96.

192 Z. Xia, F. Leonardi, M. Gobbi, Y. Liu, V. Bellani, A. Liscio, A. Kovtun, R. Li, X. Feng, E. Orgiu, P. Samorì, E. Treossi and V. Palermo, *ACS Nano*, 2016, **10**, 7125–7134.

193 G. L. C. Paulus, Q. H. Wang and M. S. Strano, *Acc. Chem. Res.*, 2013, **46**, 160–170.

194 J. M. Englert, C. Dotzer, G. Yang, M. Schmid, C. Papp, J. M. Gottfried, H.-P. Steinrück, E. Spiecker, F. Hauke and A. Hirsch, *Nat. Chem.*, 2011, **3**, 279–286.

195 P. Huang, H. Zhu, L. Jing, Y. Zhao and X. Gao, *ACS Nano*, 2011, **5**, 7945–7949.

196 A. Wang, W. Yu, Z. Huang, F. Zhou, J. Song, Y. Song, L. Long, M. P. Cifuentes, M. G. Humphrey, L. Zhang, J. Shao and C. Zhang, *Sci. Rep.*, 2016, **6**, 23325.

197 E. Bekyarova, M. E. Itkis, P. Ramesh, C. Berger, M. Sprinkle, W. A. de Heer and R. C. Haddon, *J. Am. Chem. Soc.*, 2009, **131**, 1336–1337.

198 C. Peng, Y. Xiong, Z. Liu, F. Zhang, E. Ou, J. Qian, Y. Xiong and W. Xu, *Appl. Surf. Sci.*, 2013, **280**, 914–919.

199 S. Rooyanian, M. Bagherzadeh, Z. Akrami and A. N. Golikand, *New J. Chem.*, 2018, **42**, 17371–17378.

200 A. Kasprzak, A. Zuchowska and M. Poplawska, *Beilstein J. Org. Chem.*, 2018, **14**, 2018–2026.

201 Z. Jin, T. P. McNicholas, C.-J. Shih, Q. H. Wang, G. L. C. Paulus, A. J. Hilmer, S. Shimizu and M. S. Strano, *Chem. Mater.*, 2011, **23**, 3362–3370.

202 P. Huang, L. Jing, H. Zhu and X. Gao, *Acc. Chem. Res.*, 2013, **46**, 43–52.

203 G. Ambrosio, A. Brown, L. Daukiya, G. Drera, G. Di Santo, L. Petaccia, S. De Feyter, L. Sangaletti and S. Pagliara, *Nanoscale*, 2020, **12**, 9032–9037.

204 C. Galli, *Chem. Rev.*, 1988, **88**, 765–792.

205 H. Liu, S. Ryu, Z. Chen, M. L. Steigerwald, C. Nuckolls and L. E. Brus, *J. Am. Chem. Soc.*, 2009, **131**, 17099–17101.

206 H. Xu and K. S. Suslick, *J. Am. Chem. Soc.*, 2011, **133**, 9148–9151.

207 X. Zhang, M. Han, S. Chen, L. Bao, L. Li and W. Xu, *RSC Adv.*, 2013, **3**, 17689.

208 F. Samadaei, M. Salami-Kalajahi and H. Roghani-Mamaqani, *Bull. Mater. Sci.*, 2016, **39**, 229–234.

209 S. Sarkar, E. Bekyarova, S. Niyogi and R. C. Haddon, *J. Am. Chem. Soc.*, 2011, **133**, 3324–3327.

210 S. Sarkar, E. Bekyarova and R. C. Haddon, *Acc. Chem. Res.*, 2012, **45**, 673–682.

211 C. K. Chua, A. Ambrosi and M. Pumera, *Chem. Commun.*, 2012, **48**, 5376–5378.

212 T. Sainsbury, M. Passarelli, M. Naftaly, S. Gnaniah, S. J. Spencer and A. J. Pollard, *ACS Appl. Mater. Interfaces*, 2016, **8**, 4870–4877.

213 L.-H. Liu, G. Zorn, D. G. Castner, R. Solanki, M. M. Lerner and M. Yan., *J. Mater. Chem.*, 2010, **20**, 5041.

214 T. A. Strom, E. P. Dillon, C. E. Hamilton and A. R. Barron, *Chem. Commun.*, 2010, **46**, 4097–4099.

215 H. He and C. Gao, *Chem. Mater.*, 2010, **22**, 5054–5064.

216 J. Choi, K. Kim, B. Kim, H. Lee and S. Kim, *J. Phys. Chem. C*, 2009, **113**, 9433–9435.

217 L. H. Liu, M. M. Lerner and M. Yan, *Nano Lett.*, 2010, **10**, 3754–3756.

218 K. Liu, S. Chen, Y. Luo, D. Jia, H. Gao, G. Hu and L. Liu, *Compos. Sci. Technol.*, 2013, **88**, 84–91.

219 S.-Y. Bae, I.-Y. Jeon, J. Yang, N. Park, H. S. Shin, S. Park, R. S. Ruoff, L. Dai and J.-B. Baek, *ACS Nano*, 2011, **5**, 4974–4980.

220 J.-M. Seo, L.-S. Tan and J.-B. Baek, *Adv. Mater.*, 2017, **29**, 1606317.

221 P. M. Shellard, T. Srisubin, M. Hartmann, J. Butcher, F. Fei, H. Cox, T. P. McNamara, T. McArdle, A. M. Shepherd, R. M. J. Jacobs, T. A. Waigh, S. L. Flitsch and C. F. Blanford, *J. Mater. Sci.*, 2020, **55**, 10284–10302.

222 S. Rani, M. Kumar, R. Kumar, D. Kumar, S. Sharma and G. Singh, *Mater. Res. Bull.*, 2014, **60**, 143–149.

223 N. Alzate-Carvajal, E. V. Basiuk, V. Meza-Laguna, I. Puente-Lee, M. H. Farías, N. Bogdanchikova and V. A. Basiuk, *RSC Adv.*, 2016, **6**, 113596–113610.

224 S. Verma and R. K. Dutta, *J. Environ. Chem. Eng.*, 2017, **5**, 4547–4558.

225 Z. Jia and Y. Wang, *J. Mater. Chem. A*, 2015, **3**, 4405–4412.

226 R. Kumar, M. Kumar, A. Kumar, R. Singh, R. Kashyap, S. Rani and D. Kumar, *Mater. Today Proc.*, 2019, **18**, 1556–1561.

227 S. Qudsia, M. I. Ahmed, Z. Hussain and S. Soomro, *J. Mater. Sci. Mater. Electron.*, 2017, **28**, 6664–6672.

228 S. S. Abbas, G. J. Rees, N. L. Kelly, C. E. J. Dancer, J. V. Hanna and T. McNally, *Nanoscale*, 2018, **10**, 16231–16242.

229 A. Ahmadi, B. Ramezanzadeh and M. Mahdavian, *RSC Adv.*, 2016, **6**, 54102–54112.

230 C. Y. Lee, Q. Van Le, C. Kim and S. Y. Kim, *Phys. Chem. Chem. Phys.*, 2015, **17**, 9369–9374.

231 S. Pourhashem, M. R. Vaezi and A. Rashidi, *Surf. Coatings Technol.*, 2017, **311**, 282–294.

232 S. Gadipelli and Z. X. Guo, *Prog. Mater. Sci.*, 2015, **69**, 1–60.

233 G. Liu, W. Jin and N. Xu, *Chem. Soc. Rev.*, 2015, **44**, 5016–5030.

234 S. Han, D. Wu, S. Li, F. Zhang and X. Feng, *Adv. Mater.*, 2014, **26**, 849–864.

235 Y. Wang, M. Yang, W. Liu, L. Dong, D. Chen and C. Peng, *J. Mater. Chem. C*, 2019, **7**, 9248–9256.

236 Z. Yan, W. Yao, L. Hu, D. Liu, C. Wang and C.-S. Lee, *Nanoscale*, 2015, **7**, 5563–5577.

237 K. S. W. Sing, D. H. Everett, R. A. W. Haul, L. Moscou, R. A. Pierotti, J. Rouquerol and T. Siemieniewska, in *Handbook of Heterogeneous Catalysis*, Wiley-VCH Verlag GmbH & Co. KGaA, Weinheim, Germany, 2008, vol. 37, pp. 515–531.

238 F. Rouquerol, J. Rouquerol, K. S. W. Sing, P. Llewellyn and G. Maurin, *Adsorption by Powders and Porous Solids: Principles, Methodology and Applications*, Academic Press, 2nd edn., 2014.

239 M. Thommes, K. Kaneko, A. V Neimark, J. P. Olivier, F. Rodriguez-Reinoso, J. Rouquerol and K. S. W. Sing, *Pure Appl. Chem.*, 2015, **87**, 1051–1069.

240 S. Lowell, J. E. Shields, M. A. Thomas and M. Thommes, *Characterization of Porous Solids and Powders: Surface Area, Pore Size and Density*, Springer Netherlands, Dordrecht, 2004, vol. 16.

241 T. Yang, H. Lin, X. Zheng, K. P. Loh and B. Jia, *J. Mater. Chem. A*, 2017, **5**, 16537–16558.

242 M. D. Fischbein and M. Drndić, *Appl. Phys. Lett.*, 2008, **93**, 113107.

243 D. Fox, A. O'Neill, D. Zhou, M. Boese, J. N. Coleman and H. Z. Zhang, *Appl. Phys. Lett.*, 2011, **98**, 243117.

244 K. Celebi, J. Buchheim, R. M. Wyss, A. Droudian, P. Gasser, I. Shorubalko, J.-I. Kye, C. Lee and H. G. Park, *Science*, 2014, **344**, 289–292.

245 S. P. Koenig, L. Wang, J. Pellegrino and J. S. Bunch, *Nat. Nanotechnol.*, 2012, **7**, 728–732.

246 S. C. O'Hern, M. S. H. Boutilier, J.-C. Idrobo, Y. Song, J. Kong, T. Laoui, M. Atieh and

R. Karnik, *Nano Lett.*, 2014, **14**, 1234–1241.

247 P. Russo, A. Hu, G. Compagnini, W. W. Duley and N. Y. Zhou, *Nanoscale*, 2014, **6**, 2381–2389.

248 Z. Fan, Q. Zhao, T. Li, J. Yan, Y. Ren, J. Feng and T. Wei, *Carbon N. Y.*, 2012, **50**, 1699–1703.

249 E. Poirier, *Int. J. Hydrogen Energy*, 2001, **26**, 831–835.

250 P. Bénard and R. Chahine, *Scr. Mater.*, 2007, **56**, 803–808.

251 G. Aguilar-Armenta, M. E. Patiño-Iglesias and R. Leyva-Ramos, *Adsorpt. Sci. Technol.*, 2003, **21**, 81–91.

252 J. R. Li, R. J. Kuppler and H. C. Zhou, *Chem. Soc. Rev.*, 2009, **38**, 1477–1504.

253 F. Guo, M. Creighton, Y. Chen, R. Hurt and I. Külaots, *Carbon N. Y.*, 2014, **66**, 476–484.

254 O. N. Shornikova, E. V Kogan, N. E. Sorokina and V. V Avdeev, *Russ. J. Phys. Chem. A*, 2009, **83**, 1022–1025.

255 T. Liu, L. Zhang, B. Cheng, X. Hu and J. Yu, *Cell Reports Phys. Sci.*, 2020, **1**, 100215.

256 H. Huang, Z. Song, N. Wei, L. Shi, Y. Mao, Y. Ying, L. Sun, Z. Xu and X. Peng, *Nat. Commun.*, 2013, **4**, 2979.

257 H. Fang, F. Meng, J. Yan, G. Chen, L. Zhang, S. Wu, S. Zhang, L. Wang and Y. Zhang, *RSC Adv.*, 2019, **9**, 20107–20112.

258 R. Kumar, V. M. Suresh, T. K. Maji and C. N. R. Rao, *Chem. Commun.*, 2014, **50**, 2015.

259 J. Sun, F. Morales-Lara, A. Klechikov, A. V. Talyzin, I. A. Baburin, G. Seifert, F. Cardano, M. Baldrighi, M. Frasconi and S. Giordani, *Carbon N. Y.*, 2017, **120**, 145–156.

260 A. Nordenström, A. Iakunkov, J. Sun and A. V. Talyzin, *RSC Adv.*, 2020, **10**, 6831–6839.

261 M. Georgakis, G. Stavropoulos and G. P. Sakellaropoulos, *Microporous Mesoporous Mater.*, 2014, **191**, 67–73.

262 C. R. Wood, N. T. Skipper and M. J. Gillan, *J. Solid State Chem.*, 2011, **184**, 1561–1565.

263 G. Srinivas, A. Lovell, C. A. Howard, N. T. Skipper, M. Ellerby and S. M. Bennington, *Synth. Met.*, 2010, **160**, 1631–1635.

264 B. Mi, *Science*, 2014, **343**, 740–742.

265 G. Mercier, A. Klechikov, M. Hedenström, D. Johnels, I. A. Baburin, G. Seifert, R. Mysyk and A. V. Talyzin, *J. Phys. Chem. C*, 2015, **119**, 27179–27191.

266 A. Klechikov, G. Mercier, T. Sharifi, I. A. Baburin, G. Seifert and A. V. Talyzin, *Chem. Commun.*, 2015, **51**, 15280–15283.

267 I. A. Baburin, A. Klechikov, G. Mercier, A. Talyzin and G. Seifert, *Int. J. Hydrogen Energy*, 2015, **40**, 6594–6599.

268 J. W. Burress, S. Gadipelli, J. Ford, J. M. Simmons, W. Zhou and T. Yildirim, *Angew. Chemie Int. Ed.*, 2010, **49**, 8902–8904.

269 C. E. Flores-Chaparro, C. J. Castilho, I. Külaots, R. H. Hurt and J. R. Rangel-Mendez, *J. Environ. Manage.*, 2020, **259**, 110044.

270 K. Morishige and T. Hamada, *Langmuir*, 2005, **21**, 6277–6281.

271 M. Herrera-Alonso, A. A. Abdala, M. J. McAllister, I. A. Aksay and R. K. Prud'homme, *Langmuir*, 2007, **23**, 10644–10649.

272 A. B. Bourlinos, D. Gournis, D. Petridis, T. Szabó, A. Szeri and I. Dékány, *Langmuir*, 2003, **19**, 6050–6055.

273 F.-G. Zhao, Y.-T. Kong, B. Pan, C.-M. Hu, B. Zuo, X. Dong, B. Li and W.-S. Li, *J. Mater. Chem. A*, 2019, **7**, 3353–3365.

274 V. Dhinakaran, M. Lavanya, K. Vigneswari, M. Ravichandran and M. D. Vijayakumar, *Mater. Today Proc.*, 2020, **27**, 824–828.

275 X. Zhang, B. R. S. Rajaraman, H. Liu and S. Ramakrishna, *RSC Adv.*, 2014, **4**, 28987–29011.

276 T. S. Tran, N. K. Dutta and N. R. Choudhury, *Adv. Colloid Interface Sci.*, 2018, 261, 41–61.

277 A. Claypole, J. Claypole, T. Claypole, D. Gethin and L. Kilduff, *J. Coatings Technol. Res.*, 2021, **18**, 193–203.

278 D. S. Saidina, N. Eawwiboonthanakit, M. Mariatti, S. Fontana and C. Hérold, *J. Electron. Mater.*, 2019, **48**, 3428–3450.

279 C. I. L. Justino, A. R. Gomes, A. C. Freitas, A. C. Duarte and T. A. P. Rocha-Santos, *TrAC Trends Anal. Chem.*, 2017, **91**, 53–66.

280 M. Liu, R. Zhang and W. Chen, *Chem. Rev.*, 2014, 114, 5117–5160.

281 J. Liu, J. Dong, T. Zhang and Q. Peng, *J. Control. Release*, 2018, 286, 64–73.

282 L. S. Walker, V. R. Marotto, M. A. Rafiee, N. Koratkar and E. L. Corral, *ACS Nano*, 2011, **5**, 3182–3190.

283 W. Kong, H. Kum, S. Bae, J. Shim, H. Kim, L. Kong, Y. Meng, K. Wang, C. Kim and J. Kim, *Nat. Nanotechnol.*, 2019, **14**, 927–938.

284 Head Sport GmbH, https://www.head.com, (accessed 25 May 2021).

285 Inov-8, https://www.inov-8.com, (accessed 25 May 2021).

286 Versarien PLC, http://www.versarien.com, (accessed 25 May 2021).

287 R. Vajtai, in *Springer Handbook of Nanomaterials*, Springer Berlin Heidelberg, Berlin, Heidelberg, 2013, pp. 39–82.

288 B. Huang, Q. Wang, Y. Li, M. Zhang and X. Wei, *Mater. Res. Innov.*, 2015, **19**, S9344–S9350.

289 S. Eigler and A. M. Dimiev, in *Graphene Oxide*, John Wiley & Sons, Ltd, Chichester, UK, 2016, pp. 85–120.

290 A. Ul-Hamid, *A Beginners' Guide to Scanning Electron Microscopy*, 2018.

291 A. Z. M. Badruddoza, R. Chepyala and K. Ashraf, in *Biomedical Applications of Graphene and 2D Nanomaterials*, Elsevier, 2019, pp. 43–86.

292 Z. Luo, *A practical guide to transmission electron microscopy*, Momentum Press, 1st edn., 2016.

293 J. Kim, F. Kim and J. Huang, *Mater. Today*, 2010, **13**, 28–38.

294 Ludwig Reimer, *Scanning Electron Microscopy: Physics of Image Formation and Microanalysis*, Springer-Verlag Berlin Heidelberg, 2nd edn., 1998.

295 F. GÜNEŞ, G. H. HAN, K. K. KIM, E. S. KIM, S. J. CHAE, M. H. PARK, H.-K. JEONG, S. C. LIM and Y. H. LEE, *Nano*, 2009, **04**, 83–90.

296 Y. M. Kim, S. J. Pennycook and A. Y. Borisevich, *Ultramicroscopy*, 2017, **181**, 1–7.

297 H. Zhang, J. Huang, Y. Wang, R. Liu, X. Huai, J. Jiang and C. Anfuso, *Opt. Commun.*, 2018, **406**, 3–17.

298 C. J. Shearer, A. D. Slattery, A. J. Stapleton, J. G. Shapter and C. T. Gibson, *Nanotechnology*, , DOI:10.1088/0957-4484/27/12/125704.

299 Z. Liu, W. Liu, X. Xie, W. Zhao, Y. Wen, Q. Wang and B. Ou, *IOP Conf. Ser. Earth Environ. Sci.*, 2019, **252**, 022022.

300 H. Lee and J. Y. Park, *Rev. Sci. Instrum.*, 2019, **90**, 103702.

301 K. S. Novoselov, D. Jiang, F. Schedin, T. J. Booth, V. V Khotkevich, S. V Morozov and A. K. Geim, *Proc. Natl. Acad. Sci. U. S. A.*, 2005, **102**, 10451–10453.

302 N. M. Huang, *Int. J. Nanomedicine*, 2011, **6**, 3443.

303 D. Bougeard, M. Buback, A. Cao, K. Gerwert, H. M. Heise, G. G. Hoffmann, B. Jordanov, W. Kiefer, E.-H. Korte, H. Kuzmany, A. Leipertz, E. Lentz, J. Liquier, A. Roseler, H. Schnockel, B. Schrader, H. W. Schrotter, M. Spiekermann, E. Taillandier and H. Willner, *Infrared and Raman Spectroscopy, Method and Applications*, VCH Verlagsgesellschaft mbH, Weinheini (Federal Republic of Gcrmany) VCH Publishers. Inc., New York, NY (USA), 1995.

304 A. Downes and A. Elfick, *Sensors*, 2010, **10**, 1871–1889.

305 F. Tuinstra and J. L. Koenig, *J. Chem. Phys.*, 1970, **53**, 1126–1130.

306 M. A. Pimenta, G. Dresselhaus, M. S. Dresselhaus, L. G. Cançado, A. Jorio and R. Saito, *Phys. Chem. Chem. Phys.*, 2007, 9, 1276–1291.

307 S. Niyogi, E. Bekyarova, M. E. Itkis, H. Zhang, K. Shepperd, J. Hicks, M. Sprinkle, C. Berger, C. N. Lau, W. A. DeHeer, E. H. Conrad and R. C. Haddon, *Nano Lett.*, 2010, **10**, 4061–4066.

308 A. C. Ferrari and J. Robertson, *Phys. Rev. B*, 2000, **61**, 14095–14107.

309 M. M. Lucchese, F. Stavale, E. H. M. Ferreira, C. Vilani, M. V. O. Moutinho, R. B. Capaz, C. A. Achete and A. Jorio, *Carbon N. Y.*, 2010, **48**, 1592–1597.

310 R. P. Vidano, D. B. Fischbach, L. J. Willis and T. M. Loehr, *Solid State Commun.*, 1981,

39, 341–344.

311 S. Claramunt, A. Varea, D. López-Díaz, M. M. Velázquez, A. Cornet and A. Cirera, *J. Phys. Chem. C*, 2015, **119**, 10123–10129.

312 A. C. Ferrari, J. C. Meyer, V. Scardaci, C. Casiraghi, M. Lazzeri, F. Mauri, S. Piscanec, D. Jiang, K. S. Novoselov, S. Roth and A. K. Geim, *Phys. Rev. Lett.*, 2006, **97**, 187401.

313 C. H. Lui, Z. Li, Z. Chen, P. V. Klimov, L. E. Brus and T. F. Heinz, *Nano Lett.*, 2011, **11**, 164–169.

314 A. Gupta, G. Chen, P. Joshi, S. Tadigadapa and Eklund, *Nano Lett.*, 2006, **6**, 2667–2673.

315 R. C. Reynolds, in *Modern Powder Diffraction*, eds. D. L. Bish and J. E. Post, De Gruyter, Berlin, Boston, 1989, pp. 1–18.

316 T.-A. Lin, I.-S. Tsai and P.-C. Hsu, *Micro & Nano Lett.*, 2014, **9**, 922–926.

317 H. K. Jeong, P. L. Yun, R. J. W. E. Lahaye, M. H. Park, H. A. Kay, J. K. Ick, C. W. Yang, Y. P. Chong, R. S. Ruoff and H. L. Young, *J. Am. Chem. Soc.*, 2008, **130**, 1362–1366.

318 C. Hontoria-Lucas, A. J. López-Peinado, J. d. D. López-González, M. L. Rojas-Cervantes and R. M. Martín-Aranda, *Carbon N. Y.*, 1995, **33**, 1585–1592.

319 Z. Fan, K. Wang, T. Wei, J. Yan, L. Song and B. Shao, *Carbon N. Y.*, 2010, **48**, 1686–1689.

320 L. Stobinski, B. Lesiak, A. Malolepszy, M. Mazurkiewicz, B. Mierzwa, J. Zemek, P. Jiricek and I. Bieloshapka, *J. Electron Spectros. Relat. Phenomena*, 2014, **195**, 145–154.

321 F. T. Johra, J. W. Lee and W. G. Jung, *J. Ind. Eng. Chem.*, 2014, **20**, 2883–2887.

322 J. B. Gilbert, M. F. Rubner and R. E. Cohen, *Proc. Natl. Acad. Sci.*, 2013, **110**, 6651–6656.

323 S. Klassen, *Sci. Educ.*, 2011, **20**, 719–731.

324 S. Hüfner, *Photoelectron Spectroscopy*, Springer Berlin Heidelberg, Berlin, Heidelberg, 2003.

325 J. F. Moulder, W. F. Stickle, P. E. Sobol and K. D. Bomben, *Handbook of X Ray Photoelectron Spectroscopy: A Reference Book of Standard Spectra for Identification and Interpretation of Xps Data*, 1979.

326 J. C. Vickerman and I. S. Gilmore, Eds., *Surface Analysis: The Principal Techniques*, Wiley, New Jersey, 2nd edn., 2009.

327 A. Kovtun, D. Jones, S. Dell'Elce, E. Treossi, A. Liscio and V. Palermo, *Carbon N. Y.*, 2019, **143**, 268–275.

328 J. Ederer, P. Janoš, P. Ecorchard, J. Tolasz, V. Štengl, H. Beneš, M. Perchacz and O. Pop-Georgievski, *RSC Adv.*, 2017, **7**, 12464–12473.

329 R. Al-Gaashani, A. Najjar, Y. Zakaria, S. Mansour and M. A. Atieh, *Ceram. Int.*, 2019, **45**, 14439–14448.

330 J. D. Menczel and R. B. Prime, Eds., *Thermal Analysis of Polymers*, John Wiley & Sons, Inc., Hoboken, NJ, USA, 2009.

331 R. Parameshwaran, A. Sarı, N. Jalaiah and R. Karunakaran, 2018, pp. 519–572.

332 F. Liu, M. Wang, Y. Chen and J. Gao, *J. Solid State Chem.*, 2019, **276**, 100–103.

333 F. Farivar, P. Lay Yap, R. U. Karunagaran and D. Losic, *C*, 2021, **7**, 41.

334 M. El-Azazy, in *Infrared Spectroscopy - Principles, Advances, and Applications*, ed. M. El-Azazy, IntechOpen, 2019.

335 S. Gurunathan, J. W. Han, J.-H. Park, E. S. Kim, Y.-J. Choi, D.-N. Kwon and J.-H. Kim, *Int. J. Nanomedicine*, 2015, **10**, 6257.

336 R. Tekenya, K. Pokpas, N. Jahed and E. I. Iwuoha, *Anal. Lett.*, 2019, **52**, 373–398.

337 T.-T. Do, M. Celina and P. M. Fredericks, *Polym. Degrad. Stab.*, 2002, **77**, 417–422.

338 A. A. Bunaciu, S. Fleschin and H. Y. Aboul-Enein, *Rev. Roum. Chim.*, 2015, **60**, 415–426.

339 M. Aziz, F. S. Abdul Halim and J. Jaafar, *J. Teknol.*, 2014, **69**, 11–14.

340 M. B. Structures, *NMR Spectroscopy Basic Principles, Concepts and Applications in Chemistry*, Wiley-VCH Verlag GmbH & Co. KGaA, Germany, 3rd edn.

341 N. J. Rankin, D. Preiss, P. Welsh, K. E. V. Burgess, S. M. Nelson, D. A. Lawlor and N. Sattar, *Atherosclerosis*, 2014, **237**, 287–300.

342 A. S. Mazur, M. A. Vovk and P. M. Tolstoy, *Fullerenes, Nanotub. Carbon Nanostructures*, 2020, **28**, 202–213.

343 S. Brunauer, P. H. Emmett and E. Teller, *J. Am. Chem. Soc.*, 1938, **60**, 309–319.

344 E. P. Barrett, L. G. Joyner and P. P. Halenda, *J. Am. Chem. Soc.*, 1951, **73**, 373–380.

345 P. I. Ravikovitch, G. L. Haller and A. V Neimark, *Adv. Colloid Interface Sci.*, 1998, **76**–**77**, 203–226.

346 G. Q. Lu and X. S. Zhao, *Nanoporous Materials: Science and Engineering*, Published by Imperial College Press and Distributed by World Scientific Publishing Co., 2004, vol. 4.

347 B. Coasne and R. J. M. Pellenq, *J. Chem. Phys.*, 2004, **120**, 2913–2922.

348 C. Sangwichien, G. . Aranovich and M. . Donohue, *Colloids Surfaces A Physicochem. Eng. Asp.*, 2002, **206**, 313–320.

349 K. Sing, in *Colloids and Surfaces A: Physicochemical and Engineering Aspects*, 2001, vol. 187–188, pp. 3–9.

350 Y.-S. Bae, A. Ö. Yazaydın and R. Q. Snurr, *Langmuir*, 2010, **26**, 5475–5483.

351 K. S. W. Sing, *Pure Appl. Chem.*, 1985, **57**, 603–619.

352 F. J. Sotomayor, K. A. Cychosz and M. Thommes, *Acc. Mater. Surf. Res*, 2018, **3**, 34–50.

353 R. Bardestani, G. S. Patience and S. Kaliaguine, *Can. J. Chem. Eng.*, 2019, **97**, 2781–

2791.

354 K. C. Kim, T.-U. Yoon and Y.-S. Bae, *Microporous Mesoporous Mater.*, 2016, **224**, 294–301.

355 J. Villarroel-Rocha, D. Barrera, A. A. G. Blanco, M. E. R. Jalil and K. Sapag, *Adsorpt. Sci. Technol.*, 2013, **31**, 165–183.

356 J. Deboer, *J. Catal.*, 1965, **4**, 649–653.

357 J. H. Gross, *Mass Spectrometry: A Textbook*, Springer International Publishing, 2017.

358 E. Hoffmann and V. Stroobant, *Mass Spectrometry Principles and Applications*, John Wiley & Sons, Ltd, Chichester, 3rd edn., 2016, vol. 1040.

359 R. L. Graham, C. Graham and G. McMullan, *Microb. Cell Fact.*, 2007, **6**, 26.

360 A. J. Slate, D. A. C. Brownson, A. S. Abo Dena, G. C. Smith, K. A. Whitehead and C. E. Banks, *Phys. Chem. Chem. Phys.*, 2018, **20**, 20010–20022.

361 E. A. Group, Evans Analytical Group, https://pdfs.semanticscholar.org/a930/19ce14124010573e648bf8cb320d3ebbb0c6.pdf, (accessed 17 February 2021).

362 K. Miyoshi, *Surface Characterization Techniques: An Overview*, 2002.

363 A. Fasolino, J. H. Los and M. I. Katsnelson, *Nat. Mater.*, 2007, **6**, 858–861.

364 J. M. Carlsson, *Nat. Mater.*, 2007, **6**, 801–802.

365 Z.-S. Wu, W. Ren, L. Gao, B. Liu, C. Jiang and H.-M. Cheng, *Carbon N. Y.*, 2009, **47**, 493–499.

366 J. A. Morán-Meza, J. Cousty, C. Lubin and F. Thoyer, *Phys. Chem. Chem. Phys.*, 2016, **18**, 14264–14272.

367 Y. Yu, *Appl. Sci. Converg. Technol.*, 2019, **28**, 51–54.

368 P. Nemes-Incze, Z. Osváth, K. Kamarás and L. P. Biró, *Carbon N. Y.*, 2008, **46**, 1435–1442.

369 P. Cao, K. Xu, J. O. Varghese and J. R. Heath, *J. Am. Chem. Soc.*, 2011, **133**, 2334–2337.

370 O. Ochedowski, B. K. Bussmann and M. Schleberger, *Sci. Rep.*, 2015, **4**, 6003.

371 M. S. Seehra, U. K. Geddam, D. Schwegler-Berry and A. B. Stefaniak, *Carbon N. Y.*, 2015, **95**, 818–823.

372 A. Ruammaitree, H. Nakahara, K. Akimoto, K. Soda and Y. Saito, *Appl. Surf. Sci.*, 2013, **282**, 297–301.

373 B. Andonovic, M. Temkov, A. Ademi, A. Petrovski, A. Grozdanov, P. Paunović and A. Dimitrov, *J. Chem. Technol. Metall.*, 2014, **49**, 545–550.

374 W. J. Wolfgong, in *Handbook of Materials Failure Analysis with Case Studies from the Aerospace and Automotive Industries*, Elsevier, 2016, pp. 279–307.

375 B. V. Crist, *J. Electron Spectros. Relat. Phenomena*, 2019, **231**, 75–87.

376 M. Pirveysian and M. Ghiaci, *Appl. Surf. Sci.*, 2018, **428**, 98–109.

377 G. Yang, D. Bao, H. Liu, D. Zhang, N. Wang and H. Li, *J. Inorg. Organomet. Polym. Mater.*, 2017, **27**, 1129–1141.

378 S. Khan, A. Achazhiyath Edathil and F. Banat, *Sci. Rep.*, 2019, **9**, 18106.

379 A. Hashimoto, K. Suenaga, A. Gloter, K. Urita and S. Iijima, *Nature*, 2004, **430**, 870–873.

380 J. C. Meyer, F. Eder, S. Kurasch, V. Skakalova, J. Kotakoski, H. J. Park, S. Roth, A. Chuvilin, S. Eyhusen, G. Benner, A. V. Krasheninnikov and U. Kaiser, *Phys. Rev. Lett.*, 2012, **108**, 196102.

381 R. H. Telling and M. I. Heggie, *Philos. Mag.*, 2007, **87**, 4797–4846.

382 D. Teweldebrhan and A. A. Balandin, *Appl. Phys. Lett.*, 2009, **94**, 013101.

383 I. Childres, L. A. Jauregui, M. Foxe, J. Tian, R. Jalilian, I. Jovanovic and Y. P. Chen, *Appl. Phys. Lett.*, 2010, **97**, 173109.

384 K. Murakami, T. Kadowaki and J. Fujita, *Appl. Phys. Lett.*, 2013, **102**, 043111.

385 P. Mendes, M. Belloni, M. Ashworth, C. Hardy, K. Nikitin, D. Fitzmaurice, K. Critchley, S. Evans and J. Preece, *ChemPhysChem*, 2003, **4**, 884–889.

386 A. Adenier, E. Cabet-Deliry, A. Chaussé, S. Griveau, F. Mercier, J. Pinson and C. Vautrin-Ul, *Chem. Mater.*, 2005, **17**, 491–501.

387 I. B. Seiple, S. Su, R. a Rodriguez, R. Gianatassio, Y. Fujiwara, A. L. Sobel and P. S. Baran, *J. Am. Chem. Soc.*, 2010, **132**, 13194–13196.

388 Y. Fujiwara, V. Domingo, I. B. Seiple, R. Gianatassio, M. Del Bel and P. S. Baran, *J. Am. Chem. Soc.*, 2011, **133**, 3292–3295.

389 S. Park, J. An, R. D. Piner, I. Jung, D. Yang, A. Velamakanni, S. T. Nguyen and R. S. Ruoff, *Chem. Mater.*, 2008, **20**, 6592–6594.

390 P. A. Wheeler, J. Wang, J. Baker and L. J. Mathias, *Chem. Mater.*, 2005, **17**, 3012–3018.

391 M. Sheng, D. Frurip and D. Gorman, *J. Loss Prev. Process Ind.*, 2015, **38**, 114–118.

392 R. N. Butler, *Chem. Rev.*, 1975, **75**, 241–257.

393 M. Thiemann, E. Scheibler and K. W. Wiegand, in *Ullmann's Encyclopedia of Industrial Chemistry*, Wiley-VCH Verlag GmbH & Co. KGaA, Weinheim, Germany, 2000.

394 A. Dickschat and A. Studer, *Org. Lett.*, 2010, **12**, 3972–3974.

395 N. Uchiyama, E. Shirakawa, R. Nishikawa and T. Hayashi, *Chem. Commun.*, 2011, **47**, 11671.

396 D. Liu, C. Liu, H. Li and A. Lei, *Angew. Chemie Int. Ed.*, 2013, **52**, 4453–4456.

397 G. Yan, M. Yang and X. Wu, *Org. Biomol. Chem.*, 2013, **11**, 7999.

398 G. Cheng and M. Luo, *European J. Org. Chem.*, 2011, **2011**, 2519–2523.

399 A. D. Sagar, R. H. Tale and R. N. Adude, *Tetrahedron Lett.*, 2003, **44**, 7061–7063.

400 A. Theodosiou, B. F. Spencer, J. Counsell and A. N. Jones, *Appl. Surf. Sci.*, 2020, **508**, 144764.

401 J. A. Gardella, S. A. Ferguson and R. L. Chin, *Appl. Spectrosc.*, 1986, **40**, 224–232.

402 J. Y. Kim, S. Lee, T.-Y. Kim and H.-T. Kim, *Electrochim. Acta*, 2014, **134**, 418–425.

403 Y. Furikado, T. Nagahata, T. Okamoto, T. Sugaya, S. Iwatsuki, M. Inamo, H. D. Takagi, A. Odani and K. Ishihara, *Chem. - A Eur. J.*, 2014, **20**, 13194–13202.

404 G. Srinivas, J. W. Burress, J. Ford and T. Yildirim, *J. Mater. Chem.*, 2011, **21**, 11323.

405 V. K. Kaushik, *J. Electron Spectros. Relat. Phenomena*, 1991, **56**, 273–277.

406 J. C. Fuggle, E. Källne, L. M. Watson and D. J. Fabian, *Phys. Rev. B*, 1977, **16**, 750–761.

407 A. M. Ferraria, A. P. Carapeto and A. M. Botelho do Rego, *Vacuum*, 2012, **86**, 1988–1991.

408 R. Zhang, Y. Du, D. Li, D. Shen, J. Yang, Z. Guo, H. K. Liu, A. A. Elzatahry and D. Zhao, *Adv. Mater.*, 2014, **26**, 6749–6755.

409 J. A. Rodríguez-Manzo, O. Cretu and F. Banhart, *ACS Nano*, 2010, **4**, 3422–3428.

410 J. R. Araujo, B. S. Archanjo, K. R. de Souza, W. Kwapinski, N. P. S. Falcão, E. H. Novotny and C. A. Achete, *Biol. Fertil. Soils*, 2014, **50**, 1223–1232.

411 V. T. Nguyen, H. D. Le, V. C. Nguyen, T. T. Tam Ngo, D. Q. Le, X. N. Nguyen and N. M. Phan, *Adv. Nat. Sci. Nanosci. Nanotechnol.*, 2013, **4**, 035012.

412 K. S. Subrahmanyam, S. R. C. Vivekchand, A. Govindaraj and C. N. R. Rao, *J. Mater. Chem.*, 2008, **18**, 1517.

413 N. B. S. Circular, .

414 T. Barth and G. Lunde, *Zeitschrift für Phys. Chemie*, 1926, **121U**, 78–102.

415 A. M. B. N. H. T. E. W. R. H. Illguth, *Neues Jahrb. Miner. Monatsh*, 1978, 408–421.

416 A. L. Patterson, *Phys. Rev.*, 1939, **56**, 978–982.

417 R. Sharma, N. Chadha and P. Saini, *Indian J. Pure Appl. Phys.*, 2017, **55**, 625–629.

418 W. L. Bragg, *Proc. Camb. Philol. Soc.*, 1913, **17**, 43–57.

419 N. Saravanan, R. Rajasekar, S. Mahalakshmi, T. Sathishkumar, K. Sasikumar and S. Sahoo, *J. Reinf. Plast. Compos.*, 2014, **33**, 1158–1170.

420 F. A. Miller and F. E. Kiviat, *Spectrochim. Acta Part A Mol. Spectrosc.*, 1969, **25**, 1577–1588.

421 D. Konios, M. M. Stylianakis, E. Stratakis and E. Kymakis, *J. Colloid Interface Sci.*, 2014, **430**, 108–112.

422 A. Fujii, E. Fujimaki, T. Ebata and N. Mikami, *J. Chem. Phys.*, 2000, **112**, 6275–6284.

423 S. H. Brewer, A. M. Allen, S. E. Lappi, T. L. Chasse, K. A. Briggman, C. B. Gorman and S. Franzen, *Langmuir*, 2004, **20**, 5512–5520.

424 M. Domingo-García, F. . López-Garzón and M. Pérez-Mendoza, *Carbon N. Y.*, 2000, **38**, 555–563.

425 T. Szabo, P. Maroni and I. Szilagyi, *Carbon N. Y.*, 2020, **160**, 145–155.

426 Y. Hernandez, M. Lotya, D. Rickard, S. D. Bergin and J. N. Coleman, *Langmuir*, 2010, **26**, 3208–3213.

427 K. Müller, C. Faeh and F. Diederich, *Science*, 2007, **317**, 1881–1886.

428 V. H. Dalvi and P. J. Rossky, *Proc. Natl. Acad. Sci.*, 2010, **107**, 13603–13607.

429 N. M. Kovalchuk, A. Trybala, V. Starov, O. Matar and N. Ivanova, *Adv. Colloid Interface Sci.*, 2014, **210**, 65–71.

430 B. Dehghanzad, M. K. Razavi Aghjeh, O. Rafeie, A. Tavakoli and A. Jameie Oskooie, *RSC Adv.*, 2016, **6**, 3578–3585.

431 G. Zhang, M. Wen, S. Wang, J. Chen and J. Wang, *RSC Adv.*, 2018, **8**, 567–579.

432 Y. Devrim and A. Albostan, *J. Electron. Mater.*, 2016, **45**, 3900–3907.

433 P.-G. Ren, D.-X. Yan, X. Ji, T. Chen and Z.-M. Li, *Nanotechnology*, 2011, **22**, 055705.

434 S. Deng and V. Berry, *Mater. Today*, 2016, **19**, 197–212.

435 J. Ma, D. Alfè, A. Michaelides and E. Wang, *Phys. Rev. B - Condens. Matter Mater. Phys.*, 2009, **80**, 1–4.

436 F. Ancilotto, M. Da Re, S. Grubišić, A. Hernando, P. L. Silvestrelli and F. Toigo, *Mol. Phys.*, 2011, **109**, 2787–2796.

437 Y. Zeng, L. Prasetyo, S. J. Tan, C. Fan, D. D. Do and D. Nicholson, *Chem. Eng. Sci.*, 2017, **158**, 462–479.

438 C. Fan, Y. Zeng, D. D. Do and D. Nicholson, *Phys. Chem. Chem. Phys.*, 2014, **16**, 12362.

439 J. C. Groen, L. A. A. Peffer and J. Pérez-Ramírez, *Microporous Mesoporous Mater.*, 2003, **60**, 1–17.

440 C. G. . Burgess and D. . Everett, *J. Colloid Interface Sci.*, 1970, **33**, 611–614.

441 L. Qi, X. Tang, Z. Wang and X. Peng, *Int. J. Min. Sci. Technol.*, 2017, **27**, 371–377.

442 I. C. Medeiros-Costa, C. Laroche, J. Pérez-Pellitero and B. Coasne, *Microporous Mesoporous Mater.*, 2019, **287**, 167–176.

443 B. Gurzęda, T. Buchwald, M. Nocuń, A. Bąkowicz and P. Krawczyk, *RSC Adv.*, 2017, **7**, 19904–19911.

444 J. H. de Boer, B. C. Lippens, B. G. Linsen, J. C. P. Broekhoff, A. van den Heuvel and T. J. Osinga, *J. Colloid Interface Sci.*, 1966, **21**, 405–414.

445 W. D. Harkins and G. Jura, *J. Chem. Phys.*, 1943, **11**, 430–430.

446 A. M. Dimiev and J. M. Tour, *ACS Nano*, 2014, **8**, 3060–3068.

447 M. J. Yoo and H. B. Park, *Carbon N. Y.*, 2019, **141**, 515–522.

448 H. Yu, B. Zhang, C. Bulin, R. Li and R. Xing, *Sci. Rep.*, 2016, **6**, 36143.

449 M. Toupin and D. Bélanger, *Langmuir*, 2008, **24**, 1910–1917.

450 P. A. Denis and F. Iribarne, *J. Phys. Chem. C*, 2013, **117**, 19048–19055.

451 R. Berenguer and E. Morallón, *Front. Mater.*, 2019, **6**, 1–14.

452 M. D. P. Lavin-Lopez, A. Romero, J. Garrido, L. Sanchez-Silva and J. L. Valverde, *Ind. Eng. Chem. Res.*, 2016, **55**, 12836–12847.

453 F. Guo, F. Kim, T. H. Han, V. B. Shenoy, J. Huang and R. H. Hurt, *ACS Nano*, 2011, **5**, 8019–8025.

454 I. K. Moon, J. Lee, R. S. Ruoff and H. Lee, *Nat. Commun.*, 2010, **1**, 73.

455 A. Iakunkov, V. Skrypnychuk, A. Nordenström, E. A. Shilayeva, M. Korobov, M. Prodana, M. Enachescu, S. H. Larsson and A. V.Talyzin, *Phys. Chem. Chem. Phys.*, 2019, **21**, 17901–17912.

456 J. Shen, M. Shi, N. Li, B. Yan, H. Ma, Y. Hu and M. Ye, *Nano Res.*, 2010, **3**, 339–349.

457 R. Liu, T. Gong, K. Zhang and C. Lee, *Sci. Rep.*, 2017, **7**, 9761.

458 P. Montes-Navajas, N. G. Asenjo, R. Santamaría, R. Menéndez, A. Corma and H. García, *Langmuir*, 2013, **29**, 13443–13448.

459 J. Li, J. Cui, Z. Yang, H. Qiu, Z. Tang and J. Yang, *New Carbon Mater.*, 2018, **33**, 19–25.

460 C. Zhang, W. W. Tjiu, W. Fan, Z. Yang, S. Huang and T. Liu, *J. Mater. Chem.*, 2011, **21**, 18011.

461 S. M. Alhassan, S. Qutubuddin and D. A. Schiraldi, *Langmuir*, 2012, **28**, 4009–4015.

462 J. Yoo, S. B. Lee, C. K. Lee, S. W. Hwang, C. Kim, T. Fujigaya, N. Nakashima and J. K. Shim, *Nanoscale*, 2014, **6**, 10824.

463 D. K. Chouhan, A. Kumar, S. K. Rath, S. Kumar, P. S. Alegaonkar, G. Harikrishnan and T. Umasankar Patro, *J. Polym. Res.*, 2018, **25**, 60.

464 T. U. Patro and H. D. Wagner, *J. Polym. Sci. Part B Polym. Phys.*, 2016, **54**, 2377–2387.

465 S. Ye, Z. Yang, J. Xu, Z. Shang and J. Xie, *R. Soc. Open Sci.*, 2019, **6**, 181439.

466 I. A. Ramphal and M. E. Hagerman, *Langmuir*, 2015, **31**, 1505–1515.

467 H. Z. Cummins, *J. Non. Cryst. Solids*, 2007, **353**, 3891–3905.

468 K. Suman and Y. M. Joshi, *Langmuir*, 2018, **34**, 13079–13103.

469 E. Bourgeat-Lami, N. Sheibat-Othman and A. M. Dos Santos, in *RSC Nanoscience and Nanotechnology*, ed. Vikas Mittal, Royal Society of Chemistry, 2010, pp. 269–311.

470 F. Roquerol, J. Rouquerol and K. Sing, *Adsorption by Powders and Porous Solids: Principles, Methodology and Applications*, Academic Press, 1st edn., 1999.

471 K. A. Cychosz and M. Thommes, *Engineering*, 2018, **4**, 559–566.

472 Z. Yang, H. Peng, W. Wang and T. Liu, *J. Appl. Polym. Sci.*, 2010, **116**, 2658–2667.

473 S. Zhang, H. Wang, J. Liu and C. Bao, *Mater. Lett.*, 2020, **261**, 127098.

474 T. Nicolai and S. Cocard, *J. Colloid Interface Sci.*, 2001, **244**, 51–57.

475 T. B. Becher, C. B. Braga, D. L. Bertuzzi, M. D. Ramos, A. Hassan, F. N. Crespilho and C. Ornelas, *Soft Matter*, 2019, **15**, 1278–1289.

476 J. H. Rouse, S. T. White and G. S. Ferguson, *Scanning*, 2004, **26**, 131–134.

477 A. de M. F. Guimarães, V. S. T. Ciminelli and W. L. Vasconcelos, *Mater. Res.*, 2007, **10**, 37–41.

478 Y. M. Joshi, *J. Chem. Phys.*, 2007, **127**, 081102.

479 S. Jatav and Y. M. Joshi, *Langmuir*, 2017, **33**, 2370–2377.

480 U. Hofmann, A. Frenzel and E. Csalán, *Justus Liebigs Ann. Chem.*, 1934, **510**, 1–41.

481 S. Ghosh, S. K. Goswami and L. J. Mathias, *J. Mater. Chem. A*, 2013, **1**, 6073.

482 D. Meroni, L. Lo Presti, G. Di Liberto, M. Ceotto, R. G. Acres, K. C. Prince, R. Bellani, G. Soliveri and S. Ardizzone, *J. Phys. Chem. C*, 2017, **121**, 430–440.

483 L. D. White and C. P. Tripp, *J. Colloid Interface Sci.*, 2000, **232**, 400–407.

484 E. Valeur and M. Bradley, *Chem. Soc. Rev.*, 2009, **38**, 606–631.

485 L. M. Daniel, R. L. Frost and H. Y. Zhu, *J. Colloid Interface Sci.*, 2008, **321**, 302–309.

486 A. Issa and A. Luyt, *Polymers (Basel).*, 2019, **11**, 537.

487 A.-P. S. Mandair, P. J. Michael and W. R. McWhinnie, *Polyhedron*, 1990, **9**, 517–525.

488 N. N. Herrera, J. M. Letoffe, J. L. Putaux, L. David and E. Bourgeat-Lami, *Langmuir*, 2004, **20**, 1564–1571.

489 M. Asgari and U. Sundararaj, *Appl. Clay Sci.*, 2018, **153**, 228–238.

490 K.-P. Hoh, H. Ishida and J. L. Koenig, *Polym. Compos.*, 1990, **11**, 121–125.

491 N. N. Herrera, J. Letoffe, J. Reymond and E. Bourgeat-lami, 2005, 863–871.

492 K. A. Carrado, L. Xu, R. Csencsits and J. V. Muntean, *Chem. Mater.*, 2001, **13**, 3766–3773.

493 S. Borsacchi, M. Geppi, L. Ricci, G. Ruggeri and C. A. Veracini, *Langmuir*, 2007, **23**, 3953–3960.

494 F. Xie, F. Yan, M. Chen and M. Zhang, *RSC Adv.*, 2014, **4**, 29502–29508.

495 W. Gao, L. B. Alemany, L. Ci and P. M. Ajayan, *Nat. Chem.*, 2009, **1**, 403–408.

496 I. S. Protsak, Y. M. Morozov, W. Dong, Z. Le, D. Zhang and I. M. Henderson, *Nanoscale Res. Lett.*, 2019, **14**, 160.

497 L. A. Straasø, Q. Saleem and M. R. Hansen, in *Annual Reports on NMR Spectroscopy*, Elsevier Ltd., 1st edn., 2016, vol. 88, pp. 307–383.

498 I. Kuźniarska-Biernacka, A. R. Silva, A. P. Carvalho, J. Pires and C. Freire, *Langmuir*, 2005, **21**, 10825–10834.

499 D. Briggs and G. Beamson, *High Resolution XPS of Organic Polymers: The Scienta ESCA300 Database*, Wiley & Sons, Chichester, 1992.

500 P. Das, A. R. Silva, A. P. Carvalho, J. Pires and C. Freire, *J. Mater. Sci.*, 2009, **44**, 2865–2875.

501 K. N. Wood and G. Teeter, *ACS Appl. Energy Mater.*, 2018, **1**, 4493–4504.

502 N.-Y. Cui, C. Liu and W. Yang, *Surf. Interface Anal.*, 2011, **43**, 1082–1088.

503, DOI:10.18434/T4T88K.

504 B. V. Rami Reddy, R. Ravikumar, C. Nithya and S. Gopukumar, *J. Mater. Chem. A*, 2015, **3**, 18059–18063.

505 T. R. Gengenbach, R. C. Chatelier and H. J. Griesser, *Surf. Interface Anal.*, 1996, **24**, 611–619.

506 C. Rodríguez-González, H. E. Cid-Luna, P. Salas and V. M. Castaño, *J. Nanomater.*, , DOI:10.1155/2014/940903.

507 T. L. Clare and N. A. Swartz, in *Intelligent Coatings for Corrosion Control*, Elsevier, 2015, pp. 641–671.

508 G. R. Mahdavinia, S. Ettehadi, M. Amini and M. Sabzi, *RSC Adv.*, 2015, **5**, 44516–44523.

509 H. Sanaeepur, A. Kargari and B. Nasernejad, *RSC Adv.*, 2014, **4**, 63966–63976.

510 N. Agasti and N. K. Kaushik, *Am. J. Nanomater.*, 2014, **2**, 4–7.

511 L. H. Jones and E. Mclaren, *J. Chem. Phys.*, 1954, **22**, 1796–1800.

512 B. Smith, *Infrared Spectral Interpretation*, CRC Press, 1st edn., 2018.

513 M. P. Landoll and M. T. Holtzapple, *Biomass and Bioenergy*, 2012, **45**, 195–202.

514 S. M. Salili, A. Ataie, M. R. Barati and Z. Sadighi, *Mater. Charact.*, 2015, **106**, 78–85.

515 S. S. Das, Neelam, K. Hussain, S. Singh, A. Hussain, A. Faruk and M. Tebyetekerwa, *Curr. Pharm. Des.*, 2019, **25**, 424–443.

516 Z. Xue, Y. Cao, N. Liu, L. Feng and L. Jiang, *J. Mater. Chem. A*, 2014, 2, 2445–2460.

517 D. Li and Z. Guo, *J. Colloid Interface Sci.*, 2017, **503**, 124–130.

518 Y. Wang and X. Gong, *J. Mater. Chem. A*, 2017, **5**, 3759–3773.

519 A. A. Al-Majed, A. R. Adebayo and M. E. Hossain, *J. Environ. Manage.*, 2012, **113**, 213–227.

520 X. Zhu, W. Tu, K. H. Wee and R. Bai, *J. Memb. Sci.*, 2014, **466**, 36–44.

521 M. Antonietti, S. Henke and A. Thünemann, *Adv. Mater.*, 1996, **8**, 41–45.

522 S. J. Hutton, J. M. Crowther and J. P. S. Badyal, *Chem. Mater.*, 2000, **12**, 2282–2286.

523 R. A. Lampitt, J. M. Crowther and J. P. S. Badyal, *J. Phys. Chem. B*, 2000, **104**, 10329–10331.

524 J. Yang, L. Yin, H. Tang, H. Song, X. Gao, K. Liang and C. Li, *Chem. Eng. J.*, 2015, **268**, 245–250.

525 J. Yang, Z. Zhang, X. Xu, X. Zhu, X. Men and X. Zhou, *J. Mater. Chem.*, 2012, **22**,

2834.

526 H. Yoon, S.-H. Na, J.-Y. Choi, S. S. Latthe, M. T. Swihart, S. S. Al-Deyab and S. S. Yoon, *Langmuir*, 2014, **30**, 11761–11769.

527 P. S. Brown and B. Bhushan, *Sci. Rep.*, 2015, **5**, 8701.

528 P. S. Brown and B. Bhushan, *Sci. Rep.*, 2015, **5**, 14030.

529 X. Du, X. Li and J. He, *ACS Appl. Mater. Interfaces*, 2010, **2**, 2365–2372.

530 R. N. Wenzel, *Ind. Eng. Chem.*, 1936, **28**, 988–994.

531 H. Sawada, Y. Ikematsu, T. Kawase and Y. Hayakawa, *Langmuir*, 1996, **12**, 3529–3530.

532 J. A. Howarter and J. P. Youngblood, *Adv. Mater.*, 2007, **19**, 3838–3843.

533 J. A. Howarter and J. P. Youngblood, *Macromol. Rapid Commun.*, 2008, **29**, 455–466.

534 T. Saito, Y. Tsushima and H. Sawada, *Colloid Polym. Sci.*, 2015, **293**, 65–73.

535 A. Okado, T. Nikaido, M. Ikeda, K. Okada, J. Yamauchi, R. M. Foxton, H. Sawada, J. Tagami and K. Matin, *Dent. Mater. J.*, 2008, **27**, 565–572.

536 A. B. D. Cassie and S. Baxter, *Trans. Faraday Soc.*, 1944, **40**, 546.

537 M. Liu, S. Wang, Z. Wei, Y. Song and L. Jiang, *Adv. Mater.*, 2009, **21**, 665–669.

538 L. Li, Y. Wang, C. Gallaschun, T. Risch and J. Sun, *J. Mater. Chem.*, 2012, **22**, 16719.

539 Y. Wang, J. Knapp, A. Legere, J. Raney and L. Li, *RSC Adv.*, 2015, **5**, 30570–30576.

540 Y. Wang, J. Sun and L. Li, *Langmuir*, 2012, **28**, 6151–6156.

541 H. Dautzenberg, E. Görnitz and W. Jaeger, *Macromol. Chem. Phys.*, 1998, **199**, 1561–1571.

542 M. J. Allen, V. C. Tung and R. B. Kaner, *Chem. Rev.*, 2010, **110**, 132–145.

543 D. Chen, H. Feng and J. Li, *Chem. Rev.*, 2012, **112**, 6027–6053.

544 B. Kim, H. Park and W. M. Sigmund, *Langmuir*, 2003, **19**, 2525–2527.

545 B. Kim and W. M. Sigmund, *Langmuir*, 2003, **19**, 4848–4851.

546 J. H. Rouse and P. T. Lillehei, *Nano Lett.*, 2003, **3**, 59–62.

547 D. Yang, J. Rochette and E. Sacher, 2005, **62**, 4481–4484.

548 S. Wang, D. Yu, L. Dai, D. W. Chang and J.-B. Baek, *ACS Nano*, 2011, **5**, 6202–6209.

549 S. N. Lim, W. Ahn, S.-H. Yeon and S. Bin Park, *Chem. - An Asian J.*, 2014, **9**, 2946–2952.

550 C. Zhu, P. Wang, L. Wang, L. Han and S. Dong, *Nanoscale*, 2011, **3**, 4376.

551 Y. Xiang, M. K. Banks, R. Wu, W. Xu and S. Chen, *Mater. Chem. Phys.*, 2018, **220**, 58–65.

552 S. Yang, X. Feng, S. Ivanovici and K. Müllen, *Angew. Chemie*, 2010, **122**, 8586–8589.

553 A. Lerf, H. He, M. Forster and J. Klinowski, *J. Phys. Chem. B*, 1998, **102**, 4477–4482.

554 T. Szabó, O. Berkesi, P. Forgó, K. Josepovits, Y. Sanakis, D. Petridis and I. Dékány, *Chem. Mater.*, 2006, **18**, 2740–2749.

555 D. A. Allison, G. Johansson, C. J. Allan, U. Gelius, H. Siegbahn, J. Allison and K. Siegbahn, *J. Electron Spectros. Relat. Phenomena*, 1972, **1**, 269–283.

556 S. Wang, X. Wang and S. P. Jiang, *Phys. Chem. Chem. Phys.*, 2011, **13**, 6883.

557 A. Marinoiu, M. Raceanu, M. Andrulevicius, A. Tamuleviciene, T. Tamulevicius, S. Nica, D. Bala and M. Varlam, *Arab. J. Chem.*, 2020, **13**, 3585–3600.

558 L. Dong, X. Zhang, S. Ren, T. Lei, X. Sun, Y. Qi and Q. Wu, *RSC Adv.*, 2016, **6**, 6436–6442.

559 I. Moeez, H.-D. Lim, J.-H. Park, H.-G. Jung and K. Y. Chung, *ACS Energy Lett.*, 2019, **4**, 2060–2068.

560 M. Antonietti, C. Burger, J. Conrad and A. Kaul, *Macromol. Symp.*, 1996, **106**, 1–8.

561 P. M. Macdonald and A. Tang, *Langmuir*, 1997, **13**, 2259–2265.

562 M. Antonietti, J. Conrad and A. Thuenemann, *Macromolecules*, 1994, **27**, 6007–6011.

563 J. Drelich, J. L. Wilbur, J. D. Miller and G. M. Whitesides, *Langmuir*, 1996, **12**, 1913–1922.

564 C. W. Extrand and Y. Kumagai, *J. Colloid Interface Sci.*, 1997, **191**, 378–383.

565 J. Yong, F. Chen, Q. Yang, J. Huo and X. Hou, *Chem. Soc. Rev.*, 2017, **46**, 4168–4217.

566 J. B. Boreyko, G. Polizos, P. G. Datskos, S. A. Sarles and C. P. Collier, *Proc. Natl. Acad. Sci.*, 2014, **111**, 7588–7593.

567 J. T. Edwards, in *55th AIAA Aerospace Sciences Meeting*, American Institute of Aeronautics and Astronautics, Reston, Virginia, 2017, pp. 1–58.

568 H. J. Butt, I. V Roisman, M. Brinkmann, P. Papadopoulos, D. Vollmer and C. Semprebon, *Curr. Opin. Colloid Interface Sci.*, 2014, 19, 343–354.

569 F. Sultanov, C. Daulbaev, B. Bakbolat, O. Daulbaev and Z. Mansurova, *J. Eng. Phys. Thermophys.*, 2020, **93**, 409–415.

570 F. R. Sultanov, C. Daulbayev, B. Bakbolat and Z. A. Mansurov, *Eurasian Chem. J.*, 2018, **20**, 195.

571 S. Li, S. Yang, X. Zhu, X. Jiang and X. Z. Kong, *Cellulose*, 2019, **26**, 6813–6823.

572 S. Lowell and J. E. Shields, *Powder Surface Area and Porosity*, Springer Netherlands, Dordrecht, 3rd edn., 1991.

573 W. Sun, W. Liu and Y. Hu, *J. Cent. South Univ. Technol.*, 2008, **15**, 373–377.

574 W. Chen, X. Zhang, M. Mamadiev and Z. Wang, *RSC Adv.*, 2017, **7**, 927–938.

575 F. Li, Z. Wang, S. Huang, Y. Pan and X. Zhao, *Adv. Funct. Mater.*, 2018, **28**, 1706867.

576 P. S. Brown, O. D. L. A. Atkinson and J. P. S. Badyal, *ACS Appl. Mater. Interfaces*, 2014, **6**, 7504–7511.

577 J. Li, L. Yang, H. Liu, G. Li, R. Li, Y. Cao and H. Zeng, *ACS Appl. Mater. Interfaces*,

2020, **12**, 45266–45273.

578 Y. Pan, S. Huang, F. Li, X. Zhao and W. Wang, *J. Mater. Chem. A*, 2018, **6**, 15057–15063.

579 C.-T. Hsieh, J.-M. Chen, R.-R. Kuo, T.-S. Lin and C.-F. Wu, *Appl. Surf. Sci.*, 2005, **240**, 318–326.

580 J. S. J. Hargreaves, *Catal. Struct. React.*, 2016, **2**, 1–5.

581 J. Yang, Z. Zhang, X. Men, X. Xu and X. Zhu, *New J. Chem.*, 2011, **35**, 576–580.

582 A. Steele, I. Bayer and E. Loth, *Nano Lett.*, 2009, **9**, 501–505.

583 B. Li, J. Zhang, Z. Gao and Q. Wei, *J. Mater. Chem. A*, 2016, **4**, 953–960.